

**APPLICATION OF FT-IR SPECTROSCOPY TO STUDY HYDROCARBON REACTION CHEMISTRY**

Peter R. Solomon, David G. Hamblen, Robert M. Carangelo,  
James R. Markham and Michele R. Chaffee

Advanced Fuel Research, Inc., 87 Church Street, East Hartford, CT 06108, USA

Fourier Transform Infrared Spectroscopy (FT-IR) is one of the most versatile analytical techniques available for the study of fossil fuel structure and reaction chemistry. Among its advantages are: (i) its ability to study feedstocks and reaction products as solids, liquids and gases, since almost all have characteristic absorptions in the infrared; (ii) its sensitivity, allowing the study of highly absorbing materials such as coal and char and the use of difficult techniques such as photoacoustic or diffuse reflectance spectroscopy; (iii) its speed (instruments commercially available can obtain a complete spectrum every 20 milliseconds) allowing the possibility of following chemical reactions on-line; (iv) its inherent rejection of stray radiation, allowing transmission measurements at elevated temperatures to be made in-situ; (v) its ability to measure emission spectra to determine temperature as well as chemical changes of reactants at elevated temperature.

Because of these advantages, FT-IR spectroscopy has achieved increasing use in fuel science. This paper will review some of its applications. Recent progress has been made in the use of FT-IR for the quantitative determination of hydrogen functional groups in solid hydrocarbons. Developments in this area are important since uncertainties in the hydrogen distribution have hindered investigations of coal structure. The paper will discuss the present convergence being obtained in the determination of aliphatic hydrogen and the uncertainties remaining in the determination of aromatic hydrogen. A second area to be considered will be the application of the functional group determination to the study of coal pyrolysis. The paper will consider the changes in the functional group composition of coal during primary pyrolysis and its relationship to the pyrolysis products which are formed. Finally, recently developed methods employing both emission and transmission spectroscopy will be considered to monitor, in-situ, the coal particle temperature and chemical changes which occur during pyrolysis.

**DETERMINATION OF AROMATIC AND ALIPHATIC HYDROGEN IN COAL**

While several techniques are available for obtaining infrared spectra of coal, only the KBr pellet technique has been pursued extensively for quantitative analysis. Methods for quantitative preparation of samples have been described in a number of publications (1-7) and it appears that with a representative sample of coal and care in sample preparation, spectra can be repeated with less than 5% variation. Typical KBr pellet spectra for two bituminous coals and a lignite are illustrated in Fig. 1. They have peaks due to their functional groups and mineral components which are identified in the figure. In general, all coals have these absorption bands and the major variation with rank is in their relative magnitude. There are three features of the KBr spectra whose interpretation has been controversial. The first is the large peak at 1600 wavenumbers, which evidence now suggests is an aromatic ring stretch whose intensity is greatly enhanced by the presence of hydroxyl groups on the ring and nitrogen in the ring (2-4,6). The second is the sloping baseline which has generally been attributed to scattering (rather than absorption) of the transmitted radiation by the particles of coal in the KBr pellet. A straight line correction has sometimes been used to obtain a spectrum more "representative" of the absorption. Figure 2 compares a baseline corrected spectrum of coal (a) in Fig. 1. to a spectrum of the same coal obtained by photoacoustic absorption spectroscopy (PAS) (8,9). The PAS technique which is sensitive only to the absorption of energy does not have a sloping baseline and is quite similar in appearance to the baseline-corrected KBr pellet spectrum. The baseline correction appears to be accurate for coals and chars

up to about 90 percent carbon. At high carbon concentrations, a broad slopping absorption is also present. Comparison of the two spectra suggest some distortion of the aliphatic band in the KBr pellet spectrum may occur due to the Christiansen effect. This distortion could influence measurements of the aromatic hydrogen if the 3100 wavenumber band is used. PAS spectra also appear to exaggerate the mineral peaks. A third controversial feature is the hydroxyl band. Is it really as broad as it appears (due to hydrogen bonding) and can the band associated with water incorporated during the pellet preparation be eliminated by drying the pellet? Results of Ref. 1 suggest that drying removes almost all of the water and good results have been obtained using the optical density at 3200 wavenumbers to determine the hydroxyl content. Comparison of the dry KBr pellet spectrum with the PAS spectrum in Fig. 2. suggests that the broad absorption peak of the hydroxyl groups in the dried pellet is real.

To obtain aromatic and aliphatic hydrogen concentrations,  $H(ar)$  and  $H(al)$ , it is necessary to integrate the areas  $A(ar)$  and  $A(al)$  under the appropriate peaks (spectra are normalized to 1 mg per square cm) and divide by appropriate integral absorptivities  $a(ar)$  and  $a(al)$  (in abs. units  $\times$  wavenumbers/mg/cm<sup>2</sup>) to relate the areas to the hydrogen concentrations. The former task has been automated by employing a synthesis routine which uses a set of preselected peaks whose position and width are held fixed and whose amplitude is varied to reproduce the experimental spectrum (2-4). The technique has the advantage that integrated areas will be obtained in a consistent manner for all samples. Excellent fits have been obtained for hundreds of coal samples using one set of 45 Gaussian peaks (2). To obtain the absorptivities for coal samples, a method was derived (2-4) in which  $H(al) = A(al)/a(al)$  and  $H(ar) = A(ar)/a(ar)$  was equated to the total hydrogen,  $H$ , minus the hydroxyl hydrogen,  $H(OH)$  and rearranged to yield the following equation,

$$\frac{1}{a(al)} \left[ \frac{A(al)}{H - H(OH)} \right] = 1 - \frac{1}{a(ar)} \left[ \frac{A(ar)}{H - H(OH)} \right] \quad (1)$$

If the absorptivities are independent of coal composition, than the two unknowns,  $a(ar)$  and  $a(al)$  can be determined from  $A(al)$ ,  $A(ar)$ ,  $H$  and  $H(OH)$  for two samples.  $H(OH)$  can be determined chemically or by FT-IR (1,5).  $A(al)$  is usually obtained from the set of peaks near 2900 wavenumbers which are strong and do not have any interfering peaks nearby.  $A(ar)$  can be obtained from the peaks near 800 wavenumbers which are strong but have interference from mineral peaks (which must be subtracted) and long methylene chains (which are weak and can be subtracted) or from the peak near 3100 wavenumbers which are weak and have interference from the aliphatic and hydroxyl bands. The problem of determining the area for the 3100 wavenumber peak is substantial for low rank coals as will be discussed below.

In practice, coals do not have different enough ratios of  $H(al)$  and  $H(ar)$  to determine accurately the absorptivities from two samples, so large numbers of coals are used to define a straight line by plotting the two terms in brackets. But, even this method is not accurate because the coals tend to be tightly clustered. To alleviate this problem, coal derived chars and tars, which have related chemical structures were also included to provide a wider range of aliphatic to aromatic ratios (2-4). This will work only if the absorptivities for these additional samples are the same as for coals. A set of chars produced by heating a bituminous coal at 30°C/sec to different final temperatures is illustrated in Fig. 3. As can be seen  $A(ar)/A(al)$  increases continuously with pyrolysis temperature. The chars produced above 600°C have little aliphatic hydrogen and thus provide an excellent sample for determining  $a(ar)$ . Using the 800 wavenumber region for  $A(ar)$ , the bracketed terms in Eq. 1 are plotted in Fig. 4 with some additional chars and tars from a Pittsburgh Seam coal of similar carbon content. The chars form a regular series along a straight line with intercepts at  $a(ar) = 684$  and  $a(al) = 744$ . The results are in excellent agreement with previously derived values of 686 and 746 for all bituminous coals, chars and tars (2). Model compounds were also examined to provide guidance in the possible absorptivity values (2-4). The  $a(ar)$  value is 11% lower than the average value of  $a(ar) = 768$  for 25 model compounds containing C and H only. The same model compounds give an average value of

$a(ar) = 220$  for the 3100 wavenumber band. This corresponds to  $\epsilon(ar) = .60$  in good agreement with the value derived in Refs. 7 and 10.

Using these absorptivities, values of  $H(ar)$  and  $H(al)$  have been derived for a set of bituminous coals from the Exxon premium sample collection. The results are plotted as a function of rank in Fig. 5a. The values of  $H(ar)$  lie in a narrow band which shows a smooth variation with rank. Values of  $H(al)$  are more scattered. The scatter in the data appear to reflect real variations in  $H(al)$ , since  $H(al) + H(ar)$  is in good agreement with  $H - H(OH)$  as shown in Fig. 6a. The data form a band with a random variation of  $\pm 10\%$ . The slight slope in Fig. 6a suggests a variation of the absorptivity with carbon concentration.

The problem of obtaining absorptivities using coals alone (i.e., defining a line through data points clustered in a small region) was recently discussed extensively by researchers at Penn State University (7,10). They used an error minimization procedure (equivalent to the graphical method discussed above) to evaluate the absorptivities for a group of coals and lignites. The 3100 wavenumber region was chosen for  $H(ar)$  instead of the 800 wavenumber region. The same method was used on pyridine extracts (7) and it was determined that the absorptivities match reasonably with absorptivities derived from proton nmr. The absorptivity value derived for  $a(al)$  was 665, 11% lower than our value of 745. Note the conversion factor  $\epsilon(al) = .20$  in Ref. (10) is the reciprocal of  $a(al)$  multiplied by 100 (weight fraction to weight %) and by 1.33 (mg per pellet to  $mg/cm^2$ ). The results are shown in Fig. 5b. The  $H(al)$  values are about 10% higher than ours and are in agreement with the differences in  $a(al)$ . The 10% extra hydrogen in the  $H(al)$  values must be made up in the  $H(ar)$  values which are up to 30% to 50% lower than our values at low carbon concentration. A comparison of  $H(al) + H(ar)$  to  $H - H(OH)$  is made in Fig. 6b. The random variation is similar to our results ( $\pm 12\%$  vs.  $\pm 10\%$ ) but the dependence on carbon concentration is greater. While Reisser et al. (10) have attributed all the discrepancies between  $H(al) + H(ar)$  derived by FT-IR and  $H - H(OH)$  derived by elemental analysis and FT-IR to random errors in KBr pellet sample preparation, some of the variation is clearly a systematic rank dependence caused by variations in the absorptivities with rank. This variation was observed in our earlier work and we derived separate absorptivity values for lignites and subbituminous coals (2). The rank variation in the absorptivities using the 3100 wavenumber region appear to be greater than what we have obtained using the 800 wavenumber region. This observation will be discussed below. We believe that the values of  $H(ar)$  reported originally (3) were too high because of the influence of the rank variation when using rank independent absorptivities.

Considering the above results, how accurate is the FT-IR method for determining hydrogen functional group concentrations? Both sets of data derived by FT-IR (Figs. 5a and 5b) produce similar values of  $H(al)$ . Values of  $H(ar)$  are in reasonably narrow bands which agree above 85% carbon. The method in its current state of development (using rank independent absorptivities) can, therefore, determine  $H(al)$  to  $\pm 10\%$  and relative trends for  $H(ar)$ . The FT-IR technique appears capable of providing accurate absolute values for the hydrogen functional group distribution provided the proper absorptivity can be determined for  $H(ar)$  below 85% carbon. As guidance in determining the proper absorptivities, data for  $H(ar)$  in coal derived by dipolar dephasing (11) are presented in Fig. 5c and data for pyridine extracts (12,13), vacuum distillates (14) and coals (13) obtained by proton nmr and IR are presented in Fig. 5d. Among these data for  $H(ar)$  the dipolar dephasing data (Fig. 5c) are the highest. The data from this work (Fig. 5a) are similar to the data on coal like materials (Fig. 5d) and are within the range of the dipolar dephasing data. The data of Reisser et al. (10), (Fig. 5b) are the lowest and appear outside the range of the dipolar dephasing data.

Another comparison is made in Table I using the average values determined for the ratios of  $H(ar)$  to  $H(al)$  in the range of 80-85% carbon (10-16). The value of 0.35, determined by Reisser et al., (10) is 24% lower than the cumulative average of 0.46. The value of 0.52 from the present results is 13% too high. The value of 0.2 originally determined by Brown (15) is too low and the value of 0.70 determined by

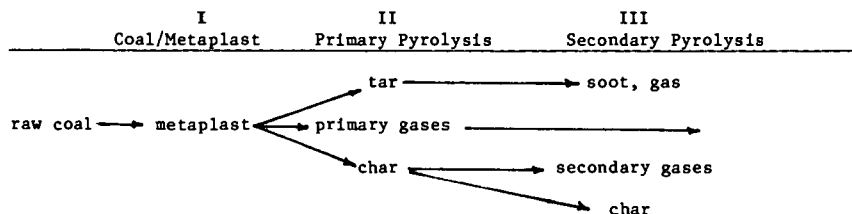
Wilson et al. (11) using dipolar dephasing appears too high.

Some of the discrepancy in the FT-IR values may be due to the choice by the Penn State group (7,10) of the 3100 wavenumber band for H(ar). This band appears to shrink more rapidly with decreasing rank than do the 800 wavenumber bands. A comparison is made in Fig. 7 between these two regions for a lignite, its tar and its char. These samples are low in mineral content. The spectra are presented without baseline or mineral corrections. While the coal shows a distinct band near 800 wavenumbers it is very difficult to distinguish a band at 3100 wavenumbers. The tar and char produced in pyrolysis show large peaks at 800 wavenumbers but only the char has a clearly defined peak at 3100 wavenumbers. The amplitude at 3100 wavenumbers is either weakened or partially hidden by the presence of the hydroxyl band. The ratio of areas of the 3100 to 800 wavenumber bands for the Exxon coals are plotted in Fig. 8a. The ratio goes to zero with increasing rank. A similar effect is observed for model compounds in Fig. 8b. The stretch region appears more sensitive to the oxygen concentration than the wag. For example, a(ar) goes from 220 (25 model compounds without oxygen) to an average value of 122 (8 model compounds with an average of 11% oxygen). For the same model compounds a(ar) for the 800 wavenumber region goes from 768 (no oxygen) to 889 (with oxygen). While this ratio depends on the way the bands are fit (i.e. integration limits and baseline) it is very difficult to avoid very small areas in the 3100 wavenumber region for low rank coals.

The decreasing 3100 wavenumber band intensities for low rank coals would explain the low values of H(ar) in Fig. 5b and the slope in Fig. 6b. Resolution of this issue and improved accuracy in the technique requires the following advances: i) an agreed upon procedure for obtaining peak areas, ii) use of rank dependent absorptivities, iii) a premium set of reproducible samples of coals, vacuum distillates and pyridine extracts for round robin tests at different laboratories using FT-IR, proton nmr and  $C^{13}$  nmr with dipolar dephasing. Even with its limitations, the present technique appears to be the best routine method to obtain hydrogen functional group concentrations.

#### THE VARIATIONS IN FUNCTIONAL GROUP COMPOSITION DURING COAL PYROLYSIS

An application of the analysis method described above was made in the study of coal pyrolysis where the evolution of pyrolysis products may be related to the chemical changes occurring in the coal as determined by FT-IR spectroscopy. Pyrolysis has been described in terms of the following stages:



During, stage I the coal may undergo some bond breaking reactions and reduction of hydrogen bonding which may lead to melting. Some light species which exist as guest molecules or are formed by the breaking of very weak bonds are released. During stage II, further bond breaking occurs leading to evolution of tar and gases and the formation of char. During stage III the products can continue to react. The char can evolve secondary gases, mainly CO and H<sub>2</sub> while undergoing ring condensations. The tars can crack to form soot, coke and gases and the gases can crack to form lighter gases and soot.

To demonstrate the relationship between the "extent of pyrolysis" and the functional group composition, we consider an experiment in which samples of a bituminous coal were heated at a constant rate of 30°C/min starting at 150°C and ending at a series of

temperatures between 350 and 950°C. Slow heating is useful in separating the stages of pyrolysis, which can overlap in rapid heating experiments. Figure 3 shows the infrared spectra obtained for the product chars (at several temperatures) by quantitative FT-IR spectroscopy. There are substantial changes in the spectra as the peak pyrolysis temperature is increased. To relate these changes to the stages of pyrolysis, the functional group compositions from these spectra are compared in Fig. 9 to the weight loss and evolution of tar and gases measured during the experiment.

Substantial changes occur during the primary pyrolysis, stage II. Figure 9a compares the weight loss with the rate of tar evolution. The maximum rate of weight loss at 470°C compares with the maximum rate of tar evolution. Figure 9b shows the rate of aliphatic gas evolution compared to the loss of aliphatic hydrogen, H(al), in the char. There is also an increase in H(ar), Fig. 9e, which occurs as the tar picks up hydrogen from hydroaromatic rings, converting them to aromatic sites. The loss of tar, aliphatic gases and H(ar) are closely coupled events which dominate the primary pyrolysis. The loss of H(al) indicates the end of stage II. The loss of H(al) also signals the loss of plasticity and swelling as described in (17).

At 30°C/min heating rate, secondary pyrolysis, stage III, began above 550°C. Figure 9c compares the evolution of methane with the concentration of methyl groups in the char. The methyl group concentration first increases during primary pyrolysis (due to bond breaking and stabilization) and then decreases as methane is formed. The events occurring during the later parts of stage III include the elimination of ether linkages coupled with the evolution of CO (Fig. 9d) and the elimination of aromatic hydrogen, H(ar), (Fig. 9e) which occurs during ring condensation coupled with evolution of hydrogen gas (not measured in this experiment). Since ring condensations also eliminate active sites for oxygen attack, H(al) should be a good parameter to correlate with intrinsic char reactivity. Figure 9f shows the evolution of CO<sub>2</sub> and H<sub>2</sub>O. The evolution of water appears to correlate with the increase in the ether oxygen suggesting that two hydroxyls may combine to form a water and an ether link.

For these experiments, the changes in the functional group composition as determined by FT-IR provide a good chemical description of the pyrolysis stages which are in turn correlated with the evolved products. It has been demonstrated that this relationship between the pyrolysis events and the functional group composition is quite general, being independent of coal rank and temperature (3,17-20). The sequence of functional group changes is the same in high heating rate experiments as for the slow heating case and corresponds in the same way to the pyrolysis events. FT-IR spectra provide a good method to determine the "extent of pyrolysis".

#### IN-SITU MONITORING OF COAL TEMPERATURE AND SPECTRAL EMITTANCE

As a final example of the FT-IR's versatility, we consider its application in the on-line, in-situ monitoring of coal conversion. In this application the sample volume is in the reacting stream rather than in a KBr pellet. Both emission and transmission measurements are made to provide data on the coal's temperature and spectral emittance (which is related to its chemical composition). As described in a previous publication (21), the transmittance measurement is used to determine the total emitting surface of the coal particles so that a normalized emission, (emission/(1-transmittance)) can be compared in both shape and amplitude to a theoretical black-body. In the work described below, the coal flow rate was monitored to insure that both measurements be made under the same conditions. Also, the emission from several phases (tar in particular) and diffraction effect required additional care in the computation of the normalized emission. Compared to other techniques for measuring temperature the FT-IR normalized emission measurement has the following advantages: 1) A complete spectrum is obtained, not just two or three colors; 2) Measurements are made in the infrared where the emission is strongest and where measurements of emission and optical properties are relevant to practical conversion processes; 3) Measurements are possible with mixed phase (particles, soot and gas); 4) For grey-bodies, the measurement of normalized emittance allows the use of the spectral shape to obtain temperature and the

amplitude, to obtain emissivity; 5) Measurements are fast. A complete spectrum can be obtained in 20 milliseconds using a commercial FT-IR. With this speed, tomographic techniques to obtain point measurements may be practical; 6) Determination of temperature distributions are possible; 7) The technique is applicable to measurements in process equipment.

The spectra which we consider were obtained for pyrolysis measurements made in a tube reactor described in another paper presented at this meeting (22) and combustion measurements made in an entrained flow reactor (17). Both reactors allow optical access to the high temperature products. For these experiments, the FT-IR measurement can provide a direct measurement of the coal particle temperature. The technique has been validated by making measurements under conditions where the particle temperatures are known. A simple case is illustrated in Fig. 10a. For this case, sufficient time was allowed for the coal to reach the asymptotic tube temperature of 935°C (1208 K) and for primary pyrolysis to have occurred. The normalized emission spectrum is in good agreement with a theoretical black-body at 1190 K with an amplitude corresponding to an emissivity of 0.9. The measured temperature is in excellent agreement with the tube temperature, as a 10°C drop in temperature is expected between the end of the tube, and the measuring point at 0.75 cm below the end.

The measurement of temperature before and during pyrolysis is not as simple, since for the size of coal particles used here, only specific bands (corresponding to the absorbing bands in coal) provide sufficient absorbance for the spectral emittance to reach 0.9. Then, only these regions can be used to compare to the black-body. Examples for a 200 x 325 mesh fraction of a Montana Lignite injected at 3 grams/min into the tube reactor at 800°C (1173 K) with a cold helium velocity of 4 m/sec are presented in Figs. 10b and 10c. The same coal with a cold velocity of 28 m/sec is shown in Fig. 10d. The spectrum is noisier due to the lower density of coal at the higher velocity, but has a shape similar to Fig. 10b where the coal is at a comparable temperature. The spectra are decidedly non-black or non-grey. Measurements show that the particle's emissivity is size, rank and temperature dependent. The result can be understood by remembering that a particle's emittance is related to its absorbance. Only the region between 1000 and 1600 wavenumbers has sufficient absorbance to fully attenuate the incident light over the particle thickness. It is only in this region that the normalized emission can be compared to the black-body. The aliphatic and hydroxyl bands are questionable.

Figures 10b to 10d contain the best fit grey-body curve ( $\epsilon = 0.9$ ) in the 1000 to 1600 wavenumber region and a grey-body curve ( $\epsilon = 0.9$ ) corresponding to the thermocouple measurement at the FT-IR focus. The grey-body curves are fit, excluding the region around 1500 wavenumbers where there is interference from water. The differences between the FT-IR and thermocouple measurements were 30°C, 40°C, and -13°C for measurements at 853 K, 953 K, and 913 K, respectively. The three cases are for transit distances of 10, 30 and 50 cm in the tube reactor. The spectra change with particle temperature and with changes in composition as ring condensation (which takes place during pyrolysis) makes the char more graphitic. The emission spectrum approaches a grey-body like Fig. 10a, only after sufficient time at elevated temperature (after primary pyrolysis is complete). The spectrum of Fig. 10c is almost a grey-body ( $\epsilon = 0.9$ ). The spectrum for the same coal at 935°C, Fig. 10a, is even closer. To determine the change under even more severe pyrolysis conditions, chars of the same coal were prepared at 1300°C and then injected into the tube reactor at 800°C. The spectrum in Fig. 10e shows a grey-body with an emissivity of  $\epsilon = 0.70$ , close to that expected for graphite.

The spectral emittance is also particle size dependent. Figure 10f shows a spectrum for a -400 mesh fraction of the same lignite. Except for the 1200 to 1600 wavenumber region, the spectral emittance is much lower than 0.9. As pyrolysis proceeded and particle mass was lost, the spectral emittance decreased even in the 1200 to 1600 region. These data show that raw coal of a size used for pulverized coal combustion does not have anywhere near the 90% absorption of radiation which is usually assumed in

calculating the particle heating rates. The average spectral emittance in the mid IR (where furnace radiation is a maximum) is about 0.5 for the 200 x 325 mesh fraction and 0.2 for the -400 mesh fraction.

Figure 10g shows that temperature was determined as low as 300°C. Figures 10h and 10i show temperature determinations during combustion. Under identical conditions, the lignite, at 1650 K is much more reactive than the bituminous coal at 1350 K. The particles spectral emittance have fallen to about 0.70 in agreement with the results of Fig. 10e.

#### ACKNOWLEDGMENT

The support of the Morgantown Energy Technology Center is gratefully acknowledged for the work on coal pyrolysis and on FT-IR emission/transmission spectroscopy. We wish to thank Dr. John McClelland of Ames Laboratory who obtained the photoacoustic spectrum in Fig. 2 and Richard Neavel, at the Exxon Corporation, for permitting the use of data on the Exxon samples.

#### REFERENCES

1. Solomon, P.R. and Carangelo, R.M., *Fuel*, **61**, 663, (1982).
2. Solomon, P.R., Hamblen, D.G., and Carangelo, R.M., "Applications of Fourier Transform IR Spectroscopy in Fuel Science", ACS Symposium Series **205**, pg. 77, (1982).
3. Solomon, P.R., *Advances in Chemistry Series*, Vol. **192**, "Coal Structure", 95, (1981).
4. Solomon, P.R. and Carangelo, R.M., "Characterization of Wyoming Subbituminous Coals and Liquefaction Products by Fourier Transform Infrared Spectrometry", EPRI Final Report, Project No. 1604-2, (1981).
5. Kuehn, D.W., Snyder R.W., Davis, A., and Painter, P.C., *Fuel*, **61**, 682, (1982).
6. Painter, P.C., Starsinic, M., Squires, E., and Davis, A.A., *Fuel*, **62**, 742, (1983).
7. Sobkowiak, M., Reisser, E., Given, R., and Painter, P., *Fuel*, **63**, 1245, (1984).
8. McClelland, J.F., *Anal. Chem.*, **55**, 89A, (1983).
9. Vidrine, D.W., *Fourier Transform Infrared Spectroscopy*, **3**, 125, (1982).
10. Reisser, B., Starsinic, M., Squires, E., Davis, A., and Painter, P.C., *Fuel*, **63**, 1253, (1984).
11. Wilson, M.A., Pugmire, R.J., Karas, J., Alemany, L.B., Woolfenden, W.R., Grant, D.M., and Given, P.H., *Analytical Chemistry*, **56**, 993, (1984).
12. Retcofsky, H.L., *Applied Spectroscopy*, **31**, 116, (1977).
13. Durie, R.A., Shewchuk, Y., and Sternhell, S., *Fuel*, **45**, 99, (1966).
14. Brown, J.K., Ladner, W.R., and Sheppard, N., *Fuel*, **39**, 79, (1960).
15. Brown, J.K., *J. Chem. Soc.*, 744, (1955).
16. Mazumdar, B.K., *Fuel*, **43**, 78, (1964).
17. Solomon, P.R., Hamblen, D.G., Carangelo, R.M., and Krause, J.L., 19th Symposium (Int.) on Combustion, The Combustion Institute, Pittsburgh, PA, pg. 1139 (1982).
18. Solomon, P.R. and Hamblen, D.G., *Finding Order in Coal Pyrolysis Kinetics*, Topical Report Submitted to the U.S. Department of Energy, under Contract #DE-AC21-FE05122 (1983).
19. Solomon, P.R. and Hamblen, D.G., *Measurement and Theory of Coal Pyrolysis Kinetics in an Entrained Flow Reactor*, EPRI Final Report for Project RP 1654-8 (1983).
20. Solomon, P.R., Hamblen, D.G., and Best, P.E., *Coal Gasification Reactions with On-Line In-Situ FT-IR/Analysis*, DOE Quarterly Reports, Contract #DE-AC21-81FE05122 (1981-1983).
21. Best, P.E., Carangelo, R.M. and Solomon, P.R. *ACS Division of Fuel Chem*, **29**, 249 (1984).
22. Solomon, P.R., Serio, M.A., Carangelo, R.M. and Markham, J.R., *Very Rapid Pyrolysis*, ACS Div. of Fuel Chemistry Preprints, **30** (1985).

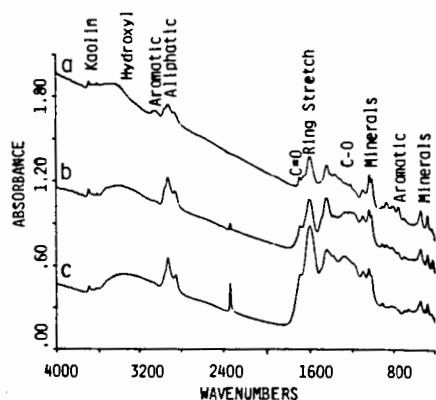


Figure 1. FT-IR Spectra for  
a) a Low Volatile Bituminous Coal,  
b) a High Volatile Bituminous Coal,  
and c) a Lignite.

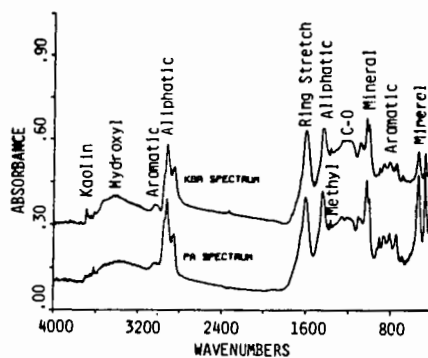


Figure 2. Comparison of KBr  
Pellet and Photoacoustic Spectra.

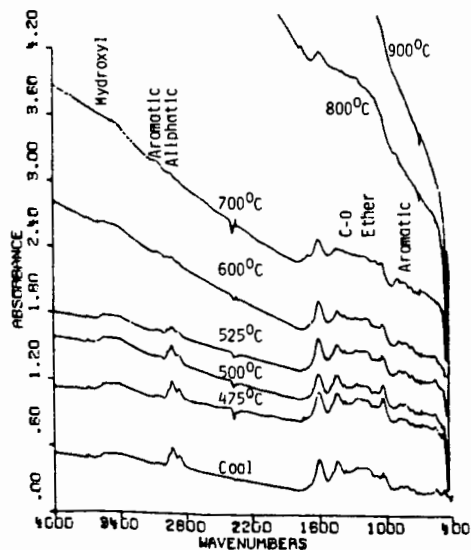


Figure 3. FT-IR Spectra for Chars Produced  
by Heating at 30°C/min to the Indicated  
Temperatures.

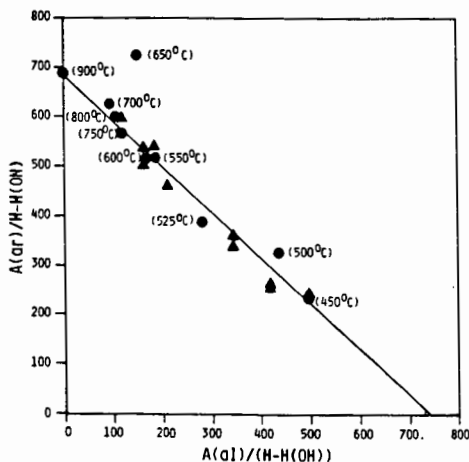


Figure 4. Regression Analysis to Determine  
Aromatic and Aliphatic Absorptivities for  
Bituminous Coals, Tars and Chars.



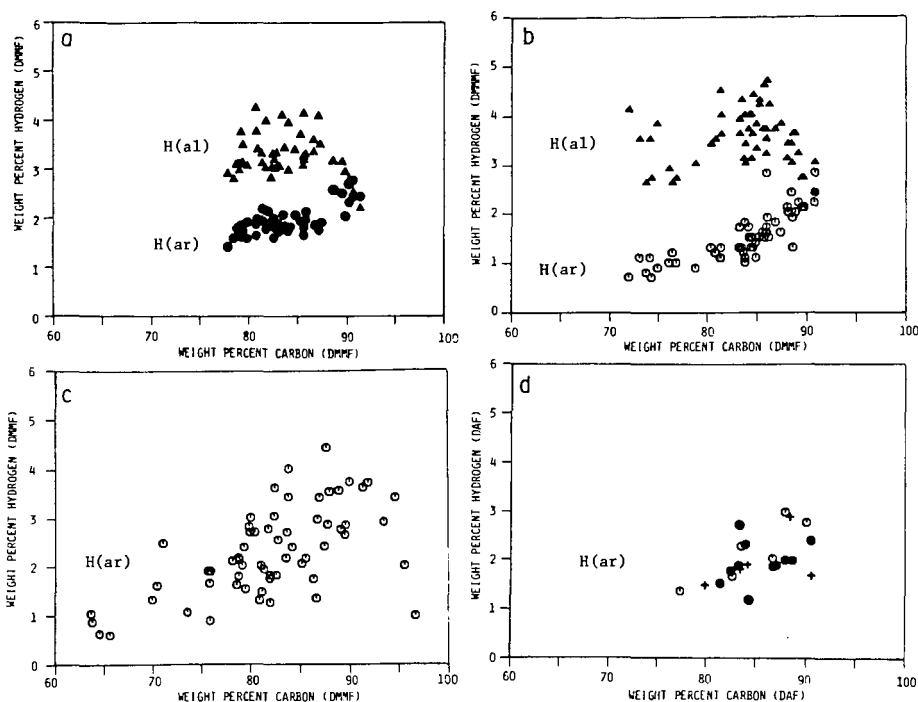


Figure 5. Aliphatic and Aromatic Hydrogen Concentration as a Function of Carbon Concentration. a) FT-IR, Present Results, b) FT-IR (10), c)  $^{13}\text{C}$ NMR with Dipolar Dephasing (11), and d) Proton NMR (12), (13), + (14).

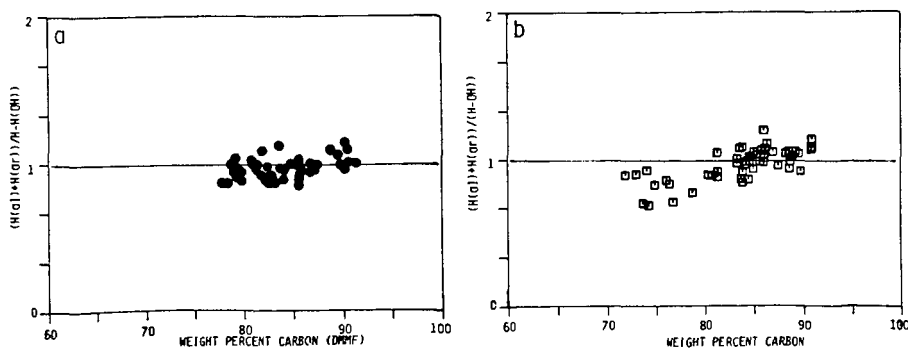


Figure 6. Hydrogen Balance,  $(\text{H}(\text{al}) + \text{H}(\text{ar})) / (\text{H} - \text{H}(\text{OH}))$  as a Function of Carbon Concentration a) FT-IR, Present Results and b) FT-IR (10).

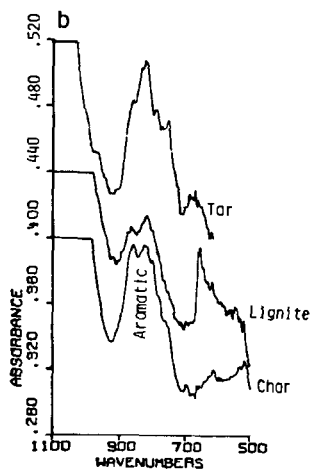
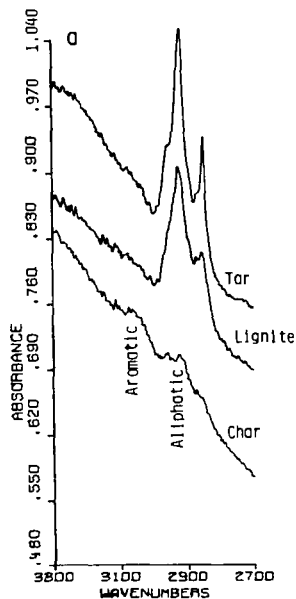


Figure 7. Comparison of Aromatic Hydrogen Stretch at 3100 Wavenumbers and Wag at 800 Wavenumbers.

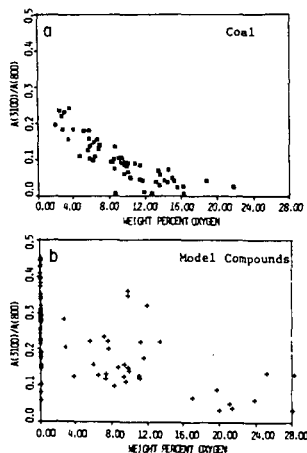


Figure 8. Ratio of Aromatic Stretch (3100 wavenumbers) to Aromatic Wag (800 wavenumbers) Absorption Bands as a Function of Oxygen Concentration.

TABLE I

Author	Ref.	H(al)/H(ar)
Brown	15	0.20
Brown et al.	14	0.33
Reisser et al.	10	0.35
Durie, et al.	13	0.38
Summary of other data		
Retcofsky	12	0.48
Present Results		0.52
Durie, et al.	13	0.56
Mazumdar	16	0.59
Summary of data		
Wilson et al.	11	0.70
Coals and Vitrinities		
Average		0.46

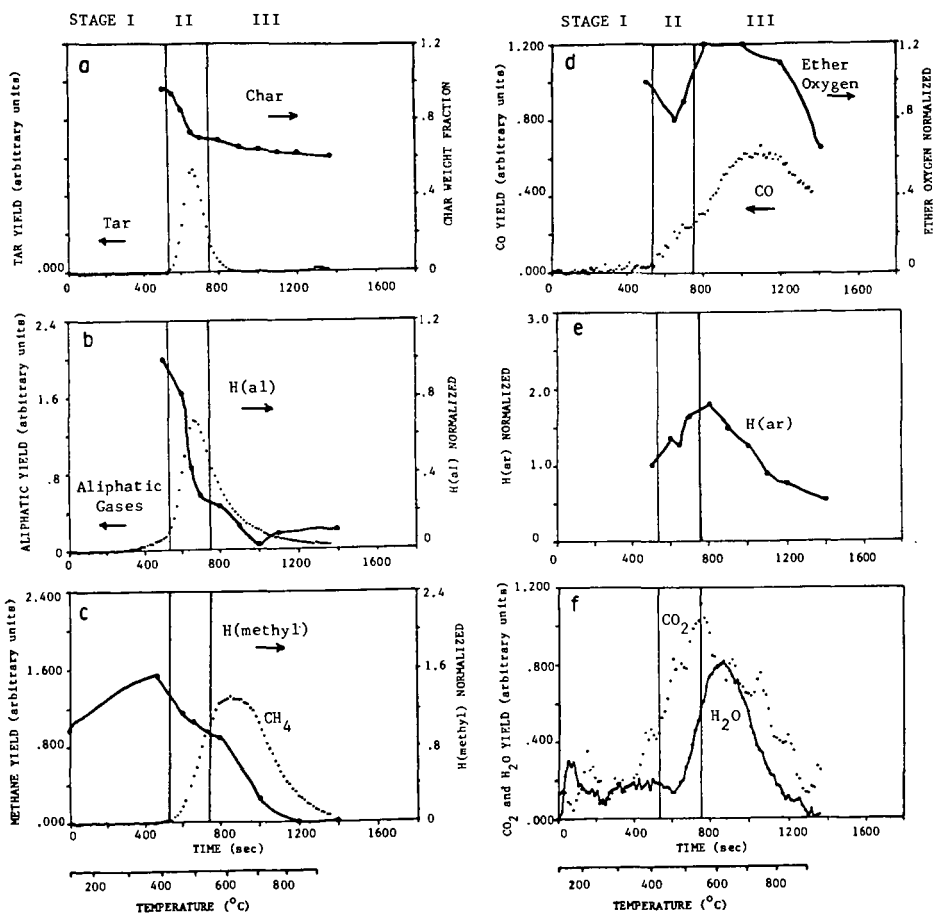


Figure 9. Comparison of Functional Group Composition and Evolved Gases in Slow Pyrolysis.

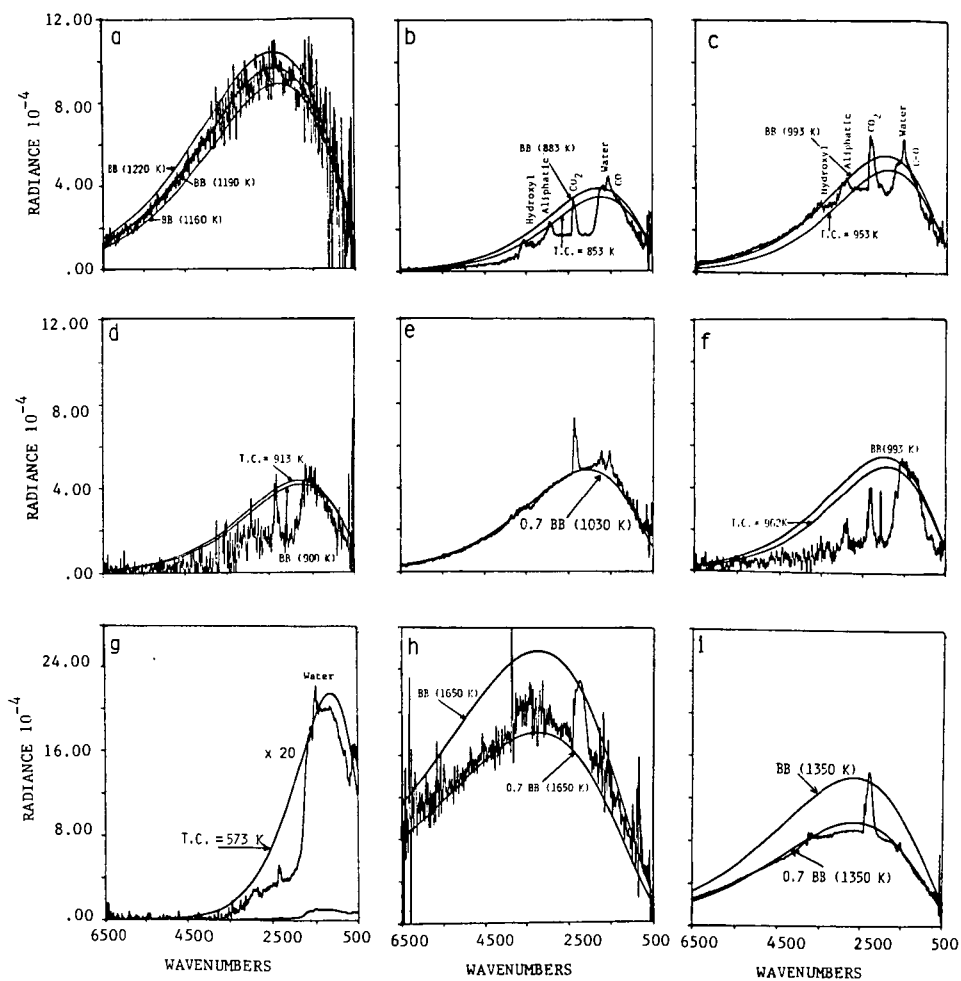


Figure 10. Normalized Emission Spectra for Coal and Char. a) Char in Stage III, b) Coal, c) and d) Char During Stage II, e) Char after Stage III, f) Char During Stage II, g) Coal, h) Lignite Char During Combustion, and i) Bituminous Char During Combustion.

# COMPARISON OF FOURIER TRANSFORM INFRARED-PHOTOACOUSTIC SPECTROSCOPY (FTIR-PAS) AND CONVENTIONAL METHODS FOR ANALYSIS OF COAL OXIDATION

P.-L. Chien, R. Markuszewski, J. F. McClelland

Ames Laboratory\*, US DOE, Iowa State University, Ames, Iowa 50011

## ABSTRACT

Fourier Transform Infrared-Photoacoustic Spectroscopy (FTIR-PAS) has been used to study variations in coal oxidation produced under laboratory-controlled conditions (temperatures of 140 and 150°C and exposure times up to 72 hours). Prominent oxidation-induced spectral changes were monitored by the peak heights of carbonyl (1690  $\text{cm}^{-1}$ ) and carboxylate (1575  $\text{cm}^{-1}$ ) bands. Changes in these peak heights have been plotted against conventional test data which are sensitive to the oxidation level of coal. Good linearity was observed for comparisons with the U.S. Steel oxidation test by alkali extraction and with measurements of the heating value. Advantages demonstrated for the FTIR-PAS method of monitoring coal oxidation include speed of analysis (several minutes), non-destructive character, minimal sample preparation (coarse powder), insensitivity to sample mass, and flat spectral baselines without hydroxyl band interference common to KBr-pellet IR transmission spectroscopy.

## INTRODUCTION

It is well known that exposure of fresh coal to air will deteriorate its coking propensity as well as heating value, floatability, and other properties. The oxidation of coal begins with adsorption (physical adsorption and chemisorption) of oxygen on accessible aromatic and aliphatic surface sites to form acidic functional groups, in particular,  $-\text{COOH}$ ,  $=\text{CO}$ , and phenolic  $-\text{OH}$  (1). If moisture is generated from chemically combined hydrogen in coal, some chemisorbed oxygen will produce peroxide or hydroperoxide complexes. The breaking down of these hydroperoxide groups at higher oxidation temperature (140°C) is responsible for the loss of CH groups (2). At later stages of oxidation, the acids produced combine with phenol to generate esters or anhydrides (2,3,4). Conventional oxidation testing methods (including free swelling, Gieseler plasticity, U. S. Steel oxidation transmission, and heating values) not only need a considerable time to complete a single measurement but also offer no information about the detailed chemical changes of coal. For instance, the U. S. Steel oxidation transmission test can only indicate whether or not coal is good for metallurgical use (5) while heating values provide only caloric data.

Methods based on diffuse reflectance (4,7,8), transmission (2,3,6), and photoacoustic (7,8) Fourier Transform Infrared (FTIR) spectroscopy have been used extensively in recent years in studies of oxidation associated coal beneficiation products. These methods can help reveal the detailed mechanisms of coal oxidation. Painter et al. (2,3,6) applied the transmission FTIR method to study oxidation mechanisms. They attributed the formation of ester links as responsible for the loss of free swelling characteristics and suggested that loss of aliphatic CH groups during oxidation is responsible for reduction of Gieseler plasticity. The groups of Hamza (7) and Lynch (8) have deduced that coal oxidation is initiated at aliphatic carbon adjacent to aromatic rings and that the initial generation of hydroperoxides and cyclic peroxides precedes the formation of carbonyl functionality which can reduce the hydrophobicity of coal surfaces, resulting in decreased floatability. On the contrary, Spitzer (9) believes that the decrease of floatability of coal after oxidation is associated with decreasing alkyl content and not with increasing oxygen content.

\* Ames Laboratory is operated for the U. S. Department of Energy by Iowa State University under Contract No. W-7405-Eng-82.

Although there are controversies in explaining the oxidation results characterized by FTIR methods, the information provided enables insights into detailed reaction mechanisms. However, there are several inherent disadvantages in diffuse reflectance and transmission methods including difficulty in obtaining a suitable reference spectrum in diffuse reflectance measurements, variable moisture content in KBr-pellet transmission spectroscopy, tedious sample preparation, severe background scattering, difficulty in selection of correct scaling factors for spectral subtraction, and uncertainty of pressure effects in making KBr pellets. The FTIR-PAS method is able to provide the same quality of results as the other FTIR methods in analyzing coal beneficiation products but with fewer problems. In this paper, capabilities of the FTIR-PAS method for characterizing coal oxidation are demonstrated with comparisons of FTIR-PAS results to those of conventional coal analysis data.

#### EXPERIMENTAL

FTIR-PAS spectra were measured with an IBM Instruments IR-98 FTIR system (8 cm<sup>-1</sup> resolution, 128 scans) and a photoacoustic cell designed and constructed at the Ames Laboratory. The cell sample cup volume was less than 0.1 cm<sup>3</sup> and contained helium gas during measurements to enhance the signal amplitude. The photoacoustic interferogram signal was detected in the frequency range 90 to 900 Hz by a model 4176 pre-polarized Bruel and Kjaer microphone with 50 mV/Pa sensitivity. Signals were amplified by a thousand gain preamplifier before being fed into the FTIR instrument for processing. After the interferogram was Fourier transformed, spectra were subtracted using the IR-98 software and difference spectra plotted, usually without spectral smoothing.

The Illinois No. 6 coal used in this oxidation study was obtained from the Ames Laboratory Coal Library (11). It came from the Captain Mine in Randolph County, IL. The description of the coal is given in Table 1.

Table 1. Analysis of Illinois No. 6 Coal Performed at Ames Laboratory

Proximate Analysis, (%):	Sulfur Forms (dry)							Heating Value (Btu/lb) Dry
	Moisture	Volatile Matter	Ash	Sulfur Forms (dry)			Organic Sulfur (by diff.)	
				Total Sulfur	Pyritic Sulfur	Sulfate Sulfur		
	8.14	33.65	13.12	3.45	2.03	0.14	1.28	12,189
Ultimate Analysis, (%):	C	H	S(total)		N	O(by diff.)		
	62.17	4.13	3.45		1.60	15.53		

Controlled oxidation of the Illinois coal was performed at Ames Laboratory by placing samples in an oven at either 140 or 150°C for varying times up to 72 hours with an air flow rate of 42 ml per second. The particle size ranged from 44 to 125 micrometers (120 to 325 mesh). FTIR-PAS spectra, heating value measurements, and U. S. Steel oxidation transmission tests on the Illinois #6 coal were also completed in this Laboratory. The amount of sample needed for acquiring FTIR-PAS spectra was roughly 15 mg. No sample preparation after sieving was required for this measurement. Raw or oxidized coal was poured directly into the photoacoustic cell's sample holder and the spectra were measured. Since the photoacoustic signal is rather insensitive to the amount of sample used for measurements, volume sampling is adequate.

and it is unnecessary either to weigh out samples for analysis or to adjust the spectrum weighting factor during spectral subtraction. The FTIR-PAS spectral acquisition time is typically three minutes (128 scans) per sample. The degree of oxidation as characterized by this method is determined by the changes in peak heights of carbonyl ( $1690\text{ cm}^{-1}$ ) and ionized carboxyl ( $1575\text{ cm}^{-1}$ ) bands which can be quantitatively measured by spectral subtraction.

Measurements for the U. S. Steel oxidation transmission test (5) were performed by: adding 1g of coal sample to 100 ml of 1 N NaOH; adding one drop of Tergitol to the caustic-coal slurry; boiling the caustic-coal slurry for 3 minutes; cooling and filtering the slurry through a 45 micrometer Whatman filter paper; diluting the filtrate with distilled water to a total volume of 80 ml; and measuring the percent transmission of the solution with a spectrophotometer set at 520 nm. The heating values were determined using the standard ASTM method (D2015).

## RESULTS AND DISCUSSION

Spectra 1a and 1b of Figure 1 are for raw Illinois #6 coal acquired by conventional transmission FTIR and FTIR-PAS methods, respectively. Besides the problems of background scattering and uncertainty of hydroxyl bonds ( $1600$  and  $3400\text{ cm}^{-1}$ ) in spectrum 1a, these two methods give qualitatively similar results. Spectrum 1c was acquired by the FTIR-PAS method on the same Illinois #6 coal after oxidation in air at  $140^\circ\text{C}$  for 24 hours. Spectrum 1d shows the spectral differences between the oxidized and the raw coal after spectral subtraction. No weighting factor adjustment was used or was necessary because scaling of the FTIR-PAS spectrum is insensitive to sample mass.

Besides the increases of carbonyl ( $1690\text{ cm}^{-1}$ ) and carboxylate ( $1575\text{ cm}^{-1}$ ) bands as well as the decrease of aliphatic CH groups ( $\sim 2900\text{ cm}^{-1}$ ), there also appear to be slight losses in aromatic CH ( $\sim 3050\text{ cm}^{-1}$ ) and in hydroxyl OH ( $\sim 3550\text{ cm}^{-1}$ ) groups. The observations at  $1690$ ,  $1575$ , and  $2900\text{ cm}^{-1}$  are consistent with Painter's results (3,6), while all of the features observed are in agreement with Smyrl's results (4). Apparently Painter's failure to see the features near  $3050$  and  $3550\text{ cm}^{-1}$  is due to the moisture interference and subtraction factor selection problems associated with transmission. Smyrl applied an in-situ diffuse reflectance method to characterize coal oxidation which, like the present work, is free from worries of moisture interference and subtraction factor selection.

Although there is controversy about which portions of coal are consumed during oxidation, the carbonyl, carboxylate and ester groups produced by the reaction have never been doubted. Therefore, these functional groups were selected to correlate with the results from conventional characterization methods. For instance, Figure 2 shows the increase of carbonyl and ionized carboxyl peak heights measured by the FTIR-PAS method and the variations of percent transmission measured by the U. S. Steel oxidation transmission test versus time of oxidation for Illinois #6 coal samples at  $140^\circ\text{C}$ . Similar saturation trends for FTIR-PAS and U. S. Steel tests are evident for oxidation conducted at both  $140$  and  $150^\circ\text{C}$ , resulting in the asymptotic behavior of carbonyl and carboxylate group changes. Figure 3 shows that the FTIR-PAS and U. S. Steel test data are linearly correlated. Data for coal oxidized at  $140^\circ\text{C}$  and  $150^\circ\text{C}$  are plotted in this figure to show that linearity is maintained for two different oxidation conditions. The linear correlation was found for both temperatures to better than 6% transmission units.

Two hypotheses regarding coal oxidation behavior are suggested by the linear correlation observed. First, the loss of coking properties of coal during oxidation is due to the formation of oxygen functional groups. Since the U. S. Steel test is a measurement of coking properties, the linear relationship of these two methods

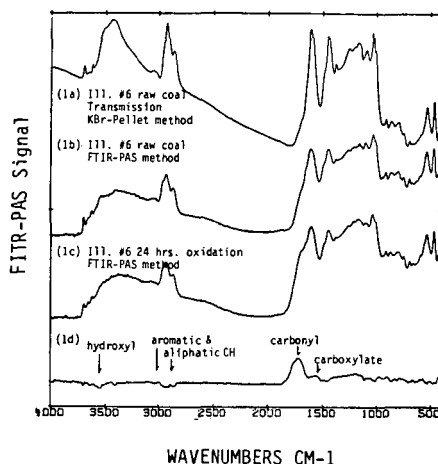


Figure 1. Comparison of Illinois #6 coal spectra, measured by transmission and photoacoustic methods and an example of a spectral subtraction result using photoacoustic spectra to show oxidation induced spectra changes.

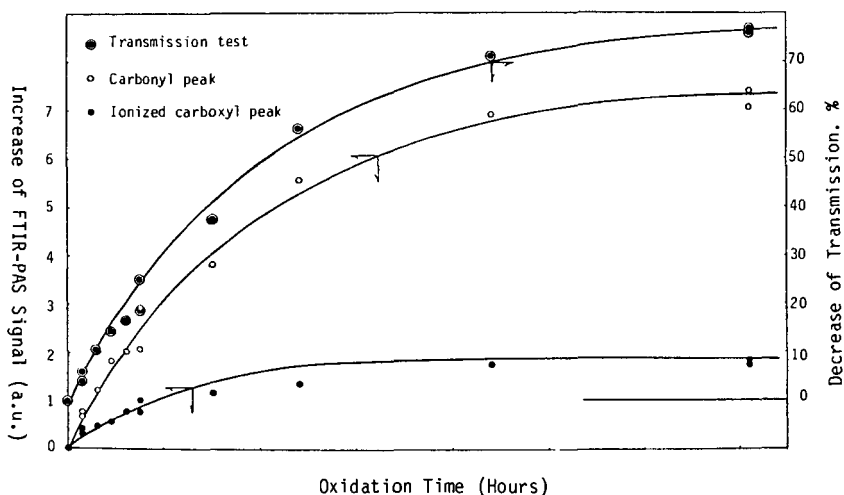


Figure 2. Progress of oxidation measured by the FTIR-PAS method and U. S. Steel alkali extraction transmission test (a.u.=arbitrary units).



suggests that both the degradation of coal in coking ability and the U. S. Steel transmission value are due to the formation of oxygen functional groups. Second, the coal particles in the size range explored appear to be oxidizing uniformly throughout their volume rather than to a decreasing degree with depth as would be the case for a diffusion limited process. The hypothesis is based on the fact that for this size coal sample, particles are opaque and the FTIR-PAS measurement senses a surface layer whereas the U. S. Steel test is a bulk determination. Since the data of the two methods have a linear correlation, the surface and bulk regions appear to be uniformly oxidized. To test this hypothesis further, the coal samples oxidized at 140°C were ground to the micrometer size range to permit the FTIR-PAS measurement of the bulk material oxidation changes since the particles are no longer opaque. To prevent additional coal oxidation during the grinding process, the grinder capsule which contained coal was cooled by liquid nitrogen. The results obtained from the FTIR-PAS spectra of ground, oxidized coal are plotted in Figure 4 against the results before grinding. The linear relation found in this plot indicates the same time evolution for oxidation of surface and bulk regions of the samples. Hence, the oxidation processes do not appear to be either separate surface-bulk processes or diffusion-limited processes but rather processes occurring uniformly throughout the bulk for the experimental conditions used.

There are two heating value estimating formulas available for coal, the Dulong and the Dulong-Berthelot formulas (Ref. 1, p. 35). In these two formulas the heating value decreases linearly with increasing oxygen content of coal. This implies that the decrease of heating value during oxidation can be correlated linearly with the amount of oxygen functional groups produced. Figure 5 is a plot of the decrease in the ASTM heating value versus increase in coal oxidation as monitored by changes in the sum of peak amplitudes associated with carbonyl and carboxylate bands of Illinois #6 coal. A common linear relation was found between these two methods for both 140 and 150°C oxidation conditions. This linear relationship between heating value degradation and FTIR-PAS data may enable optimization of coal beneficiation processes when coal oxidation occurs during the process. Since the beneficiation process includes demineralization, the decrease of mineral contents of coal can also be monitored by the same FTIR-PAS spectrum. Hence, the trade-off between mineral removal and loss of heating value can be evaluated based on one sample and a single data acquisition effort. Furthermore, the correlation between the U. S. Steel test and FTIR-PAS data can also be used to determine whether or not demineralized coal still has coking properties for metallurgical use.

Samples of coal oxidized by natural weathering, which were provided by the Koppers Company, were also studied and the FTIR-PAS spectra were measured. Linear correlations were found between our FTIR-PAS results and results obtained previously (10) for the U. S. Steel oxidation transmission, free swelling index, and Gieseler plasticity tests. These findings, which will be reported fully elsewhere, suggest that FTIR-PAS data can be correlated and substituted for data from these conventional coal tests which demand more time.

In the above discussions, only spectral changes of oxygen-containing functional groups generated during oxidation of coal were used to correlate with conventional testing method results. If the other features of FTIR-PAS subtraction spectrum 1d (as shown in Figure 1) are also involved in the data manipulation, more relations may be found that will provide a better understanding of the oxidation process.

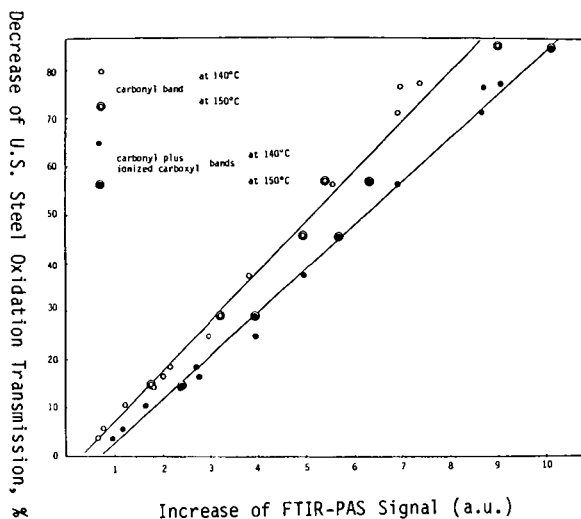


Figure 3. Comparison of FTIR-PAS signal to U. S. Steel oxidation transmission tests at the oxidation temperatures of 140 and 150°C (a.u.=arbitrary units).

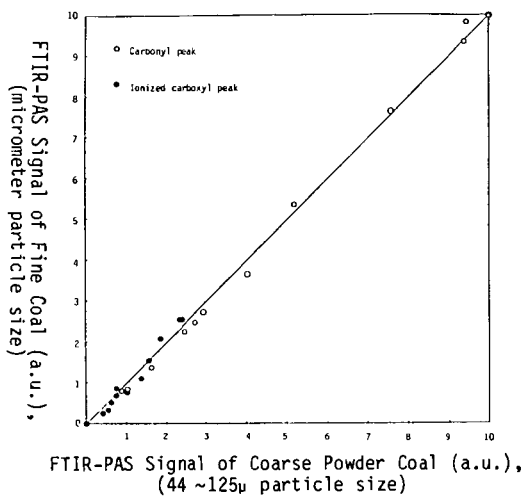


Figure 4. Plot of the photoacoustic signal for coarse opaque versus signal for fine non-opaque coal powders showing that oxidation has occurred uniformly through the coarse powder volume (a.u.=arbitrary units).

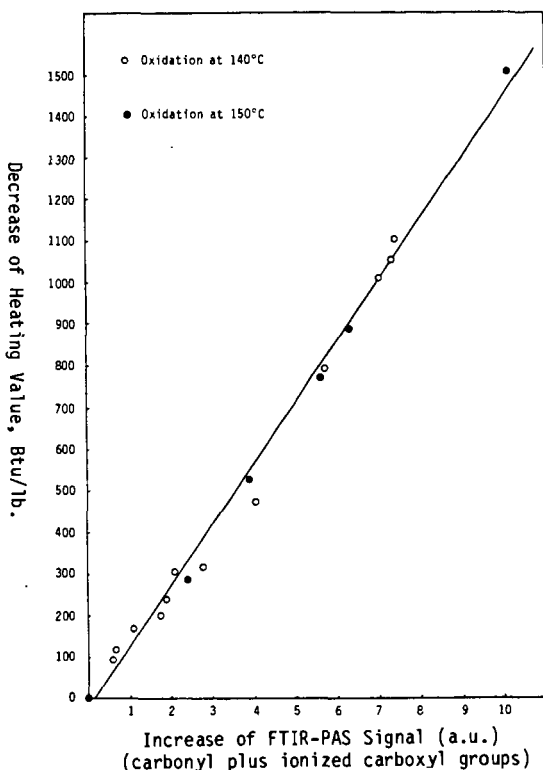


Figure 5. Comparison of FTIR-PAS signal to heating value measurement at the oxidation temperatures of 140 and 150°C (a.u.=arbitrary units).

#### CONCLUSIONS

FTIR-PAS spectral changes induced by coal oxidation have been found to correlate linearly with results of conventional coal analysis methods that are sensitive to coal oxidation. Advantages demonstrated for the FTIR-PAS method of monitoring coal oxidation include speed of analysis (several minutes), non-destructive character, minimal sample preparation (coarse powder), insensitivity to sample mass, and flat spectral baselines without hydroxyl band interference common to KBr-pellet IR transmission spectroscopy.

## REFERENCES

1. N. Berkowitz, "An Introduction to Coal Technology", Academic Press, New York, 1979, pp. 95-104.
2. C. A. Rhoads, J. T. Senftle, M. M. Coleman, A. Davis, and P. C. Painter, Fuel, **62**, 1387 (1983).
3. P. C. Painter, R. W. Snyder, D. E. Pearson, and J. Kwong, Fuel, **59**, 282 (1980).
4. N. R. Smyrl and E. L. Fuller, "Chemistry and Structure of Coals - Diffuse Reflectance IR Fourier Transform (DRIFT) Spectroscopy of Air Oxidation," in Coal and Coal Products: Analytical Characterization Techniques, ACS Symposium Series 205, E.L. Fuller, ed., 1982, pp. 133-145.
5. D. E. Lowenhaupt and R. J. Gray, International J. of Coal Geology, **1**, 63 (1980).
6. P. Painter and C. Rhoads, ACS Division of Fuel Chemistry Preprints, **26**(1), 35 (1981).
7. H. A. Hamza, K. H. Michaelian, and N. E. Andersen, Proc. 1983 International Conference on Coal Science, Pittsburgh, PA, pp. 248-251.
8. B. M. Lynch and A. M. MacEachern, Proc. 1983 International Conference on Coal Science, Pittsburgh, PA, pp. 653-654.
9. D. P. Spitzer, Proc. Pittsburgh Coal Conference, 1984, Pittsburgh, PA, pp. 858-872.
10. J. Markiewicz and R.J. Gray, Task Group Report on Alkali Extraction Test for Oxidized Coal, ASTM Meeting, Louisville, KY, May 9-11, 1983.
11. D.L. Biggs, D.H. Birlingmair, R.W. Fisher, R.T. Greer, R.A. Kaelin, R. Markuszewski, B.F. Smith, T.G. Squires, C.G. Venier, and T.D. Wheelock, "Status Report on the Collection and Preparation of Coal Samples for the Ames Laboratory Coal Library," presented at the Coal Sample Bank Workshop at the Am. Chem. Soc. Meeting, Atlanta, GA, March 27-28, 1981.

## ACKNOWLEDGEMENTS

This work was performed for the Ames Laboratory, operated for the U. S. Department of Energy by Iowa State University under Contract No. W-7405-Eng-82, and was supported by the Assistant Secretary of Fossil Energy, Division of Coal Utilization, through the Pittsburgh Energy Technology Center, Coal Preparation Branch. The authors would like to express gratitude to Dr. John Markiewicz at the Koppers Company for providing naturally weathered coal samples and test results, as well as to N. Adams, G. Norton, and R. Bachman at Ames Laboratory for conducting coal oxidation, heating value, and U. S. Steel oxidation tests.

# A SPECTROSCOPIC STUDY OF THE PRODUCTS OF REDUCTIVE ALKYLATION OF AN ILLINOIS COAL

Leon M. Stock and Reid S. Willis

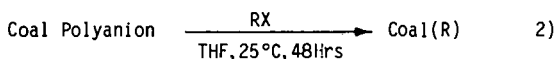
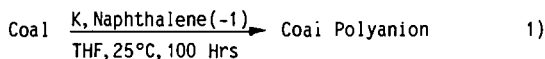
Department of Chemistry, University of Chicago, Chicago, IL 60637

## INTRODUCTION

Mild chemical reactions such as alkylation and reductive alkylation provide techniques for the conversion of coal macromolecules into substances that are soluble. The soluble products of such reactions can be investigated by one and two dimensional, high resolution NMR spectroscopy to obtain structural information that is often difficult to obtain by the investigation of solids. Moreover, the soluble products can be subjected to selective chemical transformations to obtain additional information to guide the interpretation of the spectroscopic results. This article concerns the use of a selected series of chemical reactions and nuclear magnetic resonance spectroscopy for the definition of the structural characteristics of the reactive carbanions and oxygen anions formed during the reductive alkylation of an Illinois No. 6 coal.

## RESULTS AND DISCUSSION

The reductive alkylation (1,2) of a representative Illinois No. 6 coal,  $C_{100}H_{87.0}O_{13.1}S_{1.9}N_{0.75}$ , with 8.2 % ash, was carried out as shown.



The reactions were performed and the products were isolated as described previously (3) using methyl, methyl- $d_3$ , methyl- $^{13}C$ , and ethyl iodide as the alkylating agents. The yield of tetrahydrofuran-soluble products ranged from 48 to 68% in 15 experiments. Infrared spectroscopy established that the alkylation reaction was complete. In particular, the very typical, broad oxygen-hydrogen stretching frequency was absent in the spectra of the products. The molecular weight distribution of the soluble, alkylated coal was examined by vapor pressure osmometry (4). The results imply that the number average molecular weight of the material obtained after filtration and gel permeation chromatography is about 2000 in pyridine solution.

Several different measurements indicate that about 22 equivalents of potassium are consumed per 100 carbon atoms of this coal during reductive alkylation (3). Analyses of the soluble reaction products obtained in the reaction with methyl- $d_3$  iodide for deuterium by deuterium nuclear magnetic resonance spectroscopy and by combustion mass spectroscopy (5) indicate that the most soluble products contain  $11 \pm 1.5$  alkyl groups per 100 carbon atoms. The difference between the amount of potassium consumed in the reduction and the degree of alkylation arises, in part, because the reactive

intermediates generated in the reduction reaction abstract hydrogen from tetrahydrofuran. The occurrence of this reaction was demonstrated by conducting the reduction in the presence of labeled tetrahydrofuran and quenching the reaction in water. We estimate that not less than 5 hydrogen atoms are incorporated into the coal macromolecules from the solvent on the basis of the degree of incorporation of deuterium in the experiment and the anticipated primary kinetic isotope effect.

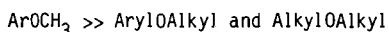
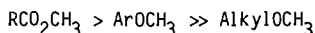
**C-Alkylation.**--Quantitative analyses of the reaction products obtained using methyl- $^{13}\text{C}$  iodide by carbon NMR spectroscopy indicate that about equal quantities of C- and O-alkylation products are formed (3). Following a leading observation by Ignasiak and his coworkers (6), we also examined the carbon NMR spectrum of the products obtained in a reductive ethylation reaction. There were 5 prominent absorption bands in the spectrum as outlined in Table 1. The resonance at 8.5 ppm is surprisingly intense and implies that the concentration of ethyl groups at saturated, quaternary carbon atoms is quite high. Indeed, quantitative analysis of the spectral data suggest that the carbon alkylation reactions occur preferentially at highly substituted positions and at primary benzylic positions and are compatible with the idea that this coal contains three distinct structures--reactive aryl methyl groups, activated trisubstituted methane fragments, and aromatic structures--that may be alkylated.

**O-Alkylation.**--The assignments of the resonances of the O-methylation products observed in regions 1, 2, and 3 obtained in the reactions with methyl- $^{13}\text{C}$  iodide, Figure 1, are summarized in Table 2. The assignments presented in column A are based upon chemical shift data exclusively. To obtain more definite information about the structures of the compounds responsible for these resonances, we carried out a series of selective chemical transformations.

First, the soluble reaction products were hydrolyzed using tetrabutylammonium hydroxide in aqueous tetrahydrofuran for 24 hours at room temperature. The solution was acidified with dilute hydrochloric acid and the product was isolated and dried prior to the reexamination of its carbon spectrum. Quantitative measurements of the absorption at 51 ppm revealed that over 98% of the intensity was removed. Hence, the resonances in region 3 arise, virtually exclusively, from alkyl and aryl carboxylic acid esters.

Second, acid hydrolysis was carried out to examine the proposal of Haenel and coworkers (7) that enol methyl ethers may, in part, be responsible for the resonance signals in region 1. The reaction was carried out with 2N hydrochloric acid in aqueous tetrahydrofuran for 48 hours at room temperature. The product was recovered and the NMR spectrum recorded. There was no change in the absolute intensities of the resonance signals in regions 1 and 2. Thus, methyl vinyl ethers are not formed to a measurable degree in the reductive alkylation of the Illinois coal.

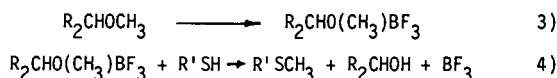
Third, a selective displacement reaction was used to distinguish the methyl alkyl ethers from the methyl aryl ethers. The reaction of the soluble coal with lithium iodide in collidine at 170°C for 24 to 48 hours was used for this purpose. The chemical literature indicates that this reaction is highly selective for the displacement of methyl groups (8).



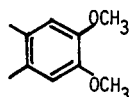
Appropriate control experiments with collidine indicated that the alkylated coal could be recovered unchanged from the reaction medium in the absence of lithium io-

dide. However, when the reaction was carried out with in the presence of the iodide there was a 70% decrease in solubility in tetrahydrofuran. The product was alkylated with unlabeled ethyl iodide to yield a material that was more than 80% soluble in pyridine. The carbon NMR spectrum of this product is greatly altered, Figure 2A. Specifically, the areas of regions 1, 2, and 3 are decreased by 96, 89, and 100%, respectively.

Fourth, it is known (9) that primary and secondary alkyl methyl ethers and benzyl methyl ethers can be cleaved selectively by boron trifluoride-etherate and a thiol, equations 3) and 4).



This reaction was performed with the  $^{13}\text{C}$  enriched demethylated coal using 1,2-ethanedithiol at room temperature. The product of the reaction was quite soluble in organic solvents. The changes in the intensities of the resonances at 55 and 58 ppm, Figure 2B, are particularly informative. The signal at 58 ppm has disappeared from the spectrum but the signal at 55 ppm is unaltered. These results imply that the compounds responsible for the residual signal at 58 ppm in Figure 2A are aliphatic methyl ethers and that the compounds responsible for the residual signal at 55 ppm in Figures 2A and 2B are aryl methyl ethers that resist dealkylation by both lithium iodide and borontrifluoride-ethanedithiol. The observations are most consistent with the presence of dimethoxyaryl compounds.



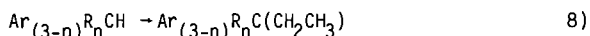
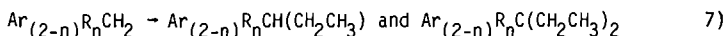
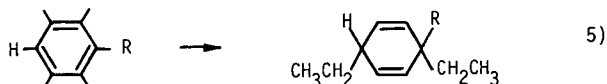
These compounds are known to resist demethylation with lithium iodide and to be inert toward acid-catalyzed cleavage. Thus, we infer that about 4% of the methyl groups added to this coal appear in such structures. The existence of compounds of this type may also be inferred from the differences observed in the nuclear Overhauser effect for the compounds in region 2 relative to the NOE for the other O-alkylation products.

The fact that the acid-catalyzed ether cleavage reaction eliminates the resonance at 58 ppm confirms the assignment of this weak signal to an aliphatic methyl ether. The chemical shift observed for this resonance is in accord with the resonance expected for the carbon atom of the methyl group in a primary alkyl methyl ether, but is incompatible with the signal expected for a simple primary benzyl methyl ether.

## CONCLUSION

Reductive alkylation adds about 12.5 alkyl groups/100 carbon atoms to the Illinois No. 6 coal. Broadly speaking 5.5 of these groups are bonded to carbon atoms and 7 are bonded to oxygen atoms. Only very small quantities of nitrogen and sulfur alkylation products can be detected. The spectroscopic results for the reductively

ethylated coal suggest that the C-alkylation reactions proceed via reductive alkylation to yield substituted dihydroaromatic compounds, equation 5), and via base-catalyzed alkylation to yield substituted arylmethanes as shown in equations 6) - 8).



The occurrence of the latter reactions strongly suggests that this Illinois coal contains three or four reasonably strong carbon acids per 100 carbon atoms. The existence of these reaction sites offers new opportunities for other selective transformation reactions.

The results obtained in the spectroscopic investigations of the chemically transformed O-alkylation products provide a reasonable basis for the definition of the relative abundances of the different O-alkylation products. The outcome of the analysis is shown in Column B of Table 2. The new observations provide definite information regarding the occurrence of low, but observable, quantities of alkyl methyl ethers, the presence of significant amounts of highly hindered aryl methyl ethers and dimethoxyaryl compounds and carboxylic acid esters. Our results also exclude several types of compounds. Thus, primary benzylic methyl ethers, secondary and tertiary alkyl methyl ethers as well as vinyl methyl ethers are not present in detectable amounts. We infer that the observed distribution of products in the alkylated coal is comparable to the distribution of these functional groups in the original coal. As a consequence, the new results provide a more secure basis for the discussion of the structure and reactivity of this coal.

#### REFERENCES

- 1) H.W. Sternberg, C.L. Delle Donne, P. Pantages, E.C. Moroni, and R.E. Markby, Fuel, **50**, 432 (1971).
- 2) The subject has been reviewed, L.M. Stock, Coal Science, **1**, 161 (1982).
- 3) L.B. Alemany and L.M. Stock, Fuel, **61**, 250 (1982).
- 4.) This determination was performed by J.W. Larsen and his students.
- 5) The combustion mass pectral analysis was carried out by Gollob Laboratories.
- 6) N. Cyr, M. Gawlak, D.W. Carson, and B.S. Ignasiak, Fuel, **62**, 412 (1983).
- 7) M.W. Haelnel, R. Mynott, K. Niemann, U.-B. Richter and L. Schanne, Angew. Chem. Int. Ed. Eng. **19**, 636 (1980).
- 8) J.E. McMurry, Org. Reactions, **24**, 187 (1976).



- 9) M. Node, H. Hari, and E. Fujita, J. Chem. Soc. Perkin Trans. I, 2237 (1976).

ACKNOWLEDGEMENT

It is a pleasure to acknowledge the support of this research by the United States Department of Energy and by the Illinois Department of Energy and Natural Resources.

Table 1. The Assignment of Resonances in the Carbon NMR Spectrum of Reductively Ethylated Coal.

Chemical Shift (ppm)	Assignment Resonance of Ethyl Group, Reaction
8.5	Methyl, ethylation at tertiary carbanionic center to form quaternary product, $R_3C(CH_2CH_3)$
12.5	Methyl, ethylation at secondary carbanionic center to form tertiary product, $R_2CH(CH_2CH_3)$
15	Methyl, ethylation at primary carbanionic center to form secondary product, $RCH_2(CH_2CH_3)$ Methyl, ethylation at oxygen, $ArO(CH_2CH_3)$
65	Methylene, ethylation at unhindered aryl oxygen, $ArO(CH_2CH_3)$
69	Methylene, ethylation at hindered aryl oxygen, $R_2ArO(CH_2CH_3)$

Table 2. Column A. The Assignments of the Resonances in the O-Alkylation Region of the Carbon NMR Spectrum of Reductively Methylated Illinois No. 6 Coal. Column B. The Relative Abundances of the O-Alkylation Products Defined by Chemical Conversions and Carbon NMR Spectroscopy.

Column A Possible NMR Assignments	Column B Relative Abundance <sup>a</sup>
1. Region Centered at 61 ppm	Region Centered at 61 ppm
Vinyl ethers	
Primary alkyl ethers	Primary alkyl ethers 0.1
Primary benzyl ethers	
Hindered aryl ethers	Hindered aryl ethers 2.2
2. Region Centered at 55 ppm	Region Centered at 55 ppm
Secondary alkyl ethers	
Unhindered aryl ethers	Unhindered aryl ethers
Dihydroxyaryl compounds	Dihydroxyaryl compounds 0.6
Simple aryl ethers	Simple aryl ethers 3.3
3. Region Centered at 51 ppm	Region Centered at 51 ppm
Tertiary alkyl ethers	
Aryl- and Alkylcarboxylic acid esters	Aryl- and Alkylcarboxylic acid esters 0.8

<sup>a</sup>The results have been normalized on the basis of the analytical results which suggest that there are 7 O-methyl groups per 100 carbon atoms in the alkylated products.

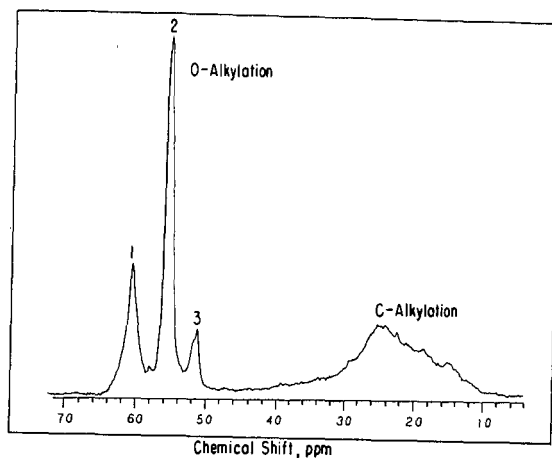


Figure 1.--The carbon nuclear magnetic resonance spectrum of an intermediate molecular weight, gel permeation chromatography fraction of the product of reductive methylation of Illinois No. 6 coal.

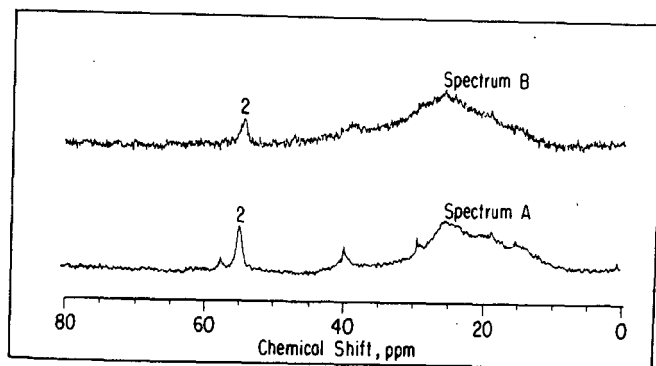


Figure 2.--The carbon nuclear magnetic resonance spectrum of the material shown in Figure 1 (A) after treatment with lithium iodide in collidine and (B) after subsequent treatment with boron trifluoride and ethanedithiol.

A DETAILED STRUCTURAL CHARACTERIZATION OF HEAVY CRUDE  
ATMOSPHERIC TOWER BOTTOMS

by

D. W. Grandy, D. A. Danner, T. L. Youngless,  
G. P. Feulmer, D. C. Young, and L. Petrakis

As the petroleum industry finds itself faced with increasing proportions of heavy sour crude, researchers must address the problem of how to upgrade this material to be compatible with existing refinery processes and product slates. The first problem to be faced in upgrading a heavy crude or residue is how to characterize the material well enough to understand the chemistry of the upgrading process. Crude residues are far more complex than coal liquids for they not only contain a variety of aromatic and heterocyclic units, but they also contain naphthenic and alkyl substituents of almost infinite variety on these simpler units as well as heavy alkanes.

The samples that will be discussed here were derived from a Maya (Mexico) crude (API gravity 19.1°). Since we are primarily interested in the chemistry of the residue, the crude was distilled at 680°F (360°C) to obtain an atmospheric tower bottom (ATB). The Maya ATB is 61% of the crude and has an API gravity of 7.7° and a sulfur content of 4.7%.

In order to simplify the characterization and upgrading chemistry, the Maya ATB was separated chromatographically into asphaltene, three acid, three base, neutral oil and neutral resin fractions on a preparative scale (1 kg) (1, 2). The separation yields and elemental analysis of the fractions are shown in Table I. A wide variety of characterization techniques were then applied to many of these fractions, including <sup>1</sup>H NMR, <sup>13</sup>C NMR (conventional and INEPT (3)), high resolution mass spectrometry (4) (HRMS), GC-MS (5), and atom specific GC (6).

Flame ionization detector (FID) and flame photometric detector (FPD) gas chromatograms of the Maya ATB neutral oil are shown in Figure 1 (5). The chromatograms were obtained on a Varian 3700 using a 10 ft long, 1/8 inch OD column packed with 10% OV-1 on acid-washed Chromasorb W. The FID trace shows an alkane series from n-C<sub>17</sub> to n-C<sub>34</sub> superimposed on a broad unresolved hump. The sulfur specific FPD trace shows some resolution of a few peaks at the low boiling end of the chromatogram and a similar unresolved hump. Other than the normal alkane series, no specific compounds were identified in the chromatogram. In spite of the rather small amount of information obtained on this sample, gas chromatographic techniques were found to be useful in monitoring changes in the hydrocarbon and sulfur species upon upgrading.

In order to eliminate interferences from saturates, the neutral oil was further separated into saturates, aromatics and polars by HPLC. This was done on a Waters HPLC using a dry silica (22-47 mesh) column.

The aromatic fraction was analyzed using a Kratos MS 50 high resolution mass spectrometer (HRMS) operated with an ionizing voltage of 70 eV, to obtain quantitative information on the aromatic and heterocyclic compounds in the neutral oil (4). Table II is a summary of the HRMS results, giving the weight percentage of the various species by Z number and the average number of carbon atoms in each Z class. For example, dibenzothiophenes were 3.32% of the sample and had an average of about six carbon atoms attached to the basic dibenzothiophene unit. Searching through the list of specific compounds in the sample reveals that dibenzothiophene accounts for 0.19% of the sample, methyl dibenzothiophene 0.43%, etc., through the series of alkyl dibenzothiophenes up to mass 408, C<sub>10</sub> dibenzothiophenes. Several hundred individual mass peaks are identified by carbon number, Z class, heteroatom content and weight percentage. This specific information allows the monitoring of the reactivity of particular molecules or molecular types.

GC-MS was also applied to the aromatic cut of the Maya ATB neutral oil. A Finnigan 4500 system with a 60-meter DB-5 fused silica capillary column was used. Due to the poor GC separation (see Figure 1), few GC peaks could be identified. However, knowing the masses of the sulfur species in the sample from HRMS, specific ion chromatograms were generated to obtain isomer number information and to observe the relative reactivity of these isomers in hydroprocessing (6). Figure 2 shows the mass chromatograms for dibenzothiophene (DBT) (m/z = 184) and substituted DBT through C<sub>7</sub>.

Proton and <sup>13</sup>C NMR spectra were obtained on most of the fractions from the Maya ATB on a Varian XL-200 FT NMR instrument. Table III gives some of the results from the <sup>13</sup>C NMR data on the fractions. Note that the neutral oils are the least aromatic fraction, being comprised of aromatics and "polars," which are only about one third aromatic, and 25% saturates, which gave no detectable signal in the aromatic region. Figures 3 and 4 show the normal <sup>13</sup>C NMR and INEPT spectra of the aromatic cut of the neutral oil (3). The INEPT technique causes the NMR signals due to CH and CH<sub>3</sub> to be inverted and virtually eliminates the signals due to carbons with no protons attached, such as those with a chemical shift around 140 ppm in the normal <sup>13</sup>C NMR spectra. A complete analysis of the spectrum gives much more structural detail.

The <sup>1</sup>H NMR spectrum of the Maya ATB neutral oil aromatics is shown in Figure 5. Although the spectrum is not rich in detail, due to the complex mixture in the sample, it can be analyzed by the technique of Clutter, Petrakis et al. to give average molecule information (7). These data are presented in Table IV. Compared to the <sup>13</sup>C NMR technique, the proton data give a somewhat lower aromaticity (0.27 versus 0.34) and a much lower (15.6% versus 28%) naphthenic carbon content. <sup>13</sup>C NMR techniques are believed to give the more reliable data. <sup>1</sup>H NMR, however, is better for determining the number of alkyl substituents.

While some of these types of data can be formally integrated to produce concentrations of functional groups (8), the general picture of the Maya ATB neutral oils that can be synthesized from the data is that the material is a very complex mixture of hydrocarbons and sulfur heterocycles. It contains about 25% saturates with alkanes from C<sub>17</sub> to about C<sub>40</sub>, alkyl

naphthenes, and very few isoprenoids. About 75% of the neutral oil is alkyl aromatics and thiophene-based compounds that are mostly from 1 to 5 rings, have some naphthene substituents, and are substituted, on the average in three to four positions with alkyl groups that range from methyl to about C<sub>16</sub>. The ratio of methyl to longer chains is 1.5:1 and the average length of the alkyl chain is about 5. Qian et al. give data from an aromatic cut of a petroleum pitch which has similar aromaticity, but a higher molecular weight and longer alkyl chains (9).

Due to their very complex nature, these petroleum residues require extensive separation and as many analyses as are available and affordable. While their absolute accuracy in describing the molecules in the mixture may be subject to a variety of errors, the strength of the analytical techniques described here is in measuring changes in the molecular structures upon hydroprocessing.

#### References

- (1) L. Petrakis, R. G. Ruberto, D. C. Young, and B. C. Gates, Ind. Eng. Chem. Process Des. Dev., 22, 292 (1983).
- (2) D. M. Jewell, E. W. Albaugh, B. E. Davis, and R. G. Ruberto, Ind. Eng. Chem. Fundam., 13, 278 (1974).
- (3) "<sup>13</sup>C NMR Multi-Pulse Sequences for the Analysis of Coal and Petroleum Products," R. Gerhards, in "Magnetic Resonance. Introduction, Advanced Topics and Applications to Fossil Energy," L. Petrakis and J. P. Fraissard, eds., D. Reilel Publishing Co., Dordrecht, The Netherlands, 1984, pp. 377-407.
- (4) I. P. Fisher and P. Fischer, Talanta, 21 (8), 867 (1974).
- (5) "Detectors," M. J. O'Brien, in "Modern Practice of Gas Chromatography," R. L. Grob, ed., John Wiley and Sons, New York, 1977, pp. 266-269.
- (6) "Techniques of Combined Gas Chromatography/Mass Spectrometry: Applications in Organic Analysis," W. H. McFadden, John Wiley and Sons, New York, 1973, p. 252.
- (7) D. R. Clutter, L. Petrakis, R. L. Stenger, and R. K. Jensen, Anal. Chem., 44, 1395 (1972).
- (8) L. Petrakis, D. T. Allen, G. R. Gavalas, and B. C. Gates, Anal. Chem., 54, 1557 (1983).
- (9) S. A. Qian, C. F. Li, and P. Z. Zhang, Fuel, 63, 268 (1984).

TABLE I  
Yield and Elemental Composition of Maya ATB Fractions

<u>Yield %</u>	<u>C %</u>	<u>H %</u>	<u>O %</u>	<u>N %</u>	<u>S %</u>	<u>Total</u>	
Maya ATB	-	84.26	10.40	0.47	0.51	4.70	100.34
Stral Oil	69.68	84.30	11.31	0.82	1.53	3.79	101.75
Asphaltene	24.14	82.65	7.83	1.41	1.12	6.97	99.98
Very Weak Base	0.86	81.78	9.42	2.48	0.15	5.00	98.83
Weak Base	0.07	49.49	6.32	18.95	0.30	6.04	81.10
Strong Base	0.01	53.98	6.86	12.87	3.34	7.55	84.60
Very Weak Acid	0.17	80.32	8.02	4.93	1.60	4.02	98.89
Weak Acid	0.04	61.81	6.65	14.13	0.85	1.72	85.16
Strong Acid	1.23	58.39	6.97	16.79	3.74	0.20	86.09
Neutral Resin	<u>2.39</u>	76.28	8.43	3.14	0.81	5.08	93.74
Total Recovery %	98.58						



TABLE II

High Resolution Mass Spectrometry Data on Maya ATB Neutral Oil Aromatics

<u>Z # Hydrocarbon Type</u>	<u>AV C #</u>	<u>Wt%</u>	<u>Total Wt</u>
Monoaromatics			28.01
-6 Alkylbenzenes	14.03	12.75	
-8 Indans	15.37	7.08	
-10 Indenes	15.16	8.18	
Diaromatics			19.88
-12 Naphthalenes	15.96	7.79	
-14 Biphenyls	18.08	5.29	
-16 Fluorenes	18.80	6.81	
Triaromatics			10.61
-18 Phenanthrenes	19.86	4.48	
-20 Phenanthrocyloparaffins	20.78	6.13	
Tetraaromatics			7.48
-22 Pyrenes	21.50	3.54	
-24 Chrysenes	22.92	3.94	
Pentaaromatics			10.04
-26 Chrysocycloparaffins	24.48	3.77	
-28 Benzpyrenes	25.20	2.75	
-30 Dibenzanthracenes	26.48	3.52	
Polyaromatics			8.03
-32	25.73	3.53	
-34	27.07	2.29	
-36	28.40	2.21	
Thiophenes			15.35
-10S Benzothiophenes	20.38	2.52	
-12S	20.41	2.59	
-14S	20.22	0.58	
-16S Dibenzothiophenes	18.14	3.32	
-18S	20.47	1.28	
-20S	18.28	1.03	
-22S Benzonaphthothiophenes	21.05	1.36	
-24S	22.65	1.15	
-26S	22.00	0.90	
-28S	23.97	0.62	
Phenols/Furans			0.60
-60 Phenols	6.00	0.04	
-160 Dibenzofurans	15.28	0.18	
-180	16.36	0.13	
-220 Benzonaphthofurans	18.56	0.25	

AV C NO 19.33

AV Z NO -16.88

C/H = 1/1.127

TABLE III  
Carbon Distribution in Fractions by  $^{13}\text{C}$  NMR

	<u>% Aromatic</u>	<u>% Naphthenic</u>	<u>% Saturate</u>	
Neutral Oils		25% (calc)		
Aromatics	60.0*	34%	28%	38%
Saturates	25.7*	0%	34%	66
Polars	14.3*	32%	ND	ND
Very Weak Acid		62%	12	26
Weak Acid		54%	17%	29%
Strong Acid				
Very Weak Base		45%	22	33
Weak Base		44%	23%	33%
Strong Base		52%	ND	ND

\*Percentage of neutral oil.

TABLE IV  
Average Molecule Data on Maya ATB Neutral Oil Aromatics from  $^1\text{H}$  NMR

Aromaticity:	0.27	% Monoaromatics:	43.8
Aromatic Rings/Molecule:	1.7	% Diaromatics:	46.9
Aromatic Ring Carbons/Molecule:	8.6	% Triaromatics:	9.3
Average Molecular Formula:	C31.7 H43.4	Average Molecular Weight:	423.9
% Alkyl Carbon:	72.8	Nonbridge Aromatic Carbons/Molecule:	7.3
Alkyl Substituents/Molecule:	3.6	% Subst. of Nonbridge Arom. Carbons:	57.8
Carbons/Alkyl Substituent:	6.4	Naphthene Rings/Molecule:	1.4
% Nonbridge Aromatic Ring Carbons:	23.1	% Naphthenic Carbon	15.6

NOTE: Average mol wt is based only on C and H and does not account for O, S, N, etc.

FIGURE 1  
FID and FPD Chromatograms  
of Maya ATB Neutral Oil

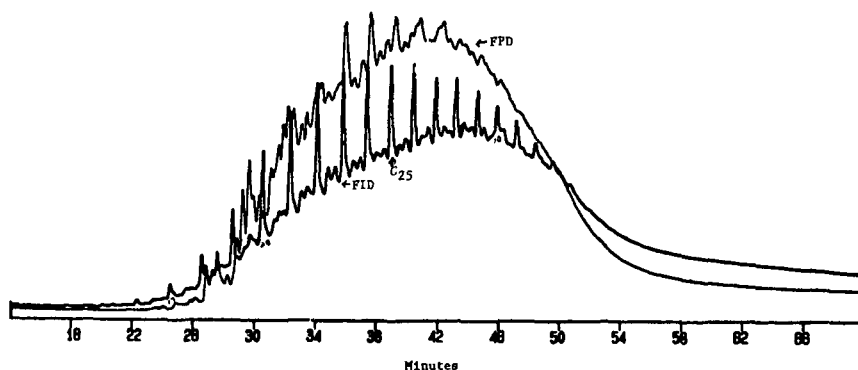
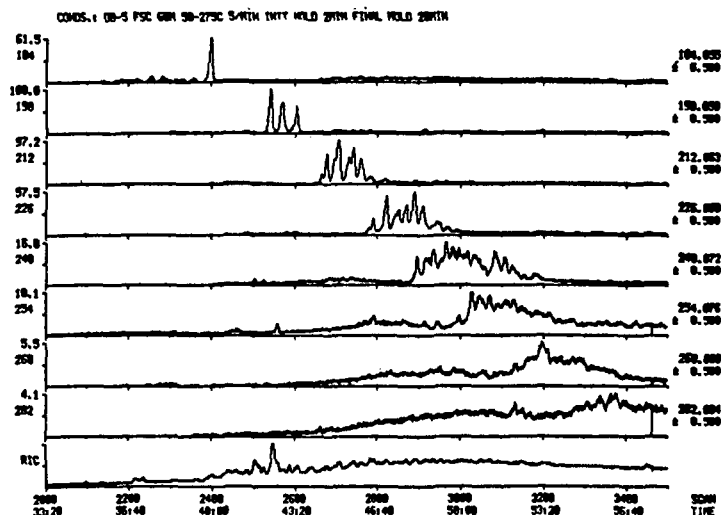


FIGURE 2  
Specific Ion Chromatograms for Dibenzothiophene and  
Substituted Dibenzothiophenes in Maya ATB Neutral Oil, Aromatic Fraction



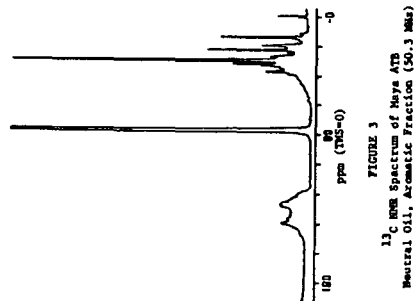


FIGURE 3

$^{13}\text{C}$  NMR Spectrum of Maya ATB  
Neutral Oil, Aromatic Fraction (50.3 Mhz)

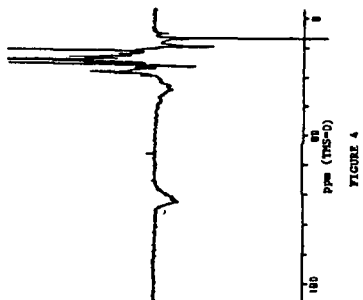


FIGURE 4

$^{13}\text{C}$  INEPT Spectrum of Maya ATB  
Neutral Oil, Aromatic Fraction (50.3 Mhz)

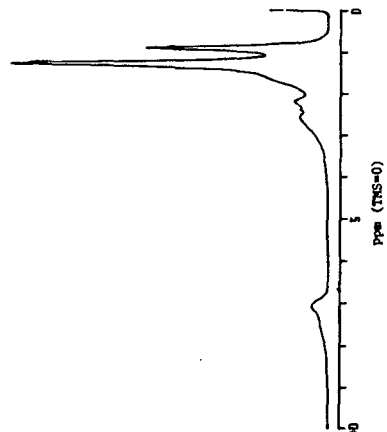


FIGURE 5

200 MHz  $^1\text{H}$  NMR Spectrum of Maya ATB  
Neutral Oil, Aromatic Fraction

## MEASUREMENT OF ORGANIC SULFUR IN FOSSIL FUELS

K.C. Hsieh, B.T. Tseng, M. Buckentin and C.A. Wert  
Materials Research Laboratory and Department of Metallurgy and Mining  
Engineering, University of Illinois, Urbana, IL 61801  
and

Gary Dyrkacz  
Chemistry Division, Argonne National Laboratory  
Argonne, IL 60439

### ABSTRACT

A method of direct determination of the organic sulfur content of solid fossil fuels has been developed using the transmission electron microscope. The technique uses the detection of the  $K\alpha$  line of sulfur to measure the presence of sulfur and the volume from which this radiation comes is measured using the bremsstrahlung radiation counted simultaneously with the sulfur line. Applications have been made to the organic sulfur content of whole and treated coals, to amber and to kerogen in oil shale. The greatest value of the method is its ability to measure the variation of organic sulfur content over extremely fine distances.

### INTRODUCTION

Sulfur is found in coal in two principal forms: mineral sulfur (principally pyrites) and organic sulfur distributed through the carbonaceous matter. The conventional method of determination of the organic sulfur content is a two step process (1). First, total sulfur is measured. Then the pyritic and sulfatic sulfur is determined after selective dissolution of the minerals with acids. The organic sulfur is calculated as the difference between the total sulfur and the mineral sulfur. This commonly used ASTM procedure (method D 2492) is apparently sound when applied to raw coals, but there may be problems with analysis of chemically processed coals (2,3). Furthermore, this method provides only an average sulfur concentration and is unable to distinguish among possible variations either spatially or among the maceral types.

A number of investigators have examined the possibility of direct measurement of organic sulfur in coal which does not depend upon this difference technique. These methods have commonly utilized the x-ray emission lines of sulfur to detect its presence and have used a variety of standardization techniques to provide numerical data and to differentiate among the variety of sulfur forms which may be present. Several earlier papers have described these techniques (4-11). Among them, the extensive work of Raymond and Gooley and of Straszhheim and Greer should be especially noted. The resolution of these techniques using either the electron microprobe or the SEM is about  $5\mu$ , so the volume of each measurement is immensely less than that of the standard ASTM technique. Determination of average values using the microprobe or SEM instruments does require the averaging over a number of individual observations to take account of possibility of variability in organic sulfur content from place to place in the coal.

We have extended this electron-optical technique to even finer spatial resolution using the transmission electron microscope. The specimens are either finely divided powders or foils of coal which are thin enough to be practically transparent to the electron beam. The technique has been adapted from methods developed by Hall and his collaborators for measurement of organically dispersed elements in biological tissue (12-15). We have developed applications of the technique, standardized the method for our microscope and have presented first results in a publication in Fuel (16). We refer only briefly to the chief features of the technique here.

## THE TEM METHOD

The geometry of the measurement is sketched in Fig. 1. An electron beam is incident upon a coal foil which is less than  $1\ \mu$  thick. Ionizing collisions with atoms in the irradiated volume cause the emission of characteristic x-ray lines which can be counted by an appropriate detector. At the same time, the background radiation is counted from the same volume. The  $K\alpha$  line of sulfur has an energy of about 2300 eV and we measure the bremsstrahlung radiation over the range 10-18 keV; a typical spectrum is sketched in Fig. 2. The organic sulfur concentration of the volume being irradiated by the electrons is simply related to the ratio of these two count rates:

$$S(\text{wt}\%) = A C_S / C_b \quad 1)$$

We have found this equation to be well satisfied for thin specimens and have determined the proportionality constant A using known sulfur standards. For our instrument and the geometry of our detector, A has the value 1.6. This number varies slightly among the coals because the bremsstrahlung radiation is somewhat dependent on the C/O ratio in the hydrocarbon matrix. This variation is slight however, being only a few percent for coals from the sub-bituminous to anthracite range.

We emphasize that success of the method is achieved only if the coal foil is thin enough that the electron beam is essentially undiminished in passing through the foil so that the intensity of ionization of the elements in the coal is uniform throughout the irradiated volume. Furthermore no absorption of either the sulfur line or the bremsstrahlung radiation should occur in the specimen. For coal foils less than  $1\ \mu$  in thickness, these conditions are amply met.

## APPLICATIONS TO COAL

### Measurement of the Average Organic Sulfur Content

We have tested the technique using a high organic sulfur bituminous coal and a low organic sulfur anthracite. Ten thin foils from each coal were prepared and five measurements were made on each foil. The total of fifty measurements for each coal is averaged to give the organic sulfur content. The organic sulfur content of a third coal, a low sulfur bituminous, was determined by examining the sulfur content of powdered macerals. The graph in Fig. 3 shows that results from this method compare very well with those from the standard ASTM method for these three coals. We could make additional measurements of this type, but we have elected to utilize the most valuable feature of this technique, namely the spatial variation.

### Spatial Variation of the Organic Sulfur Content

A measurement was made over a coal maceral (presumably vitrinite) in an Illinois #5 coal. That variation is sketched in Fig. 4. The average value is about 2.6 wt% organic sulfur with a variation of about 25% about this mean. At one point in the maceral a slight excursion away from the edge showed a much higher organic sulfur content locally, some 3.5%.

We have made additional measurements of variation of sulfur concentration around mineral particles in coal, and find some variation. We were not completely sure that that variation was not a function of the maceral type in which the mineral was located, rather than being due to the mere presence of a mineral. Consequently, we need to carry out additional work to show the factors on which this variation depends. In particular, we are interested to see whether the organic sulfur varies as one approaches closely to a sulfide particle or whether it remains constant right up to the edge of the particle. Further, we would like to see whether the organic sulfur concentration in the vicinity of a sulfide is

altered as the coal is heated into the temperature range where sulfides are known to decompose (some 700 K). Measurements of both types are in progress.

#### Variation of Organic Sulfur Between Submaceral Types

We wished to see whether the variation we observed in organic sulfur content in repeated measurements on some coals was due to random spatial variation or whether it might be due to variation in sulfur content of maceral types. It is known that the organic sulfur content of coals varies in the order  $S(\text{exinite}) > S(\text{vitrinite}) > S(\text{inertinite})$ . Our technique seems to have the capability of determining this on a fine scale. We have made measurements on a coal which had been separated into maceral fractions. We used an Indiana bituminous coal, PSOC 106, which had been separated into maceral fractions by the gradient-centrifuge method employed at the Argonne National Laboratory (17,18). Our first measurements on the gross maceral types showed the expected general trend. For the inertinite the average was 0.428 wt%, for the vitrinite, 0.61 wt% and for the exinite 1.2 wt%. Multiplying these numbers by the known fractions of the maceral types gave an average value of 0.64 wt% S, observations made by Dyrkacz independently gave an average value of 0.57 wt%. His measurements are discussed further in more detail (19).

The most significant feature of these measurements was not the average values, but the range of organic sulfur content for the three maceral types. In particular, the exinites gave wide variation, from 0.03 to 2.31 wt% for the fifty-five observations made on that maceral type.

We then took maceral fractions separated on an even finer scale so that the organic sulfur content of submaceral types could be determined independently of each other. We took 12 density fractions of this coal, 5 exinites, 3 vitrinites and 4 inertinites. Each was measured independently. Data for these three vitrinites are displayed in Fig. 5. These graphs show the organic sulfur content measured over many micron size particles of particular density fractions. The averages are listed on the graphs and the spread about the averages is evident.

A plot of the average organic sulfur content of all 12 maceral fractions is shown in Fig. 6. One sees a gradual curve, rising from the dense inertinites toward the lighter vitrinites into the exinite. Then the curve goes through a high value at a density around 1.18, and falls off toward the lighter fractions.

The peak value of organic sulfur content about the density 1.18 is striking. Since it is believed that the maceral sporinite has about this density, we elected to measure the organic sulfur content of an individual sporinite maceral embedded in whole coal, not separated from its surrounding by fine grinding. A specimen of Illinois #5 coal was examined by reflectance microscopy until a sporinite maceral was observed embedded in surrounding vitrinite macerals. A hole appropriate for electron microscope observation was milled at this point. The organic sulfur content of this area was measured from one vitrinite maceral through the sporinite into the other vitrinite maceral. As was expected, the organic sulfur content of the sporinite maceral was much higher than that of the surrounding vitrinite macerals, see Fig. 7. Furthermore, the organic sulfur content rises sharply at the boundary between the vitrinite and sporinite macerals.

This poses an interesting question. Is the high organic sulfur of sporinite a function of high organic sulfur in the initial spore and would it be true for pollens as well? We are examining these questions.

## AMBER

Amber is a fossilized resin from either deciduous trees or needle trees. It is akin to the resinite maceral type in coal. Therefore we desired to measure the organic sulfur content of amber to see how it would fit in this scheme. A measurement on an amber of Dominican origin showed that the organic sulfur content was low, much less than 1%, and that it varied from about 0.14 to 0.3 with an average value over six measurements of 0.2 wt% sulfur. Similar measurements for a Baltic amber gave an average value of about 0.33% organic sulfur with only a small variation about this mean. These measurements are consistent with the data in Fig. 6 which indicate that resinite, a low density maceral, should be on the lower end of a curve such as that in Fig. 6. We are now examining resinite maceral fractions taken from whole coals to determine the validity of this observation.

Amber also has other lines in the x-ray emission spectrum showing that other elements may be present in organically distributed form, see Fig. 8. In addition to the  $K\alpha$  line of sulfur, lines for Cl, K and Ca are present. We believe that these elements too are organically distributed, although one cannot rule out the possibility of there being tiny precipitates below the limits of resolution of the electron microscope (some 20 Å or so). Since lines for Al, Si and heavy metals are absent, precipitates of a clay-like nature or of minerals containing iron, copper and other heavy metals are not to be seen. The measurement does show that organic elements other than sulfur might be detected and measured using the electron microscope technique, with appropriate standardization of the constant A in Equation 1.

## OIL SHALE

Oil shale contains carbonaceous matter distributed in pores in the massive mineral crystals and also as an interparticle film between the mineral crystals. An electron microscope observation of a thin foil of a Green River shale from the mahogany zone is shown in Fig. 9. The kerogen is the light material between the dark mineral blocks. One also sees that smaller minerals are also embedded within the kerogen film; in this particular specimen they are a phosphate. We have measured the organic sulfur content along a line in a kerogen film over a distance of about 100  $\mu\text{m}$ . Six observations were made; they range in value from 0.2 wt% to 1.3 wt% with an average value over 6 randomly spaced points of about 0.4 wt% sulfur.

We emphasize that this technique is a valuable method of measuring the organic sulfur content of the carbonaceous matter in oil shale in situ. Furthermore, the variation over different regions in the kerogen could readily be determined.

## SUMMARY

The technique we have described measures the organic sulfur content of fuel materials directly. It must be standardized to a particular microscope and detecting system. Small variations in the proportionality constant A exist among the various carbonaceous matrices, but these are at most 5-10%. The technique is probably not valuable for measuring the average organic sulfur content of coals where the standard ASTM method might be employed, since the electron microscope is expensive to use and demands careful specimen preparation. However, it has high potential for measuring the organic sulfur content of kerogen, tar sands and other carbonaceous material in situ. Its greatest value, though, seems to lie in its ability to measure small spatial variations in organic sulfur content and in determining the variation of organic sulfur concentration among maceral types in either whole or treated coals. Finally it has promise in determination of changes in organic sulfur content which accompany heat treatments or chemical treatments.



#### ACKNOWLEDGEMENTS

Support for staff of the University of Illinois were supported by the Division of Materials Research, DoE, under contract DE-AC02-76ER01198. Part of the support for K.C. Hsieh and M. Buckentin also came from the Center for Research on Sulfur and Coal through the State of Illinois affiliated with the University of Illinois.

#### REFERENCES

1. Annual Book of ASTM Standards, ASTM D2492, Standard Test Method for Forms of Sulfur in Coal, 347 (1983)
2. Suhr, N. and Given, P.H., Fuel, 60, 541 (1981)
3. Gladfelter, W.L., and Dickerhoof, D.W., Fuel, 55, 355 (1976)
4. Raymond, R. Jr., and Gooley, R., Scanning Electron Microscopy/1978/I, 93 (1978)
5. Raymond, R. Jr., Gregory, T.G., and Gooley, R., Proc. Annual Conf. Microbeam Analytical Soc., 12, 177A (1977)
6. Raymond, R. Jr., Proc. Annual Conf. Microbeam Analytical Soc., 14, 93 (1979)
7. Raymond, Robert, Jr., ACS Symposium Series, No. 205, COAL AND COAL PRODUCTS: ANALYTICAL CHARACTERIZATION TECHNIQUES. Ed. Fuller, E.L. Amer. Chem. Soc. Washington, DC (1982)
8. Sutherland, J.K., Fuel, 54, 132 (1975)
9. Solomon, P.R., and Manzione, A.V., Fuel, 56, 393 (1977)
10. Straszheim, W.E., and Greer, R.T., Scanning Electron Microscopy/1982/III, 1013 (1982)
11. Clark, C.P., Freeman, G.B. and Hower, J.C., Scanning Electron Microscopy/1984/II, 537 (1984)
12. Hall, T.A., Physical Techniques in Biological Research: Optical Techniques, 2nd Ed., Vol. 1A, Ed. G. Oster, 157 (1971)
13. Hall, T.A., Anderson, H.C., and Appleton, T., Jour. of Microscopy, 99, Pt. 2, 177 (1973)
14. Hall, T.A., Jour. of Microscopy, 117, Pt. 1, 145 (1979)
15. Hall, T.A., Microbeam Analysis in Biology, Ed: Lechene, C.P. and Warner, R.R., Academic Press, NY, 185 (1979)
16. Hsieh, K.C., and Wert, C.A., Fuel, in press
17. Dyrkacz, G.R., and Horwitz, E.D., Fuel, 61, 3 (1982)
18. Dyrkacz, G.R., Bloomquist, C.A.A., Ruscio, L., and Horwitz, E.P., 1983 International Conference on Coal Science, International Energy Agency, Pittsburgh, August, 1983, p. 393-396
19. Dyrkacz, G.R., Bloomquist, C.A.A., and Ruscic, L., Fuel, in press

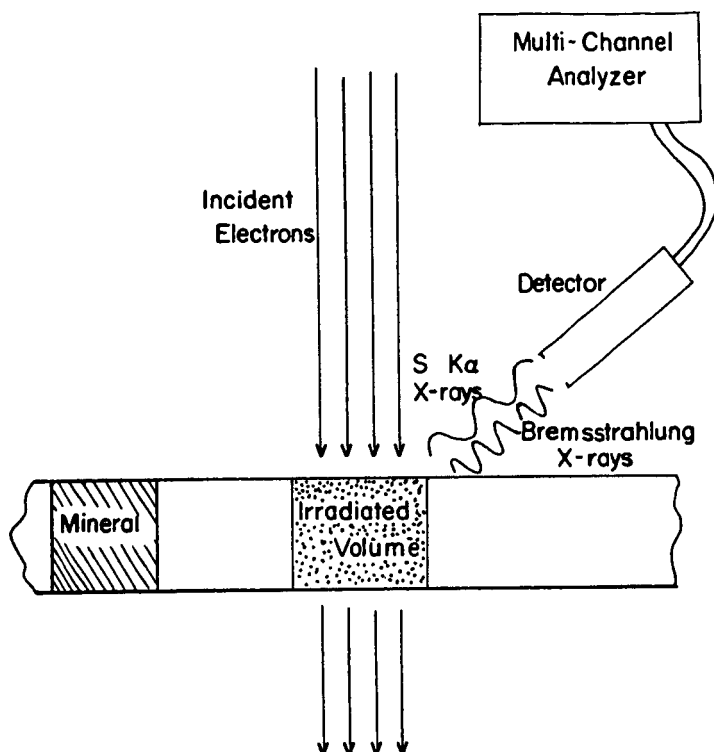


Figure 1. Sketch of x-ray detection system.

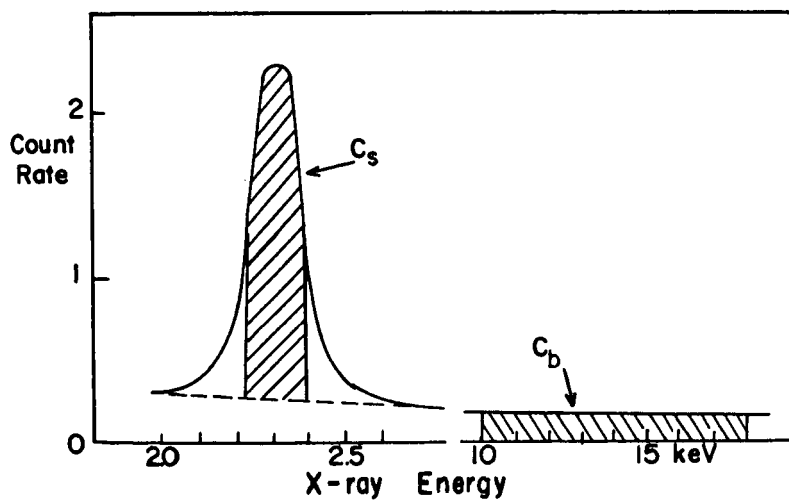


Figure 2. Schematic of counting signals.

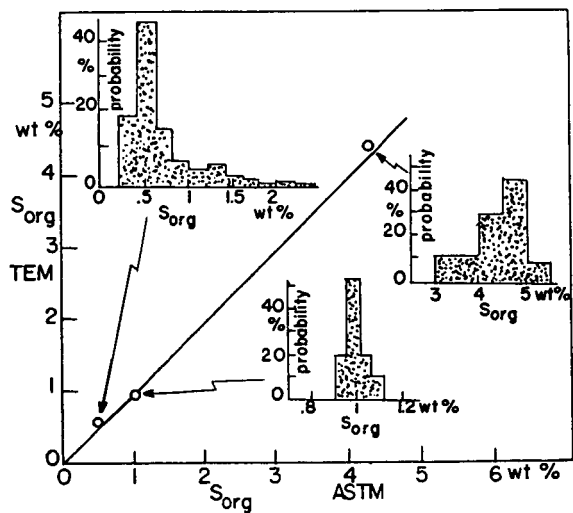


Figure 3. Correlation of measuring techniques.

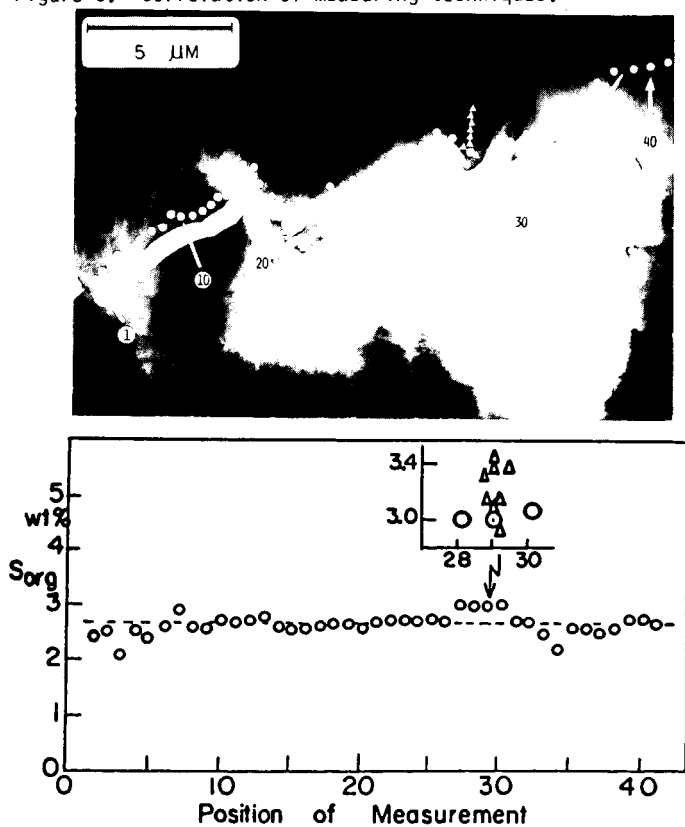


Figure 4. Spatial variation of organic sulfur.

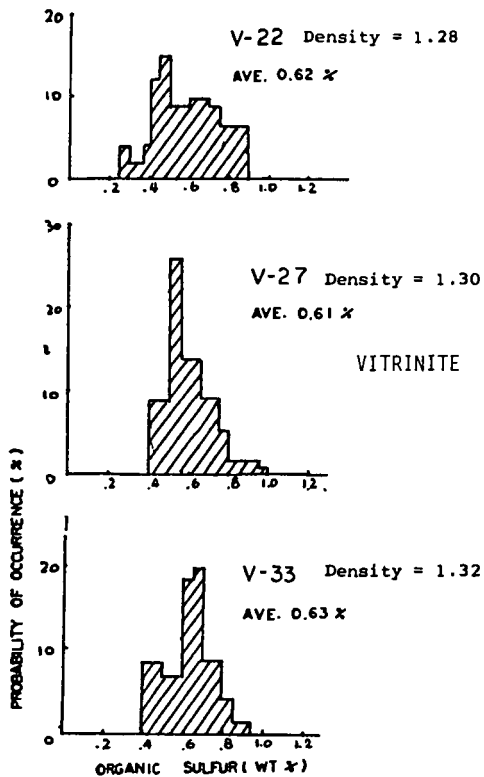


Figure 5. Distribution of  $S_{org}$  concentration.

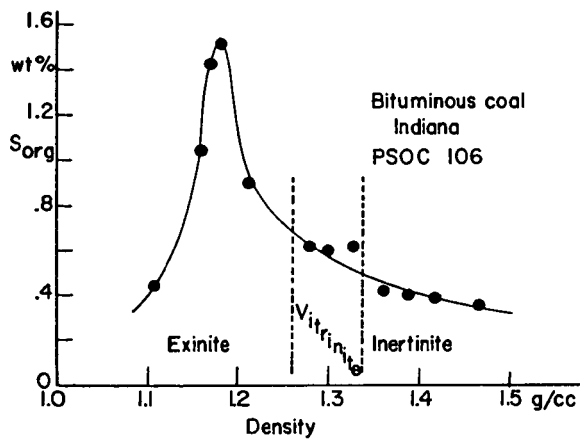


Figure 6. Variation of  $S_{org}$  by maceral type.

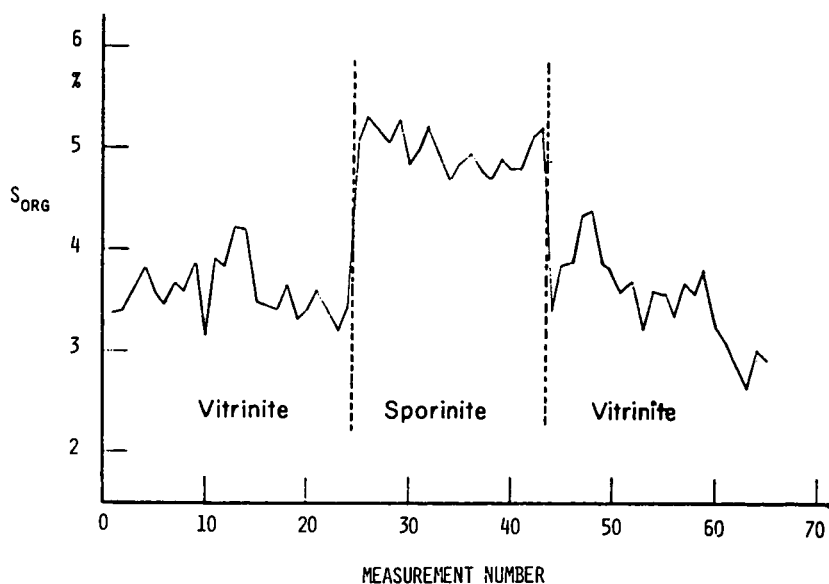
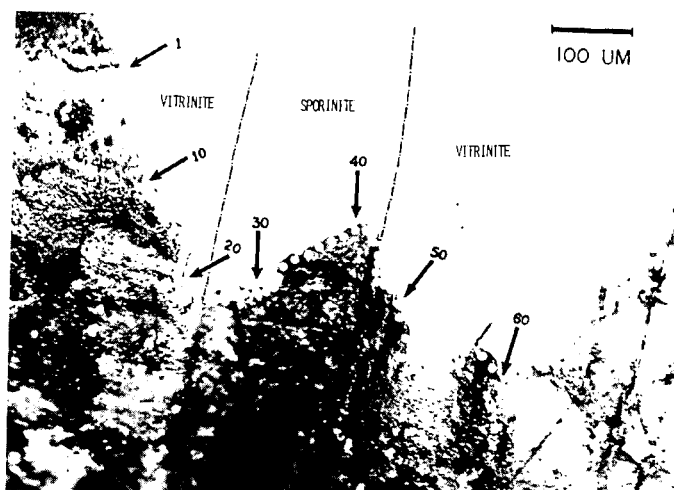


Figure 7. Variation of  $S_{org}$  across a sporinite maceral.

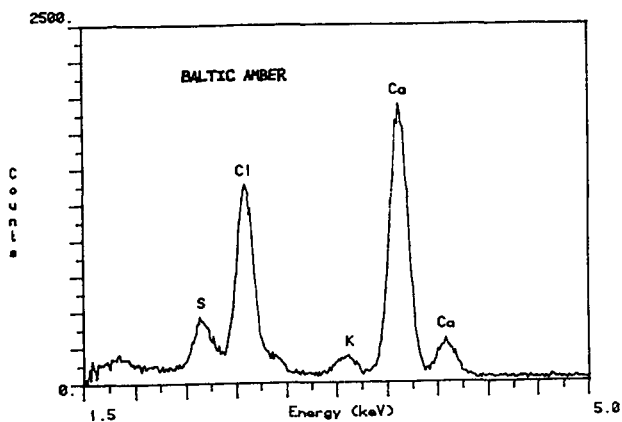


Figure 8. X-ray emission spectrum for amber.



Figure 9. Electron micrograph of oil shale.

# APPLICATION OF SCANNING ELECTRON MICROSCOPY AND AUTOMATED IMAGE ANALYSIS FOR CHARACTERIZATION OF MINERAL MATTER IN COAL

Warren E. Straszheim and Richard Markuszewski

Ames Laboratory\* and Department of Engineering Science and Mechanics  
Iowa State University, Ames, IA 50011

## INTRODUCTION

The value of the scanning electron microscopy in providing in-situ information on the microstructure of materials such as coal is well known. It is particularly suited for examining the finely distributed mineral particles found in finely-ground coal. In polished cross section, a wealth of size, shape, roughness, and association data can be provided. Addition of an energy-dispersive x-ray analyzer permits chemical analysis to be performed on these minute features, thus allowing a tentative identification of the mineral phase.

The use of automated image analysis (AIA) in conjunction with scanning electron microscopy (SEM) and energy-dispersive x-ray analysis (EDX) is gaining ever wider acceptance as a powerful tool for the in-situ characterization of mineral matter in coal (1). The SEM-AIA technique is able to combine data from SEM and EDX measurements to provide detailed information on sample character that is not available from other analytical methods. The unique features of AIA include information generated for size, shape, composition, and association of mineral phases with the coal matrix.

The SEM-AIA technique is applicable to a wide variety of characterization problems. Because the in-situ nature of this capability can provide quantitative information on the distribution of the mineral species present in coal, it lends itself particularly well to the characterization of minerals in raw and processed coals. Distribution of minerals by both phase and particle size is of great importance to almost any work on coal, but it is especially useful to coal plant operators in determining the steps necessary for effective and efficient removal of undesirable mineral phases during cleaning (2). It is not adequate to know only the relative amounts of the mineral phases present; such information is available from x-ray diffraction or infra-red spectroscopy. But the size of the minerals and their relation to the coal matrix is just as important. Such information was provided in a recent publication of our studies (3). In that work, the mineral matter distribution in raw coals and coals supercleaned by float-sink techniques was described.

In this work, the SEM-AIA technique as an analytical method for coal will be described. The discussion will include particle detection and measurement, mineral phase identification by x-ray analysis using a file of chemical definitions, and the number of particles needed to develop reliable results and adequate reproducibility between samples. In addition, attention will be given to problems in the application of AIA techniques to coal, including difficulties arising from a wide spread in the minimum and maximum particle sizes, problems in the apparent enrichment of pyrite content due to instrumental factors, and the special case of characterizing chemically treated coals.

\* Ames Laboratory is operated for the U. S. Department of Energy by Iowa State University under Contract No. W-7405-Eng-82.

The SEM-AIA techniques have been applied at the Ames Laboratory to many samples of bituminous and sub-bituminous coals to characterize their mineral content for studies of cleanability. Results from some of those studies will be used to illustrate the application and limitations of this technique.

#### BACKGROUND

Combined SEM-EDX techniques have been able to provide much information with manual operation, but results were qualitative and subject to operator judgment. The development of automated control for the SEM has permitted the same information to be extracted objectively, quantitatively and less tediously. The main limitation of the manual techniques is the human factor, since the analysis of particles for size and elemental composition is tedious. Human operators are severely limited in the rate and amount of data that they can reasonably produce. There is also a possibility of operator bias in not treating all particles alike. The intelligence of a human operator is a fantastic advantage, but the limitations on the operator are also significant.

The task of the automated image analyzer is to assume the repetitive duties of the SEM operator in such a way that statistically significant number of particles can be analyzed in a reasonable amount of time and to tabulate the data in a meaningful format. The following paragraphs describe the operations involved.

The first requirement of particle characterization is feature identification and sizing. A human operator is able to work with gross signal contrast and rather subtle edge effects to determine feature outline. As a rule, the microcomputers and electronics used in image analysis in the lab are presently restricted to determining particle boundaries, or extents, from the rather gross measure of contrast in the signal level. Therefore, sufficient contrast is required in the video signal between two phases of interest to permit differentiation of the phases. Backscattered electron imaging is very sensitive to the average atomic number of a phase and, therefore, provides high contrast between minerals of relatively high atomic number and lower atomic number coal and mounting material. A specialized analog-to-digital converter, called a "threshold selector," is used to inform the computer which pixels are above threshold and belong to a phase of interest, and which pixels are below threshold and therefore indicate background phase. The computer is thus able to discern which picture elements belong to coal, mineral, or background.

The mode of extracting information on the particle extents is complicated. In many image analysis systems built around optical microscopes and TV cameras, the whole image is digitized for processing. For SEM operations this is often not practical. Often the signal from an SEM exhibits a relatively low signal-to-noise ratio requiring that several frames be averaged to provide an adequate signal. Also, some older SEM instruments do not respond well to the scanning speed demands of TV imaging rates. In addition, it is only recently that backscattered electron detectors have become available that can operate at TV-rates. Therefore, it has been common for SEM-based image analyzers to employ some form of digital beam control to direct the beam on the sample in such a fashion as to extract the most information in the least time. A number of software algorithms are available with our AIA system to discern particle extents.

Once the particle extents have been determined, the chemical identity of a particle is determined. The image analyzer directs the SEM beam to the center



of the particle of interest and directs the EDX analyzer to collect an x-ray spectrum. Whereas a human operator can quickly scan the entire x-ray spectrum to locate and identify the significant x-ray peaks, the image analyzer must monitor regions of interest defined about x-ray lines of interest. For many mineral analyses, only 11 common elements are necessary. They are, in increasing atomic number: Na, Mg, Al, Si, P, S, Cl, K, Ca, Ti, and Fe. Additional elements can be also monitored if they are suspected to occur in trace quantities. Based on the relative intensities of the x-ray signals, particles are classified into one of several mineral categories according to definitions such as those given in Table 1. For many AIA applications, including coal mineral analyses, it is reasonable to define the chemical categories rather loosely and still to discern the various mineral components. In fact, for many minerals, it is necessary only to define the elements that must be present to define a mineral. Quartz and calcite are examples for which only a single element is needed (Si and Ca, respectively). However, for the clay minerals, more sophisticated definitions are necessary to differentiate the phases.

Table 1. Ranges of Elemental Compositions, Ratios, and Other Features for mineral phase definitions.<sup>a</sup>

Mineral Phase	Chemical Definition in % Range <sup>b</sup>	Density
Pyrite	S 10-80, Fe 10-70	5.00
Kaolinite	Al 15-80, Si 15-85 Al/Si ratio 0.4-2.5	2.65
Illite	Al 15-80, Si 20-85, Fe 0-40, K 2.5-35, Na 0-20	2.75
Montmorillonite	Al 10-75, Si 19-80, Na 0-30, Ca 0-30	2.30
Quartz	Si 60-100	2.65
Calcite	Ca 70-100	2.80
Minors (included are the following categories)		
Gypsum	S 10-80, Ca 10-70	2.30
Dolomite	Mg 5-60, Ca 60-100	2.90
Iron-rich (e.g. siderite)	Fe 90-100	3.90
Chlorite	Al 10-75, Si 10-80, Mg 0-30, Fe 0-30 (Mg or Fe required)	3.00
Rutile	Ti 70-100	4.50
Al-Rich	Al 75-100	4.00
Apatite	P 10-40, Ca 30-100	3.20
Silicates	Si 40-100	2.70
Miscellaneous	All other elemental compositions not specifically defined	2.00
Not included	Signals with <1000 total x-ray count	

<sup>a</sup> Modified after Reference 3.

<sup>b</sup> Additional specifications are often given for other elements that are allowed to be present. Although such specifications allow the presence of minor elements not specifically listed in the chemical definition, they place an upper limit on the allowable amount.

#### EXPERIMENTAL

The AIA-SEM system at Iowa State University consists of a JEOL (Japan Electron Optics Laboratory) model JSM-U3 scanning electron microscope, a LeMont Scientific B-10 image analyzer, and a Tracor Northern TN-2000 energy-dispersive x-ray spectrometer. The software-based AIA system contains associated electronics for SEM beam

control, image amplification, and thresholding. For AIA, the software base allows selection of the appropriate analysis algorithm for the particular sample and image conditions encountered.

Actual analyses were performed on pellets of coal mounted in an epoxy or polyethylene matrix according to standard petrographic procedures. The pellets were polished to a cross section and coated with carbon to render the surface electrically conductive for SEM examination. Samples were analyzed in the SEM under 50-500x magnification, using 25 kV beam voltage, 1-2 nA sample currents, and backscattered electron imaging. A point density of 1024 pixels across the screen was used to provide  $\pm 10\%$  accuracy on measurements as small as 1% of the field of view. X-ray data were collected for four seconds per particle at a typical rate of 1000 counts per second. The intensities of 30 elements were set to be monitored in regions of interest. Approximately 4000 particles were analyzed per sample, at a rate of 200 particles per hour.

The AIA procedures classify mineral particles into both size and chemical classes. Area-equivalent diameter was used as the size parameter for data presentation. This measurement is the diameter of a circle with the same area as that measured for the mineral particle. Area-equivalent diameter was used instead of a simple length or width measurement because the outline of mineral particles in coal is often complex enough to render such measurements meaningless. The equivalent diameter measurement allows particles to be classified by the area of the particle and yet reported in terms of a linear dimension. Using available literature values for the specific gravity of the individual minerals, the data were then expressed as the weight fraction of the mineral matter within a given mineral/size category. The weight fraction data could then be normalized according to the mineral matter content calculated from ash values by using a modified Parr formula (4) to present mineralogical estimates on a dry coal basis. Such a presentation provides a common base for comparing the coals before and after processing.

#### DISCUSSION OF RESULTS AND PROBLEMS

A major problem encountered in the analysis of coal samples arose from the wide size range of particles present. The weight distribution is heavily influenced by the particles in the largest size categories. However, most of the particles are found in the smallest categories. This problem is especially troublesome for relatively coarse samples of where the particle diameter can range from 1 to 1000  $\mu\text{m}$ . As an example, Table 2 presents actual data for such a case, using an Illinois No. 6 coal characterized more fully elsewhere (3).

Since analysis time per particle is dominated by the time of x-ray acquisition which is independent of particle size, it becomes necessary to allocate analysis time among the size categories in order to include a significant number of particles of all sizes. Therefore, analyses were conducted at several magnifications for restricted ranges of particle sizes. A relatively small area was analyzed at high magnification to collect data on small particles, and a much larger area was then analyzed at lower magnification to collect data on large particles. Data were then combined by correcting the weight of particles analyzed in each size range for the area of sample analyzed for that size range. The table of weight fractions was then normalized to 100%. For samples with particularly wide size ranges, three or more size partitions were required to obtain a representative size distribution. As can be seen from Table 2, the actual number of particles counted parallels the weight distribution much closer than does the unadjusted count fraction.

Table 2. Weight and Count Distribution for an Illinois No. 6 Coal  
(Nominally 70-80% less than 200 mesh or 75  $\mu\text{m}$ )

	Area Equivalent Diameter (in $\mu\text{m}$ )					
	0-4	4-7	7-12	12-20	20-36	>36
Count fraction	16.3	51.1	23.3	7.1	1.7	0.6
Weight fraction	2.5	15.3	20.4	21.0	14.4	26.3
% of particles counted	13.6	42.6	25.3	7.8	7.9	2.8
Number of particles counted	654	2055	1221	374	382	136

The statistical distribution involved in AIA analysis is a multinomial distribution, for which the standard deviation of the counts measured for a category is equal to the square root of the count. Thus a count of 100 particles would yield to a relative standard deviation of 10%. Relative error in the weight distribution results can be calculated from the number of particles collected in each category. For a system of four predominant minerals with approximately equal particle abundances, and six size categories, approximately  $4 \times 6 \times 100 = 2400$  particles would be needed for a relative standard deviation of 10% in the data.

This assumption has been borne out in analyses of multiple pellets of the same coal. Five pellets each of three coals were analyzed by AIA. A total of 1500 particles was characterized for each pellet. Standard deviations were calculated from the five estimates of weight fraction in each size/chemical category and compared with the relative error expected from the particle count. Agreement was excellent for categories containing more than ~30 particles.

A problem of artificial enrichment of one phase relative to the others arises when one phase appears much brighter in the image being analyzed than do the remaining phases. In our work with coal minerals (3,5) and in the work of others (6) such a problem was experienced with the mineral pyrite. Typically the pyrite content found by SEM-AIA is substantially higher than what is estimated by the ASTM wet chemical technique (see Table 3). The problem arises in our AIA system since it employs what is known as "global thresholding". In it, a threshold level is established against which image signal levels are compared to determine whether a pixel is part of a particle or part of the background. The recommended procedure is that the threshold be set midway between background and full signal brightness to allocate equally any noise on the particle edges between particle and background. For coal minerals this is strictly not possible. The intensity of backscattered electron image used for analysis is highly dependent on the average atomic number of the material in view. Pyrite is so much heavier than the other mineral phases that the threshold, set at a level at which the clays can be consistently detected, crosses pyrite particles at the 20-30% level and increases the possibility that individual pyrite particles will be measured larger than they are. To compensate for this bias, the U.S. Steel workers (6) recommended an empirical factor of 0.75 for scaling down the pyrite values.

Another possible explanation is that the brighter signal for pyrite causes small particles of the mineral to have a better chance of rising above threshold as opposed to the signal being diminished to a level below the threshold by the fact that a large percentage of the electrons pass completely through the particle before backscattering, causing the signal brightness to be lower than the signal from a massive particle. However, this explanation does not account for much of the error

observed since only a relatively small amount of the pyrite is found in the smallest size ranges.

Table 3. Comparisons of ASTM and SEM-AIA Estimates of Pyrite and Pyritic Sulfur Sulfur Content for Raw and Supercleaned Coals (recalculated from data of Reference 3)

	Illinois No. 6		Pittsburgh No. 8	
	Raw	Cleaned	Raw	Cleaned
<u>Pyritic Sulfur</u>				
ASTM	2.37	0.22	1.35	0.03
AIA	4.22	0.63	2.50	0.52
<u>Pyrite/Mineral Matter<sup>a</sup> Ratio</u>				
ASTM	22.93	13.48	30.55	1.66
AIA	40.86	38.53	56.54	28.59
Fe by XRF (%)	2.01	0.38	1.64	0.44
Total S (ASTM)	5.10	2.54	3.17	1.82
Organic S (ASTM)	2.36	2.27	1.42	1.67
Mineral Matter <sup>a</sup>	19.32	3.05	8.26	3.37

<sup>a</sup> Mineral matter = 1.13 (ash) + 0.47 (pyritic sulfur), as in reference 4.

For chemically processed coals, problems arise with the chemistry definitions. New mineral phases may be formed during processing that bear little resemblance to the original minerals. It may become necessary to analyze the material with alternate techniques, such as x-ray diffraction, in order to determine what phases are present. Then the necessary chemical definition can be built into the file knowing the chemistry of the new phases. Alternatively, an automatic classification option can be employed to sort particles routinely based on the relative amounts of the elements present.

Some of our work with the direct determination of organic sulfur in raw and chemically treated coal by an SEM-EDX technique (7) and additional analysis of mineral matter in those samples by FTIR spectroscopy (8) indicate that the AIA values for pyrite may be correct for at least some samples. The analyses were performed on samples of Illinois No. 6 coal, raw and chemically cleaned by the Gravimelt Process at TRW Inc., in California (8). The samples were analyzed by ASTM techniques for moisture, ash, and sulfur forms; by SEM-AIA for mineral phases; by SEM-EDX for organic sulfur; and by FTIR for mineral phases. The results are presented in Tables 4 and 5.

For the raw coal, the pyritic sulfur values obtained by AIA agreed well with those obtained at TRW. However, they were somewhat higher than the ASTM values obtained at Ames. For the cleaned coal, the pyrite values obtained by AIA and the organic sulfur values obtained by SEM agreed very well with the Ames ASTM results.

The comparison of FTIR data with AIA results in Table 5 shows good agreement for all components except kaolinite. Since the coal had to be low-temperature ashed for the FTIR analyses, and the cleaned coal did not have much ash left, the FTIR results on the cleaned coal are not as informative as the AIA results. The FTIR techniques could not identify much of the mineral matter in the cleaned coal, adding most of it

to the miscellaneous category. Since AIA does not require mineral standards and is not particularly dependent on crystal structure, more particles could be categorized by the chemical definition file.

Table 4. Analysis of Illinois No. 6 Treated by the Gravimelt Process at TRW  
(Values reported as wt. % on a dry basis, except for moisture)

	RAW COAL			TREATED COAL		
	TRW Results	ASTM At Ames Lab	SEM/AIA Results	TRW Results	ASTM At Ames Lab	SEM/AIA Results
Moisture	15.81	1.84	----	----	6.33	-----
Ash	9.97	9.23	----	0.51	0.53	-----
Mineral Matter <sup>a</sup>	-----	10.92	----	----	0.61	-----
Total S	4.21	4.03	----	0.57	0.59	-----
Pyritic S	1.36	1.04	1.46	----	0.02	0.026
Sulfate S	0.05	0.09	----	----	0.02	-----
Organic S	2.80	2.90	2.13	----	0.35	0.32

<sup>a</sup> Mineral Matter = 1.13 (ash) + 0.47 (pyritic sulfur), as in reference 4.

Table 5. FTIR and AIA Results of Raw and Chemically Treated Illinois No. 6 Coal  
(values expressed as wt. % of total mineral matter present)

	RAW		TREATED	
	FTIR	AIA	FTIR	AIA
Kaolinite	12.0	7.4	4.0	8.4
Illite	31.5	29.8	----	10.2
Quartz	19.0	20.0	10.0	13.9
Calcite	1.5	1.3	----	3.7
Pyrite	----	23.3	----	8.4
Miscellaneous	36.0	18.1	86.0	46.0

In addition, the AIA technique provided information on particle size distribution as well as mineral phase identification (see Table 6). Such information, of course, cannot be provided by the FTIR technique.

#### CONCLUSIONS

The SEM-AIA technique has been shown to be a useful tool in characterizing the mineral matter of coal by chemical composition as well as particle size distribution. The fundamental aspects of this analytical technique have been described, including the method of defining mineral phases by chemical composition, requirements for the number and size of particles to be samples for reliable and reproducible results, comparison of this technique with other methods of characterizing coal mineral matter, and some problems associated with the application of this technique to measurements of pyrite and analysis of chemically treated coals.

TABLE 6. AIA Classification of Mineral Matter in Illinois No. 6 Coal by Chemistry and Area-Equivalent Diameter of Particles (in  $\mu\text{m}$ ), Expressed as Weight Percent of the Total Mineral Matter Only.

Mineral Phase	<u>Raw Coal</u> Particle size ( $\mu\text{m}$ )						Total <sup>a</sup>
	< 6.3	6.3-19	20-62	63-199	200-632	>632	
Pyrite	2.16	7.97	7.02	6.14	0.00	0.00	23.29
Kaolinite	1.34	3.81	1.52	0.70	0.00	0.00	7.37
Illite	4.27	7.29	4.90	5.08	8.28	0.00	29.82
Quartz	4.47	9.15	3.95	1.98	0.51	0.00	20.06
Iron-rich	0.04	0.22	0.49	1.16	0.00	0.00	1.91
Calcite	0.05	0.06	0.08	0.21	0.92	0.00	1.32
Silicates	1.57	2.19	1.38	1.47	0.98	0.00	7.59
Miscellaneous	1.64	4.13	0.70	0.40	1.73	0.00	8.60
Total <sup>a</sup>	15.54	34.83	20.04	17.15	12.42	0.00	100.00

Mineral Phase	<u>Clean Coal</u> Particle size ( $\mu\text{m}$ )						Total <sup>a</sup>
	< 6.3	6.3-19	20-62	63-199	200-632	>632	
Pyrite	2.74	4.54	1.09	0.00	0.00	0.00	8.37
Kaolinite	4.20	3.35	0.89	0.00	0.00	0.00	8.43
Illite	5.78	4.41	0.00	0.00	0.00	0.00	10.19
Quartz	6.82	6.42	0.67	0.00	0.00	0.00	13.91
Iron-rich	1.93	2.66	0.00	0.00	0.00	0.00	4.59
Calcite	1.63	2.06	0.00	0.00	0.00	0.00	3.69
Silicates	1.71	2.50	0.64	0.00	0.00	0.00	4.85
Miscellaneous	14.34	21.60	10.03	0.00	0.00	0.00	45.97
Total <sup>a</sup>	39.15	47.53	13.32	0.00	0.00	0.00	100.00

<sup>a</sup> Totals may be slightly off due to rounding.

#### ACKNOWLEDGEMENT

This work was supported by the Assistant Secretary for Fossil Energy, Division of Coal Utilization, through the Pittsburgh Energy Technology Center Coal Preparation Branch. The authors wish to thank Drs. R.A. Meyers and W.D. Hart from TRW, Inc., for supplying the Gravimelt-treat coal samples, Dr. P. Painter at Pennsylvania State University for obtaining the FTIR data, and G. Norton from Ames Laboratory for supplying the ASTM analyses.

REFERENCES

1. F.E. Huggins, G.P. Huffman, and R.J. Lee, in Coal and Coal Products: Analytical Characterization Techniques, E.L. Fuller, Jr., ed., ACS Symp. Series 205, Am. Chem. Soc., Washington, D.C., 1982, pp. 239-258.
2. T.D. Wheelock and R. Markuszewski, in The Science and Technology of Coal and Coal Utilization, B.R. Cooper and W.A. Ellingson, eds., Plenum Press, New York, 1984, pp. 47-123.
3. W.E. Straszheim and R. Markuszewski, Am. Chem. Soc. Div. of Fuel Chem. Preprints 29(4), 310-318, (1984).
4. P.H. Given and R.F. Yarzab, in Analytical Methods for Coal and Coal Products, Vol. II, C. Karr, Jr., ed., Academic Press, New York, 1978, pp. 3-41.
5. R. Markuszewski, G. Norton, and W. Straszheim, in Fossil Energy Quarterly Report (April 1, 1983 - June 30, 1983), IS-4548, Ames Laboratory, Iowa State University, Ames, IA, 50011, pp. 35-47.
6. F.E. Huggins, D.A. Kosmack, G.P. Huffman, and R.J. Lee, Scanning Electron Microscopy/1980, Vol. I, pp. 531-540.
7. W.E. Straszheim, R.T. Greer, and R. Markuszewski, Fuel 62(9), 1070-1075 (1983).
8. R. Markuszewski and W. Straszheim, in Fossil Energy Quarterly Report (January 1 - March 31, 1983), IS-4835, Ames Laboratory, Iowa State University, Ames, IA, 50011, pp. 43-50.

## CHARACTERIZATION OF COAL MORPHOLOGY BY SMALL ANGLE X-RAY SCATTERING (SAXS)

Mark Foster and Klavs F. Jensen

Department of Chemical Engineering and Materials Science  
University of Minnesota, Minneapolis, MN 55455

### INTRODUCTION

To fully understand heterogeneous reactions involving porous substances such as coal, one must have a good picture of the pore structure. This picture must reflect characteristic dimensions of the pores, their connectedness, and the surface area available for reaction on the pore walls. While the chemical structure of the coal determines the kinetics of fluid-coal reactions at the surface, the porous structure dictates how much surface is available for reaction, and what role mass transfer will play in the overall rate of reaction.

Conventional techniques for investigating pore structure, e.g. gas adsorption and Hg porosimetry, have played important roles in providing our present understanding of this structure. However, data from these methods often lead to incomplete and contradictory conclusions. Adsorption works well when measuring surface areas of nonporous or macroporous substances with chemically homogeneous surfaces. However, porosity of size scale less than 30Å is difficult to characterize with adsorption. Chemically inhomogeneous surfaces are also difficult to study. The adsorption probe molecule may adsorb preferentially on specific sites and these sites may or may not be active sites in a fluid-solid heterogeneous reaction of interest. Mercury porosimetry also works best with macroporosity. Depending on the compressibility of the sample matrix, the lower limit of pore diameter one probes may vary from 200Å to 40Å for coals (1).

Small angle x-ray scattering (SAXS) is an attractive alternative characterization technique because, above all, it is nonintrusive. Since x-rays readily penetrate the entire sample, all pores are accessible to investigation including isolated pores, i.e. those not connected to a pore leading to the particle surface. Furthermore, SAXS can study micropores as small as 10Å in diameter as well as macropores of up to 500Å in diameter. These limits may be extended using x-ray cameras designed for studying high angles or very low angles. The most exciting characteristic of SAXS is its potential for in-situ studies where the sample structure may be continually probed as it is subjected to reaction conditions.

### EXPERIMENTAL METHODS

The objectives of the present SAXS studies are 1) to measure the specific surface area of the sample and 2) to infer a pore size distribution. In pursuing these objectives three types of samples are used; a model microporous carbon, three coals, and a porous  $\gamma$ -alumina. The model carbon is Carbosieve-S, a pure carbon molecular sieve distributed by Supelco, Inc. The manufacturer quotes a surface area of 860 m<sup>2</sup>/g for this product, but does not specify the measurement technique. Conventional N<sub>2</sub> BET analysis yields a value of 1100 m<sup>2</sup>/g. The carbon's highly homogeneous microporosity has been imaged with transmission electron microscopy by Fryer (2).

Basic data on the three coal samples is summarized in Table I. The anthracite coal, with its low mineral matter content and high carbon content provides the best approximation to a true two phase system of carbon and void. Anthracite, more than lower rank coal, also has microporosity similar to that in Carbosieve. The first scattering experiments with coal were therefore performed with anthracite. The other two coals were used in a study of pore change with pyrolysis due to their higher volatile matter content.

The Carbosieve and coal samples were gasified in pure CO<sub>2</sub> at 825°C and 1 atm in a thermogravimetric apparatus (TGA). The proper precautions were taken to ensure



Table I. PSOC Coal Samples

Type	PSOC #	Name	% C	% Mineral
Anthracite	870	Primrose	93.05	2.90
Low Volatile Bituminous	127	Lower Kittanning	84.45	5.16
High Volatile Bituminous	980	Gentry	80.40	3.97

that this reaction proceeded without mass transfer limitations. The coal samples were slowly pyrolyzed in  $N_2$  in the TGA at a heating rate of  $8^\circ C/sec$  before beginning gasification. A pyrolysis reactor containing a heated wire mesh was used for preparing samples at higher heating rates (up to  $260^\circ C/sec$ ) for the study of varying pyrolysis conditions.

The third type of sample studied here is a porous alumina powder provided by W.R. Grace, Davison Chemical Division. Pore distributions from both  $N_2$  adsorption and Hg porosimetry are provided by the manufacturer. The maximum of the adsorption pore volume distribution lies at a pore radius of  $32\text{\AA}$ , and the pore volume median radius is  $41\text{\AA}$ . The  $N_2$  BET surface area is  $339\text{ m}^2/g$ . Traditional analysis of the porosimetry data yields a radius of  $35\text{\AA}$  for the maximum of the pore volume distribution.

#### SMALL ANGLE X-RAY SCATTERING

X-ray diffraction or "scattering" results from boundaries between phases of sufficiently different electron densities. The large electron density difference between carbon and void generates strong scattering. Figure 1 shows schematically how the x-rays are collimated, diffracted, and detected in the University of Minnesota's modified Kratky camera (3). This configuration allows simultaneous collection of scattering data for values of the scattering vector,  $h$  from 0.015 to 0.43, where

$$h = 4\pi \sin\theta/\lambda \quad 2\theta = \text{scattering angle}$$

The data, once corrected for sample transmission coefficient and parasitic scattering, is most profitably plotted as log intensity against  $\log(h)$ , as in Figure 4. Scattering from small inhomogeneities appear at large values of  $h$ .

All the data presented here were collected with the sample at room temperature. However, a high temperature sample cell, shown in Figure 2, has been designed and constructed for in-situ studies of coal gasification. A carbon sample may be gasified in the reaction chamber while x-rays directed through the boron nitride windows probe the change in pore structure.

Two quantities characteristic of the sample may be obtained from SAXS data without assuming a model of the pore geometry. The first is an estimate of the surface per unit volume and the second is the radius of gyration,  $R_g$ . The specific surface may be estimated from the behavior of the scattering curve for values of  $h$  such that

$$hd_m > 5.0 \quad 1)$$

where  $d_m$  is the minimum dimension of the inhomogeneity. The relationship between the scattering intensity in this region and the sample's specific surface is known as Porod's law (4). Invoking this relationship assumes that the boundaries between phases in the sample are sharp. In practice this calculation is difficult because accurate data are required for a sizeable range of  $h$  where condition 1) is met and the scattering intensity must be accurately measured to small angles also.

The radius of gyration,  $R_g$ , is more widely used and may be calculated by fitting the experimental curve with the Guinier approximation at the lowest angles (5). However, a meaningful  $R_g$  is found only for systems with nearly monodisperse inhomogeneities. Also, in order to relate  $R_g$  to a precise dimension (e.g. radius) of the inhomogeneities one must assume a model for their geometry. In general, it is best to regard  $R_g$  as a persistence length characteristic of the structure.

A great deal of information lies in the middle region of the scattering curve, but it is neglected by a Porod or Guinier analysis alone. When the system under study is polydisperse, the Guinier approximation should not be used. Information about sizes of the inhomogeneities may be derived from fitting the entire curve with a reasonable model of the structure. We have considered two models for analysis of SAXS curves from coal and chars, the Voronoi model (6) and the Fully Penetrable Polydisperse Spheres (FPPS) model. We believe this is the first application of FPPS to the modelling of small angle scattering. Thus this work represents an extension of the work of Chiew and Glandt (7) and Torquato and Stell (8).

The most convenient model for deriving a pore size distribution is one which assumes the pores are discrete spheres (9). Such a model is obviously not consistent with the interconnected nature of coal porosity. The geometric regularity of these models and cylindrical pore models used by engineers studying gasification is inconsistent with the irregularity of actual char structure. Both the Voronoi and FPPS models correspond to interconnected, random porous structures with irregular pore sizes and shapes.

The theoretical scattering from the Voronoi model is completely determined by the measurement of  $\phi_v$ , the void fraction of the sample and the choice of  $c$ , the Poisson point density (6). Empirically,  $c$  may be related to an apparent  $R_g$  of the model which reflects a mean size of cells in the structure. To fit our curve one varies  $R_g$ . Though the Voronoi model contains a distribution of cell sizes, a choice of two characteristic  $R_g$ 's, one for macropores, one for micropores, becomes necessary for a bimodal porous sample (10).

The pores in coal char are so polydisperse that several Voronoi cell sizes would have to be used to represent the experimental scattering curves. However, the Voronoi model no longer seems applicable in this case, so the FPPS is used. A two-dimensional representation of one possible combination of pore sizes and shapes constructed by the FPPS model is shown in Figure 3. For a single mode in the pore size distribution the theoretical scattering from the FPPS model is completely specified by three quantities, the void fraction  $\phi_v$ , and two parameters defining the distribution of sphere sizes. In this work we consider the Schulz distribution

$$f(r) = \frac{1}{\Gamma(b)} \left(\frac{b}{r_0}\right)^b r^{b-1} \exp\left(-\frac{br}{r_0}\right) \quad (2)$$

where  $r_0$  is a mean sphere radius, and  $b$  is a parameter that measures the sharpness of the distribution. Chiew and Glandt (7) discuss the use of this distribution with FPPS to model the surface area of a porous medium.

Considering  $\phi_v$  as a measurable quantity we see that two parameters,  $r_0$  and  $b$ , are required to fit experimental data with a unimodal FPPS model, while only one parameter is required with the unimodal Voronoi model. Thus, greater flexibility in fitting the curves is obtained at the price of one new parameter. The parameters  $r_0$  and  $b$  are determined by performing a least squares fit of the model to the data. Given the values of  $r_0$  and  $b$  which minimize the error in approximating the curve, the total surface area, complete pore size distribution, and surface area distribution are obtained analytically (7).

## RESULTS

Scattering curves for three samples of Carbosieve-S are shown in Figure 4 along with parametric fits of the Voronoi model to the data. The curve for untreated Carbosieve and the curve for the sample gasified to 16.6% conversion exhibit similar behavior. Both have distinct regions reflecting scattering from micropores and macropores. The scattering intensity attributable to a particular size of pore,  $d$  should fall off sharply for values of  $hd > 5.0$ . The sharp decrease in intensity for  $0.015 < h < 0.025$  is therefore due to macropores and the drop-off for  $h > 0.2$  is due to micropores. Consequently, two Voronoi cell sizes are required to represent curves 1 and 2. At a conversion of 80% the scattering due to macropores has become much

Table II. Voronoi Model Surface Areas: Change with Conversion

Conversion	Porosity	$R_{g,micro}$ (Å)	$R_{g,macro}$ (Å)	S(m <sup>2</sup> /g)
0.00	0.375	4.5	250	1730
0.166	0.479	4.0	250	2080
0.30	0.563	4.0	250	1820
0.41	0.631	4.5	250	1720
0.68	0.80	5.0	-	1070
0.80	0.875	5.5	-	660

less important relative to that from the growing micropores, so only a micropore cell size is needed. The parameters used in fitting the curves and surface areas calculated from the Voronoi model are given in Table II. The surface areas attain a maximum at about 16% conversion.

The surface areas are greater than those previously reported (14). However, the earlier values were determined by Porod's law at insufficiently large angles. The present technique is more accurate and the values compare favorably with the large microporosity and surface areas reported by Jánosí and Stoeckli (15).

The effect of pyrolysis heating rates on char structure have been studied for two coals, Gentry and Lower Kittanning. Final results of that work will be presented at the meeting. Preliminary results for both coals suggest a small decrease in macroporosity following pyrolysis independent of heating rate over the range studied (0.8-260°C/sec). However, samples of both coals pyrolyzed slowly at 0.8°C/sec and 5°C/sec all showed similar increases in microporosity. No change was seen in the microporosity of the fast pyrolysis samples.

Scattering data collected for the anthracite coal, PSOC 870, are shown in Figure 5. The raw coal shows a more gradual decrease in intensity at low values of  $h$  than does the Carbosieve. This reflects the presence of significantly more mesoporosity. Microporosity is present here, as indicated by the scattering persisting to high values of  $h$ , but there is no drop-off in intensity for the micropore region. A small amount of conversion seems to create a large change in the curve. However, some of this change occurs with pyrolysis. The further increase in intensity at middle values of  $h$  for the 50% conversion sample demonstrates a continued growth in mean pore size.

The FPPS model was used to fit the experimental scattering curve of our characterized porous alumina sample. Figure 6 presents the comparison of experimental and theoretical scattering curves. The FPPS approximation yields values of 15Å for  $r_0$ , and 2 for  $b$ , which corresponds to a broad distribution. These results indicate a surface area of 350 (m<sup>2</sup>/cm<sup>3</sup> particle volume) or 440 m<sup>2</sup>/g compared to 339 m<sup>2</sup>/g from N<sub>2</sub> BET analysis. Further refinement of the FPPS model allowing for noninteger values of  $b$  should improve the approximation.

#### DISCUSSION AND CONCLUSIONS

Changes in the porous structure with conversion are clearly evident in scattering data from both the model carbon and anthracite coal. Growth of the micropores in Carbosieve and of both micro- and mesopores in the coal is seen in the increasing intensity at intermediate values of  $h$ . Also, the intensity drop-off at high values of  $h$  moves in toward the mesopore scattering.

Scattering from microporosity lies at the highest values of  $h$  available with most SAXS cameras, but the microporosity contains the vast majority of surface area and must be followed. Equipment for obtaining data at still higher values of  $h$  would be very helpful. Another challenge in collecting data in the micropore region is the appearance of a broad, weak intensity maximum at  $h = 0.25$  for some coal and vitrain samples (11,12). This feature may be caused by interactions between scat-

tering units made up of layers of aromatic ring structure (11,13). The models presented here do not account for this phenomena and it has not been observed in our samples.

The Voronoi and FPPS models are better for analyzing SAXS than traditional discrete models since they correspond to interconnected, random porous structures with irregular pore sizes and shapes. The Voronoi model can be used with the model carbon which appears to have a bimodal distribution with pore sizes closely grouped about the modes. However, the FPPS model, which allows for broad distributions, is more widely applicable. The FPPS model closely approximates the scattering from a characterized sample with polydisperse porosity. However, there is a marked difference between the pore size distributions derived from SAXS and those derived from N<sub>2</sub> adsorption and Hg porosimetry. This could be explained in terms of the inability of the two conventional techniques to appropriately characterize microporosity. However, more comparative studies of the techniques are needed.

#### REFERENCES

1. Nelson, J.R., Ph.D. Thesis, The Pennsylvania State University (1979).
2. Fryer, J.R., Characterization of Porous Solids, Proc. of Symposium, S.J. Gregg, D.S.W. Sing and H.F. Stoeckli, Eds., London: Society of Chemical Industry, 41 (1979).
3. Kaler, E.W., Ph.D. Thesis, University of Minnesota (1982).
4. Porod, F., Kolloid Zeitschrift 124, 83 (1951).
5. Guinier, A. and G. Fournet, Small-Angle Scattering of X-Rays, John Wiley and Sons, Inc., New York (1955).
6. Kaler, E.W. and S. Prager, J. Coll. Int. Sci. 86, 357 (1982).
7. Chiew, Y.C. and E.D. Glandt, J. Coll. Int. Sci. 99, 86 (1984).
8. Torquato, S. and G. Stell, J. Chem. Phys. 79, 1505 (1983).
9. Lin, J.S., R.W. Hendricks, L.S. Harris and C.S. Yust, J. Appl. Cryst. 11, 621 (1978).
10. Brumburger, H. and J. Goodisman, J. Appl. Cryst. 16, 83 (1983).
11. Kalliat, M., C.Y. Kwak and P.W. Schmidt, New Approaches in Coal Chemistry, ACS Symposium Series, 169, B.D. Blaustein, B.C. Bockrath and S. Friedman, Eds., ACS: Washington, D.C., 3 (1981).
12. Chiche, P., S. Durif and S. Pregermain, J. Chim. Phys. 60, 825 (1963).
13. Hirsch, P.B., Proc. Roy. Soc. A226, 143 (1954).
14. Foster, M.D. and K.F. Jensen, Proc. Int. Conf. Coal Science, Aug. 1983, 464 (1983).
15. János, A. and H.F. Stoeckli, Carbon 17, 465 (1979).

#### ACKNOWLEDGEMENT

The work was supported by DOE (DE-FG22-82PL 50806).

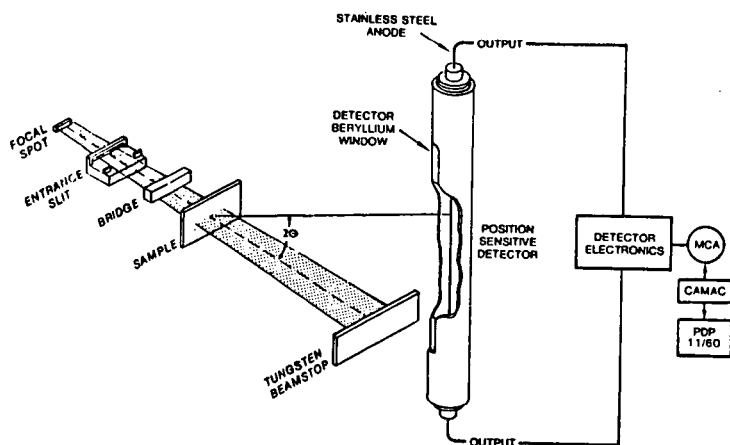


FIGURE 1. Kratky SAXS camera collimation system and detector. (From Kaler (3))

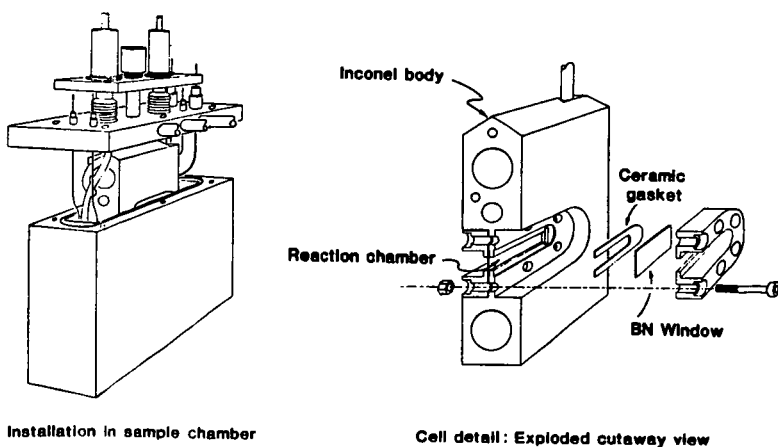


FIGURE 2. High temperature cell for in situ SAXS.

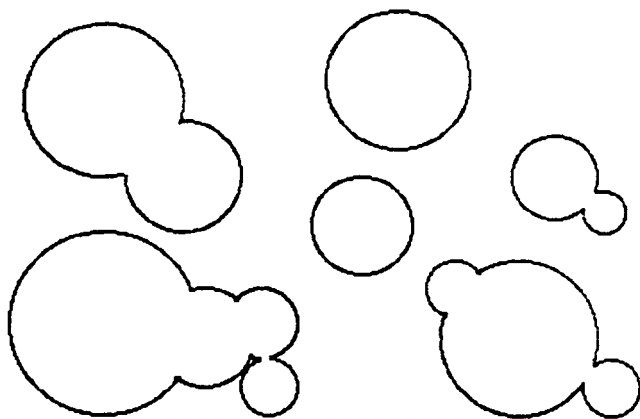


FIGURE 3. Two dimensional representation of FPPS model porous structure.

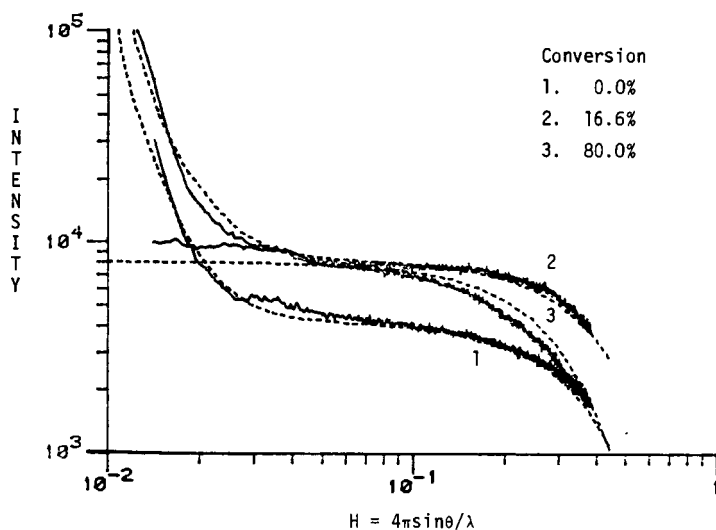


FIGURE 4. Comparison of Voronoi model approximation (----) with experimental SAXS curves (—) for Carbosieve gasified in  $\text{CO}_2$  at  $825^\circ\text{C}$ .

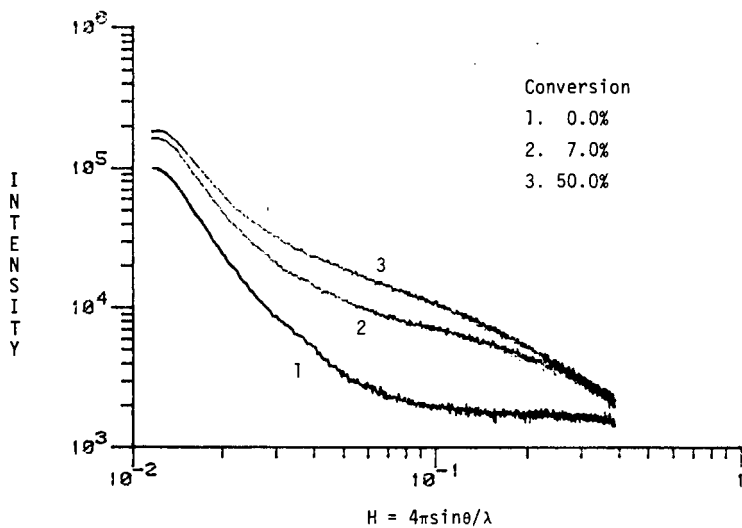


FIGURE 5. SAXS curves for Primrose anthracite (PSOC 870).

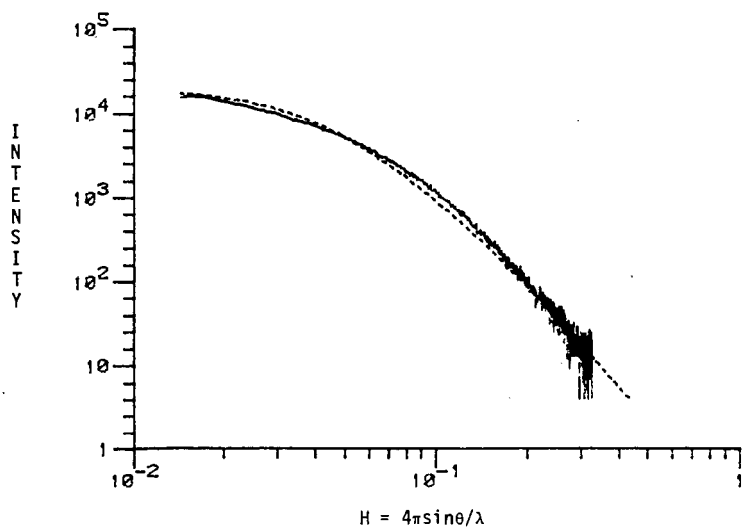


FIGURE 6. Comparison of FPPS model approximation (----) with experimental SAXS curve (—) for porous  $\gamma$ -alumina.

## THERMOPLASTIC AND VISCOELASTIC PROPERTIES OF COALS

Barbara D. Barr-Howell, John M. Howell, and Nikolaos A. Peppas

School of Chemical Engineering  
Purdue University  
West Lafayette, IN 47907

### INTRODUCTION

The modern structural view of the organic phase of bituminous and other coals is one of a crosslinked network structure (Larsen and Kovac, 1978; Lucht and Peppas, 1981 a, b; Lucht and Peppas, 1984a; Peppas and Lucht, 1984). In a recent publication (Peppas and Lucht, 1984) we have presented experimental evidence of the crosslinked structure using equilibrium swelling studies and we have offered a model that can be used to analyze it. Dynamic swelling studies using penetrants (Peppas *et al.*, 1983; Lucht and Peppas, 1984b; Peppas *et al.*, 1984; Barr-Howell and Peppas, 1985) have contributed to our understanding of this macromolecular structure.

If coal is a macromolecular network it should be possible to analyze it using theories and experiments widely applicable to polymers, basically theories of viscoelastic and rheological behavior. Since coal is a more complex and inhomogeneous structure, rheological and other analyses can give only an approximate picture of the coal structure, one that will not satisfy the purists, but still one that can offer important new insight.

Of particular importance is any information that can be obtained of the coal structure at temperatures approaching the liquefaction temperatures (300–350°C). It is known (Peppas, 1983) that coal exhibits a glass transition temperature in this range depending on its carbon content and other characteristics. The process of liquefaction is one that involves diffusive, reactive and thermal degradative phenomena; exact molecular information becomes quite difficult to obtain at high temperature. However, by using thermal analysis techniques or a combination of thermal analysis and diffusive techniques it is possible to investigate the relative importance of diffusion and degradation in the overall process. In addition, the associated viscoelastic changes of the coal network, which are expected to occur even significantly below  $T_g$  can be quantified by use of simple or sophisticated mechanical experiments (Howell and Peppas, 1984).

It is known that coal at high temperatures, close to the liquefaction temperature of 300–350°C, softens and behaves as a highly viscoelastic material. Its viscosity becomes dependent on the conditions of application of stress or strain. For example, Nazem (1980) studied the non-Newtonian behavior of carbonaceous mesophase pitch at high temperatures using a Haake viscometer and established the non-Newtonian behavior in terms of the viscosity as a function of the shear rate. Briggs investigated the viscosity of coal tar pitch as a function of temperature. Covey and Stanmore (1980) attempted to present a constitutive equation for the rheological behavior of Victorian brown coals of Australia.

An alternative approach of investigation of the viscoelastic behavior of coals is through thermal analysis at high temperatures. The early work of Bangham and Franklin (1946) established characteristics of the change and expansion of the coal structure at high temperatures. Sanada and Honda (1963) used creep deformation of various Japanese coals to establish their mechanical behavior at high temperatures. Gryaznov *et al.* (1977) and Lazarov (1983) examined the thermoplastic behavior of coals and discussed the results of several thermal analysis techniques. They examined the plasticizing phenomena of coals at high temperatures, their anisotropic liquid crystalline formations and their rheological behavior.

Thermogravimetric studies for the purpose of elucidating the thermoplastic behavior has been presented by Rovenskii and Melnik (1975), Ciuryla *et al.* (1979) and Elder and Harris (1984). Probably the most interesting recent studies on this subject are those of the group of Jenkins (Jenkins and Khan, 1982; Khan and Jenkins, 1984 a,b) who used a microdilatometer to investigate changes in the stress-strain behavior of certain coals.

### EXPERIMENTAL PART

Coal samples, packed under nitrogen, were supplied by the Pennsylvania State University Coal Bank. They were sieved to the desired mesh size and stored under nitrogen until use.



For the pyridine sorption studies at high temperatures, a thermogravimetric analyzer (Perkin Elmer, model TGA-2, Norwalk, Conn.) and an associated sorption system were used. Approximately 5 mg of the coal sample was placed in a platinum pan which was suspended from a lever arm balance. The system was then emerged in a microfurnace and purged with nitrogen. After one hour pyridine was allowed to bubble through the system and over the coal sample. Changes in weight due to sorption were recorded. The sorption experiments were carried out at constant temperature of 50 °C, 100 °C, 150 °C, 250 °C, 300 °C, and 350 °C.

For the creep experiments a thermomechanical analyzer was used. The flat coal samples for these studies were prepared under nitrogen by slicing coal chunks along their fault lines, and grinding the resulting slabs smooth with a diamond wheel (Peppas *et al.*, 1984). The size of each sample was approximately 2.5 mm<sup>2</sup> in surface area, by 0.6 to 0.9 mm in thickness. The flat samples were cut to the size of the TMA probe and tested using the thermomechanical analyzer (Perkin Elmer, model TMS-2) in the penetration mode under continuous purging with nitrogen. The initial temperature was 35 °C and a scanning rate of 10 °C/min was used. The surface area of the cylindrical probe tip used was 0.6207 mm<sup>2</sup>. Each sample was tested using applied loads of 10, 20, 30 and 40 g with corresponding stresses of 0.158, 0.316, 0.474 and 0.632 MPa. Changes due to deformation were recorded.

## RESULTS AND DISCUSSION

### *Dynamic Swelling at High Temperatures*

Dynamic swelling experiments with coal particles were performed at various temperatures to establish the transport mechanism in the presence of a solvent and the degradation reaction of coal. The studies presented here were performed with PSOC 312 coal particles of 20-30 mesh at 35, 50, 100, 150, 200, 250 and 300 °C.

The results of these studies are presented in Figures 1 and 2. At low temperatures, 35 and 50 °C, significant pyridine uptake is observed with minimum degradation. At 100 °C degradation is prominent, and the overall change of weight is smaller than at lower temperatures. Above 150 °C the degradation is significant. To further investigate this phenomenon similar coal samples were run in the TGA equipment in the absence of pyridine vapors and the degradation was recorded as shown in Figure 3. Experiments at 35 °C, 50 °C, 100 °C and 150 °C showed no measurable degradation over a period of 15 hours. Then, the data of Figure 1 and 2 were corrected for the loss of weight due to degradation and the corrected values are reported in Figure 4.

The overall penetrant uptake does not, and should not be expected to, correlate with temperature, since, due to the degradation process, the coal structure changes radically, leading to significant changes of the thermodynamic interactions between pyridine and coal network as well as, most probably, the porous structure. However, the inflection points and overshoots observed especially at 200 °C, 250 °C, and 300 °C are "real" observations, since the experimental error of the technique was determined to be less than 0.1 %. The data of 150 °C show that at this temperature the degradation is more significant than the pyridine uptake.

In general we may conclude that the pyridine transport through the significantly altered coal network at temperatures approaching its glass transition temperature is highly non-Fickian, that macromolecular relaxations become extremely important (as exhibited by the strong overshoots observed), and that the affinity of pyridine for the network is dramatically altered at high temperatures. Obviously, more detailed studies are needed to quantitatively elucidate this very fascinating phenomenon.

In the presence of 70-150 % pyridine in coal particles at 250-350 °C the coal network is in the rubbery state, only slightly above its  $T_g$  values (Peppas, 1983) and the highly anomalous transport mechanism should be expected, due to the value of the Deborah number which is of the order of one (Peppas *et al.*, 1984). The macromolecular relaxation, and the associated anomalous transport, lead to a drastically increased penetrant flux in the coal network, since the pseudo-convective contribution to anomalous transport becomes extremely important. In fact, no experimental data have been observed before, where at equilibrium the pyridine uptake is as high as 2.3 times the weight of coal, when Fickian diffusion predominates.

#### *Viscoelastic Behavior at Low and High Temperatures*

Figures 5 and 6 present the compressive strain versus temperature (and time, since the scanning speed was 10 °C/min) curves for samples of PSOC-312 with 78.33 % C and PSOC-853 with 80.15 % C, for different applied stresses.

Each curve on Figure 5 shows an induction period, followed by a change of the strain, usually starting at about 115-150 °C. At about 350 °C, where the sample is near its glass transition temperature, the compressive strain is only about 3-3.5 % of the total thickness, a typical value of compressive strain for porous, glassy polymers. Almost all the samples show that at low applied stresses and up to 300 °C a significant "negative strain" (namely expansion) of the coal samples is exhibited, which is, of course, characteristic of the traditional "swelling" of coals when heated in an inert atmosphere. With higher applied stress, the overall effect is compression and therefore an increase in compressive strain.

To further understand the viscoelastic behavior of coal below and near  $T_g$ , one may have to further examine Figure 6 which shows the strain versus temperature behavior up to the glass transition region. All the curves are smooth (a minor inflection point of unknown origin appears at about 250 °C) and quite typical of the similar behavior of glassy polymers. The porous structure should not be of major concern in this analysis. Since coal is glassy in most of the range of temperatures studied here, major pore compression would be unlikely to occur.

At a specific temperature, the creep behavior is highly similar to that of conventional macromolecular structures (Figure 7). A smooth increase in compressive strain is observed, which at 250 °C (for PSOC-853) seems to level off at about 20 %, whereas at 300 °C it reaches 65 %. It should be noted that the  $T_g$  value for this coal is 305 °C.

Figure 7 shows also the effect of repeated loadings (or creep experiments) on the compressive strain at constant temperature. For example, at 300 °C the creep behavior was followed for 200 hours at which time (point A) the load was removed and the recovery process was followed. The sample attained a certain compressive strain of 0.50 (permanent plastic deformation). Upon reapplication of the same stress at 260 hours (point B) a very fast creep behavior was observed. It must be noted that the new values of the compressive strain were on the extrapolated curve of the first creep experiment (see dashed line of Figure 7). A similar behavior is obtained at 250 °C, although of much smaller magnitude since the coal network is still glassy at this temperature.

One important comment must be made here. In a previous note (Howell and Peppas, 1984) we had discussed our first data with this technique, using coal samples which were bigger than the probe size of the TMA and we had concluded that some coal samples exhibit unusual "plateau" regions during their temperature-dependent creep behavior. In a private communication, Dr. D. Brenner of Exxon pointed out that the phenomenon studied before was that of "squeezing flow" in a viscoelastic matrix. The new studies reported here are with TMA probe-size coal samples (and with much improved preparation techniques which provide samples of truly uniform thickness (Ritger, 1985)), and they truly represented a creep behavior. The plateau region observed in the "squeezing flow" type studies has disappeared here, although a weak inflection point can be seen in some of the samples in the same region where the plateau was before. Obviously, studies towards this direction will continue.

## REFERENCES

- D.H. Bangham and R.E. Franklin, *Trans. Faraday Soc.*, **42B**, 289 (1946).
- B.D. Barr-Howell and N.A. Peppas, *Fuel Chem. Prepr.*, this volume (1985).
- V.T. Ciuryla, R.F. Weimer, D.A. Bivans and S.A. Motika, *Fuel*, **58**, 748 (1979).
- G.H. Covey and B.R. Stanmore, *Fuel*, **59**, 124 (1980).
- J.P. Elder and M.B. Harris, *Fuel*, **63**, 262 (1984).
- N.S. Gryaznov, L.V. Kopeliovich and Y.A. Nechaev, *Khim. Tverd. Topl.*, **11** (3), 104 (1977).
- J.M. Howell and N.A. Peppas, *Fuel Chem. Prepr.*, **29** (1), 207 (1984).
- R.G. Jenkins and M.R. Khan, EPRI Report AP-2337, Palo Alto, CA 1982.
- M.R. Khan and R.G. Jenkins, *Fuel Process. Techn.*, **8**, 307 (1984a).
- M.R. Khan and R.G. Jenkins, *Fuel*, **63**, 109 (1984b).
- J.W. Larsen and J. Kovac, in *Organic Chemistry of Coal*, J.W. Larsen, ed., ACS Symposium Series, Vol. 71, 36, Washington, D.C., 1978.
- L. Lazarov, *Koks i Khimiya*, (2), 13 (1983).
- L.M. Lucht and N.A. Peppas, in *New Approaches in Coal Chemistry*, B.D. Blaustein, B.C. Bockrath and S. Friedman, eds., ACS Symposium Series, Vol. 169, 43, Washington, D.C., 1981a.
- L.M. Lucht and N.A. Peppas, in *Chemistry and Physics of Coal Utilization*, B.R. Cooper and L. Petrakis, eds., Amer. Inst. Physics, Vol. 17, 18, New York, N.Y., 1981b.
- L.M. Lucht and N.A. Peppas, *Fuel Chem. Prepr.*, **29**, (1), 213 (1984).
- L.M. Lucht and N.A. Peppas, in *Advances in Rheology: Fluids*, B. Mena, A. Garcia-Rejon and C. Rangel-Nafaile, eds., Vol. 2, 631, UNAM, Mexico City, 1984b.
- F.F. Nazem, *Fuel*, **59**, 851 (1980).
- N.A. Peppas, Final Report to DOE, FG-28-80PC30222, Lafayette, IN, 1983.
- N.A. Peppas, L.M. Lucht, J.M. Larson and G.W. Sinclair, *Procecd. Intern. Coal Confer.*, **2**, 280 (1983).
- N.A. Peppas, B.D. Barr-Howell, J.M. Howell and P.L. Ritger, Annual Report to DOE, FG-22-83PC60792, Lafayette, IN, 1984.
- N.A. Peppas and L.M. Lucht, *Chem. Eng. Commun.*, **30**, 291 (1984).
- P.L. Ritger, M.S. Thesis, Chem. Engineering, Purdue University, 1985.
- V.I. Rovenskii and N.A. Melnik, *Khim. Tverd. Topl.*, **9** (4), 36 (1975).
- Y. Sanada and H. Honda, *Fuel*, **42**, 479 (1983).

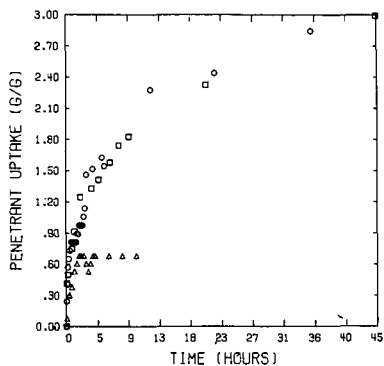


Figure 1: Effect of Swelling Temperature on Pyridine Uptake on Coal Particles of PSOC-312. Temperatures: 35 °C (○), 50 °C (□) and 100 °C (Δ).

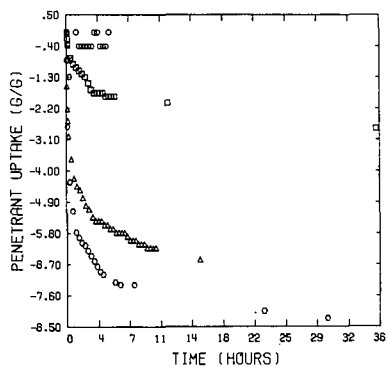


Figure 2: Effect of Swelling Temperature on Pyridine Uptake on Coal Particles of PSOC-312. Temperatures: 150 °C (○), 200 °C (□), 250 °C (Δ), and 300 °C (◇).

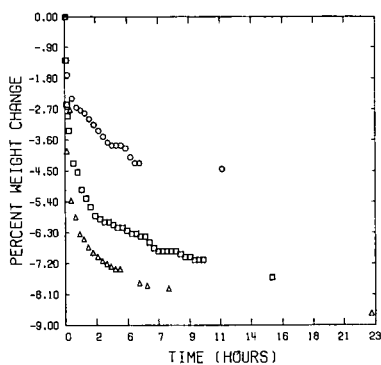


Figure 3: Coal Weight Loss as a Function of Time for PSOC-312. Temperatures: 200 °C (○), 250 °C (□), 300 °C (Δ).

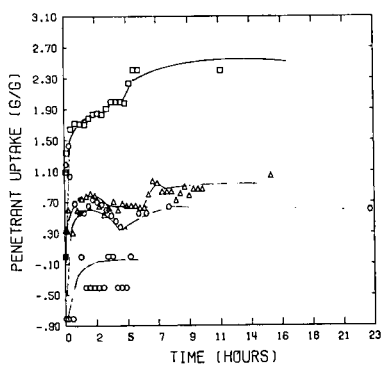


Figure 4: Corrected Pyridine Uptake of PSOC-312. Temperatures: 150 °C (○), 200 °C (□), 250 °C (Δ), 300 °C (◊).

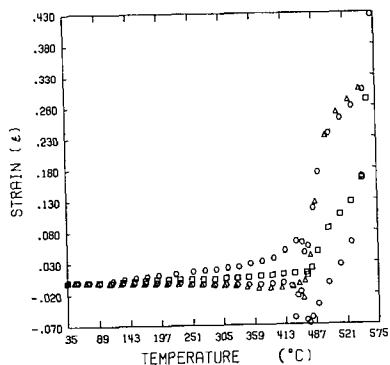


Figure 5: Compressive Strain as a Function of Temperature for Flat Coal Section of PSOC-312 with Applied Stress of 0.158 (○), 0.316 (□), 0.474 (Δ), and 0.632 (◇) MPa.

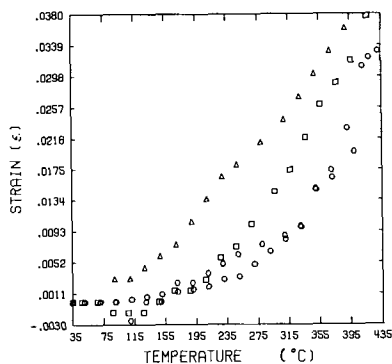


Figure 6: Compressive Strain as a Function of Temperature for Flat Coal Section of PSOC-853 with Applied Stress of 0.158 (○), 0.316 (□), 0.474 (Δ), and 0.632 (◇) MPa.

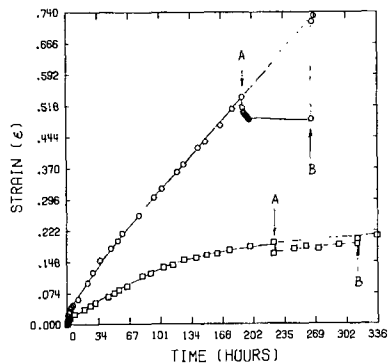


Figure 7: Compressive Strain as a Function of Time for PSOC-853 Coal Samples under Applied Stress of 0.474 MPa at 250 °C (□) and 300 °C (○). Creep period (from 0 to point A); recovery period (from A to B); second creep period (after point B).

## DIFFUSIVE UPTAKE OF FLUIDS BY COAL PARTICLES -- EFFECTS OF PARTICLE SHAPE AND PARTICLE SIZE DISTRIBUTION

D. Brenner and P. S. Hagan

Corporate Research Science Laboratories  
Exxon Research and Engineering Company  
Annandale, NJ 08801

### INTRODUCTION

Diffusion into coals is of considerable technological importance since many coal modification processes, such as direct liquefaction, desulfurization, demineralization, and chemical modification, involve diffusion of liquids or gasses into the coal. Additionally, much of the fundamental chemical research on coals requires diffusion of liquids or dissolved reagents into the coal so that reactions can occur. Precise interpretation of these experiments often requires an understanding of the diffusional behavior. The rate that reactants diffuse into the particles is often a rate-limiting step. The variety of shapes and sizes of particles in the coal slurry greatly complicates the overall diffusion kinetics, and unless this heterogeneity is properly taken into account it can lead to erroneous analyses of the process. There is information in the literature on the diffusive uptake of fluids by differently shaped single particles for various concentration-dependent diffusion coefficients (1), and there is some literature on diffusion into coals (2,3). However, no information concerning the effect of the particle size distribution on the diffusive uptake of coals in a slurry is available. The objective of this paper is to determine the range of diffusive uptake behaviors which can result from the different particle shapes and the particle size distribution.

Coal samples are commonly prepared by breaking down the coal until it is below a selected mesh size. This procedure results in a wide distribution of particle sizes. Sometimes mesh cuts of the coal are taken in which only that coal which passes through a selected larger mesh size, but not through a selected smaller mesh size, is utilized. This reduces the breadth of the size distribution, but even in the limit of an infinitely narrow mesh cut there will still be considerable variations in the diffusive uptake of the various particles due to the wide range of shapes that result from the breakdown or fracture process, and also due to the cracks and heterogeneity of the coal's microstructure.

To assess the effects of the different particle shapes and of the particle size distribution, we adopted the following strategy. First, since typical distributions of particle shapes present in coal samples are unknown, to determine the range of diffusive uptake behavior caused by having different particle shapes in the slurry, we calculate diffusive uptakes for both slab-shaped particles (with infinite height-to-width ratios) and spherical particles. Most other particle shapes can be considered to be intermediate between these two shapes, so their uptakes can be expected to fall in between these two extreme cases. Thus, these pairs of uptake calculations bracket the range of diffusive uptakes for most particle shapes, and therefore bracket the uptakes for most distributions of particle shapes.

To determine the effects of the distribution of particle sizes, for each particle shape (slab or sphere) we calculate the diffusive uptakes of both a single particle and a slurry of differently sized particles with that shape. The particle size distribution used was obtained from an experimental study of ball milling of coal by P. Luckie, *et al.* at Pennsylvania State University (4), so the distribution is relevant to actual coal slurries. While these investigators found that there were some variations in the measured particle size distribution depending on the experimental conditions, a typical distribution is approximated by

$$(1) \quad W(R) = 1 \text{ for } 0 \leq R \leq R_0, \\ = 0 \text{ for } R > R_0,$$

where  $W(R)dR$  is the weight fraction (or volume fraction) of particles whose size  $R$  is between  $R$  and  $R + dR$ .  $R_0$ , of course, gives the upper limit on the sizes of the particles. For spherical particles  $R$  is the particle radius. For slab-shaped particles,  $R$  is the half-thickness of the particle. The particle size distribution given by Eq. 1 is the distribution we use for all slurry calculations in this paper.

Besides the variations in particle shapes and sizes, there are a number of other factors which complicate diffusion in coal. These factors include the cracks and holes through the coal, the variety of macerals having different chemical and physical properties which make up the coal, the heterogeneity of the structure even within individual macerals, and the effects of intermaceral interfaces and mineral matter (5). These heterogeneities of the coal structures will not be explicitly treated in this paper, but they may cause substantial deviations from the usual diffusional behavior. The effects of particle shape and particle size distributions which are treated here should give a qualitative indication of the sorts of deviations which might result from these heterogeneities.

#### FORMULATION OF THE MODELS

In this section the diffusion models being considered are discussed briefly, and the mathematics describing the models is formulated. Two distinct modes of diffusion are treated, Fickian diffusion (6) and Case II diffusion (7). Fickian diffusion is the common form of diffusion in which the rate of flow of the penetrant is related to the concentration gradient by a proportionality factor,  $D(c)$ , which is called the diffusion coefficient. For Fickian diffusion, the concentration  $c(t,x)$  of the penetrant within a particle obeys the following equation:

$$(2) \quad \frac{\partial c}{\partial t} = \nabla \cdot D(c) \nabla c$$

For Fickian diffusion,  $D$  is either a constant or is an explicit function of the concentration  $c$ . Diffusion coefficients which are non-decreasing functions of concentration can be expected for the diffusion of most penetrants into coal, so only these are considered in this paper.

We impose the boundary and initial conditions

$$(3.1) \quad c = c^* \quad \text{at the particle's surface} \\ (3.2) \quad c = 0 \quad \text{at time } t = 0 \text{ within the particle.}$$

Here the (fixed) concentration  $c^*$  is the concentration of penetrant within the coal particle which would be in equilibrium with the concentration of penetrant in the solution; i.e.,  $c^*$  is the saturation concentration of the penetrant within the coal. By using Eq. 3.1, we are assuming that the external surface of the particle is in equilibrium with the solution. By taking  $c^*$  to be constant in time, we are assuming that the slurry is well-stirred and that the depletion of the penetrant in the solution is negligible. (Maintaining the proper boundary conditions in experiments we wish to interpret is crucial. For example, a frequent experimental procedure is to allow a penetrant to diffuse from a liquid reservoir through an inert gas to reach the particles. However, this procedure generally will not maintain the boundary condition (Eq. 3.1) sufficiently accurately, which may greatly perturb the results). The initial condition, Eq. 3.2 simply states that the particles contain no penetrant at the start of the experiment. Once the penetrant concentration  $c(t,x)$  within a particle has been determined from Eqs. 2, 3.1 and 3.2, the particle's uptake of penetrant at time  $t$ ,  $m(t)$ , is found by integrating over the particle's volume:

$$(4) \quad m(t) = \iiint c(t, \vec{x}) dV.$$



For the conditions of Eqs. 3, the uptake will be proportional to  $\sqrt{t}$  for a semi-infinite medium so for any reasonably shaped particle it will be proportional to  $\sqrt{t}$  at small enough times.

There is an important class of problems which do not involve pure diffusion, but which are also governed by Eqs. 2-4. If a substance undergoes both Fickian diffusion and chemical reaction within the particles, and if the reaction proceeds much more rapidly than the diffusion (so diffusion is the rate-limiting step), then the diffusive uptake of the substance by a particle is again given by Eqs. 2-4.

Among all non-decreasing diffusion coefficients  $D(c)$ , there are two cases which represent extremes in the concentration dependence. One extreme case is simply a constant diffusion coefficient

$$(5.1) \quad D(c) = D_0 \quad \text{for all } c.$$

The other extreme case is found by considering a diffusion coefficient which is zero up to nearly the saturation concentration  $c^*$ , but just short of this concentration the coefficient jumps to a large value and remains fixed until saturation. Mathematically, this diffusion coefficient is

$$(5.2) \quad D(c) = 0 \quad \text{for } c \leq c^* - \epsilon \\ = \frac{A}{\epsilon} \quad \text{for } c^* - \epsilon < c \leq c^*,$$

where  $A$  is a constant, and  $\epsilon/c^* < 1$ . This second extreme case is obtained by letting  $\epsilon$  become arbitrarily small and thereby take the limit as  $\epsilon \rightarrow 0$ .

We assert that the normalized uptake curve  $m(t)$  for any non-decreasing diffusion coefficient  $D(c)$  always lies in between the normalized uptake curves calculated for the two extreme cases given by Eq. 5.1 and Eq. 5.2 (in the limit of  $\epsilon \rightarrow 0$ ). (The normalization of the uptake curves is discussed in the next section.) Thus, the uptake curves calculated using the two extreme diffusion coefficients bracket the range of uptake curves for all non-decreasing diffusion coefficients  $D(c)$ . We have tested this assertion with a very large number of different concentration dependent diffusion coefficients including, for example, diffusion coefficients which increase exponentially with concentration. In all cases the uptake curves remained between the two extremes. As we shall see, for slurry systems these two extreme cases yield normalized uptake curves which lie surprisingly close together. So the curves for all non-decreasing diffusion coefficients lie close together.

Case II diffusion is distinctly different from Fickian diffusion and cannot be described by similar equations. In Case II diffusion there is a sharp penetration front that propagates into the matrix material at a constant velocity, so the initial uptake of penetrant is linear in time. Ahead of the front the concentration is nearly zero, and behind the front the concentration is nearly constant. Then for Case II diffusion, the concentration  $c(t, x)$  of penetrant at position  $x$  in a particle is given by

$$(6) \quad c(t, x) = c^* \quad \text{if } s \leq vt \\ = 0 \quad \text{if } s > vt,$$

where  $s$  is the distance from the point  $x$  to the particle's surface, and  $v$  is the velocity of the penetration front. Case II diffusion often occurs where the absorption of the penetrant results in a transition of the matrix material from a plastic to a rubbery or viscous state. Since some liquids are known to transform some coals from a plastic to a rubbery state (8,9), Case II diffusion or behavior intermediate between Case II and Fickian diffusion is a possibility for coals.

One of the most common and easiest methods of characterizing the diffusional behavior of a system is to expose the material to the fluid at  $t = 0$ , and to monitor the uptake as a function of time. This is the approach taken in this study. For this approach there are two aspects of these diffusional systems

that we are particularly interested in: (1) given the uptake behavior, what can be learned about the diffusion coefficient  $D(c)$ ; and (2) how well can the uptake be predicted without having detailed knowledge of the diffusion coefficient. To address these issues, the uptakes were calculated for the systems that were described above.

The uptakes were calculated from Eqs. 1-6 using numerical methods on a digital computer. The method used was the Crank-Nicolson scheme (10). The results were calculated to an accuracy of better than 0.1%, so any residual deviations from the exact results would not be observable in the figures.

#### METHOD OF PRESENTATION OF DATA

Results for each of the models with the conditions discussed in the Formulation Section are presented in this paper in graphical form. A few words are needed to describe the mode of presentation of the graphical data. The approach taken in this study is that the experimenter does not know anything a priori about the diffusive behavior of his system; rather he measures the penetrant uptake as a function of time and then attempts to determine such characteristics as the type of diffusion (e.g. Fickian, or Case II, or an intermediate behavior), and the concentration dependence of the diffusion coefficient. Our procedure, then, is to compute theoretical curves based on various models to which the experimenter can compare his data and attempt to determine the diffusive character of his system. The data computed for the different hypothetical models are conveniently displayed as normalized graphs or curves. The vertical axis measures the fraction of penetrant taken up by the medium, where 1.0 is the maximum value which occurs at saturation (i.e., equilibrium). The horizontal axis is the time axis. For Fickian diffusion having the boundary condition of constant concentration of penetrant at the fluid-solid interface, the uptake curve for any reasonably shaped particle will be proportional to  $\sqrt{t}$  at small enough times. Since a linear curve (initially) is easy to evaluate visually, the time axis in the figures is scaled as  $\sqrt{t}$ . What remains is to scale the absolute magnitude of time along the time axis. We have found that a convenient criterion is to match the slopes of the various curves in a figure at zero time. Then the curves start off together and it is easy to observe how they deviate from the original slopes as time progresses. For the single particle data for Fickian diffusion, the scaling of the system is arbitrarily chosen to produce initial slopes of 45°. The uptake curves produced by plotting fractional uptake versus the square root of time, where the initial slopes are scaled to be 45°, will be referred to as "normalized uptake curves".

#### RESULTS

##### Fickian Diffusion

###### a. Fickian diffusion in a single slab-shaped particle

Figure 1 shows the normalized uptake curves for Fickian diffusion in a slab, for a constant diffusion coefficient and for the diffusion coefficient defined in Eqs. 5.2. (Recall that the normalized uptake curve for any non-decreasing diffusion coefficient lies in between these two curves). The lower curve is for the constant diffusion coefficient and the upper curve is for the coefficient which is zero except for concentrations very near saturation. The curves are straight and virtually indistinguishable up to an uptake of roughly 0.6. This behavior is not surprising since it is well known that for Fickian diffusion in a semi-infinite medium with the boundary condition described in Eq. 3.1, the curves would be straight for all time for any concentration dependence of the diffusion coefficient. A deviation from the straight line can only occur when there is an appreciable overlap of fluid diffusing in from one side of the slab with fluid which diffused in through the other side. That is, only when the fluid achieves an appreciable concentration at the center plane of the slab do differences occur between the finite thickness slab and a semi-infinite slab.

The diffusional behavior for the diffusion coefficient defined by Eqs. 5.2 is readily pictured physically. Since for this diffusion coefficient there can be no diffusion unless the fluid concentration is essentially at saturation, the fluid propagates into the medium as a sharp front with concentration zero ahead of the front, and it is essentially at its saturation value behind the front. The front propagates with a decreasing velocity which is proportional to  $1/\sqrt{t}$ . Only when the fronts propagating in from opposite sides of the slab meet, does the system recognize that the slab is not semi-infinite. Since Fickian uptake curves for non decreasing diffusion coefficients always remain concave towards the  $\sqrt{t}$  axis (11), it is clear that the diffusion coefficient of Eqs. 5.2, which maintains the 45° straight line all the way to saturation gives an upper bound to the cumulative uptake at any time.

#### b. Fickian diffusion in a single spherical particle

In Figure 2, the same two diffusion coefficients used in Figure 1 are again utilized, but this time for a spherical particle. In addition, an intermediate concentration dependence is included -- the exponential concentration dependence  $D(c) = e^{2c}$ . The exponential diffusion coefficient gives the intermediate curve in Figure 2, which illustrates our general finding that the normalized uptake curve for any diffusion coefficient (that is non-decreasing with concentration) always lies in between the normalized uptake curves obtained from the extreme diffusion coefficients in Eq. 5.1 and Eqs. 5.2. For spherical particles the difference in the normalized uptake curves for the two diffusion coefficients which give the upper and lower bounds is much less evident than for the slab case. In fact, unless an experimental uptake curve had a very high accuracy, it would be difficult to determine whether the observed behaviour was produced by the most strongly concentration dependent diffusion coefficient possible (the upper curve) or by a constant diffusion coefficient (the lower curve), much less some intermediate concentration dependence.

It is seen in Figure 2, that the uptake curves depart from the initial straight line much earlier than for the slab. The deviation from the straight line by the upper curve, for which the penetrant propagates into the material as a sharp front, is caused by the smaller and smaller area of the surface defined by the front as it propagates towards the center of the sphere.

#### c. Fickian diffusion in a slurry of slab-shaped particles

Figure 3 shows the effect of the particle size distribution on the uptake behavior of slab-shaped particles. The curves in this slurry graph are scaled such that if all of the volume of the sample was used in making up particles of the same size as the largest particle in this distribution, then the curves would start out at 45° on this plot. Of course the presence of the smaller particles in the distribution results in a larger surface area than if the same volume resided in larger particles, so the initial slope for the slurry is considerably greater than 45°.

The top and bottom curves in Figure 3 are for the same diffusion coefficients as in Figure 1. It is immediately obvious by comparing Figures 1 and 3 that the particle size distribution dramatically changes the behavior of the normalized uptake curves. For example, for this slurry of slab-shaped particles there is significantly less difference between the uptake curves for the two extreme concentration dependencies shown than for the single particle case. In fact, the curves for the slurry of slab-like particles in Figure 3 are significantly closer together than the curves for the single spherical particle in Figure 2.

It is seen that the uptake curves in Figure 3 fall well below the initial slope at a much lower uptake value than even for the single spherical particle case. Qualitatively the reason for this early deviation is clear. The smaller particles in the distribution approach saturation quickly and then contribute little to the uptake. The close correspondence of the two curves at all times and the

dramatic differences between the curve shapes in Figures 1 and 3 suggest that the particle size distribution is the dominant factor in the uptake behavior.

#### d. Fickian diffusion in a slurry of spherical particles

Figure 4 presents slurry data for spherical particles calculated using the diffusion coefficients described previously. This figure should be compared with the single spherical particle curves of Figure 2. The uptake curves in Figure 4 lie very close together, even though the curves represent the two extreme cases of concentration dependence for (monotonically increasing) Fickian diffusion coefficients. It is clear from these results that for the sort of particle distribution used, it is extremely difficult, if not impossible, to get reliable concentration dependence information for the diffusion coefficient from the shape of the uptake curve.

#### Case II Diffusion and Comparison with Fickian Diffusion

As described previously, Case II diffusion exhibits behavior which is fundamentally different from Fickian diffusion, regardless of the concentration dependence of the Fickian diffusion coefficient. Case II diffusion is easy to visualize since it involves the propagation of a sharp front into the medium, with zero concentration ahead of the front and saturation behind the front. In this respect it is similar to the Fickian diffusion described by Eqs. 5.2, and discussed previously. However, physically and mathematically these two modes of diffusion are fundamentally different. For example, whereas (regardless of the concentration dependence) a Fickian front propagates into a semi-infinite medium at a velocity proportional to  $1/\sqrt{t}$  (assuming the usual fixed concentration of penetrant at the surface), the Case II front propagates at a constant velocity.

#### a. Case II diffusion in a single slab-shaped particle

Figure 5 shows the penetrant uptake curve for Case II diffusion in a single slab-like particle. In this figure the Case II diffusion is compared to the two extremes of Fickian diffusion previously shown in Figure 1. The curve which starts off lowest in Figure 5 is from Case II diffusion, the other two curves are identical to the ones in Figure 1. The Case II uptake curve can not be conveniently normalized to a initial slope of  $45^\circ$  on this graph because of its initial linear-in-t time dependence. Therefore, the Case II curves were normalized in a different manner. In all of the remaining figures, the Case II curve is scaled along the square-root-of-t horizontal axis by requiring that the area under its curve be equal to the area under the curve for the constant Fickian diffusion coefficient. The dramatic difference in behavior between Case II diffusion and Fickian diffusion for any monotonically increasing concentration dependence is obvious from Figure 5. Presumably uptake curves for Fickian diffusion coefficients having any concentration dependence which is a non-decreasing function of concentration will fall between the two Fickian curves in Figure 5, whereas the Case II curve is far out of this range. While the Case II curve appears to be highly curved in this  $\sqrt{t}$  plot, actually the Case II curve would be a straight line if the graph utilized a linear-in-t horizontal axis.

#### b. Case II diffusion in a slurry of slab-shaped particles

Figure 6 shows the uptake curve for Case II diffusion for a slurry of slab-like particles. The particle size distribution is given by Eqs. 1. The corresponding Fickian uptake curves for this particle shape and particle size distribution, which were shown in Figure 3, are displayed in Figure 6 for comparison. It is seen that there is slightly closer correspondence between the Fickian and Case II curves for the slurry than in Figure 5 for the individual particles, but the curves are still quite different. Comparing the Case II curve for the individual slab of Figure 5 with the Case II curve for the slurry of Figure

6, it is seen that in the region up to an uptake of about 0.8 the curve in Figure 6 has much less curvature than in Figure 5. In fact, over more than half of the entire uptake curve, from below 0.2 up to nearly 0.8, the Case II uptake curve in Figure 6 is very nearly straight. This is surprising since with our boundary conditions a straight line plot of uptake versus square root of time is commonly taken as the signature of Fickian diffusion. To add to the confusion, the Fickian curves in Figure 6 have much more curvature than the Case II curve. So, if the very early time curvature of the Case II curve were neglected (for example, there are frequently experimental difficulties or uncertainties at small times), it is possible that an experimenter would misinterpret the Case II curve as signifying Fickian diffusion, and would misinterpret the Fickian curves as signifying a non-Fickian type of diffusion. Recall also that the particle size distribution used for these calculations is not an arbitrary one, but is a fit to an experimentally derived curve from the ball milling of a coal. Therefore, it is crucial that an experimenter understand the effective particle size distribution of his sample before attempting to interpret diffusional data from uptake curves. A particle's effective size will be affected by the exact shape of the particle, and in fact, the effective particle size may be quite different from the particle's geometrical size. This distinction can be especially important for heterogeneous, crack-containing, and porous materials, such as coals, for which the geometrical surface and the region rapidly penetrated by fluids may differ substantially (5).

The change in shape of the Case II uptake curve for the slurry in Figure 6, as compared to the single particle uptake in Figure 5, is caused by the saturation of the smaller particles so that they no longer contribute to fluid uptake.

#### c. Case II diffusion in a single spherical particle

Figure 7 shows the Case II uptake curve for a single spherical particle. Also shown on the graph are the Fickian uptake curves for the corresponding system. The Case II uptake curve for the sphere differs from the linear-in-time behavior for the slab, because as the diffusion front propagates into the sphere towards the center, the position of the front describes a smaller and smaller sphere. It is noteworthy that for the single spherical particle, the Case II uptake curve has a long, relatively straight region from about 0.2 to 0.8 on the square-root-of-time plot. This is a longer (approximately) straight region than for the corresponding Fickian curves. Of course, the large curvature in the region below an uptake of 0.2 gives away the non-Fickian behavior of the Case II curve for this system.

#### d. Case II diffusion in a slurry of spherical particles

Figure 8 shows the uptake curve for Case II diffusion in a slurry of spherical particles whose size distribution is again given by Eqs. 1. The Fickian curves for the corresponding systems (i.e. Figure 4) are also shown. What is remarkable about this Case II curve is that it is nearly straight all the way from an uptake of about 0.05 to 0.7 uptake. If the particle size distribution was not taken into consideration one could very easily conclude (mistakenly) that this uptake curve is the result of Fickian diffusion.

It is clear from the above results that for slurry systems it is very difficult to determine the concentration dependence of the diffusion coefficient, or even the type of diffusion, from the usual continuous fluid uptake curve. If concentration dependent diffusional information is desired for a system, more effective, though less convenient, methods must be used, such as equilibrating the sample at various concentrations and making differential uptake measurements.

#### CONCLUSIONS

This study has shown that the fluid uptake behavior of particles in slurries can differ drastically from the uptake behavior of individual particles. Therefore, fluid uptake profiles for single particles must not be utilized to

interpret diffusional data on slurries without taking into consideration the particle size distribution. For a particle size distribution produced by the ball mill grinding of coal, it was found that the effect on the penetrant uptake was sufficiently severe that the initial uptake rate for Fickian diffusion was highly non-linear on a square-root-of-time plot. However, surprisingly, with this same particle size distribution, Case II diffusion gave a nearly linear graph on a square-root-of-time plot. So Case II diffusion might easily be mistaken for Fickian diffusion for this system. Thus faulty analysis of the diffusional system can readily occur.

This study also brought to light an unexpected similarity in the shape of fluid uptake curves for diffusion coefficients having drastically different concentration dependencies. For a coal slurry having a typical particle size distribution, the fluid uptake profiles for diffusion coefficients having extremes in concentration dependence are quite similar for slab-shaped particles, and for spherical particles the curve shapes are almost indistinguishable. These results show that the concentration dependence of diffusion coefficients can not be readily determined for slurry systems using continuous fluid uptake measurements. Other less convenient methods must be used, such as differential uptake measurements.

For coals and other micro-heterogeneous and micro-cracked materials, the problem of determining diffusional behavior is particularly complex because the external surface geometry may not satisfactorily indicate the rate of penetration of the fluid into the particles. In coal, for example, the uptake of fluid through holes, cracks, along maceral interfaces and along regions of mineral matter may contribute substantially to the diffusion process. In addition, the various macerals or microcomponents of the coal will have different diffusional characteristics. Even within the vitrinite classification different pieces of material may exhibit substantially different diffusion characteristics.

#### REFERENCE

1. Crank, J., "The Mathematics of Diffusion", Second Edition, Clarendon Press, Oxford (1975).
2. Walker, P. L. Jr., and Mahajan, O. P., in "Analytical Methods for Coal and Coal Products", Edited by C. Karr, Jr., Vol. I, Chapt. 5, Academic Press, NY (1978).
3. Larsen, J. W., Lee, D., Fuel, 62, 1351-1354 (1983).
4. Luckie, P. T., Annual Progress Report for Sept. '76-Sept. '77, ERDA Contract EX-76-C-01-2475, NTIS Report # FE-2475-13 (1977).
5. Brenner, D., "Thin Section Microscopic Studies of the Diffusion of Oxygen into Coal at Elevated Temperatures", Corporate Research Report CR.25BN.84 (1984).
6. Crank, J., "The Mathematics of Diffusion", Second Edition, Chp. 1, Clarendon Press, Oxford (1975).
7. Alfrey, A., Gurnee, E. F., and Lloyd, W. G., J. Polym. Sci., C12, 249 (1966).
8. Brenner, D., "The Macromolecular Nature of Bituminous Coal", Corporate Research Report CR.22BN.82 (1982).
9. Brenner, D., Nature, 306, No. 5945, 772 (1983).
10. Crank, J., and Nicolson, P., Proc. Camb. Phil. Soc. Math. Phys. Sci., 43, 50, (1947).
11. Crank, J., "The Mathematics of Diffusion", Second Edition, p. 180, Clarendon Press, Oxford (1975).

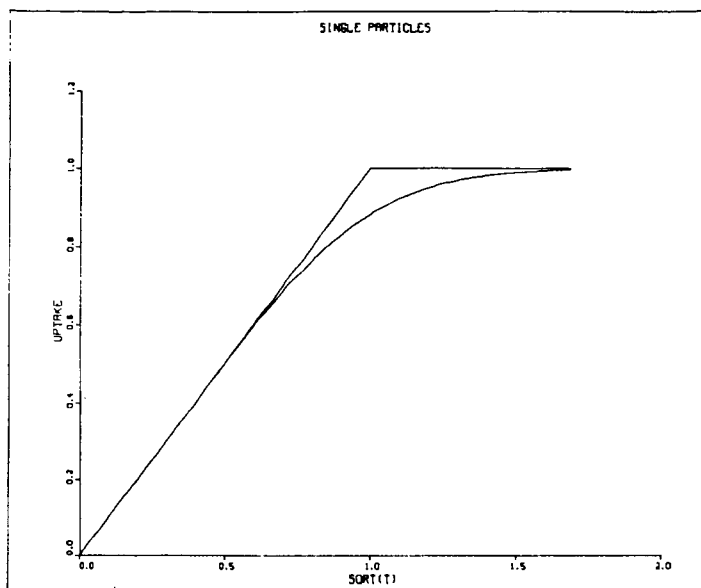


Figure 1. Solvent uptake for a single slab-shaped particle  
a) Lower curve is for constant diffusion coefficient (concentration independent)  
b) Upper curve is for extreme concentration dependent Fickian diffusion

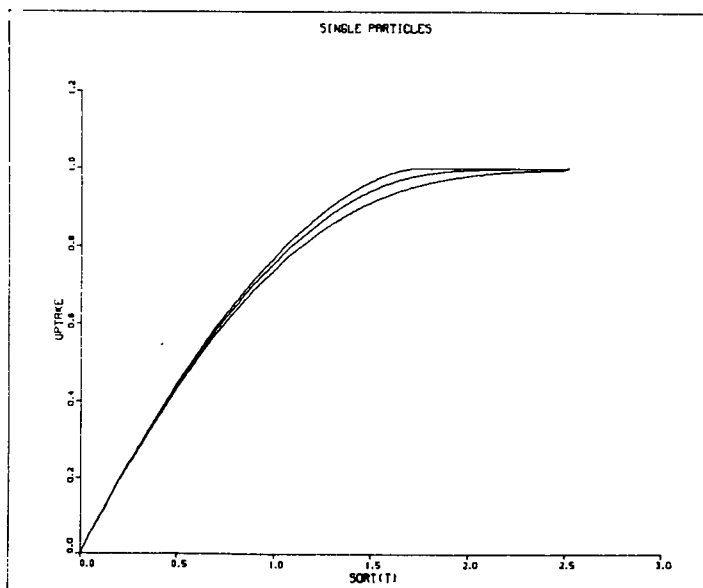


Figure 2. Solvent uptake for a single spherical particle  
a) Lower curve is for constant diffusion coefficient (concentration independent)  
b) Middle curve is for exponentially concentration dependent diffusion coefficient  
c) Upper curve is for extreme concentration dependent Fickian diffusion

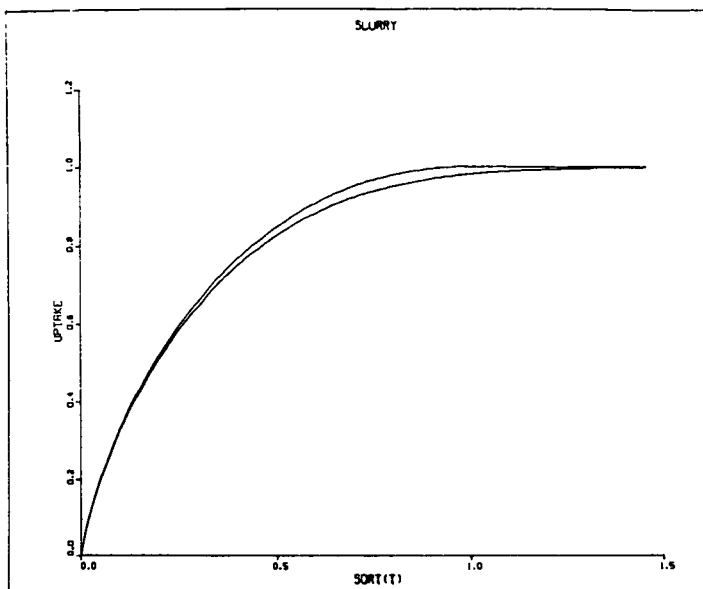


Figure 3. Solvent uptake for a slurry of slab-shaped particles

- a) Lower curve is for constant diffusion coefficient (concentration independent)
- b) Upper curve is for extreme concentration dependent Fickian diffusion

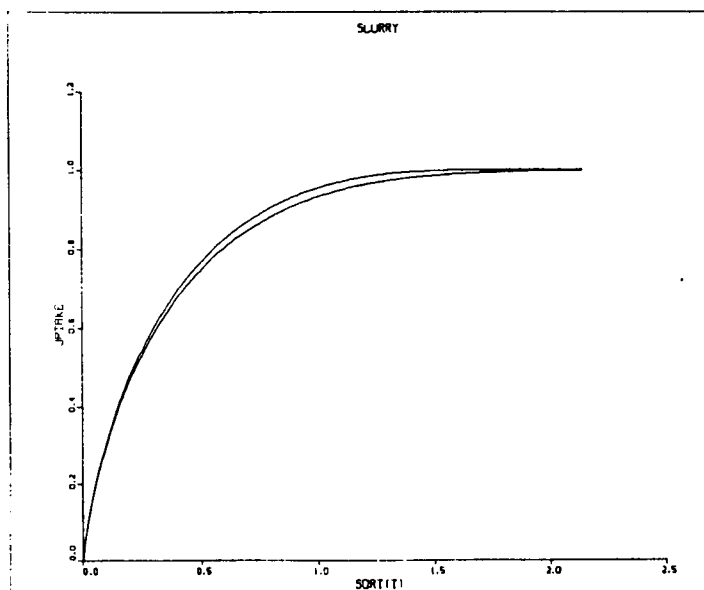


Figure 4. Solvent uptake for a slurry of spherical particles

- a) Lower curve is for constant diffusion coefficient (concentration independent)
- b) Upper curve is for extreme concentration dependent Fickian diffusion



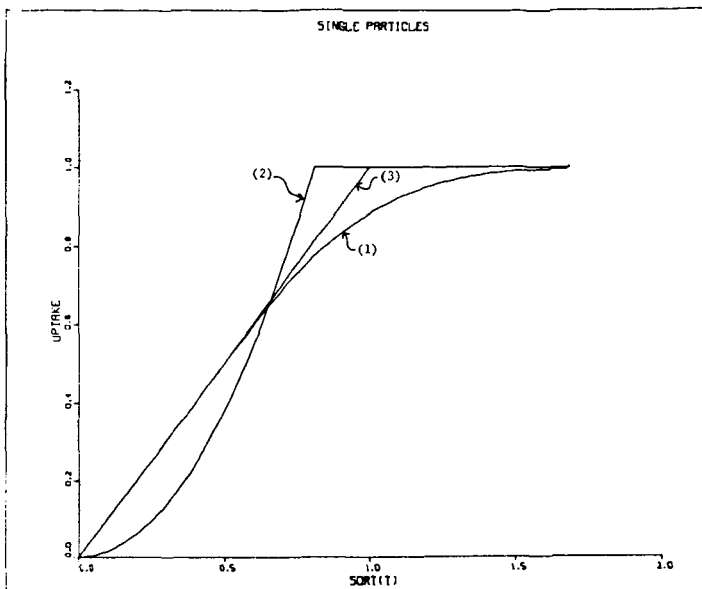


Figure 5. Solvent uptake for a single slab-shaped particle  
 a) Curve 1 is for constant diffusion coefficient (concentration independent)  
 b) Curve 2 is for extreme concentration dependent Fickian diffusion  
 c) Curve 3 is for Case II diffusion (constant velocity)

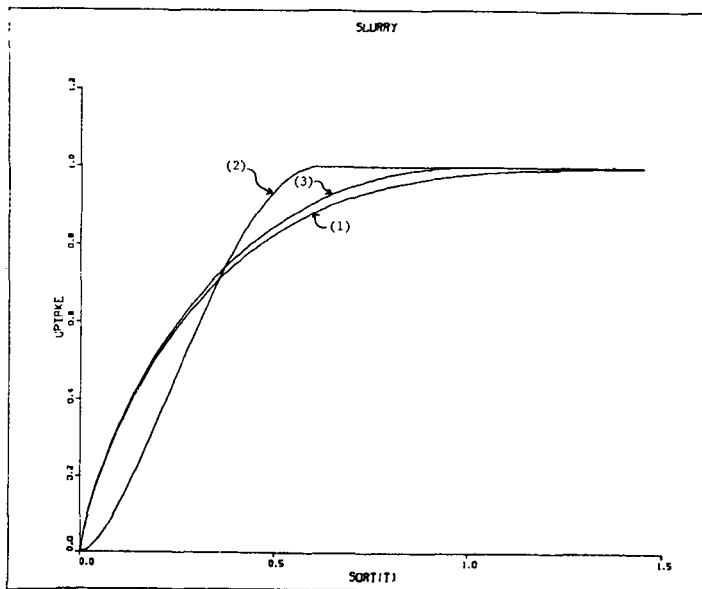


Figure 6. Solvent uptake for a slurry of slab-shaped particles  
 a) Curve 1 is for constant diffusion coefficient (concentration independent)  
 b) Curve 2 is for extreme concentration dependent Fickian diffusion  
 c) Curve 3 is for Case II diffusion (constant velocity)

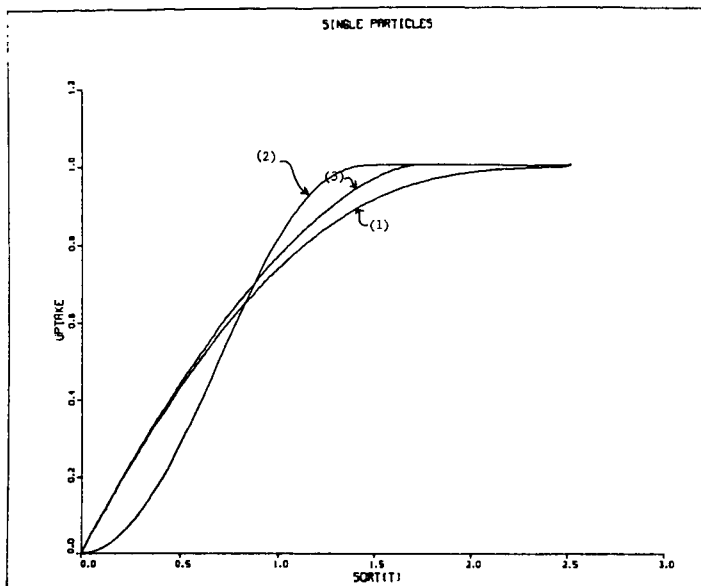


Figure 7. Solvent uptake for a single spherical particle  
a) Curve 1 is for constant diffusion coefficient (concentration independent)  
b) Curve 2 is for extreme concentration dependent Fickian diffusion  
c) Curve 3 is for Case II diffusion (constant velocity)

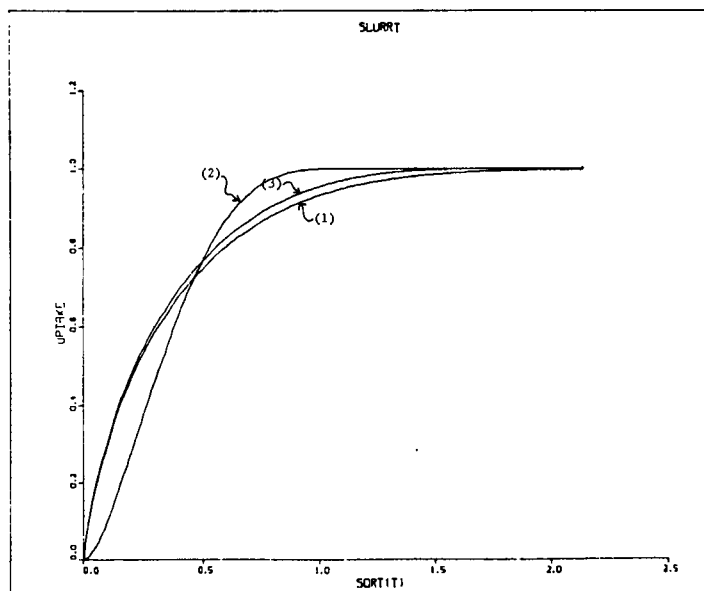


Figure 8. Solvent uptake for a slurry of spherical particles  
a) Curve 1 is for constant diffusion coefficient (concentration independent)  
b) Curve 2 is for extreme concentration dependent Fickian diffusion  
c) Curve 3 is for Case II diffusion (constant velocity)

## "IN SITU" OBSERVATIONS OF LIQUID DIFFUSION IN THIN SECTIONS OF COAL

D. Brenner

Corporate Research Science Laboratories  
Exxon Research and Engineering Company  
Annandale, NJ 08801

### INTRODUCTION

The objectives of this study are to advance our understanding of how liquids penetrate through the microstructure of coals and to use diffusion to probe the macromolecular and microstructure of coals. Diffusion of liquids and of solids dissolved in liquids is of considerable importance in many areas of coal technology and science. Many coal liquefaction processes involve the penetration of a liquid into coal; in particular, this is the case for many slurry-based liquefaction processes. There are a number of coal beneficiation processes actively being investigated which rely on diffusion of reagents into the coal to modify its structure or to remove undesired mineral or organic components. Similarly, many chemical pretreatments of coals depend on diffusion for the reagents to reach the reactive sites in the coal. Mass transfer is crucial to many fundamental chemical investigations of coal structure which utilize wet chemical techniques since reagents must diffuse to reactive sites within the structure. From a fundamental viewpoint a better understanding of diffusion in coal will advance our overall comprehension of the underlying macromolecular structure and microstructure of coals.

The escape of reaction products, mobile coal molecules, or molecular fragments from the coal structure are other diffusional processes in coal which are of substantial technological importance. For example, they occur in most conversion processes. In liquefaction, liquids or gases produced within the coal or molecular fragments of the coal dissolved in the liquids must escape from within the coal particles. In gasification molecular fragments from the degraded coal structure must diffuse to the surface of the particle before they can evaporate into the surrounding gas.

In this study we focus on a reasonably well-defined system in order to better understand diffusion phenomenon. We investigate the diffusion of good liquid swelling agents into a high volatile bituminous coal. Since the diffusing swelling agents greatly enhance the mobility of the macromolecular chain segments within the coal, this system is particularly well suited for probing macromolecular aspects of the coal structure.

The diffusion of liquids in materials is commonly studied by fluid uptake and/or desorption as a function of time. For simple or well-behaved materials this approach is effective, but for coal which is highly heterogeneous varying markedly from sample to sample and from micro-region to micro-region within each sample, this approach can give only averaged and incomplete information. A technique utilized with polymers is to characterize diffusion by observing the movement of colored solvents, liquids colored with dyes, or index of refraction gradients in the material. These methods have not been successfully applied to coals because of the high opacity of coals and the difficulty in fabricating satisfactory samples.

In this study we report the first successful "in situ" microscopic observations of diffusion in coals. The techniques involved first producing uncontaminated thin section specimens of coals using methods developed in our laboratory. Then special procedures were developed for securing the specimen, shielding the top and bottom surfaces from the penetrant and exposing the edge of the thin section to the selected solvent. This technique enables one to follow the kinetics of the diffusion in detail under the microscope in transmitted light as the solvent penetrates the coal. In this manner the maceral composition, mineral matter, and other aspects of the microstructure are observed directly during the diffusion process, and the heterogeneity of the coal can be accounted for

explicitly. This is crucial to the understanding of the diffusion phenomenon in coals since for adequate evaluation it is necessary to be able to measure the progress of the solvent into each of the micro-components which are being penetrated within the coal.

## EXPERIMENTAL

The coal used in these studies was Illinois No. 6 from the Monterey No. 1 mine which is of high volatile C bituminous rank. Because coal is so highly absorbing in the visible region of the spectrum, transmitted light optical microscopy can only be done with very thin specimens. Unfortunately, coal is a fragile material in thin pieces and it readily breaks into small fragments. For this reason special techniques must be used to prepare the thin section specimens. To avoid fragmentation of the thin slivers of coal, the specimens are normally embedded in an adhesive cement such as an epoxy adhesive. However, the diffusional characteristics of such embedded specimens are affected by the adhesives, so they are not satisfactory for diffusion studies. Canada Balsam has been used by many investigators as a securing agent for the coal. It can be mostly removed, but it leaves behind residues which are undesirable contaminants in the coal and may affect diffusion in unpredictable ways. The sample preparation procedure used to prepare the samples for this study utilized an adhesive which is completely soluble. The adhesive is a paraffin-based embedding wax (1). It is soluble in hexane which has a minimal effect on the coal. This sample preparation procedure has been described previously (2) and will not be described further here. The samples were cut perpendicular to the bedding plane. The thin sections were about 15 micrometers thick and roughly 0.5 mm across.

All of the experiments described in this paper were at room temperature and atmospheric pressure. The diffusing liquid used in this study was reagent grade pyridine.

Once satisfactory thin section specimens have been prepared they cannot simply be immersed in the solvent. If the whole surface of the sample were exposed to the solvent, then penetration would occur from all sides and the specimen would be rapidly penetrated in its thin direction from solvent coming through the top and bottom. The kinetics of this process would be difficult to interpret and even more difficult to quantify. Rather, it is desirable to prevent the solvent from penetrating through the top or bottom of the thin section and to allow it to penetrate only from one edge. Unfortunately, because of the tiny size and delicate character of the specimens one can not simply dip one edge of the sample in the solvent.

Two different techniques for holding the thin section samples and exposing them to the penetrating liquid were developed. Each of the techniques has advantages and disadvantages depending on the particular type of information which most interests the investigator. In the "grease-immersion" technique the solvent is prevented from contacting most of the top and bottom surfaces of the thin section by coating most of these surfaces with a grease. The grease must itself be an adequate barrier to the solvent. Some of the materials which were found usable were fluorinated greases (3) and a low molecular weight uncrosslinked butyl rubber (4). A small area of the top and bottom surfaces is left uncoated to avoid getting grease on the edge. The thin section is then placed between two glass slides. A schematic diagram of the grease-immersion setup is shown in Figure 1. At the start of the experiment a drop of liquid solvent is placed in contact with the uncoated edge of the thin section. The liquid then penetrates through one edge and propagates into the thin section of coal parallel to the surface.

In the weighted coverglass method the thin section of coal is sandwiched between a 1 mm thick glass slide on the bottom and a No. 1-1/2 glass coverslip on top. Weights are put along the edges of the coverslip so that good contact between the coal and the glass surfaces is insured. While it might be thought that the solvent would very rapidly wick along the glass surfaces and thereby quickly penetrate the coal from the top and bottom surfaces, this did not tend to occur in practice. Apparently, where the solvent does penetrate in between the glass and the

top or bottom of the thin section, the coal swells. This swelling effectively plugs up the channels where the solvent was penetrating -- right where the plug was needed. Additionally, where the solvent penetrated along the surface of the coal, it transformed the surface coal material into a rubbery state. The rubbery surface-coal acted as a gasket preventing any appreciable further penetration by the solvent.

During a diffusion experiment the solvent can not be directly observed within the coal because it is transparent. Rather, the swelling caused by imbibition of the solvent renders the diffusion observable. When the solvent swells the coal it appears to be a lighter color. This lighter color occurs primarily because for the swollen coal there is less material per unit cross sectional area of the coal in the path of the light passing through the sample. There may also be an effect caused by the change in index of refraction of the pore space as it becomes filled with fluid, but this effect is far less than from swelling for the pyridine-Illinois No. 6 coal system.

An "in situ" diffusion experiment was started by bringing a drop of solvent into contact with the edge of the coal thin section which was properly set-up as described in the previous section. The time of liquid contact was recorded and the sample was observed on the microscope stage in transmitted light. Periodically photomicrographs were taken and the time was noted in order to record the kinetics of the process. The liquid was kept in contact with the edge of the coal throughout the experiment.

## RESULTS AND DISCUSSION

### Diffusion of Pyridine in relatively homogeneous vitrinite

A thin section sample of Illinois No. 6 coal consisting of relatively homogeneous vitrinite was used for a diffusion experiment. The sample was placed in the grease-immersion setup. Liquid pyridine was brought into contact with the exposed edge of the sample. The thin section was then observed in the microscope as the liquid penetrated into the edge of the sample and diffused into the coal parallel to the surface of the thin section. Figure 2 shows the sample after 50 minutes exposure to the pyridine. The circle of light on the sample is caused by the field diaphragm of the microscope which is partially closed to keep light from passing around the sides of the sample. Illuminator light which does not pass through the coal is very bright and the haze caused by it tends to obscure the more dimly illuminated structural features of the coal. In Figure 2 a very abrupt change in coloration at the diffusion front is evident. Just ahead of the diffusion front the coal is the dark red color of the unchanged coal whereas just behind the front the coal is a much lighter orange-yellow color. This sharp diffusion front having an abrupt change in penetrant concentration demonstrates that the diffusion of the liquid in the coal is highly concentration dependent. A strong concentration dependence is characteristic of many macromolecular materials, especially in cases where the imbibition of the liquid transforms the macromolecular substance from a glassy material to a rubbery or viscous state and/or where the solvent swells the sample. In the coal behind the diffusion front where the solvent has already penetrated to an appreciable concentration there is relatively little change in the color of the coal. Since the color of the coal is related to its degree of swelling or the concentration of imbibed solvent, it is seen that there is relatively little change in the concentration of the solvent in the coal behind the diffusion front.

There are several particular modes of diffusion which could cause the very abrupt change in solvent concentration at the diffusion front along with the small change in solvent concentration behind the front. For example, a system where some of the penetrant can react with the matrix and the reaction is faster than the diffusion, can exhibit a relatively sharp front. Also, a relatively sharp front will result from a Fickian diffusion coefficient which is small at low concentrations of penetrant, but which abruptly jumps up to a much larger value at some concentration.

We had demonstrated previously (5) that swelling of this coal with pyridine depresses the glass transition temperature of the coal below room temperature and transforms it into a rubbery state. For polymers, when a liquid plasticizes it to above its glass transition, the diffusion is sometimes of Case II type (6). Case II is the name given to diffusion which has the following characteristics (7). There is a very sharp diffusion front. The diffusion front propagates into the material at constant velocity. And, there is extremely small variation in the concentration of the penetrant in the region behind the diffusion front. We have shown that the diffusion of pyridine into vitrinite in Illinois No. 6 coal has the first and last of these characteristics. The velocity of movement of the diffusion front will be discussed later.

The diffusion front in Figure 2 has substantial curvature and is somewhat irregular. The curvature may be caused by the exterior geometry of the sample and/or the shape of the region where the liquid pyridine contacts the coal. The irregularity of the diffusion front is caused by the micro-heterogeneity of the vitrinite -- even though it appeared relatively homogeneous under the microscope.

Large regions of variable coloration are seen trailing behind the diffusion front in Figure 2. The pattern of the coloration suggests that it is caused by strains in these flexible regions of the sample behind the diffusion front which are restricting solvent uptake. Such strains might be caused by stresses resulting from the swelling, which is highly anisotropic in the vicinity of the diffusion front. Strains could also have been caused by deformation of the coal at some earlier stage in its evolution. Another possibility is that this coloration comes from regions having variable composition which results in a variable rate of swelling. However, the relationship between these regions of variable color and the position of the diffusion front makes it most likely that this behavior is a direct consequence of the diffusion and/or the resultant swelling.

The diffusion front is somewhat ragged, but it is not grossly irregular. There are bits of unswollen vitrinite just behind the front. There is a prominent "finger" of vitrinite which has not yet been swollen by the pyridine; however, there are some channels of swollen material in it which have been penetrated by the pyridine. This finger of vitrinite clearly must be appreciably different from the surrounding vitrinite.

Figure 3 shows the sample after 78 minutes exposure to the pyridine. The shape of the diffusion front has changed considerably. It is seen that the finger of Figure 2 has been completely penetrated by the pyridine and is now indistinguishable from the surrounding vitrinite. It is also seen that the small bits of unpenetrated vitrinite behind the front in Figure 2 have been penetrated and swollen. It was observed that when these small regions begin to change to a lighter color in one part they then tend to change relatively quickly to the lighter color overall. It appears as if there is some sort of barrier to the solvent surrounding these small regions, perhaps a membrane or coating. Then, once the barrier becomes penetrated by the solvent the whole inside is relatively rapidly penetrated. It is clear from these photographs that the "homogeneous-appearing" vitrinite is far from homogeneous, but rather there is considerable variation from region to region within it.

A potential difficulty with the grease-immersion technique used in this experiment is that transfer of solvent either into or out of the top or bottom surfaces of the thin section may occur via the grease. The greases utilized were selected to minimize this effect. In addition, during the "in situ" experiment the sample was carefully monitored for evidence of appreciable solvent transfer through the grease. For example, appreciable direct transfer of solvent from the liquid reservoir through the grease to the coal would be expected to produce thin solvent-swollen regions along the edges of the sample, or at least to perturb the solvent concentration at the junction of the diffusion front with the edge of the sample. No evidence of either of these effects was observed. However, an estimate of the magnitude of loss or gain of solvent through the grease would be desirable to reliably evaluate its effect on the kinetics of the diffusion process.

When the sample was observed through the optical microscope in transmitted light between crossed polarizers, a thin, orange-colored line stood out against the

darkened thin section. With time, this thin line moved further into the sample. When the polarizers were removed, it was seen that the thin orange line corresponded to the position of the diffusion front; that is, it occurred at the position where the color of the coal changed from the dark red color of the unswollen coal to the light orange color of the expanded coal. The thin orange-colored line which is observed between crossed polarizers at the position of the diffusion front is apparently caused by the orientation of the coal structure in this region. The expanding coal behind the diffusion front is constrained by the unswollen coal ahead of the diffusion front. This can be expected to stretch and align the macromolecular network in this region. Such partially oriented macromolecular chains cause a significant difference in the index of refraction parallel and perpendicular to the direction of orientation. This causes a rotation in the direction of polarization of light passing through the specimen. The result is that some light passes through the second of the crossed polarizers. A short distance behind the diffusion front there is enough flexibility that the macromolecular orientation is diminished and the orange line is no longer seen. The orientation of the structure in the region of the diffusion front and the relaxation of the orientation behind the front are further evidence for the macromolecular nature of the coal and the transition of the coal from a rigid to a rubbery material.

#### Diffusion of pyridine in coal having a heterogeneous striated structure

A thin section of Illinois No. 6 coal having a heterogeneous striated structure was used in a diffusion experiment. The sample was about 15 micrometers thick and, as in the other samples, its surface was perpendicular to the bedding plane. Figure 4 shows the sample after its edge has been in contact with liquid pyridine for 4 minutes. The dark gray material seen in the photomicrograph is the vitrinite or wood-derived component of the coal. In this sample it is seen to occur as strands which are approximately parallel to the bedding plane. The bedding plane is seen edge-on in the photograph. The lighter bits of material are the liptinite which is the more hydrocarbon-rich waxy component. This component is derived from non-woody parts of plants such as spores, pollen, and stem and leaf coatings.

A sharp diffusion front is seen in Figure 4. The front is similar to that seen in the homogeneous vitrinite sample of Figure 2. The front here, though, is more ragged because of the different macerals present in the sample. It is also seen that some of the vitrinite strands behind the diffusion front are far more darkly colored than the other vitrinite behind the front. Apparently these particular vitrinite macerals are more slowly penetrated by the pyridine. In time, though, these macerals are penetrated and swollen and become light-colored.

Figure 5 shows the sample after 52 minutes exposure to pyridine. Although the coal specimen in Figure 5 is quite heterogeneous, the diffusion front is not far from being straight. There are, however, a number of small fragments of vitrinite behind the front which appear to be very slightly, if at all, penetrated by the pyridine. These bits of vitrinite may have a coating or membrane surrounding them which retards penetration by the pyridine, or this material may have a less permeable structure which the pyridine penetrates more slowly. However, with time almost all of these darker fragments behind the diffusion front are swollen and become light-colored. It is also evident from comparing Figures 4 and 5 that there has been substantial swelling in the pyridine of the large liptinite maceral in the left center of the photomicrograph.

#### Diffusion rates parallel and perpendicular to the bedding plane

In order to compare the diffusion rates of the solvent parallel and perpendicular to the bedding plane of the coal all four edges of a thin section were simultaneously exposed to the pyridine. This sample had a striated structure. Its surface was perpendicular to the bedding plane; the bands of material ran parallel to the bedding plane and the direction perpendicular to the bands was perpendicular to the bedding plane. Figure 6 shows this thin section after 15 minutes in contact

with the liquid pyridine. It is seen that the penetration rates of the pyridine in the directions parallel and perpendicular to the bedding plane are comparable.

Some investigators have reported that the diffusion rates of various fluids in coals is much faster parallel to the bedding plane than perpendicular (8,9). An important difference between these prior investigations and our current studies is that we are observing primarily intra-maceral diffusion whereas earlier work was more effected by larger scale diffusion. We showed earlier (9) that major routes for rapid penetration of the coal structure included intermaceral interfaces, cracks, holes, and regions containing mineral matter accumulations. These types of irregular regions within the coal tend to extend along the bedding plane. Therefore, on a large scale faster diffusion can be expected parallel to the bedding plane. Our studies however, are more concerned with the finer structures of the coal. We have focused on the diffusional behavior within individual vitrinite macerals within the coal. Within the individual macerals or for groups of macerals which are in intimate contact with each other and which do not contain substantial irregular regions, the diffusion rates parallel and perpendicular to the bedding plane are comparable.

#### Self-sealing in coal undergoing solvent-swelling

A thin section sample of vitrinite was exposed to pyridine using the weighted coverglass method. In Figure 7, the sample is shown after 60 seconds contact with the pyridine. Note the lightened areas indicating solvent penetration and solvent swelling along the edges of the large crack in the sample as well as along the edges of the sample. The sample is shown in Figure 8 after 100 seconds exposure to the pyridine. Note that the large crack has fully closed. Also, whereas the diffusion front has moved substantially in from the outer edges of the sample there has been relatively little movement of the diffusion front along the edges of what was the large crack. Figure 9 shows the sample after a total of 210 seconds exposure to the pyridine. There has been considerable additional movement of the diffusion front into the coal from the edges. However, along what was the large crack there has been little change in the coal.

These observations illustrate one important mechanism which can occur during the diffusion of good swelling solvents into coals. The swelling of the coal may seal-off cracks and holes in the coal and thereby stop or diminish penetration of the solvent through these routes. Although such routes may constitute a very small volume of the coal, if they were not sealed by the swelling they can be major routes for uptake of the solvent. For example, our prior work on diffusion of oxygen into coals (9) has shown that the cracks and holes provide paths for rapid penetration of oxygen into the interior of the coal.

The self-sealing effect may also have important consequences on the sub-microscopic scale. Pores within the coal, or inter-maceral interfaces in the coal which have previously been shown can be routes for rapid penetration by fluids (9) may be sealed by swelling if the solvent starts to penetrate them. On the other hand, porosity within mineral matter accumulations is less likely to be plugged by swelling (unless there is a substantial concentration of swellable organic matter within the region of mineral matter. Note, however, that the sealing mechanism is only expected to be operable in localized regions which swell in advance of surrounding materials. If all of a region swells isotropically, then cracks and holes in the region will also swell and sealing will not occur. It should be kept in mind, however, that the converse of self-sealing frequently occurs; that is, stresses produced during solvent swelling often produce cracks in coal particles (10).

#### Kinetics of Diffusion and Re-diffusion

The movement of diffusion fronts as they penetrated into thin section specimens was quantified for several samples. For each sample the rate of propagation of the diffusion front into the sample was quantified. The results were somewhat variable, probably because of the heterogeneous nature of the coal. For



all samples measured, though, there was a pronounced slowing down of the velocity of the diffusion front with increasing time, as the front penetrated deeper into the sample. This would suggest that the diffusion is not Case II. However, because the amount of solvent penetrating through the grease, or between the glass slide and the coal into the top and bottom surfaces of the coal has not been accurately quantified (though qualitative checks were made -- see earlier in this section), it would be desirable to corroborate these results either through an accurate evaluation of this contribution to solvent uptake or by using alternate techniques.

After the diffusion front had propagated well into the thin section, the pyridine was removed and the sample was allowed to dry at room temperature in nitrogen gas for several days. Then the same diffusion experiment as before was repeated. Figure 10 shows graphically the results for both the original diffusion and the second exposure after drying. It is evident that the movement of the diffusion front is much more rapid for the second run, after the sample has previously been swollen by the pyridine and dried. This faster diffusion in the second run had been observed in our previous work where thin sections were fully immersed in liquid pyridine and penetration occurred primarily through the top and bottom surfaces (11).

There are several possible contributions to the more rapid penetration of the pyridine the second time. When the sample is dried after the initial swelling, some of the pyridine remains in the coal (12). So, less pyridine diffuses into the coal the second time. In addition, the residual pyridine probably weakens some of the inter-molecular interactions so that the new pyridine diffusing in encounters a looser structure and can therefore swell the coal more readily. Another possibility is that the initial swelling and drying causes microcracks in the structure so that subsequent diffusion can utilize these new routes. However, in the regions where the diffusion rate was measured, no diffusion via microcracks was observable in the optical microscope. There may also have been some effect on the diffusion rate from some bitumen being extracted from the coal during the first diffusion run.

## CONCLUSIONS

Diffusion into coal has been observed "in situ" at the microscopic level for the first time. This technique which utilizes uncontaminated thin sections of coal enabled the study of true intra-maceral diffusion as distinguished from the usual concurrent diffusion in a variety of maceral structures, or diffusion via cracks, mineral matter, macropores, or maceral interfaces. For diffusion of a good solvent into a high volatile bituminous coal, a sharply defined front occurred, and the diffusive flow was highly concentration dependent. The movement of the front slowed with depth of penetration into the coal. When the sample was placed between crossed polars, a thin light line was seen along the diffusion front against the dark background. This indicates that orientation of the macromolecular network occurs as a result of the stresses in the vicinity of the front. For intra-maceral diffusion in vitrinite there was no obvious difference between the rates of movement of the front parallel versus perpendicular to the bedding plane. When the liquid was desorbed and then reabsorbed, the diffusion rate was considerably faster the second time. Liquid penetration into cracks in vitrinite was initially rapid, but the swelling which resulted often sealed the cracks, greatly reducing further penetration.

## ACKNOWLEDGEMENTS

The encouragement and support of M. Siskin and M. L. Gorbaty in this investigation is gratefully acknowledged. The technical assistance of M. S. Beam in the preparation of the thin section samples is greatly appreciated.

## REFERENCES

1. Paraplast is a paraffin-based embedding wax having a melting point of 57°C. It is manufactured by the Lancer Co., St. Louis, MO, USA.
2. Brenner, D. in "Coal Structure" (Ed. R. A. Meyers), Academic Press, New York, 1982, pp 254-263.
3. Some usable fluorinated greases are Krytox, manufactured by DuPont and Fomblin manufactured by Montedison.
4. LM Butyl, manufactured by Exxon Chemical Company.
5. Brenner, D., Nature, 306, No. 5945, 772 (1983).
6. Crank, J., "The Mathematics of Diffusion", Second Edition, Chapter 11, Clarendon Press. Oxford (1975).
7. Alfrey A., Gurnee, E. F., and Lloyd, W. G., J. Polym. Sci., C12, 249 (1966).
8. Attar, A., and Warren, D., "Division of Fuel Chemistry Preprints", 26, No. 3, pp. 172-177, Am. Chem. Soc. National Meeting, New York, New York (1981).
9. Brenner, D., "Division of Fuel Chemistry Preprints", 26, No.1, pp. 42-49, Am. Chem. Soc. National Meeting, Atlanta, Georgia (1981).
10. Brenner, D., Fuel, 62, 1347, (1983).
11. Brenner, D., Fuel, 63 pp 1324-1328, (1984).
12. Collins, C. J., Hagaman, E. W., Jones, R. M. and Raaen, V. F. Fuel, 60, 359 (1981).

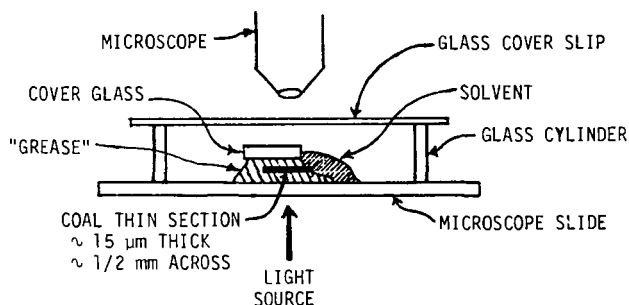


Figure 1. Grease-immersion setup for "in situ" microscopic observations of solvent diffusion in coals.



Figure 2. Diffusion of pyridine in relatively homogeneous vitrinite, after 50 minutes contact of edge with liquid pyridine.



Figure 3. Diffusion of pyridine in relatively homogeneous vitrinite, after 78 minutes contact of edge with liquid pyridine.



Figure 4. Diffusion of pyridine in a heterogeneous striated coal structure, after 4 minutes contact of edge with liquid pyridine.



Figure 5. Diffusion of pyridine in a heterogeneous striated coal structure, after 52 minutes contact of edge with liquid pyridine.



Figure 6. Comparison of diffusion rates parallel versus perpendicular to the bedding plane.

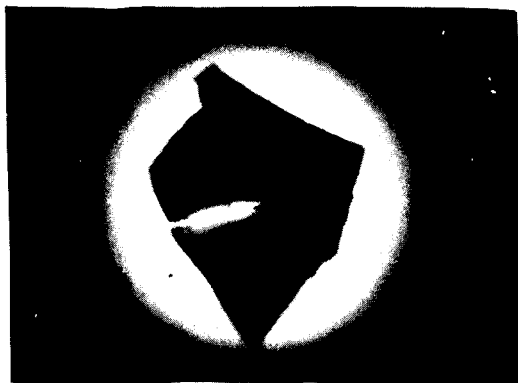


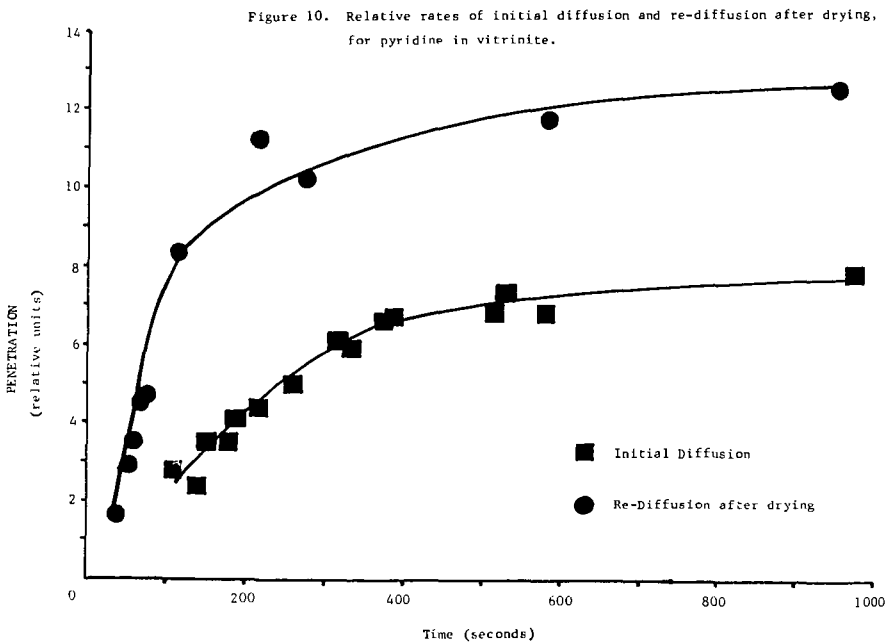
Figure 7. Thin section with crack, after 60 seconds exposure to pyridine.



Figure 8. Crack in thin section sealed by swelling, after 100 seconds exposure to pyridine.



Figure 9. Thin section with sealed crack, after 210 seconds exposure to pyridine.



## SOLVENT SWELLING OF COAL 1. DEVELOPMENT OF AN IMPROVED METHOD FOR MEASURING SWELLING PHENOMENA

Tetsuo Aida and Thomas G. Squires

Ames Laboratory\*  
Iowa State University  
Ames, Iowa 50010

### INTRODUCTION

Although the polymeric nature of coal was established over a quarter of a century ago (1), many phenomena which derive from its cross-linked, macromolecular structure are still not well understood. This includes one of the most important aspects of coal chemistry, the accessibility of solvents and/or chemical reagents to sites buried within the solid coal matrix (2). Thus, the rate and extent of chemical conversion and/or solubilization of these interior sites are governed by penetration of the macromolecular structure by an appropriate chemical agent. Generally, penetration of cross-linked, macromolecular solids by organic chemicals has been investigated using swelling techniques.

The swelling induced by contacting coal with organic solvents has been investigated intensively in recent years; and several convenient methods using both liquids and saturated vapors have been developed for measuring coal swelling properties (3). The liquid phase swelling behavior is particularly interesting because it is a reasonable measure of a solvent's ability to penetrate the coal matrix. Previously, investigators of this phenomenon have utilized some variation of the test tube technique developed by Dryden (4). In this method, the initial height of a dry coal bed,  $h_i$ , is compared to the final swollen height,  $h_f$ , after equilibration with solvent. These values are used to compute the equilibrium swelling ratio,  $Q = h_f/h_i$ , for each solvent.

However, the accuracy of this method is not satisfactory, particularly at lower ( $Q < 1.3$ ) and higher ( $Q > 3.0$ ) swelling ratios; and it is also quite difficult to investigate dynamic swelling behavior. Moreover, the  $Q$ -value reflects not only interactions between solvent and coal, but is also grossly affected by complicated elastic restoring forces in the coal network due to covalent bond cross-linking, hydrogen bonding, or  $\pi$ - $\pi$  interactions between condensed aromatics. On the other hand, initial swelling rates may isolate interactions between solvent and coal by minimizing the involvement of such complicated restoring forces.

On the basis of these considerations, we have developed a new method for the dynamic measurement of liquid phase solvent swelling phenomena which is 100 times more accurate than conventional methods. We have used this technique to determine  $Q$ -values and initial swelling rates for Illinois No. 6 Coal with a variety of solvents. Here we present our initial experimental results and compare these findings with those obtained using conventional methods.

---

\* Operated for the U.S. Department of Energy by Iowa State University under Contract No. W-7405-Eng-82.

## EXPERIMENTAL

### Materials

Illinois No. 6 Coal from the Ames Laboratory Coal Library was used in these studies. This coal has the following ultimate analysis (dmmf basis): 78.82% C; 5.50% H; 1.59% N; 2.29% S<sub>org</sub>; and 10.05% ash. Prior to use, this coal was ground, sized, and dried at 110°C overnight under vacuum. Except for commercial "Gold Label Grade" reagents (Aldrich Co.) which were used without further purification, solvents were distilled by ordinary procedures before use.

### Apparatus

As shown in Figure 1, this apparatus is similar in principle to an osmotic pressure measurement device, except that coal and solvent are separated by 10  $\mu$  stainless steel filter. In each experiment, the movement of the piston as a function of time was recorded; and the initial swelling rate ( $V_i$ ) was determined graphically as shown in Figure 1. The Q-value was calculated by dividing the final volume,  $S_0 + \Delta S$ , by the initial volume,  $S_0$ .

### General Procedure

In a typical experiment, 500 mg. of Illinois No. 6 Coal was placed in the cylinder bottom and covered by the piston. The pressure on the piston was adjusted to 5.0 g/cm<sup>2</sup> and was maintained at this level throughout the experiment. After positioning the piston, the entire system was evacuated to 0.20 - 0.15 mm Hg for 10 minutes. The valve of the solvent container was then opened allowing the solvent to contact the coal; and the movement of the piston was recorded as a function of time.

## RESULTS AND DISCUSSION

### Comparison of New Method and Conventional Method

Conventional swelling measurements were carried out using a 10 mm x 75 mm test tube, 2.0 g of Illinois No. 6 Coal, and 8.0 ml. of THF. The height of coal bed was read at five minute intervals after shaking the mixture vigorously each time. As shown in Figure 2, there is an interesting contrast in swelling behavior as measured by the two methods. In the case of the conventional method, the rate is retarded in the early stages of swelling, possibly because many pores are filled with air and the solvent cannot achieve intimate contact with the coal surface during this initial stage.

For the more interactive solvents, a higher Q-value was observed using the new method. This is probably because, in contrast to the conventional method, there is no mechanical agitation of the coal bed; and the integrity of the coal bed is thus maintained throughout the swelling measurement. In support of this hypothesis, the new apparatus was found to be quite sensitive to mechanical shock which usually resulted in an instant drop in the reading.



### Sensitivity of New Method

In a 500 mg. experiment, our new apparatus can detect a volume change of  $10^{-4}$  ml, that is the Q-value can be determined to  $\pm 0.0001$ . However, for practical reasons, we prefer to report the data to  $\pm 0.01$  Q-value units. Typical Q-values measured by this method are included in Table I along with data obtained by conventional measurements.

Table I. Comparison of Methods for Measuring Q-values<sup>a</sup>

SOLVENT	Benzene	Toluene	p-Xylene	Methanol	THF	0.5N <sup>b</sup> Bu <sub>4</sub> NOH
Q <sub>N</sub> <sup>c</sup>	1.04	1.06	1.06	1.24	2.20	4.15
Q <sub>C</sub> <sup>d</sup>	~1.3	~1.3	~1.3	1.4	1.8	--

a. Illinois No.6 Coal measured at 21.0°C

b. Solution in pyridine/methanol (1:1 vol.)

c. Present method

d. Conventional method

Our new method exhibits some obvious advantages, both at lower and higher swelling conditions, which will allow us to examine subtle differences in swelling behavior. An interesting contrast in the two methods is found in the relative Q-values for methanol and hydrocarbons. The reason for the difference is not clear at the present time, but may involve non-swelling volume increase processes like particle-particle repulsions. In the new method such forces are apparently overcome by the pressure of the piston. At the other extreme, Q = 4.15 for the tetrabutyl ammonium hydroxide solution is the highest swelling ratio which we have ever measured for Illinois No. 6 Coal.

### Determination of Initial Swelling Rate

In order to evaluate the capability of this method for investigating kinetic phenomena, several experiments were conducted. The effect of particle size on coal swelling rates was first examined. As expected, swelling rates are very sensitive to particle size. As shown in Figure 3, 200 x 400 mesh Illinois No. 6 Coal swells in THF at approximately 10 times the rate of 25 x 60 mesh coal. The temperature dependence of the THF-coal interaction in the range of 20 to 40°C was also examined. Interestingly, the Q-value was not affected by temperature, while the initial swelling rate increased by 15% for each 10°C increase (see Figure 4).

Although the actual penetration of the solvent and/or chemical reagent will not always be reflected by the Q-value or initial swelling rate, we believe that they provide a quite useful basis for designing chemical conversions or extractions of coal. One such basis for evaluating solvents is presented in Table II. Here, the swelling rates of common solvents, including some hydrogen donor solvents, are compared using a new parameter,  $\tau_{10}$ , which is defined as the time which would be necessary to swell the initial volume by 10%. This value is calculated on the basis of the initial swelling rate.

Table II. Comparison of Swelling Rates Using  $\tau_{10}$ <sup>a</sup>

Solvent	$\tau_{10}$	Solvent	$\tau_{10}$
n-Propylamine	10 sec.	Benzene	1.7 hrs.
Pyridine	48 sec.	Quinoline	5.0 hrs.
DMSO <sup>b</sup>	1.8 min.	Indoline	16.6 hrs.
THF <sup>c</sup>	1.6 min.	THQ <sup>d</sup>	2.0 mos.
Acetone	2.7 min.	Tetralin	>1.0 year
Methanol	3.1 min.		
Dichloromethane	4.7 min.		

a. Illinois No.6 Coal, 60 x 100 mesh, measured at 21°C.

b. Dimethylsulfoxide

c. Tetrahydrofuran

d. 1,2,3,4-Tetrahydroquinoline

Relation Between Initial Swelling Rate ( $V_i$ ) and Q-Value

Prior to undertaking these experiments, we expected a direct relationship between Q-values and  $V_i$ 's because we understood that both are a measure of the relative affinity of solvent for coal. The results obtained are presented in Table III.

Table III. Comparison of Q-Value and  $V_i$ <sup>a</sup>

SOLVENT	Q-Value	$V_i \times 10^2$
Methanol	1.24	3.2
CH <sub>2</sub> Cl <sub>2</sub>	1.23	2.1
Acetone	1.50	3.7
THF	2.20	6.2
Quinoline	2.35	0.03
n-Propylamine	2.45	58.6
NH <sub>2</sub> CH <sub>2</sub> CH <sub>2</sub> NH <sub>2</sub>	2.60	46.4
DMSO	2.80	4.8
Pyridine	2.90	12.5

a. Illinois No.6 Coal, 60 x 100 mesh, measured at 21°C.

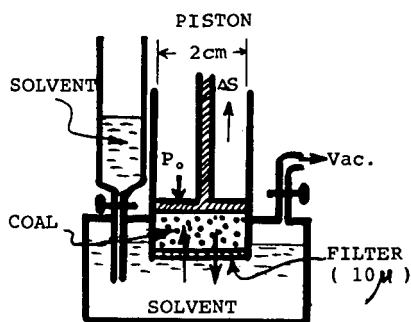
We are puzzled by the lack of correlation between  $V_i$  and Q-value. However, two possible explanations come to mind. Initial swelling rates could be more sensitive than Q-values to solvent viscosities and steric requirements. A more detailed study of these factors, especially steric requirements for solvent swelling of coal, will be presented in the next paper.

## ACKNOWLEDGEMENTS

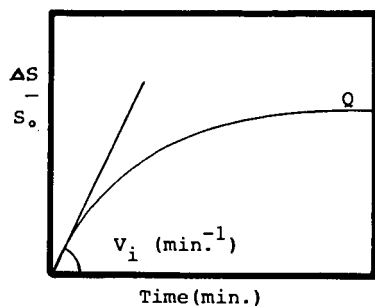
We wish to thank Professors R. S. Hansen and D. K. Finnemore for their useful discussion and encouragement. We are grateful for support from The State of Iowa, and from the U. S. Department of Energy through the Ames Laboratory under Contract No. W-7405-ENG-82. The opinions, findings, and conclusion expressed herein are those of the authors, and do not necessarily reflect the views of DOE or the State of Iowa.

#### REFERENCES

1. van Krevelen, D. W., "Coal" Elsevier Publishing Co., Amsterdam, 1961, pp. 433-452.
2. Larsen, J. W.; Green, T. K.; Choudhury, P.; Kuemmerle, E. W. Adv. Chem. Series 1981, 192, 277.
3. Key references are cited in a recent paper by Green, T. K.; Larsen, J. W. Fuel 1984, 63, 1539.
4. Dryden, I. G. C. Fuel 1951, 30, 145.



$P_0$ : Initial Pressure  
 $\Delta S$ : Increased Volume



$S_0$ : Initial volume of coal  
 $V_i$ : Initial swelling rate

Figure 1. Method for Measuring Liquid Phase Solvent Swelling of Coal.

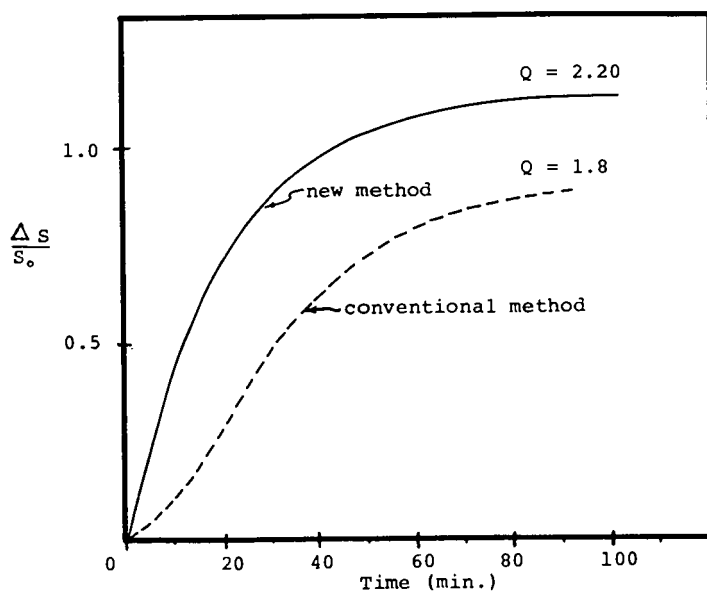


Figure 2. Comparison of THF Swelling Patterns for Illinois No. 6 Coal at 21.0°C.

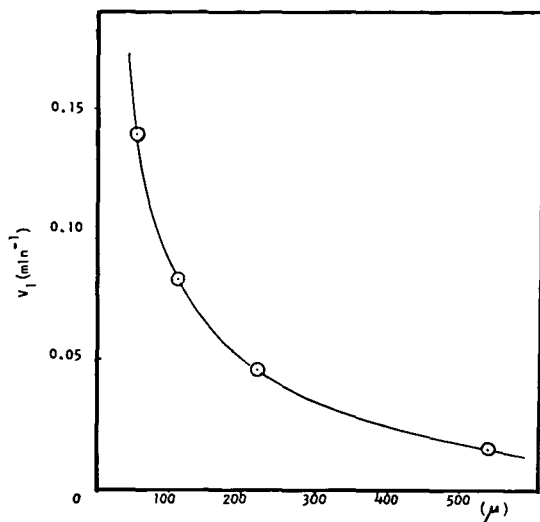


Figure 3. Effect of Particle Size on Initial THF Swelling Rate of Illinois No. 6 Coal (21.0°C).

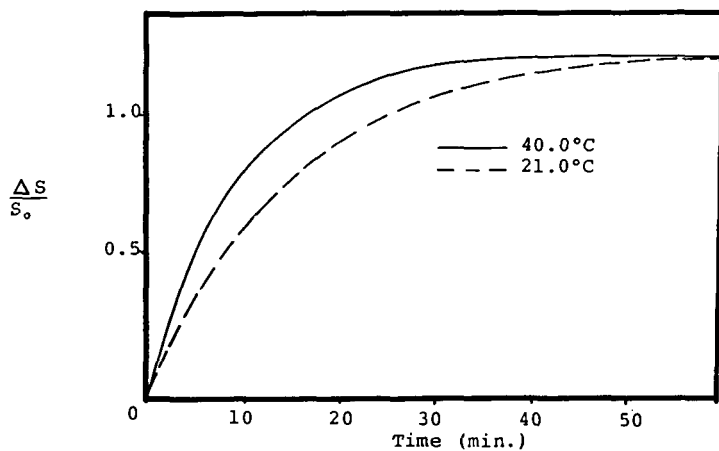


Figure 4. Temperature Effect on THF Swelling Behavior of 60 x 100 mesh Illinois No. 6 Coal

## SOLVENT SWELLING OF COAL 2. INVESTIGATION OF STERIC REQUIREMENTS

Tetsuo Aida and Thomas G. Squires

Ames Laboratory\*  
Iowa State University  
Ames, Iowa 50011

### INTRODUCTION

Some time ago it was established that, as a solid, microporous material, coal behaves as a molecular sieve (1), i.e. it discriminates among molecules diffusing into the pore system on the basis of size, shape, and functionality. It seems to us that the process by which solvent molecules penetrate the solid coal matrix should be similarly selective. The investigation of such phenomena is important, not only from the perspective of understanding the accessibility of chemical agents to sites within the coal matrix (2), but for the rational design of chemical conversion processes.

Recently, we developed a new method for accurately measuring both the dynamic and equilibrium solvent swelling behavior of coal (3). Here, we report the initial application of these techniques to the investigation of accessibility phenomena. From this study, which examines the steric interactions between solvent and coal, we expect to obtain a better understanding of the mechanism by which chemical agents penetrate the coal matrix.

### EXPERIMENTAL

The swelling measurements were carried out as described in the previous paper (3); and the initial swelling rates were determined graphically. All coals used in these studies were from the Ames Laboratory Coal Library. Prior to use, the coals were ground, sized to 100 x 200 mesh, and dried at 110°C overnight under vacuum. Except for commercial "Gold Label Grade" reagents (Aldrich Co.) which were used without further purification, solvents were distilled by ordinary procedures before use.

### RESULTS AND DISCUSSION


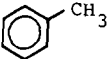
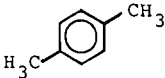
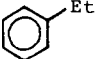
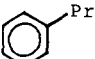
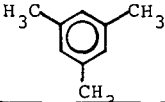
#### Swelling of Illinois No. 6 Coal in Hydrocarbon Solvents

The swelling data obtained with hydrocarbon solvents are shown in Table I. There apparently is no simple relationship between the initial swelling rate,  $V_i$ , and the equilibrium swelling ratio,  $Q$ , for this series of solvents. Neither is there an obvious relationship between viscosity and swelling behavior. However, with the exception

---

\*Operated for the U.S. Department of Energy by Iowa State University under Contract No. W-7405-Eng-82.

Table I. Swelling Behavior of Illinois No. 6 Coal in Hydrocarbons<sup>a</sup>

Hydrocarbon	Q	V <sub>Ret</sub> <sup>b</sup>	η <sub>20</sub>
	1.04	1.00 <sup>c</sup>	0.65
	1.06	0.40	0.59
	1.06	1.18	0.65
	--	4.00	0.69
	--	16.7	--
	--	30	--

a. 100-200 mesh, measured at 21.0°C

b. Rate Retardation Factor:  $V_i(\text{benzene})/V_i(\text{hydrocarbon})$ c.  $V_i = 2.73 \times 10^{-4} \text{ min.}^{-1}$ 

of toluene which initially swells about 2.5 times as fast as benzene, the sharp decrease in  $V_i$  from benzene to mesitylene suggests that there is a steric component to the rate constant for solvent penetration of the coal matrix.

#### Solvent Swelling Behavior of Illinois No. 6 Coal in Alcohols

The initial swelling rates ( $V_i$ ) and equilibrium swelling ratios (Q) were measured for C<sub>1</sub> through C<sub>4</sub> alcohols, and the results are summarized in Table II.<sup>1</sup> Except for methanol, Q-values for the unbranched primary alcohols were almost identical, while, with increasing chain length, a twelve-fold decrease in initial swelling rates was noted for this series. Although the latter behavior is consistent with that predicted on the basis of steric considerations, it is also consistent with the trend in solvent viscosities.

However, comparison of the initial swelling rates of *n*-propyl and isopropyl alcohol reveals a rate retardation factor ( $V_{\text{Ret}}$ ) of 4 for the branched isomer despite almost identical viscosities. Similar behavior is exhibited by the butyl alcohol series: compared to *n*-butyl alcohol, the initial swelling rates of isobutyl and *sec*-butyl alcohol are retarded by factors of 9 and 40, respectively. These large effects cannot be rationalized on the basis of viscosities.

Table II. Swelling Behavior of Illinois No. 6 Coal in Alcohols<sup>a</sup>

Alcohol	Q	$V_{Ret}^b$	$\eta_{20}$
MeOH	1.23	1.00 <sup>c</sup>	0.60
EtOH	1.34	1.92	1.2
n-PrOH	1.36	3.96	2.3
i-PrOH	--	14.18	2.3
n-BuOH	1.34	12.17	2.9
i-BuOH	--	103.4	4.2
s-BuOH	--	499.0	3.9

a. 100-200 mesh, measured at 20.0°C

b. Rate Retardation Factor:  $V_i(\text{methanol})/V_i(\text{alcohol})$ c.  $V_i = 3.18 \times 10^{-2} \text{ min.}^{-1}$ Solvent Swelling Behavior of Illinois No. 6 Coal in Amines

The swelling behavior of Illinois No. 6 Coal in various aliphatic amines was also examined. Once again, we can ascertain no significant differences among the Q-values for the entire series of amines. On the other hand, initial swelling rates for this series vary over a range of  $10^6$  and provide an unambiguous basis for establishing the importance of steric requirements. In fact, the evidence is so compelling that the results are simply reported, with minimum discussion, in Tables III-VI.

Table III. Swelling Behavior in Primary Amines.<sup>a</sup> Effect of Chain Length.

Structure	Q	$V_{Ret}^b$
$\text{CH}_3\text{CH}_2\text{CH}_2\text{NH}_2$	2.45	1.00 <sup>c</sup>
$\text{CH}_3(\text{CH}_2)_2\text{CH}_2\text{NH}_2$	2.64	2.05
$\text{CH}_3(\text{CH}_2)_4\text{CH}_2\text{NH}_2$	2.19	9.31

a. Illinois No. 6 Coal (100 x 200 mesh), measured at 21.0°C

b. Rate Retardation Factor:  $V_i(\text{n-Propylamine})/V_i(\text{amine})$ c.  $V_i = 5.86 \times 10^{-1} \text{ min.}^{-1}$ Table IV. Swelling Behavior in Primary Butyl Amines.<sup>a</sup> Effect of Chain Branching

Structure	Q	$V_{Ret}^b$
$\text{CH}_3(\text{CH}_2)_2\text{CH}_2\text{NH}_2$	2.64	1.00
$(\text{CH}_3)_2\text{CHCH}_2\text{NH}_2$	2.46	4.38
$(\text{CH}_3)_3\text{CNH}_2$	1.95	732

a. Illinois No. 6 Coal (100 x 200 mesh), measured at 21.0°C

b. Rate Retardation Factor:  $V_i(\text{n-Butylamine})/V_i(\text{amine})$



Table V. Swelling Behavior in  $C_6H_{13}N$  Amines.<sup>a</sup> Comparison of Primary, Secondary and Tertiary Isomers

Structure	Q	$V_{Ret}^b$
$CH_3(CH_2)_4CH_2NH_2$	2.19	1.00
$(CH_3CH_2CH_2)_2NH$	2.05	15.4
$(CH_3CH_2)_3N$	--	$1.5 \times 10^5$

a. Illinois No. 6 Coal (100 x 200 mesh), measured at 21.0°C

b. Rate Retardation Factor:  $V_i(n\text{-Hexylamine})/V_i(\text{amine})$

Table VI. Swelling Behavior in Secondary  $C_6H_{13}N$  Amines.<sup>a</sup> Effect of Chain Branching.

Structure	Q	$V_{Ret}^b$
$(CH_3CH_2CH_2)_2NH$	2.05	1.00
$[(CH_3)_2CH]_2NH$	--	1830

a. Illinois No. 6 Coal (100 x 200 mesh), measured at 21.0°C

b. Rate Retardation Factor:  $V_i(\text{Di-n-Propylamine})/V_i(\text{amine})$

The nature and divergency of these comparisons leave little doubt that steric factors play an important role in coal accessibility phenomena and can provide answers to a number of troublesome questions. For example, the lack of coal solubility in solvents such as triethyl amine and hexamethyl phosphoramide (HMPA), which (because of their "solubility parameters") should be good solvents (4), is clearly consistent with steric inhibition of coal matrix penetration by these hindered solvents.

#### Effect of Coal Rank on Solvent Swelling Behavior

In a final series of experiments, the rank dependent solvent swelling behavior of coals in three isomers of primary butyl amine was investigated. While we found small differences in the equilibrium swelling ratios for various coal/amine systems, we can detect no systematic relationship between rank and Q-values; and we have focused our attention on initial swelling rates. In order to correlate this data, we have defined two swelling parameters,

$$\theta_s = V_n/V_s \quad \text{and} \quad \theta_t = V_n/V_t$$

where  $\theta_s$  and  $\theta_t$  represent the steric sensitivity of coal toward secondary and tertiary branching in the butylamine isomers, and  $V_n$ ,  $V_s$ , and  $V_t$  are the initial swelling rates of coal in n-butylamine, sec-butylamine, and t-butylamine, respectively. These rate parameters, analogous equilibrium parameters, and carbon contents of the coals used in these studies are presented in Table VII.

Table VII. The Effect of Coal Rank on Steric Sensitivity.

Coal <sup>a,b</sup>	C(% dmmf) <sup>c</sup>	$\theta_s$	$\theta_t \times 10^3$	$Q_n/Q_s^d$
A	72.2	18.8	--	1.136
B	72.2	17.3	60.8	1.120
C	74.8	10.3	0.83	1.078
D	80.4	4.5	0.62	1.073
E	82.4	10.89	4.7	1.083
F	84.9	19.16	--	1.040

a. 100-200 mesh, measured at 21.0°C

b. A: Hanna No. 80; B: Dietz No. 1 & 2; C: Adaville No. 11;  
D: Illinois No. 6; E: West Kentucky No. 9; F: Pittsburgh No. 8

c. mm = 1.08 Ash + 0.55 S

d.  $Q_n$ : Q-value in n-butylamine;  $Q_s$ : Q-value in sec-butylamine

We have plotted  $\theta_s$  versus carbon content for the six coals used in this investigation. There appears to be some relaxation of steric requirements around 80% carbon content. While it is too early to speculate about the underlying basis for this behavior, we believe that it is related to the balance between covalent and non-covalent (hydrogen bonded) crosslinking (4). Investigation of these phenomena will be the target of future efforts.

#### ACKNOWLEDGEMENTS

We wish to thank Professors R. S. Hansen and D. K. Finnemore for their useful discussion and encouragement. We are grateful for support from The State of Iowa, and from the U. S. Department of Energy through the Ames Laboratory under Contract No. W-7405-ENG-82. The opinions, findings, and conclusion expressed herein are those of the authors, and do not necessarily reflect the views of DOE or the State of Iowa.

#### REFERENCES

1. van Krevelen, D. W., "Coal" Elsevier Publishing Co., Amsterdam, 1961, pp. 139-143.
2. Aida, T.; Squires, T. G., "Solvent Swelling of Coal. 1. Development of an Improved Method for Measuring Swelling Phenomena," Prepr. Pap.-Am. Chem. Soc., Div. Fuel Chem. Previous paper presented at this meeting (1985).
3. Key references are cited in a recent paper by Green, T. K.; Larsen, J. W. Fuel 1984, 63, 1539.
4. Green, T. K.; Brenner, D.; Kovac, J.; Larsen, J. W., "Coal Structure" (Ed. R. A. Meyers), Academic Press, New York, 1982.

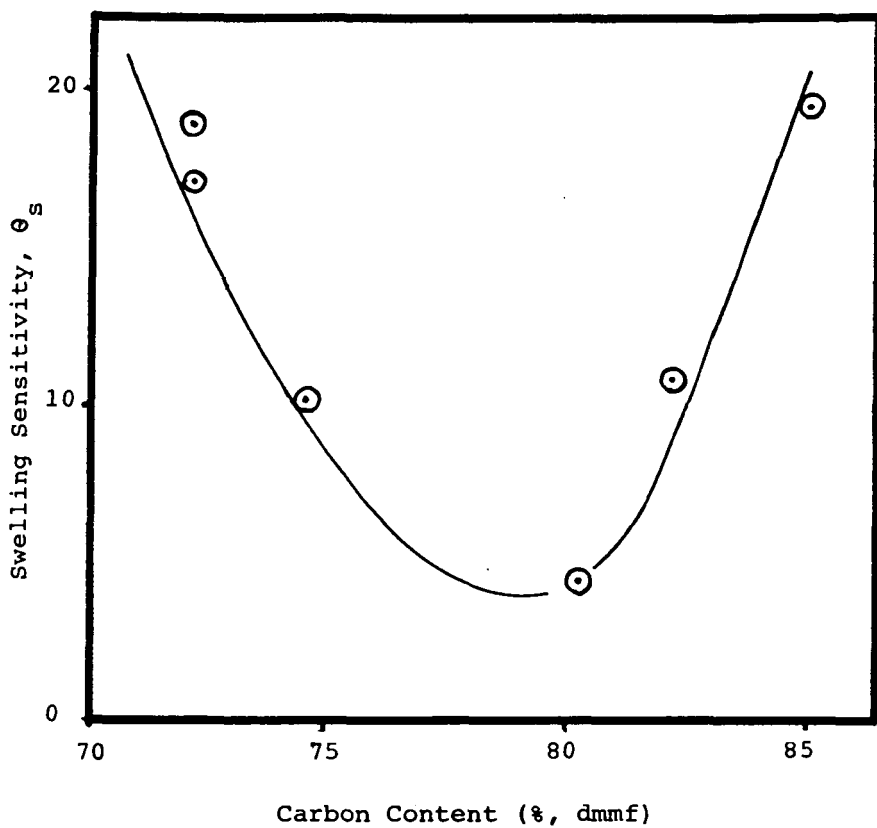


Figure 1. Dependence of Swelling Sensitivity on Coal Rank.

## MECHANISMS OF AMINE TRANSPORT IN COAL PARTICLES

Barbara D. Barr-Howell and Nikolaos A. Peppas

School of Chemical Engineering  
Purdue University  
West Lafayette, Indiana 47907

### INTRODUCTION

There exists considerable evidence in the literature which suggests that the organic phase of coal is a highly crosslinked macromolecular network. This analysis is supported by the fact that the organic phase of coals can swell in thermodynamically compatible solvents to twice its original volume without complete dissolution (Larsen and Kovac, 1978; Lucht and Peppas, 1981 a,b; Lucht, 1983). To aid in the study of the highly crosslinked coal network, Lucht and Peppas (1981a) proposed a simplified description of the organic phase, containing tetrafunctional and multifunctional crosslinks, unreacted functionalities, chain ends, entanglements, chain loops, and effective network chains. Physical crosslinks occur because the system is highly entangled. The chains have limited mobility and therefore are unlikely to disentangle. Chemical crosslinks result from chemical reactions and are stable under a variety of conditions.

Analysis of dynamic swelling results from macromolecular coal networks swollen by good solvents yields important information about solvent-network interactions and the structure of the network. Diffusion studies can be used to determine the thermodynamic state of the network, i.e., whether the network exists in the glassy or rubbery state. It is also possible to determine the type of solvent uptake which occurs in the network. The solvent uptake can occur by Fickian diffusion, anomalous transport, Case-II transport, or Super Case-II transport.

When a macromolecular network such as coal exists in the thermodynamic glassy state all large molecular chain motions are restricted, but the segmental motions are not necessarily limited. As the temperature of the network is increased to the glass transition temperature, large molecular chain motions become important and the network shifts to its thermodynamic rubbery state. The exact glass transition temperature of the macromolecular network is dependent on its chemical and physical nature. The presence of solvent can increase large molecular chain motions at lower temperatures thereby effectively lowering the glass transition temperature of the network. Anomalous diffusion occurs only below the glass transition temperature and at fairly high penetrant activities. Fickian diffusion occurs both in the glassy state and the rubbery state. Concentration-independent Fickian diffusion occurs generally at low penetrant activities or low temperatures.

A convenient method used in the analysis of sorption data employs fitting the sorption data to equation (1).

$$\frac{M_t}{M_\infty} = kt^n \quad (1)$$

Here  $M_t$  is defined as the mass of solvent uptake at time  $t$ ,  $M_\infty$  is the mass of solvent uptake as time approaches infinity,  $k$  is a constant dependent on the structural characteristics of the network, and  $n$  is the exponent which indicates the type of solvent uptake. Table 1 relates the exponent  $n$  to the various types of diffusion.

Table 1.  
Analysis of diffusional behavior using equation (1)

Exponent $n$	Type of diffusion
0.5	Fickian diffusion
$0.5 < n < 1.0$	Anomalous transport
1.0	Case-II transport
$> 1.0$	Super Case-II transport

Equation (1) is valid only in the analysis of the first 60% of the final mass of solvent uptake. It also cannot be used to analyze inflections or overshoots.

For Fickian diffusion with constant boundary conditions and a constant diffusion coefficient, the sorption and desorption kinetics in spheres is given by equation (2) (Crank, 1975).

$$\frac{M_t}{M_\infty} = 1 - \frac{6}{\pi^2} \sum_{n=1}^{\infty} \frac{1}{n^2} \exp(-Dn^2\pi^2t/r^2) \quad (2)$$

Here  $M_t$  is the mass of solvent uptake at time  $t$ ,  $M_\infty$  is the mass of solvent uptake as time approaches infinity,  $r$  is the radius of the sphere, and  $D$  is the concentration-independent diffusion coefficient. An important approximate solution to equation (2) at  $M_t/M_\infty = 0.5$  is given by equation (3).

$$D = \frac{0.00766d^2}{t_{1/2}} \quad (3)$$

Here  $t_{1/2}$  is the diffusional half-time in seconds and  $d$  is the sphere diameter in centimeters. Equation (3) gives a useful relationship for the calculation of the diffusion coefficient in  $\text{cm}^2/\text{sec}$ .

For Case-II transport which usually occurs at high penetrant activity and is relaxation-controlled, the desorption and sorption data in a sphere are expressed by equation (4) (Ensore *et al.*, 1977).

$$\frac{M_t}{M_\infty} = 1 - \left(1 - \frac{k_0 t}{C_0 r}\right)^3 \quad (4)$$

Here  $k_0$  is defined as the Case-II relaxation constant in  $\text{mg}/\text{cm}^2 \text{ min}$  and is assumed to be a constant;  $C_0$  is the equilibrium concentration of the penetrant and  $r$  is the radius of the sphere.

Most diffusion data do not follow Fickian diffusion or Case-II transport kinetics but are explained by a combination of the two kinetic models. Anomalous transport may be described by coupling of the relaxation process with the diffusion process. This idea of coupling led Berens and Hopfenberg (1978) to propose a model to describe this process; the model is given in equation (5).

$$1 - \frac{M_t}{M_\infty} = \phi_F \left[ \frac{6}{\pi^2} \sum_{n=1}^{\infty} \frac{1}{n^2} \exp(-4\pi^2 n^2 D t / d^2) \right] + \phi_R \exp(-kt) \quad (5)$$

Here  $\phi_F$  and  $\phi_R$  are the fractions of sorption contributed by Fickian diffusion and the relaxation process respectively,  $D$  is the diffusion coefficient for the Fickian portion of the transport, and  $k$  is the first-order relaxation constant. If diffusion occurs rapidly in comparison to the relaxation, both  $D$  and  $k$  can be determined from the sorption data (Ensore *et al.*, 1977).

## EXPERIMENTAL PART

The coal samples, packed under nitrogen, were supplied by the Pennsylvania State University Coal Bank. The samples were sieved to the desired mesh size and stored in nitrogen until use.

Untreated coal samples of 1-2 g were dried and weighed to  $\pm 0.005$  g on a Mettler top loading balance. The samples were then placed in 10 ml beakers which were suspended in a dessicator over a pool of solvent. The solvents used in the studies were n-propylamine, butylamine, diethylamine, and dipropylamine. The dessicator was sealed and suspended in a water bath to maintain a constant temperature of  $35 \pm 0.5^\circ\text{C}$ . At set time intervals, the coal samples were removed, weighed, and then returned to the dessicator.

## RESULTS AND DISCUSSION

Dynamic swelling studies were performed on seven untreated coal samples. In the first set of experiments, the effect of carbon content on the sorption of n-propylamine vapor was studied. The samples were prepared for experimentation by drying, and then exposed to n-propylamine vapor at  $35^\circ\text{C}$  until equilibrium swelling had been reached. The mass of solvent uptake per mass of coal sample (dmmf) was calculated as a function of time. The results for PSOC 418 with 69.94%C (dmmf), PSOC 312 with 78.38%C (dmmf), and PSOC 9129 with 88.19%C (dmmf) are shown in Figure 1. The results for PSOC 791 with 72.25%C (dmmf), PSOC 853 with 80.12%C (dmmf), and PSOC 402 with 82.48%C (dmmf) are shown in Figure 2.

The first major observation from this set of experiments was the dramatic effect of carbon content on the final solvent uptake per mass of coal sample (dmmf). This is shown graphically in Figure 3. The solvent uptake is shown to decrease with increasing carbon content.

The mathematical analysis of the sorption data initially involved fitting the data to equation (3) for the first 60% of the final solvent mass uptake. The results from this analysis are tabulated in Table 2. The results show no direct correlation between carbon content and exponent  $n$ ; however, all the values fall between 0.5 and 1.0 and therefore all the sorption processes may be classified as anomalous transport.

Table 2.

Analysis of the Sorption Data from Dynamic Swelling Studies for n-Propylamine using Equation (1)

PSOC	%C (dmmf)	k	Exponent n	r
418	69.94	.07	.74	.998
791	72.25	.05	.83	.999
247	75.53	.024	.981	.993
312	78.38	.05	.79	.993
853	80.23	.04	.79	.996
402	82.48	.05	.68	.994

The model of Berens and Hopfenberg given in equation (1.10) was used to determine diffusion coefficients and relaxation constants. The results from this analysis are tabulated in Table 3. Here both the relaxation constants and the diffusion coefficients are found to decrease with increasing carbon content.

Table 3.

Diffusion Coefficients and Relaxation Constants  
from the n-Propylamine Studies

PSOC	%C (dmmf)	k (sec <sup>-1</sup> )	D(cm <sup>2</sup> /sec)
418	69.94	$1.1 \times 10^{-6}$	$7.5 \times 10^{-9}$
791	72.25	$5.5 \times 10^{-6}$	$2.8 \times 10^{-9}$
247	75.53	$6.2 \times 10^{-6}$	$2.2 \times 10^{-9}$
312	78.38	$7.9 \times 10^{-6}$	$3.2 \times 10^{-9}$
853	80.12	$5.8 \times 10^{-6}$	$2.2 \times 10^{-9}$
402	82.48	$4.3 \times 10^{-6}$	$5.6 \times 10^{-9}$

The final mathematical analysis of this data involved calculating the Case-II relaxation constant using the relaxation controlled model given by equation (4). The results from this analysis are tabulated in Table 4. Here the calculated relaxation constants show a decrease as the carbon content increases.

Table 4.

Case-II Relaxation Constants for  
n-Propylamine Studies Using Equation (4)

PSOC	%C (dmmf)	k <sub>0</sub> (g/cm <sup>2</sup> sec)
418	69.94	$5.1 \times 10^{-7}$
791	72.25	$3.0 \times 10^{-7}$
247	75.53	$3.1 \times 10^{-7}$
312	78.38	$2.7 \times 10^{-7}$
853	80.12	$2.8 \times 10^{-7}$
402	82.48	$1.6 \times 10^{-7}$

The second set of experiments were designed to determine the effect of particle size on solvent transport. Again the samples were pre-dried and then exposed to n-propylamine vapor at 35°C until equilibrium swelling had been reached. The results from these experiments were plotted as the mass of solvent uptake per mass of coal sample (dmmf) as a function of time; these results are given in Figure 4, for PSOC 312 with 78.38%C (dmmf) with sizes of 850-600  $\mu$ m, 600-425  $\mu$ m, 425-250  $\mu$ m, 250-180  $\mu$ m, and 180-150  $\mu$ m.

The results from the analysis of exponent n using equation (1) are tabulated in Table 5. A decrease in particle size has a resulting decrease in the value of the exponent n; there is a shift from anomalous transport in the larger particles to Fickian diffusion in the smaller particles.

Table 5

Analysis of the Sorption Data for Varying Particles (PSOC 312)  
Sizes Using Equation (1)

Particle Size	k	Exponent n	r
850-600 $\mu$ m	.05	.79	.993
600-425 $\mu$ m	.07	.72	.997
425-250 $\mu$ m	.10	.67	.997
250-180 $\mu$ m	.12	.62	.999
180-150 $\mu$ m	.13	.54	.998

### Acknowledgements

This work was supported by DOE grant No. DE-PG22-83PC 60792.

### REFERENCES

- Berens, A.R. and H.B. Hopfenberg, *Polymer*, **19**, 490 (1978).
- Crank, J., *The Mathematics of Diffusion*, 2nd ed., Oxford Press, London, 1975.
- Ensore, D.J., H.B. Hopfenburg, and V.T. Stannett, *Polymer*, **18**, 793 (1977).
- Larsen, J.W. and J. Kovac, in J.W. Larsen, (ed.) *Organic Chemistry of Coal*, ACS Symposium, **71**, 36, Washington, D.C., 1978.
- Lucht, L.M. and N.A. Peppas, in B.D. Blaustein, B.C. Bockrath, and S. Friedman, eds., in *New Approaches in Coal Chemistry*, ACS Symposium, **169**, 43, Washington, DC (1981a).
- Lucht, L.M. and N.A. Peppas, in B.R. Cooper and L. Petrakis, eds., *Chemistry and Physics of Coal Utilization*, American Institute of Physics, New York, NY, 18 (1981b).
- Lucht, L.M., "Macromolecular Network Structure of Coals: Interpretation of Equilibrium and Dynamic Swelling Experiments," Ph.D. Thesis, School of Chemical Engineering, Purdue University, West Lafayette, IN, 1983.

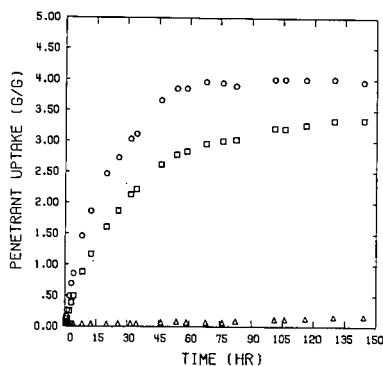


Figure 1: Uptake of n-Propylamine Vapor at 35°C a Function of Time for PSOC 418 (69.94%C, ○), PSOC 312 (78.38%C, □) and PSOC 989 (88.19%C, △).



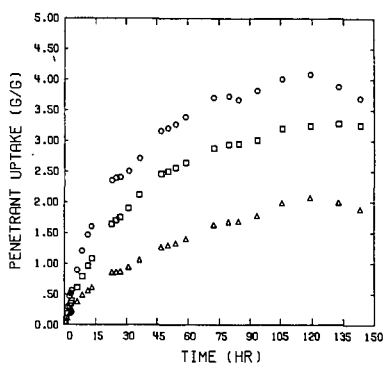


Figure 2: Uptake of *n*-Propylamine Vapor at 35° as a Function of Time for PSOC 791 (72.25%C, ○), PSOC 853 (10.12%C, □) and PSOC 402 (81.48%C, △).

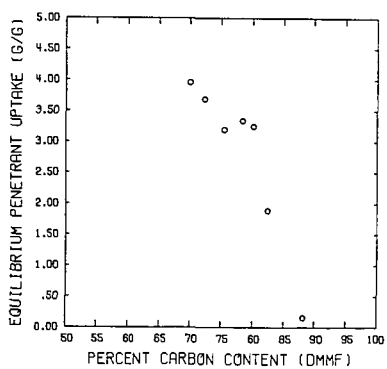


Figure 3: Final Solvent Uptake as a Function of Carbon Content for *n*-Propylamine Studies.

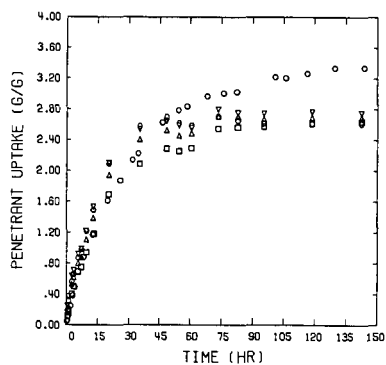


Figure 4: Uptake of n-Propylamine Vapors by Coal Particles as a Function of Time. Studies with PSOC 312 (78.38%C) and with Particles Sizes of 850-600  $\mu\text{m}$  (○), 600-425  $\mu\text{m}$  (□), 425-250  $\mu\text{m}$  (△), 250-180  $\mu\text{m}$  (◇), and 180-150  $\mu\text{m}$  (▽).

## Plastic Behavior of Coal Under Rapid-Heating High-Temperature Conditions

William S. Fong, Yehia F. Khalil, William A. Peters, and Jack B. Howard

Department of Chemical Engineering and Energy Laboratory  
Massachusetts Institute of Technology  
Cambridge, Massachusetts 02139

### Introduction

Bituminous coals upon heating undergo a number of physical and chemical changes. The solid coal passes through a transient plastic (fluid) phase before it resolidifies to form coke. This transient fluidity results in caking and agglomeration of the coal particles in the processing of many bituminous coals. Industrially, these phenomena may contribute to desirable process performance such as a strong and reactive product in metallurgical coke manufacture, or to undesirable operating behavior such as bed bogging in fixed or fluidized bed gasifiers. More fundamentally, the presence of the fluid phase can influence the pyrolysis rate process. A basic understanding of the plastic behavior of coal is therefore essential in the development of quantitative understanding of modern coal conversion and combustion processes.

The mechanism of coal plasticity is poorly understood. One picture is that softening is initiated by a superposition of physical melting and pyrolysis of the coal. A plasticizing agent (metaplast) generated by these processes maintains fluidity until evaporation, repolymerization, and thermal cracking reduce its concentration to a subcritical value causing resolidification (1-3). Previous studies of coal plasticity have mainly been performed under conditions pertinent to metallurgical coke making; i.e., low heating rate carbonization of packed bed samples. A standard instrument is the Gieseler plastometer which operates at a heating rate of  $5 \times 10^{-2} \text{ K s}^{-1}$  to final temperatures around 800 K. Plasticity data are needed at the high heating rates and temperatures (up to  $15,000 \text{ K s}^{-1}$  and 700 - 1300 K, respectively), and elevated hydrogen pressures (up to 10 MPa) of interest in coal conversion.

A new apparatus (4) has been developed that allows the rapidly changing plasticity of softening coal to be measured as a function of the following operating conditions, each varied independently over the stated range: heating rates 40 -  $800 \text{ K s}^{-1}$ , temperatures 600 - 1250 K, particle diameters less than 100  $\mu\text{m}$  and pressures of inert or reactive gases from vacuum to 10 MPa. This paper presents the findings of a detailed study of the plasticity of a high volatile Pittsburgh No. 8 seam bituminous coal using this instrument. Typical results are presented and compared to predictions of a preliminary mathematical model of coal plasticity. The inventory of fusible material within the coal was independently determined by pyridine extraction of rapidly quenched flash-pyrolyzed chars and correlated with the plastic behavior. The effect of the time-temperature history of the coal on the molecular weight of this extract was determined by gel permeation chromatography.

### Experimental

#### (a) Plastometer

The plastometer is described in detail elsewhere (4). Briefly, the technique involves measuring the torque required to rotate at constant speed, a thin shearing disk embedded in a thin layer of coal initially packed as fine particles, and confined between two heated metal plates. The unit is enclosed in a high-pressure vessel that can be evacuated or charged with hydrogen or inert gas. One end of the torque transducer is joined to the shaft of the shearing disk, while the other end is driven by a gear motor. Response time of the piezoelectric transducer is less than 10 ms.

The details of the coal shearing device are illustrated in Figure 1. The shearing chamber consists of a 0.50 mm thick shearing disk of 3.75 mm radius in a 38.1 mm x 0.76 mm slot formed by upper and lower bounding plates held together by a pair of stainless steel/ceramic clamps. The thin coal layer between the disk and each bounding plate is thus 0.13 mm (or about two particle diameters for the size of particles tested). The shearing disk and bounding plates are machined from a nickel superalloy for high-temperature strength, corrosion resistance, and high electrical resistivity. Measurement of temperature is by a thin-foil thermocouple of 0.013 mm thickness (response time 2 - 5 ms) attached to the outside surface of the upper metal plate of the shearing chamber. Heating is by sequentially passing two constant pulses of current of pre-selected magnitude and duration through the metal plates for heating up and holding the sample temperature, respectively. Currents as high as a few hundred A are drawn from the 12 volt DC source for sample heatup. A loading device (not shown here) (4) is used to permit reproducible loading of the coal particles into the shearing chamber and alignment of the rotating disk with the axis of the transducer shaft. The assembled and loaded shearing chamber is placed between the two electrodes in the viscometer before the experiment, and the couplings to the transducer are then connected. To protect the transducer against overload during startup, the shearing disk is rotated manually one or two turns until a torque in a measurable range of  $4 - 5 \times 10^{-2}$  Nm is attained. The unit is then evacuated to approximately 5 Pa and flushed twice with helium at 0.1 MPa. Then the test gas is admitted until the desired test pressure is established. The drive motor is started 0.5 s before the heating circuits are activated. The torque vs time, and temperature vs time profiles throughout the entire run are each recorded on an electronic recorder at a rate of 200 points/s, digitized, and stored for subsequent data processing.

#### (b) Screen Heater Reactor

The weight loss and extract yield data are obtained from an enlarged and modified version of the screen heater reactor described by Anthony (5). Coal particles (~30 mg) of the same size used in the plastometer study (63 - 75  $\mu$ m) are spread in a thin layer between two faces of 425 mesh stainless screen of 14 cm x 7 cm size. The screen is mounted between two electrode blocks and heated by the same high-current circuits used for the plastometer. One of the electrodes is spring-loaded so that the screen is held tight throughout the entire run. Volatiles readily escape the immediate neighborhood of the screen and are diluted by the ambient reactor gas (usually helium). At the end of the preset heating interval, a cooling valve is automatically activated, and sprays pressurized liquid nitrogen onto the screen, resulting in a substrate quenching rate exceeding  $1100 \text{ K s}^{-1}$ . The weight loss of coal is determined by weighing the loaded screen before and after the run. The extract yield is then determined by Soxhlet extracting the screen and char with pyridine, drying the extracted screen and char in a vacuum oven at 120°C for 4 hours, and reweighing.

### Results and Discussion

The objectives of this work are to determine the separate effects of temperature, heating rate, pressure, reactive gaseous atmosphere, inorganic additives and pretreatment on coal plastic behavior and to formulate kinetic models for coal plasticity. Experiments to date have employed a Pittsburgh seam bituminous coal of 39% volatile matter and 63-75  $\mu$ m particle diameter. The coal, which was from the same mine as the samples used previously in this laboratory, was freshly ground under nitrogen, washed, sieved and then vacuum dried at 383 K for 4 hours.

#### (a) Typical Plastometer Results

Figures 2 and 3 present typical data obtained under 0.1 MPa and 3.5 MPa of helium, respectively, at a disk rotational speed of 0.67 rpm (corresponding to an average shear

rate of  $1.32 \text{ s}^{-1}$ ). In Fig. 2 the sample was heated at  $461 \text{ K s}^{-1}$  to a final temperature of  $874 \text{ K}$  and then held at this temperature for  $6.0 \text{ s}$ . As the temperature increases, the torque decreases to a low value due to liquid formation. After a period of low viscosity, the viscosity of the molten coal rises to a high value due to progressive resolidification of the melt. However, continued rotation of the disk breaks up the resultant coke formed by resolidification, and the torque vs time curve gradually decreases thereafter.

The stages of physical change of the coal are illustrated in Fig. 3. For the given shear rate, the torque is related to the absolute viscosity by  $1.0 \times 10^{-2} \text{ Nm} \equiv 2.6 \times 10^4 \text{ Pa s}$ , obtained by calibrating the instrument with viscous liquid standards at room temperature using a method described elsewhere (4). Essentially, the shearing geometry is regarded as two sets of concentric parallel disks. A calibration factor is introduced to account for the slight deviation of the actual instrument geometry from the parallel disk geometry. The apparent Newtonian viscosity is then obtained using the standard equation for a concentric rotating disk viscometer and the calibration factor.

To show how different types of particles behave when heated in the plastometer, samples of Montana lignite (dried,  $53\text{--}88 \text{ }\mu\text{m}$ ), quartz ( $<106 \text{ }\mu\text{m}$ ), Pittsburgh No. 8 coal (dried,  $63\text{--}75 \text{ }\mu\text{m}$ ) and the same Pittsburgh coal pre-extracted with pyridine (dried,  $63\text{--}75 \text{ }\mu\text{m}$ ) were separately tested. Fig. 4 compares these results. In the case of quartz, which does not change its physical form when heated, there is an initial drop in torque due to the slight thermal expansion of the shearing chamber when heated. A high but fluctuating torque signal reflects shearing of particles with rigid edges. Montana lignite, which undergoes pyrolysis without softening under these conditions, retains its solid form but experiences a decrease in volume due to weight loss. Its torque curve thus shows a gentle decrease to a steady value. The Pittsburgh coal shows a plastic behavior very different from the above solids. A low minimum torque value and a distinct plastic period are clearly present. Finally, the pyridine pre-extracted coal shows a delayed softening. Resolidification is faster and the plastic interval is shorter as compared with the untreated coal, presumably due to the prior removal of some metaplast precursor by pyridine.

#### (b) Typical Screen Heater Results

Information on the time-resolved kinetics of devolatilization, the amount of extractables formed within the coal and on the molecular weight distribution and chemical makeup of these extracts provides independent but complementary information about the mechanism of plasticity. Fig. 5 is a time resolved plot of yields of volatiles (i.e. weight loss), pyridine extractables from char, and the pyridine insoluble material in the char, for a heating rate of  $448 \text{ K s}^{-1}$  to a holding temperature of  $858 \text{ K}$ . After different holding times, the sample is rapidly quenched with liquid nitrogen (dotted line). The weight average molecular weight  $M_w$  of the extract is determined by a Waters Associates ALC/GPC 201 system using two series-connected  $100 \text{ }\text{\AA}$  and  $500 \text{ }\text{\AA}$  Microstyragel columns. Fig. 6 is a similar plot for a higher holding temperature. The quantity  $M_w$  is found to increase in both cases. Pre-extraction of the coal removes part of the liquid precursor, and less extract would be expected upon subsequent pyrolysis as was observed. This behavior can significantly affect the plastic behavior of coal. Fig. 7 compares the yields of pyrolysis-derived extracts from raw coal samples with those from pyridine pre-extracted samples, subjected to identical temperature-time histories. A second set of comparisons, for a different heating history, are also shown.

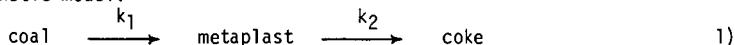
#### (c) Discussion of Results

The mechanism of plasticity in coals is not well understood for rapid heating and high temperature conditions. Plasticity and related phenomena such as swelling

and agglomeration are direct consequences of liquid formation by heating. Physical melting of part of the coal first occurs when the temperature is sufficiently high. Subsequent pyrolytic bond breaking generates additional liquid. The initial liquid generated by physical melting may also dissolve part of the solid coal material. At the same time, liquid is lost through evaporation of its lighter molecules (volatiles) from the particle, and through repolymerization and cracking reactions. This picture is supported by our present data. The kinetics of extract generation and destruction as inferred from the screen heater experiments correlates well with the plasticity data, as shown in Fig. 8. It seems reasonable to assume that the amount of extract is an indication of the instantaneous liquid metaplast content of the coal. Initially, we can extract 27% of pyridine solubles from the unheated raw coal. This amount would correspond to the material that is solid at low temperature but undergoes physical melting as temperature exceeds the 'melting' point. Our observation with the plastometer, that initial softening occurs around 580 K independent of heating rate ( $50 - 700 \text{ K s}^{-1}$ ), is consistent with the above observation as seen from Fig. 9. If this initial 27% of material is pre-extracted, and afterwards the coal is subjected to pyrolysis, the metaplast (extract) formed by pyrolysis alone is much less as seen from Fig. 7. The pre-extracted coal is expected to soften at a later time (higher temperature) and the duration of plasticity is shorter, as is observed (Fig. 4d).

The relation of extract inventory to the duration of plasticity and to resolidification rate is illustrated from the pyridine insoluble curves in Figs. 5 and 6. The amount of insolubles reaches a minimum and then rises to an asymptotic value determined by the competition of devolatilization and resolidification rates. The rising portion of the curves indicates either repolymerization reaction or cracking of metaplast to a light gas and a solid, or both. Repolymerization seems likely since the molecular weight of the metaplast increases with heating time (Figs. 5, 6). However, this can also be caused by selective evaporation of light molecules from the metaplast. The devolatilization rate also seems to be proportional to the instantaneous amount of metaplast in coal. At higher holding temperatures ( $\geq 973 \text{ K}$  for heating rates around  $500 \text{ K s}^{-1}$ ) the plasticity and extract curves do not correlate well. The extract curve has shorter width than the plasticity curve. This behavior may in part reflect an apparatus artifact since the mass transfer resistance for volatiles escape in the plastometer is much greater than in the screen heater.

The duration of plasticity and the resolidification rate are quite sensitive to temperature-time history (Figs. 9, 10). Fig. 10 shows how these vary for plastometer runs at  $450 \text{ K s}^{-1}$  to four different holding temperatures. This behavior leads to the conceptually simple mathematical model based in part on Fitzgerald's metaplast theory (6). He considered the formation and destruction of metaplast to be described by a first order kinetic model.



To simplify its implementation here, equivalent component densities and negligible weight loss are assumed. To relate metaplast concentration to the apparent viscosity of the melt, an expression for concentrated suspensions by Frankel and Acrivos (7) is employed. The relative viscosity  $\mu$  of a suspension at high solids concentration is given by,

$$\mu = \frac{\mu^*}{\mu} = \frac{9}{8} \left[ \frac{(\phi/\phi_m)^{1/3}}{1 - (\phi/\phi_m)^{1/3}} \right] \quad (2)$$

where  $\mu^*$  is the viscosity of a suspension with a solids volume fraction  $\phi$ ,  $\phi_m$  being the maximum value of  $\phi$  possible, and  $\mu$  is the viscosity of the continuous (solids-free) phase. We approximate  $\phi = 1 - M$  where  $M$  is the metaplast weight fraction. Since the sample is initially a packed bed of solids,  $\phi_m$  is assumed to be unity. This condition is possible if the solid elements of the suspension are thin slabs

(lamellae) which is a reasonable representation of the layered structure of vitrinite. Solving Equation 1 for metaplast concentration with the given temperature profile (constant linear heating followed by a constant holding temperature) and using Equation 2 allows  $\bar{\mu}$  to be calculated if the rate constants  $k_1$  ( $=k_{01} \exp[-E_{A1}/RT]$ ) and  $k_2$  ( $=k_{02} \exp[-E_{A2}/RT]$ ) are known. These quantities can be estimated from laboratory data. At a late stage of resolidification, the metaplast formation rate is very small, so

$$\frac{dM}{dt} = -k_2 M \quad (3)$$

At small values of  $M$  ( $M < 0.1$ ), Equation 2 with the approximation  $\phi_m = 1.0$  is reduced to

$$\bar{\mu} = \frac{27}{8} \left( \frac{1}{M} \right) \quad (4)$$

It then follows that

$$\frac{d \ln \bar{\mu}}{dt} = k_2 = k_{02} \exp[-E_{A2}/RT] \quad (5)$$

The holding temperature is a good approximation for  $T$  when resolidification occurs well after the holding temperature is reached (such as in Fig. 2). The experimental rate of increase of the logarithm of torque is identical to the left-hand term of Equation 5. A plot of the logarithm of this quantity vs reciprocal holding temperature gives a straight line corresponding to an activation energy  $E_{A2}$  of  $133 \text{ kJ mole}^{-1}$  and  $k_{02}$  of  $2.0 \times 10^8 \text{ s}^{-1}$ . Actual viscosities are measured in the range  $1 \times 10^3 -$

$1 \times 10^5 \text{ Pa s}$ . Nazem (8) measured the viscosities of carbonaceous mesophase pitch at around  $623 \text{ K}$  and found them to be between  $30 - 200 \text{ Pa s}$ . Hence  $\bar{\mu}$  would be of order  $10 - 1,000$  if we assume the solids free metaplast has a similar viscosity. For illustration purpose,  $\mu$  is taken to be  $120 \text{ Pa s}$ . Values of  $k_{01} = 245 \text{ s}^{-1}$  and  $E_{A1} = 40.7 \text{ kJ mole}^{-1}$  are found to fit the plastic period of the experiments at  $450 \text{ K s}^{-1}$  heating rate (4). The temperature dependence of viscosity of the solids-free metaplast is not considered here. Calculated plasticity curve in Fig. 11 shows the same form of dependence of viscosity on reaction time as the observed data in Fig. 10. Fig. 12 shows that the calculated plastic period (smooth curve), defined as the time interval when  $\mu^* < 3.6 \times 10^4 \text{ Pa s}$ , fits the laboratory data well.

The above model is of preliminary nature and offers opportunities for improvement. Weight loss has not been considered in defining metaplast concentration. Generation of metaplast is described only by a first order chemical reaction, i.e. physical melting is neglected. This seems particularly suspect since curve fitting the present data with this model gave a low value of  $E_{A1}$  more suggestive, in the present context, of kinetics dominated by physical transport or phase change. Further, Equation 2 relating metaplast concentration to relative viscosity was derived for the highly simplistic case of solid spheres.

The plastic behavior under vacuum and high inert gas pressure was also investigated. For both vacuum and  $3.5 \text{ MPa}$  ambient helium pressure, the plastic period is shorter ( $4.5$  and  $4.2 \text{ s}$  respectively, compared to  $6.4 \text{ s}$  at  $0.1 \text{ MPa}$  helium pressure). The resolidification rates for both cases are faster than under  $0.1 \text{ MPa}$  helium. Under vacuum, the metaplast may escape faster from the particle, resulting in shorter plasticity duration. High pressure may favor repolymerization reactions, hence the resolidification rate. The effect of high pressure on fluidity agrees with inferences by Halchuk et al. (9) based on analyses of char particles from screen heater pyrolysis. They found that the fluidity of a HVA Pittsburgh No. 9 seam coal during rapid pyrolysis at  $760^\circ\text{C}$  was lower at pressures above  $0.45 \text{ MPa}$ , than that at  $0.1 \text{ MPa}$ .

## Conclusions

A new plastometer for measuring the apparent viscosity of plastic coals under rapid-heating, high temperature conditions has been developed and found to give reproducible data that are generally consistent with expected plasticity behavior. Under rapid heating conditions ( $40 - 800 \text{ K s}^{-1}$ ) the duration of plasticity and its rate of disappearance for a Pittsburgh No. 8 bituminous coal depended strongly on pressure, temperature, and heating rate. However, the initial softening temperature was insensitive to heating rate. Pre-extraction of the coal with pyridine at 389 K, typically yielded 25 - 30 wt% organic matter and strongly retarded plasticity on subsequent heating by delaying its onset and shortening its duration.

The effects of temperature on the duration of plasticity were correlated by a preliminary mathematical model relating viscosity of solid-liquid suspensions to the transient concentration of a plasticizing agent generated and depleted by single first-order chemical reactions in series. This simple kinetic picture is also in qualitative accord with the other observations described above. However, quantitative prediction of metaplast molecular weights, effects of pressure and particle size on plasticity, and of softening temperatures will require that transport processes and physical melting be included in the modelling. More detailed modelling will also be needed to describe other softening related phenomena, such as swelling and agglomeration of particles in coal conversion processes and the role of plasticity in liquefaction kinetics.

## Acknowledgements

Financial support of this work is provided by the United States Department of Energy under Contract No. DE-AC21-82MC-19207, and is gratefully acknowledged.

## References

1. Habermehl, D., F. Orywal, and H. D. Beyer, "Plastic Properties of Coal" in Chemistry of Coal Utilization, 2nd Suppl. Vol., M. A. Elliott, ed., J. Wiley & Sons, New York, 1981.
2. Loison, R., A. Peytavy, H. F. Boyer, and R. Grillo, "The Plastic Properties of Coal" in Chemistry of Coal Utilization, Suppl. Vol., H. H. Lowry, ed., J. Wiley & Sons, New York, 1963.
3. Kirov, N. Y. and J. N. Stephens, "Physical Aspects of Coal Carbonization" Kingsway Printers, Caringbah, Australia, 1967.
4. Fong, W. S., W. A. Peters, and J. B. Howard, submitted for Review for Publication, Rev. Sci. Instrum., 1984.
5. Anthony, D. B., J. B. Howard, H. P. Meissner, and H. C. Hottel, Rev. Sci. Instrum. 45, 992 (1974).
6. Fitzgerald, D., Fuel 36, 389 (1957).
7. Frankel, N. A. and A. Acrivos, Chem. Eng. Sci. 22, 847 (1976).
8. Nazem, F. F., Fuel 59, 851 (1980).
9. Halchuk, R. A., W. B. Russel, and D. A. Saville, Proc., Int. Conf. on Coal Science, Pittsburgh, 1983, pp. 491-3.



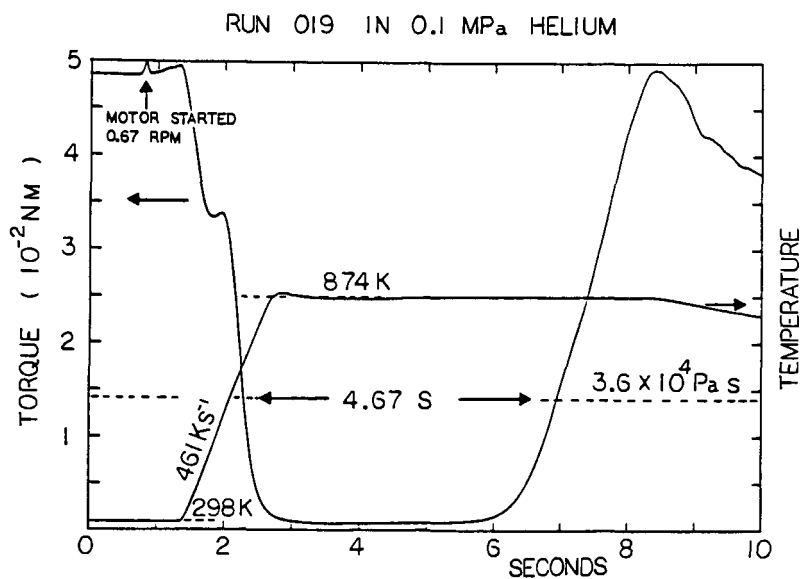


Figure 2 Typical Raw Data from Plastometer. Total Pressure = 0.1 MPa

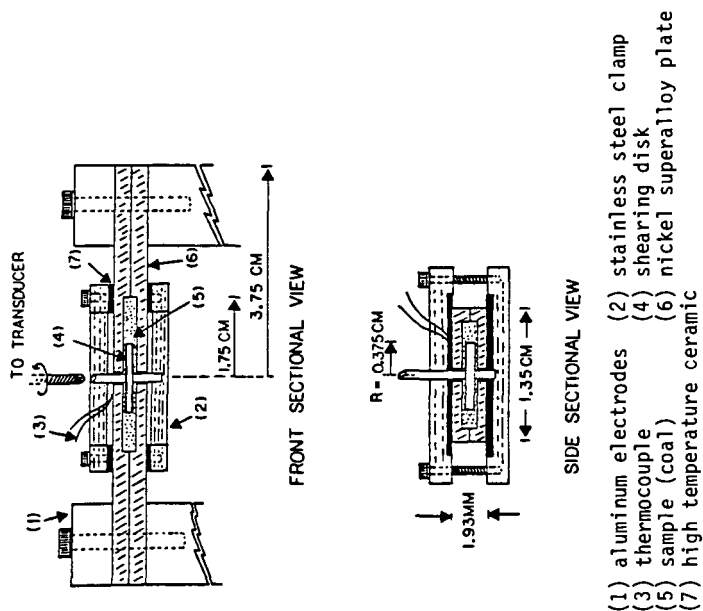


Figure 1 Details of Shearing Chamber

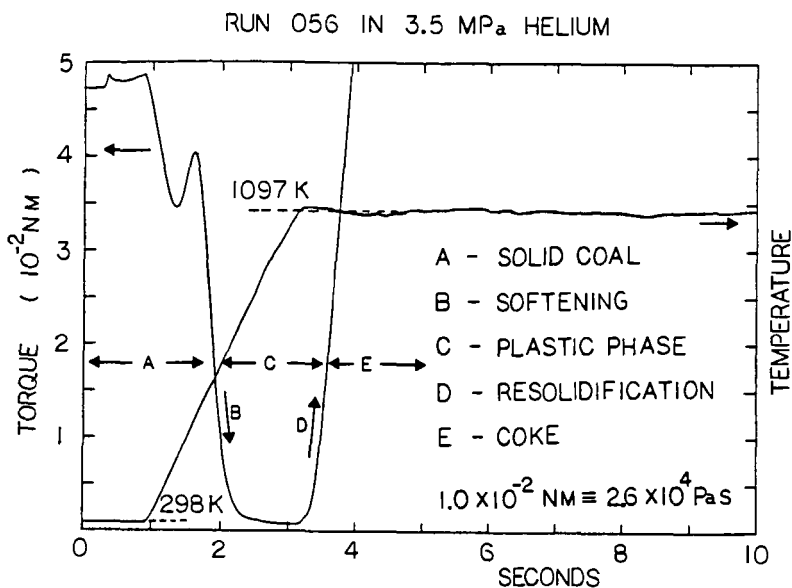


Figure 3 Typical Raw Data from Plastometer. Total Pressure = 3.5 MPa

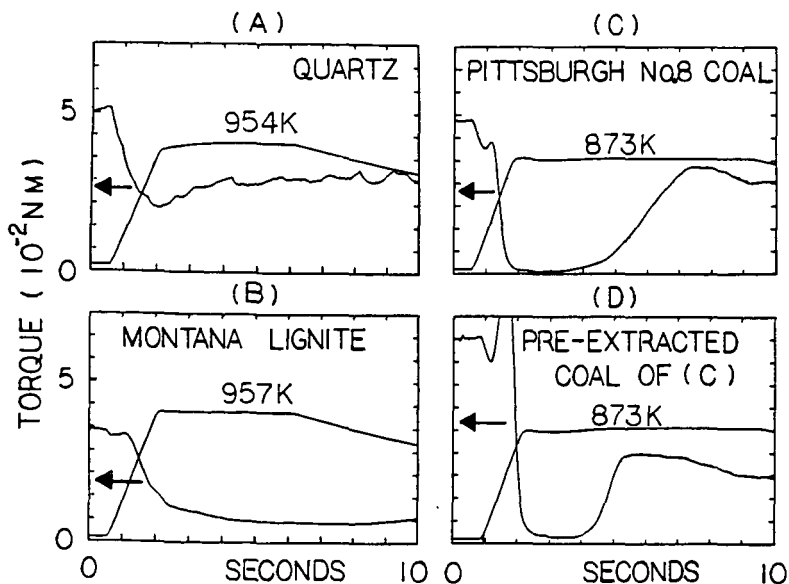


Figure 4 Behavior of Different Particles in the Plastometer

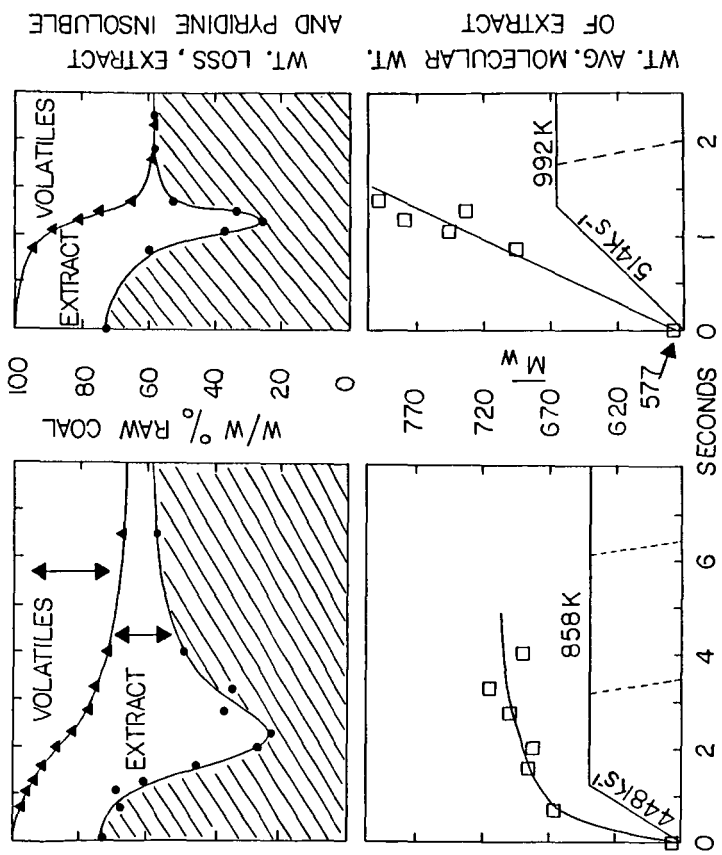


Figure 5  
Figure 6  
Figures 5,6 Weight Loss of Raw Coal, Pyridine Extract and Insoluble from Char and Weight Average Molecular Weight of Extract from Screen Heater Experiments.  
Temperature-time histories indicated.

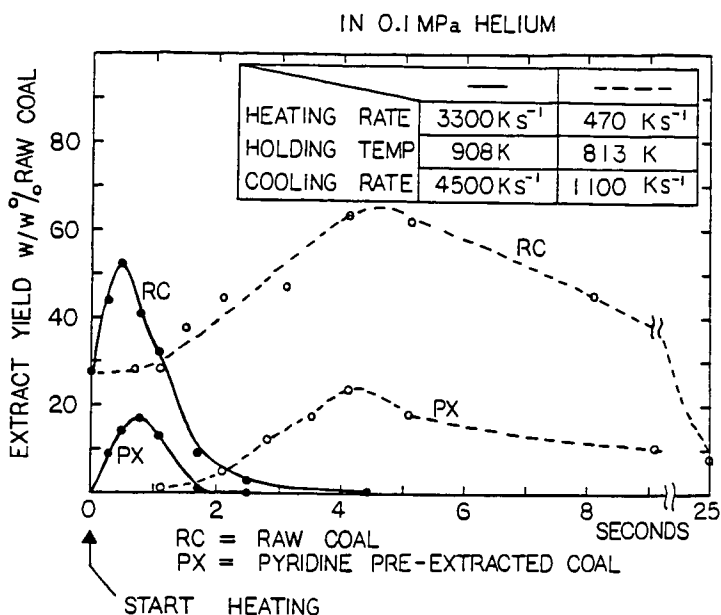


Figure 7 Comparison of Extract Yields for Raw Coal and Pre-extracted Coal

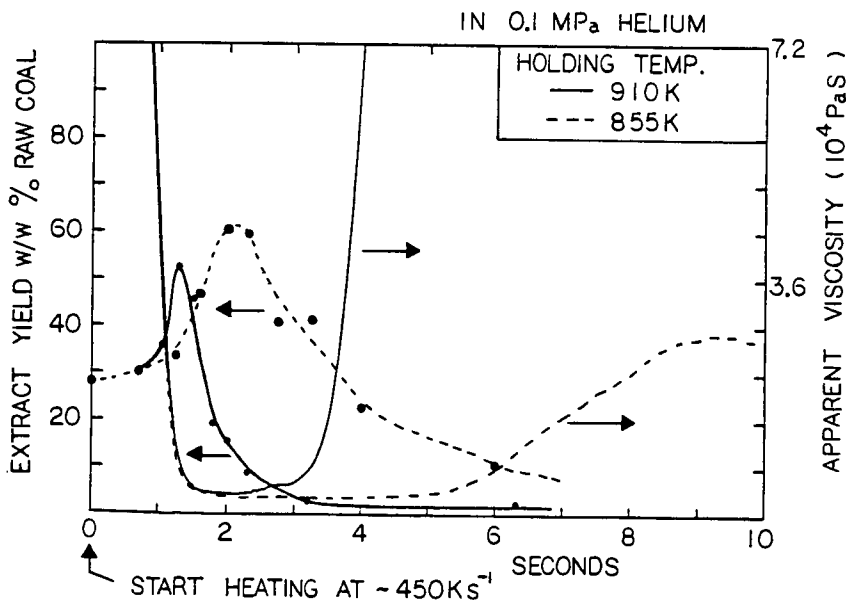


Figure 8 Comparison of Plastic Behavior and Extract Formation/destruction

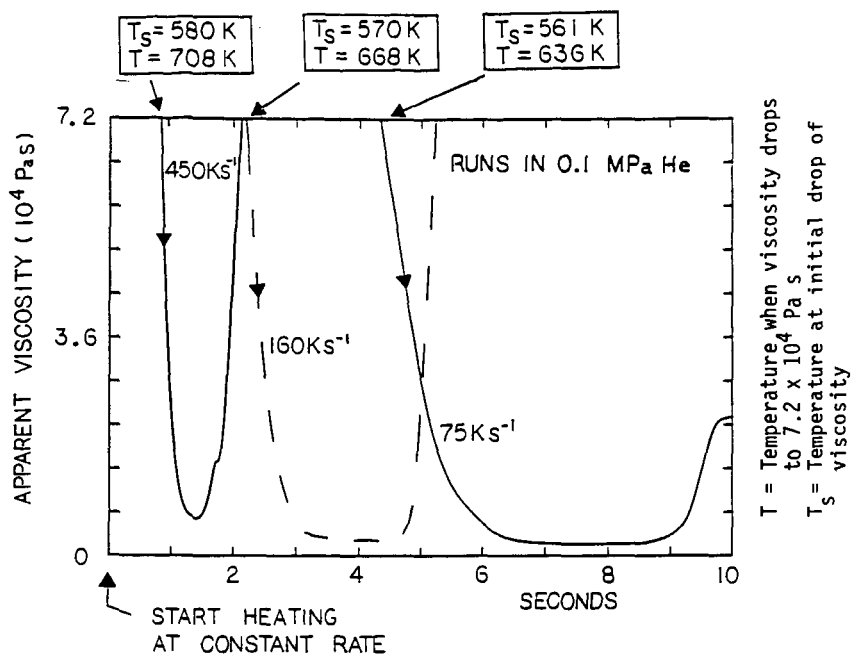


Figure 9 Plasticity Data for Constant Heating Rate Runs

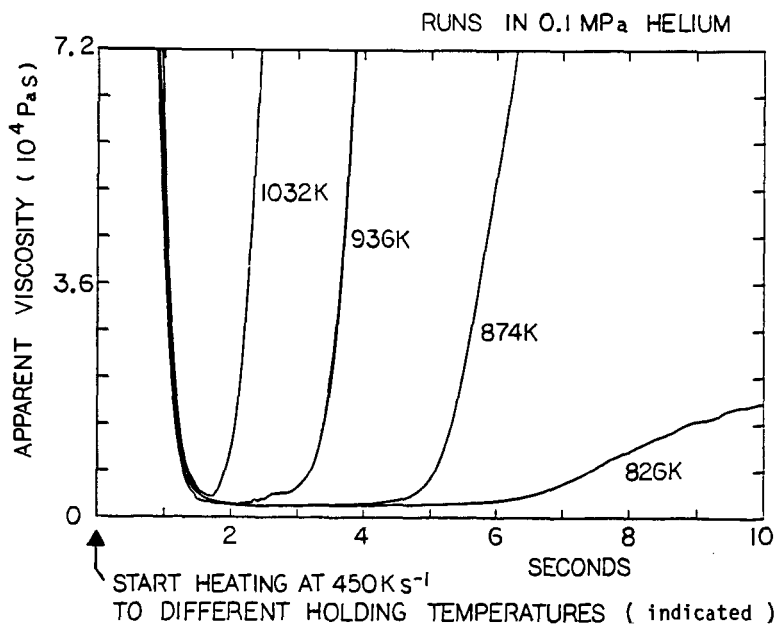


Figure 10 Plasticity Data for Holding Temperature Runs

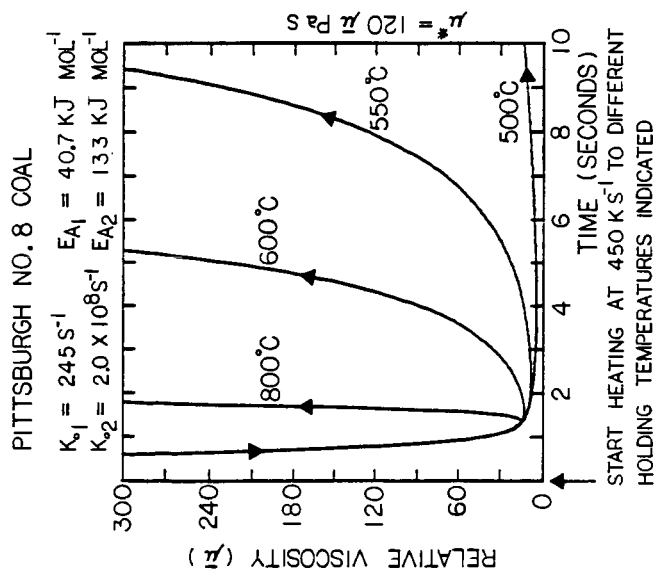


Figure 11 Calculated Viscosity Curve according to Single First Order Reaction Model

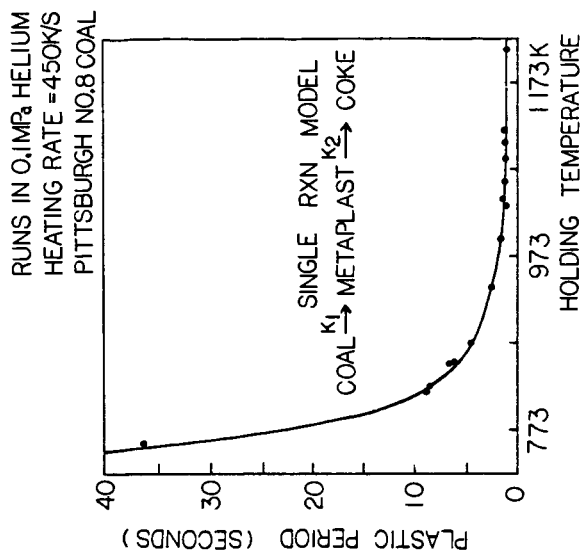


Figure 12 Calculated Plastic Period (curve) and experimental data (solid circles)

## INTERNAL FRICTION AND DYNAMIC YOUNG MODULUS OF A BITUMINOUS COAL

H. M. Ledbetter and M. W. Austin

Fracture and Deformation Division, Center for Materials  
Science, National Bureau of Standards

J. E. Callanan

Chemical Engineering Science Division, Center for Chemical  
Engineering, National Bureau of Standards,  
Boulder, Colorado 80303

### INTRODUCTION

Elastic properties of coal provide three types of information. First, elastic constants such as Young modulus and Poisson ratio provide essential engineering-design parameters. These parameters enter calculations for load-deflection, thermo-elastic stress, buckling instability, and crack propagation. Second, elastic constants provide valuable material characterization. They reflect differences in thermal-mechanical history, in void and crack content, and in chemical composition. Third, elastic constants relate closely to interatomic arrangements and interatomic forces. From interatomic force constants ("spring constants"), one can specify the complete set of elastic constants (two for isotropic symmetry, nine for orthotropic symmetry). Because coal exhibits three macroscopic orthogonal mirror planes, it must exhibit orthotropic elastic symmetry. Recently, for isotropic solids, Ledbetter [1] described elastic constants and their interrelationships with other physical properties.

As described by Nowick and Berry [2], internal friction, or anelasticity, amounts to the imaginary part of either elastic stiffness or elastic compliance. Internal friction manifests itself in many ways: width of a resonance peak, amplitude decay of a stress wave, phase lag of strain behind stress, and area within an elastic-region stress-strain loop. Each of these manifestations provides a possible measurement method. As described below, we used resonance-peak width. In crystalline solids, internal friction usually arises from various relaxations: point defects, dislocations, grain boundaries, phonons, magnetoelastic couplings, and electron configurations. In amorphous polymers, the principal relaxation arises from the glass transition, attributed to large-scale rearrangements of the principal polymer chain. At lower temperatures, one observes secondary relaxations caused by side groups capable of independent hindered rotations. Adapted from Houwink and de Decker [3], Fig. 1 shows for four polymers the internal friction versus temperature, which we often call the mechanical-loss spectrum. Most polymers fit the general pattern suggested in Fig. 1.

Recently, Szwilski [4] described a method for determining the anisotropic elastic moduli of coal. He reported seven previous studies of coal's elastic constants. Besides these seven, at least six other experimental studies exist: Constantino and Trettennero [5] and Wert, Weller, and Völker [6-10].

Wert and Weller [6-10] used a torsional pendulum at frequencies near 1 Hz to measure between 10 and 450 K the temperature dependence of both the torsional modulus,  $G$ , and the internal friction,  $\tan \delta = Q^{-1}$ . These authors were first to report coal's internal-friction spectrum, which reveals mechanical-relaxation phenomena. See Fig. 2. Based on their experimental studies, Weller and Wert support a polymeric model for coal. In the above temperature range, these authors detected three peaks (denoted  $\alpha$ ,  $\beta$ ,  $\gamma$ ) and possible evidence for a low-temperature peak ( $\delta$ ) near 50 K. These peaks correspond closely to those observed in most polymers. Wert and Weller [7] ascribe the  $\alpha$ -peak to massive motion of macromolecules, related probably to the

glass transition. They ascribe the  $\beta$ -peak to reorientation under stress of side units, perhaps associated with water. They ascribe the  $\gamma$ -peak to twisting or other reorientation of segments of a linear section of  $\text{CH}_2$  units. They believe this peak decreases with coal's increasing carbon content (rank).

The present study relates closely to those of Wert and Weller [6-10]. The principal differences are three: (1) We used larger specimens by a factor of approximately 40 in volume. (2) We used higher frequencies: 45 kHz to their 1 Hz. (3) We studied a Young-modulus (extensional) deformation mode while they studied a torsional mode. Twisting induces no volume changes while uniaxial stress involves both shear and dilatation.

#### MATERIAL

We studied a high-volatile Eastern-Kentucky bituminous coal studied previously by Wert and Weller [7], who reported a composition of 81.8% carbon (wt. pct. daf). Specific gravity measured at 293 K by Archimedes's method was 1.316.

#### SPECIMENS

We prepared square-cross-section rod specimens, 0.48 cm by 2.43 cm, by sawing. The specimen reported on here lay in the coal's bedding plane and along the major cleat direction. We determined this orientation visually, based on easily discernible striae and longitudinal markings.

#### MEASUREMENTS

For measuring the Young modulus,  $E$ , and internal friction,  $Q^{-1}$ , we used a Marx-composite-oscillator method [11-14]. At  $T = 293$  K, the composite-oscillator resonance frequency was 45 kHz. Our version of this apparatus operates between 20 and 100 kHz in the fundamental mode. Using overtones permits higher frequencies. Cooling to liquid-nitrogen temperature (76 K) was achieved with a probe-and-dewar arrangement described elsewhere [13]. To obtain the Young modulus, one uses the relationship

$$E = 4\rho f_0^2 l^2 \quad (1)$$

where  $\rho$  denotes mass density,  $f_0$  specimen resonance frequency for the fundamental (half-wavelength) mode, and  $l$  specimen length. In a Young-modulus deformation mode, the rod cross-section is immaterial, if it is uniform along the specimen length. To obtain internal friction, one uses the relationship

$$Q^{-1} = (f_2 - f_1)/f_0 \quad (2)$$

where  $f_1$  and  $f_2$  denote the frequencies at the half-power points of the resonance peak and  $f_0$  denotes resonance frequency. Thus, versus frequency, one measures strain amplitude detected as the voltage generated in a piezoelectric quartz gage crystal. We did not correct for coal's contraction during cooling. Cooling rates were 2 K/min. A sweep over the resonance-frequency range required 40 s. Measurements made at lower cooling rates should show less scatter.

Concerning measurement uncertainties, our limited experience with this material precludes a precise statement. We guess that  $E$  is accurate within a few percent and  $Q^{-1}$  within about 20 percent. Scatter in Fig. 3 indicates the imprecisions.



## RESULTS

Figure 3 shows the principal results:  $E$  and  $Q^{-1}$  versus temperature between 293 and 76 K. We show  $E$  as a dimensionless ratio to the ambient-temperature value.

## DISCUSSION

Our ambient-temperature value,  $E = 6.4$  GPa, exceeds considerably the range for coal reported by Constantino and Trettenero [5], 3.0 to 4.5 GPa, measured perpendicular to the bedding plane. But it falls within the 2.1 to 9.5 GPa range reported by Szwilski [4] for the bedding plane. To minimize effects of microcracks, Szwilski applied a small confinement force, which would not affect the intrinsic elastic constant. Compared with polymers, this Young modulus is only slightly lower. For example, for four technical polymers, Athougies et al. [15] reported the dynamic Young modulus which showed a range of 7 to 9 GPa.

The extrapolated increase in  $E$  during cooling to zero temperature,  $E(0)/E(293) \cong 1.7$ , lies considerably below the torsional-modulus increase found by Wert and Weller [7],  $G(0)/G(293) \cong 2.6$ . For isotropic materials,  $E$  and  $G$  relate simply through the bulk modulus,  $B$ :

$$E = 9BG/(3B+G). \quad (3)$$

By differentiation

$$\frac{\Delta E}{E} = \frac{1}{(3B+G)} \left( G \frac{\Delta B}{B} + 3B \frac{\Delta G}{G} \right). \quad (4)$$

Taking the Poisson ratio to be  $1/3$ , then [1]

$$\frac{\Delta E}{E} = \frac{1}{9} \left( 8 \frac{\Delta G}{G} + \frac{\Delta B}{B} \right). \quad (5)$$

Thus, the large  $\Delta G/G$  relative to  $\Delta E/E$  must arise from another source, not from a smaller  $\Delta B/B$  change, which contributes approximately one-ninth. One can identify four possible sources: measurement frequency, strain amplitude, temperature-dependent relaxation strength, and material anisotropy. Without further study, we can not comment on these possibilities.

Usually, one can describe the  $E(T)$  behavior by a relationship [16]

$$E(T) = E(0) - s/\exp(t/T) \quad (6)$$

where  $E(0)$  denotes zero-temperature Young modulus,  $s$  an adjustable parameter related to zero-point vibrations,  $t$  the Einstein temperature, and  $T$  temperature. This relationship fits the  $E(T)$  measurements only approximately because of the irregularities in  $E(T)$  that arise from cooling through some relaxation mechanisms, principally the  $\gamma$  peak. From a least-squares fit to the  $E(T)$  results shown in Fig. 3, we obtain  $t = 345$  K, a rough estimate of coal's effective Einstein temperature. In a preliminary study, Merrick [17] modeled coal's specific heat with an Einstein model. He made the usual Einstein-model interpretation: "the characteristic temperatures ... reflect the average properties of the bonds." For the temperature range 0-800°C, Merrick obtained  $t = 1200$  K. A second approach used a two-Einstein-temperature model with  $t_1 = 380$  K and  $t_2 = 1800$  K. This model recognizes anisotropic binding forces: strong forces within layers and weaker forces between layers. It gives a lower  $C_p(T)$  curvature and better agreement with measurement. We compare these

results with graphite where Komatsu [18] used a lattice-vibration model and the  $C_{44}$  elastic constant to predict that  $t_1 = 135$  K and  $t_2 = 1860$  K. We take this latter characteristic temperature as the upper bound of any "lattice" vibrations representing binding forces in coal. A better upper bound may arise from the  $t = 1680$  K Einstein temperature of diamond [1], where the carbon-carbon tetrahedral-covalent bond strength exceeds that of any other known material.

We turn now to internal friction. Figure 3 shows a broad peak centered near 240 K, which we interpret as the Wert-Weller  $\gamma$  peak detected at 130 K. From eq. (3.5-5) in Nowick and Berry

$$Q = k \ln (\omega_2/\omega_1) (T_{p1}^{-1} - T_{p2}^{-1})^{-1} \quad (7)$$

where  $k$  denotes Boltzmann's constant,  $Q$  denotes activation energy,  $\omega$  denotes angular frequency, and  $T_p$  denotes peak temperature, we obtain  $Q = 0.26$  eV compared with 0.18 eV obtained by Wert and Weller [10].

The upturn in Fig. 3 just above 76 K signifies a strong low-temperature ( $\delta$ ) peak only suggested in some of the Wert-Weller studies. This peak requires further study by cooling to lower temperatures. This  $\delta$  peak may appear stronger in our study because our higher measurement frequency (by a factor of  $5 \cdot 10^5$ ) approaches more closely the  $\delta$ -peak resonance frequency. From eq. (3.5-4) in Nowick and Berry

$$T_p = \frac{-Q}{k} \frac{1}{\ln \omega t_0} \quad (8)$$

where  $t_0 = \nu_0^{-1}$  denotes a fundamental relaxation time and  $\nu_0$  a fundamental frequency related to a mechanical-relaxation mechanism. Thus, a lower  $T_p$  corresponds to either lower  $Q$  or lower  $\nu_0$ . Lower  $T_p$  usually corresponds to a smaller vibrating unit.

#### CONCLUDING REMARKS

Given that coal is a polymer, then the enormous body of pre-existing polymer physics should transfer to coal. This physics includes measurement methods, mechanical models (Kelvin, Maxwell, etc.), molecular interpretations, structure geometry, viscoelasticity theory, and anisotropic phenomena. Many books summarize the state of polymer physics; several relate especially to dynamical-mechanical properties: Alfrey [19], Tobolsky [20], Ferry [21], Heijboer [22], McCrum, Read, and Williams [23], Christensen [24], Ward [25], Baer and Radcliffe [26], Nielsen [27], Read and Bean [28], and Murayama [29].

From the materials-science viewpoint, the most important relationships are those between structure and macroscopic properties. For polymers, Murayama [29] summarized the dynamical-mechanical studies:

The investigation of the dynamic modulus and internal friction over a wide range of temperatures and frequencies has proven to be very useful in studying the structure of high polymers and the variations of properties in relation to end-use performance. These dynamic parameters have been used to determine the glass transition region, relaxation spectra, degree of crystallinity, molecular orientation, crosslinking, phase separation, structural or morphological changes resulting from processing, and chemical composition in polyblends, graft polymers, and copolymers.

Thus, one expects similar possible results in applying dynamical-mechanical methods to coal.

Our preliminary measurements show that, by dynamic methods, one can measure coal's elastic constants and mechanical-relaxation spectrum in a Young-modulus mode at kilohertz frequencies.

Boyer [30] pointed out that in studying the relaxation spectra of polymers one can focus on five different aspects: (1) experimental methods; (2) individual spectra as a characterization; (3) spectra features common to many materials; (4) correlation of loss peaks with other physical and mechanical properties; (5) molecular mechanisms of loss peaks. The second aspect includes effects of thermal history, crystallinity, measurement frequency, external force field, molecular orientation, and other variables.

Further studies at NBS could include eight principal efforts: (1) refine our preliminary measurements and extend them to both lower and higher temperatures; (2) determine the complete nine-component elastic-constant tensor; (3) attempt to relate the mechanical-relaxation peaks to mechanisms; (4) determine by measurement the changes of these peaks produced by variables such as moisture, heating, aging; (5) possibly relate microstructure to physical properties; (6) model the macroscopic elastic constants in terms of those of constituents; (7) determine complete damping tensor; (8) focus especially on the low-temperature  $\delta$ -peak, which appears larger in our measurements than in previous ones.

#### ACKNOWLEDGMENT

Professor C.A. Wert (Urbana) helped us get started on this study by providing samples, reprints, and encouraging advice. Dr. M. Weller (Stuttgart) provided critical, useful comments.

#### REFERENCES

- [1] Ledbetter, H.M., in *Materials at Low Temperatures* (Amer. Soc. Metals, Metals Park, 1983), p. 1.
- [2] Nowick, A.S. and Berry, B.S., *Anelastic Relaxation in Crystalline Solids* (Academic, New York, 1972).
- [3] Houwink, R. and de Decker, H.K. (eds.), *Elasticity, Plasticity, and Structure of Matter* (Cambridge U.P., London, 1971), p. 161.
- [4] Szwilski, A.B., *Int. J. Rock Mech. Min. Sci. Geomech. Astr.* **21**, 3 (1984).
- [5] Constantino, M. and Trettenero, S., *J. Appl. Phys.* **54**, 76 (1983).
- [6] Wert, C.A. and Weller, M., *J. Physique* **42**, C5-581 (1981).
- [7] Wert, C.A. and Weller, M., *J. Appl. Phys.* **53**, 6505 (1982).
- [8] Weller, M., Völkl, J., and Wert, C., in *Proc. 1983 International Conference on Coal Science* (Pittsburgh, August 1983), p. 283.
- [9] Weller, M. and Wert, C.A., *J. Physique* **44**, C9-191 (1983).
- [10] Weller, M. and Wert, C., *Fuel* **63**, 891 (1984).
- [11] Marx, J., *Rev. Sci. Instrum.* **22**, 503 (1951).
- [12] Robinson, W.H. and Edgar, A., *IEEE Trans. Son. Ultrason.* **SU-21**, 98 (1974).
- [13] Weston, W.F., *J. Appl. Phys.* **46**, 4458 (1975).
- [14] Ledbetter, H.M., *Cryogenics* **20**, 637 (1980).
- [15] Athougies, A.D., Peterson, B. T., Salinger, G.L., and Swartz, C.D., *Cryogenics* **12**, 125 (1972).
- [16] Varshni, Y.D., *Phys. Rev.* **82**, 3952 (1970).
- [17] Merrick, D., *Fuel* **62**, 540 (1983).
- [18] Komatsu, K., *J. Phys. Soc. Japan* **10**, 346 (1955).
- [19] Alfrey, T., *Mechanical Behavior of High Polymers* (Interscience, New York, 1948).

- [20] Tobolsky, A.V., Properties and Structure of Polymers (Wiley, New York, 1960).
- [21] Ferry, J.D., Viscoelastic Properties of Polymers (Wiley, New York, 1961).
- [22] Heijboer, J., Physics of Noncrystalline Solids (North-Holland, Amsterdam, 1965).
- [23] McCrum, N.G., Read, B.E., and Williams, G., Anelastic and Dielectric Effects in Polymeric Solids (Wiley, London, 1967).
- [24] Christensen, R.M., Theory of Viscoelasticity (Academic, New York, 1971).
- [25] Ward, I.W., Mechanical Properties of Solid Polymers (Wiley, New York, 1971).
- [26] Baer, E. and Radcliffe, S.V., Polymeric Materials (Amer. Soc. Metals, Metals Park, 1974).
- [27] Nielsen, L.E., Mechanical Properties of Polymers and Composites (Dekker, New York, 1974).
- [28] Read, B.E. and Dean, G.O., The Determination of Dynamic Properties of Polymers and Composites (Wiley, New York, 1978).
- [29] Murayama, T., Dynamic Mechanical Analysis of Polymeric Material (Elsevier, Amsterdam, 1978).
- [30] Boyer, R.F., in ref. [26], p. 277.

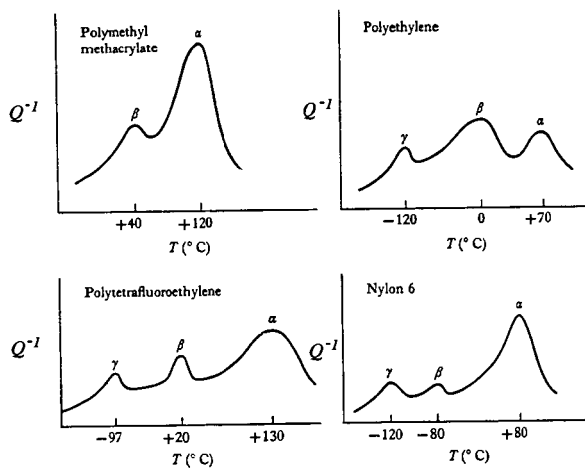


Fig. 1. Dynamic loss modulus versus temperature for four polymers; from Houwink and de Decker [3].

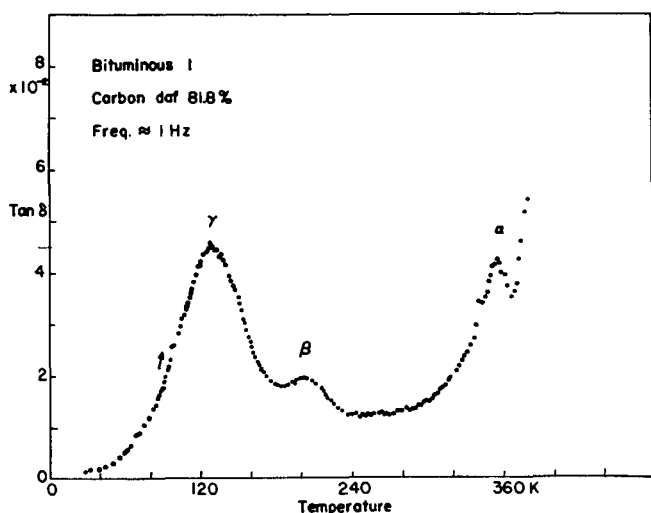


Fig. 2. Internal-friction spectrum of a bituminous coal; from Wert and Weller [7].

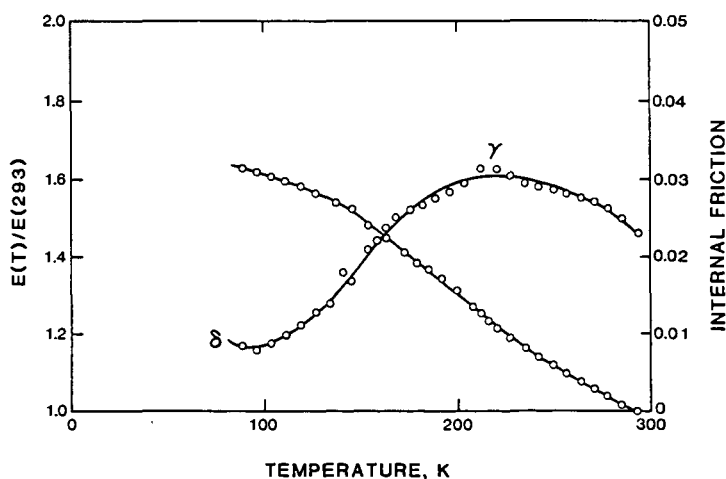


Fig. 3. Dynamic Young modulus and internal friction versus temperature measured near 50 kHz. A strong mechanical relaxation ( $\gamma$ ) occurs near 240 K. A strong low-temperature peak ( $\delta$ ) is suggested below 75 K.

## THE USES OF DIELECTRIC SPECTRA AND IMMERSIONAL CALORIMETRY IN THE CHARACTERIZATION OF LOW-RANK COALS

C. Tye, R. Neumann, and H.H. Schobert

University of North Dakota Energy Research Center  
Box 8213, University Station  
Grand Forks, North Dakota 58202

### Introduction

Moisture in low-rank coals is believed to involve at least two fundamentally different mechanisms for binding water to the coal matrix (1). The first type of moisture behaves as if were "free"; the vapor pressure versus temperature behavior is that of pure water. The second type occurs at sites where it is bound more tightly, resulting in a lowering of the vapor pressure relative to that of pure water at the same temperature. Such moisture may be hydrogen bonded to oxygen-containing functional groups or it may be incorporated as water of hydration of ion-exchangeable cations. There might also be tightly entrained moisture, in the pore structure, between the thermodynamically "free" moisture and the chemically bonded moisture. The objective of our work was to investigate the application of two experimental techniques, dielectric relaxation spectroscopy and immersional calorimetry, to the characterization of moisture content and pore structure of low-rank coals.

Dielectric techniques can sometimes prove valuable in studying bulk matter containing specific polar molecules (2, 3). From a theoretical standpoint, a parallel plate capacitor with a vacuum between its electrodes ceases to behave as a pure capacitance (at all frequencies) when a condensed matter dielectric is inserted. If an alternating voltage is applied to the capacitor containing a dielectric, the current and voltage will no longer be precisely  $\pi/2$  radians out of phase,  $\pi/2$  being the value for a vacuum-filled capacitor. The degree of departure from  $\pi/2$  radians as expressed by the angle  $\delta$ , depends on the "lossyness" of the dielectric.

The process of absorption (defined as the concentration of a substance on a surface where the substance, the absorbate, is in a gas or liquid form and the absorbent a solid) is spontaneous and is characterized by a fall in the entropy of the system and a decrease in surface free energy. This necessitates the absorption process to be exothermic, the resultant energy being referred to as the heat of immersion or heat of wetting. Therefore the exothermic heat liberated when a porous solid is immersed in a liquid is related to the surface energy of the solid and the measurement of it can be used to determine the surface area of various solid samples.

### Apparatus and Materials

#### (a) Dielectric Cell.

The dielectric cell was constructed from two stainless steel electrodes attached to corresponding outer stainless steel supports by means of a screw sandwiching a disk of insulating Teflon (see Figures 1 and 2). One electrode was 63 mm in diameter. The other, 50 mm in diameter, was surrounded by a 6 mm wide stainless steel annulus from which it was insulated by Teflon tape. This outer guard ring was kept at ground potential to eliminate fringing fields, edge effects and surface conduction across the dielectric being studied. The impedance measuring instrument used was a General Radio 1621 precision capacitance measuring system. This experimental setup enables the measurement of the equivalent parallel capacitance and resistance of the cell to be made at a given temperature and

frequency. For the subambient temperature measurements, the cell was placed in a styrofoam box and cooled with liquid nitrogen to the starting temperature.

(b) Differential Calorimeter.

The differential calorimeter consists, in essence, of two discrete units, each a calorimeter in its own right (see Figures 3 and 4). Each would have its own (identical to the other) paddle stirrer mechanism, heater circuit, temperature sensing circuit and Dewar flask. This twin calorimeter unit would then be operated in differential mode; i.e., a similar amount of wetting liquid would be put into each calorimeter Dewar, the calorimeters being imbedded in a metal heat sink for the thermal stability required, and the coal or carbon sample would be added to one Dewar. The temperature measuring circuit consists of a pair of matched thermistors, inserted into opposing arms of a Wheatstone bridge. Thus the heat liberated when the solid sample was added to the working Dewar would upset the balance conditions of the Wheatstone bridge due to the resistance change of the working Dewar's thermistor, with respect to the reference Dewar's thermistor resistance, and would produce an out-of-balance current that can be directly measured on a potentiometric chart recorder. This method of temperature measurement has the advantage that it is referenced to ambient conditions and not, for example, to the temperature of melting ice. The heat sink was fabricated from a 38 x 30 x 23 cm aluminum block. Two holes were bored in the heat sink of diameter slightly larger than the diameter of the Dewars, to enable them to be easily lowered inside. The stirring mechanism was designed to rapidly mix the material to be tested with the wetting liquid, producing a maximum dispersion of the material in the liquid with a minimum production of heat from the work of stirring. The work of stirring should ideally be constant. The rotating paddle type of stirrer was used, the glass paddle being mounted inside a guide tube which was in turn supported in a ground glass cone.

(c) Coal Samples.

Two coals were chosen for study: Gascoyne (North Dakota) lignite and Yampa (Colorado) subbituminous. The samples were obtained from the University of North Dakota Energy Research Center coal sample library. Composition data is given in Table I.

### Testing Procedures

(a) Dielectric Measurement.

Samples of several forms were used in the dielectric cell. Initial tests were performed with 63 mm diameter, 3 mm thick disks of coal sawn from solid blocks. Subsequent work involved 16, 30, 60, and -60 mesh powders. The connected and loaded cell was lowered into the styrofoam box and liquid nitrogen added to cool the cell and contents to around -190°C. The capacitance bridge was balanced and then the cell was allowed to warm up, during which time the measurements of T, temperature; F, frequency; C, capacitance, and G, conductance were performed. These variables would then subsequently be inserted into Equation 1 to determine the phase shift  $\tan \delta$  at a given frequency. The phase shift, expressed as the phase angle between voltage and current, is a function of the specific resistance of the coal, which in turn is dominated by the presence of its conductive phase, water.

$$\tan \delta = \frac{G}{2\pi FC} \quad 1)$$

A typical experiment involved taking data over a temperature range of -170° to 0°C at 0.1, 1.0 and 10.0 kHz. The temperature was measured by means of a chromel-alumel thermocouple attached to the guard ring. Plots of  $\tan \delta$  against temperature yielded the required dielectric spectra for that frequency.

Table I. ~ Characteristics of Coal Samples.

Sample	Gascoyne	Yampa
Rank	Lignite	Subbituminous
Mine Location	Bowman Co., North Dakota	Routt Co., Colorado
Heating Value (maf), Btu/lb	11677	13524
<u>Proximate Analysis, (As Rec'd); wt%:</u>		
Moisture	37.60	10.30
Volatile Matter	29.06	32.20
Fixed Carbon	0.00	44.00
Ash (ASTM)	9.70	13.50
<u>Ultimate Analysis (maf); wt%:</u>		
Carbon	69.05	80.81
Hydrogen	4.73	4.50
Nitrogen	1.04	2.53
Oxygen	23.15	11.30
Sulfur	2.03	0.79

(b) Differential Calorimetry.

The technique used with the differential calorimeter was to add 75 ml of wetting fluid (methanol or tetralin) to each of the clean, dry Dewar vessels. The top sections, complete with sensing and stirring apparatus were then lowered into the Dewars. Two grams of sample in a stoppered bottle was placed on top of the heat sink so that it could attain the same temperature as the rest of the system. The chart recorder was started after the bridge had been adjusted to its optimum operating conditions (250 mV). When the temperature remained constant, shown by a straight horizontal line on the trace, the calibration heater was switched on for 60 seconds (A to B, Figure 5). During this time, the voltage across the heater and the current passing through it were determined. After a reasonable portion of the cooling curve had been recorded for extrapolation purposes (B to C, Figure 5), the weighed sample was introduced to the working Dewar by means of the funnel mounted in the cone (C to D, Figure 5). A reasonable portion of the cooling curve was again recorded (D to E, Figure 5) and later another application of the heater for a known time period was applied to the working Dewar with the resulting temperature rise (E to F, Figure 5).

The heat of wetting in calories per gram is given by:

$$H = \frac{VIT}{J\sigma_h} \times \frac{\sigma_w}{W} \quad 2)$$

where V is the heater voltage in volts.

I is the heater current in amps.

T is the time the heater was switched on for (in seconds)

which produced the corrected temperature deflection of  $\sigma_h$ .

$\sigma_w$  is the corrected temperature deflection when the sample was wetted with the wetting liquid.

J = A constant = 4.18 joules per calorie.

W = weight of sample in grams.



Note that the second application of the heater (after the addition of the sample) will always produce a lower deflection, due the contribution of the sample to the total specific heat capacity of the Dewar and contents. The expression for describing the thermal capacity of the system is:

$$C = C_F + M_L S_L + M_C S_C \quad 3)$$

where  $C$  = thermal capacity of system,  
 $C_F$  = thermal capacity of fixed apparatus in the Dewar  
 (heat supports, stirrer, Dewar, etc.),  
 $M_L$  = mass of liquid,  
 $S_L$  = specific heat capacity of wetting liquid,  
 $M_C$  = mass of sample,  
 $S_C$  = specific heat capacity of sample.

It should therefore be possible to get an idea of the heat capacity of the sample by the difference in deflections between the first and second applications of the calibration heater.

The heat of wetting per unit area for any given liquid on a particular surface is a constant for that liquid provided the liquid wets the surface of the solid perfectly. The value of this constant is given by Bond and Spencer (4) as 10.7 for methanol. In order to convert the heat of wetting results into surface areas, Bond and Spencer measured the heat of wetting of a non-porous carbon black having a surface area of 230 m<sup>2</sup>/gm. Thus, the heat of wetting per m<sup>2</sup> = 10.7/230 calories. Alternatively, 1 calorie of heat is liberated when 21.5 m<sup>2</sup> of carbon surface is wetted by methanol.

The corrected temperature rises were obtained (6) by extrapolating the cooling curve until it crossed the vertical line drawn from the point when the heater was initially switched on, or the point when the coal was added. In this way the effect of the cooling of the Dewar, which would occur during the time the heater was on, would be nullified. Therefore, each time the heater was turned on or the coal was added, enough time had to elapse afterwards for a representative amount of the cooling curve to be recorded for an accurate extrapolation to be made. This vertical distance would be measured and treated as the corrected temperature rise.

In most cases, the slope of the temperature against time curve before and after heat input was the same, making the actual time at which the corrected temperature rise was determined not critical.

## Results and Discussion

Figure 6 shows the  $\tan \delta$  versus temperature behavior for a Yampa (Colorado) subbituminous coal of 10% to 12% moisture; the coal had been stored under water and air-dried before insertion into the cell. No appreciable weight loss occurred during air drying. Between -60° and 0°C (not shown) the  $\tan \delta$  increases without bound; this is most likely caused by an ionic double layer formed by mobile ions present in the coal. The peaks show a simple Debye-like behavior in that they are relatively narrow and the temperature maxima shift to higher temperatures with increasing frequency. The solitary curve at the bottom of the figure is a 0.1 kHz  $\tan \delta$  plot for the same sample after it had been freeze-dried for two days at 10 microns pressure. The total loss of moisture was approximately 10% of the original weight of the coal. The complete loss of the large dispersion upon water removal is taken to be evidence that the dispersion is indeed caused by the relaxation of water molecules. When the coal sample was reconstituted with water after freeze-drying, there was no significant difference in dielectric spectra with the original spectra from the mine fresh sample. Figure 7 shows the dielectric characteristics of this Yampa coal on removing and replacing the moisture for one frequency.

Figure 8 is the resultant dielectric spectra of the Gascoyne lignite sample. Here there are two distinct sets of peaks; one set at  $-102^{\circ}$ ,  $-92^{\circ}$ , and  $-80^{\circ}\text{C}$ , the other set at  $-60^{\circ}$ ,  $-50^{\circ}$ , and  $-36^{\circ}\text{C}$ . The latter set is likely attributable to the presence of macroscopic crystals of ice. Accurate dielectric measurements on pure bulk ice have placed the spectrum in this vicinity (5). Figure 9 presents the spectrum of the same lignite after air drying for several days until a constant weight had been achieved. The upper set of peaks is missing and the lower set appears at  $-108^{\circ}$ ,  $-100^{\circ}$ , and  $-90^{\circ}\text{C}$ . The peak locations are virtually identical to those in the Colorado subbituminous coal. Finally, freeze-drying resulted in the loss of more water and produced the 1 kHz spectrum shown at the bottom of the Figure. Note again the evidence for associating the large relative maxima with the presence of water.

When the Gascoyne sample was reconstituted with water after freeze-drying, two distinct set of peaks were again apparent; the spectrum was not significantly different from that of Figure 8. These experiments indicate that this lignite incorporates 80% of its moisture in a loosely-bound form which freezes to ice below  $0^{\circ}\text{C}$  and that the remaining 20% is present in the coal possibly as water of hydration, which does not crystallize into ice. The Colorado subbituminous coal contains only the latter type of bound moisture. These results are consistent with the conclusion about two types of bound water, based on vapor pressure studies (3).

Samples of -60 mesh Yampa subbituminous and Gascoyne lignite were tested to see what effect powdering had on the dielectric spectral quality. The spectra displayed in Figures 10 and 11, respectively, show resolved  $\tan \delta$  peaks at approximately the same temperature locations observed for the solid disk experiments. This proves that the powdered coal samples show  $\tan \delta$  peaks of sufficient quality to alleviate the need for preparing solid disk samples.

A series of experiments were conducted to test the effect of different mesh sizes of coal granules on spectral peaks and spectral quality, to determine if particle size had an effect on the type or amount of water content of the coal. Yampa (Colorado) subbituminous was sieved into mesh sizes 16, 30, 60, and fines less than -60. The spectral quality for the first set of peaks (presumably corresponding to the tightly-bound water of hydration) improves as the size of the specimen particle decreases. The spectral peaks are much more clearly defined for the -60 mesh size than for those at 16 mesh.

The interpretation of the dielectric spectra and correlations of dielectric results with other measurable coal characteristics is still in progress. However, the size, location, and number of peaks in dielectric spectra provide a significant quantity of information on the state and behavior of the coal's intrinsic moisture. There are many ways in which water may be attached to the coal, either loosely as water in the pore structure or chemically bonded to the coal matrix as, for example, water of hydration. Measurement of dielectric properties of this water present in the coal has indicated the distinction between at least two of the mechanisms of the water bonding.

A sample of the Gascoyne lignite was tested in the immersion calorimeter with methanol. Its heat output (determined from Figure 12) was found to be 65.74 joules per gram (15.49 calories, per gram). Using a 10.7 conversion factor (4) gives a surface area of  $165.72 \text{ m}^2\text{gm}^{-1}$ . A similar sample of Yampa subbituminous coal was tested and gave rise to the output shown in Figure 13. It is interesting to note the key difference between these two figures, that of the nearly instantaneous heat output of the lignite (the exothermic heat of wetting was liberated in a few seconds) in comparison with that of the subbituminous coal. In the latter case, the heat output occurred over several hours, presumably as the methanol wetting liquid explored the system of micropores which were approaching molecular dimensions. The specific and corresponding surface area were not calculated due to the difficulty in obtaining a corrected temperature deflection  $\alpha_w$  from Figure 13.

Further testing was carried out on various mesh sizes of Gascoyne lignite to determine if the external or apparent surface area was a significant factor in the total (including internal pores) surface area value. Mesh sizes of 16, 30, 60, and

powder less than -60 were used without significant variation in the heat output. The total surface area of a coal is therefore very tolerant of sample powder size, the internal pore surface area term being dominant when compared to the external or apparent surface area term. This is the expected result if the pores are very small.

A probe liquid of larger molecular volume than methanol should not be so able to penetrate the porous structure, especially the micropore region which can account for up to 95% of the total surface area. Tetrahydronaphthalene (tetralin) was thus used because of its relatively large sized molecules and because of its interest as a hydrogen donor in liquefaction. Yampa subbituminous and Gascoyne lignite were then tested in the calorimeter using tetralin. The results of the surface area determinations are tabulated in Table II along with the corresponding results for the two coals in methanol.

Table II. Surface Area of Coals Using Different Wetting Liquids.

Coal Sample	Surface Area ( $\text{m}^2/\text{gm}$ )	
	Methanol	Tetralin
Colorado Subbituminous	>200	9.05
Gascoyne Red lignite	165.72	5.15

Since the tetrahydronaphthalene is a larger molecule than methanol, it is unable to penetrate the smallest pores in the coal. Heat is only liberated from the very large pores and the external or apparent surface as if the porous coal had transformed into a non-porous carbon black. In future experiments the use of probe liquids of intermediate molecular sizes between those of methanol and tetrahydronaphthalene will yield information on the relative amounts (distributions) of micro, transitional and macropores.

#### Acknowledgment

The authors are pleased to acknowledge the valuable assistance of Wayne Kinney in carrying out some of the experimental measurements of this project.

#### Literature Cited

1. Schobert, H.H. "Characterization of Low-Rank Coals Important in Their Utilization." Oral presentation at Penn State; short course on coal. November 1-5, 1982.
2. McCrum, N.G.; Read, B.E.; and Williams, G. "Anelastic and Dielectric Effects in Polymeric Solids." Wiley, New York, 1967.
3. Daniel, V.V. "Dielectric Relaxation", Academic Press, New York, 1967.
4. Bond, R.L. and Spencer, W.D. Proceedings of the 1957 conference on carbon (University of Buffalo), 1958, p. 357.
5. Mahajan, O.P. "Coal Structure." Meyers, R.A., Ed., Academic Press, New York, p. 65, 1982.
6. Tye, C. "Design, Building and Operation of a Differential Calorimeter." Final year project, University of Salford, U.K., April 1983.

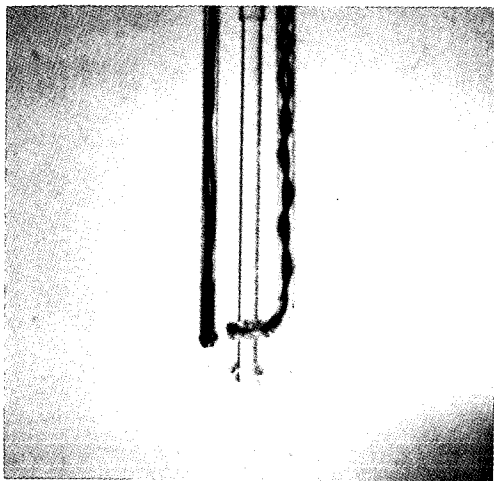


Figure 3. Shows details of one calorimeter.

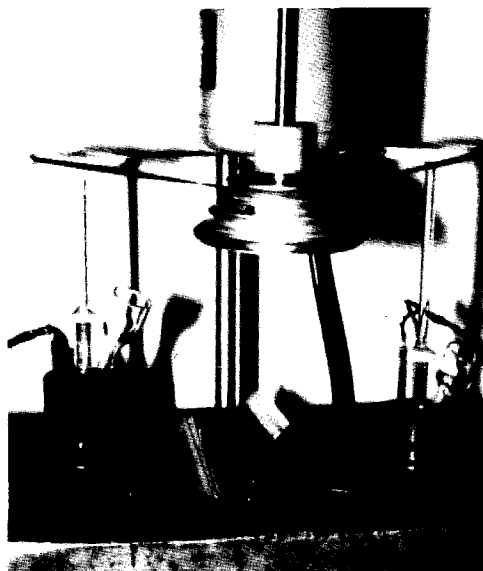


Figure 4. Shows overall differential calorimetry system.

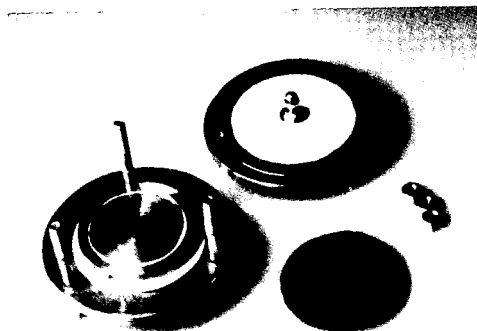


Figure 1. The disassembled cell and a water-saturated solid sample of Gascoyne Red lignite.

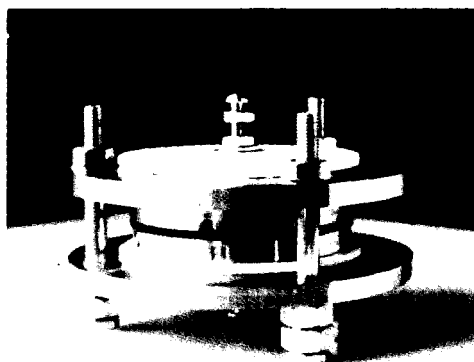


Figure 2. The assembled dielectric cell.

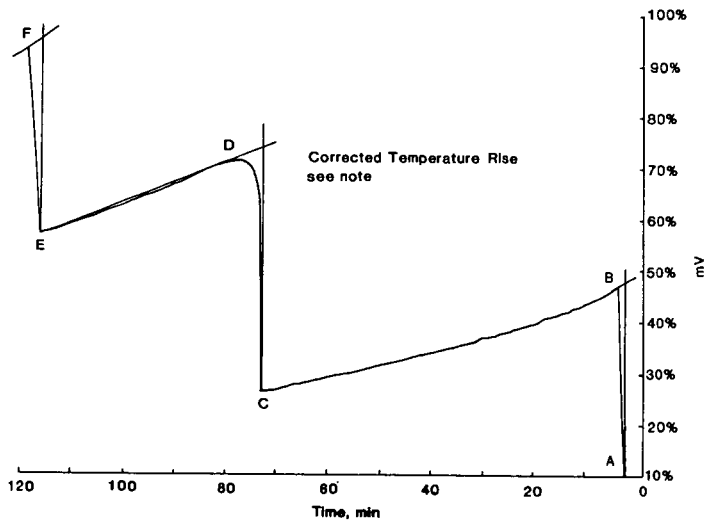


Figure 5. Trace for activated coconut shell carbon (2 mV full scale deflection 120 mm per hour).

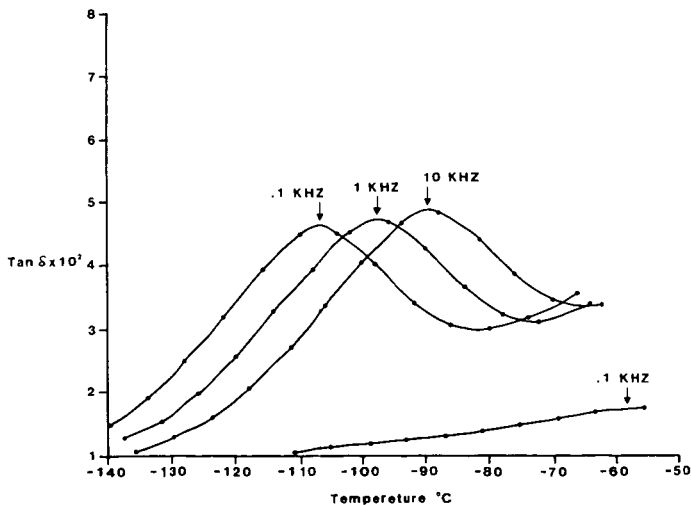


Figure 6. Phase shift vs. temperature for air-dried Yampa (Colorado) subbituminous coal.

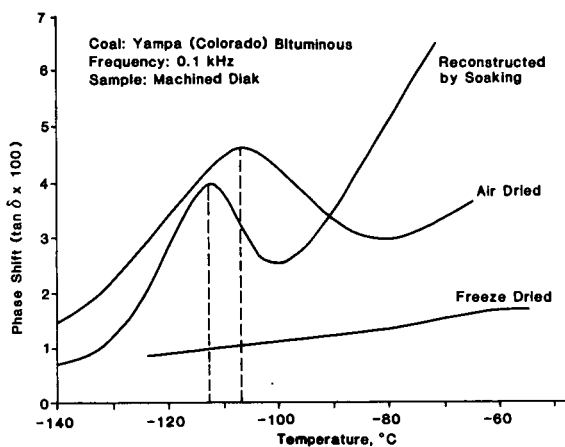


Figure 7. Dielectric characteristics of a subbituminous coal, showing effect of removal and replacement of tightly bound moisture.

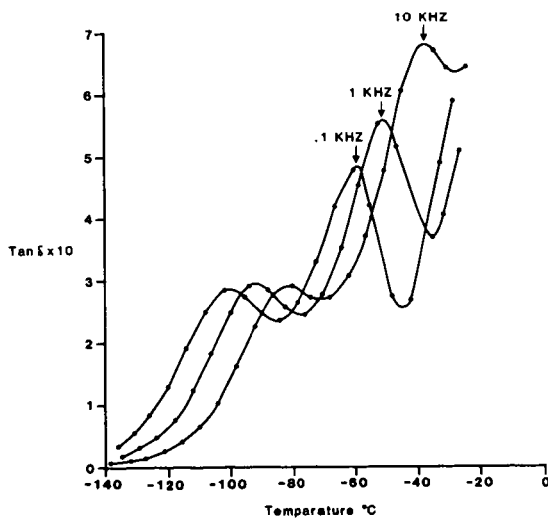


Figure 8. The temperature dependence of  $\tan \delta$  is depicted for the water-saturated Gascoyne Red lignite.

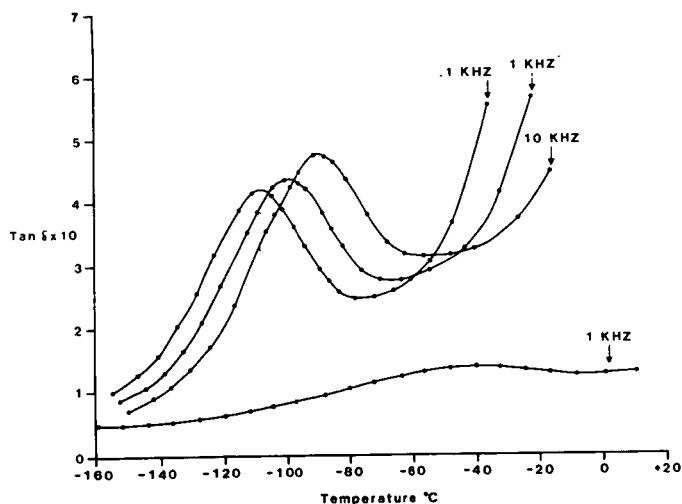


Figure 9. The temperature dependence of  $\tan \delta$  is depicted for the air-dried Gascoyne lignite. The lower (kHz) dispersion is for the freeze-dried coal.

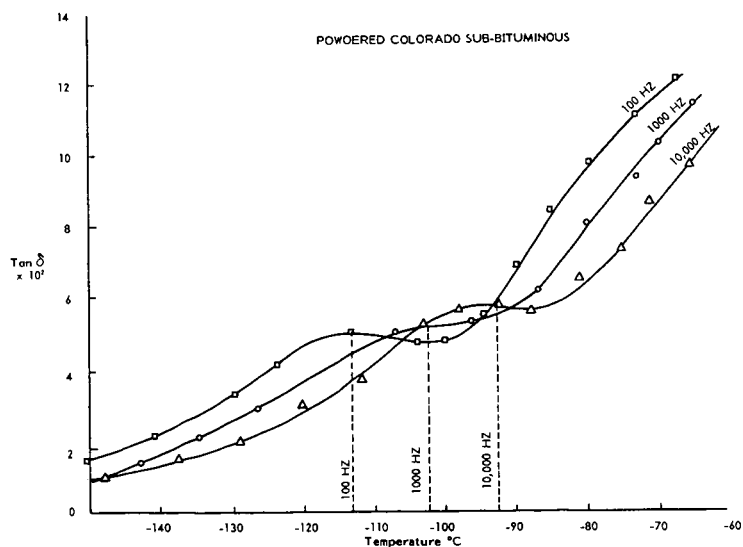


Figure 10. Spectra for powdered Yampa subbituminous.



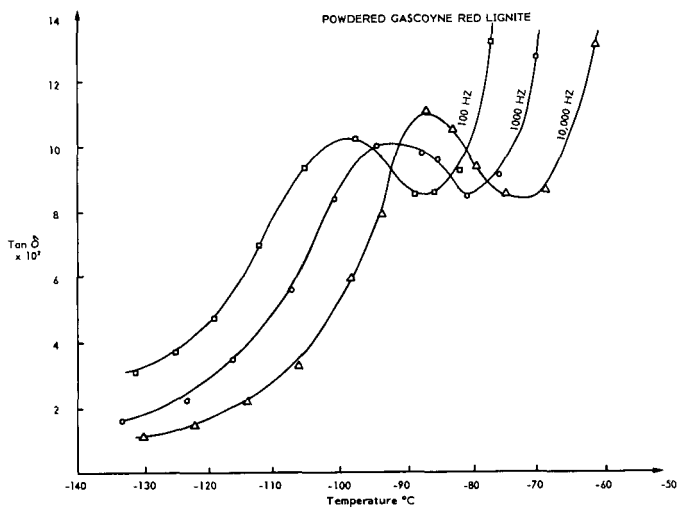


Figure 11. Spectra for powdered Gascoyne Red lignite.

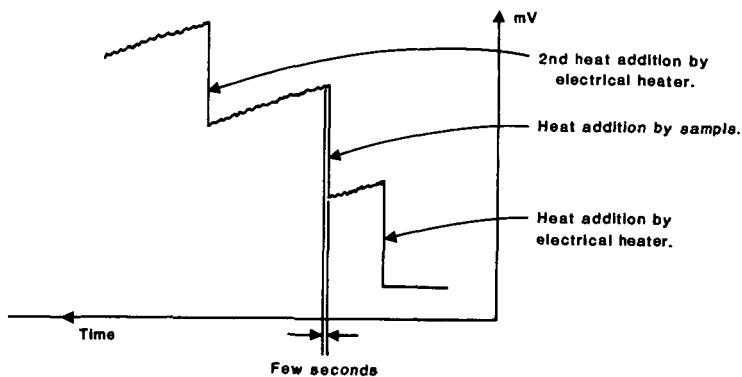


Figure 12. Characteristic of lignite type coals.

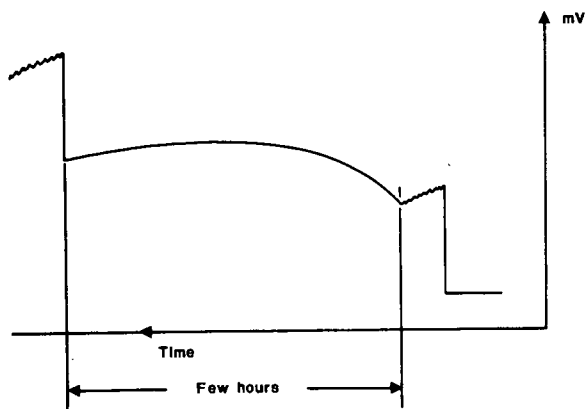


Figure 13. Characteristic of subbituminous type coals.

SEPARATION OF COAL LIQUIDS BY SIZE  
EXCLUSION CHROMATOGRAPHY - GAS CHROMATOGRAPHY (SEC-GC)

C.V. Philip and R.G. Anthony

Kinetic, Catalysis and Reaction Engineering Laboratory  
Dept. of Chemical Engineering, Texas A&M University  
College Station, Texas 77843

Introduction

The high efficiency gel columns packed with 5 $\mu$ m particles have increased the efficiency and decreased the analysis time of size exclusion chromatography (SEC). Since relatively large samples can be separated in a time as short as 20 minutes, SEC can be used as a preliminary separation technique prior to other analytical techniques such as gas chromatography (GC) and gas chromatography-mass spectroscopy (GC-MS). Such SEC separation of coal liquids, petroleum crudes and their distillation cuts into four or five fractions, followed by the analysis of the SEC fractions by GC and GC-MS have been reported elsewhere (1-14). The fraction collection and concentration of fractions were performed manually. This procedure was inefficient, and susceptible to human error. The Automated fraction collection followed by injection of the fraction into the GC reduces analysis time, and offers an option for collecting a desired number of fractions at predetermined time intervals.

The SEC separates coal liquids into fractions containing species with similar linear molecular sizes. Since similar molecular size species in coal liquid happened to have similar functionalities, the size separation enables the separation of fractions containing similar chemical species. When tetrahydrofuran (THF) is used as the mobil phase the coal liquid can be separated into four fractions containing heavy nonvolatiles, long chain alkanes mixed with light nonvolatile, phenols and aromatics. When the number of fractions are increased, less complex chromatograms with fewer peaks are obtained. The results of SEC-GC analysis of coal liquids indicate that the coal liquids are composed of a very large number of species but with similar structural blocks and functional groups. Lumping of similar components into four distinct groups such as nonvolatiles, alkanes (nonaromatic hydrocarbons) alkylated phenols and aromatics is seen as practical means of characterizing coal liquids. The instrumentation, analysis of coal liquid samples including recycle solvents are discussed in detail in this paper.

---

**Disclaimer:** This report was prepared as an account of work sponsored by an agency of the United States Government. Neither the United States Government nor any Agency thereof, nor any of their employees, makes any warranty, express or implied, or assumes any legal liability or responsibility for the accuracy, completeness, or usefulness of any information, apparatus, product, or process disclosed, or represents that its use would not infringe privately owned rights.

## Experimental

A Western Kentucky Synthoil and four recycle solvents from the Energy Research Center, University of North Dakota were the samples used for the analysis. Dry additive free tetrahydrofuran (THF) under helium atmosphere was used for preparing sample solutions and as the mobil phase in the size exclusion chromatograph (SEC). Although the synthoil could be injected without dilution, a 50% solution was preferred in order to reduce possible peak spreading and tailing. Since the recycle solvents were very viscous, 25% solutions were used. All the solutions were filtered through 0.5 Millipore filters using modest heat, but not high enough to boil THF, from a hot air gun and 30 psi Nitrogen pressure.

The instrumentation included a liquid chromatograph (LC, Waters ALC/GPC Model 202) equipped with a 60 cm, 5  $\mu$ m 100 Å PL gel column (Polymer Laboratories) and a refractive index detector (Waters Model R401) a Varian Chromatographic system (GC, VISTA 44) equipped with a 30 meter x 0.32 mm ID DB-5 capillary column (bonded phase fused silica column manufactured by J&W Scientific Co.) an autosampler (Varian 8000), a flame ionization detector (FID) and a nitrogen specific detector (thermionic ion specific - TSD) and a microcomputer system (IBM CS 9000) with 1000 K bytes RAM and dual 8" floppy disc drives for collecting raw chromatographic data.

The continuous sample separations on the gel column followed by the GC analysis of selected fractions was achieved by the operation of two sixport valves and a 3/4 port valve (All from Valco Instrument Company) as illustrated in figure 1. Sample injection into the LC was performed by a sixport valve ( $V_1$ ) with a 2 ml sample loop and fitted with a syringe-needleport for variable sample size injection. The combined operation of another sixport switching valve and the 3/4 port valve ( $V_2$ ) with 16 sample loops (100  $\mu$ l) enabled the linking of the liquid chromatograph with the autosampler of the gas chromatograph. The autosampler was modified to handle 100  $\mu$ l samples directly from the fraction collection loops of  $V_3$ . When  $V_2$  was turned clockwise, it kept  $V_3$  in line of LC effluents so that the fractions of separated sample could be collected and also the autosampler was bypassed.  $V_2$  at its counter clockwise position kept  $V_3$  in line with the autosampler for sample injection but bypassed the LC stream. Generally 0.1  $\mu$ l sample size was used for GC analysis. The stream from the capillary column was split (50/50) for the simultaneous monitoring by the FID and TSD. The real time monitoring of the GC was possible on both Varian and IBM systems and the raw chromatographic data were stored on the 8" floppy discs. The fraction collection, sample injection into the GC as well as the data collection was performed by the integrated system composed of a Varian Automation System (VISTA 401) and the IBM microcomputer (CS 9000). For each sample injection into the GPC column, up to 16 fractions were collected and analyzed by the GC using appropriate gas chromatographic programs stored in the memory without any manual interaction.

## Results and Discussions

The effluents from the GC capillary column are split into two streams and monitored by a flame ionization detector (FID) and a nitrogen specific detector (TSD). The analysis of a coal liquid derived naphtha (produced from western Kentucky coal-synthoil) is shown in Figure 2. The GC-MS analysis of coal liquid can miss several nitrogen compounds due to complex fragmentation pattern and low concentration. The FID output shows signs of overloading and most peaks are unresolved. Such overloading does not appear to affect the separation of nitrogen compounds. The use of a nitrogen specific detector in addition to FID enables one to identify the nitrogen species easily and GC-MS can be used for their structural identification.

Molecular size parameters such as molecular weight, molecular volume and hydrodynamic volume are used very effectively as the basis for SEC separation of polymers with identical building blocks or monomers (16-21). These molecular parameters need correction factors which vary depending on the individual structure of species (20), in order to use them as the basis for the SEC separation of mixtures of species especially the low molecular size compounds.

The SEC studies on a number of small molecular size species (5) such as alkanes, aromatics, phenols, amines and complex mixtures (15) such as coal liquids (1-11), petroleum crudes and their distillates (12,14), indicate that linear molecular size or the length of the molecule measured from its valance bond structure, is a better basis for explaining the mechanism of size separation by SEC (12). The effective linear molecular size of a species depends on its tendency to hydrogen bond with the solvent resulting in an increase of linear molecular size compared to nonhydrogen bonding species. Tetrahydrofuran, the SEC mobil phase, can increase the length of certain hydrogen bonding species such as phenols, amines and alcohols while the size of compounds such as benzene, pyridine, thiophene and alkanes are unaffected. This phenomenon enables the separation of phenols and aromatics in coal liquid into separate fractions.

SEC separation of recycle solvent obtained by the liquefaction of Wydak coal is illustrated in Figure 3a. The SEC effluents can be divided into four fractions based on elution time. The longer species appears first and are collected in Fraction 1. Since they are not volatile enough for GC-MS analysis, they are termed as heavy nonvolatiles. The second fraction is composed of volatiles, mostly straight chain alkanes ( $n\text{-C}_{14}\text{H}_{30}$  -  $n\text{-C}_{44}\text{H}_{90}$ ), and light nonvolatiles. Some olefins whose concentration may depend on the severity of liquefaction process, and branched alkanes such as pristane and phytane are also found in the second fraction. The third fraction is enriched mostly with alkylated phenols, indanols and naphthols. Some long structured aromatics such as biphenyls and binaphthyls may appear in this fraction. If the coal liquids are refined by cracking process resulting in naphthenic materials - a mixture of olefins and cyclic hydrocarbons, the third fraction may contain these materials also. The fourth fraction is composed of alkylated benzenes, indans, naphthalenes and heavy fused ring aromatics such as pyrenes and benzopyrenes.

When valve  $V_2$  and  $V_3$  are engaged the SEC Effluents (Figure 1) can be collected on the sample loops of  $V_3$  at specific intervals. The refractive index detector output shows the effect of such fraction collections as negative peaks (compare Figure 3a and 3b). Although sixteen is the maximum number of fractions, which can be collected at one time, more than sixteen fractions can be collected for a sample by repeating the procedure aimed at different elution times. Figure 4a shows SEC of a synthoil produced from western Kentucky coal. Twentythree fractions were collected. The FID output of 18 fractions, leaving the first three and the last two, are shown in Figure 5. The synthoil sample was analyzed by GC-MS prior to SEC-GC analysis and the major components were identified as alkanes ranging from  $n\text{-C}_{10}\text{H}_{22}$  to  $n\text{-C}_{44}\text{H}_{90}$ , phenols such as alkylated phenols, indanols and naphthols and aromatics such as alkylated benzenes, indans and naphthalenes. The first GC in Figure 5 shows the FID output of SEC fraction 4 of synthoil. All the peaks shown are straight chain alkanes. The next GC shows that the volatiles in fraction 5 are composed of relatively smaller alkanes. As the elution time increases the alkane chain length decreases. The fractions with short alkanes has overlap from heavy phenols (Fig. 5 GC, 6-9). The heavy phenols are not resolved but appear as a base line shift which is due to a large number of phenolic species eluting unresolved. As the fraction number increases smaller phenols appear as well resolved peaks (Fig. 5 GC, 9,14). When the molecular weight of phenolic species are increased by adding alkyl groups the probable number of isomers are increased and more isomers are possible for heavier phenols. The heavy and light aromatics appear in the last fractions (Fig. 5 GC 15-18). The fused ring aromatics such as pyrene and benzopyrenes appear after light aromatics (12).

At the Energy Research Center of the University of North Dakota, anthracene oil distillate was initially used as the solvent for coal liquefaction. The solvent along with dissolved liquefaction products were reused several times and solvent grade products mixed with the original solvents were supplied as recycle solvents. Four recycle solvents derived from four coals were analyzed by SEC-GC. The gas chromatograms of similar SEC fractions of these liquids are shown in Figures 3 and 4. Gas chromatograms of three similar fractions from each of the four solvents are presented in Figure 6. Examination of GCs indicate that these solvents contain similar volatile components.

### Conclusions

Although SEC and GC are two powerful chromatographic techniques, their combined use for analyzing complex mixtures has been limited due to the time consuming steps involved. The two valve interface which links the liquid chromatograph to gas chromatograph and the computer system which automate the system, reduce the analysis time as well as the frequency of manual interaction during the analysis which may take 8-10 hours for a coal liquid sample. By adding a mass spectrometer as a third detector to the GC, an extensive analysis of a rather complex sample such as coal liquid, petroleum crude and their refinery products is possible.

### Acknowledgements

The financial support of the U.S. Department of Energy, (Project Number DE-AC18-83FC10601) Texas A&M University Center for Energy and Mineral Resources and Texas Engineering Experiment Station is gratefully acknowledged. Energy Research Center at University of North Dakota furnished samples for the study.

### Literature Cited

1. Philip, C.V., Anthony, R.G., **Fuel Processing Technology**, 1980, 3, 285.
2. Philip, C.V., Anthony, R.G., **Proc. Coal Technology**, 1978, 2 p. 710.
3. Philip, C.V., Anthony, R.G., **Preprints ACS Org. Coat & Polym. Div.**, 1980 (August 20).
4. Zingaro, R.A., Philip, C.V., Anthony, R.G., Vindiola, A., **Fuel Processing Technology**, 1981, 4, 169.
5. Philip, C.V., Anthony, R.G., **Am. Chem. Soc. Div. Fuel Chem. Preprints**, (1979), 24, (3), 204.
6. Philip, C.V., Zingaro, R.A., Anthony, R.G., **Am. Chem. Soc. Fuel Chem. Preprints**, 1980, 25, (1), 47.
7. Philip, C.V., Zingaro, R.A., Anthony, R.G. in "Upgrading of Coal Liquids," Ed. Sullivan, R.F., **ACS Symposium Series No. 156**, 1981; p. 239.
8. Philip, C.V., Anthony, R.G., **Am. Chem. Soc. Div. Fuel Chem. Preprints**, 1977, 22, (5), 31.
9. Philip, C.V., Anthony, R.G. in "Organic Chemistry of Coal," Ed. Larsen, J.W., **ACS Symp. Series**, 1978, p. 258.
10. Philip, C.V., Anthony, R.G., **Fuel**, 1982, 61, 351.
11. Philip, C.V., Anthony, R.G., **Fuel**, 1982, 61, 357.
12. Philip, C.V. and Anthony, R.G., "Size Exclusion Chromatography", Ed. Proudler, T., **ACS Symp. Series**, 1984, 245, 257.
13. Philip, C.V., Anthony, R.G. and Cui, Z.D., "Chemistry of Low-Rank Coals, Ed. Schobert, H.H., **ACS Symp. Series**, 1984, 264, 287.
14. Philip, C.V., Bullin, J.A. and Anthony, R.G., **Fuel Processing Technology**, 1984, 9, 189.
15. Sheu, Y.H.E., Philip, C.V., Anthony, R.G. and Soltes, E.J., **Chromatographic Science**, 1984, 22, 497.
16. Hendrickson, J.G., **Anal. Chem.**, 1968, 40: 49.
17. Majors, R.E.J., **Chromatog. Sci.**, 1980, 18: 488.
18. Hendrickson, J.G. and Moore, J.C., **J. Polym. Sci. Part A-1**, 1966, 4: (1966).
19. Cazes, J. and Gaskill, D.R., **Sep. Sci.**, 1969 4: 15.
20. Krishen, A. and Tucker, R.G., **Anal. Chem.**, 1977 49: 898.
21. Snyder, R.L. and Kirkland, J.J., **Introduction to Modern Liquid Chromatography**, John Wiley and Sons, Inc., New York, 1974.

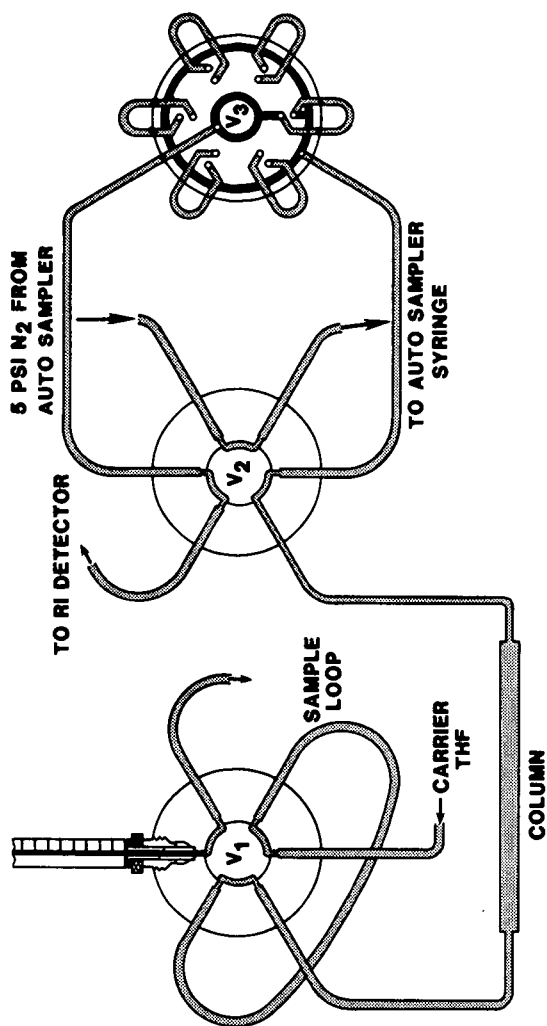


Figure 1. LC - GC interface. Note: V<sub>3</sub> has sixteen loops instead of six shown.



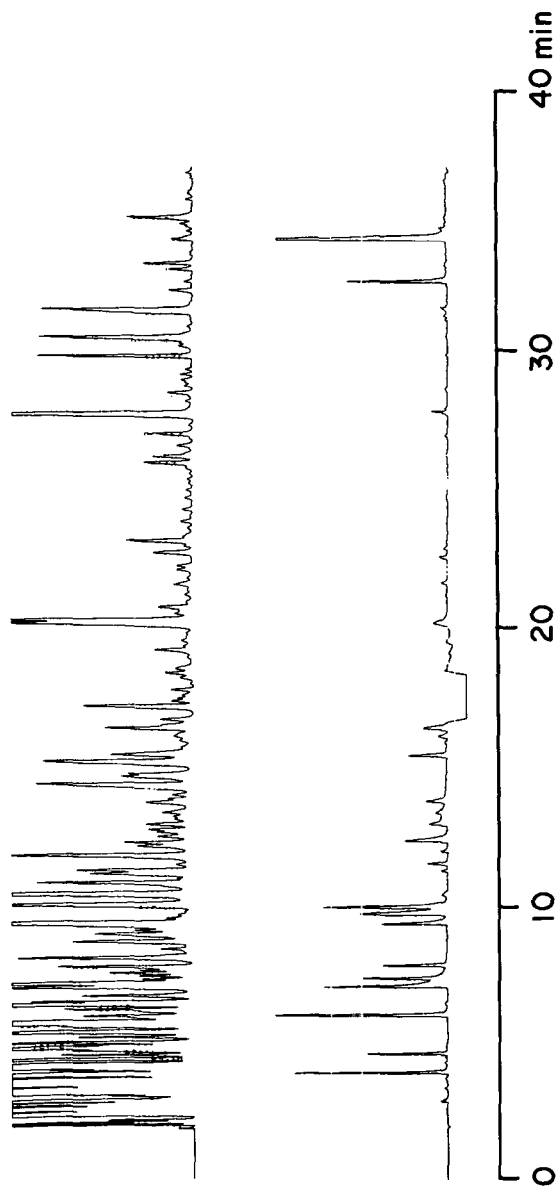


Figure 2. Gas chromatographic analysis of coal derived naphtha with duel detectors. The gas chromatograph is equipped with a bonded phase fused silica capillary column and an outlet stream splitter (1:1). Temperature program: 3 min hold at 40°C, 2°C/min to 80°C, 2°C/min to 120°C and 4 min hold at 120°C. One stream is monitored by an FID detector (top) and the other is monitored by a nitrogen specific detector (bottom).

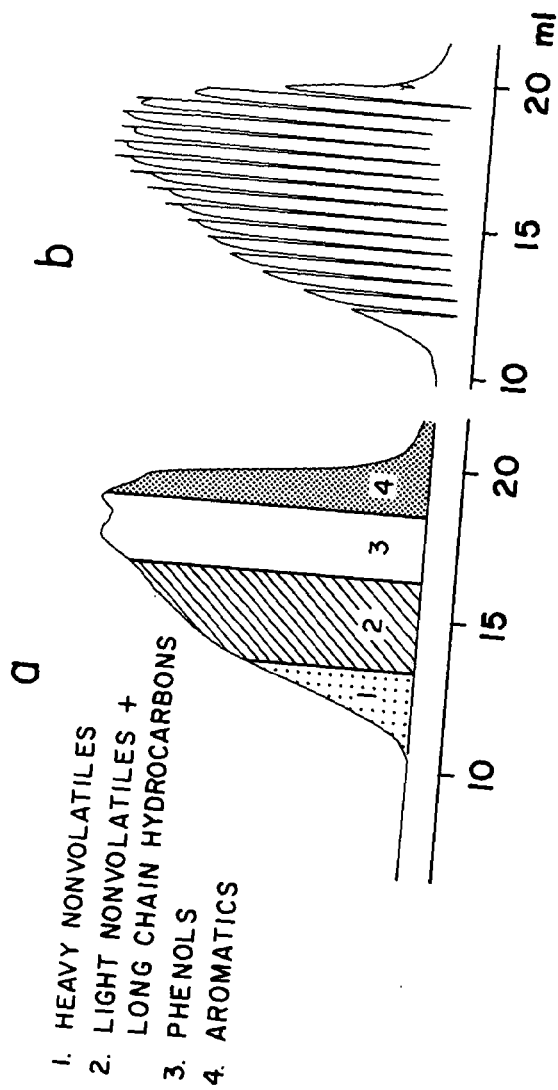


Figure 3. SEC separation of Wydak coal derived recycle solvent (a) LC-GC interface bypassed (b) 16 fraction were collected by LC-GC interface.

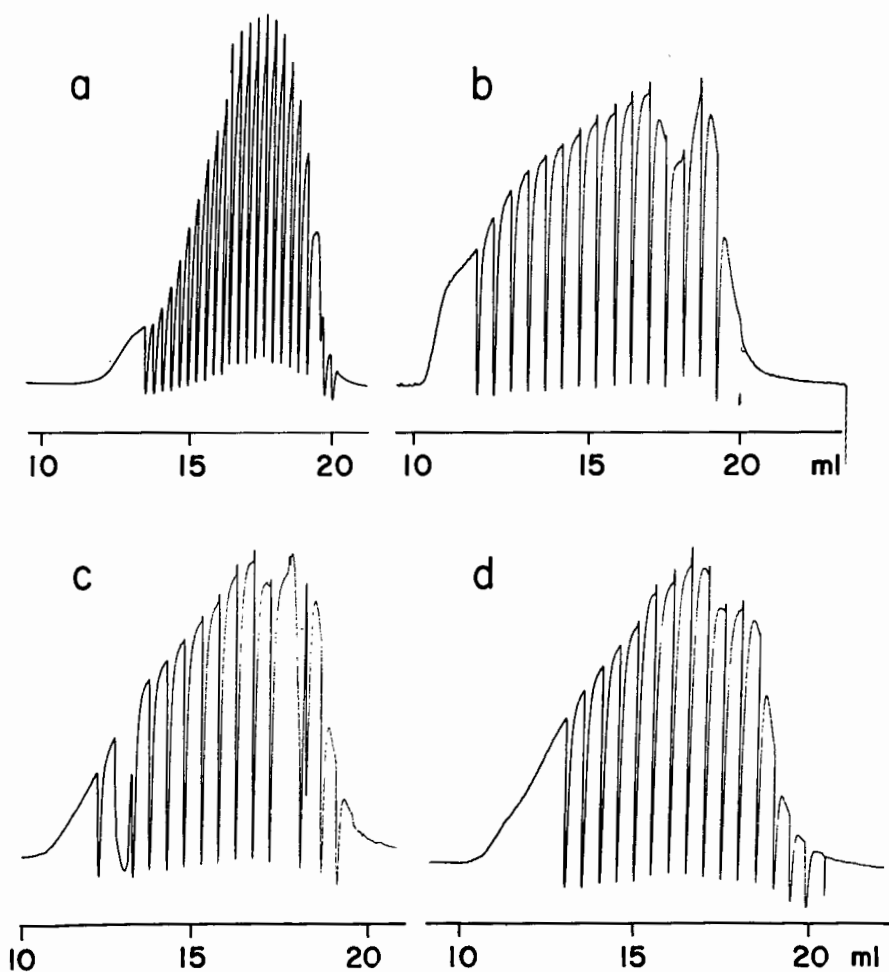


Figure 4. 100  $\mu$ l fractions are collected from the SEC effluents (a) Western Kentucky Synthoil. Recycle Solvents (b) Texas Big Brown (c) Beulah (d) Zap-2.

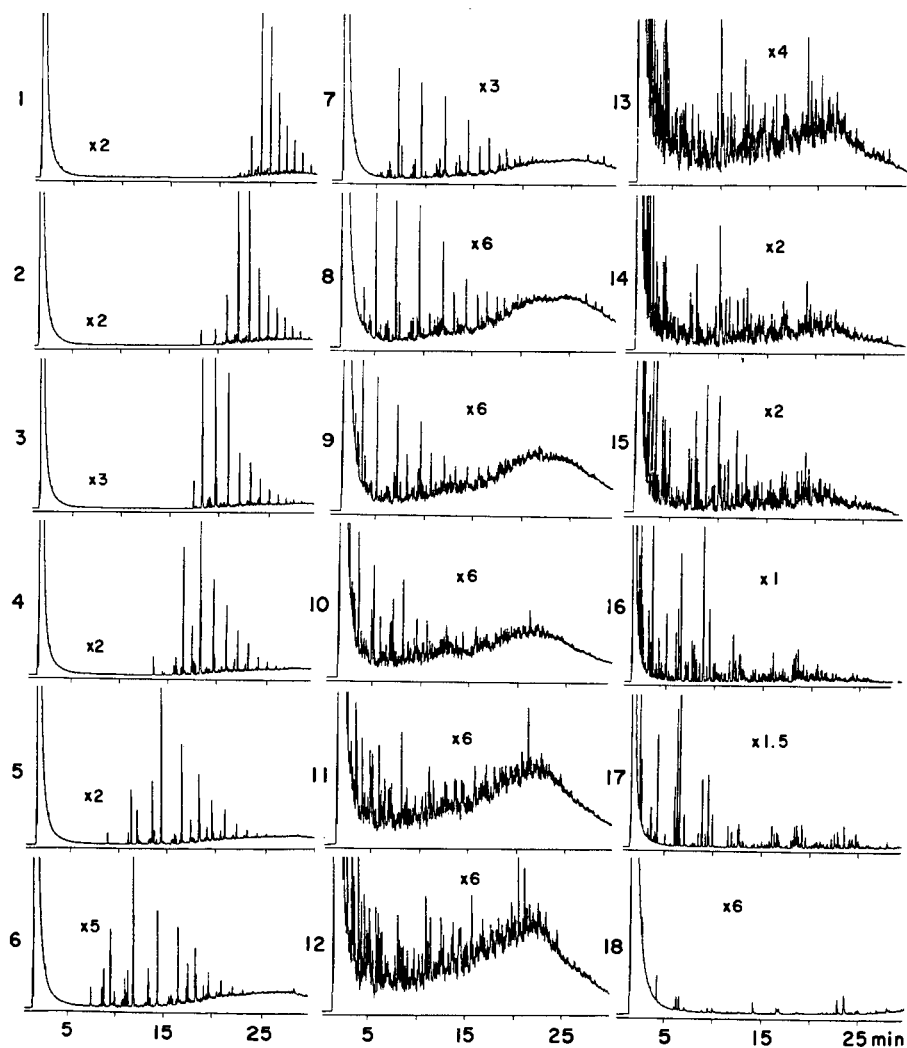


Figure 5. Gas Chromatograms of fractions from Western Kentucky Synthoil (Figure 4a) temperature program: 80-120°C at 4°C/min, 120-280°C at 10°C/min and 4 min. hold at 280°C.

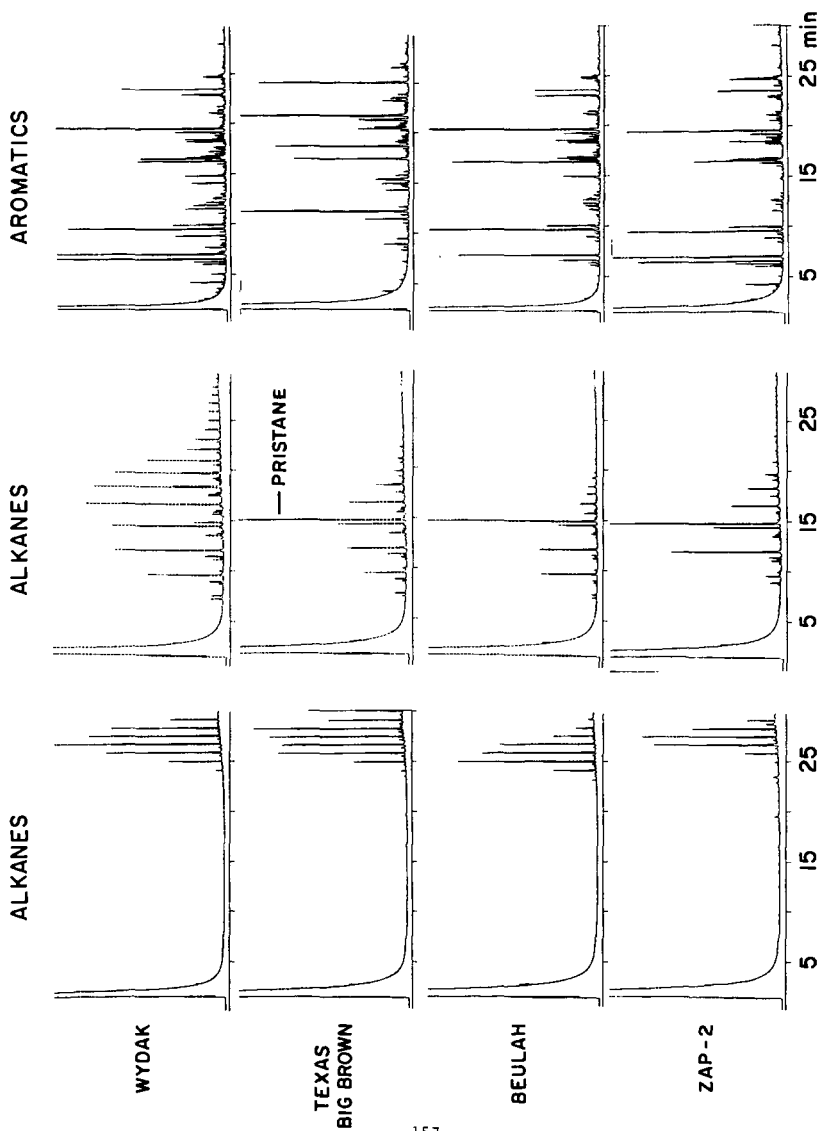


Figure 6. Gas chromatograms of similar fractions of four recycle solvents. GC conditions are same as in Figure 5.

UNDERSTANDING THE POUR POINT DEPRESSION MECHANISM-  
I. HPLC AND GPC ANALYSIS OF CRUDE OILS

C. A. Irani, D. S. Schuster, and R. T. Yin

Gulf Oil Research & Development, Production Research Center,  
P. O. Box 37048, Houston, TX 77236

SUMMARY

This study offers a preliminary explanation for the high pour point phenomena in waxy crudes, and attempts to differentiate between crude oils that do and do not respond to pour point depressants. Twelve internationally located crude oils were first subjected to a standard wax separation procedure, and the collected waxes were further analyzed by GPC and HPLC methods. The isolated wax fraction was found to be composed of aromatic, polar and hexane insoluble components in addition to the crystallizable saturate components. Based on GPC analysis of the molecular size distribution of the wax components isolated from the crudes, the 12 crudes could be categorized into three types. Regression analysis was successfully used to correlate pour point to the wax content and the saturates in the waxes. The saturates content gave the better correlation. GPC analysis of the saturate cuts was facilitated by the development of a saturates calibration curve to replace the existing polystyrene standard.

INTRODUCTION

Numerous problems occur during the production and transportation of waxy crudes. These crudes have high pour points (often over 100°F) and leave troublesome wax deposits in pipelines and production equipment. When cooled below the temperature for wax precipitation the precipitating waxes tend to form an interacting three-dimensional structure that can effectively tie up the lighter fractions of the crude and cause congealing to occur. A number of previous publications<sup>(1-10)</sup> have discussed the problems associated with the production and transportation of these crudes, and the methods that have been proposed for minimizing these problems.

Two approaches are commonly taken for handling these crudes. The obvious approach would be to always maintain the crude temperature above its pour point, but this is not always technically or economically feasible. The second approach is to use chemical pour point depressants to modify the interactions between the precipitating waxes, thus reducing the pour point and improving the flow characteristics. The problem arises in that the wax-additive interaction is extremely complex and very poorly understood, so that no prior judgement can be made as to the efficacy of a particular additive for depressing the pour point of a particular crude. The data presented in Table 1 serves to better demonstrate this point by comparing the properties of Cabinda (West Africa) and Handil (Kalimantan) crudes. Both crudes have similar API gravities and wax contents, yet their pour points are quite different. Additionally, Cabinda responds quite well to low concentrations of a

certain additive, yet Handil shows little response to most available additives.

Table 1  
Comparison of Two Waxy Crudes

Crude	API Gravity	Wax Content Wt. %	Pour Point °C (°F)	Depressed <sup>1</sup> Pour Point °C (°F)
Cabinda	32.1	16.3	21.1 (70)	-17.8 (0) <sup>2</sup>
Handil	32.1	16.5	32.2 (90)	21.1 (70) <sup>3</sup>

1. Maximum pour point depression seen with screening 50 pour point depressants.
2. 100 ppmw of Additive A.
3. 1000 ppmw of Additive B.

Based on the performance of these two crudes it was concluded that the wax-additive interaction is complex and poorly understood, and that a detailed analytical evaluation of at least the wax fractions in the crude oil would help in developing a better understanding of the interaction. More Specific questions that the study also attempted to address included: (1) The relationship between precipitated waxes and actual saturates; (2) The relationship between the pour point and the amount and composition of the wax fraction collected; (3) The nature of the waxes collected from different crudes; (4) An understanding of why there appeared to be a specific temperature for many crudes below which the pour point could not be chemically depressed.

Gel Permeation Chromatography (GPC) and High Pressure Liquid Chromatography (HPLC) were the major analytical tools used in this study to try and answer some of the questions raised above.

#### EXPERIMENTAL

Waxes were first isolated by an in-house procedure frequently used to determine the wax content of crudes and petroleum product. The procedure is a modification of ASTM D-721, and calls for diluting 1 gram of sample with 100 ml of methylethyl ketone. The solution is heated to 65.5°C (150°F) to dissolve the sample, and filtered at this temperature to remove the insoluble components (such as bulk asphaltenes). The solution is cooled to -17.8°C (0°F) and filtered through Whatman No. 50 filter paper to recover the wax precipitate. This fraction is referred to as the TOTAL waxes present in the crude oil.

HPLC was used to further separate this wax fraction into saturates, aromatic, polar, and hexane insoluble if present. The HPLC equipment and procedure has been discussed elsewhere.<sup>(11)</sup>

GPC was also used to classify the TOTAL waxes, as well as the saturates isolated from the TOTAL waxes by HPLC. The GPC consists of the following columns: 3-  $\mu$  styragel, ( $10^4$ ,  $10^3$ , 500 Å), and 2 $\mu$  spherogel (50 Å). Tetrahydrofuran solvent was used (20 mg/ml sample dilution). The injection volume was 100  $\mu$ l and a 2 ml/min flow rate was maintained. A differential refractometer detector was used. The elution of the sample was automatically monitored by a computer. At the end of the run, the computer integrates the chromatogram, calculates the molecular weight distribution, and prints out the results in digital and graphic form.

A special calibration curve was generated for the GPC analysis of the saturate fractions. For this purpose the saturates present in the wax fraction were separated by elution time in a preparative GPC. A Knauer Vapor Pressure Osmometer was used to determine their actual molecular weights, and their elution times on the analytical GPC were obtained. This molecular weight and elution time data was then combined to develop a calibration curve applicable to the saturate fractions.

## RESULTS AND DISCUSSIONS

Twelve waxy crude oils from fields around the world were analyzed in this study. Table 2 identifies the crude oils and presents some of their general properties (API gravity, pour point, wax content, HPLC analysis). Working on the premise that a difference in the composition of the wax fractions amongst these various crudes was responsible for the difference in behavior and response to chemical additives, the wax fractions were isolated and subject to further analysis.

GPC analysis of the wax precipitates provided molecular size distribution data based on which the crudes could be separated into three types. HPLC further indicated that what was being separated as a wax phase was actually a complex mixture of aromatic, polar, asphaltene and crystallizable saturate-type components. By employing a preparative HPLC method, large samples of the saturate fractions were collected and further analysed by GPC in order to identify distinguishing traits in the saturates present in the different crudes. Molecular weight distributions of the saturate components was facilitated by use of an in-house developed calibration curve specifically generated for this application to improve on the results available through the use of the existing polystyrene curve.

Even though the waxy components in a crude are directly responsible for the high pour point, previous attempts to correlate the pour point with the wax content of a crude have not proven very successful. For the 12 crudes used in this study, regression analysis showed a fair fit between the pour point and the wt. % waxes present, and a very good fit with the wt. % saturates present in the collected waxes. Details of this and other results are presented in the following sections.

### GPC Calibration Curve

GPC proved a valuable tool for both whole wax and saturates analysis. However, for pure saturates analysis the use of a polystyrene



based calibration curve was felt to give erroneous results. An attempt was made to correct this by developing a calibration curve specifically suited for saturates analysis. Both pure alkanes and saturate fractions isolated from a waxy crude were used to generate the necessary calibration curve. The waxes were first separated from the whole crude using the precipitation method described above, and preparative HPLC then used to isolate the saturates present in the wax cut. The saturates were further cut by preparative GPC into individual fractions, and the retention volume for each fraction established. The molecular weights of each saturate fraction were determined using vapor pressure osmometry. Molecular weight determinations were hampered by the low solubility of the saturates in the solvents used, and special handling procedures had to be used to overcome this problem. The calibration curves obtained are presented in Figure 1, which compares the polystyrene curve to the saturates curve and the pure alkane curve.

The pure alkane curve is limited in scope because pure alkanes were not available above a carbon number of 34, and yet it closely matches the saturates curve which could be taken to higher molecular weights. A substantial discrepancy exists between the saturates curve and the polystyrene curve, so that use of the saturates calibration curve gave a more reasonable molecular weight distribution of the saturates.

#### Composition of the Wax Fractions

Whereas pure saturates can be expected to be colorless or at most white, the actual wax fractions isolated were highly colored, leading to the conclusion that polar and/or aromatic type components were also present in the collected wax precipitates. Preparative HPLC was used to separate the wax fractions into saturates, aromatics, polars and asphaltenes, with the results shown in Table 2.

TABLE 2

#### HPLC ANALYSIS OF WAX FRACTIONS

Crude	API Grav.	Pour Point (°F)	Wax Content* Wt. %	Wt. % Sats.	Wt. % Arom.	Wt. % Polars	Wt. %* Asph.
Bentayan	22.6	110	36.4	55.0	14.2	28.1	2.7
Wasatch	41.8	105	37.1	90.0	8.2	1.7	0.1
Green River	30.3	95	26.8	61.4	16.5	14.9	6.6
Handil	32.3	90	16.5	88.8	6.0	4.0	1.6
Mibale	30.5	85	20.5	62.5	16.9	10.0	0.6
Cabinda	32.1	70	16.3	62.0	11.6	25.4	1.0
Lucina	39.6	60	12.2	73.0	12.5	9.4	5.1
Brega	43.1	50	6.4	73.5	9.7	13.3	3.5
Escravos	36.1	50	6.8	60.9	11.8	27.0	0.3
Mesa	30.4	50	7.3	62.9	15.6	21.0	0.5
Zaire GCO-4	30.4	50	14.2	39.3	11.7	36.0	13.0
Murban	39.7	15	4.8	72.9	17.5	8.6	1.0

\*Used in Regression Analysis

Clearly the wax precipitate is actually a very complex mixture of these crude oil components, a fact that compares well with field observations of paraffin deposits. Only in highly paraffinic and low asphaltic crudes do these deposits appear to have characteristics of pure saturates. Generally, depending on the composition of the crude, the deposits range from being high in saturates to almost asphaltic in nature. It is also generally recognized that successful chemical depression of the pour point requires that the additive modify the structure of the precipitating wax as the temperature is lowered. In untreated crude the precipitating waxes are capable of forming a complex, interacting three-dimensional structure which essentially ties up the lighter components of the crude thus reducing its fluidity. Consequently, for a chemical to successfully depress the pour point of a crude oil, it must first successfully destroy the interaction mechanism between these chemically complex species. Because no two crude oils have the same composition, no two wax precipitates can be expected to display a similar chemical interaction. Consequently a large discrepancy in performance between the response of various crudes to the same additive results. This also helps to explain why different crudes with similar saturate distributions show differing response, because the actual interaction is chemically more complex than a simple saturates interaction. For many refined streams, diesel oil for example, the pour point problem is more specific to the saturates present, and additives are capable of showing a much broader response. It is the complexity of the crude oil precipitates that limits the applicability of pour point depressants for their treatment.

#### Waxy Crude Classification

Review of the molecular size distribution data obtained by GPC for the 12 crudes under study indicated that it might be possible to use this information to classify the crudes. This was attempted, and three types were defined. Even though this classification may be considered loose, and has only been explored for the 12 crudes, the results are sufficiently encouraging to warrant extending this study to a larger number of crudes.

Type-1 crudes, as defined by the molecular size distribution of the total waxes, is shown in Figure 2. Many of the West African crudes fall in this category, which is characterized by a bimodal molecular size distribution. However, even though the C-25 and lower carbon numbers are well represented, the bulk of the wax components are in the higher molecular weight range. Extrapolation of this observation implies that the higher pour point crudes could perhaps fall in this type.

Type-2 crudes are presented in Figure 3. A bimodal distribution persists but there is a reversal in the relative contributions by the low and high carbon number fractions. The C-25 species are now more dominant, with the C-25+ species providing a hump at the tail end of the distribution. The remaining four crudes are classed together as Type-3 (Figure 4), but this is a weaker correlation. The primary trend for Type 3 crudes is towards a narrower distribution range as shown in Figure 4. Two of the crudes, Brega and Murban, show a continuation of this trend, with the two distinct peaks of the Type 2 crudes replaced by a single

peak in the C-25-30 range, and a declining contribution by the C-30+ fractions. Handil crude is an extreme example, in which almost the entire contribution is from the C-25-30 range material and only a limited contribution is from the C-30+ material. The one exception appears to be Escravos crude for which a distinct C-25-30 peak is present, but a very substantial contribution by components of very high carbon number is also observed.

Based on these noted differences in crude types it is now feasible to attempt to explain differences in crude responses to chemical additives. For example, the difference in behavior of Cabinda and Handil crudes can be attributed to the differences in the nature and distribution of the wax components in the two crudes, wherein a much narrower distribution of waxes is present in Handil relative to Cabinda. The response of these two crudes to additives would also be substantially different. Any additive in Handil crude would be swamped by a large amount of wax precipitating over a very narrow temperature range, whereas with Cabinda the effect would be much more gradual, with the additive capable of modifying the initial wax precipitate, which in turn could serve to modify the interaction between successive wax precipitates.

However, an intriguing question that remained unanswered was whether the differences in behavior of the two crudes could be attributed more to the differences in the saturate fractions present in the crudes, or to the more complex combination of material that represented the precipitated wax fraction. To this end preparative HPLC was used to isolate the pure saturate fractions from a number of crudes, and these saturate fractions analysed by GPC. The results, presented in Figure 5, indicated that the pure saturates are remarkably similar in size distribution, and consequently differences in behavior must be dependent on the chemical nature of the complexes formed between the saturates and aromatic, polar and asphaltene type components also present in the crudes.

#### Correlating Wax Content to the Pour Point

Numerous previous attempts to correlate the pour point to the wax content of a crude oil have not been very successful. Our studies have shown that the complex chemistry of the interactions involved would preclude any general correlation. Regression analysis was used to explore possible correlations between the pour point and the wax content of the crudes or the saturates present in the waxes. Table 3 presents the several variables ( $x_1 - x_{12}$ ) explicitly defined as functions of wax content and saturates in wax respectively.

TABLE 3

## Variables for Multiple Regression analysis

$x_1 = x$	$x_5 = x^2$	$x_9 = 1/e^x$
$x_2 = 1/x$	$x_6 = 1/x^2$	$x_{10} = \ln x/x^2$
$x_3 = \ln x$	$x_7 = 1/e^{\ln x}$	$x_{11} = (1-x)^2$
$x_4 = e^x$	$x_8 = e^{\ln x}$	$x_{12} = x(\ln x)$

$x$  = Wt. % Wax or Wt. % of Saturates in Wax

Functions  $x_4$ ,  $x_7$  and  $x_9$  were not used as they did not correlate well with the available data. Even though the remaining nine functions were used in multiple regression analysis, not all appear in the final regression equations, since the occurrence of singularities in the coefficient matrix indicated that the regression coefficient could not be solved simultaneously.

Equation 1 presents the relationship between the wax content and pour point.

$$\text{Pour Point (°F)} = -44522.14 - 1333.95x_1 + 15754.08x_3 + 41954.46x_6 + 69462.51x_{10} + 226.71x_{12} \quad 1)$$

The correlation coefficient for this equation is .9423. A much higher correlation coefficient (0.9978) was obtained for the correlation between the pour point and the amount of saturates present in the wax fraction. Equation 2 is the necessary equation for this case.

$$\text{Pour Point (°F)} = 49395.11 - 416.66x_1 + 50834.54x_2 - 14439.62x_3 - 2.78x_6 - 125575.07x_6 - 103337.73x_{10} \quad 2)$$

CONCLUSIONS

The pour point phenomena in waxy crudes is a complex chemical event which is influenced both by the amount of the saturates present in the crude and the chemical composition of the crude. GPC characterization of the wax precipitates allowed classifying the 12 crudes into three distinct types. HPLC analysis of the wax precipitates indicated that they are comprised of a complex mixture of saturate, aromatic, polar and asphaltic material. Differences in the behavior of the crudes and in their response to additives can be attributed to the differences in the distribution and composition of the wax fractions.

ACKNOWLEDGEMENTS

The assistance of the following Gulf personnel was greatly appreciated: J. Suatoni, R. Ruberto, and G. Chao for the GPC and HPLC analysis, and M. Greco for the VPO studies.

#### REFERENCES

1. Perkins, T. K. and J. B. Turner, "Starting Behavior of Gathering lines and Pipelines Filled with Gelled Prudhoe Bay Oil," Journal of Petroleum Technology, March, 1971, pp. 301-308.
2. Barry, E. G., "Pumping Non-Newtonian Waxy Crude Oils," Journal of the Institute of Petroleum, Vol., 57, No. 5534, March, 1971.
3. SPE Rocky Mountain Regional Meeting, May 23-25, 1983, "Paraffin Deposition and Rheological Evaluation of High Wax Content Altamont Crude Oils," by W. J. Matlach and M. E. Newberry.
4. Meyer, R. F. and C. T. Steel, ed., The Future of Heavy Crude Oils and Tar Sands, "Pipeline Transportation of Heavy Oils," A. Sloan, R. Ingham, and W. L. Mann, (Edmonton, Alberta, Canada, 1979), Chapter 86.
5. Rossemyr, L. I., "Cold Flow Properties and REsponse to Cold Flow Improver of Some Typical Fuel Oils," Ind. Eng. Chem. Prod. Res. Div., Vol. 18, No. 3, (1979).
6. SPE 55th Annual Fall Technical Conference and Exhibition, September 21-24, 1980, "Flow Properties of Utah Shale Oils," by W. H. Seitzer and P. F. Lovell, SPE 9500.
7. SPE Annual Technical Conference and Exhibition, October 5-7, 1981, "Pipeline Transportation of High Pour Handil Crude," by C. A. Irani and J. Zajac, SPE 10145.
8. Harvey, A. H., R. Briller, and M. D. Arnold, "Pipelining Oils Below Their Pour Point--Part I," Oil & Gas Journal, August 23, 1971, p. 96.
9. Harvey, A. H., R. Briller, and M. D. Arnold, "Pipelining Oils Below Their Pour Point--Part II," Oil & Gas Journal, August 30, 1971, p. 62.
10. Ford, P. E., J. W. Ells, and R. J. Russell, "What Pressure is Required for Restarting Gelled Line?" Oil & Gas Journal, May 17, 1965, pp. 134-136.
11. Suatoni, J. and R. E. Swab, "Preparative Hydrocarbon Type Analysis by High Performance Liquid Chromatography," Journal of Chromatography Science, Vol. 14, November 1976, pp. 535-537.

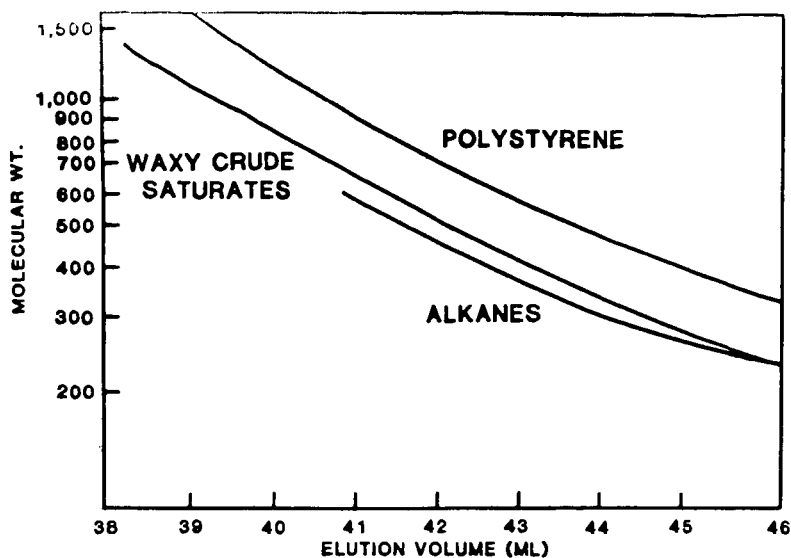


Fig. 1 WAXY CRUDE SATURATES CALIBRATION CURVES

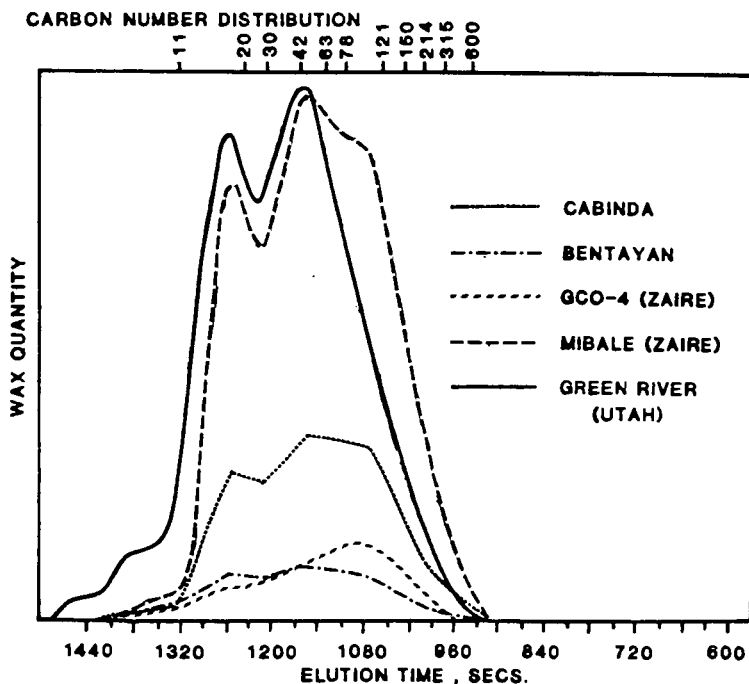


Fig.2 TYPE - I CRUDES

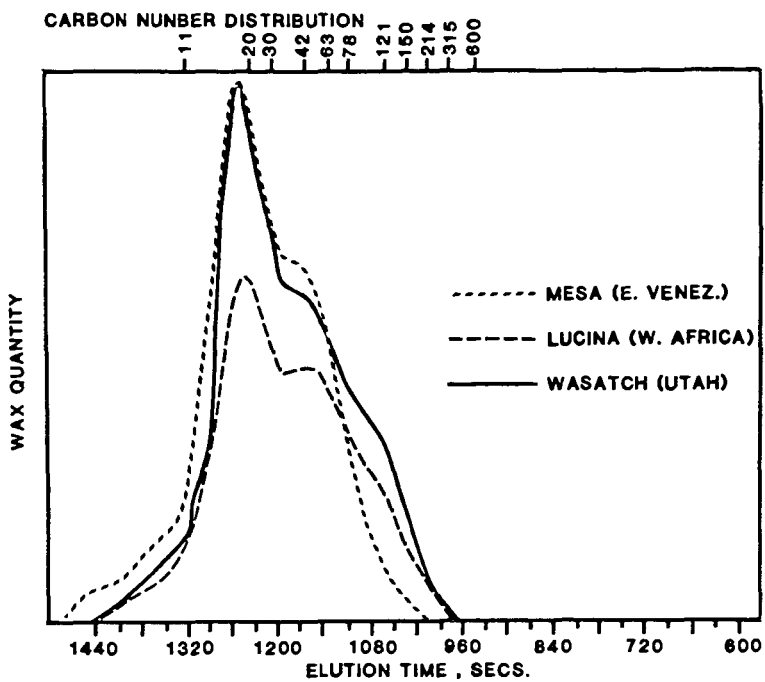


Fig.3 TYPE II CRUDES

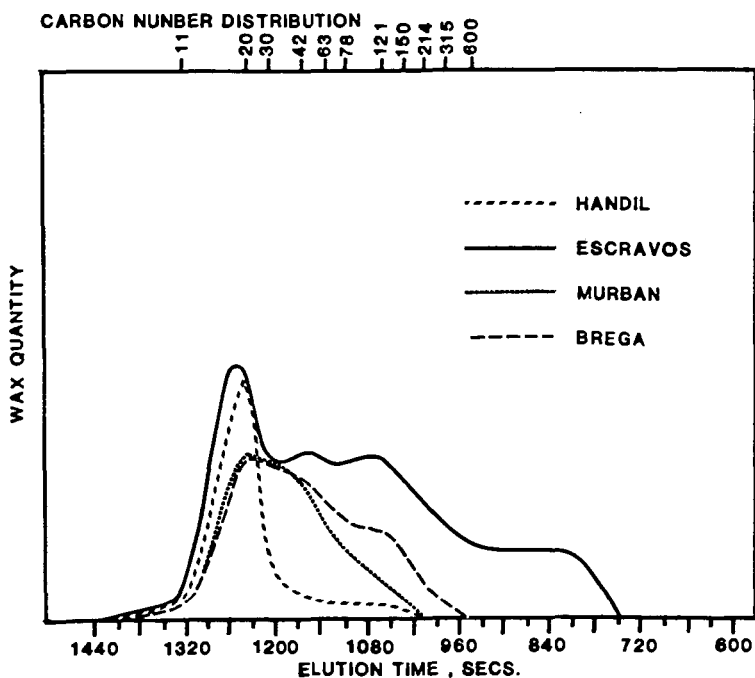


Fig.4 TYPE III CRUDES

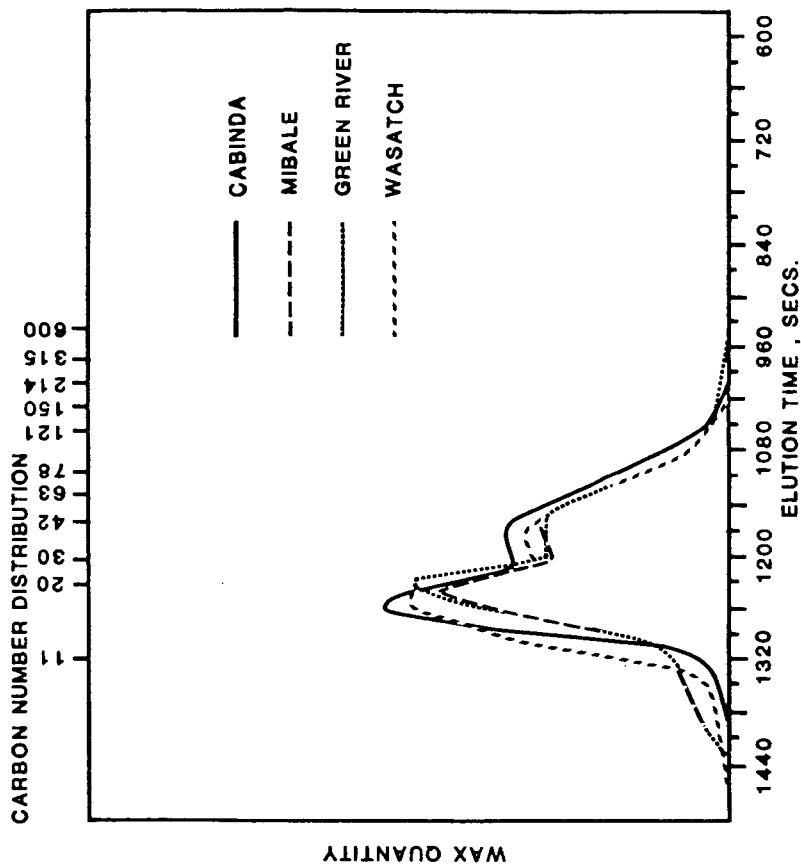


Fig.5 COMPARISON OF SATURATES FRACTIONS



## UNDERSTANDING THE POUR POINT DEPRESSION MECHANISM-II MICROFILTRATION ANALYSIS OF CRUDE OILS

D. S. Schuster and C. A. Irani

Gulf Oil Research & Development, Production Research Center,  
P. O. Box 37048, Houston, TX 77236

### SUMMARY

This study helps to explain the high pour point phenomena in waxy crudes and begins to explain differences in crude oils that do and do not respond to pour point depressants. Microfiltration was used to separate the waxes that precipitate out at the various temperatures in waxy crude oils. These waxes, which can be composed of saturates, aromatic, polars and asphaltenes, vary in molecular weight and composition with their temperature of precipitation in a waxy crude. Waxes that precipitate out of the crude oil solution at temperatures above the pour point are of higher molecular weight and have a high asphaltene content. The waxes that precipitate at lower temperatures have lower molecular weights and contain mostly saturates. Detailed chemical analysis showed that the temperature where asphaltenes are no longer associated with the waxes represents the maximum degree of pour point depression obtainable. This trend was verified for six waxy, high pour point crudes.

### INTRODUCTION

As pointed out in the preceding paper, treating waxy crudes with pour point depressants often offers a solution to high pour point problems. However, a major uncertainty with the chemical additive treatment for reducing the pour point is that many waxy crudes only show a limited response to the pour point depressant. Additionally, the mechanism of pour point reduction, while often hypothesized, still remains unknown.

Four questions concerning pour point depression were posed in the last paper. That paper demonstrated the answers to the first three questions and indicated that the pour point is a function of the amount of saturates in the wax fraction, the waxes are composed of aromatic, polar and asphaltic components in addition to the saturates, and that the waxes in different waxy crudes can be classified into three types. Thus, when dealing with waxy crudes, the polar, aromatic and asphaltic components must be considered.

This paper attempts to answer the remaining questions posed in the last paper, and a number of questions that follow from it. Specifically, 1) What happens at the pour point temperature? 2) Why can't the pour point of many crudes be depressed beyond a certain temperature? and 3) Why are pour point depressants effective on only certain crudes?

## EXPERIMENTAL

### Wax Fractionation

As presented in the previous paper, a method was defined to obtain the total amount of wax in a hydrocarbon fraction at a predetermined temperature of  $-17.8^{\circ}\text{C}$  ( $0^{\circ}\text{F}$ ). This procedure was modified to fractionate the waxes over distinct temperature ranges so that a more continuous analysis of the changing wax composition could be undertaken.

The crude was diluted (100:1) with methyl ethyl ketone and heated to  $150^{\circ}\text{F}$ . Bulk asphaltenes were removed by filtration at this temperature. The diluted sample was cooled through a series of  $5.5^{\circ}\text{C}$  ( $10^{\circ}\text{F}$ ) temperature intervals, with the precipitated wax being removed from the sample at each interval. The end results is a totally dewaxed oil at  $-17.8^{\circ}\text{C}$  ( $0^{\circ}\text{F}$ ) with the waxes separated out in successive  $5.5^{\circ}\text{C}$  ( $10^{\circ}\text{F}$ ) temperature ranges. The separated waxes were then further analyzed by the HPLC and GPC methods discussed in the previous paper.

### Centrifuge Study

Treatment with additives often does not reduce the crude's pour point to a sufficient degree. Indications are that the additive is successful with the initial range of waxes, but the either the additive is ineffective with the next range of waxes (which gives rise to the depressed pour point) or its effectiveness is inhibited by the deposition of waxes. The purpose of the centrifuge study was to separate the first precipitate of treated waxes, so that the succeeding wax fractions could be isolated for treatment and analysis. If a significant pour point reduction was obtained on this next set of waxes, the two treatments were then combined into a single treatment for the entire crude.

The basic experimental procedure was:

- 1) Treat the crude sample with the most successful additive package.
- 2) Remove the crude from the predetermined optimum oven cycle and transfer to centrifuge tubes at  $22.2^{\circ}\text{C}$  ( $40^{\circ}\text{F}$ ) above the treated crude's pour point.
- 3) Transfer the centrifuge tubes to a waterbath and cool the samples at  $1^{\circ}\text{C/hr.}$  ( $0.6^{\circ}\text{F/hr.}$ ) to  $11.1^{\circ}\text{C}$  ( $20^{\circ}\text{F}$ ) above the treated crude's pour point.
- 4) Preheat the centrifuge to the same temperature as in Step 3 above, and centrifuge the samples for five minutes.
- 5) Decant the top liquid phase from the settled waxes.

The top liquid phase was subjected to further treatment for pour point depression, and both the wax phase and the top liquid phase were further analyzed.

## RESULTS AND DISCUSSION

This study resulted in several interesting findings which are presented below. First, an analysis of the waxes obtained at different temperatures showed that the waxes precipitating above the pour point have a high molecular weight and contain significant amounts of asphaltenes. Another finding was that a strong association exists between asphaltenes and waxes that precipitate at various temperatures. The lowest temperatures at which asphaltenes are still present with the wax appears to indicate the maximum amount of pour point reduction achievable by the use of chemical additives. Further details are offered below.

### Wax-precipitation Temperature Trends

Analysis of the waxes separated at various temperatures from a crude indicates that the waxes that precipitate at temperatures above the 35°C (95°F) congealing temperature differ from those that precipitate at lower temperatures.

The first difference is shown by the GPC molecular size distribution curves (Figure 1) for Bu Attifel crude. The wax fractions isolated at 32.2°C (90°F) and 37.8°C (100°F) indicate that the waxes that precipitate below the congealing temperature is reached are composed of higher molecular weight components. Each size distribution curve represents a contribution from both higher and lower molecular weight species which show up as two distinct peaks. A reversal in the relative contributions from the two species takes place between 32.3°C and 37.8°C. At the higher temperatures (above the congealing temperature), the more sizeable contribution is from the higher molecular weight species (peak on the left), but at 32.2°C the major contribution is from the lower molecular weight components (peak on the right).

The second trend indicates that above the 35°C (95°F) congealing temperature, the wax fractions are primarily composed of asphaltenes, but at temperatures below the congealing temperature the waxes contain mostly saturates (Table I). Therefore, possible nucleating sites for wax crystal growth that precipitate at temperatures above the congealing temperature are primarily asphaltenes. These asphaltenes were initially removed by filtration during the wax separation. Apparently, some type of asphaltenes must be associated with the waxes, and they are not removed by bulk deasphalting.

TABLE I

HPLC ANALYSIS OF BU ATTIFEL WAXES SEPARATED BY MODIFIED G-281

TEMPERATURE- WAX REMOVAL	(G-281)	HPLC of the Waxes			
	WT. % WAXES	WT. % SATURATES	WT. % AROMATICS	WT. % POLARS	WT. % ASPHALTENES
100°F	1.8	4.7	0.3	---	95.0
100	1.1	24.0	0.7	0.3	75.0
95	1.0	95.5	2.1	0.4	2.0
90	0.4	95.9	2.8	0.7	0.6
80	1.7	89.7	1.7	0.2	8.4
70	1.6	89.0	2.5	0.2	8.3
60	5.6	95.9	3.5	0.1	0.4
50	2.3	94.6	4.4	0.6	0.4
40	2.4	96.6	3.0	0.4	---
30	3.6	97.2	2.7	0.1	---
20	4.1	95.7	3.6	0.7	---
0	5.0	96.8	2.7	0.5	---
-20	4.3	96.3	3.2	0.5	---

Aside from the uncertainty as to the source of the asphaltenes, it is understandable why the higher temperature waxes are composed of asphaltenes. Asphaltenes are high molecular weight species and can be viewed as being more peptized (less flocculated) at the higher temperatures. Therefore, asphaltenes would tend to associate with the higher temperature waxes. The presence of these asphaltenes with the higher temperature waxes could also explain why the GPC molecular size distribution contains two peaks. The peak on the left probably represents the asphaltenes, while the peak on the right might represent the saturates and associated polars and aromatics.

This reasoning does not, however, explain either how or why the asphaltenes are associated with any of these waxes, since a bulk deasphalting step should have removed them. Further analysis of this asphaltene association yielded some interesting results which are outlined below.

#### Asphaltene Effect

As noted, asphaltenes are associated with the waxes, even though they should have been removed by a bulk deasphalting step during the wax separation. This association was verified by determining the saturates, aromatics, polar, and asphaltene content of Bu Attifel in two different manners.

First, Bu Attifel crude was directly separated by group type into saturates, polars, aromatics, and asphaltenes and volatiles by HPLC. Conversely, by total wax separation at 0°F, the crude was separated into the total wax, oil and bulk asphaltene fractions. These fractions were then analyzed by HPLC to yield the group types contained in the fractions. The same total amounts of the saturates, aromatics, polars and asphaltenes should be obtained for both separation methods.

As can be seen in Table II, this does not appear to be true for the asphaltenes and saturates. Only when the saturates and asphaltenes are added together is conservation of mass satisfied. Apparently, the saturates and asphaltenes are associated with one another and do not totally separate from one another during the bulk deasphalting step. Asphaltenes have been reported to be associated with polar and aromatic components during deasphalting, but in this case, the deasphalting step is leaving asphaltenes behind.

TABLE II

BU ATTIFEL CRUDE COMPONENT ANALYSIS

HPLC Analysis After Separation Into Wax,  
Asphaltenes, and Oil By Gulf Method 281

Components	Wt. %	Saturates	Insolubles (asphaltenes)	Polars	Aromatics	Volatiles
Wax	29.5	= 27.317	+ 1.475	+ .059	+ .649	+ 0
Asphaltenes	3.9	= .17	+ 3.72	+ 0	+ 0	+ 0
Oil	41.0	= 36.018	+ 0	+ .241	+ 4.751	+ 0
Volatiles	25.6	= 0	+ 0	+ 0	+ 0	+ 25.6

---

Total	100.00	= 63.505	+ 5.195	+ .3	+ 6.40	+ 25.6
		68.7				

HPLC Analysis of the Total Crude

Total Crude	100.00	= 67.8	+ 0.9	+ .31	+ 5.79	+ 25.6
		68.7				

It is interesting to note the precipitation temperature at which the waxes no longer contain asphaltenes (Table I). No asphaltenes are found with the waxes that precipitate at temperatures below 10°C (50°F). It should be noted that Bu Attifel crude's pour point has never been depressed below this temperature.

Similar analysis of Cabinda Crude (Table III) verifies the Bu Attifel results. As with Bu Attifel crude, asphaltenes are associated with the saturates at higher precipitation temperatures. Asphaltenes are, however, found with all of the waxes that precipitate out to -17°C (0°F). This is especially interesting since this wax precipitation temperature also represents the maximum depressed pour point obtained for Cabinda crude by using chemical additives.

TABLE III

## HPLC ANALYSIS OF CABINDA WAXES SEPARATED BY MODIFIED G-281

TEMPERATURE- WAX REMOVAL (°F)	(G-281)	HPLC of the Waxes			
	WT. % WAXES	WT. % SATURATES	WT. % AROMATICS	WT. % POLARS	WT. % ASPHALTENES
100	2.1	12.4	4.1	8.3	75.2
90	0.3	20.4	7.2	28.8	43.6
80	3.1	57.0	13.6	24.4	1.7
70	2.0	70.5	11.6	17.5	0.4
60	1.4	70.3	12.2	17.4	0.1
50	2.2	70.3	12.7	16.6	0.4
40	3.7	60.0	16.4	23.3	0.3
20	4.4	66.7	16.3	16.9	0.1
0	3.3	66.2	18.5	15.1	0.2

Additional analysis of six crude oils confirms that asphaltenes are associated with the level of pour point depression. Table IV summarizes the maximum effect of pour point depressants on the crudes. Note that this temperature also represents the temperature at which the asphaltene-saturate association ends.

TABLE IV

## ASPHALTENE - POUR POINT DEPRESSION TREND

CRUDE	WASATCH	GREEN RIVER	HANDIL	GOBBS
Pour Point (°F)	105	95	90	85
Maximum Depressed Pour Point (°F)	105	60	70	30

Temperature-  
Wax Removal

## HPLC Indication of Asphaltene

110	*	*	*	*
100		*	*	*
95		*	*	*
90		*	*	*
80		*	*	*
70		*	*	*
60		*		*
50				*
40				*
30				*
20				
0				

\*Denotes presence of asphaltenes.

The treated and untreated waxes in Bu Attifel crude were isolated by the centrifuge method and analyzed with HPLC. This study indicated (Table V) that the untreated portion of Bu Attifel crude contained no asphaltenes.

TABLE V  
ANALYSIS OF UNTREATED, CENTRIFUGED BU ATTIFEL WAXES

(G-281)		HPLC OF THE WAXES				
TEMPERATURE- WAX REMOVAL (F°)	WT. % WAXES	WT. % SATURATES	WT. % AROMATICS	WT. % POLARS	WT. % VOLATILES	WT. % ASPHALTENES
0	33.9	70.9	6.5	0.4	22.2	0.0

Based on these results it appears that the presence of asphaltenes with waxes indicates that the waxes will be susceptible to wax crystal modification and subsequent pour point reduction induced by chemical additives. It is apparent that the asphaltenes are either a symptom of a wax crystalline form that is susceptible to modification, or themselves caused a weak link in the wax crystal and thus cause the wax to be susceptible to modification.

Past research has suggested that asphaltenes can aid or act as wax crystal modifiers (pour point depressants), but it was never possible to predict their effect on a given crude or distillate. Therefore, these results also begin to explain some of the ambiguities encountered with using asphaltenes as pour point depressants. Plain bulk asphaltenes may never be associated with or interfere with a given wax structure, but specific asphaltenes, such as those associated with the waxes in Cabinda crude may be necessary.

#### CONCLUSIONS

- 1) Waxes that precipitate at temperatures above the congealing temperature contain mainly asphaltenes. These waxes also are composed of higher molecular weight species than the waxes that precipitate at temperatures below the congealing temperature.
- 2) Asphaltenes appear to play an important role in pour point reduction. They either symptomize waxes that are susceptible to chemical additives, or else interfere with the congealing mechanism. The presence of asphaltenes with waxes indicates that the waxes will be modified by chemical additives.
- 3) Different high pour crudes have different wax precipitation temperature limits of the wax-asphaltene association. Therefore, the maximum pour point depression attainable with each crude appears to be a function of the precipitation temperature where asphaltenes are no longer associated with the waxes.

- 4) The bulk asphaltenes may be chemically different from the asphaltenes found associated with the Bu Attifel and Cabinda waxes.

#### ACKNOWLEDGEMENTS

The assistance of the following is greatly appreciated: R. Hutchison for the asphaltene separations and R. Ruberto for the GPC and HPLC analysis. Both were GR&DC employees at the time of this study.



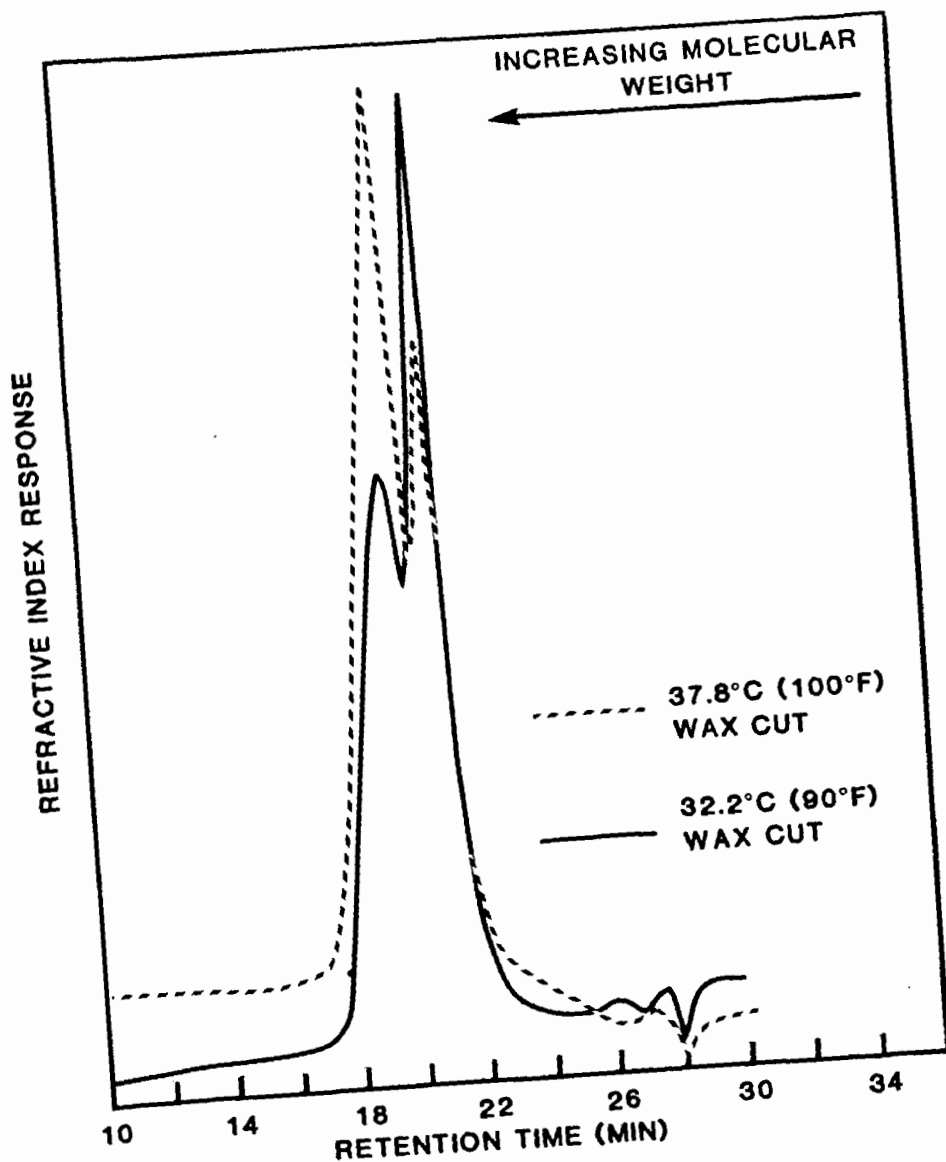


Fig.1 MOLECULAR WEIGHT DISTRIBUTION TREND  
CHANGE BETWEEN BUATTIFEL WAX FRACTIONS

## APPLICATIONS OF PERCOLATION THEORY TO THE ANALYSIS OF COAL GASIFICATION

Sebastián Reyes and Klavs F. Jensen

Department of Chemical Engineering and Materials Science  
University of Minnesota, Minneapolis, MN 55455

### INTRODUCTION

The changes in pore structure, internal surface area, and transport characteristics of porous carbonaceous materials play a major role in their gasification behavior. To describe the complex interactions of physical and transport properties during char gasification, it is essential to have a realistic model for the evolution of geometrical and topological features of the pore space. Several models for the structural changes during gas-solid reactions have been developed (1-11) resulting in important contributions to the understanding of char gasification reactions. Nevertheless, refinements are needed since available models can successfully predict only a subset of experimental observations. Even though available structural models include key features of pore branching, important topological effects are lost when the influence of closed porosity is not taken into account and effective diffusion coefficients are evaluated through tortuosity factors. Another key topologically dependent property is the eventual fragmentation of the particle at a critical porosity. The uniform development of porosity in the kinetic regime causes particle disintegration preferentially at high conversions. On the other hand, when diffusional resistances are important, the critical porosity of fragmentation is reached first at the particle surface, causing the continuous shrinkage of the particle from the early stages of conversion. Consequently, the overall conversion is not only determined by the conversion level of the shrinking particle but also by the history of released fragments. An interesting treatment of particle shrinkage during char particle combustion has been presented by Gavalas (9). However, more detailed analysis is required to relate the critical porosity of fragmentation to the topology of the internal structure.

The objective of this paper is to present an application of percolation theory to the analysis of coal gasification. It is well known that inorganic impurities naturally present in char particles can catalyze gasification reactions (12). However, our primary objective is to improve the structural models. Realistic extensions may then be made to include catalytic effects. The present particle description focuses on structural and topological features not included in previous models. The use of percolation theory provides a natural framework for understanding and evaluating the role of pore opening, pore enlargement and pore overlap in the evolution of porosity and internal surface area. Moreover, it accurately describes the fundamental influence of pore topology on transport characteristics of the internal structure, as well as particle fragmentation phenomena at high porosities.

### PERCOLATION CONCEPTS AND STRUCTURAL PROPERTIES

A general description of char gasification requires a model relating physical and transport properties to local structural changes. This model should accurately describe the accessible porosity ( $\phi^A$ ), accessible internal surface area per unit volume ( $\hat{a}^A$ ), and effective transport coefficients ( $\epsilon^B$ ) as functions of local carbon conversion. The potential contributions from closed pores to the total surface area ( $\hat{a}$ ) and total porosity ( $\phi$ ) can be locally described through the relations:

$$\phi^A = \phi - \phi^I \quad 1)$$

$$\hat{a}^A = \hat{a} - \hat{a}^I \quad 2)$$

where the superscript I on  $\phi$  and  $\hat{a}$  identify the isolated porosity and surface area. Equations 1 and 2 are necessary to account for pore opening by chemical reactions of the internal structure.

The effective transport coefficients are strongly dependent on the development of  $\phi^A$  as well as on the size and geometry of the pores. That is,  $\phi^A$  reflects the main topological features of the internal structure, such as dead ends and tortuous paths, which determine the extent of mass transport through the pore space. Moreover, if Knudsen diffusion is significant, the evolution of the pore size distribution also becomes a key factor in predicting transport.

Since a complete characterization of pore space morphology cannot be obtained by regular geometrical and topological simplifications, it is desirable to resort to some statistical description. This is supported by the observation that the majority of porous solids exhibit highly disordered structures. Consequently, the statistical means of percolation theory are ideally suited for evaluating  $\phi^A$ ,  $\hat{a}^A$  and  $\epsilon^E$  in terms of  $\phi$ . Percolation theory, first introduced by Broadbent and Hammersley (13), has been successfully applied to describe numerous physical and mechanical phenomena in disordered media. Key concepts and details of the theory can be found in available review papers (e.g. (14-16)).

Transport and reactions in porous solids can be modelled, in principle, by constructing large space filling random structures. However, the computational effort involved surpasses available resources even in large scale computing facilities. Fortunately, key features of these models are captured by simple networks. Reyes and Jensen (17) have recently demonstrated that a network model of pore topology, a so-called Bethe network may be used to evaluate  $\phi^A$  and  $\epsilon^E$  in porous solids. A Bethe network is an endlessly branching tree lacking reconstructions and completely characterized by its coordination number  $z$ . The coordination number is the number of bonds connecting each site. If a fraction  $\phi$  of randomly selected bonds are labeled as "pores",  $\phi^A$  is a unique function of  $\phi$  and  $z$ . If  $\phi$  is less than a nonzero threshold value  $\phi_c$ , called the percolation threshold, the pore space consists of disconnected regions, i.e. isolated pores. The threshold value for Bethe networks is given by (18):

$$\phi_c = 1/(z-1) \quad 3)$$

The network thus defined can be conveniently used to simulate topological features in porous solids. Since its topological properties are preserved by increasing or decreasing the length and/or the cross-section of the bonds, the experimentally measured porosity,  $\phi^A$ , and pore size distribution,  $f(r)$ , can be readily matched to the network model by randomly removing a fraction  $1-\phi(\phi^A, z)$  of bonds and distributing sizes to a fraction  $\phi(\phi^A, z)$  according to  $f(r)$ . To completely specify the appropriate network model simulating the pore space of the porous solid, the coordination number of the Bethe network must be selected. This number is chosen to match the percolation threshold of the Bethe network and the porous solid.  $\phi_c$  for the solid can be determined from fragmentation studies (19) through the relation:

$$\phi_c = 1 - \phi^* \quad 4)$$

where  $\phi^*$  is the critical porosity of fragmentation. An alternative approach is to directly determine  $z$  from experimental data on effective diffusion coefficients (17). A schematic representation of accessible pore space simulated by a 3-coordinated Bethe network is shown in Figure 1 for arbitrary inputs of  $\phi^A$  and  $f(r)$ . The attractiveness of this approach is that effective transport coefficients can be exactly evaluated for binary mixtures without resorting to tortuosity factors while explicitly accounting for the influences of narrow necks, tortuous paths and dead ends. Close agreement has been found between predictions with this method and published experimental data on effective diffusion coefficients (17). As an example, Table 1 shows experimentally measured diffusion coefficients for the pair CO-CO<sub>2</sub> in porous

electrode graphite (20), and predicted values with a 5-coordinated Bethe network. Predicted values are in excellent agreement with measurements for a wide range of temperatures (18-900°C) and pressures (0.1-10 atm). Moreover, this approach allows a natural extension for evaluating  $\epsilon^E$  in changing structures, since input values of  $\phi$  and  $f(r)$ , characterizing the local morphology, can be determined from independent balance equations.

By using the present Bethe network representation of the pore space, particle fragmentation may be modelled by Equations 3 and 4. Once the appropriate coordination number has been selected, both  $\phi_c$  and  $\phi^*$  are determined. However, it should be emphasized that  $\phi^*$  is based solely on topological features of two-phase structures leading to particle breakup by reactions, and not to mechanical phenomena, such as abrasion. The mass distribution of released fragments may be estimated as (21):

$$g(r, z) = \frac{z((z-1)n)!}{(n-1)!((z-2)n+2)!} \cdot \frac{(z-2)^{(z-2)n+2}}{(z-1)^{(z-1)n+2}} \quad (5)$$

where  $n$  is an integer number representing the size of the cluster whose mass is  $m_f$ , with  $m_f$  being the mass of the smallest fractal unit characterizing the structure.

To complete the framework for a gasification model, the accessible internal surface area must be related to the local structure. Consistent with the Bethe network formulation, and based on probabilistic arguments,  $\hat{a}^A$  can be estimated as (21):

$$\hat{a}^A = K[\phi(1-\phi) - \phi I(\phi, z)[1 - \phi I(\phi, z)]] \quad (6)$$

The constant  $K$  is related to the mass per unit volume of a fractal unit, and can be obtained by matching  $\hat{a}^A$  to a single surface area determination. The important implications of this approach are that effects of pore enlargement and pore overlap become natural consequences of increasing  $\phi$  in a random fashion.

#### GASIFICATION MODEL

Gasification of a single char particle in  $\text{CO}_2$  is chosen to illustrate the percolation based approach outlined in the previous section. It is further assumed that there are no catalytically active mineral impurities in the char. The evaluation of physical, transport and fragmentation properties require initial data readily available by conventional characterization of porous solids (e.g.  $\phi_0^A$ ,  $\hat{a}_0^A$ ,  $f_0(r)$ ), except for the coordination number of the network. This number can be implied from experimental data on diffusion coefficients or fragmentation studies. However, here it is considered as a parameter to simulate gasification behavior of char particles with various levels of pore space connectivity. Typical values fall in the range 4 to 8 (17).

The reaction is considered to be first order in  $\text{CO}_2$ . Since this reaction leads to an increase in the number of moles, mass transfer contributions from both concentration and pressure gradients must be included in the model equations. The derivation of the appropriate equations describing the gasification behavior for the above conditions has been presented elsewhere (22). In dimensionless form, modelling equations may be summarized as:

Mass balances for gaseous components:  $i \neq j = \text{CO}, \text{CO}_2$

$$0 = \frac{1}{\eta} \frac{1}{\xi} \frac{\partial}{\partial \xi} \left[ \xi^2 \epsilon_{ij}^{ED} \lambda \frac{\partial X_i}{\partial \xi} + \xi^2 \epsilon_{ij}^{EP} X_i \frac{\partial \lambda}{\partial \xi} \right] + v_i \psi_0^2 S \lambda X_{\text{CO}_2} \quad (7)$$

$$X_i(\xi, 0) = 0 \quad (8)$$

$$\partial X_i(0, \tau) / \partial \xi = 0 \quad (9)$$

$$\left\{ \epsilon_{ij}^{ED} \lambda \frac{\partial X_i}{\partial \xi} + \epsilon_{ij}^{EP} X_i \frac{\partial \lambda}{\partial \xi} \right\} \Big|_{\xi=1} = \eta B_{m1} (X_{ib} - X_i(1, \tau)) \quad (10)$$

Mass balance for solid phase:

$$\frac{d\phi}{d\tau} = \sigma_0 S \lambda X_{CO_2} + \frac{\xi}{\eta} \frac{\partial \phi}{\partial \xi} \frac{d\eta}{d\tau} \quad (11)$$

$$\eta(\xi, 0) = \phi_0 \quad (12)$$

Rate of particle shrinkage:

$$\frac{d\eta}{d\tau} = - \left\{ \lambda X_{CO_2} \right\} \Big|_{\xi=1} \quad \tau < \tau^* \quad (13)$$

$$\eta(0) = 1$$

$$\frac{d\eta}{d\tau} = - \eta \left\{ \frac{\sigma_0 S \lambda X_{CO_2}}{\partial \phi / \partial \xi} \right\} \Big|_{\xi=1} \quad \tau > \tau^* \quad (14)$$

$$\eta(\tau_+^*) = \eta(\tau_-^*)$$

Pore growth:

$$\zeta(\xi, \tau) = F(\xi, \tau) / S(\xi, \tau) \quad (15)$$

The dimensionless variables were chosen to facilitate the numerical solution of the modeling equations and expose time constants for key physicochemical processes involved.  $S$ ,  $\zeta$ ,  $\lambda$ ,  $X$  are dimensionless surface area, pore radius, pressure and gas concentration, respectively.  $\epsilon_{ij}^{ED}$  and  $\epsilon_{ij}^{EP}$  are dimensionless local effective diffusion and permeability coefficients, respectively. By defining  $\eta = r^*/r_{oc}$  and  $\xi = r/r^*$ , where  $r^*$  is the instantaneous particle radius, the moving boundary problem is transformed to a fixed one. The second term on the right hand side of Equation 11 accounts for the effect of the moving boundary arising from shrinking particle size. The external surface of the particle recedes by two major mechanisms: chemical reaction on the external surface and perimeter fragmentation, as described by Equations 13 and 14, respectively.  $\tau^*$  is the dimensionless time at which  $\phi$  in Equation 11 reaches the critical porosity of fragmentation  $\phi^*$ . The complete specification of the modelling equations requires working expressions for  $\phi^A(\phi, z)$  and  $\epsilon^E(z, \phi, f(r), L(r))$  developed in Reyes and Jensen (17).

#### GASIFICATION IN THE KINETIC REGIME

In the kinetic regime  $CO_2$  is uniformly distributed throughout the particle so only the rate of carbon consumption, according to Equation 11, is required to describe the gasification behavior. Furthermore, since only a negligible particle shrinkage occurs due to chemical reaction on the external surface, the second term on the right hand side of Equation 11 can be neglected. Because of the uniform porosity increase throughout the particle, Equation 14 predicts an instantaneous disintegration of the particle when  $\phi$  reaches  $\phi^*$ . For  $\phi > \phi^*$  it can be shown that (21):

$$\phi = \frac{\phi^*}{\phi^* + (1-\phi^*) \exp\{-Kr_{oc}[\tau-\tau^*]\}} \quad (16)$$

where  $r_{oc}$  is the initial particle radius, and  $\phi$  is now a pseudo-porosity whose complementary fraction  $(1-\phi)$  represents the remaining fraction of the initial solid

material. If conversion is related to  $\phi$  through the relation:

$$X_{cp} = \frac{\phi - \phi_0}{1 - \phi_0} \quad (17)$$

then the gasification rate is evaluated as:

$$\frac{dX_{cp}}{d\tau} = \frac{\{\sigma_0 \lambda X_{CO_2} / (1 - \phi_0)\} S}{K_{r_{oc}} \phi^* (1 - \phi^*) \exp\{-K_{r_{oc}}[\tau - \tau^*]\}} \quad , \tau < \tau^* \quad (18a)$$

$$\frac{dX_{cp}}{d\tau} = \frac{K_{r_{oc}} \phi^* (1 - \phi^*) \exp\{-K_{r_{oc}}[\tau - \tau^*]\}}{(1 - \phi_0) \{\phi^* + (1 - \phi^*) \exp\{-K_{r_{oc}}[\tau - \tau^*]\}\}^2} \quad , \tau > \tau^* \quad (18b)$$

Therefore, by using Equations 11, 16, 17 and 18 the complete gasification behavior of a char particle can be simulated. Typical kinetic and physical parameters chosen for this purpose are summarized in Table 2. It is assumed that micro- and mesopores are primarily responsible for the surface area and that they account for 2/3 and 1/3 of the pore volume, respectively. By using the general model equations it was verified that the parameter values in Table 2 correspond to gasification under kinetically controlled conditions. Figure 2 summarizes gasification behavior for porous char particles with different initial accessible porosities. A coordination number of  $z=7$  was chosen to simulate a complex random structure giving a critical porosity of fragmentation of approximately 5/6, similar to values observed by Dutta et al. (23) and Kerstein and Niksa (19). The solid lines describe the gasification before particle disintegration. As expected, the higher the initial porosity the lower the conversion at which particle disintegration takes place. Beyond this critical conversion, the gasification of fragments is described by the dashed lines, as evaluated by Equations 16, 17 and 18b. The shapes of the rate curves reflect competition between surface area enlargement due to pore growth at low conversion, and surface area decay due to pore coalescence at larger porosities. With increasing values of initial porosities the coalescence process becomes important at shorter times, causing the maximum rate to decrease and shift towards lower values of conversion. Further increases in porosity cause the maximum to disappear.

The existence of closed pores, a topological feature of the internal structure, also plays a role in the gasification. Their existence has been experimentally determined by several investigators (e.g. 20, 25). This effect can be readily illustrated by analyzing the behavior of char particles with different pore space connectivities. As observed from Figure 3, for a  $\phi_0^* = 0.20$ , the more connected the internal structure is the higher the conversion at which particle disintegration takes place. In addition, as the connectivity is increased, the maximum rates decrease in magnitude and shift toward higher values of conversion. These phenomena are readily explained by noting that the lower the connectivity of the pore space is, the greater the amount of closed pores that can be made accessible by chemical reactions of pore walls. This in turn causes the accessible surface area to increase but also makes the rate of pore coalescence dominant at low conversions.

#### GASIFICATION IN THE DIFFUSIONAL REGIME

To clearly focus on transport limitations caused by intraparticle phenomena, it will be assumed that there is no boundary layer resistance for mass transport to the external surface (i.e.  $B_{m1} \gg 1$ ). The existence of boundary layer resistance can readily be included in the numerical solution but the interpretation of the results become unnecessarily more complicated. The modelling equations 7-15 were solved numerically by using orthogonal collocation on finite elements (23).

Once the onset of perimeter fragmentation has been reached, the global conversion and gasification rate depend not only on the gasification behavior of the

shrinking particle but also on the gasification history of the released fragments. By integrating Equation 17 throughout the particle and dividing by the particle volume, the global particle conversion is evaluated as:

$$\hat{x}_{cp}(\tau) = 3 \int_0^1 \hat{x}_{cp}(\xi, \tau) \xi^2 d\xi \quad (19)$$

Since released fragments react in a kinetic regime (21), their conversions and gasification rates are obtained by Equations 16, 17 and 18b. The global conversion of the fragments released at time  $\tau_1$  is evaluated as:

$$\hat{x}_{cf}(\tau, \tau_1) = \frac{1 - \phi_0 \{1 + ((1 - \phi^*)/\phi^*) \exp[-K_{rc}(\tau - \tau_1)]\}}{(1 - \phi_0) \{1 + ((1 - \phi^*)/\phi^*) \exp[-K_{rc}(\tau - \tau_1)]\}} \quad , \quad \tau > \tau_1 > \tau^* \quad (20)$$

By weighting contributions from the shrinking particle and released fragments, the overall conversion behavior may be evaluated as:

$$\hat{x}_{cg}(\tau) = \eta^3(\tau) \hat{x}_{cp}(\tau) - \int_{\tau^*}^{\tau} \hat{x}_{cf}(\tau, \tau') \frac{dn^3(\tau')}{d\tau'} d\tau' \quad (21)$$

The corresponding overall gasification rate,  $d\hat{x}_{cg}(\tau)/d\tau$ , is obtained by taking the time derivative of  $\hat{x}_{cg}(\tau)$  in Equation 21.

In order to illustrate the model predictions, the gasification behavior of a char particle at 1000°C with  $\phi_0 = 0.20$  and simulated with  $z=7$  is presented. Other conditions as those in Table 2. Figure 4 shows CO<sub>2</sub> concentration profiles for different levels of carbon conversion. It is observed that as conversion increases, the profiles flatten out and approach the bulk concentration. This increase in concentration with burnoff is primarily caused by improved transport characteristics of the internal pore structure, as pore space is widened and made accessible. Since conversion increases most rapidly near the external surface, where the CO<sub>2</sub> concentration is high, the initial porosity for fragmentation is first reached at the particle surface when  $\hat{x}_{cg} = 0.65$ . While negligible particle shrinkage occurs because of chemical reaction on the particle surface, a rapid decrease in particle radius takes place by perimeter fragmentation.

The evolution of the dimensionless accessible surface area with carbon conversion is shown in Figure 5. In the early stages of conversion the surface area gradually grows due to pore enlargement as well as the contributions from closed pores. However, with increasing conversion, pore overlap between growing neighboring surfaces dominates over pore enlargement, causing the surface area to decrease. Because of the radially nonuniform conditions within the particle, the same qualitative surface area behavior occurs at each radial position but at different times. Even though this figure illustrates typical behavior during char gasification, it was previously shown that the surface area will not exhibit a maximum under conditions where pore overlap is already dominant from the beginning of the gasification.

The overall gasification curve for the above example is shown in Figure 6. This curve represents the often observed behavior where the rate goes through a maximum at some intermediate conversion. As intuitively expected, the conversion for maximum rate shifts toward higher values when the temperature is increased from a kinetic to a diffusional regime. Further temperature increase causes the critical conversion to decrease again, and eventually the maximum disappears, since in the limit of high temperature the particle reacts with a purely shrinking core behavior (SC). At  $\hat{x}_{cg} = 0.65$  the onset of perimeter fragmentation is observed. At this point the rate exhibits an increase in its slope, which indicates an acceleration in the gasification process due to fragmentation phenomena. This acceleration effect is small in the present example because the high surface area of the particle segregates the solid structure into very small fragments (21), whose concentration before their

release is not much different from the bulk concentration. In this case, the acceleration is primarily due to the higher rates in the shrinking particle because of increasing overall transport rates with decreasing particle size. A much stronger effect would have been observed if external mass transport resistances were significant (i.e.  $B_{mi} \ll 1$ ).

Figure 7 illustrates the change in particle size with particle conversion for different temperatures. At low temperatures the particle gasifies in the kinetic regime and disintegrates spontaneously when the critical porosity is reached. As diffusion resistance increases in importance with higher temperatures, perimeter fragmentation occurs at lower conversions. In the limit of very high temperatures (i.e. reaction rates) perimeter fragmentation takes place from the beginning and the particle then follows the classical shrinking core (SC) behavior.

#### CONCLUSION

The application of percolation theory concepts to modelling of a single particle char gasification has been summarized. Emphasis has been placed on the interpretation and evaluation of transport and fragmentation properties of the changing pore structure during gasification. The qualitative behavior of the model in both the kinetically and the diffusionally controlled regimes clearly reflect the strong influence of structural properties on gasification. Furthermore, the good agreement between these model predictions and reported experimental observations (11,20,24-33) are encouraging for further use of percolation theory in modelling changing coal structures.

#### REFERENCES

1. Petersen, E. E., *AIChE J.* 3, 443-448 (1957).
2. Szekely, J. and J.W. Evans, *Chem. Engng. Sci.* 25, 1091-1097 (1970).
3. Hashimoto, K. and P.L. Silveston, *AIChE J.* 19, 259-268 (1973).
4. Simons, G.A. and M.L. Finson, *Combust. Sci. Technol.* 19, 217-225 (1979).
5. Simons, G.A., *Combust. Sci. Technol.* 19, 227-235 (1979).
6. Bhatia, S.K. and Perlmutter, D.D., *AIChE J.* 26, 379-386 (1980).
7. Bhatia, S.K. and Perlmutter, D.D., *AIChE J.* 27, 247-254 (1980).
8. Gavallas, G.R., *AIChE J.* 26, 577-585 (1980).
9. Gavallas, G.R., *Combust. Sci. Technol.* 24, 197-210 (1981).
10. Zygourakis, K., L. Arri and N.R. Amundson, *Ind. Eng. Chem. Fundam.* 21, 1-12 (1982).
11. Tseng, H.P. and T.F. Edgar, *AIChE Annual Meeting*, Los Angeles, CA (1982).
12. Reyes, S. and K.F. Jensen, *Ind. Eng. Chem. Fundam.* 23, 223-229 (1984).
13. Broadbent, S.R. and J.M. Hammersley, *Proc. Camb. Phil. Soc.* E3, 629-641 (1957).
14. Frisch, H.L. and J.M. Hammersley, *J. SIAM*, 11, 894-918 (1963).
15. Shante, V.K.S. and S. Kirkpatrick, *Adv. Phys.* 20, 325-357 (1971).
16. Hughes, B.D. and S. Prager, "The Mathematics and Physics of Disordered Media," Springer-Verlag, New York, 1-108 (1983).
17. Reyes, S. and K.F. Jensen, *Annual AIChE Meeting*, San Francisco, CA, Paper 35a (1984).
18. Fisher, M.E. and J.W. Essam, *J. Math. Phys.* 2, 609-619 (1961).
19. Kerstein, A.R. and S. Niksa, *Int. Conference on Coal Science*, Pittsburgh, PA, 743-746 (1983).
20. Turkdogan, E.T., R.G. Olson and J.V. Vinters, *Carbon* 8, 545-564 (1970).
21. Reyes, S. and K.F. Jensen, submitted to *Chem. Engng. Sci.*
22. Reyes, S. and K.F. Jensen, submitted to *Chem. Engng. Sci.*
23. Carey, G.F. and B.A. Finlayson, *Chem. Engng. Sci.* 30, 587-596 (1975).
24. Dutta, S., C.Y. Wen and R. J. Belt, *Ind. Eng. Chem. Process Des. Dev.* 16, 20-30 (1977).
25. Kawahata, M. and P.L. Walker, Jr., *Proceedings 5th Carbon Conference*, Pergamon Press, London, 251-263 (1962).



26. Walker, P.L. Jr., R.J. Foresti, Jr. and C.C. Wright, Ind. Eng. Chem. 45, 1703-1710 (1953).
27. Petersen, E.E., P.L. Walker, Jr. and C.C. Wright, Ind. Eng. Chem. 47, 1629-1630 (1955).
28. Walker, P.L. Jr. and E. Raats, J. Phys. Chem. 60, 364-369 (1956).
29. Berger, J., T. Siemieniewska and K. Tomkow, Fuel 55, 9-15 (1976).
30. Tomkow, K., A. Jankowska, F. Czechowski and T. Siemieniewska, Fuel 56, 101-106 (1977).
31. Dutta, S. and C.Y. Wen, Ind. Eng. Chem. Process Des. Dev. 16, 31-37 (1977).
32. Hashimoto, K., K. Miura, F. Yoshikawa and I. Imai, Ind. Eng. Chem. Process Des. Dev. 18, 72-80 (1979).
33. Foster, M. and K.F. Jensen, Int. Conference on Coal Science, Pittsburgh, PA, 464-467 (1983).

#### ACKNOWLEDGEMENT

This work was supported by DOE (DE/FG22-82PC50806) and the Graduate School of the University of Minnesota.

Temperature	Pressure	$D_{CO-CO_2}^E$ (a)	$D_{CO-CO_2}^E$ (b)
$^{\circ}C$	atm.	$cm^2/s$	$cm^2/s$
18	1.0	0.0018	0.0014
500	1.0	0.0060	0.0069
600	1.0	0.0072	0.0083
700	0.1	0.043	0.041
700	0.2	0.035	0.032
700	0.5	0.018	0.019
700	1.0	0.0099	0.011
700	10.0	0.0012	0.0014
800	1.0	0.012	0.011
900	1.0	0.014	0.013

Table 1. Experimental and predicted effective diffusion coefficients in porous electrode graphite. (a) Experimental value, Turkdogan et al. (20), (b) Bethe network predictions ( $z=5$ ).

Preexponential factor	: $k = 5.0 \times 10^3$ (m/s)
Activation energy	: $E_a = 60.0$ (kcal/mol)
Specific surface area	: $S_o = 300.0$ (m <sup>2</sup> /gr)
Particle radius	: $r_{oc} = 200$ ( $\mu m$ )
Carbon density	: $\rho_p = 1500$ (kg/m <sup>3</sup> )
<u>Rayleigh distribution</u>	
smallest micropore radius	: $r_{\mu o} = 10A$
average micropore radius	: $r_{\mu a} = 20A$
smallest mesopore radius	: $r_{Mo} = 50A$
average mesopore radius	: $r_{Ma} = 200A$

Table 2. Kinetic and structural parameters used in the present simulations.

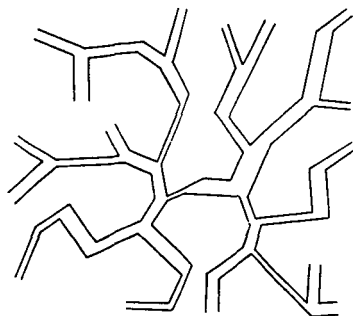


Figure 1. A schematic simulation of accessible pore space with a 3-coordinated Bethe network for arbitrary data of porosity and pore size distribution.

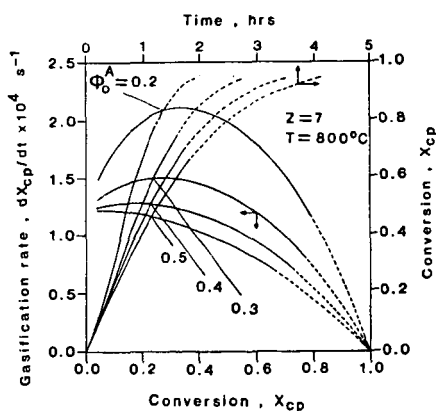


Figure 2. Conversion vs. time and gasification rate vs. conversion for a char particle for various initial porosities.

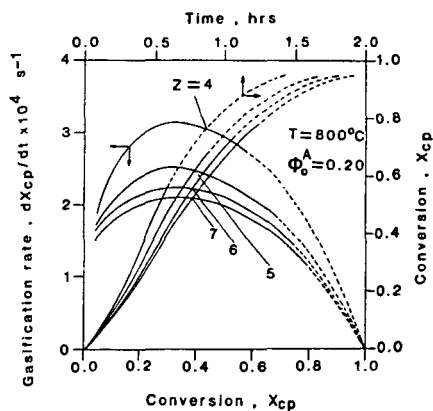


Figure 3. Conversion vs. time and gasification rate vs. conversion for a char particle with different pore space connectivities.

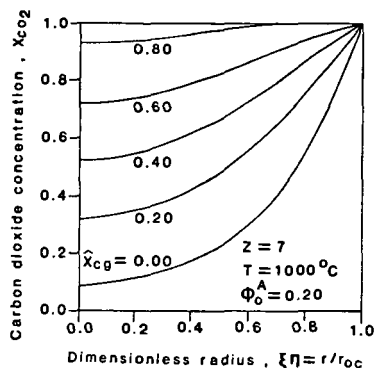


Figure 4. Carbon dioxide concentration profiles at various levels of overall conversion.

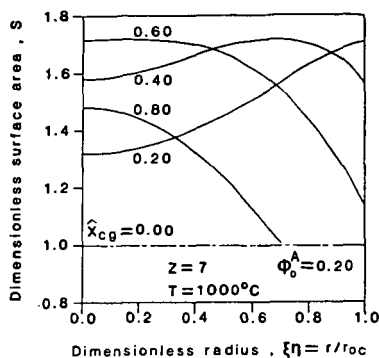


Figure 5. Dimensionless surface area profiles at various levels of overall conversion.

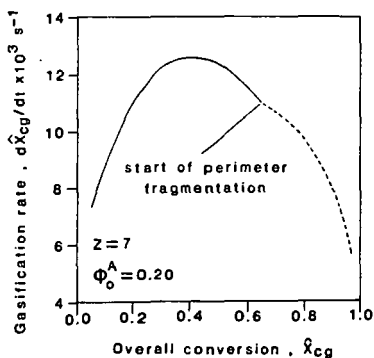


Figure 6. Gasification rate vs. conversion for a char particle at 1000^\circ C.

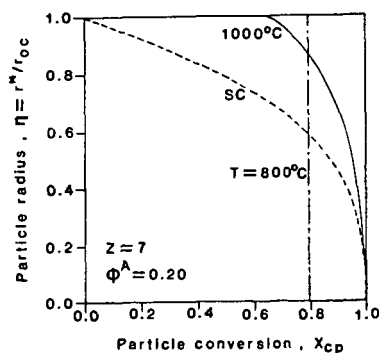


Figure 7. Particle radius as a function of particle conversion for a char particle for various reaction temperatures.

QUANTITATIVE ANALYSIS OF COALS AND COAL DERIVATIVES BY  
CP/MAS- $^{13}\text{C}$ -NMR SPECTROSCOPY

E. W. Hagaman and R. R. Chambers

Chemistry Division  
Oak Ridge National Laboratory  
P. O. Box X  
Oak Ridge, Tennessee 37831 USA

This paper reports experiments which are designed to ascertain the degree to which the CP/MAS- $^{13}\text{C}$ -nmr technique can be used in a quantitative sense in analysis of coal and coal derivatives. The quantitative capability of the experiment as applied to diamagnetic organic molecules is well documented (1). The uncertainty in the analysis of coals arises from the presence of a substantial organic-based free-electron spin density and from the uncertainty in the hydrogen distribution in these typically low H/C materials. The possibility exists that a fraction of the carbon in a coal experiences electron-nuclear interactions which render the signal invisible, broadened and/or paramagnetically shifted, or is in an environment depleted of hydrogen and unable to yield a  $^1\text{H}$ - $^{13}\text{C}$  CP signal.

To what extent are the carbons in coal detected with unit intensity response? The experiment selected to address this question entails introducing into the coal a known quantity of carbon designed to yield unit intensity response under the analysis conditions. The experimentally measured area ratio representing introduced carbon/native coal carbon from the CP/MAS- $^{13}\text{C}$ -spectrum is then compared with the same ratio determined in an unambiguous, independent experiment.

Chemical Modification of ILL. #6-Vitrain

The introduced carbon is incorporated by methylation of the heteroatoms of the coal which undergo base-catalyzed alkylation. In ILL. #6 vitrain these sites are predominantly (80-85%) phenolic residues. The balance of the introduced methyl groups are bonded to other functional groups. There is clear chemical shift evidence for methyl ester and aminomethyl groups and perhaps a small amount of sulfhydryl or select carbon methylation.

The methylation is performed with  $^{14}\text{C}$ ,  $^{13}\text{C}$ -double-labelled methyl iodide. The measure of introduced carbon is obtained by  $^{14}\text{C}$ -radioassay techniques, which, together with elemental analysis of the coal derivative, provides the benchmark ratio needed to evaluate the nmr integrations.

Large errors in the  $^{14}\text{C}$  and  $^{13}\text{C}$  ratio determinations can occur if solvents and/or reagents used in the derivitization contaminate the product. The extent of such unwanted incorporation in the present experiments have been measured by using  $^{14}\text{C}$ -labeled solvents and reagents in parallel experiments.

Initial methylations were performed using tetra-*n*-butyl ammonium hydroxide in aqueous THF following literature procedures (2). Repeated attempts to remove  $(\text{nBu})_4\text{N}^+\text{X}^-$  salts from the product using published methods were unsuccessful in our hands. The reagent can be removed by methanol washing, but a significant fraction of the coal is also solubilized by this solvent.

To prepare an O- $\text{CH}_3$  coal derivative free of carbon-containing reagents, a procedure for alkylation of coal using KOH in aqueous THF was developed. The methylation of ILL. #6 vitrain using this system introduced 4.6 methyl groups/100 coal carbons after 5 days reaction, ca. 10% fewer than obtained with the tetra-*n*-butylammonium

hydroxide/aqueous THF system. For the present purpose, complete alkylation is not required; the product, Ill. #6-OCH<sub>3</sub>, obtained following a single methylation step is analyzed in Table 1. Another product listed in Table 1, Ill. #6-XCH<sub>3</sub>, has been prepared by stirring Ill. #6 vitrain and methyl iodide (91.2% <sup>13</sup>C-enriched, 3-fold molar excess based on five acidic sites/100 coal carbons) in THF for five days. Under these conditions little aromatic methylether formed. The incorporation of methyl groups occurs predominantly on acid and amine functional groups.

THF retention in the coal products is minimal (<0.8 wt%) in all alkylation procedures.

#### CP/MAS-<sup>13</sup>C-NMR Analysis

The aromatic carbon fraction of coals,  $f_a$ , derived from CP/MAS-<sup>13</sup>C-nmr measurements are generally determined from aromatic and aliphatic carbon resonance area measurements taken from a single spectrum recorded under optimum or near optimum signal-to-noise conditions (cross polarization contact time = 1 ms). Reported  $f_a$  values determined in this fashion assume that the conditions for quantitative signal intensity response in this experiment, namely

$$T_{CH} \ll t_{cp} \ll T_{1\rho H}$$

are applicable.  $T_{CH}$  is the <sup>1</sup>H-<sup>13</sup>C cross polarization time constant under the Hartmann-Hahn condition,  $t_{cp}$  is the experimental cross polarization contact time, and  $T_{1\rho H}$  is the proton spin-lattice relaxation time in the rotating frame. Single spectrum analysis of  $f_a$  requires that a homogeneous  $T_{1\rho H}$  characterize the entire sample.

It has been shown that the aromatic and aliphatic resonance envelopes of coals generally display nearly homogeneous but different  $T_{1\rho H}$  behavior (3). The ratio  $T_{1\rho H}(\text{aromatic})/T_{1\rho H}(\text{aliphatic})$ , with typical values of 0.8-1.2 for Ill. #6 vitrain derivatives, can be altered by chemical modification.

While the inequality  $T_{CH} \ll t_{cp} = 1 \text{ ms}$  is valid for protonated carbon sites in coals, it is only marginally met for the non-protonated aromatic carbon fraction of Ill. #6, which reveals an average  $T_{CH}$  of  $350 \pm 100 \mu\text{s}$ . This value should not differ significantly for other bituminous coals.

These considerations indicate that it is worthwhile to evaluate CP/MAS-<sup>13</sup>C-nmr data of coals more critically to assess the errors which may be introduced by single spectrum analysis.

The general expression given by Mehring (4) which describes the development of carbon signal intensity in the spin-lock, CP/MAS-<sup>13</sup>C-nmr experiment with non-negligible  $T_{1\rho H}$  relaxation is

$$A(t) = KN \frac{T_{1\rho H}}{T_{1\rho H} - T_{CH}} (e^{-t/T_{1\rho H}} - e^{-t/T_{CH}}) \quad 1)$$

where  $A(t)$  is <sup>13</sup>C signal intensity at  $t = t_{cp}$ ,  $N$  represents the number of acquisitions and  $K$  is a constant proportional to the number of <sup>13</sup>C spins and spectrometer sensitivity. By restricting the cross polarization contact time to values for which  $t_{cp} \gg T_{CH}$  and  $e^{-t_{cp}/T_{CH}} \ll e^{-t_{cp}/T_{1\rho H}}$ , Equation 1 reduces to

$$A(t) = KN \frac{T_{1\rho H}}{T_{1\rho H} - T_{CH}} (e^{-t/T_{1\rho H}}) \quad 2)$$

Examination of typical  $T_{1\rho H}$  and  $T_{CH}$  values for the coal derivatives under consideration shows that the use of cross polarization times  $> 2$  ms satisfy the restrictions which lead to Equation 2. To evaluate  $f_a$  the spectrum is recorded at five contact times  $> 2$  ms and the separate aromatic and aliphatic resonance areas are non-linear least-squares fit to Equation 2.  $K$  is evaluated at  $t_{cp} = 0$  as

$$K = A_0 \frac{T_{1\rho H} - T_{CH}}{T_{1\rho H}} \quad 3)$$

and  $f_a$  is given by  $K(\text{arom})/[K(\text{arom}) + K(\text{aliph})]$ .

The application of Equation 3 requires estimates of  $T_{CH}$  for several carbon types in coals. Previous studies of coals indicate that  $T_{CH}$  values of 35, 65 and 350  $\mu$ s for protonated carbons (aromatic and aliphatic), methyl carbons (methylether) and non-protonated aromatic carbons, respectively are acceptable estimates for the present analysis. The aliphatic resonance band is considered to have a negligible fraction of non-protonated carbons and 60% of the aromatic resonance band is considered to be non-protonated carbon (5).

Table 1 summarizes the aromaticity values for Ill. #6 vitrain calculated using Equation 3. Intensity data over the range of contact times 1.0-8.0 ms yields  $f_a$  of  $.660 \pm .003$ . The same data set, minus the intensity data for the 1 ms  $t_{cp}$ , yields a calculated  $f_a$  of  $.707 \pm .006$ . The 1 ms data strongly influences the calculation. Equation 3 is not an appropriate expression for analysis of the 1.0 - 8.0 ms data set since the inequality  $e^{-t_{cp}/T_{CH}} \ll t_{cp}/T_{CH}$  is not met for 1 ms data. Equation 1 should be used to treat this data. Note that the calculated  $f_a$  for the data for which  $t_{cp} > 2$  ms is in fair agreement with  $f_a$  determined from a single spectrum with  $t_{cp} = 1.0$  ms.

Table 1.  $f_a$  and Introduced CH<sub>3</sub>/100 Coal Carbons for Ill. #6 and Derivatives.

	$f_a$	Introduced CH <sub>3</sub> /100 Coal Carbons	
	Ill. #6	Ill. #6-OCH <sub>3</sub>	Ill. #6-XCH <sub>3</sub>
1.0-8.0ms $t_{cp}$ range	$0.660 \pm .003$	5.84	0.18
2.0-8.0ms $t_{cp}$ range	$0.707 \pm .006$	5.78	0.1
1.0ms $t_{cp}$ time	$0.697 \pm .02$	5.72	0.21

The number of methyl carbons introduced into the coal matrix is determined by assuming that  $f_a$  of Ill. #6 vitrain is valid for the original coal carbon of the products, i.e., interconversion of  $sp^2$  and  $sp^3$  carbons does not occur as a consequence of the derivitization. Hence,  $f_a$  of Ill. #6 vitrain and the aromatic resonance area of the product allow partitioning of the aliphatic resonance area into components representing native coal carbon and introduced carbon. This analysis is summarized in Table 1 for the two coal derivatives, Ill. #6-OCH<sub>3</sub> and Ill. #6-XCH<sub>3</sub>.

Note that the calculated value for the number of methyl groups introduced into Ill. #6-OCH<sub>3</sub> using the fitting procedure (Equation 3) is independent of the  $t_{cp}$  range and  $f_a$  assigned to the original coal, as long as the analysis of Ill. #6 vitrain and Ill. #6-OCH<sub>3</sub> is internally consistent. This is simply a statement that to within the error of the fit of the data to a single exponential, no detectable carbon intensity accrues in the spectrum between 1.0 and 2.0 ms. The fitting procedure simply corrects the measured areas for the differences in  $T_{1\rho H}$  between the coals and for the differences of  $T_{1\rho H}$  between the aromatic and aliphatic resonance bands of each coal.

The calculated values for the number of methyl groups introduced into the coal using single spectrum analysis with  $t_{cp} = 1.0, 2.0$  and  $3.0$  ms, is 5.72, 5.34 and 5.01, respectively, and indicate the magnitude of the error which is introduced by the  $T_{1\rho H}$  differentials between the coal and its derivative. Clearly the value at  $t_{cp} = 1.0$  ms is indistinguishable from the values obtained by the full fitting procedure. Thus a 1.0 ms cross polarization contact time is a judicious compromise value consistent with a nearly complete cross polarization signal from all carbons including detectable non-protonated carbons and minimum error introduced by differential  $T_{1\rho H}$  relaxation effects.

The methyl incorporation values shown in Table 1 for Ill. #6-XCH<sub>3</sub> show the same behavior but have larger relative error, a result of the small area changes in the product relative to Ill. #6 vitrain.

#### Comparison of <sup>13</sup>C-NMR and <sup>14</sup>C-Radioassay Analysis

The number of methyl groups found in Ill. #6-OCH<sub>3</sub> and Ill. #6-XCH<sub>3</sub> by the radioassay technique is 4.64/100 coal carbons and 0.20/100 coal carbons, respectively. The error in these values is largely determined by the error in elemental analyses and is <2%. The values determined by nmr analysis (1.0 ms CT) are  $5.72 \pm 1.1/100$  and  $0.21 \pm 0.04/100$  coal carbons, respectively. The 20% error associated with the nmr values is derived for the use of single spectrum analysis and is the worst case error calculated by allowing  $f_a$  of Ill. #6 vitrain and Ill. #6-OCH<sub>3</sub> to vary  $\pm .02$  from their measured values. We conclude that, within the estimated error of the nmr measurement, the CP/MAS-<sup>13</sup>C-nmr method does accurately monitor total carbon signal in the examined coals.

#### References

- 1a. Alemany, L. B.; Grant, D. M.; Pugmire, R. J.; Alger, T. D.; Zilm, K. W. *J. Amer. Chem. Soc.* **1983**, *105*, 2133.
- b. *Ibid* **1983**, *105*, 2142.
- 2a. Liotta, R. *Fuel* **1979**, *58*, 724.
- b. Liotta, R.; Rose, K.; Hippo, E. *J. Org. Chem.* **1981**, *46*, 277.
- c. Liotta, R.; Brons, G. *J. Amer. Chem. Soc.* **1981**, *103*, 1735.
3. Sullivan, M. T.; Maciel, G. E. *Anal. Chem.* **1982**, *54*, 1615.
4. Mehring, M. "High Resolution NMR Spectroscopy in Solids," Springer-Verlag, Berlin, **1976**, chapter 4.
5. Wilson, M. A.; Pugmire, R. J.; Karas, J.; Alemany, L. B.; Woolfenden, W. R.; Grant, D. M.; Given, P. H. *Anal. Chem.* **1984**, *56*, 933.

**Acknowledgment.** Research sponsored by the Division of Chemical Sciences/Office of Basic Energy Sciences, US Department of Energy under contract DE-AC05-84OR21400 with the Martin Marietta Energy Systems, Inc.

ANALYSIS OF MIDDLE DISTILLATE FUELS BY HIGH RESOLUTION  
FIELD IONIZATION MASS SPECTROMETRY

Ripudaman Malhotra, Michael J. Coggiola, Steven E. Young,  
Doris Tse, and S. E. Buttrill Jr.

Mass Spectrometry Program, Chemical Physics Laboratory  
SRI International, Menlo Park, CA 94025

INTRODUCTION AND BACKGROUND

During the decade following the Arab oil embargo, there has been an increase in both the variety and variability of petroleum feedstocks for the production of middle distillate fuels. As a result, the variability and the chemical constitution of the currently used middle distillate fuels are different from those used before 1970. Problems have arisen in the use of specifications developed empirically from experience with fuels of the older composition. There have even been a few instances in which a fuel which met specification on delivery quickly became so unstable in storage as to become unusable. Therefore, new fuel specifications based more directly upon the chemical constitution of the fuel are needed. This will require the development of new methods for distillate fuel analysis capable of providing rapid and detailed information on the chemical composition of the distillate fuels.

A number of methods for the analysis of fossil fuels by mass spectrometry have been reported. Many of them, including the ASTM standard, D2425-67 (1978), use electron-impact (EI) ionization. This mode of ionization causes extensive fragmentation and precludes obtaining any information on the molecular-weight distribution of the sample. To circumvent this problem, many investigators have used low-energy electron-impact ionization, and other softer modes of ionization, such as field ionization (1,2) and field desorption (3). Both field desorption, and low-energy EI display a wide range of response factors for different classes of compounds and field ionization appears to be a method of choice, at least for distillate fuels (4).

For the past several years, SRI International's unique Field Ionization Mass Spectrometer (FIMS) has provided detailed quantitative information on the composition of diesel and jet fuels derived from oil-shale, coal, and petroleum. Complete and quantitative molecular-weight distributions on all of the types of hydrocarbon compounds present in these fuels previously required a time-consuming chromatographic separation of the fuel into several fractions followed by FIMS analysis of each of these fractions. In this paper we describe the development of a high-resolution FIMS facility capable of providing a rapid and complete quantitative analysis of distillate fuels without the need for a chromatographic separation step.

By using high resolution, it will be possible to distinguish between molecular ions belonging to different hydrocarbon classes that share the same nominal mass. To resolve pairs of hydrocarbons differing by a  $C-H_{12}$  doublet, e.g., nonane and naphthalene, a resolving power of 3,200 is sufficient for all molecules of molecular weight 300 amu or less.



## DESCRIPTION OF EQUIPMENT AND SOFTWARE

### Field Ionization Mass Spectrometer

A vintage MS-9 mass spectrometer (AEI, Ltd.) was completely disassembled, cleaned, and reworked to bring it into good operating condition. In the EI ionization mode using the original ion source, a mass resolution of 30,000 was eventually obtained. The spectrometer has been interfaced with a Kratos DS-55C data system.

In order to install an SRI volcano-style field ionization (FI) source on the MS-9, the original source and mounting flange were removed along with the original solid sample probe and reentrant connection for the batch inlet system. To make room for the field ionization source and some new ion lenses, an extension of the original source housing was designed and built (5). Figure 1 shows a scale drawing of a cross-section through the modified MS-9 source housing.

The volcano-style FI source used in this work was designed at SRI by Aberth and Spindt (6). Ions produced by the field ionization of fuel molecules are accelerated to 6 kV and focused into a small diameter, round beam. The ions then pass through a dual electrostatic quadrupole lens assembly that provides: (1) focusing of the ion beam on to the entrance slit of the MS-9 mass spectrometer, and (2) a means of transforming the round ion beam into a more nearly ribbon-shaped beam that better matches the shape of the entrance slit to the mass spectrometer.

The resolution of the MS-9 equipped with the FI-source was tested with a mixture of hydrocarbons containing both saturates and naphthalenes in the molecular weight range 128 to 156. The instrument could easily resolve the molecular ions of these two classes of compounds indicating a resolution of greater than 1600. Furthermore, with a mixture of benzene and pyridine, it was possible to resolve besides the molecular ions of pyridine and benzene containing a single carbon-13 atom the doublet due to the latter ion and the 1% of protonated benzene that is present in this system. The separation of this minor ion from the molecular ion of benzene with one carbon-13 requires a resolving power of 18,800; as shown in the inset of Figure 1, this power has been slightly exceeded.

### Software for Generating z-Tables

Distillate fuels are likely to contain anywhere between 50 and 150 constituents. A list of masses and their intensities would be a very cumbersome way to present the information on the composition of these fuels. A more manageable representation would be a matrix in which homologous series of different compound classes were sorted into different columns. Since most of the fuel components are hydrocarbons, the obvious choice of compound classification is that according to the z-number, where z is defined by expressing the molecular formula of the hydrocarbon as  $C_nH_{2n+z}$ .

A mass scale which defines the  $CH_2$  unit as 14.0000 can be used to sort the different compound classes, since in this scale the mass defect of any given class will be the same throughout the mass range (7). Rather than writing a new computer code to generate a z-table from the raw data, an existing DS-55C program was modified. The original program was designed to calculate the elemental composition corresponding to each peak in the spectrum. An added advantage of this approach is that the intensities of  $^{13}C$  satellite peaks can also be easily added to the intensity of the parent peak.

Once all of the entries in the table have been computed, their intensities are summed, and renormalized to a total intensity of 100.0. The resulting table of percentages can then be printed, plotted or stored for future reference. In addition, a second program has been written that could retrieve the stored z-tables from different runs, and compute the average and standard deviation for each entry. This procedure is useful in evaluating the reproducibility of the analysis method, and any fuel composition-property correlations.

## **ANALYTICAL PROCEDURE**

### Sample Introduction

Approximately 1-2  $\mu\text{L}$  of liquid fuel together with 0.5-1  $\mu\text{L}$  of a mixture of benzene, toluene, and isooctane, which serve as mass markers, are introduced into a high temperature, glass batch-inlet system attached to the high resolution FIMS instrument. To minimize loss of volatile components during sample introduction, the fuel and the standard mass-marker mixtures are taken in micro-pipettes (Microcaps, Drummond Scientific Company, Broomall, PA) and placed inside the sample holder. Inside the evacuated glass batch-inlet system, the fuel sample vaporizes completely. A portion of the fuel sample vapor flows into the ion source of the mass spectrometer. Because all of the fuel sample is vaporized at the same time, the number of molecules of a specific type flowing into the ion source is directly proportional to the number of molecules of that type present in the original fuel.

### Ionization and Data Acquisition

The field ionization source in the mass spectrometer ionizes sample molecules into molecular ions. The molecular ions are separated according to their mass by the spectrometer, which is operated at a mass resolution of 3000 or greater, sufficient to completely separate the molecular ions of the different hydrocarbon types present in the original fuel. The mass spectrometer is scanned at a speed of 120 seconds per decade. A scan time of 110 seconds plus a magnet settling time of ten seconds allows one scan to be completed every two minutes. Typically, 10 to 15 scans are collected although the amount of sample used is sufficient to allow two to three times as many scans if so desired.

The Kratos DS-55C data system requires the presence of a large number of reference peaks in the high-resolution mass spectrum. These reference peaks are normally produced by introducing perfluorokerosene (PFK) into the electron impact ion source together with the sample. Because of their negative mass defect, the numerous fragmentation peaks of PFK are easily resolved from most of the sample peaks and provide good mass calibration. However, field ionization produces little fragmentation, and most of the commonly used reference compounds including PFK are unsuitable for use as internal mass references for our purpose. We have solved this problem by using added compounds and the common fuel components as references. A mixture of benzene, toluene, and isooctane is added together with the fuel sample. Isooctane is one of the few compounds which even under field ionization undergoes complete fragmentation to give t-butyl ions. This is advantageous since the molecular ion of isooctane would be in the mass range of interest. At the same time, isooctane is sufficiently high boiling to allow easy handling. The fragment t-butyl ion produced from isooctane and the molecular ions of benzene and toluene serve as the autostart masses for the time-to-mass conversion software. A combination of saturated hydrocarbon and alkylbenzene peaks are used as reference masses for the rest of the mass range. Several sets

of reference peak masses have been tabulated and different ones are used for different types of fuels.

Time centroid data are usually collected because they can be conveniently reprocessed in the event of an incomplete or unsatisfactory time-to-mass conversion. This can sometimes be a problem because of the highly variable fuel composition of distillate fuels from different sources. Reprocessing of the time-centroid data with a different set of reference peaks is necessary in such cases.

#### Data Processing

Each of the scans of ion peak intensity is stored in a computerized high-resolution mass spectrometer data system, which averages these individual scans and calculates the accurate masses and the elemental composition (chemical formulas) of each of the peaks in the field ionization mass spectrum of the fuel sample. This information enables the peak intensities to be sorted by compound type (z-series) and the number of carbons present in the molecule. The final result of the analysis is a table showing the relative amounts of the various compounds present in the fuel mixture organized by z-series and carbon number. The relative field ionization signals of each component of the fuel can be converted into mole-fraction of that component present in the original fuel sample by using measured relative field ionization efficiency data for known compounds.

### **RESULTS AND DISCUSSION**

#### Determination of Response Factors

Relative ionization efficiencies were determined by using a number of test mixes containing up to 30 components. The various test mixes were designed to study possible matrix effects and to determine the efficiencies of isomeric compounds. These studies also helped in developing the analytical technique. Ionization efficiencies of the various compounds were measured relative to 1-phenylheptane. Response factors were determined for several homologs within a compound class. We observed that ionization efficiencies for the various classes of compounds varies only slightly over the molecular weight range encountered with distillate fuels; 100 to 300 amu. Branching lowers the observed intensity of the molecular ion because of some fragmentation, but this effect is serious only in the case of molecules containing quaternary carbons. Polycyclic aromatics have the highest ionization efficiency and straight chain aliphatics the least.

For the purposes of analyzing fuel samples we used an average of the response factors of the various homologs belonging to that class. We had not expected compounds more unsaturated than biphenyls in diesel and jet fuels and therefore had not determined the response factors of phenanthrenes and dihydrophenanthrenes. However, we did encounter them and have used the same response factors for them as naphthalenes. The response factors used for the various classes are given in Table 1.

#### Analysis of Some Distillate Fuel Samples

We had earlier reported on the analysis of a stable and unstable fuel sample and shown that the unstable fuel had a substantially greater amount of naphthalenes (5). This result is in concert with the findings of Mayo and Lan (8).

Several other diesel fuel marine and experimental jet fuel samples have been analyzed by HR-FIMS. Results of the analysis of a very stable fuel (NRL-83-14) are shown in Table 2. The table gives the mole percent of the various constitu-

ents by their carbon number and z-series. The fuel contains 27.8% acyclic and 14.4% monocyclic saturates. No bicyclic or tricyclics were detected. This fuel is also very rich in alkyl benzenes and tetralins. It is interesting to note that the distribution of the compounds within any z-series is fairly uniform for all compound classes except naphthalenes. The compound at m/z 212.0712, identified as  $C_{17}H_8$  ( $z = -26$ , M.W. 212.0626) is most likely ethyl (or dimethyl-) dibenzthiophene (M.W. 212.0660). Composition of a model fuel used for engine tests, NRL-82-15, is given in Table 3. The fuel is less stable relative to NRL-83-14 and has somewhat of a higher naphthalene content.

### CONCLUSIONS

This work demonstrates the applicability of high-resolution FIMS as a powerful technique for rapid chemical characterization of middle distillate fuels. We have fixed most of the problems with the spectrometer, and the instrument is now operating on a routine basis. The only weak point in the entire system appears to be the heated batch inlet system. Preliminary results have shown that this technique provides accurate and reproducible data. Data analyzed thus far are too scant to make definitive fuel composition-property correlations; such studies are currently underway.

**ACKNOWLEDGMENT:** Support for this work by the Naval Research Laboratory (Contract No. N00014-81-K-2032) is greatly acknowledged.

### References

- (1) S. E. Scheppele, C. S. Hsu, T. D. Marriott, P. A. Benson, K. N. Detwiler, and N. B. Perreia, Int. J. Mass Spectrom., 1978, **28**, 335.
- (2) G. A. St. John, S. E. Buttrill, Jr., and M. Anbar, in Organic Chemistry of Coal, J. W. Larsen, Ed., ACS Symposium Series 71, Washington, DC, 1978, p. 223.
- (3) T. Aczel, J. A. Laramee, and G. T. Hansen, ASMS Proceedings, 1982, 808.
- (4) G. A. St. John and S. E. Buttrill, Jr., unpublished results.
- (5) S. E. Young and S. E. Buttrill, Jr., ASMS Proceedings, 1982, 534.
- (6) W. Aberth and C. A. Spindt, Int. J. Mass Spectrom. Ion Phys. 1977, **25**, 183.
- (7) E. Kendrick, Anal. Chem. 1963, **35**, 2146.
- (8) F. R. Mayo and B. Y. Lan, Division of Petroleum Chemistry, Preprints 1983, **28(5)**, 1209.

Table 1  
RELATIVE FIELD IONIZATION EFFICIENCIES OF VARIOUS HYDROCARBONS

<u>Compound Class</u>	<u>Z</u>	<u>Relative Response</u> <sup>*</sup>
Alkanes	2	0.34
Monocyclic alkanes	0	0.54
Bicyclic alkanes	-2	0.63
Tricyclicalkanes	-4	0.56
Benzenes	-6	0.91
Tetralins	-8	0.86
Octahydrophenanthrenes	-10	1.03
Naphthalenes	-12	1.03
Biphenyls or Tetrahydro-		
phenanthrenes	-14	1.44
Dihydrophenanthrenes	-16	1.44
Phenanthrenes or		
Anthracenes	-18	1.44

<sup>\*</sup>Relative to 1-phenylheptane.

Table 2

## COMPOSITION OF FUEL NRL-83-14\* BY CARBON NUMBER AND z-SERIES

n/z	2	0	-2	-4	-6	-8	-10	-12	-14	-16	-18	-26
10					2.58							
11					2.91	1.84		1.53				
12					2.08	2.47		5.15				
13		3.52			2.02	2.58		6.96	0.77			
14	4.89											
15	5.16	2.30			2.14							
16	5.34	2.87			1.59	2.11		1.54	1.26	0.79	0.98	
17	4.00	2.19			2.07	1.73		1.35	1.26		0.84	1.01
18	4.74	1.31			2.04	1.94			0.86			
19	3.65	2.20			1.42							
20					1.94							
SUM	27.8	14.4			20.8	12.7		16.5	4.2	0.8	1.8	1.0 †

\*A very stable fuel sample.

†The compound is most likely ethyl (or dimethyl-) dibenzthiophene.

Table 3

## COMPOSITION OF FUEL NRL-82-15\* BY CARBON NUMBER AND z-SERIES

n/z	2	0	-2	-4	-6	-8	-10	-12	-14	-16	-18
8					0.63						
9					1.00						
10					0.89						
11	1.67	0.89			0.83	1.17		4.08			
12	6.95	1.52	1.96		1.30	2.02		6.54			
13		2.75			1.69	2.50		6.55			
14	4.60										
15	3.74	2.21	2.62	0.92	1.26						
16	3.61		2.09		1.04	1.55	1.23	1.57	0.89		
17	4.64	1.48	1.24	1.32	1.43	1.24	0.80	0.78	0.47		
18	3.07	2.16	0.70		0.62	1.07	0.69				
19	2.57	2.11	0.96		0.53			0.44			
SUM	30.9	12.5	9.6	2.2	11.2	9.6	2.7	20.0	1.4		

\*Relatively unstable fuel, but not the worst.

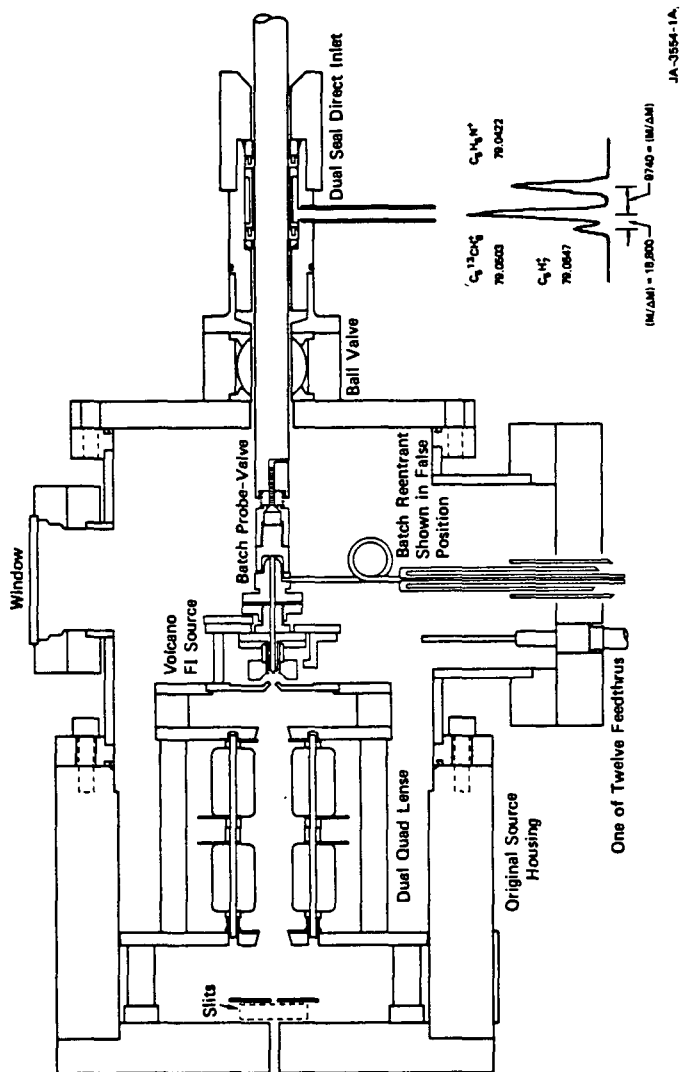


FIGURE 1 CROSS SECTION OF SOURCE HOUSING FOR MS-9

## NUMERICAL EXTRACTION OF CHEMICAL COMPONENT PATTERNS FROM PYROLYSIS MASS SPECTRA OF U.S. LIGNITES

Henk L.C. Meuzelaar, Willem Windig and G. Steven Metcalf

Biomaterials Profiling Center, University of Utah  
391 South Chipeta Way, Suite F  
Salt Lake City, Utah 84108

### INTRODUCTION

Structural characterization of lignites presents a major challenge because of the extreme complexity and heterogeneity of these low rank coals. Whereas most peats still contain macroscopically and microscopically identifiable plant remains, morphological analysis of lignites is much less straightforward. Moreover, routine coal characterization tests such as Free Swelling Index or Vitrinite Reflectance, are less readily applicable to lignites whereas sophisticated spectroscopic techniques such as IR, NMR or MS tend to give highly complex spectra due to the presence of multiple, overlapping chemical components. Although combined analytical methods such as MS/MS, GC/MS or GC/FTIR are capable of resolving and identifying many of these overlapping components, such "hyphenated" techniques tend to be costly and require time-consuming data evaluation and interpretation steps thus making it impractical to apply these methods to large sample series.

A novel approach capable of resolving overlapping signals in spectra of complex mixtures involves numerical extraction of component patterns by means of factor and discriminant analysis (1). Thus far, this numerical extraction approach has been applied especially to pyrolysis mass spectrometry (Py-MS) patterns of coals and other fossil fuels, because of the relative ease of numerical conversion of mass spectra (compared to the continuous curves obtained by IR, NMR or chromatographic techniques).

The main advantages of combining single stage analytical techniques with numerical extraction methods rather than using "hyphenated" physicochemical techniques are: high speed and relatively low cost. Moreover, numerical extraction methods are especially powerful when relatively large series of samples need to be studied. Meuzelaar *et al.* (2) demonstrated the applicability of the combined Py-MS/numerical extraction approach to a series of over 100 coal samples from the Rocky Mountain Coal Province obtained from the Penn State Coal Sample Bank. Other, smaller Py-MS studies of coals have been published by Van Graas *et al.* (3), De Leeuw *et al.* (4) and Larter (5). As listed in Table I, the Py-MS study reported here involves a selection of samples representing both U.S. coal provinces with major lignite reserves, namely the Northern Plains Province (6 samples) and the Gulf Province (16 samples).

### EXPERIMENTAL

Lignite samples were obtained from the Penn State Coal sample bank in hermetically sealed metal cans containing 500 g, 20 mesh aliquots under Argon. All further grinding and splitting operations were performed under N<sub>2</sub>, finally resulting in 10 mg, 300 mesh aliquots which were subsequently suspended in 2 1/2 ml of Spectrograde methanol. Two 5  $\mu$ l drops of these suspensions were applied to ferromagnetic wires (Curie-point temperature 610°C) and air-dried at room temperature under continuous rotation, resulting in a sample size of approx. 40  $\mu$ g. Within one hour after preparation, all coated wires were analyzed by Curie-point pyrolysis mass spectrometry using an Extranuclear 5000-1 quadrupole MS system described elsewhere (6). Py-MS conditions were as follows: temp. rise time 5 s, equilibrium temp. 610°C, total heating time 10 s, electron energy setting 11 eV, mass range scanned m/z 20-



260, scanning rate 2000 amu/s, total scanning time 20 s. Each lignite sample was analyzed in triplicate and the resulting 66 spectra were normalized using the NORMA program (7). Subsequent multivariate analysis was carried out with the SPSS program package (8) and consisted of factor analysis followed by discriminant analysis using the 11 most significant factors (eigenvalue >1), according to a procedure described previously by Windig *et al.* (9). It should be noted that each set of three duplicate analysis was assigned a separate category number in the discriminant analysis procedure, thus avoiding the creation of artificial clusters and divisions in the data set. Finally, the five most significant discriminant functions were analyzed with the aid of the variance diagram (VARDIA) procedure developed by Windig *et al.* (10). This resulted in the localization of at least six individual component axis which were then evaluated further by means of discriminant loading and spectrum plot procedures, as described by Windig *et al.* (9).

## RESULTS AND DISCUSSION

The pyrolysis mass spectra of three of the twenty two lignite samples are shown in Figure 1, demonstrating marked differences in the bulk composition of the pyrolyzates, e.g., with regard to hydroxyaromatic compound series, aliphatic hydrocarbon series and sulfur signals. Moreover, arrows in Figure 1 point to minor "biomarker" peaks at  $m/z$  234 (retene) and  $m/z$  194 (unknown biomarker) which were found to be quite characteristic for lignite samples from the Northern Plains and Gulf provinces respectively.

Before describing a more detailed chemical interpretation of the Py-MS findings, it should be pointed out that chemical labels assigned to peak series or individual peaks in Figure 1 (as well as throughout this paper) are tentative only. Generally these interpretations are based on literature data although some of the chemical identities are backed up by Py-GC/MS studies on the same lignites (11). Another factor to consider when interpreting Py-MS data on coals is the incomplete pyrolytic conversion. Under the experimental conditions employed in our study, estimated tar yields for high volatile bituminous coals are in the 50-60% range (12) whereas lignite conversion yields are basically unknown but may well fall in the same range. Moreover, not all the tar products will be detected by our mass spectrometric procedures. Ultimately, perhaps only 20-30% of the (dry) bulk of the original lignite sample contributes directly to the mass spectrum.

In view of the large number of spectra obtained and the hundreds of mass peaks in each spectrum, the use of sophisticated data reduction and correlation methods is indispensable. As described under "Experimental", factor analysis followed by discriminant analysis was applied to the Py-MS data set. This resulted in seven "significant" discriminant functions (see Table II). The scores of the first two functions are plotted in Figure 2, revealing a relatively good separation between lignites from the two different coal provinces (on DI) as well as a definite separation between lignites from different seams, fields or regions (on DII).

The nature of the underlying chemical components responsible for the clustering behavior in Figure 2 was examined by means of a novel, interactive method known as the Variance Diagram (VARDIA) technique (10), which enables us to determine the optimal location of each major chemical component in discriminant space. The VARDIA method has proven to be capable of extracting numerical components from mass spectra of complex mixtures, including fossil fuel pyrolyzates (10).

Two VARDIA plots, representing discriminant functions I and II as well as III and IV respectively, are shown in Figure 3, revealing the presence of at least six major component axes (labeled A-F) in the space spanned by these four functions. The mass spectral patterns associated with these component axes are shown in Figures 4 and 5. Component axes A and B (Figure 4a, b) obviously represent

the two bulk components seen in the lignite spectra, namely hydroxyaromatic compounds and aliphatic hydrocarbon moieties.

The nature and origin of the hydroxyaromatic compound series becomes clear when comparing the spectral pattern of component axis A (Figure 4a) with that of a softwood lignin model compound (Figure 4c). Although obvious quantitative differences exist between the two spectral patterns, the qualitative similarities strongly suggest a direct chemical relationship. That lignin-like patterns can be preserved in pyrolysis mass spectra of fossil organic matter  $10^7$  to  $10^8$  years old has also been reported in several other studies (4,6,13).

The chemical nature and origin of the aliphatic hydrocarbon pattern in Figure 4b presents a more difficult problem. Nevertheless, an intriguing qualitative match was obtained with the Py-MS pattern of Apiezon L, a high MW petroleum distillate consisting of 67% aliphatic, 28% naphthenic and 5% aromatic hydrocarbons (14). Since the petrographic analysis data available from the Penn State Coal data bank did not reveal major contributions of liptinite macerals (see Table I), it may be assumed that the hydrocarbon moieties observed by Py-MS represent maceral types easily overlooked by routine petrographic analysis, e.g., from exsudatinite or bituminite (15). An interesting speculation is that we may be dealing with hydrocarbons derived from algal precursors although major contributions from bacterial lipids (16) cannot be ruled out either.

The spectral patterns of the component axes shown in Figure 5a-c are interpreted to represent terpenoid resins (Figure 4a; e.g. retene signal at  $m/z$  234), unknown biomarker compounds (Figure 5b; e.g., signals at  $m/z$  194, 179 and 168) and sulfur moieties as well as related marine-influenced peak series (Figure 5c), respectively.

Comparison of the VARDIA plots in Figure 3 with the discriminant score plot in Figure 2 shows that component axis F (representing reduced sulfur forms such as  $H_2S$  and  $CH_3SH$ ) correlates most strongly with the Wildcat seam lignites from South-Central Texas which are known to have been deposited in marine-influenced, lagoonal environments (17). However, component axis E (representing more oxidized sulfur forms such as  $SO_2$  and  $CS_2$ ) also correlates with the Fort Union Bed lignites of Montana, which lack an obvious marine depositional influence. In these lignites, the oxidized sulfur forms may well represent the relatively high inertinite content since similar correlations were noted in previous Py-MS studies of purified coal macerals (18).

That the two biomarker signals at  $m/z$  234 and  $m/z$  194 are very characteristic, indeed, for the two coal provinces (as also indicated by a comparison of Figures 2 and 3) is confirmed by the bivariate plot in Figure 6. Apparently, the biomarker precursors (conifer resins?) of the Northern Plains province were not present in the ancient depositional environment of the Gulf province; and *vice versa*.

Finally, it should be mentioned that the above discussed interpretations of the Py-MS data were further supported by a systematic correlation with conventional coal characterization data (e.g., petrographic analysis, ultimate analysis, proximate analysis, calorific value and and vitrinite reflectance) obtained from the Penn State Coal Data Bank. The results of these data correlation efforts, e.g., using canonical variate analysis techniques (19), will be reported elsewhere (20).

In conclusion, the data analysis results presented here confirm the feasibility of numerical extraction of chemical components from the low voltage mass spectra of extremely complex lignite pyrolyzates.

## ACKNOWLEDGEMENTS

The authors are indebted to the Penn State Coal Sample Bank for providing lignite samples and especially to Dr. Peter Given for his help and advice in selecting the particular set of lignites used in this study.

The research reported here was supported by a development grant from Phillips Petroleum Company, by U.S. Department of Energy Contract #DE FG22-82PC50970 and by matching funds from the State of Utah.

## REFERENCES

1. Meuzelaar, H.L.C., Windig, W., Harper, A.M., Huff, S.M., McClennen, W.H., Richards, J.M., *Science* 226, 268 (1984).
2. Meuzelaar, H.L.C., Harper, A.M., Hill, G.R., Given, P.H., *Fuel* 63, 640 (1984).
3. G. Van Graas, J.W. De Leeuw, P.A. Schenck, in *Advances in Organic Geochemistry* A.G. Douglas and J.R. Maxwell, Eds. (Pergamon Press, Oxford, UK, 1979), pp. 485-494.
4. P.A. Schenck, J.W. De Leeuw, T.C. Viets, J. Haverkamp, in *Petroleum Geochemistry and Exploration of Europe*, J. Brooks, Ed. (Blackwell Scientific Publications, 1984), pp. 267-274.
5. S.R. Larter, in *Analytical Pyrolysis-Techniques and Applications*, K.J. Voorhees, Ed. (Butterworth, London, 1984), pp. 212-275.
6. H.L.C. Meuzelaar, J. Haverkamp, F.D. Hileman, *Pyrolysis Mass Spectrometry of Recent and Fossil Biomaterials-Compendium and Atlas* (Elsevier, Amsterdam, 1982).
7. A.M. Harper, H.L.C. Meuzelaar, G.S. Metcalf, D.L. Pope, in *Analytical Pyrolysis-Techniques and Applications* (Butterworth, London, 1984), pp. 157-195.
8. *Statistical Package for the Social Sciences (SPSS)*, N.H. Nie et al., Eds. (McGraw-Hill, New York, ed. 2, 1975).
9. W. Windig, P.G. Kistemaker, J. Haverkamp, *J. Anal. Appl. Pyrol.* 3, 199 (1981).
10. Windig, W., Meuzelaar, H.L.C., *Anal. Chem.* 56, 2297 (1984).
11. Nip, M., De Leeuw, J.W., Schenck, P.A., Meuzelaar, H.L.C., Stout, S.A., Given, P.H., Boon, J.J., *J. Anal. Appl. Pyrol.*, in press.
12. Meuzelaar, H.L.C. McClennen, W.H., Cady, C.C., Metcalf, G.S., Windig, W., Thurgood, J.R., Hill, G.R., *ACS Preprints (Div. of Fuel Chem.)*, Vol. 29, No. 5, 1984, pp. 166-177.
13. W.L. Maters, D. Van de Meent, P.J.W., Schuyt, J.W. De Leeuw, P.A. Schenck, H.L.C. Meuzelaar, in *Analytical Pyrolysis*, C.E.R. Jones and C.A. Cramers, Eds. (Elsevier, Amsterdam, 1977), pp. 203-216.
14. Personal communication by Biddle Instruments Inc., Blue Bell, PA.
15. M. Teichmüller, in *Stach's Textbook of Coal Petrology*, E. Stach et al. Eds. (Gebrüder Borntraeger, Berlin, 1982), pp. 219-294.
16. Ourisson, G., Albrecht, P. Rohmer, M., *Sci. Am.* 251, 44 (1984).
17. Kaiser, W.R., Johnston, J.E., Bach, W.N., *Geological Circular 78-4*, Bureau of Economic Geology, The University of Texas at Austin (Austin, TX), 1978.
18. Meuzelaar, H.L.C., Harper, A.M., Pugmire, R.J., Karas, J., *Coal Geology* 4, 143 (1984).

19. Halma, G., Van Dam, D., Haverkamp, J., Windig, W., Meuzelaar, H.L.C., *J. Anal. Appl. Pyrol.*, in press.
20. Metcalf, G.S., Windig, W., Hill, G.R., Meuzelaar, H.L.C., to be published.

TABLE I  
CONVENTIONAL LIGNITE CHARACTERIZATION DATA

No. 1	PSOC Code 2	Seam Name (State) 3	Maceral Conc. (%)			Ultimate Anal. (%)				% S (tot) 11
			Vit. 4	Inert. 5	Exin. 6	C 7	H 8	N 9	O 10	
1	833	Fort Union Bed (MT)	74.1	23.2	1.4	70.0	4.60	1.29	23.7	0.64
2	838	Fort Union Bed (MT)	81.7	16.9	1.4	71.3	4.74	1.08	22.3	1.34
3	1084	Sawyer (MT)	88.9	10.8	0.3	71.5	4.84	1.01	22.2	0.60
4	1087	Sawyer (MT)	82.5	16.3	1.2	71.0	4.75	1.00	23.0	0.23
5	1090	Sawyer (MT)	89.1	10.2	0.7	71.9	4.66	0.99	22.1	0.35
6	975	Anderson (WY)	79.6	8.0	12.3	73.0	5.18	0.99	20.3	0.48
7	791	A-Pit (TX)	90.7	8.4	0.9	72.3	5.39	1.20	20.2	0.99
8	792	A-Pit (TX)	94.7	4.5	0.8	72.7	5.61	1.18	19.6	0.97
9	414	Darco (TX)	80.6	17.5	1.9	73.0	5.31	1.37	19.3	1.14
10	415	Darco (TX)	83.4	14.1	2.5	73.6	5.66	1.45	18.4	0.89
11	623	Darco (TX)	81.0	17.2	1.8	74.8	5.26	1.32	17.6	1.35
12	625	Darco (TX)	83.3	15.2	1.5	74.1	4.89	1.30	18.1	2.38
13	1037	Unnamed (TX)	86.5	13.1	0.4	73.1	5.31	1.62	18.9	1.16
14	1038	Unnamed (TX)	88.1	10.8	1.1	73.6	5.02	1.65	18.5	1.39
15	427	Unnamed (TX)	90.6	8.1	1.3	72.9	5.37	1.24	19.2	1.61
16	428	Unnamed (TX)	94.5	3.7	1.8	73.3	6.02	1.28	18.0	1.78
17	786	Unnamed (TX)	87.0	12.0	1.0	73.4	5.12	1.34	18.9	1.44
18	788	Unnamed (TX)	91.6	7.9	0.5	73.5	5.46	1.20	18.7	1.15
19	421	Wildcat (TX)	87.7	10.9	1.4	71.6	5.83	1.34	19.4	2.63
20	422	Wildcat (TX)	88.7	10.1	1.2	75.5	5.86	1.39	15.6	2.03
21	424	Wildcat (TX)	90.7	6.1	3.2	73.7	6.05	1.22	17.6	2.08
22	637	Wildcat (TX)	83.8	14.6	1.6	74.8	5.28	1.32	16.6	2.75

<sup>7,8,9,10</sup>-modif. Parr dmmf (<sup>10</sup> calculated by diff.); <sup>11</sup>-daf

TABLE II  
DISCRIMINANT ANALYSIS RESULTS

Discriminant Function	Eigenvalue	Relative Percentage	Canonical* Correlation
I	341.0	61.3	.999
II	124.0	22.3	.996
III	38.2	6.9	.987
IV	23.6	4.3	.979
V	16.1	2.9	.970
VI	8.8	1.6	.948
VII	2.5	0.5	.845

\* with 11 original factors

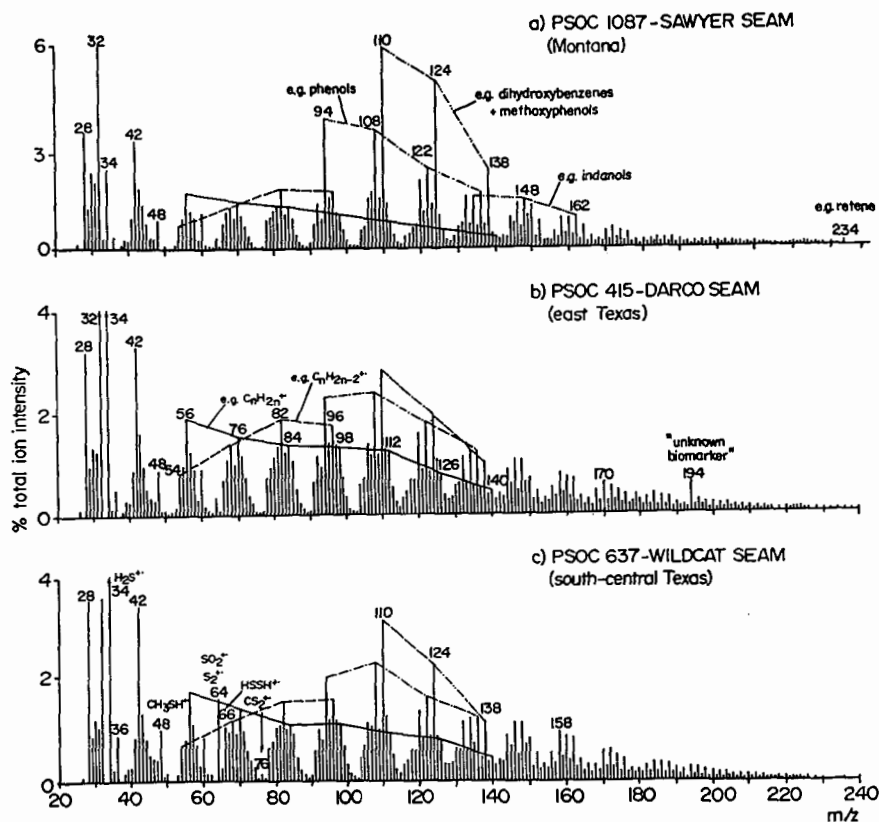


Figure 1. Low voltage pyrolysis mass spectra of three selected lignites representing the Northern Plains province (a) and the Gulf province (b and c). Note the relatively high abundance of hydroxyaromatic series in (a) compared to the more prominent aliphatic hydrocarbon series in (b) and (d). Further note the marked sulfur compounds in (c) and the small biomarker signals (arrows at  $m/z$  234 and 194 in (a) and (b), respectively).

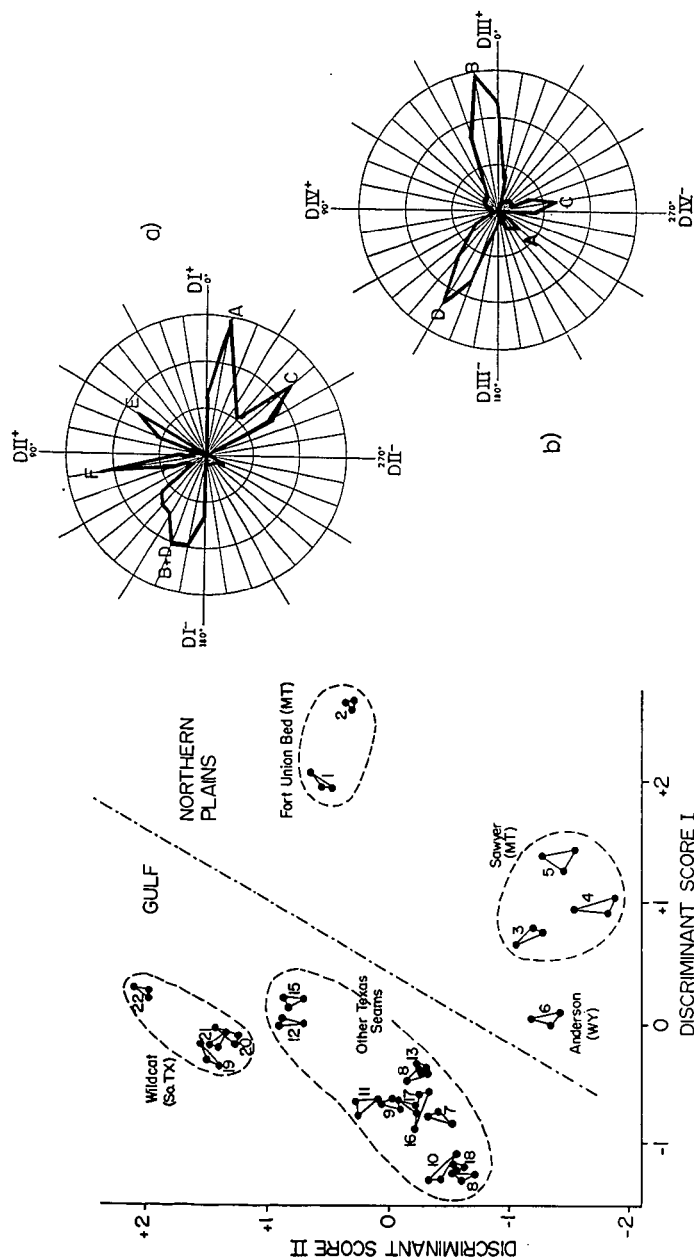


Figure 2. Scatter plot of the scores of the first two discriminant functions showing the clustering behavior of the 22 lignite samples. Triplicate analyses of the same sample are connected by solid lines. Dashed lines indicate coal seam or field relationships. For sample codes, see Table 1.

Figure 3. Variance diagrams showing the presence of six major component axes (A-F) in the space spanned by discriminant functions I, II (a) and III, IV (b), respectively.

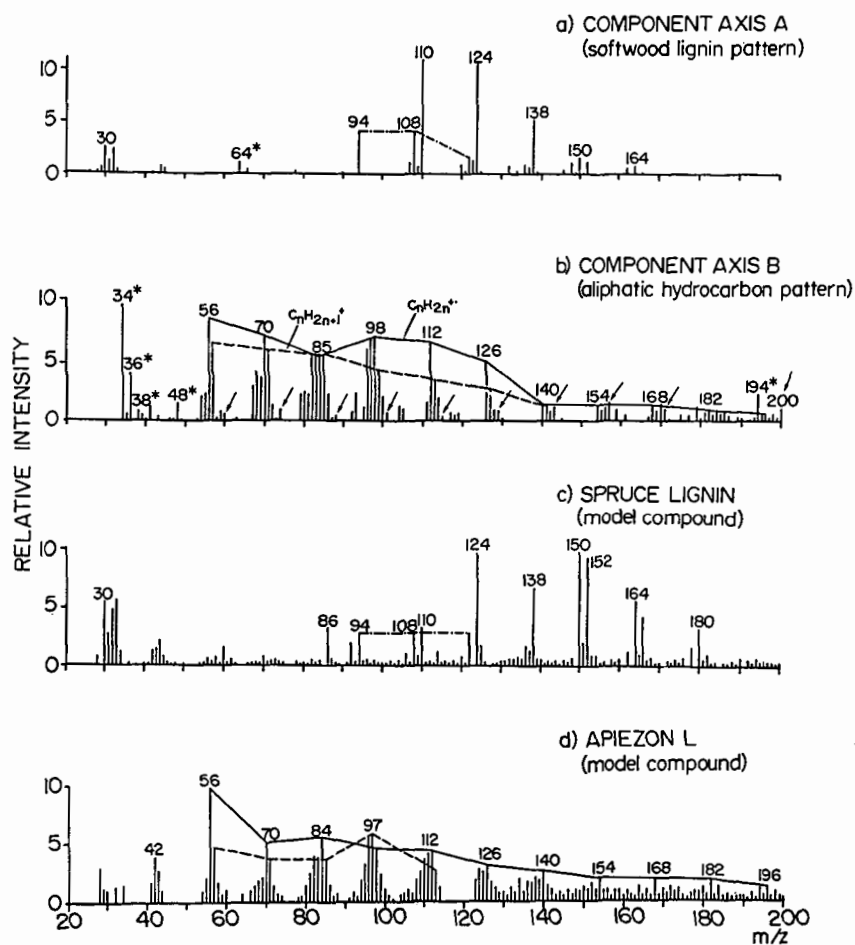


Figure 4. Comparison of the numerically extracted discriminant "spectra" of components A (a) and B (b) with the pyrolysis mass spectra of two model compounds (c and d). Mass peak intensities not optimally represented on the component axes are indicated by asterisks. Arrows point to an aliphatic carboxylic acid series in (b).

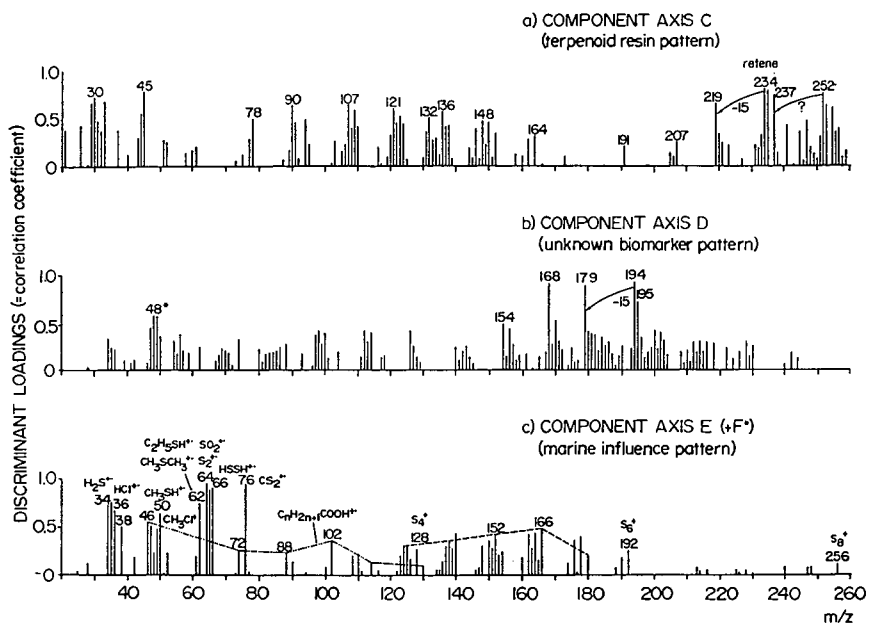


Figure 5. Loading (correlation coefficient) plots representing components C-F in Figure 3. For explanation, see text.

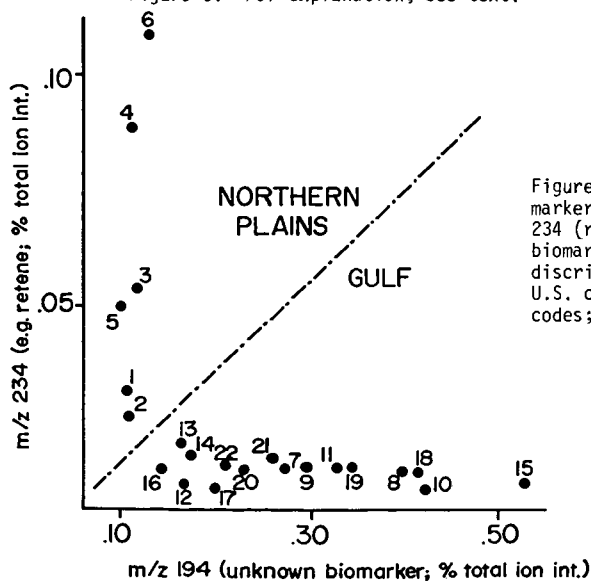


Figure 6. Scatter plot of biomarker peak intensities at m/z 234 (retene) and m/z 194 (unknown biomarker) showing the perfect discrimination between the two U.S. coal provinces. For sample codes; see Table I.



## HIGH RESOLUTION MASS SPECTROMETRIC ANALYSIS OF COAL LIQUIDS

Thomas Aczel, Steve G. Colgrove, and Stephen D. Reynolds

Exxon Research and Engineering Company  
Baytown Research and Development Division  
P. O. Box 4255  
Baytown, TX 77522-4255

### INTRODUCTION

Development of new industrial technologies requires meaningful cooperation among many scientific disciplines, including several branches of chemistry, physics, engineering, economics, and others. This is particularly true for coal liquefaction technology, that involves complex operations, deals with rather refractory materials, and represents a potentially large impact on overall consumption patterns.

Analytical chemistry is a key player in this team effort. It seeks and obtains, to an extent commensurate with effort and circumstances, information on the composition of feed, product and intermediate streams. This information is utilized for fundamental understanding of the reactions involved in coal liquefaction and the upgrading of coal liquids, for monitoring day-to-day pilot plant operations, for evaluating end-products quality and for assessing process and product impact on the environment.

This paper reviews some of the analytical approaches we use in our laboratories for the in-depth characterization of coal liquids. Emphasis will be placed on methods determining organic composition. Issues discussed will include the overall nature of coal liquids, analytical strategy and methodology, the scope of the analyses, the role of separation, mass spectrometric and other techniques, and on the calculation and/or prediction of useful physical parameters from compositional data.

### DISCUSSION

#### Overall Nature of Coal Liquids

Coal liquids are very complex liquids that contain a large variety of chemical classes and compounds. A non-exhaustive list is given in Table I. In-depth analysis generally requires the use of a variety of analytical tools, although, as we will see, these can be often reduced to mass spectrometry alone, provided that one is willing to use some assumptions and clearly understands the limitations of the short-cut method selected.

Composition is a function of both coal origin and liquefaction and/or upgrading conditions. Liquids from some western coals contain significantly lower concentrations of sulfur compounds than those from some eastern coals; while the type and severity of the upgrading process changes significantly the ratios between saturate, hydroaromatic, aromatic, and polar components. Gross composition of end-products in most cases is more affected by the type of upgrading than by coal origin.

#### Analytical Strategy

Selection of the best analytical strategy for the analysis of coal liquids depends on the nature of the information needed, the availability of analytical tools, funding for a particular project, and time. Information content and time/cost restraints are most often balanced with a compromise. A typical analytical scheme that is often used in our laboratories is shown on Figure 1. This scheme provides the user with a

very large body of information that is generally sufficient for most studies involving reaction kinetics, process behavior, end-product quality. The main roles of the various steps are summarized in the following paragraphs.

Separation into saturates, aromatics and polars yields valuable information on the overall amounts of these classes of compounds. It also facilitates the subsequent analysis. For example, saturates are difficult to characterize in detail in the presence of aromatics; and separation of aromatics and polars reduces the mass spectrometric resolving power requirements for the analysis of most nitrogen and oxygen compounds. Separation also eliminates structural uncertainties between furanic and phenolic oxygen types that even high resolution MS can not cope with in complex mixtures. Furans are concentrated in the aromatic fraction, phenolics in the polar fraction; separation thus allows a reliable structural assignment.

Low resolution, high voltage compound type analysis of the saturates determines total paraffins and one to six ring naphthenes. GC distillation and subsequent analysis of trapped cuts yields this type of information as a function of boiling range.

The main feature of the overall analysis is the high resolution, low voltage characterization of the aromatic, polar aromatic, and asphaltene fractions. As will be shown in the remainder of this presentation, this approach yields detailed information of several thousands of individual components and provides the user with a number of physical parameters that are related to composition.

Time and funding constraints might restrict the scope of the analytical scheme. If the separation step is not carried out, total saturates, aromatics and polars can be determined with reasonable accuracy from high voltage, low resolution MS data (Table II), while the aromatic and polar components can be measured accurately from the high resolution, low voltage analysis of the total stream. The decrease in information content will affect only the saturate type distribution, the relationship between saturate composition and boiling range, and the specific identification of some of the oxygenated types. This reduced approach is the only one feasible for materials in the gasoline range; separation of these streams would involve unacceptable losses of volatiles.

A further simplification consists of the substitution of a low resolution, low voltage analysis to the high resolution procedure. This approach is generally applicable to only rather severely hydrogenated coal liquids, as it determines only a few heteroatomic components, such as phenols. Separation of more and less condensed aromatics, that usually requires a resolving power of at least 1000 per 100 MW units, is accomplished through computerized deconvolution of the interfering homologous series, for example alkyltetralins and alkylpyrenes. The deconvolution calculations are based on a large number of high resolution analyses. The low resolution approach, using high voltage for determining saturates/aromatics/polars and low voltage for the determination of aromatic types and carbon number homologs, yields fast and highly reproducible analyses. The method was used extensively in monitoring the large coal liquefaction pilot plant at Baytown, Texas, with an average of two analyses every four to six hours each day, and with a response time of about one hour (1980-1982).

Special nature of some samples and research projects requires occasionally a more extensive analytical treatment than that outlined in Figure 1. These include separation of the aromatics into one, two, three, and four ring concentrates; separation of the polars into weak and strong acids, weak and strong bases, and neutral polars; and analysis of all the fractions by GC/MS,  $^{13}\text{C}$  NMR, and proton NMR. The more specific separations facilitate interpretation and yield information on components in the parts per billion range (Table III); GC/MS yields important information on individual isomers; NMR corroborates and extends the structure assignments made by MS.

### High Resolution, Low Voltage MS Analysis

This method is the cornerstone of our procedures. It has the unique ability to give both detailed quantitative data on a very large number of components and to summarize and sort these into process and/or product quality related parameters.

The underlying principle of the method is the simultaneous use of high resolution and low voltage. High resolution separates the very large number of hydrocarbons and heterocompounds that have the same nominal molecular weight but possess different formulas and thus slightly different precise masses. Such multiplets consist of six to eight peaks on the average at every mass from about mass 150 to mass 500 or 600 in coal liquids. Examples are given in Table IV. Low voltage greatly simplifies the spectra of complex mixtures by ionizing only aromatic and polar aromatic molecular ions. Low voltage is an open-ended approach that allows one to analyze as many components as are present in a sample; and calibration sets can be set up based on theoretical considerations and extrapolations. This is particularly important in complex natural products, that contain thousands of components that are not available in pure form for calibration.

The procedures involved in high resolution, low voltage analysis can be summarized as follows:

- The sample and a blend of halogenated aromatic mass reference standards are charged to a high resolution mass spectrometer, in our case a Kratos MS50, and are run at an effective voltage of 10-11 electron volts (measured by a ratio of 50 to 100 between the molecular ion, 106, and a strong fragment, 91, in m-xylene).
- A computerized data acquisition system, Kratos DS55 plus Exxon proprietary programs determines the mass and intensity of each component, assigns formulas, and sorts the components according to formula or compound type and carbon number.
- A second set of Exxon proprietary computer programs quantitates all individual concentrations and also summarizes the data into overall structural parameters. The scope of the analysis is shown in Table V; typical summary parameters calculated are listed in Table VI.

A very useful feature of the analysis is the calculation of physical and process related parameters from composition (Table VI). For samples available only in very small amounts, this is often the only means to obtain these parameters. Most of the calculations use simple stoichiometric equations; distillation is calculated by assigning each component a boiling range derived either from the literature or extrapolations; carbon and hydrogen types are expressed in NMR terms by assigning theoretical values to each component. In all cases, total sample values are obtained by weighing the theoretical values of all components by the corresponding concentrations in a particular stream and by compositing the data.

The physical parameters calculated are generally quite accurate. Table VII shows typical data for elemental analysis, Table VIII for distillation, Table IX for NMR type parameters.

### DEVELOPMENTS IN PROGRESS

While mass spectrometry is certainly the technique that yields the most detailed information on coal liquids, it also has some limitations. The major ones are the need to heat and volatilize the materials to be analyzed, and the difficulty of identifying specific isomers in complex mixtures. The volatility limitation applies to heavy ends boiling above approximately 1100°F; specific isomer identification is a

problem mainly in total coal liquids. Work is continuing in our laboratories to reduce or eliminate the impact of these factors.

The volatility requirement can be eliminated by using field desorption or fast atom bombardment for ionization. Preliminary data obtained in our laboratories show that field desorption can be used to reproducibly analyze heavy ends with molecular weights as high as 3000 for coal liquids and 4000 for petroleum liquids. The approach requires use of a high-field magnet for mass measurements up to 6000+ molecular weight and very careful standardization of the numerous experimental steps involved, including preparation of the special emitters, sample loading, source alignment, scanning and computerized data acquisition. Recognition of individual isomers can be accomplished through the use of GC/MS, in particular for the lighter components up to  $C_{12}$ , and the more outstanding ones beyond that range. GC/MS data in our labs are generally normalized to high resolution MS data on the corresponding homologs in order to account for the components that can only be identified non-specifically. We are now working on methods to interpret GC/MS data in the absence of pure compound calibrants.

#### CONCLUSION

The analytical methodology discussed above was used for literally hundreds of thousands of samples in the past decade. Many were run with the standard approach outlined in Figure 1; more with the simplified, "MS only" alternative; and several with the extended technology that included GC/MS and NMR.

Availability of the very detailed and summarizable data was demonstrably of great use in the planning, development, and evaluation of coal liquefaction and upgrading processes including very small to large scale efforts.

Table I

MAJOR COMPOUND CLASSES IN COAL LIQUIDS

<u>Class</u>	<u>Type</u>
● SATURATES	● n-paraffins, iso-paraffins, cyclopentanes, cyclohexanes, 1-8 ring condensed cycloparaffins; biological residuals (biomarkers) such as isoprenoid paraffins, steranes, hopanes, etc.
● AROMATICS	● One to eight ring aromatics, such as benzenes, naphthalenes, acenaphthenes, fluorenes, phenanthrenes, pyrenes, chrysenes, benz-pyrenes, benz-perylenes, coronenes, etc.; and the corresponding aromatic thiophenes, dithiophenes, furans, difurans, thiophenfurans.
● NAPHTHENOAROMATICS	● One to eight ring aromatics as above associated with one or more six membered naphthenic rings (hydroaromatics) and/or one or more five membered naphthenic rings. Typical hydroaromatics are tetralins, tetra and octa hydrophenanthrenes, the various hydropyrenes; typical naphtheno-aromatics are indans, benzindans, etc.
● POLAR AROMATICS	● Mono, di- and trihydroxyl-aromatics and naphtheno-aromatics; pyrroles and pyridines associated with aromatics; dinitrogen compounds (probably dipyridine types); nitrogen-oxygen compounds such as hydroxy pyridines and hydroxy pyrroles.
● ASPHALTENES	● Polar aromatics with increased amounts of poly-functional types, such as di-oxygen compounds.

Table II

MS TYPE ANALYSES ARE IN GOOD AGREEMENT WITH CHROMATOGRAPHIC SEPARATIONSA. Accuracy

<u>Sample</u>	<u>Weight Percent</u>					
	<u>Saturates</u>		<u>Aromatics</u>		<u>Polars</u>	
	<u>MS</u>	<u>Sepn.</u>	<u>MS</u>	<u>Sepn.</u>	<u>MS</u>	<u>Sepn.</u>
A	17	19	44	47	39	34
B	8	8	65	63	27	29
C	4	4	51	55	39	36

B. Reproducibility

<u>Replicate runs</u>	<u>Weight Percent</u>	
	<u>Saturates</u>	<u>Aromatics &amp; Polars</u>
1	27.69	72.31
2	27.66	72.34
3	27.71	72.29
4	27.92	72.08
5	27.68	72.32
6	27.54	72.46

Average standard deviation  
on 16 runs in one month

0.081

0.081

Table III

SEPARATION PLUS HIGH RES MS DETECTS PPB COMPONENTS

Example: Acidic Fraction of a Coal Liquid

<u>Carbon No.</u>	<u>Concentration, parts per billion</u>			
	<u>Phenols</u>	<u>Indanols</u>	<u>Hydroxy-Indenes</u>	<u>Naphthols</u>
6	4389	---	---	---
7	28400	---	---	---
8	16875	---	---	---
9	1715	301	62	---
10	450	142	43	0
11	287	58	35	15
12	21	44	30	5
13	8	49	14	0
14	0	36	0	0
15	34	18	3	0

- Separation enrichment : ~4,200-fold
- Dynamic range in high res MS run : ~18,000

Table IV  
TYPICAL MULTIPLET SITUATIONS IN COAL LIQUIDS

<u>Component Class</u>	<u>Example</u>	<u>Delta Mass</u>	<u>Resolving Power Required</u>	
			<u>Mass 300</u>	<u>Mass 600</u>
Non Condensed/Condensed Hydrocarbons	$C_{22}H_{36}/C_{23}H_{24}$	0.0939	3200	6400
Non Condensed Hydrocarbons/ Aromatic Thiophenes	$C_{22}H_{36}/C_{20}H_{28}S$	0.0905	3300	6600
Non Condensed Hydrocarbons/ Mono-Oxygen Compounds	$C_{22}H_{36}/C_{21}H_{32}O$	0.0364	8300	16600
$^{13}C$ isotopes of Hydro- carbons/N compounds	$^{13}C^{12}C_{21}H_{36}/C_{21}H_{35}N$	0.0082	37000	64000
Aromatic Thiophenes/ condensed Hydrocarbons	$C_{20}H_{28}S/C_{23}H_{24}$	0.0034	88000	176000

Table VI

PARAMETERS CALCULATED BY HIGH RESOLUTION, LOW VOLTAGE MS ANALYSISComposition

- Each component (carbon no. homolog) + weight percent
- Each homologous series
  - + weight percent
  - + Avg. C no.
  - + Avg. MW
- Overall sample
  - + Aromatic ring distribution by chemical class
  - + Avg. MW
  - + Avg. carbon no.
  - + Avg. hydrogen deficiency
  - + Weight fraction in aromatic nuclei, sidechains, saturate rings

Physical Properties

- Overall sample
  - + Atomic C, H, O, N, S, H/C
  - + C, H types as measured by NMR
- Selected classes, homologous series for suitable properties
  - + Distillation curve
  - + Density, refractive index
  - + Predicted composition of potential distillation cuts

Process Related Parameters

- Overall sample
  - + Solvent quality index in Exxon Donor Solvent process
  - + Several others



Table V

MS ANALYSIS DETERMINES VERY LARGE NUMBER OF COMPONENTS

<u>Chemical Class</u>	<u>List of Components Determined Range in Homologous Series</u>		<u>Appr. No. of Components</u>
Hydrocarbons	$C_nH_{2n+2}$	through $C_nH_{2n-50}$	700
Thiophenes	$C_nH_{2n-2}S$	" $C_nH_{2n-50}S$	550
Dithiophenes	$C_nH_{2n-6}S_2$	" $C_nH_{2n-44}S_2$	550
Furans/Phenolics	$C_nH_{2n-2}O$	" $C_nH_{2n-50}O$	1100
	$C_nH_{2n-6}O_2$	" $C_nH_{2n-40}O_2$	650
	$C_nH_{2n-6}O_3$	" $C_nH_{2n-28}O_3$	600
	$C_nH_{2n-6}O_4$	" $C_nH_{2n-28}O_4$	600
Nitrogen Cpds	$C_nH_{2n-3}N$	" $C_nH_{2n-41}N$	500
Nitrogen Oxygen Cpds	$C_nH_{2n-3}NO$	" $C_nH_{2n-41}NO$	500
Sulfur-Oxygen, Sulfur-dioxygen Cpds	$C_nH_{2n-10}SO_x$	" $C_nH_{2n-40}SO_x$	1000
DiNitrogen, Nitrogen Di-oxygen Cpds	$C_nH_{2n-6}N_xO_x$	" $C_nH_{2n-40}N_xO_x$	500
Miscellaneous highly condensed, poly- functional compounds	-----		<u>600</u>
	Total		7250

Table VII  
COMPARISON OF ELEMENTAL ANALYSES BY MS AND CHEMICAL TECHNIQUES

A. Individual Samples

Weight Percent					
Atomic H/C		Elemental N		Elemental O	
MS	Chem.	MS	Chem.	MS	Chem.
0.93	0.96	0.10	0.12	0.02	0.10
1.12	1.14	0.90	0.70	0.71	0.76
1.70	1.69	2.30	2.52	2.40	2.63
2.17	2.17	5.92	6.00	3.68	3.22

B. Composite Data on Separated Classes

Element	MS on Separated Classes			MS Composite	Chemical
	Saturates	Aromatics	Polars		
C	86.10	91.34	84.68	88.60	88.84
H	13.90	7.68	7.37	7.84	7.82
O	---	0.40	5.43	2.28	1.83
N	---	---	2.52	0.95	1.17
S	---	0.58	---	0.33	0.33

Table VIII  
COMPARISON OF MS AND GC DISTILLATIONS

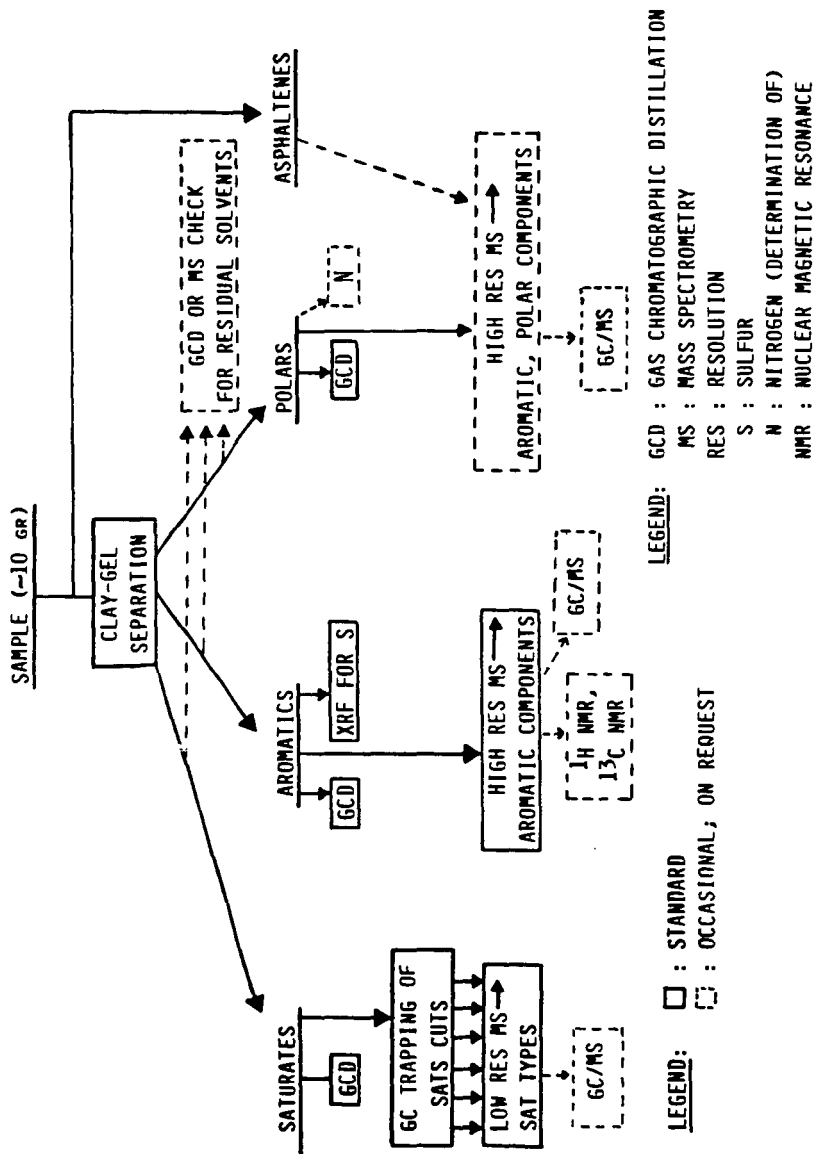
Temperature, °F	Percent Off			
	Sample A		Sample B	
	MS	GCD	MS	GCD
400	0.9	0.1	13.4	12.8
500	5.5	3.6	52.5	48.3
600	15.0	14.0	83.6	86.5
700	37.0	34.4	96.7	98.2
800	63.1	65.8	99.2	99.8
900	86.0	88.5	99.7	100.0
1000	76.8	98.3	99.9	100.0

Table IX  
COMPARISON OF CARBON TYPES BY MS AND NMR

Carbon Type	Mole Percent	
	MS	NMR
Saturate	37.1	38.7
Naphthenic	18.2	19.5
Linear	18.9	19.2
Olefinic	0.0	0.0
Aromatic	62.9	61.3

Figure 1

# ANALYTICAL PROCEDURE FOR COAL LIQUIDS



PYROLYSIS AND COMBUSTION CHARACTERIZATION OF PULVERIZED COALS  
FOR INDUSTRIAL APPLICATIONS

Nsakala ya Nsakala, Gary J. Goetz, Ramesh L. Patel and Tony C. Lao

Combustion Engineering, Inc., 1000 Prospect Hill Road, Windsor, CT 06095

James D. Hickerson and Harry J. Ritz

Department of Energy, Pittsburgh Energy Technology Center, Pittsburgh, PA 15236

ABSTRACT

This paper presents in-depth fundamental information obtained from a two-inch inner diameter laminar flow reactor referred to as the Drop Tube Furnace System (DTFS). This information consists of the following: (1) pyrolysis kinetic characteristics of four coals of various rank (Pennsylvania anthracite, Alabama high volatile bituminous coal, Montana subbituminous coal, and Texas lignite); and (2) combustion kinetic studies of chars produced from the foregoing parent coals. The combustion kinetic information obtained on the high volatile bituminous coal has been used in conjunction with Combustion Engineering's proprietary mathematical model to predict the combustion performance of the pilot scale (500,000 Btu/hr) Controlled Mixing History Furnace (CMHF). Comparison of the predicted data with the experimental results shows a virtually one-to-one scale-up from the DTFS to the CMHF.

INTRODUCTION

The Department of Energy's intent in sponsoring this and other related programs is to foster increased coal usage in the United States. To effectively use coal in existing and new applications requires a more definitive, quantitative understanding of coal properties vs. performance. The objective of this program is to develop the methodologies that most reliably characterize coals from a pyrolysis/combustion standpoint thereby permitting accurate performance predictions to be made. This will in turn allow intelligent use of our coal reserves for a multiplicity of industrial applications with the confidence levels required.

The quantitative fundamental data developed from this study indicate significant differences in coal/char chemical, physical, and reactivity characteristics, which should be useful to those interested in modeling coal combustion and pyrolysis processes. Coal selection is known to be one of the keys governing a successful coal conversion/utilization process. Practical applications of these data involve providing vital information to a designer in the area of carbon burnout and  $\text{NO}_x$  reduction for a large scale coal utilization scheme.

The primary research tools used in this program were CE's Drop Tube Furnace System (DTFS), a bench scale entrained laminar flow furnace and the Controlled Mixing History Furnace (CMHF), a pilot scale entrained plug flow furnace. Both the DTFS and CMHF by virtue of their ability to resolve combustion time into distance along their respective furnace lengths were used to examine carbon burnout phenomena. In addition, the CMHF by virtue of its staged-combustion capabilities was used to evaluate  $\text{NO}_x$  emissions and establish conditions conducive to low  $\text{NO}_x$ . The  $\text{NO}_x$  results obtained from this program will not be discussed in this paper. They will appear in the forthcoming final DOE report.

## EXPERIMENTAL FACILITIES AND PROCEDURES

### Drop Tube Furnace System (DTFS)

The DTFS (Figure 1) is comprised of a 1-inch inner diameter horizontal tube gas preheater and a 2-inch inner diameter vertical tube test furnace for providing controlled temperature conditions to study pyrolysis and/or combustion phenomena. This entrained flow reactor is capable of heating reactant gases and reacting particulates to temperatures up to 2650°F (1730°K) and obtaining particle residence times up to about one second to simulate the rapid heating suspension firing conditions encountered in pulverized coal fired boilers. The DTFS testing procedure entails the following: (1) feed the fuel at a precisely known rate through a water-cooled injector into the test furnace reaction zone; (2) allow the fuel and its carrier gas to rapidly mix with a preheated down-flowing secondary gas stream; (3) allow combustion and/or pyrolysis to occur for a specific time (dictated by the transit distance); (4) quench the reactions by aspirating the products in a water-cooled sampling probe; (5) separate the solids from the gaseous products in a filter medium; and (6) determine on-line  $\text{NO}_x$ ,  $\text{O}_2$ ,  $\text{CO}_2$ , and  $\text{CO}$  concentrations in the effluent gas stream. An ash tracer technique (1, 2) is used in conjunction with the proximate analyses of a given feed sample and the chars subsequently obtained from the test furnace to calculate the pyrolysis weight losses and/or combustion efficiencies as a function of selected operational parameters (temperature, residence time, fuel type, etc.).

### Controlled Mixing History Furnace (CMHF)

The pilot scale (500,000 Btu/hr) CMHF (Figure 1) is based on the principle of plug flow which resolves time into distance along the length of the furnace. It consists of a refractory-lined 1.5 foot inner diameter cylinder with an overall height of 22.6 ft. A mixture of pulverized fuel and primary air is fired downward into the furnace from a single burner centrally located at the top of the furnace. The furnace consists of four zones--preheat, combustion, water-cooled, and after-burner--proceeding downward from the fuel admission point. By sampling at different ports along the length of the furnace, it is possible to examine the carbon burnout and  $\text{NO}_x$  formation histories of a fuel. An ash tracer method is also used to determine the solids combustion efficiency as a function of operational parameters. Gaseous products aspirated in a sampling probe are analyzed on-line to determine  $\text{NO}_x$ ,  $\text{O}_2$ ,  $\text{CO}$ , and  $\text{CO}_2$  concentrations.

## RESULTS

### Analysis of Coals

The coals selected for this study include a ligA from Wilcox seam in Texas, a subB coal from Rosebud seam in Montana, a hvAb coal from Black Creek seam in Alabama, and an anthracite from Buck Mountain seam in Pennsylvania. The proximate and ultimate analyses and higher heating values of these coals (Table 1) are consistent with their ASTM classifications.

### Pyrolysis Characteristics of Coals

Size graded (200x400 mesh) coals were pyrolyzed in the DTFS in the presence of nitrogen atmosphere at five different temperatures (1450, 1600, 1900, 2400, and

TABLE 1  
SELECTED ANALYSES OF COALS

ANALYSIS	TEXAS (WILCOX) ligA		MONTANA (ROSEBUD) subB		ALABAMA (BLACK CREEK) hvAb		PENN (BUCK MT.) an	
	As	DAF	As	DAF	As	DAF	As	DAF
	Rec'd		Rec'd		Rec'd		Rec'd	
Proximate, Wt. Percent								
Moisture (Total)	21.2	--	23.9	--	3.6	--	5.7	--
Volatile Matter	34.7	53.6	30.7	45.0	37.7	40.3	3.5	4.1
Fixed Carbon	30.0	46.4	37.6	55.0	55.8	59.7	83.3	95.9
Ash	14.1	--	7.8	--	2.9	--	7.5	--
Ultimate, Wt. Percent								
Hydrogen	3.5	5.5	3.6	5.3	4.9	5.3	1.7	1.9
Carbon	45.6	70.5	51.6	75.5	78.5	84.0	82.7	95.3
Sulfur	0.6	0.9	0.7	1.0	0.7	0.7	0.4	0.5
Nitrogen	0.8	1.3	0.9	1.3	1.6	1.7	0.7	0.8
Oxygen (Diff)	14.2	21.8	11.5	16.9	7.8	8.3	1.3	1.5
Ash	14.1	--	7.8	--	2.9	--	7.5	--
Higher Heating Value, Btu/lb	7845	12130	8800	12080	13935	14910	12740	14675

2650°F) and residence times ranging up to 0.9 sec. Results, Figure 2, show that: (1) pyrolysis weight loss depends significantly on temperature and time for each coal; (2) and pyrolysis is virtually complete within 0.2 sec. for the lignite, subbituminous, and high volatile bituminous coals. The lignite and subbituminous coal showed, respectively, 12% and 14% volatile matter enhancements over their proximate ASTM volatile matter yields; the high volatile bituminous coal and anthracite, on the other hand, showed no volatile matter enhancements over ASTM results.

Results in Figure 2 were used to derive the pyrolysis kinetic parameters for each coal. The derivation method used by Nsakala et al. (1), Scaroni et al. (3), and Walker et al. (4) was also used here. That is, briefly:

$$C = C_0 \exp (-kt) \quad 1)$$

where  $C_0$  is the maximum obtainable weight loss referred to as  $\Delta W_\infty$ , and  $C$  is the remaining pyrolyzable material weight at time  $t$  ( $C = \Delta W_\infty - \Delta W$ , where  $\Delta W$  is the pyrolysis weight loss at time  $t$ ), and  $k$  is a pyrolysis rate constant. Plugging these values into and manipulating Equation 1 yields

$$\ln (1 - \Delta W / \Delta W_\infty) = -kt \quad 2)$$

Plotting the left hand side of Equation 2 vs.  $t$  yields straight lines (Figure 3) from which the  $k$  values can be obtained from the slopes of the least squares fits.

Now, the  $k$  values can be used in conjunction with a first order Arrhenius law to obtain

$$k = k_0 \exp (-E/RT) \quad 3)$$

where  $k_0$ ,  $E$ ,  $R$ , and  $T$  are, respectively, the pyrolysis frequency factor, the apparent activation energy, the universal gas constant, and the reaction temperature.

Plotting  $\ln k$  vs.  $1/T$  yields straight lines (Figure 4) from which the values of  $k_0$  and  $E$  can be obtained from the intercepts and slopes of the least squares fits. Results from this study are given in Table 2.

TABLE 2

KINETIC DATA FOR PYROLYSIS OF 200X400 MESH COALS IN NITROGEN ATMOSPHERE AND 1450-2650°F(1060-1730°K) TEMPERATURE RANGE

FUEL TYPE	E(cal/mole)	$k_0(\text{sec}^{-1})$	$\gamma$
Texas LigA	7980	50.8	-0.95
Montana subB	4740	13.5	-0.93
Alabama hvAb	7825	32.5	-0.98
Pennsylvania Anthracite	7755	38.7	-0.79

$\gamma$  = Correlation Coefficient

The low activation energies (4.7-8.0 kcal/mole) encountered here seem to indicate that a physical, rather than a chemical, control mechanism does control the thermal decomposition process. Various investigators (2, 3, 4, 5) employing dilute-phase reactors similar to the present DTFS have also encountered relatively low activation energies (generally less than 20 kcal/mole) for thermal decomposition of coals of various rank.

#### Combustion Characteristics of Coal Chars

A commercial grind (~70%-200 mesh) of each coal was pyrolyzed in the DTFS in nitrogen atmosphere at 2650°F. The resultant char was subsequently size graded to obtain a 200x400 mesh size fraction. The proximate and pore structural analyses of each coal char is given in Table 3. It is noteworthy that: (1) all the chars are virtually volatile matter-free; and (2) while the BET surface areas follow the

TABLE 3

PROXIMATE AND PORE STRUCTURAL ANALYSES OF 200X400 MESH DTFS-GENERATED CHARS

QUANTITY	TEXAS ligA	MONTANA subB	ALABAMA hvAb	PENN. an.
Proximate, Wt. %.				
Volatile Matter	2.3(3.5)*	2.3(2.8)*	1.5(1.6)*	1.3(1.4)*
Fixed Carbon (Diff)	64.3	80.3	94.6	92.1
Ash	31.2	14.9	3.9	5.9
$S_{BET}, m^2/g, daf$	191.3	89.9	16.4	2.6
$S_{CO_2}, m^2/g, daf$	210.9	162.9	16.3	1.6
$g_{Hg}, g/cm^3, daf$	0.79	0.69	0.86	1.62
$g_{He}, g/cm^3, daf$	1.71	2.01	1.75	1.86
$V_T, cm^3/g$	0.681	0.952	0.591	0.080
Porosity, %	53.8	65.7	50.9	12.9

\*Dry-ash-free-basis



trend ligA > subB > hvAb > anthracite, the total open porosity trend is subB > ligA > hvAb > anthracite.

Each char was burned in the DTFS in 0.03 atm. O<sub>2</sub> (in nitrogen balance) at five temperatures (1600, 1900, 2150, 2400, and 2650°F) and residence times ranging up to 0.85 sec. Results show: (1) a strong temperature and time dependence of combustion efficiencies of the ligA, subB, and hvAb chars; and (2) a relatively weak temperature and time dependence of the anthracite char combustion efficiency.

Results in Figure 5 were used to determine for each char the overall rates of carbon removal per unit external surface area (K) assuming that the reaction proceeds by a shrinking core mechanism. The K values were then used in conjunction with classically calculated corresponding diffusional reaction rate coefficients (K<sub>D</sub>) to derive the surface reaction rate coefficients (K<sub>S</sub>) according to

$$1/K = 1/K_D + 1/K_S \quad (4)$$

First order Arrhenius Equations is then applied to the data as follows

$$K_S = A \exp(-E/RT) \quad (5)$$

where A, E, R, and T are, respectively, the frequency factor, apparent activation energy, gas constant, and reaction temperature.

Plotting  $\ln K_S$  vs.  $1/T$  yields straight lines (Figure 6) from which the values of A and E can be obtained from the intercepts and slopes of the least squares fits. This calculation procedure is given in detail by Field (6, 7) and Goetz et al. (8).

Two methods were used in this derivation. The first method used the bulk gas temperatures (T). The second method entailed calculating particle surface temperatures (T<sub>s</sub><sup>g</sup>) by a heat balance method (7) as follows

$$H_g = H_c + H_r \quad (6)$$

Where H<sub>g</sub>, H<sub>c</sub>, and H<sub>r</sub> are, respectively, the rate of heat generation per unit area, the rate of heat loss by conduction, and the rate of heat loss by radiation. Differences between T<sub>s</sub><sup>g</sup> and T ranged from 20 to 197°F. These differences are reflected in the reaction kinetic parameters given in Table 4. These results depict the importance of specifying the method used in deriving combustion kinetic parameters.

TABLE 4  
SENSITIVITY OF COMBUSTION KINETIC PARAMETERS OF  
VARIOUS 200X400 MESH CHARs TO THE METHOD OF DERIVATION

FUEL TYPE	E(CAL/MOLE)		A(g/cm <sup>2</sup> sec.O <sub>2</sub> atm.)	
	METHOD 1	METHOD 2	METHOD 1	METHOD 2
Texas Lignite	21050	20350	57	35.6
Montana subB	26730	25400	593	271
Alabama hvAb	23320	22550	80	50
Pennsylvania Anthracite	17900	17840	4.3	3.7

Method 1: Using measured gas temperature (T)

Method 2: Using calculated particle surface<sup>g</sup>temperature (T<sub>s</sub>)

#### DTFS to CMHF Scale Up Studies

The combustion and  $\text{NO}_x$  characteristics of the Alabama hvAb coal were also determined in the CMHF at 500,000 Btu/hr firing rate. The DTFS-derived kinetic parameters of this coal char were used in conjunction with other coal data and an in-house mathematical model to simulate the CMHF combustion processes under various conditions. This mathematical model is essentially based upon the formulation of Field and co-workers (9), whereby the following differential equation is solved

$$du_j/dt = -S_j q_j \quad 7)$$

where  $u_j$ ,  $S_j$ , and  $q_j$  are, respectively, the weight of a particular residual char fraction at time  $t$  per unit initial weight of char, the geometric surface area of each particular fraction per unit weight of char and the rate of carbon removal per unit geometric surface area. Equation 7 assumes that the volatile matter is instantaneously released and burned. As such, the pyrolysis process is not modeled. It is noteworthy that the pyrolysis information presented in this paper can be used in developing coal pyrolysis models for incorporation in overall combustion models.

Results obtained from the present simulation study will be explained in detail in the final DOE report. Figure 7 depicts two cases: (1) a base line (no air staging, 20% excess air, commercial fuel grind); and (2) an optimum  $\text{NO}_x$  reduction (50% primary stage stoichiometry, 20% excess air, fine grind). A very good agreement exists between theoretical and experimental results, indicating a virtually one-to-one DTFS-to-CMHF scale-up. CE is beginning to use this technique for predicting carbon heat losses in utility and industrial boilers. This technique is therefore of practical uses.

#### CONCLUSIONS

- The apparent activation energies for coal pyrolyses are so low (4.7-8.0 kcal/mole) that they seem to indicate a physical rather than a chemical control of the pyrolysis process.
- The apparent activation energies for coal char combustion are in the 17.9-26.7 kcal/mole range, indicating a very significant temperature dependence of coal char combustion.
- Pore structure plays an important role during char combustion. The higher the total open porosity, generally, the greater is the char reactivity.
- Combustion performance as predicted from DTFS kinetic data and use of a mathematical model agrees very well with combustion performance as directly measured on the CMHF using the same coal.
- The fundamental data presented here have significant practical value as inputs to computer models to predict carbon heat losses.

#### ACKNOWLEDGEMENTS

We appreciatively acknowledge the Department of Energy for the financial support of this program under Contract No. DE-AC22-81PC 40267.

## REFERENCES

1. Nsakala, N., Essenhigh, R. H., and Walker, P. L., Jr., *Combustion Science and Technology*, **16**, 153 (1977).
2. Badzioch, S., and Hawksley, P. G. W., *Ind. Eng. Chem. Process Des. Develop.*, **9**, 521 (1970).
3. Scaroni, A. W., Walker, P. L., Jr., and Essenhigh, R. H., *Fuel*, **60**, 71 (1981).
4. Maloney, D. J., PhD Thesis, The Pennsylvania State University, University Park, PA, 1983.
5. Walker, P. L., Jr., Jenkins, R. G., Vastola, F. J., and Spackman, W., DOE Final Technical Report DE-AC01-79ET14882, January 1983.
6. Field, M. A., *Combustion and Flame*, **13**, 237 (1969).
7. Field, M. A., *Combustion and Flame*, **14**, 237 (1970).
8. Goetz, G. J., Nsakala, N., Patel, R. L., and Lao, T. C., EPRI Final Report AP-2601, September 1982.
9. Field, M. A., Gill, D. W., Morgan, B. B., and Hawksley, P. G. W., *Combustion of Pulverized Coal*, BCURA, Leatherhead, England, 1967, p. 211.

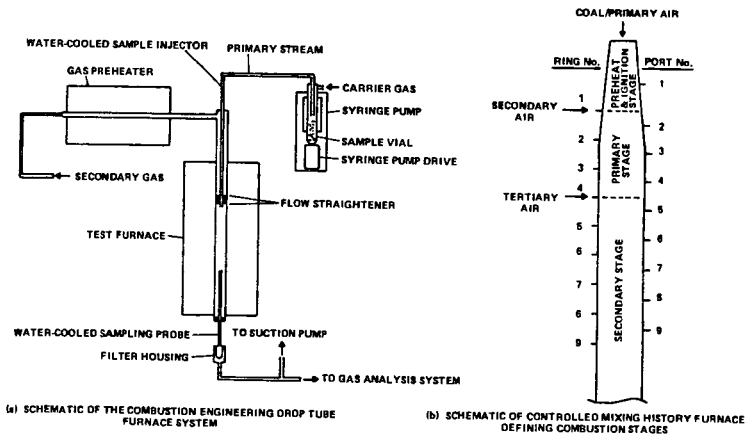


FIGURE 1 PRINCIPAL EXPERIMENTAL EQUIPMENT USED

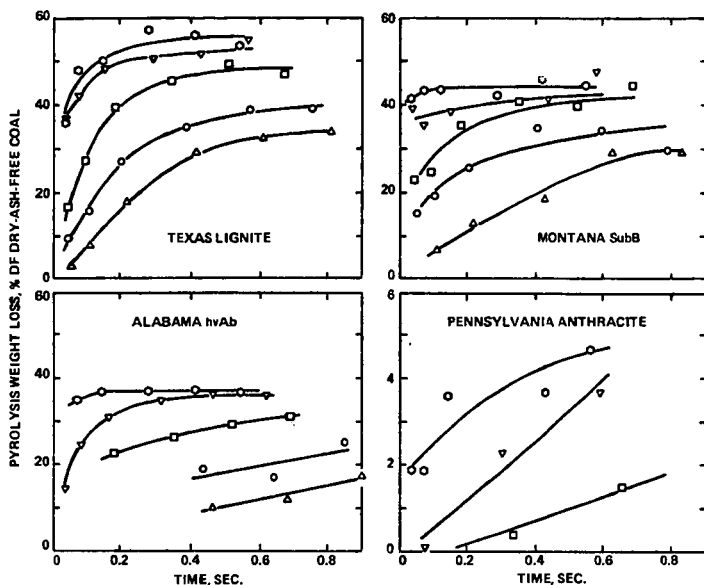


FIGURE 2 DTFS PYROLYSIS WEIGHT LOSSES OF 200 x 400 MESH COALS IN NITROGEN ATMOSPHERE AT VARIOUS TEMPERATURES (  $\Delta$  1450°F,  $\circ$  1600°F,  $\square$  1800°F,  $\nabla$  2400°F,  $\diamond$  2650°F)

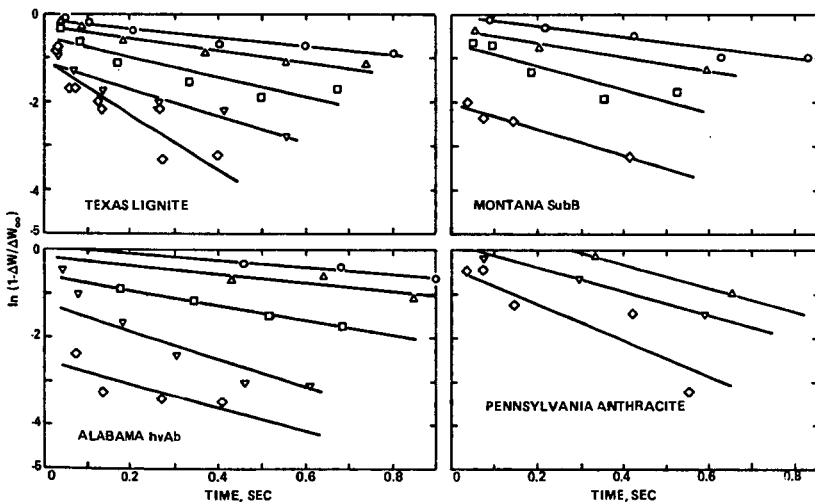


FIGURE 3 VARIATION OF  $\ln(1-\Delta W/\Delta W_{\infty})$  WITH DTFS RESIDENCE TIME FOR PYROLYSIS OF 200 x 400 MESH COALS IN NITROGEN ATMOSPHERE AT VARIOUS TEMPERATURES (  $\circ$  1450°F,  $\Delta$  1600°F,  $\square$  1800°F,  $\nabla$  2000°F,  $\diamond$  2650°F)

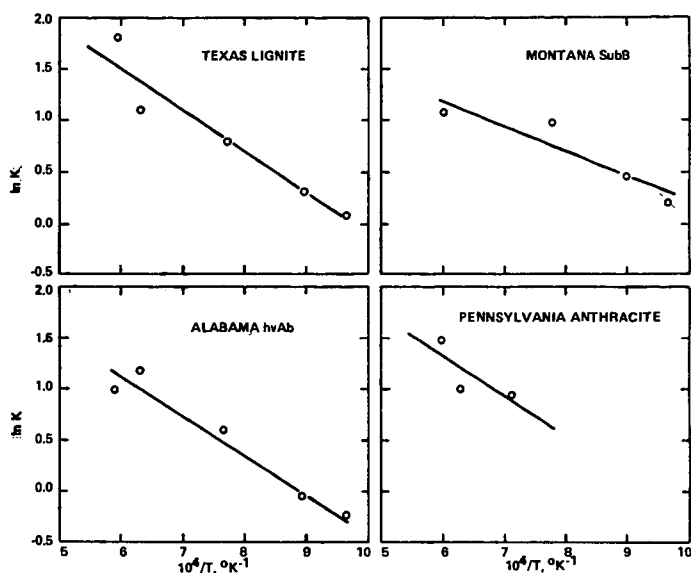


FIGURE 4 ARRHENIUS PLOTS FOR DTFS PYROLYSIS OF VARIOUS 200 x 400 MESH COALS

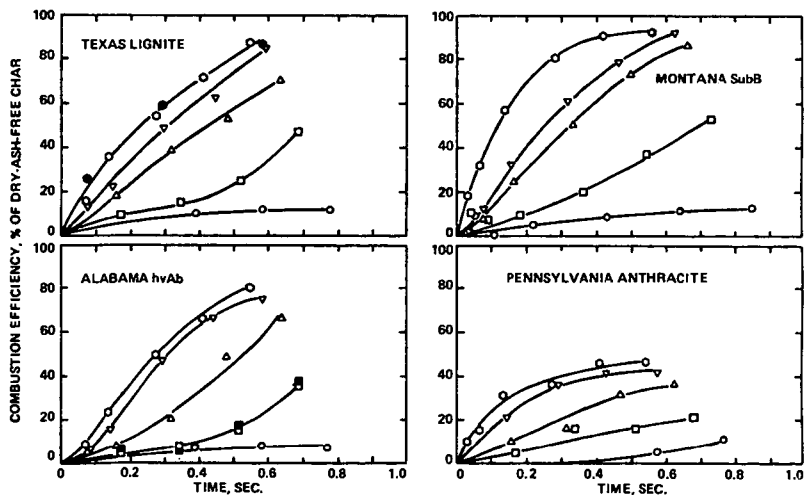


FIGURE 5 DTFS COMBUSTION EFFICIENCIES OF 200 x 400 MESH COAL CHARS IN 3% O<sub>2</sub> / 97% N<sub>2</sub> MEDIUM AT VARIOUS TEMPERATURES (○ 1600°F, □ 1800°F, △ 2150°F, ▽ 2400°F, ● 2650°F)

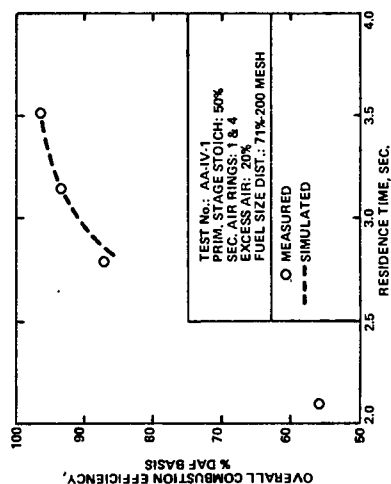
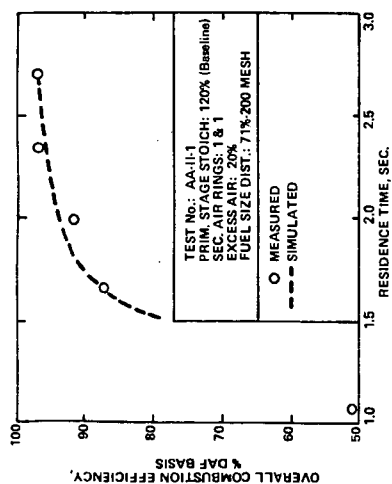


FIGURE 7 SIMULATED CMHF COMBUSTION PERFORMANCE FOR ALABAMA Ivab COAL USING DTFS KINETIC INFORMATION

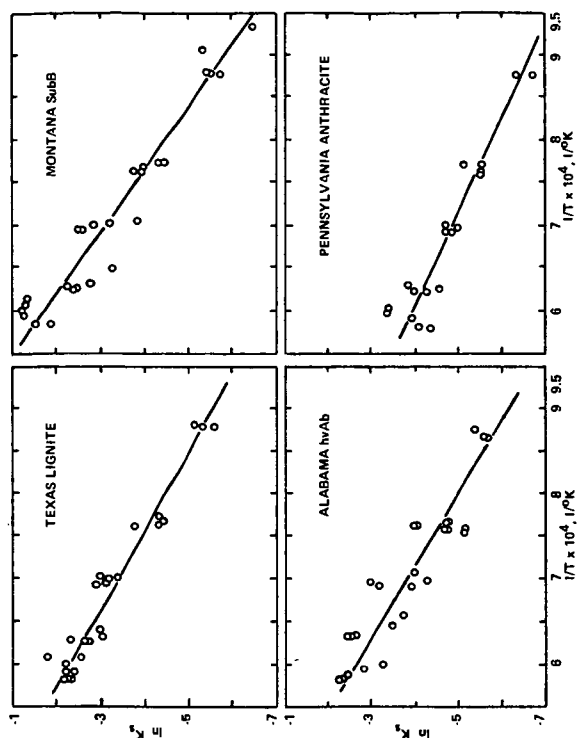


FIGURE 8 ARRHENIUS PLOTS FOR DTFS COMBUSTION OF VARIOUS 200 x 400 MESH COAL CHARS

## FLASH PYROLYSIS OF COAL IN NONREACTIVE GASES

Muthu S. Sundaram\*, Meyer Steinberg, and Peter T. Fallon  
Process Science Division  
Department of Applied Science  
Brookhaven National Laboratory  
Upton, N.Y. 11973

### ABSTRACT

Coal pyrolysis experiments were carried out with a New Mexico subbituminous coal in the presence of nonreactive He, N<sub>2</sub>, and Ar gases in an entrained downflow tubular reactor. The percent carbon conversions to CH<sub>4</sub>, C<sub>2</sub>H<sub>4</sub>, BTX, CO and CO<sub>2</sub> were determined as a function of temperature and residence time at 50 psi. In helium atmosphere, the yields of methane and CO<sub>x</sub> reached asymptotic values in about 1 sec and ethylene was produced throughout the length of the BNL reactor corresponding to a coal particle residence time of 1.7 sec. The relative yields of individual products were influenced by the pyrolysis atmosphere but the total carbon conversion remained almost unaffected. A reduction in the cationic content of coal by acid treatment enhanced the production of CO and CO<sub>2</sub> but inhibited the formation of ethylene.

### INTRODUCTION

Devolatilization plays an important role in the conversion of coal to gases and liquids. It is generally agreed that combustion and gasification of coal is preceded by the release of volatile matter from the coal particle. Under rapid heating conditions ( $>10^4$  °K/sec), volatile yields in excess of those from proximate analysis ( $<10^2$  °K/sec) have been obtained (Budzioch, 1970). Other reaction parameters which affect the volatile yields during pyrolysis of coal are: reaction temperature, particle residence time, and gas pressure. In addition, the pyrolysis product composition also depends on the nature of the entraining gas medium.

Previous research at Brookhaven mainly focused on the yields, distribution, and kinetics of formation of products in reactive hydrogen and methane atmospheres (Sundaram, 1982; Steinberg, 1982; Sundaram, 1984). An investigation was, therefore, initiated with special emphasis on determination of flash pyrolytic behavior of coal in nonreactive gases and their mixtures. This paper is specifically concerned with the effect of gaseous atmosphere on the pyrolysis product yields.

## EXPERIMENTAL

Figure 1 presents the schematics of the entrained downflow isothermal tubular reactor. A detailed description of the design, construction, and operation of the reactor is available (Sundaram, 1982). The reactor is heated electrically by four clamshell-type heaters and designed for operation at temperatures up to 1050°C and pressures up to 4000 psig. Particle heatup rates in the range  $10^4$  to  $10^5$  °K/sec are attainable in this reactor. Other carbonaceous materials such as biomass and oil shale have also been successfully run in the unit.

Coal ( $<150$   $\mu\text{m}$  in diameter) is mixed with 10 to 30% by weight of Cab-O-Sil, an inert fumed silica powder, to prevent agglomeration, and is fed by gravity into the preheated gas stream at an average flow rate of about 400 to 600 g/hr. The preheated gas is injected at an average volumetric flow rate of about 40 to 45 l/min. At the beginning of the run, the coal and gas flow rates are so adjusted that a constant solid-to-gas feed ratio of 0.15 to 0.25 g coal/l gas is maintained in order to be able to continue a dilute phase operation. The residence time of the coal particles is determined from the free-fall velocity of the solid particles using Stoke's law and from the velocity of the entraining gas molecules.

The proximate and ultimate analyses of coal used in the study are shown in Table 1. The acid-washed New Mexico subbituminous coal was prepared by treating the original coal with large excess of 1 N HCl at room temperature followed by washing with deionized water until the filtrate was free of chloride ions. All coal samples were dried in a vacuum oven for at least 24 hours before feeding into the reactor. The gases used were of 99% or higher purity. The density, heat capacity, and thermal conductivity data for experimental gases are listed in Table 2. 50-50 gas mixtures of helium and argon were prepared from pure gases on a volume percent basis.

The principal pyrolysis products were methane, ethylene, BTX, CO, and CO<sub>2</sub>. Product gas samples, corresponding to coal particle residence times variable up to 2 sec, are taken from any of the four sample taps located at 2-ft intervals throughout the length of the reactor and analyzed via on-line GC. Products heavier than BTX are formed only at low temperatures ( $<800^\circ\text{C}$ ) and collected in water-cooled condensers during isothermal runs and analyzed separately. Char containing coal ash, Cab-O-Sil, and unreacted carbonaceous material is collected in a char pot. The yields of individual carbon-containing products are reported as percent of carbon contained in the feed coal.

## RESULTS AND DISCUSSION

The product distributions from pyrolysis of coal in nonreactive gaseous atmospheres of helium, nitrogen, and argon were obtained as a function of temperature, residence time, and pressure (Steinberg, 1983). A specific purpose of this work was to find whether the heat transfer characteristics of these gases had any influence on the pyrolytic product distribution and if so, to what extent.



The yield versus coal particle residence time curves for various products obtained from the flash pyrolysis of New Mexico subbituminous coal in helium are shown in Figure 2 for different isothermal temperatures, from 700° to 1000°C. Although the total carbon conversion to hydrocarbon gases, BTX, and CO<sub>x</sub> tends to increase with coal particle residence time, one may note that most of the conversion occurs within 1 sec, and further increase in residence time does not cause significant increase in total carbon conversion. For instance, at 800°C, a carbon conversion equivalent to 10% is achieved at 1 sec and increasing the residence time by 0.6 sec increases the total carbon conversion by only 1.6%.

This is expected because the hydrogen required for stabilization of free radicals generated from coal and from pyrolysis tar is "donated" by coal itself, and the amount of "donatable" hydrogen, present mostly in the hydroaromatic rings in coal, is a fixed quantity. The extent of cracking of hydroaromatic rings to release hydrogen is probably not influenced by coal particle residence time alone. The hydroaromatic rings are connected to other units and functional groups in coal by chemical bonds of different strengths. As the temperature is increased, bonds with higher dissociation energy are thermally broken and additional hydrogen can be released from the hydroaromatic portion of coal. Initial acceleration in the reaction rate, especially during the early stages of pyrolysis, has been attributed to the occurrence of simultaneous reactions and/or to the resistance of intraparticle mass transfer (Kobayashi, 1977).

The product curves show that ultimate asymptotic yields have been obtained for methane and CO<sub>x</sub> within the residence time employed. The production characteristic of ethylene appears to be considerably different from that of methane and CO<sub>x</sub>. Polymethylene moieties present in coal are considered to be main precursors for ethylene production (Calkins, 1983). At low temperatures, ethylene is produced only at long residence times. (Similar behavior is noticed in CO<sub>x</sub> production.) At higher temperatures, ethylene is continuously produced throughout the length of the reactor and no maximum in its yield is visible from the curves. Extrapolation of the 900°C curve indicates a maximum of about 5.8% at about 2-sec coal particle residence time. At temperatures above 900°C, ethylene undergoes decomposition as can be clearly seen in Figure 3 in which the product yields are plotted as a function of temperature for various residence times. Because of lack of hydrogen, only part of the decomposed ethylene results in the formation of methane. It is seen from this Figure that at 1.5 sec ethylene yield decreases from 4.9% at 900°C to 2.3% at 1000°C (a reduction of 2.6% in absolute yield), whereas methane yield increases from 3.4% at 900°C to 5.0% at 1000°C (1.6% increase in absolute yield). The increase in the BTX yield from 1.5% at 900°C to 2.2% at 1000°C (Table 3) might be attributed to the secondary reactions of ethylene unaccounted for as above.

It appears that cracking of polymethylene groups is catalyzed by in situ mineral matter in coal. When an acid-treated New Mexico subbituminous coal containing 6.2% ash was pyrolyzed, ethylene yields

were 25 to 30% lower than those from original coal containing 22.8% ash. An increase in the temperature from 900° to 1000°C decreased the ethylene yields by approximately 50% in both cases (Table 3). The presence of coal mineral matter, however, seems to favor the formation of methane and BTX at the expense of ethylene. For example, in the case of untreated coal, the combined yields of methane and BTX increase by 2.3% C against a 2.6% decrease in the yield of ethylene. On the other hand, in the case of acid-treated coal, ethylene formed at low temperature seems to undergo secondary thermal cracking reactions at high temperature resulting in the formation of char.

As can be seen in Table 3, reduction of cationic content of coal by acid treatment increased the yields of CO and CO<sub>2</sub> gases. The decrease in ethylene and BTX yields were more than compensated by increase in CO<sub>x</sub> yield in that the overall carbon conversion to hydrocarbon gases plus BTX and CO<sub>x</sub> actually increased. From studies based on model compounds (Cypres, 1975) and coal (Schafer, 1979), it is known that phenolic functional groups in coal are mainly responsible for the production of CO. On this basis, it is suggested that coal mineral matter might catalyze the polymerization reactions involving phenolic groups or their precursors during early stages of devolatilization, thereby inhibiting the evolution of CO. In situ mineral matter seems to catalyze the dimerization of solvent radicals under coal liquefaction conditions (Sundaram, 1983-1); caution should, however, be exercised in extending these results to coal pyrolysis because of drastic changes in reaction severity.

In addition, it is also possible that the acid treatment could have caused changes in pore structure and/or chemical structure of coal, which may have influenced the pyrolysis behavior. A more thorough and systematic study is required before an acceptable mechanism can be advanced.

In any case, the preliminary results from the present study are different from recent findings by Franklin of MIT (Franklin, 1981) who pyrolyzed coal via an extensively used captive sample technique with reported heating rates of about 1000°K/sec and holding times up to 5 sec. In the later study, an acid-demineralized Pittsburgh No. 8 coal was spiked with various inorganic additives such as calcite, quartz, kaolinite, montmorillonite, etc., and calcium minerals were found to be particularly effective in cracking oxygen functional groups to produce CO. It is not clear whether the differences between the two studies are due to their experimental techniques (BNL: entrained flow, short residence time, high heating rate; MIT: captive sample, long holding time, slow heating rate) or to coal rank (BNL: subbituminous coal; MIT: bituminous coal). We intend to pursue this subject matter in more detail in the future.

The results of pyrolysis experiments in other nonreactive gases are shown in Figure 4. The total conversion includes the yields of methane, ethylene, BTX, and CO<sub>x</sub>. Because of analytical limitations in measuring CO in the presence of nitrogen or argon, CO yield data from helium pyrolysis experiments were used to determine total conversion under nitrogen and argon atmospheres. Examination of Figure 4 with

this assumption suggests that the total carbon conversion is almost unaffected by pyrolysis atmosphere under the conditions reported. An increase in total conversion in the order of  $\text{He} > \text{N}_2 > \text{Ar}$  was reported earlier (Sundaram, 1983-2). In that study, coal was pyrolyzed at a higher pressure (200 psi) and the results obtained from experiments employing somewhat nonuniform residence time conditions (3.5 to 4.7 sec) were compared, whereas in this paper results from more uniform, narrow range residence time (1.5 to 1.7 sec) experiments are compared. Pyrolysis experiments under other conditions are in progress, and the results will be published in a future report.

Even though the total carbon conversion remained almost unaffected by pyrolysis atmosphere, the relative yields of pyrolysis products seem to be altered by different nonreactive gases. A clear-cut trend in product yields, however, is not revealed in Figure 4. Nevertheless, some generalizations on product yields could be made. Conversion to methane followed the increasing order of  $\text{He} > 50\% \text{He}/50\% \text{Ar} > \text{N}_2 > \text{Ar}$ . The yield of ethylene was lower in helium atmosphere than in  $\text{N}_2$  or Ar and the ethylene yield maximized at 900°C in all gaseous atmospheres. A slightly larger amount of BTX was produced in Ar and He/Ar than in He or  $\text{N}_2$  up to 900°C; at 1000°C, the BTX yield is almost the same in all gaseous atmospheres.

The gas-film heat transfer coefficient and hence the heat-up rate of the coal particles were found to follow the order  $\text{He} > \text{N}_2 > \text{Ar}$ . It appears that the magnitude of difference in the particle heat-up rate is not large enough to significantly affect the total volatiles yield under the conditions reported herein. The effect of nonreactive gases on the physical and chemical characteristics of the resulting char is not known at present. In one investigation, the surface area of pyrolysis char was found to be affected by the pyrolysis atmosphere and it was reported to follow the order,  $\text{He} > \text{Ar} > \text{N}_2$  though for unexplained reasons (Thakur, 1982).

#### CONCLUSIONS

When a New Mexico subbituminous coal was pyrolyzed in different nonreactive gases, the relative yields of volatile products were altered but the total carbon conversion remained almost unaffected. Acid treatment of the coal enhanced the production of  $\text{CO}_x$  gases but inhibited the formation of ethylene. This suggests that the in situ mineral matter might catalyze polymerization reactions involving oxygen functionalities in coal.

#### ACKNOWLEDGMENT

This research was supported by the U.S. Department of Energy under Contract No. ACO2-76CH00016.

## REFERENCES

- Budzioch, S., and Hawksley, P.G.W., Ind. Eng. Cham. Proc. Deg. Dev., 9, 521 (1970).
- Calkins, W.H., ACS Fuel Div. Prepr., 28, 85 (1983).
- Cypres, R., and Bettens, P., Tetrahedron, 31, 359 (1975).
- Franklin, H.D., Peters, W.A., and Howard, J.B., ACS Fuel Div. Prepr., 26 (37, 35, (1981).
- Kobayashi, H., Howard, J.B., and Sarofim, A.F., Proc. 16th Intl. Symp. on Comb., 411 (1977).
- Schafer, H.N.S., Fuel, 59, 302 (1980).
- Steinberg, M., and Fallon, P.T., Hydrocarb. Proc., 61, 92 (1982).
- Steinberg, M., Fallon, P.T., and Sundaram, M.S., "Flash Pyrolysis of Coal with Reactive and Non-Reactive Gases", Ann. Tech. Rep. to U.S. DOE, Rep. No. DOE/CH/00016-1402 (DE83011264), 1983.
- Sundaram, M.S., Steinberg, M., and Fallon, P.T., "Flash Hydropyrolysis of Coal for Conversion to Liquid and Gaseous Fuels: Summary Rport", DOE/METC/82-48 (1982).
- Sundaram, M.S., and Given, P.H., ACS Fuel Div. Prepr., 28(5), 26 (1983-1).
- Sundaram, M.S., Steinberg, M., and Fallon, P.T., ACS Fuel Div. Prepr., 28, 106 (1983-2).
- Sundaram, M.S., Steinberg, M., and Fallon, P.T., ACS Fuel Div. Prepr., 29(2), 129 (1984).
- Thakur, S., and Brown, L.E., Carbon, 20, 17 (1982).

TABLE 1. ANALYTICAL DATA FOR NEW MEXICO SUB-BITUMINOUS COAL

Ultimate Analysis	(wt % dry)	Ultimate Analysis	(dry)
Carbon	: 55.9	Volatile Matter	: 34.9
Hydrogen	: 4.3	Fixed Carbon	: 42.4
Nitrogen	: 1.1	Ash	: 22.8
Sulfur	: 1.0		
Oxygen (by diff.)	: 14.9		

TABLE 2. PHYSICAL PROPERTIES OF GASES AT 900°C AND ATM. PRESSURE

	Helium	Nitrogen	Argon
$\rho_g$ (gm/cc)	$2.80 \times 10^{-3}$	$1.96 \times 10^{-2}$	$2.81 \times 10^{-2}$
$\mu_g$ (CPS)	$5.78 \times 10^{-2}$	$5.56 \times 10^{-2}$	$7.29 \times 10^{-2}$
$K_g$ (Cal/cm <sup>2</sup> °K sec)	$9.78 \times 10^{-4}$	$1.68 \times 10^{-4}$	$1.13 \times 10^{-4}$
$C_p$ (Cal/Mole °K)	7.57	4.97	4.97

TABLE 3. FLASH PYROLYSIS OF NEW MEXICO SUB-BITUMINOUS COAL IN HELIUM ATMOSPHERE AT 50 PSI TOTAL PRESSURE

Particle Residence Time : 1.3 - 1.5 sec.

Percent Carbon Conversion to Designated Products

Run No.	Untreated Coal*		Acid-Washed Coal**	
	756	754	770	770
Temperature, °C	900	1000	900	1000
<u>Product Yields:</u>				
CH <sub>4</sub>	3.4	5.0	3.7	3.8
C <sub>2</sub> H <sub>4</sub>	4.9	2.3	3.4	1.7
BTX	1.5	2.2	2.4	1.9
CO	2.7	5.6	5.8	8.1
CO <sub>2</sub>	1.1	1.8	2.0	2.5
Total	13.6	16.9	17.3	18.0

\* Ash Content: 22.8%

\*\* Ash Content: 6.2%

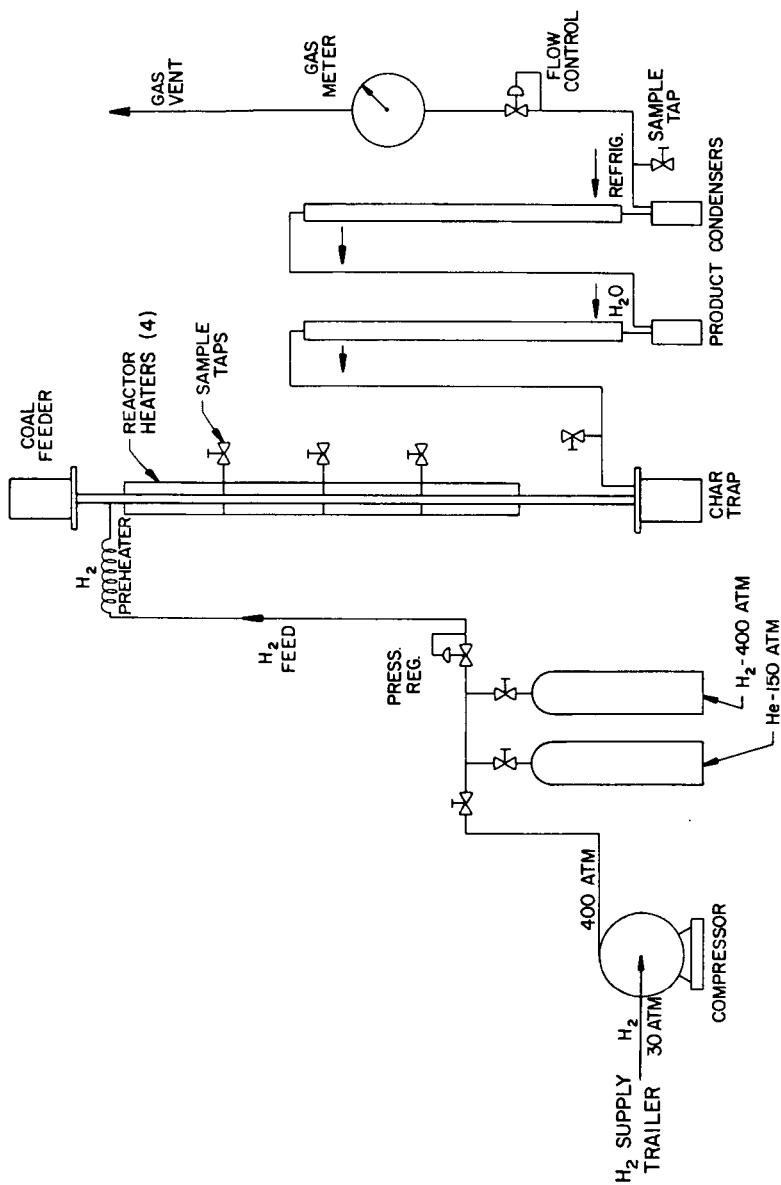


Figure 1. Schematic Representation of Pyrolysis Reactor.

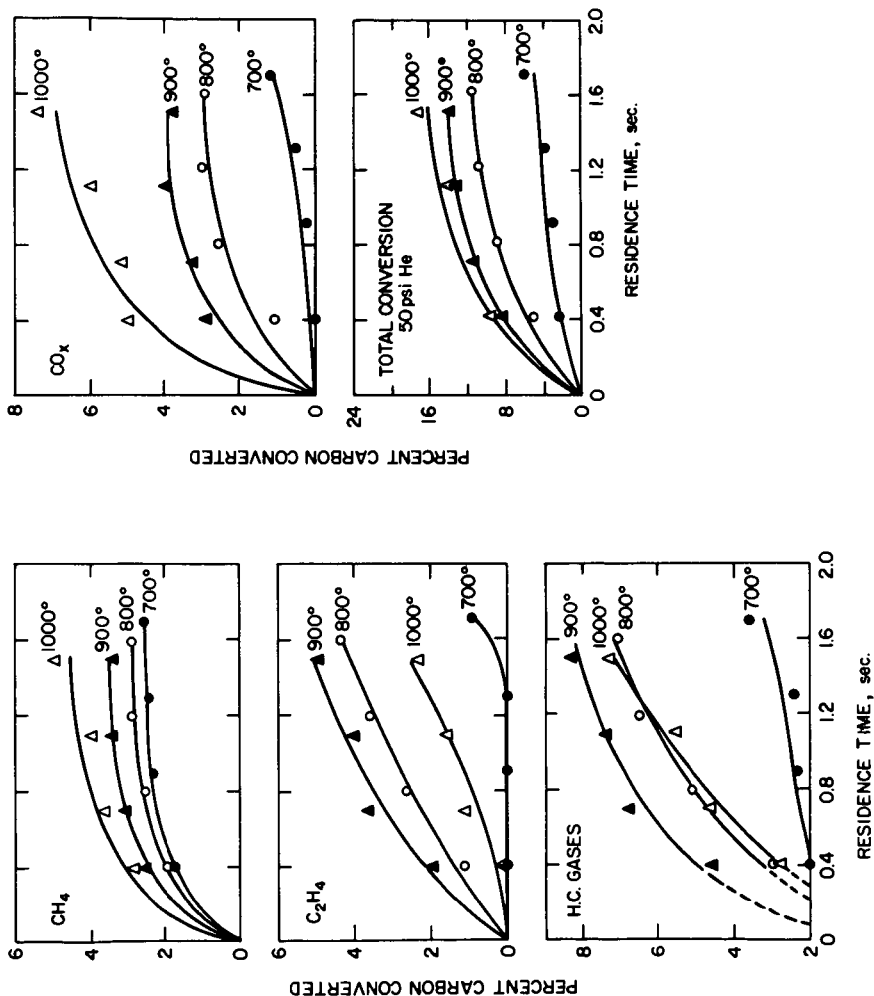


Figure 2. Flash Pyrolysis of New Mexico Sub-Bituminous Coal in Helium. Effect of Coal Particle Residence Time on Product Yields.

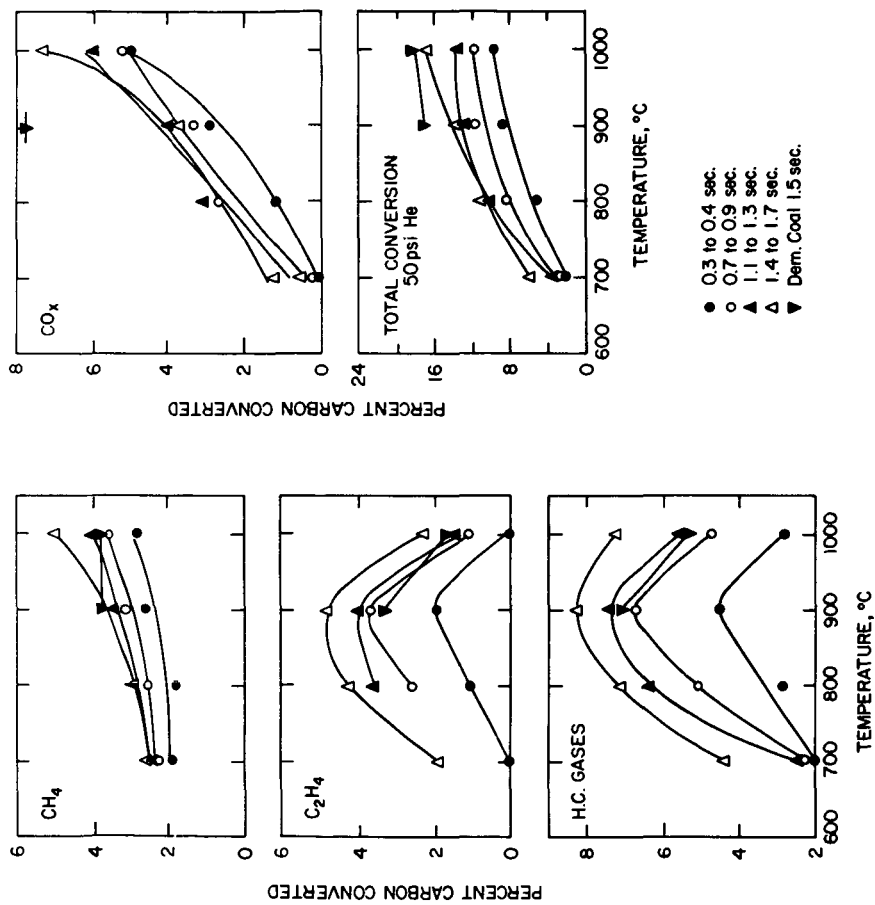


Figure 3. Flash Pyrolysis of New Mexico Sub-Bituminous Coal in Helium. Effect of Coal Temperature on Product Yields.



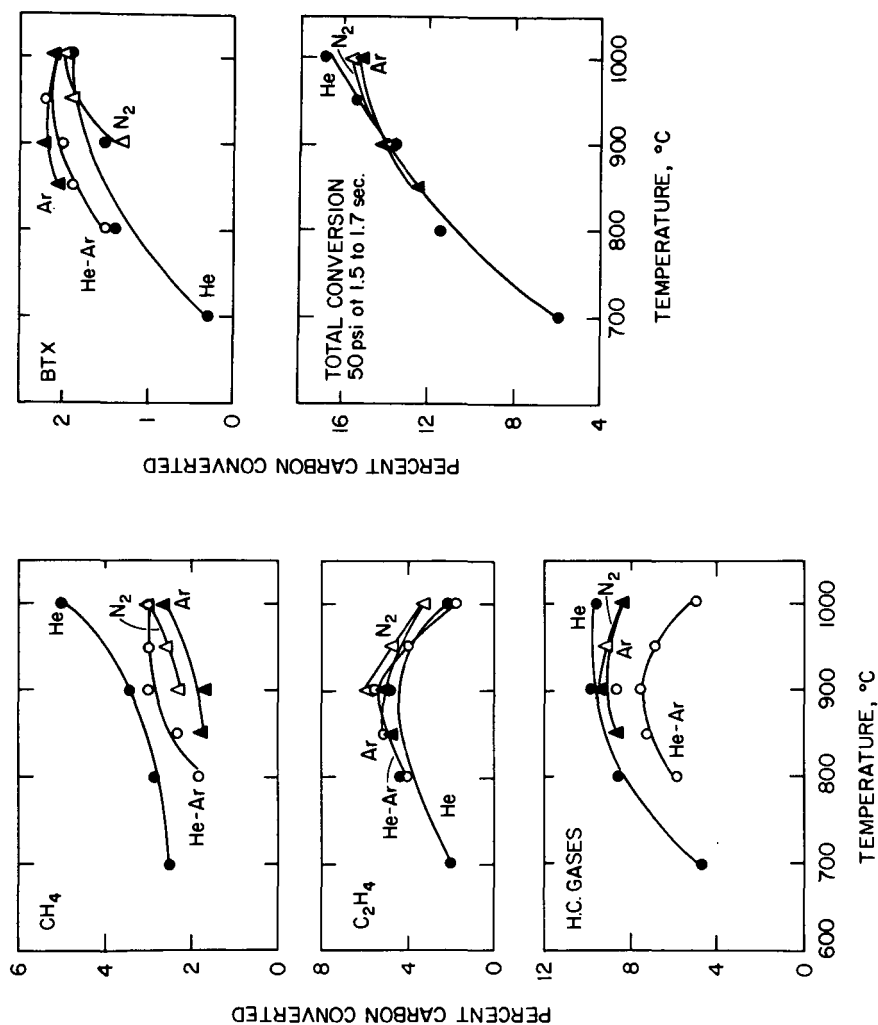


Figure 4. Flash Pyrolysis of New Mexico Sub-Bituminous Coal in He, N<sub>2</sub>, and Ar. Effect of Temperature on Product Yields.

EVOLUTION OF TARS AND GASES DURING  
DEVOLATILIZATION OF COAL IN A FIXED BED REACTOR

Gokhale, A.J., Vasudevan, T.V., and Mahalingam, R.  
Department of Chemical Engineering  
Washington State University  
Pullman WA 99164-2710  
ABSTRACT

Devolatilization of a subbituminous coal has been investigated in a laboratory fixed bed gasifier, by contacting the coal with a reactive gas mixture similar to that entering the devolatilization zone of a commercial gasifier. Two particle sizes of feed coal PSOC-241 (-2,+1 and -4,+3 mm) at a single reactor pressure (30 psig) were evaluated, in the temperature range 350 to 550 C. The tars evolved were characterized by capillary gas chromatography and gel permeation chromatography. The tar and gas evolutions are described in terms of concentration and pressure profiles, through considerations involving diffusion and pore structure. The overall devolatilization rates are evaluated through the unreacted shrinking core model.

INTRODUCTION

In coal gasification, the objective is to increase the calorific value of the original raw fuel by removing the unwanted constituent, viz., ash, and also to produce a fuel which is cheaper to transport, handle and utilize. The present discussion will be limited to a Lurgi type fixed bed coal gasifier. Figure 1 [1] shows a schematic diagram of a Lurgi fixed bed gasifier. At the present state of technology, reliable engineering data are available on the gasification and combustion zones and can be readily applied to the design of a fixed bed gasifier. This is not the case with the devolatilization zone and no systematic study of the devolatilization phenomenon in the range of operating parameters for a fixed bed gasifier, has been reported in literature. Thus, it becomes necessary to conduct experimental and modelling work on the devolatilization behavior of coals, as influenced by particle size, pressure, temperature and a reactive gas environment [2]. Such devolatilization studies on a laboratory scale fixed bed gasifier form the main objective of the work described here [3]. The operating conditions for these studies are selected based on whatever data are available in the literature on fixed bed gasifiers, the approach being to simulate the conditions existing in the devolatilization zone of a fixed bed gasifier. The composition of the reactive gases entering the reactor is approximated to that entering the devolatilization zone of a fixed bed gasifier in practice. The residence time for the flow of reactive gases through the coal bed is

selected to be maintained at 5 seconds for all the runs. The results obtained from the devolatilization of a subbituminous coal, PSOC-241, at 30 psig (0.308 MPa) reactor pressure are presented here. Two particle sizes of feed coal were evaluated: (-2,+1) mm and (-4,+3) mm. Reaction temperatures used were 350, 450 and 550 C. The H<sub>2</sub>/CO mole ratio in the feed gas was maintained at 2.5. The duration of a devolatilization run was 5, 10, 20 or 30 minutes.

## EXPERIMENTAL

A schematic representation of the experimental set-up is shown in Figure 2. The fixed bed reactor used for conducting the devolatilization studies was a 4.1 cm i.d. x 72 cm long 316 stainless steel tube provided with a wire mesh grid(0.25 mm opening), located 4 cm from the bottom, to hold the coal and char in the reactor. The reactor was placed vertically inside a furnace body. The graded coal sample was introduced into the reactor from the top under gravity by means of a Swagelok-type nut and feed pipe arrangement. Based on the reported gasification rates in a Lurgi type air blown gasifier [1,4] it was calculated that the entering gas environment in the devolatilization reactor should approximately have the following composition by volume:

Gas	H <sub>2</sub>	CO	CO <sub>2</sub>	CH <sub>4</sub>	N <sub>2</sub>	O <sub>2</sub>	Steam	Total
Volume%	18	7	14	4	25	2	30	100

Individual gases were drawn from compressed gas cylinders and mixed together with steam in a steam tube. The role of the steam tube was to convert feed water into steam, mix and preheat the steam-gas mixture to the desired devolatilization temperature. The steam tube was a 316 stainless steel tube(1.5 cm i.d. X 30 cm long), filled with inert catalyst support beads (3 mm diameter, alumina content=99% by wt. min; silica content =0.2% by wt. max; surface area=0.3 sq.m/gm; Norton Chemical Company) and was placed inside a small electric furnace. The feed gas stream entered the coal bed through a gas distributor located at the bottom of the reactor. A high pressure back pressure regulator after the condensers was used to maintain the desired pressure in the reactor system. The hot gases leaving the reactor from the top were laden with the tar generated inside the reactor; in order to quantitatively collect the tar and steam condensate, a double pipe heat exchanger was used as a condenser. Cooling water was circulated through the outer annulus and the tar laden gases were passed through the inner tube. Three such condensers (6mm i.d. X 40 cm long) were used in series to condense most of the tars. A high pressure glass fiber filter was used after the condensers as a final trap for the tar particles. After the completion of a run, methylene chloride was used as a solvent to wash down the condensers and the lines; dissolved tars and water phase were then collected from the bottom of the condensers. The yield of tar was measured in gm of tar per 100 gm of coal fed to the reactor. A Hewlett Packard 5840A gas chromatograph (with a 30 m long SE type 30 glass capillary column and a flame ionization detector (FID)) was used to quantitatively determine the species present in the tar samples. Area vs concentration curves for 30 standard species in methylene chloride were prepared. The species for standardization were selected

based on the published literature [5]. The molecular weights of tar samples were determined with a Waters Associates HPLC system. The columns used were 100 Å and 500 Å Ultrastaygel, made by Waters (columns: 7.8 mm i.d. X 30 cm long). The carrier solvent was tetrahydrofuran (THF) and a UV detector was used for absorption measurements. Polystyrene standards of known molecular weights were used to prepare a molecular weight vs elution volume curve.

The gas samples collected at 5, 10, 20 and 30 minutes from the sampling cylinders during the devolatilization run were analyzed for individual components. The permanent gases - CO<sub>2</sub>, CO, and O<sub>2</sub> - were analyzed on a CARBOSIEVE S3 column and the hydrocarbon gases were analyzed on a PORAPAK R column. Both the columns were fitted on to a Hewlett Packard gas chromatograph 5840A equipped with an ECD detector. A MOLECULAR SIEVE 5A column was used on a Carle gas chromatograph 111H, equipped with a TCD detector to analyse the H<sub>2</sub> in the gas samples. N<sub>2</sub> was obtained by difference. At the end of a 5, 10, 20 and 30 minute run, the reactor was quenched in water and the char was removed and weighed.

## RESULTS AND DISCUSSION

### Chemical Analyses of Coal Sample

Table 1 gives the proximate and ultimate analyses of the subbituminous coal, PSOC-241. The coal sample was ground to minus 200 mesh U.S. sieve size and equilibrated to room conditions. The analyses were performed by the Continental Testing and Engineering Company, Vancouver, B.C., Canada. From these analyses, the value for the ultimate yield of volatiles was obtained as 50.07% of coal, to be used later in the kinetic models. In order to determine the effect of the duration of the devolatilization run on the total weight loss, some selected devolatilization runs were conducted for durations of 60 minutes and it was observed that there was no additional weight loss after 30 minutes from the start of the run. At 550 C, the maximum weight loss occurred equal to 49% of feed coal sample weighing 100 gm.

### A. Devolatilization

#### Effect of Temperature

The principal effect of temperature on the devolatilization phenomenon is the decomposition of the organic structure of coal to yield water, hydrogen, methane, oxides of carbon and hydrocarbons. Consider the data on weight loss and tar/gas yields for the (-2,+1) mm and (-4,+3) mm size coal as shown in Tables 2 and 3. The weight loss is maximum at 550 C and is the least at 350 C. This confirms the earlier observation reported in literature about the nature of pyrolysis of

coal. At 350 C, the free moisture in the coal is removed and a small amount of tar is produced, which indicates that at this temperature, the majority of the coal chemical structure is still intact. At 550 C, most of the devolatilization is completed around 30 minutes as indicated by no additional weight loss during some runs conducted upto 60 minutes duration.

A plot of the distribution of molecular weights of tar samples is shown in Figure 3. From this it is clear that the fraction of evolving tar having molecular weight of about 300 units decreases as the run is continued. This can be attributed to the physical depolymerization of similar structures or the chemical cracking of a species to lower molecular weight as it is exposed to temperature for longer times.

The volumetric rate of evolution for all gases (Figures 4 and 5) shows a peak around 5 minutes from the start of a run and the rate then tapers off to zero around 30 minutes. In general, the rate of evolution for all gases is higher at higher temperature of reaction, i.e.  $550 > 450 > 350$  C, for all particle sizes.

#### Effect of Particle Size

The runs at 30 psig reactor pressure in the reactive gas atmosphere did not exhibit any difference in the total weight loss for the two particle sizes of coal studied, at 550 C. For the (-2,+1) mm coal, the yield of tar at 30 minutes increased with temperature as shown in Table 3; whereas for the (-4,+3) mm coal, the yield of tar showed a maximum at 450 C, as shown in Table 2. This can be attributed to the cracking of tar at 550 C, resulting in reduced yield of tar at 550 C as compared to that at 450 C. Figure 6 shows the total weight loss and tar yield data for the two particle sizes. The tar molecules have longer residence time within the larger coal particles and hence the former are amenable to dissociation by cracking. The next section shows how the internal pressure build-up and tar concentration within the coal particle also increase with the particle size.

#### B. Mathematical Models for Devolatilization

##### Single First Order Reaction Model

The earliest approach to the mathematical description of the devolatilization phenomenon was that of Pitt (1962) [6] who proposed a simple first order rate expression for the overall rate of evolution of volatiles:

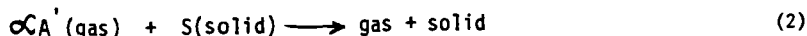
$$\frac{dV}{dt} = -kV \quad (1)$$

Anthony and Howard (1976) [7] have pointed out that this is an oversimplified description and the literature values for the activation

energy vary from as low as 4 kcal/mol to as high as 55 kcal/mol. This observation can be explained partly as being dependent on the type of the experimental set-up and operating variables, but mainly stems from the fact that when a series of parallel first order reactions are forced to be represented by a single reaction, very low values for the activation energy are bound to be obtained. In that respect, this representation is purely arbitrary but sometimes it has the ability of describing the observed rate process. Also, since there is often a limitation on analyzing the different chemical species quantitatively, such a simplified approach does have some merit. The values of activation energy and frequency factor for the subbituminous coal studied were: 11.4 kcal/mol and 0.554 1/sec for the (-2,+1) mm size coal; and 3.9 kcal/mol and 0.005 1/sec for the (-4,+3) mm size coal respectively. These indicate that although primary devolatilization involves organic reactions which have activation energy of the order of 50 kcal/mol, the first order approximation yields a very low overall value. Thus, it will be inappropriate to conclude from these low values that the devolatilization phenomenon is purely diffusion controlled. Of course there is a significant resistance to diffusion of volatiles through the ash layer, which will be evaluated later. A cross reference to the literature indicates that Shapatina et al., (1960) [8] have reported very low values for activation energy, viz., between 1 and 4 kcal/mol.

#### Unreacted Shrinking Core Model

This model was tested with the experimental data from the PSOC-241 subbituminous coal. The runs were conducted at 30 psig reactor pressure and in a reactive gas atmosphere. Two particle sizes of coal were used: (-4,+3) and (-2,+1) mm. The governing equation for this model is:



#### Fluid film resistance control

Equation (3) gives the necessary relation for fractional conversion of coal, for this case:

$$t/t^* = X, \quad t^* = R_p C_{SO} / 3k_{mA'} CA' O, \quad X = 1 - r_c^3 / R_p^3 \quad (3)$$

Based on equation (3),  $X$ , the fractional conversion of coal to volatiles was plotted against the reaction time. Figure 7 shows the data for (-2,+1) mm particle size, at 30 psig and reaction temperatures of 350, 450 and 550 C. The data points fall on straight lines, but since these lines do not pass through the origin, it is logical to assume that there is not significant resistance to diffusion in the gas film around the particles. Similar conclusions are arrived at for (-4,+3) mm size coal, as shown in Figure 8.

### Ash layer diffusion control

Equation (4) gives the necessary relation in this case:

$$t/t^* = [1 - 3(1-X)^{2/3} + 2(1-X)] , t^* = \propto R_p^2 C_{so} / 6 D_{eA} C_{A'O} \quad (4)$$

Based on equation (4),  $[1 - 3(1-X)^{2/3} + 2(1-X)]$  was plotted against time, as shown in Figures 9 and 10. It appears that there is some resistance to diffusion within the ash layer and this will be examined further through equation (6).

### Chemical reaction control

Equation (5) gives the necessary relation in this case:

$$t/t^* = [1 - (1-X)^{1/3}] , 1/3 t^* = R_p / K_s C_{A'O} \quad (5)$$

Based on equation (5),  $[1 - (1-X)]$  was plotted against time, as shown in Figures 11 and 12. These curves also indicate that there could be some reaction control on the progress of the coal devolatilization. This will also be further examined through equation (6).

### Ash layer diffusion versus chemical reaction control

Equation (6) gives the modified version of equation (4) as:

$$1/3 t/t^* = [1 - (1-X)^{1/3}]^2 , t^* = \propto C_{so} R_p^2 / 2 C_{A'O} D_{eA} \quad (6)$$

$\ln[1 - (1-X)]$  was plotted against  $\ln[t]$  as shown in Figures 13 and 14. Since the slopes of these lines are greater than two, it can be concluded that the ash layer offers the most of the resistance to the progress of coal devolatilization. This is further confirmed from Figure 15, where  $r_c/R_p$  is plotted against  $t/t^*$  as suggested by Levenspiel (1972) [10]. From this figure it is seen that the curve shows a point of inflection on the 135 degree dotted line (joining the points (0,1) and (1,0)), indicating that ash layer controls the progress of the reaction.

It must be pointed out at this stage that the above model is only 'phenomenological' and does not take into account the actual intrinsic chemical reactions. The numerous chemical species involved in devolatilization have been lumped into one hypothetical specie for the sake of mathematical simplicity and due to lack of detailed information on chemical structure. Thus this model is more qualitative in nature for this type of gas-solid system; it, however is quite informative.

### Intraparticle Diffusion Model for Subbituminous Coal [11]

This model has been described by Gavalas (1982) [11]. It describes the concentrations of tar and gas inside the coal particle as a function of radial position, temperature, pressure and experimental

yields of tar and gas. The principal equations describing this model are:

$$\frac{dC_G}{dr} = -\frac{\beta}{\mu} \frac{C_G}{D_{GK}} \frac{dp}{dr} - \frac{r}{3} \left[ \gamma_G \left( \frac{x_T}{D_{GT}} + \frac{1}{D_{GK}} \right) - \gamma_T \frac{x_G}{D_{GT}} \right] \quad (7)$$

$$\frac{dC_T}{dr} = -\frac{\beta}{\mu} \frac{C_T}{D_{TK}} \frac{dp}{dr} - \frac{r}{3} \left[ \gamma_T \left( \frac{x_G}{D_{GT}} + \frac{1}{D_{TK}} \right) - \gamma_G \frac{x_T}{D_{GT}} \right] \quad (8)$$

The analytical solution of these equations gives the dimensionless pressure build-up as:

$$W(0) - 1 = \frac{(-1 + A)}{A} \left\{ \left[ 1 + \frac{A_{at}(1 + \delta \xi_T) B}{(1 + A)^2} \right]^{1/2} - 1 \right\} \quad (9)$$

where

$$\xi = r/a, \quad V_i = C_i / (p_0 / RT), \quad (i = G, T), \quad W = p / p_0$$

$$\delta = \gamma_T / \gamma_G, \quad \xi_T = D_{GK}^* / D_{TK}^*, \quad A = 3\beta p_0 / \epsilon \mu D_{GK}^*$$

$$B = RTa^2 \gamma_G / \epsilon p_{at} D_{GK}^*$$

The parameter 'A' in this model depends on bulk pressure outside the particles and on the temperature of the reaction. The parameter 'B' depends on the square of the particle radius. The differential equations describing the variation of tar and gas concentrations within the coal particle were solved on ACSL (Advanced Computer Simulation Language) and the following plots were made: The dimensionless pressure build-up, within the coal particle is plotted against the parameter A in Figure 16. This plot indicates that the pressure build-up is higher for larger particles. A plot of tar mole fraction within the particle against the radial position is shown in Figure 17. A plot for the tar concentration at the center of the coal particle with respect to parameter A (which is a measure of the total pressure on the system), is shown in Figure 18. This figure shows that for the pressure range investigated in the runs (30 - 375 psig) [3], the tar concentration is less sensitive to pressures upto 300 psig. Also, from these plots it can be seen that at a given pressure, the tar concentration increases with particle size.

## CONCLUSIONS

The coal devolatilization experimentation reported herein involves realistic sizes of coal, and a reactive gas environment, as postulated to be present in the devolatilization zone of a Lurgi fixed bed gasifier, operating at a given pressure and temperature. No such work has been reported on a macrosample of coal and hence the results from the present work should be more meaningful. The conclusions to be drawn from the results presented are:



1. Devolatilization of coal is influenced by the operating variables.
2. The peak in molecular weight for the tar generated is around 300.
3. A first order approximation of the overall rate of devolatilization does not adequately describe the phenomenon.
4. The resistance to diffusion of tar out of the coal particle in the ash layer constitutes a major controlling mechanism in coal devolatilization.
5. Pressure build-up and tar concentration inside the coal particle both increase with particle size.

#### ACKNOWLEDGEMENT

This work has been carried out as part of a United States Department of Energy contract # DE-AC21-82MC 19208.

#### NOTATION

$a$	radius of coal particle, cm
$A$	dimensionless parameter
$A'$	component in the gas phase
$B$	dimensionless parameter
$C_{A'0}$	bulk concentration of $A'$ , gmol/cm <sup>3</sup>
$C_G$	concentration of gas evolved, gmol/cm <sup>3</sup>
$C_{S0}$	initial concentration of S, gmol/cm <sup>3</sup>
$C_T$	concentration of tar evolved, gmol/cm <sup>3</sup>
$D_{eA'}$	effective diffusivity of $A'$ , cm <sup>2</sup> /sec
$D_{GT}$	binary diffusivity, cm <sup>2</sup> /sec
$D_{iK}^*$	Knudsen diffusivity of the $i$ th component, cm <sup>2</sup> /sec
$D_{iK}$	effective Knudsen diffusivity of the $i$ th component, cm <sup>2</sup> /sec
$E$	activation energy, kcal/mol
$k, k_s$	reaction rate constant, 1/sec
$k_0$	frequency factor, 1/sec
$k_{mA'}$	gas film mass transfer coefficient, cm/sec
$p$	pressure, atm
$p_0$	total bulk pressure, atm

$P_{at}$	atmospheric pressure, atm
$r$	radial position within the coal particle, cm
$r_c$	radius of unreacted core, cm
$R$	gas constant, cal/gmol. K
$R_p$	radius of coal particle, cm
$S$	component in the solid phase
$t, t^*$	time, sec
$T$	temperature, K
$V$	yield of volatiles, gm
$w$	fractional pressure build-up
$x_T$	mole fraction of tar evolved
$x_G$	mole fraction of gas evolved
$X$	fractional conversion
$\infty$	stoichiometric coefficient
$v_T$	rate of evolution of tar, gm/gm.sec
$v_G$	rate of evolution of gas, gm/gm.sec
$\beta$	permeability of coal
$\mu$	viscosity of gaseous mixture, cm <sup>2</sup> /sec
$E$	voidage

## REFERENCES

- [1] Denn, M., J. Wei, W.C. Yu and R. Cwiklinski, 'Detailed simulation of a moving-bed gasifier', a research report prepared for the Electric Power Research Institute, AP-2576 (1982).
- [2] Talwalkar, A.T., 'A topical report on coal pyrolysis', prepared for the Morgantown Energy Technology Center of the U.S. Department of Energy, WV, Contract # DE-AC21-82MC19316 (1983).
- [3] Gokhale, A.J., 'Devolatilization behavior of coals in a fixed bed reactor', Ph.D. dissertation, Chemical Engineering, Washington State University, Pullman, WA (1985).
- [4] Probststein, R.F. and R.E. Hicks, 'Synthetic Fuels', McGraw-Hill Book Company, N.Y. (1982).
- [5] Gangwal, S.K. and D.G. Nichols, 'Coal conversion and the environment', U.S. Department of Energy- Battelle NorthWest Symposium, Richland, WA, DOE-Symp. Series 54 (1981).
- [6] Pitt, G.J., 'The kinetics of the evolution of volatile products from coal', Fuel, 41, 267 (1962).
- [7] Anthony, D.B. and J.B. Howard, 'Coal devolatilization and hydrogasification', A.I.Ch.E.J., 22, 625 (1976).
- [8] Shapatina, E.A., V.A. Kalyuzhnyi and Z.F. Chukhanov, 'Technological utilization of fuel for energy: thermal treatment of fuels (1960)', reviewed in the B.C.U.R.A. Monthly Bulletin, 25, 285 (1961).
- [9] Wen, C.Y., 'Noncatalytic heterogeneous solid fluid reaction models', Industrial and Engineering Chemistry, 9, 34-54 (1968).
- [10] Levenspiel, O., Chemical Reaction Engineering, John Wiley & Sons Inc. (1972).
- [11] Gavalas, G.R., Coal Pyrolysis, Vol 4, Elsevier Scientific Publishing Company (1982).

Table 1. Chemical Analyses of Coal Sample

Subbituminous Coal (PSOC-241)			
Proximate Analysis		Ultimate Analysis	
% Moisture	10.81	% Carbon	66.17
% Ash	6.24	% Hydrogen	4.53
% Volatiles	39.26	% Nitrogen	1.09
% Fixed Carbon	43.69	% Chlorine	0.01
	-----	% Sulphur	0.39
	100.00	% Ash	6.25
	-----	% Oxygen	21.54
Btu/lb	9941		-----
free swelling index = 0			100.00
			-----

Table 2. Volatiles, Tar and Gas Yields: PSOC-241 coal, (-4,+3)  
mm; reactor @ 30 psig; reactive gas + steam mixture

Total Volatile Yield, gm				
min	30	20	10	5
550 C	43.0	41.7	38.0	36.3
450 C	36.4	34.9	29.8	26.7
350 C	26.0	22.2	20.7	15.7
-----				
Tar Yield, gm				
min	30	20	10	5
550 C	1.75	1.07	0.77	0.31
450 C	2.17	0.89	0.80	0.74
350 C	0.75	0.53	0.45	0.28
-----				
Gas Yield, gm				
min	30			
550 C	13.7			
450 C	18.3			
350 C	6.3			

Table 3. Volatiles, Tar and Gas Yields: PSOC-241 coal, (-2,+1)  
mm; reactor @ 30 psig; reactive gas + steam mixture

Total Volatile Yield, gm				
min	30	20	10	5
550 C	42.9	42.2	37.1	35.8
450 C	37.0	36.8	33.5	31.9
350 C	24.0	23.8	23.4	21.5
-----				
Tar Yield, gm				
min	30	20	10	5
550 C	1.90	1.3	0.85	0.64
450 C	1.47	1.17	1.05	0.55
350 C	0.82	0.65	0.4	0.3
-----				
Gas Yield, gm				
min	30			
550 C	19.7			
450 C	7.3			
350 C	N.A.			

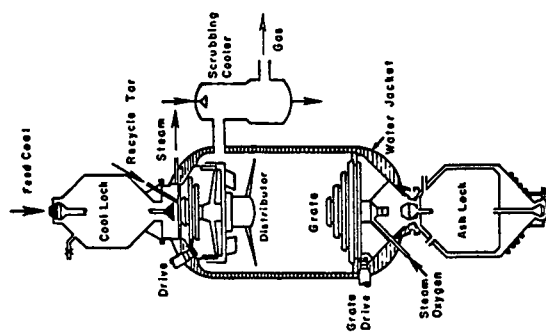


FIG. 1 - LARGE PRESSURIZED GASIFIER [1]

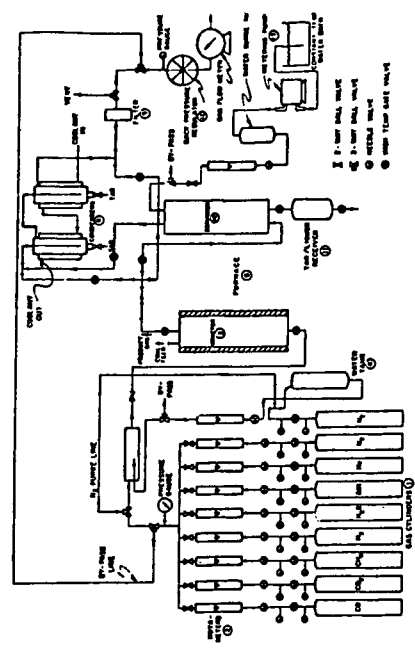


FIG. 2 - EXPERIMENTAL SET-UP [3]

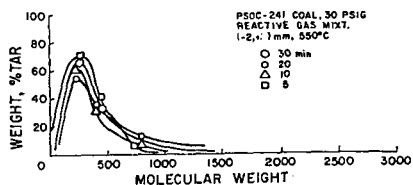


FIG. 3 - MOLECULAR WEIGHT DISTRIBUTION OF TAR

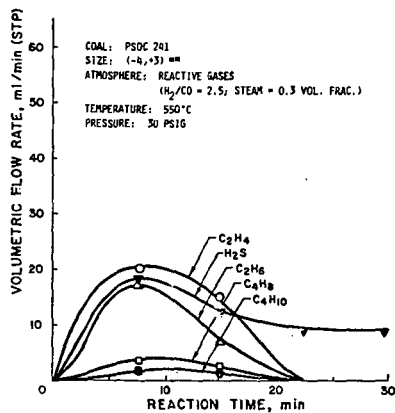


FIG. 5 - GAS EVOLUTION RATE VS. TIME  
(HYDROCARBON GASES EXCL. METHANE AND INCL.  $H_2S$ )

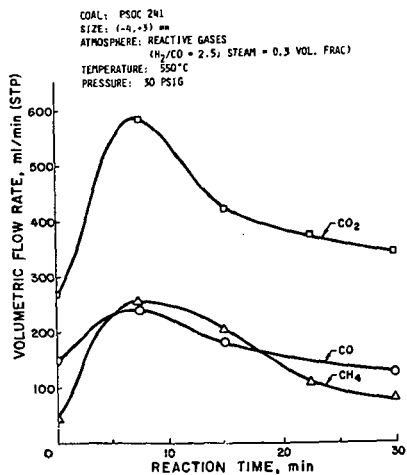


FIG. 4 - GAS EVOLUTION RATE VS. TIME  
(PERMANENT GASES INCL. METHANE)

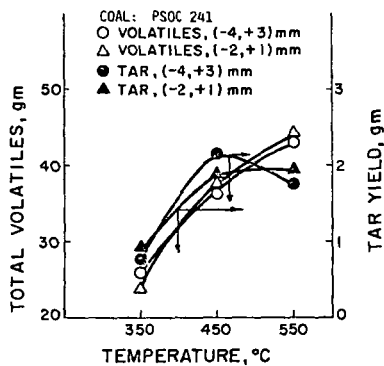


FIG. 6 - EXPERIMENTAL DATA

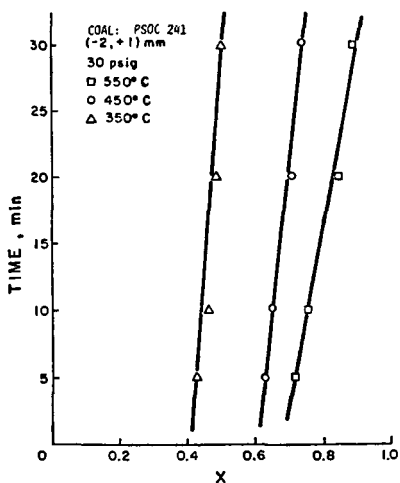


FIG. 7 - FLUID FILM RESISTANCE CONTROL, TYPE I

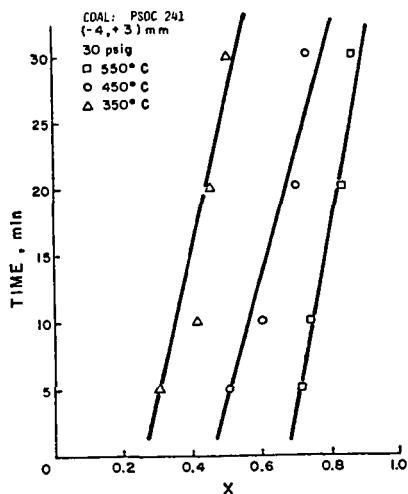


FIG. 8 - FLUID FILM RESISTANCE CONTROL, TYPE I

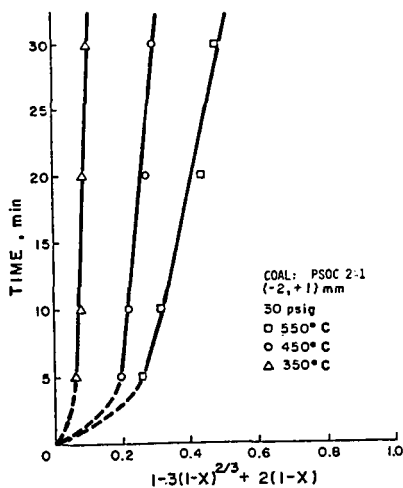


FIG. 9 - ASH LAYER RESISTANCE CONTROL, TYPE II

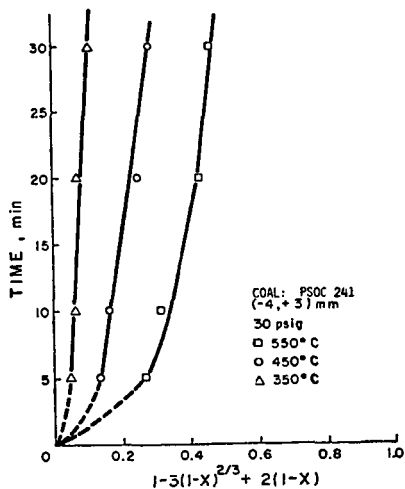


FIG. 10 - ASH LAYER RESISTANCE CONTROL, TYPE II

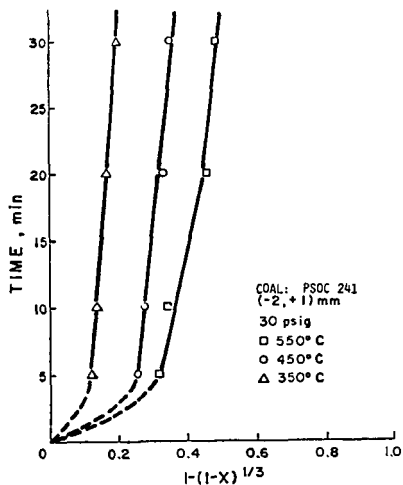


FIG. 11 - CHEMICAL REACTION CONTROL, TYPE III

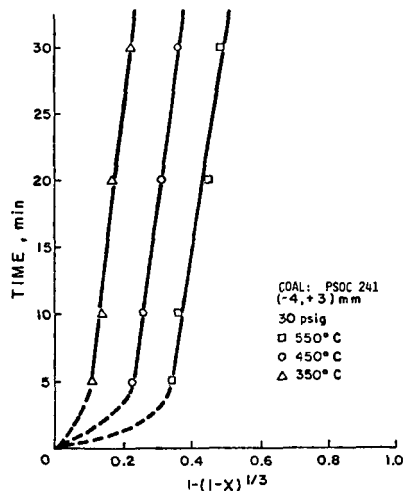


FIG. 12 - CHEMICAL REACTION CONTROL, TYPE III

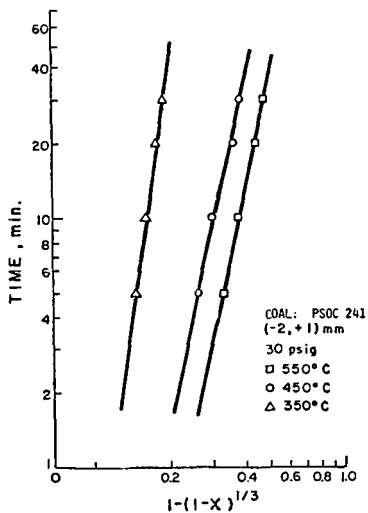


FIG. 13 - ASH LAYER RESISTANCE CONTROL, TYPE II'

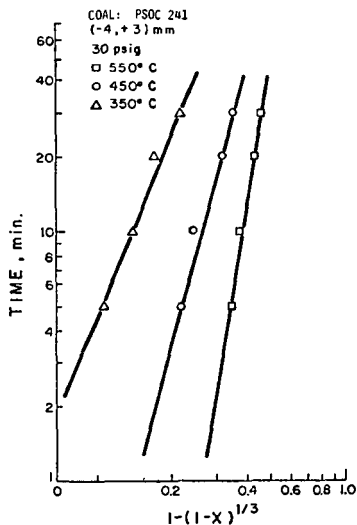


FIG. 14 - ASH LAYER RESISTANCE CONTROL, TYPE II'



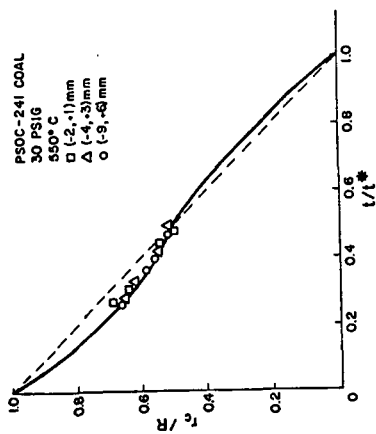


FIG. 15 - UNREACTED SHRINKING CORE MODEL

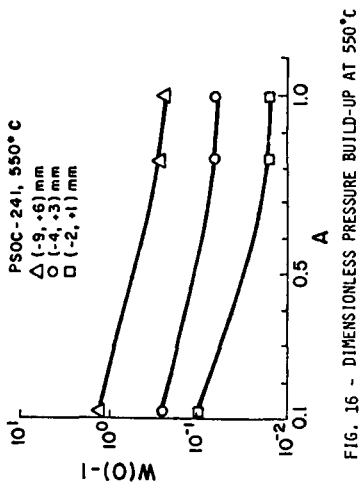


FIG. 16 - DIMENSIONLESS PRESSURE BUILD-UP AT 550°C

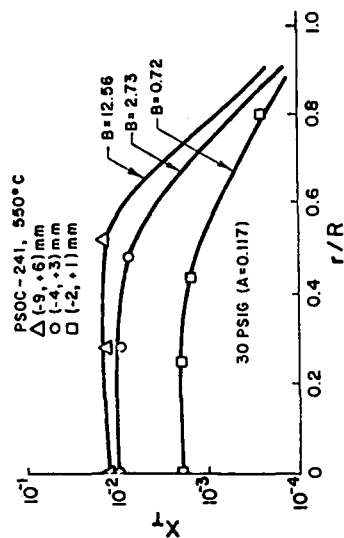


FIG. 17 - TAR MOLE FRACTION INSIDE COAL PARTICLE

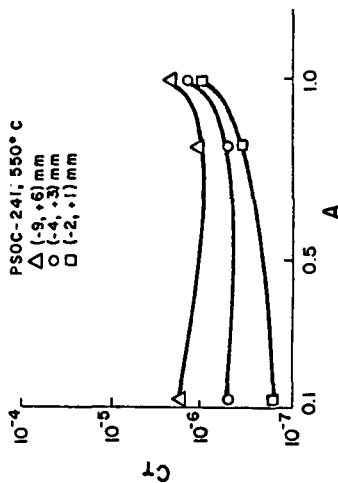


FIG. 18 - TAR CONCENTRATION AT THE CENTER OF COAL PARTICLE

## HYDROXYL FUNCTIONAL GROUP DETERMINATION IN COAL TARS AND PYROLYSIS OF O-METHYLATED COAL

Susan A. Cannon, C. Judith Chu, Robert H. Hauge and John L. Margrave

Department of Chemistry, William Marsh Rice University  
P. O. Box 1892, Houston, Texas 77251

### INTRODUCTION

The objective of this investigation was to study the hydroxyl functional groups of tar molecules and to determine their involvement in the mechanism of tar evolution during coal pyrolysis processes. Strong similarities exist between the infrared spectra of coals and their respective tars suggesting that the tar molecules are similar in structure to the parent coal and contain similar functional groups characteristic of the parent coal.(1) Clarification of the structure of tar molecules should lead to a better understanding of the parent coal structure. Our main concern has been centered on the identification of tar hydroxyl functional groups and the determination of their role in the mechanism of tar evolution. Whether hydrogen bonding through the hydroxyl functional groups is an important factor in tar evolution will be investigated through the pyrolysis studies of methylated coals. The process of methylation replaces most of the phenolic and carboxylic hydrogens in coal with methyl groups.(2,3) Thus hydrogen bonding via the phenolic or carboxylic hydrogens should be largely eliminated.

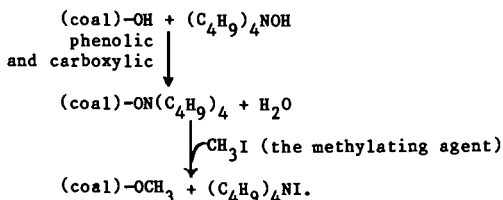
The experiments were designed so that tar molecules and other gaseous products of coal pyrolysis could exit the reaction zone rapidly and be trapped with inert nitrogen gas on a cold matrix surface. Matrix isolation studies of tar molecules produce better resolved FTIR spectra than those in a coal matrix, making structural characterization of the tar molecules a more definite possibility.

### EXPERIMENTAL

The Rice University multisurface matrix isolation apparatus was used in the pyrolysis studies of four different ranks of coal and their respective methylated products. The four coal samples studied were Pittsburgh bituminous, Illinois #6, Rawhide sub-bituminous and Texas lignite. The samples were ground and sifted under inert nitrogen atmosphere to prevent oxidation. Only the -500 mesh size coal particles were used in the experiments.

The matrix isolation FTIR apparatus possesses 60 deposition surfaces which are useful for pyrolysis studies over a wide range of temperatures. Small changes occurring as a result of variations in reaction temperature can be readily detected. Gaseous pyrolysis products including the tar molecules were trapped in a nitrogen matrix at 12°K. One surface was used for every 40-100°C increment rise in temperature over a 10 minute trapping period. The frozen matrices were later analyzed off-line with an integrated IBM-FTIR spectrometer. Tar evolution was observed to occur within the same temperature range (150-600°C) for the four coals studied. Therefore the experimental temperature range studied was from room temperature to approximately 620°C. Detailed descriptions of the MI-FTIR apparatus and the pyrolysis reactor can be found elsewhere.(4,5)

Methylation of the coal samples was performed according to the procedures described by R. Liotta in "Selective Alkylation of Acidic Hydroxyl Groups in Coal".(2) The general reaction procedure may be described using the following equations:



Only -500 mesh coal particles were used in our methylation reactions. The experimental procedure for the pyrolysis of the methylated coals was identical to that of the original coal in order to determine if methylation in any way alters the pyrolysis behavior of the original coal.

## RESULTS AND DISCUSSION

### Determination of Hydroxyl Functional Groups in Tar

Hydroxyl functional group determination in coals has been undertaken both spectroscopically (6) as well as through a combination of chemical and spectroscopic means. (7) The spectroscopic method of hydroxyl determination relied on the measurement of the broad infrared absorption region between  $3600\text{--}2000\text{ cm}^{-1}$ . This broad absorption range was complicated by the presence of KBr water absorptions as well as absorptions attributed to hydrogen bonded OH. The second method of hydroxyl functional determination involved the measurement of intensities of infrared bands (carbonyl stretching at  $1770$  and  $1740\text{ cm}^{-1}$ ) assigned to products of acetylation reactions of coal. Both methods involved indirect determination of OH functional groups in the parent coal matrix. Studies of coal pyrolysis processes using matrix isolation techniques have the advantage of actually isolating the individual tar molecules and other gaseous products in an inert matrix. Isolation of the individual tar molecules in an inert gas matrix at  $12^\circ\text{K}$  produced well resolved infrared spectra not observed in the FTIR spectra of tars in a coal matrix, thus making structural characterization of the tar molecules highly feasible. The matrix isolated tar should also be free of hydrogen bonding thus facilitating the identification of hydroxyl functional groups.

Figure 1 shows the matrix isolated FTIR spectra of the gaseous pyrolysis products of Pittsburgh bituminous from r.t. to  $621^\circ\text{C}$ . The evolution of tar molecules was initiated at temperatures as low as  $130^\circ\text{C}$  and continued until maximum evolution was reached at  $470^\circ\text{C}$ . Absorptions characteristic of tar molecules were broad bands at  $3000\text{--}2800\text{ cm}^{-1}$  due to CH stretching, and  $1550\text{--}1100\text{ cm}^{-1}$  due to CH bending and CO stretching. Study of the OH stretching region of the matrix isolated tar spectra should provide information concerning the hydroxyl functional groups present in the tar molecules. The presence of water OH stretching modes and absorptions due to water-tar complexes in this region complicated the identification of tar OH functional groups. Co-deposition of water ( $0.5\text{ H}_2\text{O}/100\text{ N}_2$ ) with tar molecules resulted in noticeable increases in absorptions due to water-tar complexes. This is shown in Figure 2 which compares the matrix isolated FTIR spectra of Illinois #6 tar molecules with the results obtained from tar-water co-deposition experiments. As can be seen, two distinct broad absorptions at  $3626.5$  and  $3580.9\text{ cm}^{-1}$  remained unaffected by the addition of water molecules. These were assigned to tar hydroxyl functional groups. The OH stretching frequencies of all four of the coal tar molecules studied are shown in Figure 3. Considerable amounts of hydroxyl functional groups were found in the tars of the two higher rank coals, Pittsburgh bituminous and Illinois #6, with Illinois #6 possessing greater amounts of hydroxyl functional groups. Considerably less hydroxyl absorption was observed for the two lower rank coal tars, Rawhide sub-bituminous and Texas lignite. The

observation of less hydroxyls for the lower rank coals is in accordance with lower rank coals possessing less aromatic character.

Comparison of OH stretching frequencies of phenol, 2-naphthol and cyclohexanol in nitrogen matrix with those of matrix isolated tar is shown in Figure 4. The broad tar OH absorption at  $3626.5\text{ cm}^{-1}$  compares favorably with the OH stretching frequencies of phenol and 2-naphthol but not with cyclohexanol. In general, the less acidic alcoholic hydroxyls have OH absorptions at frequencies higher than  $3630\text{ cm}^{-1}$  (OH stretching frequency of nitrogen matrix isolated methanol is  $3664\text{ cm}^{-1}$ ). The peak at  $3626.5\text{ cm}^{-1}$  is thus assigned to a phenolic hydroxyl. One also concludes that alcoholic hydroxyls are not present in matrix isolated tar molecules. The less intense tar OH absorption at  $3580.9\text{ cm}^{-1}$  is still under investigation. Since this absorption is lower in frequency than the phenolic OH, it is probably due to a more acidic OH functional group than the phenolic hydroxyl. Possibilities are carboxylic hydroxyls or phenolic hydroxyls with an adjacent thiophene group (hydroxy-benzothiaphene).(8)

#### Pyrolysis of O-Methylated Coal

The role of hydroxyl functional groups in the mechanism of tar evolution is of great interest. Hydrogen bonding through the hydroxyl functional groups could be an important intermolecular bond in the structure of coal. If hydrogen bonding through the hydroxyl functional groups were the predominant factor in determining the volatility of the coal (determined by the ease of tar evolution and percent weight loss), then replacing the hydroxyl hydrogens with methyl groups should eliminate this hydrogen bonding and make the coal more volatile. Hydroxyl functional groups can also undergo water elimination reactions to form new C-O-C cross linkages. The formation of these new cross linkages would also act to reduce the volatility of coal and thus increase the tar evolution temperature. Methylation of the coal would eliminate the formation of these new cross linkages. More tar might also be evolved due to the increased volatility and decreased decomposition of the O-methylated coal.

If the evolution of tar during coal thermal decomposition occurred primarily through the cleavage of weak linkages such as methylene linkages, then methylation should not effect the volatility of the coal or the tar evolution temperature.

Slow pyrolysis studies of methylated coals were performed to determine if O-methylation in any way has altered the pyrolysis behavior of the original coal. Figure 5 shows the matrix isolated FTIR spectra of the pyrolysis products of methylated Pittsburgh bituminous from r.t. to  $604^{\circ}\text{C}$ . Comparison of pyrolysis results of the methylated coal (Figure 5) with those of the original coal (Figure 1) showed several differences indicative of coal structural changes after methylation. Tar evolution temperature has been reduced by approximately  $150\text{--}200^{\circ}\text{C}$ , indicating a more volatile coal after methylation. This was observed for all four ranks of coal studied. An increase of approximately 10% volatility was also observed for all four coals after methylation. Comparisons of the matrix isolated tars with their respective methylated tars are shown in Figure 6. For all four coals, O-methylation has changed the relative intensities of  $\text{CH}_3$  to  $\text{CH}_2$  groups in the tar molecules in favor of greater  $\text{CH}_3$  absorptions as is to be expected since  $\text{CH}_2$  groups have replaced all hydroxyl hydrogens in the methylated tar. Phenolic hydroxyl absorptions at  $3626.5\text{ cm}^{-1}$  are also absent in the methylated tar molecules.

The increased volatility and the lowering of tar evolution temperature of the O-methylated coal suggest that methylene linkages are not involved in the mechanism of tar evolution. Our results from the pyrolysis of O-methylated coal suggest two possible mechanisms of tar evolution. The first involves breaking only hydrogen bonding of the hydroxyl groups as tar is evolved. A second mechanism envisions the formation of new cross linkages through decomposition of the hydroxyl groups at lower temperature. The temperature at which tar evolves in then set by the temperature at which the new cross linkages decompose. Isotopic enrichment studies are currently in progress to assist in distinguishing between the above mechanisms.

In any case, the large increase in volatility of the tar component of all four coals is quite remarkable and suggests a common bonding mechanism in all coals.

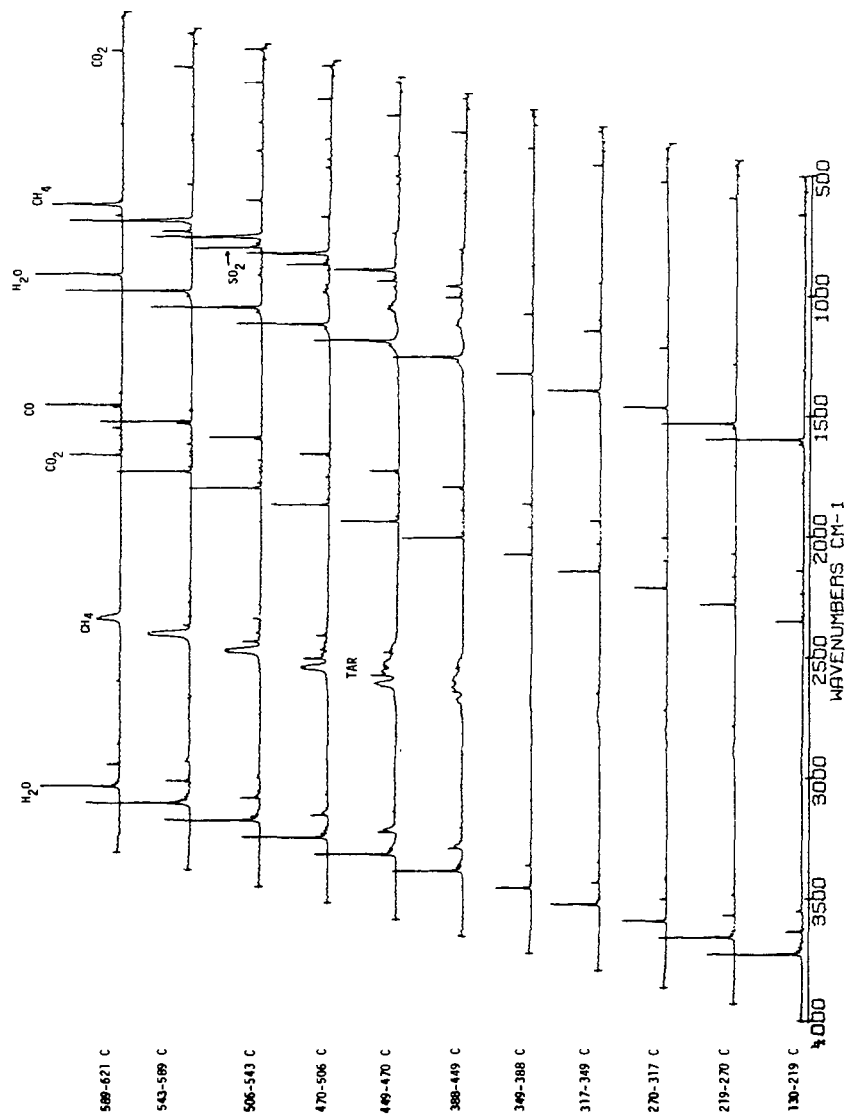
#### ACKNOWLEDGEMENT

The authors gratefully acknowledge support of this work by the Department of Energy, Morgantown, West Virginia. We also thank Exxon Research and Engineering at Baytown, Texas for supplying our coal samples.

#### REFERENCES

1. Solomon, P.R., "Relation Between Coal Structure and Thermal Decomposition Products", Coal Structure, Adv. in Chem. Series, 192, eds. Corbaty, M.L. and Ouchi, K., Am. Chem. Soc., p. 95, 1981.
2. Liotta, R., "Selective Alkylation of Acidic Hydroxyl Groups in Coal", Fuel, vol. 58, 724, 1979.
3. Liotta, R. and Brons, G., "Coal. Kinetics of O-Alkylation", J. Am. Chem. Soc., 103, p. 1735-1742, 1981.
4. C.J. Chu, L. Fredin, R.H. Hauge and J.L. Margrave, "Studies of Pyrolysis Processes of Illinois #6 and its Tar Using Matrix Isolation FTIR Spectroscopy", High Temperature Science, 1984, in press.
5. C.J. Chu, L. Fredin, R.H. Hauge and J.L. Margrave, "Pyrolysis Studies of Illinois #6 and its Tar using Matrix Isolation FTIR Spectroscopy", ACS, Div. Fuel Chemistry, Preprints, 29, (2), 49, 1984.
6. Solomon, P.R., and Carangelo, R.M., "FTIR Analysis of Coal. 1. Techniques and Determination of Hydroxyl Concentrations", Fuel, vol. 61, p. 663, 1982.
7. Snyder, R.W., Painter, P.C., Havens, J.R., and Koenig, J.L., "The Determination of Hydroxyl Groups in Coal by Fourier Transform Infrared and  $^{13}\text{C}$  NMR Spectroscopy", Applied Spectroscopy, vol. 37, no. 6, p. 497, 1983.
8. Spiro, C.L., Wong, J., Lytle, F.W., Greegor, R.B., Maylotte, K.H., and Lampson, S.H., "X-ray Absorption Spectroscopic Investigation of Sulfur Sites in Coal: Organic Sulfur Identification", Science, vol. 226, p. 48, 1984.

Figure 1: Pittsburgh Bituminous Slow Pyrolysis



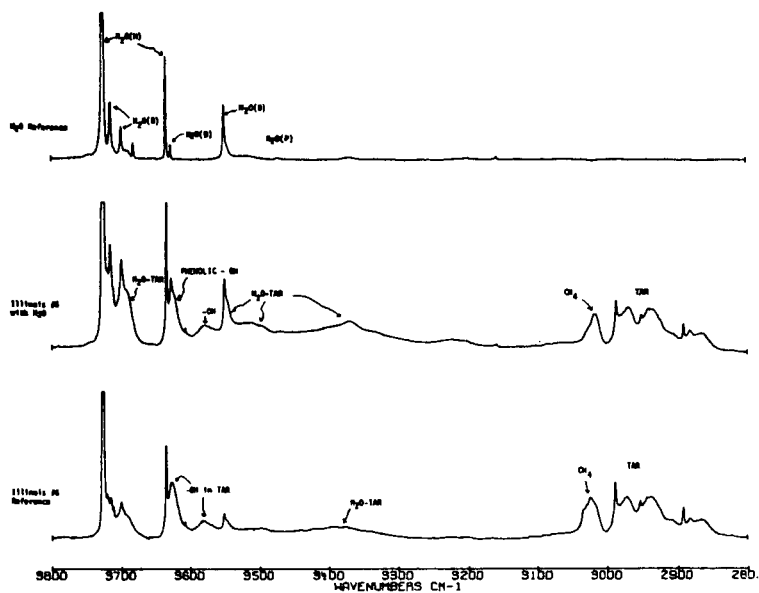


Figure 2. Co-Deposition of Illinois #6 Tar and  $H_2O$  in  $N_2$  Matrix

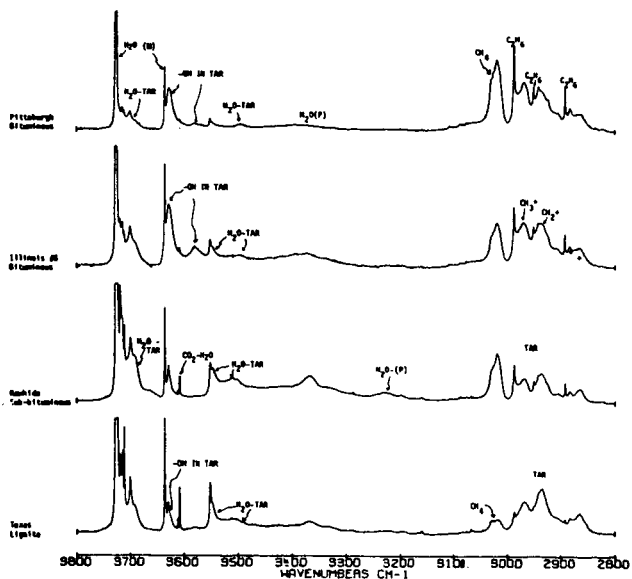
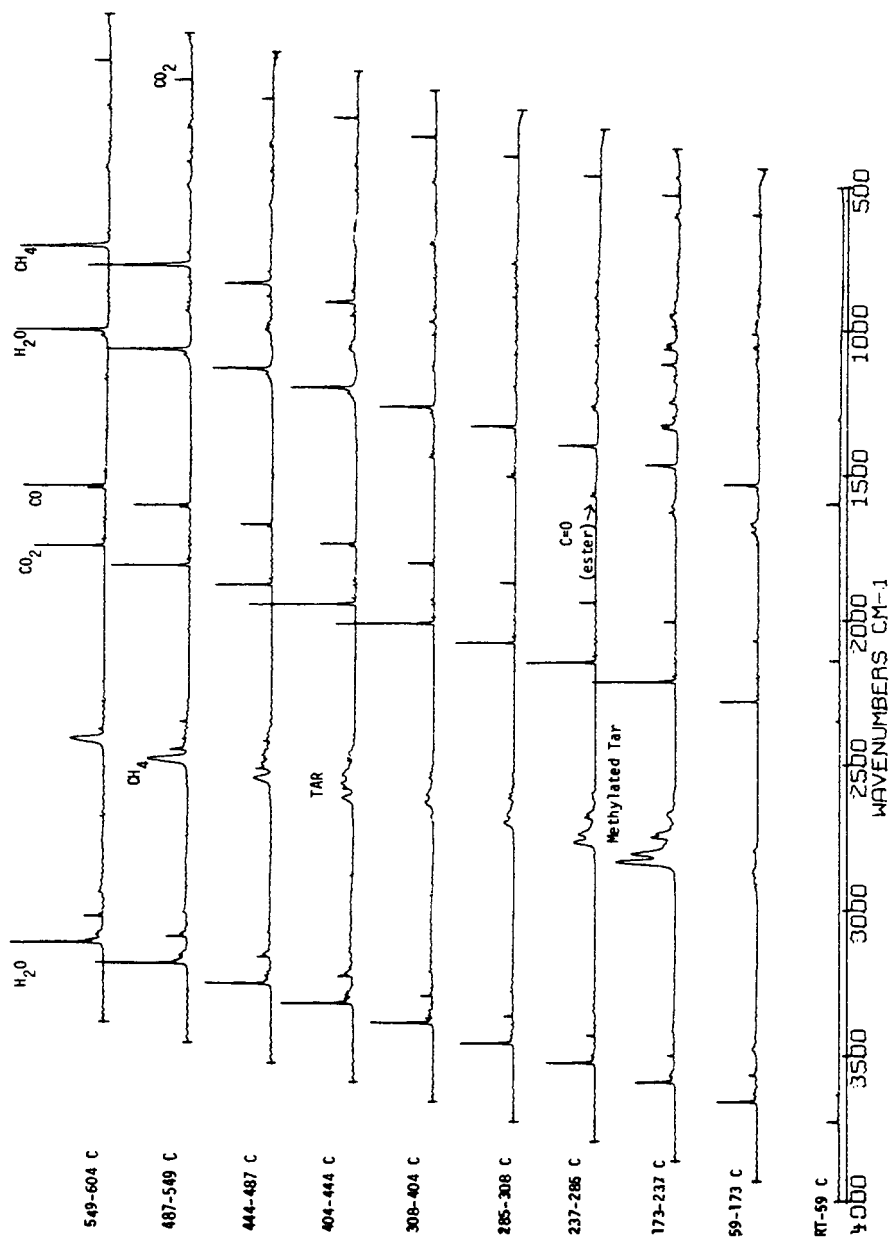


Figure 3. MI-FTIR Spectra of Four Coal Tars

Figure 5: O-Methylated Pittsburgh Bituminous Slow Pyrolysis





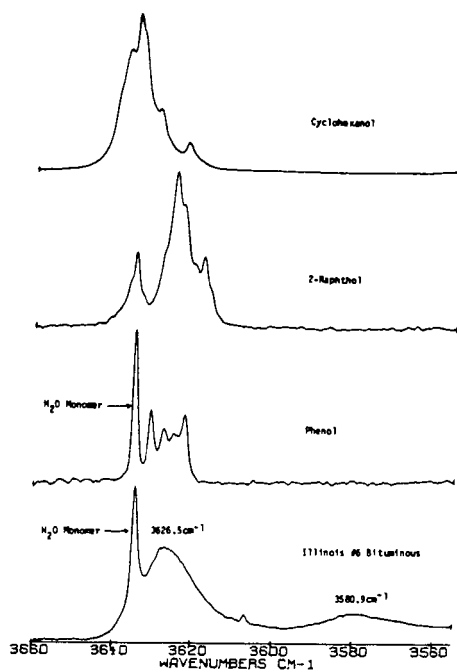


Figure 4. Comparison of Hydroxyl Stretching Frequencies in  $N_2$  Matrix

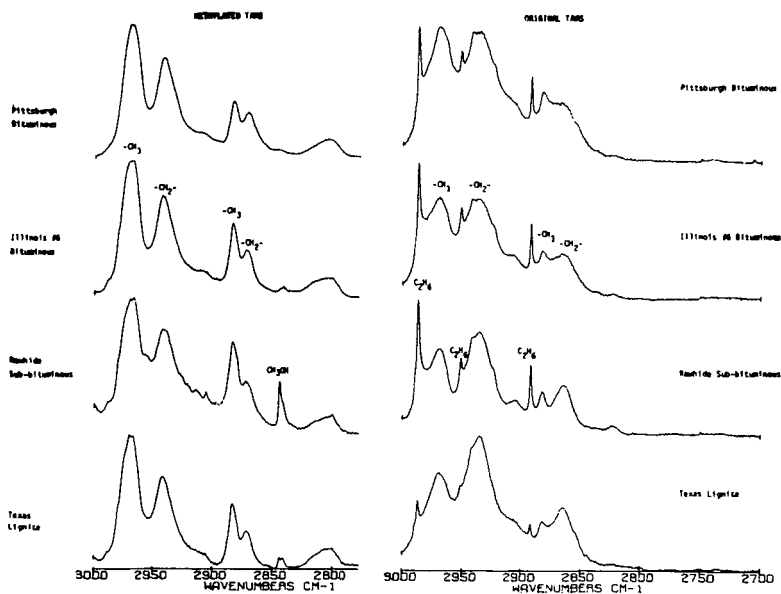


Figure 6. Comparison of CH Stretching Region of Tar and O-Methylated Tar

## VERY RAPID COAL PYROLYSIS

Peter R. Solomon, Michael A. Serio, Robert M. Carangelo and James R. Markham

Advanced Fuel Research, Inc., 87 Church St., East Hartford, CT 06108 USA

## INTRODUCTION

Considerable controversy exists concerning the rate of coal pyrolysis. For example, at 800°C, rates reported in the literature (derived assuming a single first order process to define weight loss) vary from a low of around  $1 \text{ sec}^{-1}$  (1-4) to a high near  $100 \text{ sec}^{-1}$  (5-8), with values in between (9,10). The discrepancies cannot be explained by differences in sample composition because experiments in which coal rank alone was varied typically show no more than a factor of 5 variation in rate (11). One problem is that if the higher rate is correct, then any experiment which attempts to obtain isothermal rate data at 800°C must heat the coal in a time short compared with the pyrolysis time, i.e. on the order of  $100,000^\circ\text{C}/\text{sec}$ . At higher temperatures the heating rate to obtain isothermal data must be even faster. But for most experiments at temperatures of 800°C or higher, calculations of heat up rates for pulverized coal suggest that if the higher rate is correct, pyrolysis will typically be occurring during heat up, even assuming zero heats of reaction. Under these circumstances it is necessary to know the coal particle temperature to derive kinetic rates. Coal particle temperatures during rapid pyrolysis have not generally been measured.

In an attempt to resolve this controversy, a new pyrolysis experiment was designed which provided for high heating rates and a geometry which simplified the prediction of particle temperatures (12). It used a small diameter electrically heated tube into which coal and helium carrier gas were injected. The reaction distance was varied by moving the electrode positions. The particle temperatures and the particle residence times were calculated from the measured tube wall temperatures and the gas flow rates, respectively. Even allowing for the uncertainty in these estimated values, the rates measured at asymptotic tube temperatures of 700°C, 800°C and 900°C agreed with the highest reported rates and were inconsistent with the low rates.

These heated tube experiments therefore, lent support to the high rate advocates but suffered in conclusiveness as did the other experiments in this temperature range in not having a direct measure of particle temperature (2-10,12) and reaction time (2,5,7-9,12). The tube reactor experiment was modified to eliminate these drawbacks. Temperatures of the solids were determined at the tube exit using FT-IR emission and transmission spectroscopy (13,14) and the transit time for the coal was measured using photo transistors at the top and bottom of the tube. Temperature measurements were also made inside and outside the tube with a thermocouple.

Measurements were made of the amount and composition of the tar, char and gases evolved as a function of the measured reaction time and temperature. We focus on primary pyrolysis, during which the initial rapid weight loss, the evolution of tar and lighter hydrocarbons, and the disappearance of the aliphatic (or hydroaromatic hydrogen) in the coal/char all happen at similar rates. For a 200 x 325 mesh fraction of a dry North Dakota lignite in a 115 cm long tube having an asymptotic tube temperature of 800°C, primary pyrolysis was completed in a period of 14 milliseconds based on the mean particle residence times. The extent of axial dispersion was small. During this period, the maximum coal temperature was increasing from 600 to 740°C. These data, as well as data obtained at equilibrium tube temperatures of 700°C and 935°C, are in agreement with the high pyrolysis rate originally reported (12).

This paper describes the experimental apparatus and measurement technique, and presents the results for a lignite at temperatures between 600°C and 935°C. The results are compared to the predictions of a pyrolysis model and to the literature data. Reasons for the discrepancies are discussed.

## EXPERIMENTAL

The reactor is illustrated in Fig. 1. It consists of a 0.2" i.d. Inconel 702 tube which is heated electrically. Coal entrained in cold carrier gas is injected at the top of the tube. The coal is fed using a previously described entrainment system (7,8). The coal-gas mixture enters the heated section of tube and heats rapidly. The heat transfer rate is large because of the small tube diameter, the high thermal conductivity of the helium carrier gas, and the fact that the particles collide with the hot walls of the tube. After a variable residence time, the reacting stream is quenched in a water cooled section of tube. The product collection train consists of a cyclone to separate the char followed by a collection bag to collect the gas, tar and soot. The gas from the bag is analyzed by FT-IR and the solids and liquids are collected on the bag surface and in a filter.

### Temperature Measurements

The temperature of the gas-coal mixture and outside tube temperature has been measured with a thermocouple. At constant current, the tube will reach an equilibrium temperature such that the external power loss by radiation and convection is equal to the electrical power input. With gas and coal flowing in the tube, the tube is initially cooler than the equilibrium temperature, since heat is used to raise the temperature of the gas and coal. The heat absorbed by the coal and gas can be calculated from the measured tube temperature. When the reactants reach the equilibrium temperature, the outside of the tube reaches a constant temperature.

The results for one set of measurements with coal present are presented in Fig. 2. The measurements include: a) thermocouple measurements inside and outside the tube; b) FT-IR measurements at the center of the gas/solid stream 0.75 cm below the end of the hot tube; c) thermocouple measurements at the position of the FT-IR measurement; and d) thermocouple measurements inside a water cooled tube attached to the hot tube to measure the quenching rate.

Heat transfer calculations suggest that inside the tube the thermocouple reads 10-20°C higher than the gas due to radiation from the wall. The bead temperatures at the FT-IR focal point was calculated to be lower by approximately the same amount outside the tube. The measurements of the external tube wall temperature are low due to heat loss from the thermocouple bead to the surroundings. However, the maximum effect of this error can be determined by comparing the asymptotic values of the external wall temperature and the internal gas temperature, which come to thermal equilibrium for sufficiently long distances. The knowledge of this temperature difference along with the apparent wall temperature can be used to determine the error at each measured wall temperature, which gets lower as the tube gets cooler. For example, in the 800°C experiment, the corrections ranged from +35°C at 800°C to +10°C at 500°C when using a 0.002" diameter thermocouple bead. The corrections scaled with bead diameter, as expected. The wall profile shown in Fig. 2 has been corrected for radiation errors. The temperature difference between the outside and the inside of the tube was calculated to be negligible.

Measurements of coal particle temperatures were made using FT-IR emission and transmission spectroscopy. As described in a previous publication (13), the transmittance measurement is used to determine the total emitting surface of the coal particles so that a normalized emission, (emission/(1-transmittance)) can be compared

in both shape and amplitude to a theoretical black-body. The FT-IR measurement can provide a direct measurement of the coal particle temperature during heat up. A simple case is illustrated in the insert of Fig. 2. For this case sufficient time was allowed for the coal to reach the asymptotic tube temperature of 935°C (1208 K) and for pyrolysis to have occurred. For a grey-body (such as shown here for char) the shape of the normalized emission spectrum gives the temperature and the amplitude gives the emittance. The normalized emission spectrum is in good agreement with a theoretical black-body at 1190 K with an amplitude corresponding to an emissivity of 0.9. The measured temperature is in excellent agreement with the tube temperature as a 10°C drop in temperature is expected between the end of the tube, and the measuring point at 0.75 cm below the end. The measurement of temperature before and during pyrolysis is not as simple, since for the size of coal particles used here only specific bands (corresponding to the absorbing bands in coal) provide sufficient absorbance for the spectral emittance to reach 0.9. Then, only these regions can be used to compare to the black-body. The measurement technique, the problems encountered, their solutions and the results are discussed in another paper at this meeting (14). The results at 800°C are presented as the triangles in Fig. 2.

Calculations of the temperature of the gas, the thermocouple bead, and the coal particles were performed given the tube wall temperature as a boundary condition. The calculations assume the temperature dependent heat capacity for coal derived by Merrick (15) which agrees with the measurements of Lee (16), an average spectral emittance of 0.5 for the 200 x 325 mesh particles of coals in agreement with recent FT-IR measurements (14) and zero heat of reaction. The calculations assume convective heat transfer between the tube wall and gas and between the gas and coal particle or thermocouple bead and radiative heat transfer between the wall and the coal particle or thermocouple bead. The heat transfer coefficient between the wall and the gas, which was determined from the Sieder-Tate equation (17), was validated by equating the electric power input to the power radiated and convected outside the tube (determined from the tube temperature and emissivity) plus the heat transfer to the gas inside the tube.

In order to match the measured particle temperatures in the early part of the tube (e.g., < 50 cm at 800°C) it was necessary to include a term to account for heat transfer due to collisions of relatively cold particles with the hot walls. This phenomenon, known as wall-contact heat transfer, has been described by Boothroyd (18). A heat transfer coefficient was defined by analogy to a conventional convective coefficient, i.e.  $Q_{wc} = h_{wc} (T_{wall} - T_{coal})$ .

The predicted results (lines in Fig. 2) are in good agreement with the measured temperatures. The agreement between the actual thermocouple measurements and the predicted values is a good indication that the corrected wall temperature profile is accurate. The measured particle temperatures are slightly below the predicted values in agreement with a 10°C drop from the tube end to the measuring point. Possible values for the heat of reaction were considered. A value of 250 K cal/gram of total volatile material results in a predicted temperature which is too low although the shape of the temperature vs distance curve matched the FT-IR data better than the zero heat of reaction case. Additional data are needed to determine the possible values for the heat of reaction and the chemical reactions to which it applies (e.g. tar loss, overall weight loss, etc.).

#### Particle Residence Time

The heated tube reactor was modified for particle velocity measurements. The passage of a pulse of coal through the system was measured for each electrode position by recording signals from photo transistors mounted on glass sections at the top and bottom of the reactor tube on a dual channel oscilloscope. Photographs of the oscilloscope traces allow an assessment of the mean particle residence time and the extent of axial dispersion.

A technique was developed where short, well-defined pulses could be introduced by using an electrically activated solenoid to inject the contents of a tube containing the coal charge and gas at 10 psig. In addition, the reactor was set up over the FT-IR bench in preparation for hot tests with temperature measurements. This configuration has the added advantage of using a laser from the FT-IR beam as the light source for the lower photo transistor, which improved the signal to noise significantly. It also eliminated the lower glass tube which tended to be obscured with tar after a few hot runs. The only problem was a slight spreading of the particle stream as it emerged from the tube, which meant that the measured dispersion was in excess of what actually occurred in the tube.

The photographs enabled an assessment of the particle residence time and of the particle dispersion, which impacts on the kinetic analysis. Some representative traces from cold and hot tests are shown in Fig. 3. Figure 3a indicates a transit time of approximately 60 milliseconds for the coal in the cold tube. The average transit time in the cold experiments was determined from a number of measurements to be 56 milliseconds. The particles, therefore, travel at about 80% of the gas velocity of 28 m/sec. Figures 3b-3d show the transit time when the tube is heated over increasing distances (75, 100 and 115 cm). The transit time is reduced to about 32 milliseconds when 115 cm is heated (Fig. 3d).

The extent of axial dispersion was small and was typically almost symmetrical, which would lead to a slight (approximately 10%) underestimation of the rate constant. It was neglected in the analysis of results for this paper.

Data are presented in Fig. 4 for the mean particle transit times for hot experiments. The hot data are adjusted so that the transit time in the cold part of the tube is not included. This was done by subtracting the heated length from the distance between the detectors (125 cm) and using the cold data to determine the transit time which should be subtracted from the observed transit time for the hot experiment. The adjusted data then reflect the amount of time it takes to traverse the hot zone.

The particle residence time data definitely indicate that the particles are accelerating in the hot experiments at close to the same rate as the gas except for a slowdown in the region where pyrolysis begins (~50 cm). This is reasonable in light of the small value of the characteristic drag time, 1.5 milliseconds, (which indicates the relaxation time for a particle for a step change in gas velocity) for the size fraction used in the hot experiments (~200, +325 mesh) (17). The data were fit by a model which assumes the particles are moving at 80% of the average gas velocity until primary pyrolysis is 1% complete, at 40% of the gas velocity between 1% and 75% pyrolysis, and back to 80% of the gas velocity after pyrolysis is 75% completed. The reason for the slow down during pyrolysis is not yet clear but is probably associated with evolution of gas from the coal or swelling which has been observed for this lignite under these extremely high heating rates.

Additional confirmation of the particle velocities was obtained from comparing the particle feed rate with the density of particles exiting the tube determined by FT-IR transmittance measurements, where the density of particles in the focus is inversely proportional to their velocity.

## RESULTS

The results are shown in Fig. 5 for isothermal tube temperatures of 700°C, 800°C, and 935°C. Figures 5a-c present the weight % char, tar, and gas (the sum of measured individual gas species) as a function of the reaction distance. The mass balance was between 96.5 and 101%.

The measured and calculated particle temperatures and times as functions of distance are shown in Figs. 5d-f. The calculated particle temperatures match FT-IR temperature data obtained at 800°C and 935°C and the particle times match transit time data obtained at 800°C. Confidence can be placed in the calculated temperature at 700°C because the calculations use the same heat transfer coefficients which give the validated calculations at 800°C and 930°C. The time calculations at 700°C and 935°C employ the same relative velocity between gas and particles that was measured at 800°C. For all three temperatures, pyrolysis occurs during particle heat up, even though heating rates are in excess of 40,000°C/sec.

The solid lines in Figs. 5a-5c are generated using a previously presented pyrolysis theory (8) which calculates the evolution of individual species using a distributed activation energy of the form introduced by Anthony et al. (1) for each species. The rates for tar and hydrocarbon gases are shown in Fig. 6. The gas rate is five times higher than the rate for the same species in Ref. 8. This is to account for the factor of 5 higher rates observed for lignites compared to bituminous coals, discussed in (11). An error was discovered in the calculation of tar evolution in Ref. 8. The rate in Fig. 6 is for the corrected calculation. As a further comparison, the reciprocals of the times required to achieve 63% tar yield are plotted (solid circles) in Fig. 6 as a function of the reciprocal of the average absolute temperature during this period. A single pyrolysis experiment at 600°C gave a rate constant of  $6.3 \text{ sec}^{-1}$ . These data fall close to the line defining the tar rate.

The theory is in excellent agreement with the data. At all three temperatures the observed weight loss is a result of rapid evolution of tar and slower evolution of the gases. The increase in total weight loss with increasing final temperature is the result of gas evolution (primarily CO and H<sub>2</sub>O) due to loss of tightly bound functional groups.

For comparison with previous weight loss data, a single first order weight loss has been calculated (dashed lines) using a rate  $k = 4.28 \times 10^{14} \exp(-55,400/RT) \text{ sec}^{-1}$ . This is one half  $k_{\text{tar}}$  (see Fig. 6) and represents a compromise between the rapid evolution of tar and the slower rate for gas evolution. The single first order rate does not fit the data as well. It gives a steeper weight loss than is observed and the yield does not increase with temperature. Given these limitations inherent in a single first order model, the theory is in good agreement with the data.

## DISCUSSION

The measured rate for primary pyrolysis weight loss is therefore higher than the high rates originally measured by Badzioch and Hawksley (5). The activation energy of 55 kcal is what is expected from thermochemical kinetics for ethylene bridges between aromatic rings and agrees with pyrolysis rates for model compounds and polymers where these bonds are the weak links (19). The rate is also in agreement with data obtained at much lower temperature ( $\sim 450^\circ\text{C}$ ) at a heating rate of 30°C/sec.

What are the reasons for the discrepancies between these rates and rates reported by many other investigators (1-4,9,10,20-22)? There are two reasons for the discrepancies, interpretation of the rate and knowledge of the particle temperatures. Consider first the grid experiments. The data and analysis by Anthony et al. (1) illustrates the first reason. They presented two kinetic interpretations for their data, a single first order process and a set of parallel processes with a Gaussian distribution of activation energies. Both interpretations fit the data using Arrhenius expressions for kinetic rates. The single first order process which uses an activation energy of 11 kcal/mole requires two parameters, while the distributed rated model which uses a mean activation energy of 56 kcal/mole requires a third parameter to describe the spread in rates. Niksa et al. (3) used a single first

order model with its low activation energy. Suuberg et al. (6) rejected the low activation of the two parameter fit as being chemically unreasonable, and settled for a less accurate fit but with appropriate activation energies. The problem is that a variety of interpretations may provide good fits to the data over a limited range of temperature and heating rates. The grid experiments do not provide sufficient information to choose between the possibilities, some of which lead to highly inaccurate extrapolations. It is only by performing additional experiments at higher heating rates and therefore higher pyrolysis temperatures that the ambiguities can be eliminated. The data presented in this paper indicate that the distributed activation energy model was the better choice to produce  $k \approx 100 \text{ sec}^{-1}$  at  $800^\circ\text{C}$ . Additional discrepancies are probably due to inaccurate assumptions regarding particle temperatures which have not been measured in the grid experiments.

If the high activation energy rate is the better choice, what about the data of Kobayashi et al. (2) which give a rate on the order of  $1 \text{ sec}^{-1}$  at  $800^\circ\text{C}$  and only  $100 \text{ sec}^{-1}$  at  $1700^\circ\text{C}$ ? There was no direct measurement or confirmation of the particle temperature in these experiments. Instead, an assumption was made that the particles were at the gas temperatures at the longest residence time (200 milliseconds) for a nominal furnace temperature of 1260 K where a weight loss of 26 wt. % was observed. It was assumed that the 26 wt.% point was always reached at a temperature of 1260 K in the higher temperature experiments. These assumptions were used to determine a parameter,  $\Theta$ , defined as the ratio of the momentum shape factor to the energy shape factor. The particle temperature calculations were performed assuming: a value of  $\Theta = 3$ , although a value closer to unity would be more likely; a smaller value of particle heat capacity than is now believed (15,16); a higher value for the absorption of radiation than recent data would indicate for small coal particles (13) and zero heat of pyrolysis. The resulting calculation gives a heatup time of approximately 18 milliseconds at 1260 K, in conflict with the observation that no weight loss has occurred at 70 milliseconds. Furthermore, the initial assumption is in conflict with the data presented in this paper which suggest that had the coal been at 1260 K for even 10 milliseconds, substantially more than 26% weight loss would have occurred. We believe that the particle temperatures at which pyrolysis was occurring were significantly overestimated by Kobayashi et al. (2), leading to underestimation of the kinetic rates.

There are other data which do not agree with our rates and where two color temperature measurements were made (20-22). These measurements suggest a high solids temperature. But these measurements may indicate the temperature of a hot cloud of soot surrounding the particle or hot spots on the particle surface and not reflect the temperature in the region of the particle where pyrolysis is occurring. It is also true that the assumption of constant emissivity used in interpretation of two-color data can be erroneous in some cases (13,14).

#### CONCLUSION

An experiment has been performed to determine pyrolysis rates for a lignite in which both the transit time and temperature of particles have been measured. The measured rate for weight loss is greater than  $100 \text{ sec}^{-1}$  at  $800^\circ\text{C}$ . The results suggest a reinterpretation of heated grid data which have given rates much lower than this at comparable temperatures. The results also suggest that lower rates obtained in entrained flow reactors were due to heat transfer limitations.

#### ACKNOWLEDGEMENT

This work was supported by the Morgantown Energy Technology Center of the U.S. Department of Energy under Contract No. DE-AC21-81FE05122, Holmes A. Webb, Contractor Monitor.

## REFERENCES

1. Anthony, D.B., Howard, J.B., Hottel, R.C. and Meissner, H.P., 15th Symposium (Int) on Combustion, The Combustion Institute, Pittsburgh, PA pg. 1303 (1975) and Anthony, D.B., Sc.D. Thesis, M.I. T., Dept. of Chemical Engineering, Cambridge, MA (1974).
2. Kobayashi, H., Howard, J.B. and Sarofim, A.F., 16th Symposium (Int) on Combustion, The Combustion Institute, Pittsburgh, PA, pg. 411, (1977). and Kobayashi, H., Ph. D. Thesis, M.I.T. Dept. of Mechanical Eng., Cambridge, MA (1976).
3. Niksa, S., Heyd, L.E., Russel, W.B. and Saville, D.A., On the Role of Heating Rate in Rapid Coal Devolatilization, 20th Symposium (Int) on Combustion (to be published).
4. Solomon, P.R. and Colket, M.B., 17th Symposium (Int) on Combustion, The Combustion Institute, Pittsburgh, PA pg. 131 (1978).
5. Badzioch, S. and Hawksley, P.G.W., Ind. Eng. Chem. Process Design Develop., 9, 521, (1970).
6. Suuberg, E.M., Peters, W.A. and Howard, J.B., Ind. Eng. Process. Design Develop., 17, #1, pg. 37 (1978).
7. Solomon, P.R. and Hamblen, D.G., Measurement and Theory of Coal Pyrolysis Kinetics in an Entrained Flow Reactor, EPRI Final Report for Project RP 1654-8 (1983).
8. Solomon, P.R., Hamblen, D.G., Carangelo, R.M. and Krause, J.L., 19th Symposium (Int) on Combustion, The Combustion Institute, Pittsburgh, PA, pg. 1139 (1982).
9. Maloney, D.J. and Jenkins, R.G., Coupled Heat and Mass Transport and Chemical Kinetic Rate Limitations during Coal Rapid Pyrolysis, 20th Symposium (Int) on Combustion, to be published.
10. Freihaut, J.D., A Numerical and Experimental Investigation of Rapid Coal Pyrolysis, Ph.D. Thesis, Pennsylvania State University, (1980).
11. Solomon, P.R. and Hamblen, D.G., Finding Order in Coal Pyrolysis Kinetics, DOE Topical Report for Contract No. DE-AC21-81FE05122 (1983) and Progress Energy Combustion Science, 9, 323 (1984).
12. Solomon, P.R., Hamblen, D.G., Carangelo, R.M., Markham, J.R. and DiTaranto, M.B., ACS Div. of Fuel Chem. 29, 83, (1984).
13. Best, P.E., Carangelo, R.M. and Solomon, P.R., ACS Division of Fuel Chem, 29, 249 (1984).
14. Solomon, P.R., Hamblen, D.G., Carangelo, R.M., Markham, J.R. and Chaffee, M.R., Application of FT-IR Spectroscopy to Study Hydrocarbon Reaction Chemistry, ACS Div. of Fuel Chemistry Preprints 30 (1985).
15. Merrick, D., Fuel, 62, 540 (1983).
16. Lee, A.L., ACS Div. of Fuel Chem. Preprints, 12 (3), 19 (1968).
17. Perry, R.H. and Green, D., Chemical Engineers' Handbook, 6th Edition, McGraw-Hill, NY (1984).
18. Boothroyd, R.G., Flowing Gas-Solids Suspensions, Chapman and Hall, Ltd., London (1971).
19. Solomon, P.R. and King, H.H., Fuel, 63, 1302, (1984).
20. Ballantyne, A., Chou, H.P., Orozco, N. and Stickler, D., Volatile Production during Rapid Coal Heating, Presented at the DOE Direct Utilization AR&TD Contractors Review Meeting, Pittsburgh, PA (1983).
21. Seeker, W.R., Samuelson, G.S., Heap, M.P. and Trolinger, J.D., 18th Symposium (Int) on Combustion, The Combustion Institute, pg., 1213, (1981).
22. Witte, A.B. and Gat, N., Effect of Rapid Heating on Coal Nitrogen and Sulfur Releases, Presented at the DOE Direct Utilization AR&TD Contractors Review Meeting, Pittsburgh, PA, (1983).



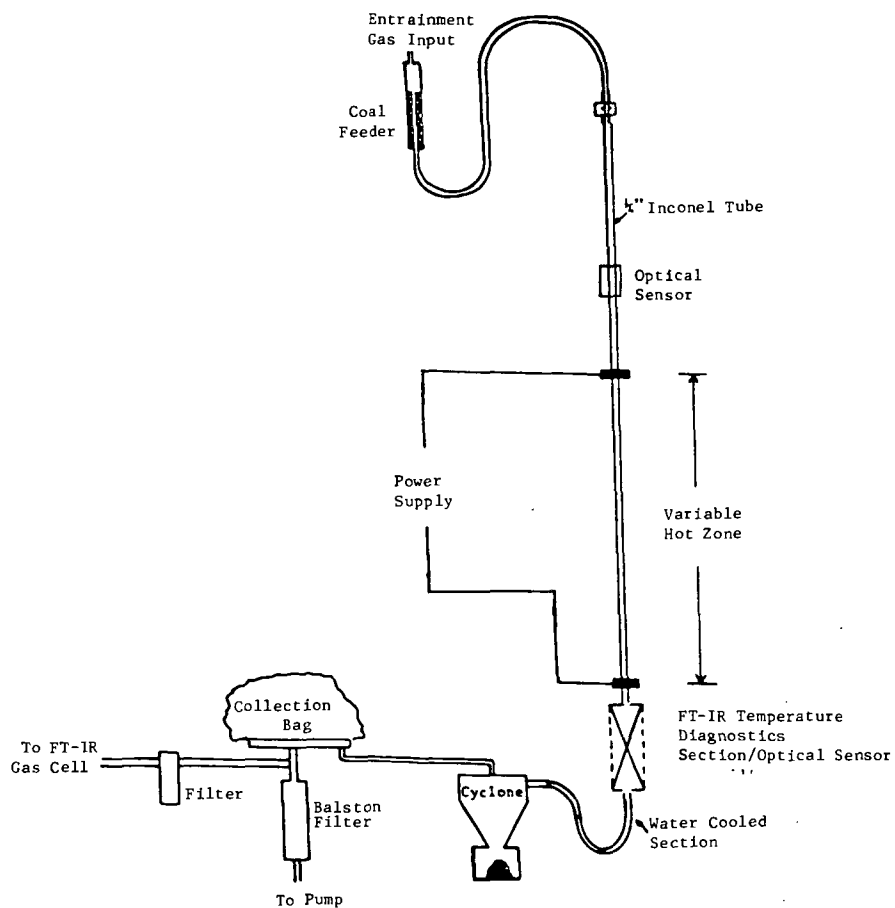


Figure 1. Schematic of Heated Tube Reactor.

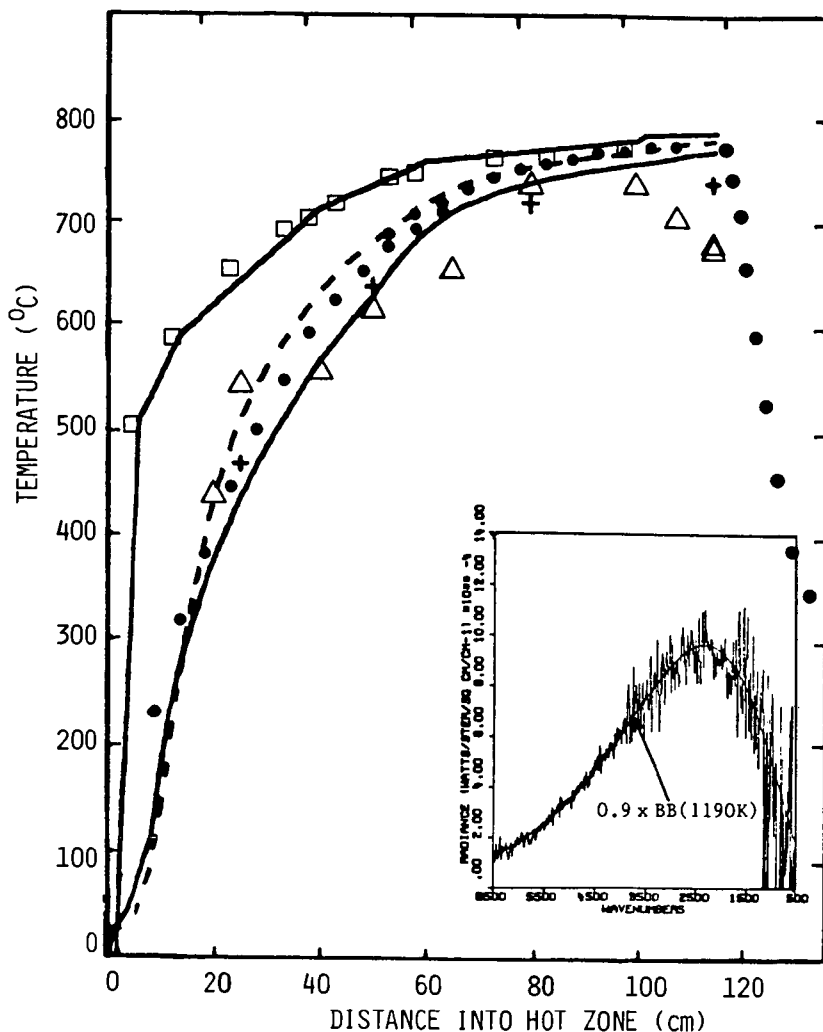


Figure 2. Measured and Calculated Temperatures in the Tube Reactor with Coal and Helium.  $\square$  Outside Tube Temperature Corrected for Heat Loss.  $\bullet$  Thermocouple Temperature Inside the Tube.  $+$  Thermocouple Temperature at FT-IR Focal Point.  $\triangle$  FT-IR Temperature of Coal Particles. Upper Line is the Wall Temperature used as Input. Lower Line is the Calculated Coal Particle Temperature. Dashed Line is the Calculated Thermocouple Temperature. Insert is a Comparison of an FT-IR Normalized Emission Spectrum with a Theoretical Black-body Assuming  $\epsilon = 0.9$ .

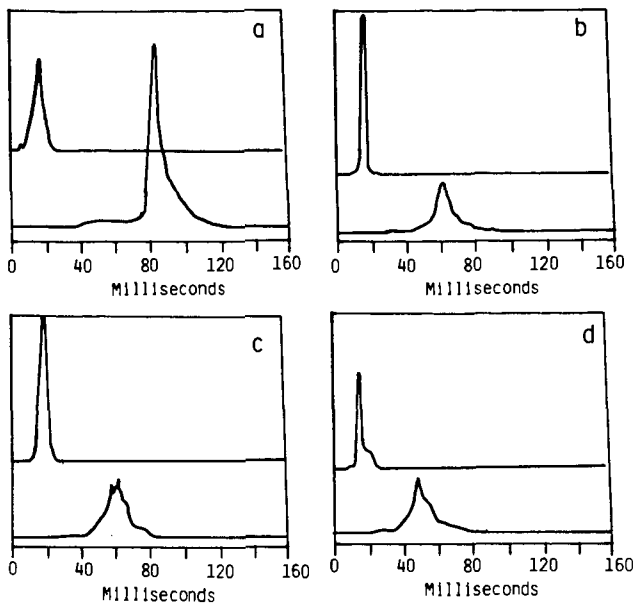


Figure 3. Phototransistor Signals Indicating Coal Particle Transit Times for 4 Electrode Positions. a) 125 cm Cold, b) 50 cm Cold, 75 cm Hot, c) 25 cm Cold, 100 cm Hot, and d) 10 cm Cold, 115 cm Hot.

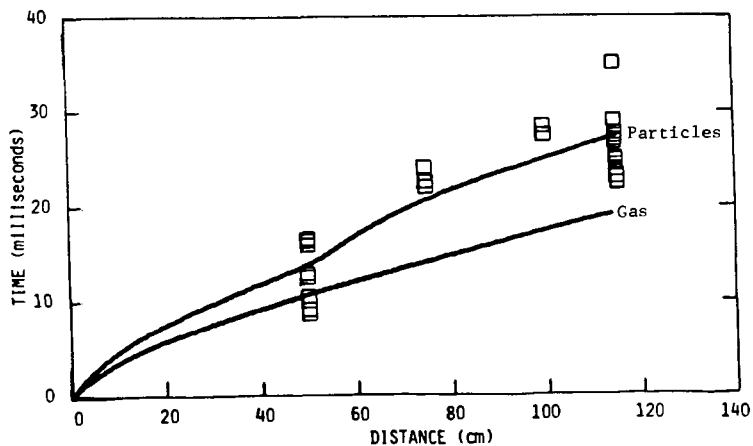


Figure 4. Measured and Calculated Particle Residence Time and Calculated Gas Residence Time in the Heated Tube Reactor. The Calculation Assumes the the Particles are at 80% of the Gas Velocity before and after Primary Pyrolysis and at 40% between 1% and 75% Weight Loss.

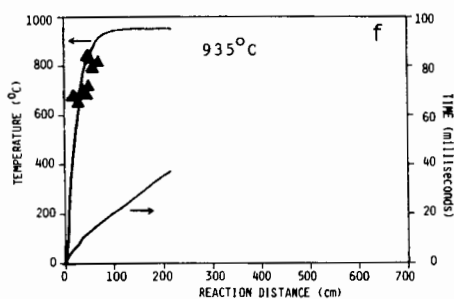
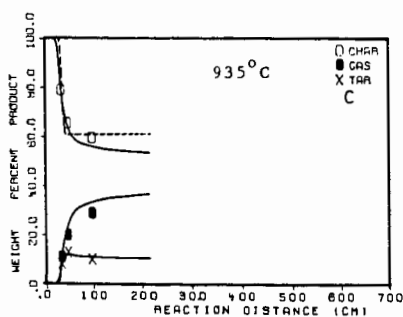
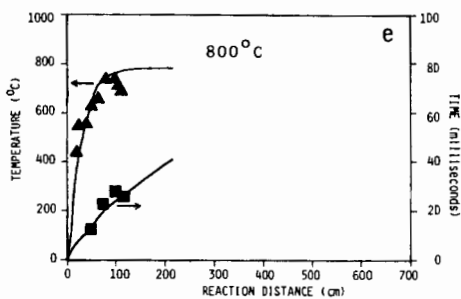
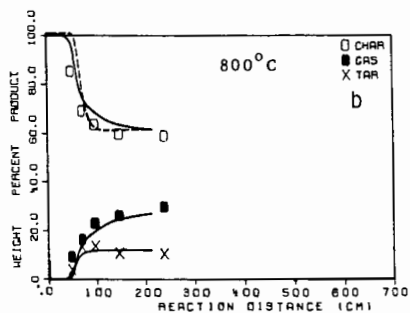
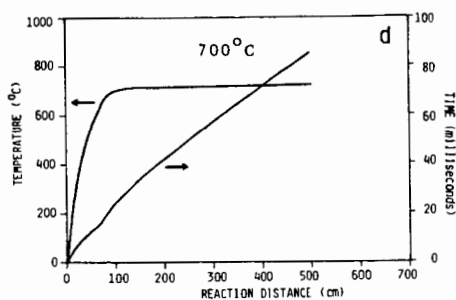
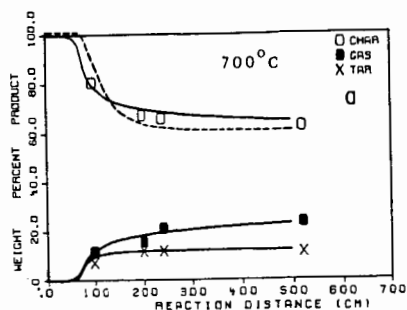


Figure 5. Pyrolysis Results Comparing the Theory and Data for Yields and Particle Time Temperature Histories. Symbols are Data, Solid Lines in a-c are from the Functional Group Model (8). The Dashed Lines are a Single Rate First Order Model. Lines in d-f are from a Heat Transfer Model.

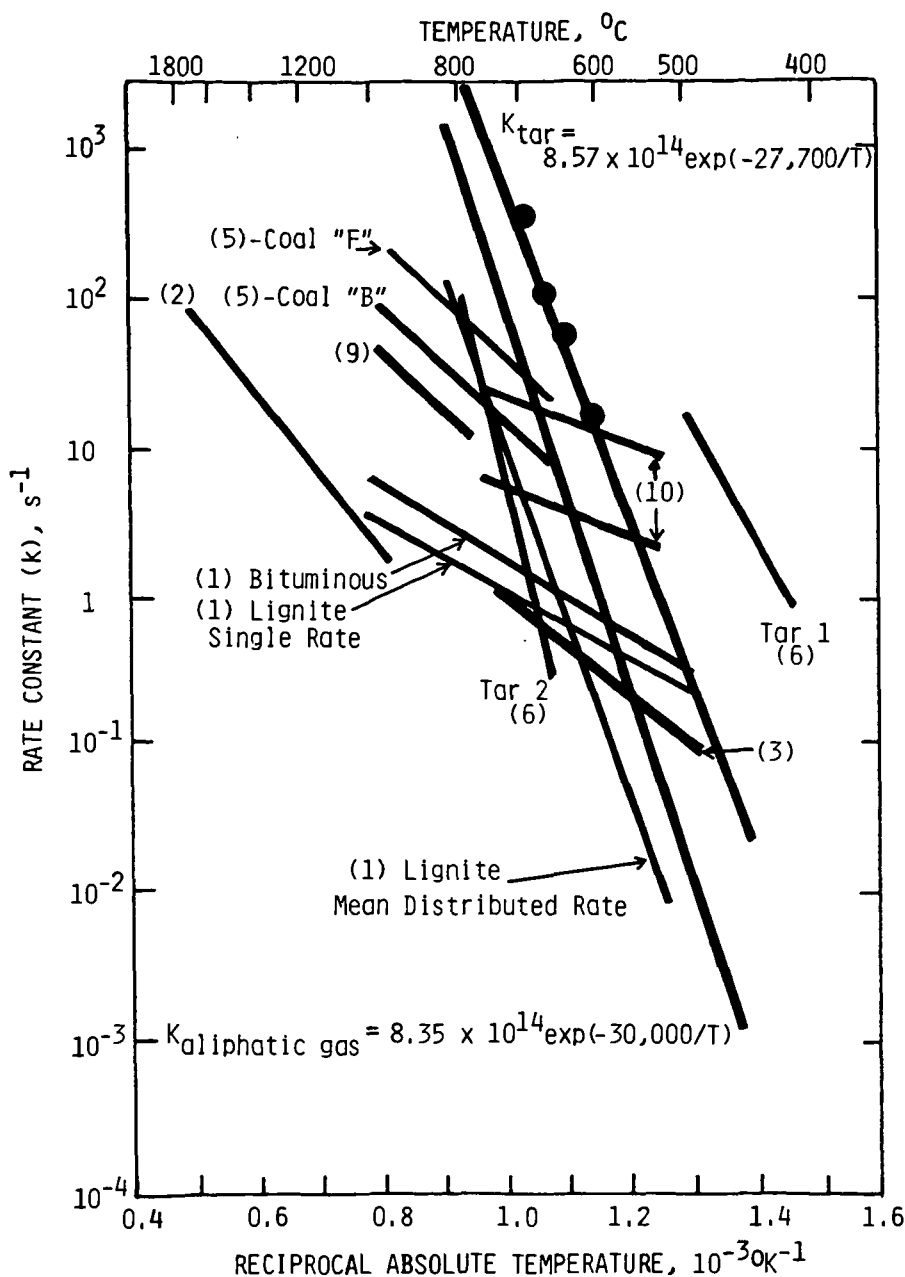


Figure 6. Comparison of Kinetic Rates for Weight Loss (or Tar Loss) from Several Investigations. The Numbers in Parentheses Indicate the Reference from which the Rates were Obtained. The Upper Lines for Reference 10 was for 53-106  $\mu$ m dia. Particles, the Lower Lines was for 850-1000  $\mu$ m dia. Particles. The Rates for Tar and Aliphatic Gas are those used in the Theoretical Calculation. Note that the Number in the Exponent is Roughly 1/2 the Activation Energy.

REACTIVITY IN AIR OF CHARS PRODUCED FROM A LIGNITE  
CONTAINING VARIOUS CATIONS

Alan W. Scaroni and Bruce A. Morgan

Fuel Science Program  
Department of Materials Science and Engineering  
The Pennsylvania State University  
University Park, PA 16802

The combustion of coal is practiced widely throughout the world. In the United States in 1982, for example, almost 600 million tons of coal were burned for electricity production (1). Nevertheless, many fundamental aspects of coal combustion are not well understood. It has been established, however, that at least two general processes occur during combustion: pyrolysis or devolatilization of the coal due to an applied thermal stress and heterogeneous combustion of the remaining char according to carbon-oxygen reactions. The relative importance of each process to the overall combustion of a particular coal is not easy to measure experimentally and is even more difficult to predict a priori.

In the sequence of events that is coal combustion, heterogeneous char combustion, which is usually referred to as char burnout, necessarily occurs last. This has led to the deduction that the char burnout is the rate determining step in the overall process. This argument then provides that to burn coal more effectively and efficiently, it is necessary to understand the mechanism, and thereby be able to affect the rate of the char-oxygen reaction.

While it is true that the rate of release and combustion of the volatiles in most practical systems are fast compared to the rate of the C-O<sub>2</sub> reactions, the yield of volatiles, which determines the amount of char which must be burned heterogeneously, is equally important in determining the char burnout time. Hence, an alternative to increasing the rate of the C-O<sub>2</sub> reaction is to decrease the required extent of the C-O<sub>2</sub> reaction by reducing the yield of char. Both aspects of the combustion of a range of coals have been addressed in the current project, but coverage in this paper is restricted to the properties of lignites which affect the yield of volatiles and the char reactivity, both of which may affect the overall combustion rate of lignites.

The heterogeneous reaction rate of a coal char with a reactant gas is influenced by such parameters as the inherent char reactivity, which is related to the number of carbon active sites, the rate of transport of the reactant gas to the active surface area and the presence of potentially catalytic inorganic species. Jenkins et al. (2,3) have shown that the air reactivity of coal chars is dependent upon the pyrolysis conditions under which the chars were prepared. As the severity of the pyrolysis conditions was increased, the number of carbon active sites in the char was found to decrease, hence, the reactivity decreased. In addition, coal char reactivity was shown to be rank dependent; chars produced from lignites being more reactive than those from higher rank coals.

The high reactivity of lignite chars has been attributed, in part, to the presence of ion exchangeable cation on the original coals. These are predominantly alkali and alkaline earth metals (4), some of which are excellent catalysts for the C-O<sub>2</sub> reaction (5,6). Their presence on low rank coal chars, as distinct from discrete mineral phases, has been shown to increase reactivity (7). However, as the severity of the pyrolysis or reaction conditions increases, the metals lose their catalytic activity due primarily to a loss of dispersion via sintering. This occurs as the holding time at temperature or the reaction temperature itself

increases (8). The objective of the current work was to determine the effect of the presence of cations, namely calcium and magnesium, on the pyrolysis of a lignite under combustion conditions and on the subsequent reactivity of partially burned chars.

### Experimental

The ion exchangeable cations on a Texas lignite, PSOC 623, were removed by acid washing in 0.04 N HCl. Alkaline earth metals, Ca and Mg, were back exchanged onto the acid washed samples using 1 M metal acetate solutions. Details of the exchange procedure have been outlined previously (9). Cation contents of the prepared samples were measured by atomic absorption spectroscopy.

The raw and modified lignite samples were pyrolyzed and partially combusted in an entrained-flow reactor at an initial reactor (gas and wall) temperature of 1173 K. A description of the reactor and its mode of operation have been provided elsewhere (10).

Reactivity data were generated on chars produced under either a  $N_2$  or air atmosphere at various residence times in the entrained flow reactor using a Fisher Thermogravimetric Analyzer (Model 260 F). The reactivities were obtained isothermally in air at atmospheric pressure and a temperature of 533 K.

For these conditions and by using only 2 mg of char spread thinly on a Pt pan, heat and mass transfer effects should not mask the reaction rate. Hence, the reported reactivities are believed to be intrinsic, chemically controlled rates. The gasification reactivities are taken from the maximum slope of the TGA recorder plot, normalized to the initial weight of dry ash free char.

### Results and Discussion

The ultimate analysis of the raw lignite and the proximate analyses of the raw and modified samples are shown in Table 1. The raw lignite contained 1.8 wt% cations on a dry basis, predominantly Ca (1.4%) and Mg (0.26%) with trace quantities of Na, K, Ba and Sr. The acid washing reduced the cation content to less than 0.01 wt%. The two cation-loaded samples chosen for comparison in the present study contained 1.9 wt% Ca and 1.6 wt% Mg, respectively.

#### Weight Loss Rate Data

Weight loss rate data for pyrolysis in  $N_2$  and combustion in air at 1173 K are shown in Figure 1 for raw and acid washed lignite. The same data for the Ca and Mg loaded lignite are shown in Figure 2. Details of the model for predicting residence times have been provided by Tsai and Scaroni (10). In addition, an analysis is provided which estimates particle and gas temperature excursions from the initial furnace temperature of 1173 K due to the superimposition of endothermic heats of pyrolysis and exothermic heats of combustion. The essence of the analysis is that the lignite particles are being heated to the furnace (gas and wall) temperature for at least 0.1 s. Upon ignition, particle temperatures exceed gas temperatures for a short period ( $< 0.1$  s) by in excess of 200 K. Hence, the weight loss rate data in Figures 1 and 2 are for nonisothermal pyrolysis and combustion for about 0.15 s.

The data shown in Figures 1 and 2 have been discussed previously (9) and can be summarized as follows. The presence of ion exchangeable cations suppresses the evolution of volatiles during pyrolysis. This is attributed to an increase in secondary char forming reactions primarily involving tars. Such reactions are catalyzed by Ca and Mg (11). In an air atmosphere, however, catalysis of the  $C-O_2$

reaction by Ca for a short time increases the weight loss by the Ca loaded lignite to above that of the acid-washed sample. No such rapid rate of weight loss occurs for the Mg-loaded coal since Mg is not a good catalyst for the  $C-O_2$  reaction. At longer residence times, weight loss rates are similar for the raw, acid-washed and Ca-loaded samples, and slightly larger for the Mg loaded sample. This implies that catalysis of the  $C-O_2$  reaction is no longer occurring. Loss of catalytic activity by Ca at high temperature has been ascribed to loss of dispersion due to sintering (7). Hence, comparing the behavior of the raw and acid washed samples, the increased weight loss due to short-lived but significant catalysis of the  $C-O_2$  reaction by the presence of cations on the raw lignite simply compensates for the reduced yield of volatiles because of their presence.

#### TGA Reactivity Data

Maximum reactivities in air at 533 K of partially combusted chars are shown in Figure 3 as a function of weight loss in the entrained flow reactor. For each form of the lignite, reactivities decrease with increasing weight loss in the reactor up to about 85-90%. For higher weight losses, reactivities are low and approximately constant at  $< 0.1$  mg/mg h. A decreasing reactivity indicates a loss of carbon active sites, whereas a constant reactivity may indicate a constant active site concentration or control of the reaction rate by oxygen diffusion to the active surface area though an ash barrier formed from the mineral matter in the coal.

Maximum char reactivities at 50, 75 and 90% weight loss and the time required to reach each level of weight loss for the variously treated lignites are given in Table 3. Note that 50% weight loss exceeds the level reached by pyrolysis in  $N_2$ . For residence times less than 0.10-0.13 s, reactivities at each level of weight loss decrease in the order  $Ca > Raw > Mg > acid-washed$ . This is in accordance with the order predicted by catalysis of the  $C-O_2$  reaction. For residence times greater than 0.10-0.13 s, reactivities are low and approximately the same. This implies an absence of significant catalysis, possibly due to temperature induced sintering of the metals. Ignition of the particles with an attendant temperature increase occurs within this time range.

The significance in relating TGA reactivity data to weight loss in the entrained flow reactor is seen by comparing the data in Table 3 for the cation containing samples. After a weight loss of 50%, reactivities decrease in the order  $Ca > Raw > Mg$  while the additional time required to reach 90% weight loss in the entrained flow reactor increases in the order  $Ca < Raw < Mg$ . In this region of the weight loss curve where heterogeneous char combustion is occurring, catalysis of the  $C-O_2$  reaction may be important implying that chemical reactivity controls the weight loss rate. Although different conditions prevail, TGA data may give a qualitative indication of behavior in this region. It is difficult to interpret the data for the acid washed lignite in this manner, however. Work is continuing to explain this apparent anomaly.

For residence times greater than 0.13 s in the entrained low reactor, which correspond to weight losses in excess of 85-90%, weight loss rates are low and approximately constant at  $3.8 \times 10^{-4}$  g/cm<sup>2</sup>s (expressed per unit external surface area). There is no apparent effect of the presence of cations in this region of the weight loss curve. It has been suggested previously that this may indicate physical rate control of the reaction mechanism (9). The TGA reactivity data can now be used to help determine the reaction Zone.

TGA reactivities at 533 K for these chars were approximately constant at  $6.1 \times 10^{-5}$  g/cm<sup>2</sup>s. Extrapolating these data to the entrained-flow reactor operating temperature of 1173 K using the Zone II Activation Energy of 21.7 kcal/mole as determined by Young (12), produces a reactivity of  $4.4 \times 10^{-4}$  gm/cm<sup>2</sup>s. This is



similar to the experimentally measured reactivity of  $3.8 \times 10^{-4} \text{ g/cm}^2 \text{ s}$ , and is considerably less than the value calculated for Zone III control,  $7.7 \times 10^{-2} \text{ g/cm}^2 \text{ s}$ .

Arrhenius parameters are currently being generated in the TGA for the  $\text{C-O}_2$  reactions appropriate for the current chars. This will eliminate the need to use Arrhenius parameters generated by others. However, if the data of Young are appropriate for use in this situation, the implication is that the same reaction zone does not exist in the TGA and entrained flow reactor, the former being Zone I, and the latter Zone II.

#### Summary

TGA reactivity data of partially combusted chars have been used to elucidate the char burnout stage of pulverized coal combustion. The absence of a significant effect of cations on char reactivity at high levels of burnoff implies the absence of catalysis of the  $\text{C-O}_2$  reaction. This was ascribed to sintering of the metal cations following ignition. The char particles then burn out slowly under Zone II control, the chars having relatively low inherent reactivities.

#### Acknowledgments

The lignite was supplied by W. Spackman from the PSU-DOE Coal Sample Bank and Data Base. Financial support for Bruce Morgan was obtained from the Coal Cooperative Program and MRI Fellowship Program at Penn State.

#### Literature Cited

1. Annual Energy Review, 1983, Energy Information Administration, DOE/EIA-0384(83), April 1984.
2. Jenkins, R. G., Nandi, S. P., and Walker, P. L., Jr., Fuel, 52, 288, 1973.
3. Radovic, L. R., Walker, P. L., Jr., and Jenkins, R. G., Fuel, 62, 849, 1983.
4. Morgan, M. E., Jenkins, R. G., and Walker, P. L., Jr., Fuel, 60, 189, 1981.
5. McKee, D. W., Fuel, 62, 170, 1983.
6. Walker, P. L., Jr., Matsumoto, S., Hanzawa, H., Muira, T., and Ismail, I. M. K., Fuel, 62, 140, 1983.
7. Radovic, L. R., Ph.D. Thesis, The Pennsylvania State University, 1982.
8. Radovic, L. R., Walker, P. L. Jr., and Jenkins, R. G., J. Catal., 82, 382, 1983.
9. Morgan, B. A. and Scaroni, A. W., in "The Chemistry of Low Rank Coals," Amer. Chem. Soc. Symposium Series 264, 255, 1984.
10. Tsai, C. Y. and Scaroni, A. W., AIME-SME Preprints, 336, 1984.
11. Tanabe, K., "Solid Acids and Bases," Academic Press, NY, 1970.
12. Young, B. C., in "The Chemistry of Low Rank Coals," Amer. Chem. Soc. Symposium Series, 264, 243, 1984.

Table 1  
ULTIMATE AND PROXIMATE ANALYSES FOR THE RAW AND MODIFIED LIGNITE

Ultimate Analysis				Proximate Analysis			
	C	H	N	S	O (by diff)		
% (daf)	70.1	5.0	1.7	1.4	21.8		
						% H <sub>2</sub> O	% Ash (dry)
						10.8	15.9
						Raw	VM(daf)
						Acid Washed	59.7
						Ca Loaded	54.9
						Mg Loaded	57.6
							57.1

Table 2  
CATION CONTENTS OF THE RAW AND MODIFIED LIGNITE

Raw	Ca	Mg	Na	K	Ba	Sr	Total	Acid Washed	Ca Loaded	Mg Loaded
wt % (dry)	1.4	0.26	0.03	0.03	0.03	0.02	1.8	<0.01	1.9	1.6
meq/g (dry)	0.7	0.2	0.01	0.01	0.002	0.002	0.9	~0	1.0	1.3

**Table 3**  
**TIME TO REACH AND MAXIMUM CHAR REACTIVITIES AT VARIOUS LEVELS OF**  
**WEIGHT LOSS IN ENTRAINED FLOW REACTOR AT 1173 K**

Weight Loss in Entrained Flow Reactor at 1173 K	Maximum Char Reactivity, mg/mg h (daf) (Time to reach weight loss, ms)			
	<u>Ca-loaded</u>	<u>Raw</u>	<u>Mg-loaded</u>	<u>Acid-washed</u>
50	2.1 (80)	0.8 (65)	0.6 (90)	0.4 (50)
75	1.2 (95)	0.7 (85)	0.4 (125)	0.3 (70)
90	<0.1 (110)	<0.1 (145)	<0.1 (290)	0.1 (140)

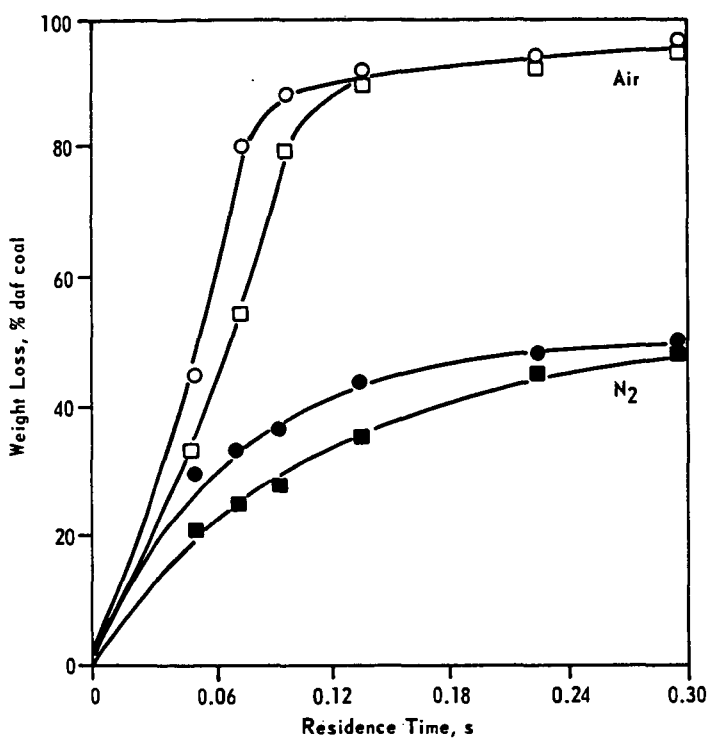


Figure 1. WEIGHT LOSS RATE IN AIR AND N<sub>2</sub> FOR RAW (□, ■) AND ACID-WASHED (○, ●) LIGNITE IN ENTRAINED FLOW REACTOR AT 1173 K

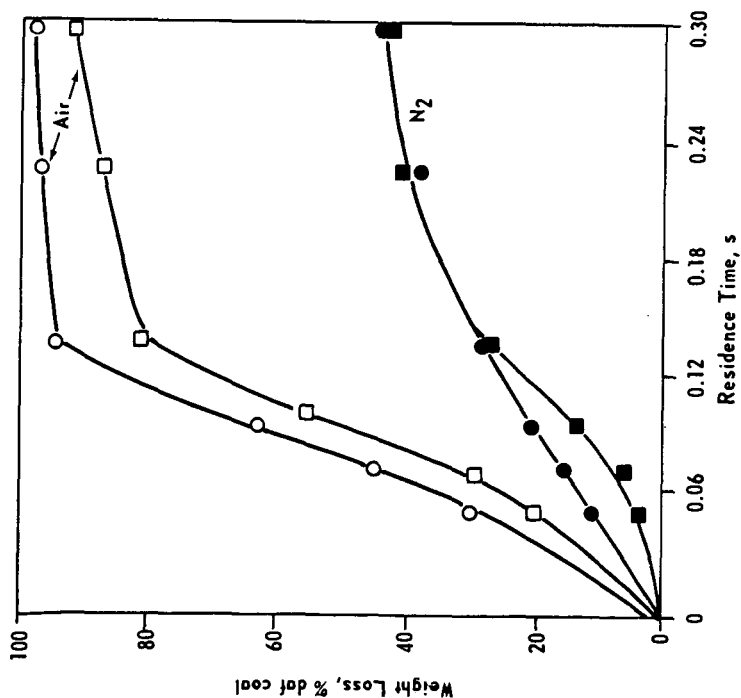


Figure 2. WEIGHT LOSS RATE IN AIR AND  $N_2$  FOR Ca (○,●) AND Mg (□,■) LOADED LIGNITE IN ENTRAINED FLOW REACTOR AT 1173 K

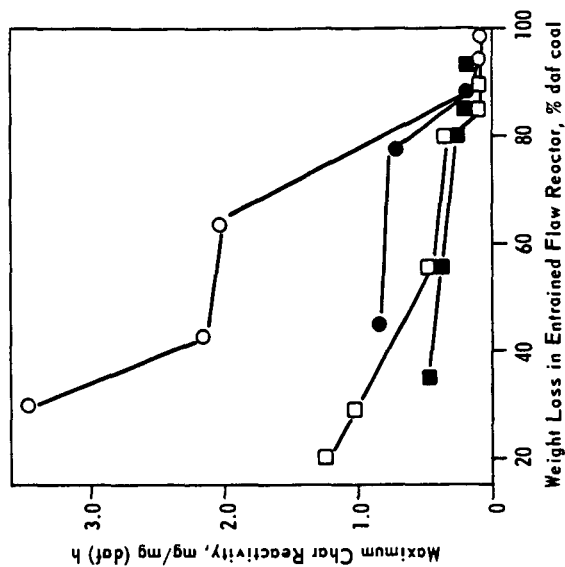


Figure 3. TGA REACTIVITIES IN AIR AT 533 K OF CHARs PRODUCED FROM Ca-LOADED (○), RAW (●), Mg-LOADED (□) AND ACID WASHED (■) LIGNITE AS A FUNCTION OF WEIGHT LOSS BY PARTIAL COMBUSTION IN ENTRAINED FLOW REACTOR AT 1173 K

## A COMPARISON OF CO<sub>2</sub> AND O<sub>2</sub> GASIFICATION OF GLASSY CARBON

S. R. Kelemen  
H. Freund  
Exxon Research and Engineering Company  
Clinton Township  
Route 22 East  
Annandale, New Jersey 08801

### Abstract

O<sub>2</sub> is known to be much more reactive than CO<sub>2</sub> toward carbon. We have separated and studied with surface spectroscopies the dissociative adsorption step from the CO formation step in the O<sub>2</sub> and CO<sub>2</sub> gasification of glassy carbon. The reactive adsorption probabilities decreased with increased coverage. At high coverage the derived activation energy for O<sub>2</sub> dissociation was 33 kcal/mole and 50-60 kcal/mole for CO<sub>2</sub>. The CO formation energy decreased from 90 kcal/mole at very low coverage to 70 kcal/mole at high coverages. The steady state oxygen coverage during CO<sub>2</sub> gasification corresponded to these high coverages with a measured activation energy of 67 kcal/mole. CO formation energetics limit the rate of CO<sub>2</sub> gasification. The increased gasification activity for O<sub>2</sub> is associated with a more facile gaseous dissociation step causing higher oxygen coverages which in turn generates lower energy CO formation sites.

### I. INTRODUCTION

It is widely recognized that O<sub>2</sub> has a much higher reactivity than CO<sub>2</sub> toward carbon; this difference has been kinetically quantified to be 10<sup>5</sup> greater at 800K and 0.1 atm pressure (1). Despite this large reactivity difference the responsible elementary processes on the carbon surface are not well understood. Oxidation and gasification reactions of carbon are a class of very difficult reactions to characterize and quantify. Gasification reactions are sensitive to the type of carbon being gasified (2). A better understanding of these systems could be achieved by detailed physical characterization of the external surface of a given carbon coupled to adsorption and reactivity studies of the reactant gases (2-4). The application of surface sensitive probes to this area is an essential component to approach the problem. These results are used to interpret observations of steady state reactivity.

### II. EXPERIMENTAL

Experiments were performed in an ultra-high-vacuum spectroscopy chamber with a base pressure lower than  $2 \times 10^{-10}$  Torr. Auger electron spectroscopy (AES) was performed with a double-pass cylindrical mirror analyzer using a 2.2 keV primary beam energy and 2V peak to peak voltage modulation.

The amount of oxygen was determined using AES. The overall amplitude of the  $dN(E)/dE$  oxygen (510 eV) to carbon (272 eV) was taken as the measure of oxygen surface concentration. A linear absolute coverage scale which corresponds to the AES O/C ratios was previously estimated and used in other studies on carbon surfaces (5-7). A coverage of one oxygen per surface carbon atom  $\theta_{\text{oxygen}} = \theta = 1$  gives a AES O/C value of 0.25. We will self consistently apply this same coverage scale throughout the course of this study.

The glassy carbon samples were cut from plates obtained from Atomergic Chemetals and were outgassed at 1300°C in UHV prior to use. The presence of small amounts of very strongly bound oxygen could be reduced further by heating to higher temperatures, but this did not significantly effect the  $\text{CO}_2$  and  $\text{O}_2$  chemistry at high oxygen coverages. Further details of the characterization of the glassy carbon substrates can be found elsewhere (6). This procedure removed oxygen which was the principal contaminant measured by AES. The initial AES carbon to oxygen ratio was near 0.01. This represents a small amount of very strongly bound oxygen.

### III. RESULTS

We have characterized the glassy carbon surface using ultraviolet photoemission spectroscopy following oxygen uptake from  $\text{O}_2$  and  $\text{CO}_2$  at 300°C. Previous UPS studies of atomically clean glassy carbon surfaces show enhanced electron emission near the Fermi level (6). This is associated with the presence of unsaturated surface carbon valences, "dangling bonds". These levels are removed upon chemically bonding to oxygen. Emission within 3 eV of the Fermi level decreases on glassy carbon as these levels become involved in bonding to oxygen (6). The emission from oxygen 2p levels was found between -4 and -11 eV following exposure to either  $\text{O}_2$  or  $\text{CO}_2$ . Features which could be identified with molecularly adsorbed  $\text{O}_2$  or  $\text{CO}_2$  were absent. The similarity between  $\text{O}_2$  and  $\text{CO}_2$  suggest that the dissociation of  $\text{CO}_2$  gives rise to surface oxygen and gaseous CO at 300°C. UPS thus gives us an indication that  $\text{O}_2$  and  $\text{CO}_2$  dissociation predominates under our conditions in these adsorption systems. This agrees with the conclusion reached for  $\text{O}_2$  adsorption on graphon based on thermal desorption and isotope labeling studies (8).

XPS was also used to characterize the oxidized carbon surface. The  $\text{O}(1s)$  XPS signals following 300°C oxidation by  $\text{O}_2$  and  $\text{CO}_2$  showed a peak at 532 eV binding energy. The carbon  $(1s)$  peak for clean glassy carbon occurred at 284.2 eV. Following oxygen uptake from either  $\text{O}_2$  or  $\text{CO}_2$ , there was a slight increase in emission at lower binding energies. The carbon  $(1s)$  peak did not, however, possess a 288.5 eV binding energy component which is associated with carbon coordinated to multiple oxygen atoms as in a carboxylic functionality (9-12). These results also indicate that similar oxygen functionalities were produced by  $\text{CO}_2$  and  $\text{O}_2$  at 300°C, and these are likely to be surface carbon atoms coordinated to one oxygen.

We have measured the increase in the oxygen AES signal following  $\text{CO}_2$  and  $\text{O}_2$  exposures at  $300^\circ\text{C}$ . We used a maximum temperature of  $300^\circ\text{C}$  in order to achieve high oxygen surface coverages but also to limit complications introduced by *in situ* gasification of carbon (13). The maximum oxygen coverages generated from  $\text{O}_2$  and  $\text{CO}_2$  corresponded to  $\theta_0 = 0.85$  and  $0.45$  respectively. The adsorption processes were placed in quantitative terms. The efficiency of reactive adsorption as a function of the amount of oxygen already present was obtained from the incremental changes of oxygen coverage with the interval of exposure to either  $\text{CO}_2$  or  $\text{O}_2$  at  $300^\circ\text{C}$ . The efficiencies were calculated for increasing intervals of one decade of exposure. Figure 1 shows these results on glassy carbon as a function of oxygen coverage. The adsorption process is characterized by relatively rapid initial uptake on the order of  $10^{-4}$  efficiency for both gases up to approximately  $\theta_0 = 0.1$  oxygen coverage. Above this coverage, there is a rapid decrease to  $10^{-10}$ . Further exposure to  $\text{O}_2$  will increase the oxygen coverage. The adsorption coefficient declines with coverage from  $10^{-10}$  to  $10^{-12}$  from  $\theta_0 = 0.25$  to  $\theta_0 = 0.85$ . At higher coverages the behavior of  $\text{O}_2$  and  $\text{CO}_2$  begin to depart.  $\text{CO}_2$  was limited in the amount of oxygen which could be deposited under these conditions. The decline in the coefficient for  $\text{CO}_2$  was more rapid with coverage and decreased to below  $10^{-14}$  near half monolayer coverage. Presumably, the coefficient declines further for  $\text{CO}_2$  at higher coverages, but we were unable to measure slower processes.

The AES oxygen thermal stability profile was measured on glassy carbon following  $\text{O}_2$  and  $\text{CO}_2$  oxidation at  $300^\circ\text{C}$ . Figure 2 shows that the surface oxygen concentration remains nearly constant up to  $600^\circ\text{C}$  in both cases. Between  $600 - 700^\circ\text{C}$ , the surface oxygen coverage begins to decrease for the  $\text{O}_2$  oxidized surface, yet for  $\text{CO}_2$  the coverage still remains almost constant. Above  $600^\circ\text{C}$  CO was the dominant desorption product. Above  $800^\circ\text{C}$  there were similar reductions in oxygen coverage in both cases. CO evolves from the surface over a very wide range of temperature.

The CO formation energies were determined from the rate of change of oxygen coverage with time during heating in UHV by assuming first order kinetics and a frequency factor of  $10^{13}$ . This formalism provides a framework to estimate the desorption energy. The results are shown in Figure 3. They are plotted as a function of oxygen coverage based on the common AES coverage scale as previously defined. The oxygen coverage dependency of the formation energy is similar for the surface oxygen derived from  $\text{O}_2$  and  $\text{CO}_2$  adsorption. At low oxygen coverages,  $\theta_0 = 0.25$ , the energy decreases from 95 to 80 kcal/mole. The formation energy exhibited much smaller changes with coverage at the higher coverages.  $\text{O}_2$  adsorption produced higher oxygen coverages. The energy ranged between 80 - 70 kcal/mole between  $\theta_0 = 0.25$  to  $0.85$ .  $\text{CO}_2$  coverage was limited to  $\theta_0 = 0.4$  but between  $\theta_0 = 0.25$ , and  $0.4$  the energies were similar as with  $\text{O}_2$ . The CO formation energy decreases with increasing oxygen coverage.



#### IV. DISCUSSION

The adsorption of  $O_2$ , and  $CO_2$  on glassy carbon surfaces were examined using AES. The study was restricted to carbon surfaces that had been previously outgassed in UHV at elevated temperature and characterized with surface sensitive techniques. In this way we were able to directly compare two gases which have widely different gasification activities.

There have been few adsorption studies on well-characterized, clean carbon surfaces. Original studies of oxygen adsorption on clean "paracrystalline" carbon (15) and sputter-damaged graphite surfaces (16) have shown complex adsorption behavior. The rate of uptake was characterized by coverage regions having a linear dependence with the log of exposure. This was interpreted as evidence for many discrete types of adsorption sites. It is believed that different oxygen adsorption sites exist on carbons with different thermal stabilities (2). Unfortunately these early studies did not relate adsorption to subsequent reactivity. A more recent study of  $O_2$  on the edge surface of graphite has shown a strong oxygen coverage dependence on the reactive adsorption efficiency (7) similar to these original studies even though the edge surface of graphite has a limited amount of site heterogeneity (14). Correlated thermal stability studies of oxygen enabled estimates of the energetics of product formation. The values that were obtained on the edge graphite surface were dependent on the oxygen coverage (10). The thermal stability of oxygen on carbon for a given site is then sensitive to the amount of nearby oxygen already present. In this study we have compared the rate of oxygen uptake from  $O_2$  and  $CO_2$  at  $300^\circ C$  on glassy carbon and have measured the thermal stabilities of the resultant oxidized surfaces.

The maximum oxygen uptake from  $O_2$  at  $300^\circ C$  on glassy carbon represented adsorption over a majority of the surface. A high absolute oxygen coverage was achieved. We observed a similar pattern of oxygen uptake on the edge surface of graphite  $300^\circ C$  (7) as on the glassy carbon samples. The similarity of the high coverage oxygen chemisorption results on the edge surface of graphite and glassy carbon is an indication that the sites on the less ordered carbon surface are actually chemically very close to those on the edge graphite surface. Although physically these surfaces are very different, microscopically their behavior is much the same.

Differences exist between  $O_2$  and  $CO_2$  uptake at  $300^\circ C$ . Under our conditions the absolute oxygen coverage reached nearly a monolayer using  $O_2$  at  $300^\circ C$ . Exposure to  $CO_2$  under the same conditions resulted in oxygen uptake only to one half monolayer coverage. Herein lies a significant difference between  $O_2$  and  $CO_2$  reactive chemisorption at  $300^\circ C$ . After saturation of the small number of very active sites, the adsorption efficiency of  $CO_2$  and  $O_2$  is approximately  $10^{-10}$ .  $O_2$  is able to sustain this efficiency to high coverages. The efficiency drops to  $10^{-14}$  for  $CO_2$  before a half monolayer oxygen coverage can be achieved. The adsorption efficiency must drop many more orders of magnitude for  $CO_2$  at higher oxygen coverage.

The thermal stability studies in UHV for the resultant 300°C oxidized surfaces yielded estimates for the energetics of product formation. The energetics are related to the absolute oxygen surface coverage. The energies are similar at constant absolute oxygen coverage for oxygen generated from either  $O_2$  or  $CO_2$ . The energies increase with decreasing oxygen coverage going from 75 kcal/mole at  $\theta_o = 0.4$  to 95 kcal/mole at  $\theta_o = 0.05$  coverage. Under our conditions,  $O_2$  is capable of generating higher oxygen coverages, and the CO formation energy decreases to 70 kcal/mole at the highest coverage.

The adsorbed oxygen species are strongly bound. The observation of large heats of adsorption and low adsorption efficiencies ( $10^{-10}$  -  $10^{-14}$ ) imply a substantial energy barrier for adsorption. We can estimate the barriers for adsorption for  $CO_2$  and  $O_2$  at several oxygen coverages by assuming a Boltzman energy distribution and the temperature of the gas equal to the surface temperature. At  $\theta_o = 0.1$  this yields a barrier height of 13 and 15 kcal/mole for  $O_2$  and  $CO_2$  respectively. At  $\theta_o = 0.4$  we find that the barrier increases to 25 kcal/mole for  $O_2$  and 35 kcal/mole for  $CO_2$ . At  $\theta_o = 0.9$  the value increases to 33 kcal/mole for  $O_2$ . The value for  $CO_2$  must be substantially greater at this high oxygen coverage. Estimates based on adsorption efficiencies at higher surface temperatures of  $CO_2$  exposure as well as extrapolation of the efficiencies at 300°C to  $\theta_o = 0.9$  yield barriers in the range of 50 - 60 kcal/mole. Marsh has used an energy-reaction coordinate diagram to help illustrate the kinetics of adsorption and CO formation (2). We have been able to quantify parts of this diagram which we just described and are also illustrated in Figure 5 for the reaction of glassy carbon with  $CO_2$  and  $O_2$  to form CO.

Higher oxygen concentrations can be developed (13) by oxidation of carbon with  $O_2$  above 400°C but this leads to in situ gasification and complicates the reaction-energy coordinate diagram. We have observed CO and  $CO_2$  as gaseous products during thermal desorption of glassy carbon oxidized above 400°C in  $O_2$ . There are several possible origins for  $CO_2$  production. Some carboxylic groups may be produced by  $O_2$  at very high oxygen coverages. Studies (17) of nitric acid oxidized glassy carbon indicate that  $CO_2$  can be produced from decomposition of carboxylic oxygen functionalities. The decomposition of surface carboxylic groups to form  $CO_2$  will complicate the  $O_2$  reaction with carbon. Another possible route at high oxygen coverages is the formation of CO with consecutive oxidation by surface oxygen to  $CO_2$ . Indications are that formation energy for CO declines further below 70 kcal/mole at very high oxygen coverages (7) but  $CO_2$  eventually becomes a competitive reaction route. We have minimized the complications of  $CO_2$  formation from  $O_2$  oxidation in our studies by limiting the concentration of surface oxygen.

Activation energy for the  $O_2$  adsorption step has been estimated at higher temperatures and presumably higher coverages and tends to higher values. Lussow et al. (13) report an activation energy of 29 kcal/mole for  $O_2$  adsorption between 450°C and 675°C. In carbon gasification studies a value near 38 kcal/mole has been reported for the  $O_2$  adsorption step. (18,19) Our

results at lower coverages show that the barrier for adsorption is greater for  $\text{CO}_2$  than for  $\text{O}_2$  at a given oxygen surface coverage and that the barrier increases for both gases as the oxygen coverage increases. The values reported for  $\text{O}_2$  at high temperatures are of the same order that we find at high oxygen coverages in our studies.

The differences in adsorption behavior of  $\text{CO}_2$  and  $\text{O}_2$  at high oxygen coverages must be related to the much greater gasification activity for  $\text{O}_2$ . Our data suggest that  $\text{CO}_2$  and  $\text{O}_2$  produce similar kinds of adsorbed oxygen species at low and medium coverages. This is most likely carbonyl type oxygen functionality, carbon which is coordinated to one oxygen. The stability of this kind of oxygen is dependent on the amount already present. This can be interpreted as oxygen bound to one carbon having the ability to modify the energetics of the interaction of neighboring free carbon sites with oxygen and  $\text{CO}_2$ . At higher coverages, there are pronounced differences between  $\text{CO}_2$  and  $\text{O}_2$ . The adsorption barrier for  $\text{CO}_2$  relative to  $\text{O}_2$  increases with increasing oxygen coverage, while the stability of the adsorbate decreases and gasification to CO becomes more facile. The observations suggest that the energy barrier for oxygen adsorption from  $\text{O}_2$  is much lower than for  $\text{CO}_2$  for sites which have lower subsequent CO formation energetics. At high oxygen coverages, the magnitude of the adsorption barrier increases while the energetics of gaseous product formation declines. For both  $\text{CO}_2$  and  $\text{O}_2$  at a given reaction temperature a steady state situation will develop. At higher temperatures the reaction coordinate energy diagram is thought to be one with a greater barrier for gas dissociation but a lower barrier for gaseous formation. The kinetics of  $\text{CO}_2$  gasification of glassy carbon has been measured near atmospheric pressure above  $650^\circ\text{C}$ . The activation energy for  $\text{CO}_2$  gasification was 67 kcal/mole (20). There is a correspondence between this value and the CO formation energetics that we observe at high oxygen coverages. In addition the oxygen coverages determined by AES following  $\text{CO}_2$  gasification are also comparable. These results imply that the steady state surface situation during  $\text{CO}_2$  gasification is close to that found for the highest oxygen coverages in this study. On the other hand greater oxygen concentration are developed with  $\text{O}_2$ . The energetics of  $\text{CO}_2$  and  $\text{O}_2$  dissociation under gasification conditions will be different and from our estimates it will be substantially lower for  $\text{O}_2$ . The increased gasification activity for  $\text{O}_2$  is associated with a more facile gaseous dissociation step at high oxygen coverages which generates lower CO formation energy sites.

## V. REFERENCES

1. P. L. Walker, Jr., F. Rusnko, L. G. Austin, *Adv. Catalysis* 11 (1959) 133.
2. H. Marsh, *Spec. Publ.-Chem. Soc.* 1977 32 (Oxygen Met. Gaseous Fuel Ind.) 133.
3. N. M. Laurendeau, *Prog. Energy Combust. Sci.* 4 (1978) 221 and references therein.
4. J. B. Donnet, *Carbon* 20 (1982) 267.
5. S. R. Kelemen and C. A. Mims, *Surface Science* 133(1983) 71.
6. S. R. Kelemen, H. Freund and C. A. Mims, *J. of Vac. Sci. and Technol. A* 2(2) (1984) 987.
7. S. R. Kelemen and H. Freund, submitted to *Carbon*.
8. P. L. Walker, Jr., F. J. Vastola and P. J. Hart, Fundamentals of Gas-Surface Interactions p. 307 (Academic Press, New York, 1967).
9. D. T. Clark in: Handbook of X-ray and Ultraviolet Photoelectron Spectroscopy (Heyden, London, 1978).
10. R. Schlögl and H. P. Boehm, *Carbon* 21 (1983), 345.
11. A. Ashitani, *Carbon* 19 (1981) 269.
12. T. Takalagi and A. Ashitani, *Carbon* 22 (1984) 43.
13. R. O. Lussow, F. J. Vastola and P. L. Walker, Jr. *Carbon* 5 (1967) 591.
14. S. R. Kelemen and C. A. Mims, *Surface Science*, 136 (1984) L35.
15. P. J. Hart, F. J. Vastola and P. L. Walker Jr., *J. Colloid Interface Sci.* 32 (1970) 187.
16. M. Barber, E. L. Evans and J. M. Thomas, *Chem. Phys. Lett.* 18 (1973) 423.
17. S. R. Kelemen and H. Freund, unpublished results
18. P. L. Walker Jr., *Carbon* 18 (1980) 447.
19. P. F. Lewis and G. A. Simons, *Combustion Sci. Tech.* 20 (1979) 117.
20. H. Freund, submitted to *Fuel*.

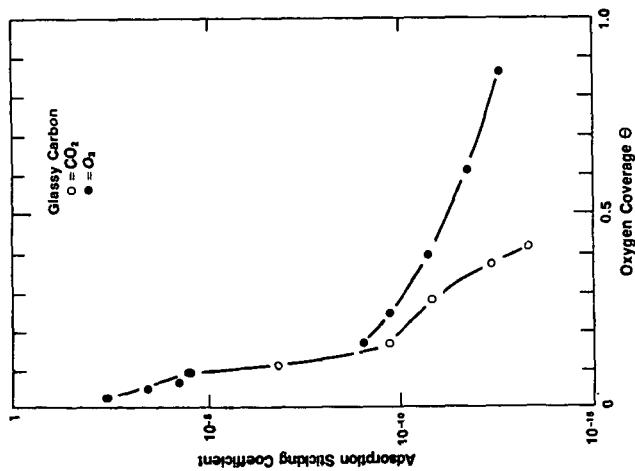


Figure 1: Reactive adsorption efficiency for  $\text{O}_2$  and  $\text{CO}_2$  as a function of the amount of oxygen already present on the glassy carbon surface held at  $300^\circ\text{C}$ .

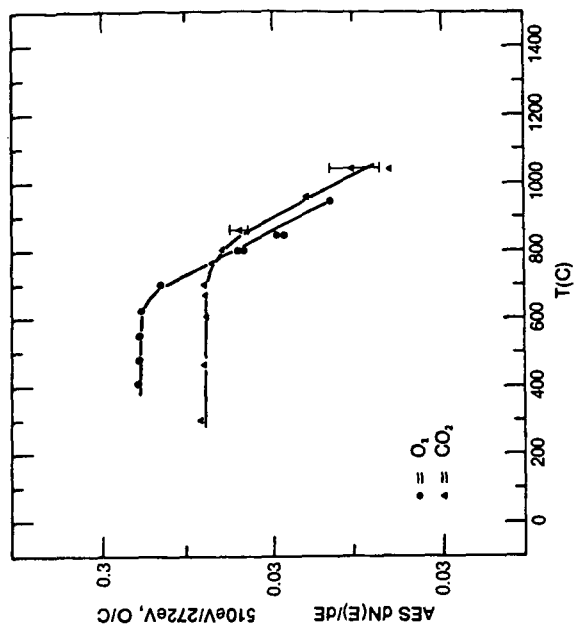


Figure 2: Oxygen AES signal after  $\text{O}_2$  and  $\text{CO}_2$  oxidation at  $300^\circ\text{C}$  and following heating in UHV for 300 sec at each data point.

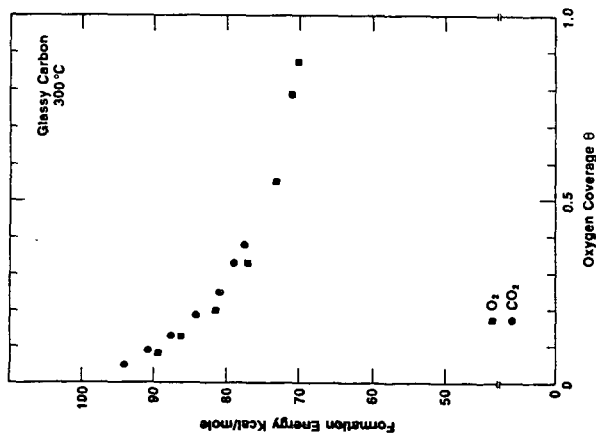


Figure 3: Formation energy of gaseous CO product as a function of oxygen coverage after  $O_2$  and  $CO_2$  oxidation at 300°C.

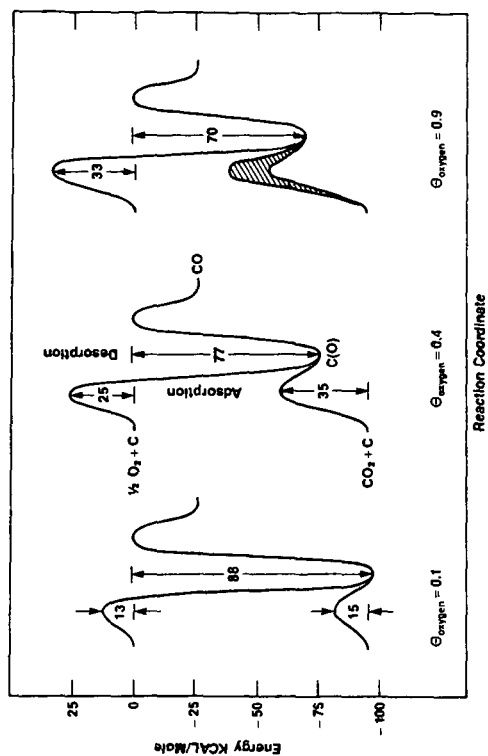


Figure 4: Energy - reaction coordinate diagram at different oxygen surface coverages in the reaction of  $CO_2$  and  $D_2$  with glassy carbon to form CO.

## TRANSIENT KINETIC STUDIES OF CHAR REACTIONS: GASIFICATION IN STEAM-ARGON MIXTURES

J.M. Cole, R. Ganapathi, and S.E. Ellison

Division of Engineering  
Brown University  
Providence, RI 02912

### I. INTRODUCTION.

In our laboratory we have been engaged in the study of the gasification behavior of chars using a transient kinetic approach. Previous work [1,2] concentrated on the development of the experimental techniques and carbon dioxide gasification. In the current communication we present some of our most recent data on the kinetic behavior of char gasification in steam-argon mixtures, and in so doing attempt to point out some of the significant advantages of transient techniques in studying the reactive behavior of chars, and in obtaining fundamental data.

The basis for this approach lies in the observation that the transient response of a reaction system to a perturbation in one or more of its state variables exhibits certain characteristics which are reflective of the "true" nature of the reaction mechanism under the appropriate experimental conditions. In comparison, steady-state rate measurements reveal relatively little concerning the detailed sequence of elementary steps that constitutes the "intrinsic" reaction mechanism. Thus, transient response data can be used in a qualitative sense to discriminate among competitive kinetic models. In addition, once an appropriate kinetic model has been identified, quantitative analysis of the transient data, using multiparameter estimation techniques, yields the model parameters. Moreover, the steady-state data, obtained at the end of each transient experiment, are available as well. The overall result of this approach is a more robust model of the reaction system under investigation.

### II. EXPERIMENTAL.

A simplified schematic of the transient kinetic apparatus that was developed for the current experimental applications is presented in Figure 1. This system consists primarily of: (1) a continuous gas flow, fixed solids, Berty-type gradientless, isothermal reactor for carrying out the reaction under well-mixed conditions; (2) a solenoid/ control valve network for generating step function changes in feed composition; (3) a modulated, supersonic molecular beam mass spectrometer for monitoring the transient response of the composition of the gas phase at the reactor effluent; and (4) automated data logging and mass programming of the mass spectrometer utilizing a PDP 11/34-IBM 7406 device coupler combination. Additional system details and data on system performance establishing the "gradientless" nature of the reactor with respect to gas phase mixing and interphase heat and mass transport have been fully documented and are available elsewhere [3,4].

For the steam-argon gasification studies reported on here, an important modification to the original apparatus involved the addition of a steam generation system and a condenser/gas-liquid separator. The steam generator, which appears in schematic in Figure 1, consisted of a stainless steel cylindrical reservoir for feed water and a high temperature evaporator. From the reservoir, the liquid water was metered into an argon carrier stream. The water flow rate was measured with a digital flowmeter (American Flow Systems AQ 300; up to 20 cm<sup>3</sup>/min). The combined water/argon flow was fed to an electric resistance-heated evaporator which produced superheated steam at the local thermodynamic conditions. All the upstream lines were heated and insulated to prevent steam condensation.

Various experimental considerations dictated that it was not desirable to attempt to maintain steam in the vapor phase downstream of the reactor up to the mass spectrometer sampling point. This would have involved heating and insulating the downstream lines, the adoption of another

method of flow rate measurement than the rotameters used in our previous studies, and would have created sampling problems due to the high fraction of water vapor expanding through the sampling orifice and condensing due to adiabatic cooling. Instead, therefore, it was decided to remove the bulk of the water immediately downstream of the reactor. This was accomplished using a specially-developed condenser. Insofar as the transient nature of the experiments is concerned, the introduction of any volume in the flow circuit of a magnitude comparable to that of the reactor would introduce an undesirable lag time in the system response, which if too large would tend to obfuscate the intrinsic transient response of the reactor. In addition, from an operational viewpoint it was essential to have whatever time lag that was ultimately introduced be invariant with the amount of collected liquid water in the condensate receiver. Of course, this could be accomplished by continuous removal of condensate; but this approach quickly leads to a complex control problem. Therefore, a simpler alternative approach was adopted. A baffle plate was installed at the bottom of the inlet dip tube to the condenser with circumferential slots for gas and condensate flow. In this manner, condensate could accumulate in the lower volume of the condenser, but the noncondensable fraction of the gas flow effectively "short-circuits" the condenser, immediately flowing to the outlet located in proximity, and thereby minimizing the imposed lag time. The effect of the condenser on the system transient response was measured by monitoring the exponential rise of an argon signal in the reactor effluent upon instantaneously switching this gas to the reactor feed line. Without the condenser in the flow circuit it was found, as previously [2], that the intrinsic time delay of the system was about 2 s. The effect of the condenser was the introduction of an additional additive lag time of 4 s, thereby making the new total system lag time about 6 s, which was found to be invariant with the liquid water level in the condensate receiver. This lag time proved to be of no practical consequence in the analysis of the data.

### III. EXPERIMENTAL PROCEDURES

The two gas phase product species that were monitored with the molecular beam mass spectrometer during the course of the transient experiments were CO ( $m/e=28$ ) and  $H_2$  ( $m/e=2$ ). Automatic mass programming allowed alternate monitoring of these two species at a sampling frequency of about 1 Hz (0.5 Hz each), which was sufficient for the experiments conducted. (It is noted that the limiting factor in the current configuration is not the mass programming, but rather the characteristic time of the lock-in amplifier which was used to extract the modulated portion of the signals.) Water, although also present in the sampled product gas, was not monitored, since the  $m/e=18$  signal simply corresponded to the saturation vapor pressure of water at room temperature, the bulk of the water having been removed upstream in the condenser.

Since all the species of interest here are also normally present in the background of the oil diffusion-pumped mass spectrometer vacuum envelope, to a greater or lesser degree, it was important to insure that the mass spectrometer signals corresponded to the instantaneous composition of the gas phase at the sampling orifice, and were not being influenced primarily by the background. A modulated beam technique was employed for this purpose. The gas at the sampling point was expanded through a 25  $\mu m$  diameter orifice into the first stage of a two-stage, differentially pumped vacuum system. In this stage (maintained ca.  $1 \times 10^{-4}$  torr) the expansion was cored by a 200  $\mu m$  diameter,  $60^\circ$  conical skimmer, and admitted into the second, mass spectrometer stage (maintained ca.  $5 \times 10^{-7}$  torr). In this stage the beam was mechanically modulated with a 200 Hz tuning fork chopper, and then passed through the ion source of the quadrupole mass spectrometer. The signal for each mass peak was then processed through a lock-in amplifier which extracted the rms value of the 200 Hz modulated signal only, thereby discriminating against the background contribution to the total signal. Mass discrimination in the sampled flow due to the jet expansion was found to be small [3], most probably due to sampling into the second stage while the beam was still relatively under-expanded.



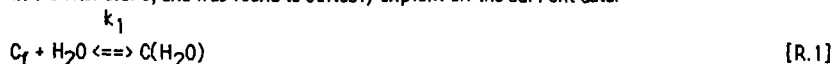
In order to insure that the CO and H<sub>2</sub> signals observed with the mass spectrometer could be entirely attributed to the steam-carbon reaction occurring within the reactor, a series of "blank" transient experiments was performed using steam-argon mixtures with non-porous glass beads in the solids basket in lieu of char. Two different reactor space times, 12 s and 18 s, were used. For each space time, experiments were performed at total pressures of 1.0, 1.3, and 2.0 MPa, and steam contents by volume of the steam-argon feed mixture of 50 and 70%. The char bed temperature in all cases was about 740 °C. No significant trace of either species was observed under these conditions. Thus, it was concluded that the CO and H<sub>2</sub> observed during the course of the transient gasification experiments originated from the steam-carbon reaction.

Another experimental concern related to the gas phase composition involved the water-gas shift reaction. This reaction is exothermic and thermodynamically favored under conditions of high steam partial pressure in the presence of CO to produce CO<sub>2</sub> and H<sub>2</sub>. It has been reported that this reaction is approximately at equilibrium at temperatures of 800°C and above in coal gasification systems [5]. However, it can be kinetically limited and, therefore, rather slow, unless it is appreciably catalyzed by impurities in the char. Insofar as the current experiments are concerned, its relative importance can be readily assessed by monitoring CO<sub>2</sub>. Although we examined the m/e=44 signal during the course of our scoping studies, no appreciable modulated signal was observed. Thus, under the current experimental conditions, the practical effects of this reaction seem to be minimal.

Transient experiments were conducted by first establishing the reactor temperature and pressure under a continuous pure argon purge. The flowrates of the pure argon purge and steam-argon reactive mixture were matched using the upstream and downstream control valve system (cf. Figure 1) such that the space time of the reactor remained constant at reactor conditions upon switching the two flows. (In order to accomplish this, the measured liquid water flowrate was converted to equivalent steam flowrate at reactor conditions.) All these operations were accomplished without exposing the char to the steam-argon mixture by alternate switching between the purge and bypass lines. (The pressure drop across the reactor is negligible in comparison to that imposed by the solenoid/control valve system, and thus the open bypass line adequately models the reactor flow resistance.) Once the pressure, temperature, and flowrates were set in the preceding manner, the transient experiment was initiated by activating the solenoid valve system to switch between the two flows. Pre-set mass programming and automated data logging were initiated simultaneously with the inception of the experiment.

#### IV. KINETIC MODELING

Various models have been proposed for the steam-carbon gasification system (e.g., see [6-10]). In the current studies, however, the complexity of the kinetic model required to explain the steam-char reaction was limited by the experimental conditions selected; i.e., only pure steam-argon feeds were used. Furthermore, for reactor space times of 12 to 18 s, the steam conversion never exceeded 10%. In addition, no significant amounts of methane or CO<sub>2</sub> were detected for the pressure and temperature ranges used. Under these conditions, the following mechanism was found to incorporate the basic features common to most of the models in the literature, and was found to suitably explain all the current data:





This mechanism is basically that of Curran et al. [10], except that reactions [R.2]–[R.4] are treated as irreversible; the latter two by virtue of the relatively low amounts of CO and H<sub>2</sub> produced in the reactor. Although this assumption seems to be quite good *a priori* for CO, it has been noted that under steady-state conditions, H<sub>2</sub> significantly inhibits the steam-char reaction, with a resultant multiplicative factor in the denominator of the Langmuir–Hinshelwood steady-state specific gasification rate expression of almost an order of magnitude greater than that for steam (e.g., see [6,8]). However, under the current transient experimental conditions with initially no H<sub>2</sub> in the reactor, and eventually very low amounts even at pseudo-steady-state, the sensitivity of the transient data to the rate of the reverse of reaction [R.4] seemed to be relatively low. Therefore, it was omitted from the current analysis on these grounds. It is noted, however, that it is certainly possible to determine this rate constant with the current techniques using either pure or high partial pressure H<sub>2</sub> feeds.

All the basic mechanisms represented in the literature employ a step like reaction [R.1] (i.e., steam adsorption); however, there is a range of treatment on subsequent details and rate-limiting steps. For example, Gadsby et al. [6] assumed essentially instantaneous decomposition of the carbon-steam surface complex to gaseous CO and H<sub>2</sub>. Ergun [11] and Strickland-Constable [12] suggested this mechanism for H<sub>2</sub>, but postulated a surface carbon-oxygen complex with an appreciable lifetime that eventually decomposes to yield gaseous CO. Long and Sykes [7] and Blackwood and McGrory [8] proposed decomposition to dual-site hydroxyl and hydrogen atom surface complexes simultaneously with steam adsorption (i.e., fast equilibration), followed by irreversible rearrangement to carbon-oxygen and carbon-hydrogen surface complexes. These differences are relatively indistinguishable from each other in the current data. Therefore, the combination of reactions [R.1] and [R.2] were selected as being most generally representative.

Once the model has been defined, the approach becomes quite similar to other general treatments of "lumped" transient kinetic models that have been presented in the literature (e.g., see [13,14]), and to our previous CO<sub>2</sub> gasification work [1,2]. The use of a "gradientless" reactor guarantees that the resultant mass balances are always ordinary differential equations (i.e., "lumped" parameter systems), although, as in the current case, they may be nonlinear. Basically, the transient continuity expressions for the various species involved in the reaction system, incorporating the rate expressions derived from the kinetic mechanism, comprise the set of ordinary differential equations which defines the model of the system.

Formulated in this fashion, the model employed to analyze our steam gasification data consisted of seven first order differential equations with a total of six parameters: C<sub>so</sub> (the "effective" concentration of active sites; g mol/g mol carbon), k<sub>1</sub>, k<sub>-1</sub>, k<sub>2</sub>, k<sub>3</sub>, and k<sub>4</sub>. The resultant system of equations is omitted from the current communication for the sake of brevity. Its derivation is relatively straightforward and is presented in reference [4].

#### V. PARAMETER ESTIMATION

The multiparameter estimation algorithm employed in the analysis of the current data was patterned after a scheme outlined by Luus and Jaakola [15]. The Luus–Jaakola (LJ) scheme is a direct random search method combined with search space reduction. Basically, the procedure is as follows. An initial range is selected for each parameter, and a number of different parameter sets are then selected on a random basis. For each parameter set the model is solved numerically and an unweighted least squares objective function value,  $\Phi$ , is determined using all the CO and H<sub>2</sub> partial pressure data over the entire course of the transient experiment; i.e.,

$$\theta = \sum_{i=1}^2 \{ \sum_j (P_{ij} - P^*_{ij})^2 \}, \quad (1)$$

where the  $P_{ij}$  and the  $P^*_{ij}$  are the measured and predicted partial pressures, respectively. After an arbitrarily large number of parameter sets have been evaluated, a fraction of the "best" resultant cases (i.e., those with the lowest  $\theta$  values) are then selected and the parameter ranges of these sets are scanned to define new reduced parameter ranges to be used for the next round of iteration. The entire procedure is then repeated until a pre-specified tolerance on the differential change in the objective function is met. The associated parameter set for the "best" value of  $\theta$  after the last iteration is taken as the final optimum parameter set for the data.

The LJ method was applied to the steam gasification data on an experimental basis, with reasonable results, as part of an ongoing investigation on multiparameter regression schemes for transient kinetic data analysis [16]. Previously [1,2] we had used a Marquardt-type search scheme employing a Green's function method [17] for determining the first order gradients required for the technique. As for all such schemes, we found both advantages and disadvantages in using the LJ scheme. Perhaps its most obvious disadvantage lies in its inherent inability to converge to the optimum parameter set if it is inadvertently not included in the initial ranges of all the parameters. If the initial range is too large, the rate of region reduction can be drastically slower than if the range is capable of being more narrowly specified. Also, since a finite, albeit large, number of parameter sets are examined, there is always the possibility of missing the "true best" parameter set. Counterbalancing these debits is a potentially significant savings in computation time due to the absence of the requirement for evaluating first order gradients and, possibly, higher derivatives. Also, in reducing the parameter search space, the LJ method increases the probability of encountering a near-optimum parameter set, in comparison to totally random search methods. However, these arguments notwithstanding, our experience with the data considered here, suggests that a more effective method might involve a hybrid scheme wherein an LJ-type algorithm is used as the "front end" of an optimization procedure for reducing the parameter search space, with a more powerful local gradient technique, such as a Marquardt scheme, used to actually focus in on the optimum parameter set. Such a scheme is currently under consideration.

Typically, in the current application of the LJ method, the parameter ranges obtained after 11 iterations, using a 5% case reduction rate, were used as the initial ranges for the subsequent set of iterations. When the "best" value of  $\theta$  did not change by more than 5%, the parameter set associated with this minimum value of the objective function was taken to be the optimum set. As an approximate average, about 25 overall iterations were sufficient to fit the experimental data with a good degree of accuracy.

## VI. RESULTS AND DISCUSSION

Two types of chars were studied in the current work: Fisher activated coconut char, and a char prepared from Darco Ignite (PSOC 623) (800°C for 2 hr. in an inert atmosphere). Typical transient experiment results are presented in Figures 2 and 3. The six model parameters were determined for each transient experiment using the LJ algorithm as described above. The apparent activation energies for each parameter were then determined from Arrhenius plots of the parameter values. The resultant parameter expressions are summarized in Table I.

From the results in Table I it can be seen that the apparent activation energies are, on the whole, higher for the lignite than for the coconut char. However, the activation energies for  $k_1$  are very nearly identical for the two chars, thereby implying that the mechanism for steam adsorption on the two chars is very similar. As in our previous CO<sub>2</sub> gasification studies, we found that the apparent activation energies of the effective active site concentrations were negative. This result, as previously, is attributed to the diminution of active sites via thermal annealing of the char upon heating [1,2,9,18,19,20]. Moreover, the  $C_{50}$  parameter expression determined in the current steam gasification studies for the coconut char is very similar to that

determined for the same char from previous CO<sub>2</sub> gasification studies: viz.,  $C_{SO} = 1.7 \times 10^{-9} \exp(+27000/RT)$  [1,2,3]. This result implies that virtually the same active carbon sites participate in steam and CO<sub>2</sub> gasification under the current experimental conditions. This is also direct evidence that the transient technique can yield good estimates of the effective active site concentrations of chars under actual gasification conditions.

It is interesting to note that  $C_{SO}$  for the lignite char is comparable to that of the coconut char, even though their total surface areas are quite different (1038 m<sup>2</sup>/g for the coconut char; and 24.7 m<sup>2</sup>/g for the lignite char). However,  $C_{SO}$  decreases more rapidly with temperature for the coconut char than for the lignite char, as evident from the relative magnitudes of their negative apparent activation energies. This result probably reflects the fact that the coconut char is "older" than the lignite char, and, thus, more graphitic in nature and more susceptible to thermal annealing, and, therefore, exhibits a stronger temperature behavior. Also, the fact that that disordered regions in char have been reported to react more rapidly than ordered regions [21], is consistent with the comparable  $C_{SO}$  values of the two chars in spite of the significant difference in total surface areas.

Although values for all the rate constants determined in the current work are not available in the literature, comparisons can be made with steady-state Langmuir-Hinshelwood expression parameter values. Setting all the time derivatives equal to zero in the transient model and solving for the pseudo-steady-state specific gasification rate,  $W_{SS}$ , yields the following expression:

$$W_{SS} = K_1 P_w / [1 + K_2 P_w], \text{ min}^{-1} \quad (2)$$

where the correspondence between the new parameters and the rate constants is given by:

$$K_1 = k_1 k_2 C_{SO} / [k_{-1} + k_2]; K_2 = k_1 [1 + k_2 (1/k_3 + 1/k_4)] / [k_{-1} + k_2] \quad (3)$$

A comparison of the parameter values calculated from these expressions with corresponding values given in the literature are presented in Table II. As can be seen, the comparison is fairly good. The primary source of the variability observed is most probably due to differences in the chars. For example, the total surface area of the coconut char used by Blackwood and McNary [8] was reported as 46.5 m<sup>2</sup>/g, in comparison to the 1038 m<sup>2</sup>/g for the activated coconut char used in the current work.

Pseudo-steady-state operation is attained at the end of each transient experiment corresponding the "leveling off" of the signal traces (e.g., after ca. 1.2 min). These data can also be analyzed in the usual steady-state fashion to show that they are consistent with traditional Langmuir-Hinshelwood kinetics. The steady-state expression given by Eq. (2) can be recast into the following form:

$$P_{w,ss}/W_{SS} = P_{w,ss} C_D RT / q P_{C,ss} = 1/K_1 + (K_2/K_1) P_{w,ss} \quad (4)$$

where the subscript "ss" denotes steady-state values,  $P_{C,ss}$  is the steady-state CO partial pressure determined from the data,  $q$  is the volumetric flowrate at the reactor exit,  $R$  is the universal gas constant, and  $T$  is the effluent gas temperature. Therefore, a plot of the lefthand side of Eq. (4) against  $P_{w,ss}$  should be a straight line. One such plot for the coconut char data is presented in Figure 3; the linear behavior is quite evident.

## VII. CONCLUDING REMARKS.

It has been shown that char gasification in steam-argon mixtures, under the current experimental conditions, is reasonably well represented by the transient kinetic model presented in this communication. Multiparameter analysis of the resultant transient kinetic data yielded separate Arrhenius temperature-dependent expressions for each of the model rate constants, as well as the effective active site concentrations for the two chars examined. Although corresponding rate constant expressions are not available for direct comparison, related kinetic parameters found in the literature agreed with the appropriate combinations of the current rate constant values.

The transient kinetic technique has been shown to be a valuable tool for examining char reaction mechanisms, and for determining rate parameters for direct use in modeling, design, and analysis of new or existing gasification and related systems. With automated data handling, the technique is capable of quickly and efficiently yielding a large amount of information concerning the reactivity and behavior of chars in various gaseous environments directly in a single type of experiment. The advantages of this technique over other more commonly accepted steady-state methods are significant.

#### ACKNOWLEDGEMENT

The authors gratefully acknowledge the support of the U.S. Department of Energy under Grant Nos. DE-F022-81PC40786 and DE-F022-83PC60800. However, any opinions, findings, conclusions, or recommendations expressed herein are those of the authors and do not necessarily reflect the views of DOE.

#### REFERENCES

1. Sy, O. and J.M. Calo, ACS Div. Fuel Chem. Prepr. **28**, 6 (1983).
2. Sy and Calo, Proc. 1983 Int. Conf. on Coal Science, Pittsburgh PA, p. 445.
3. Sy, O., "Transient Kinetic Studies of Char-Gas Reactions in a Gradientless Reactor: CO<sub>2</sub> Gasification," Master's Dissertation, Princeton University, Princeton, N.J., 1982.
4. Ganapathi, R., "Transient Kinetic Studies of Char Gasification in Steam-Argon Mixtures," Master's Dissertation, Brown University, Providence, RI, 1984.
5. Squires, A.M., Trans. Inst. Chem. Eng. (London) **39**, 3 (1961).
6. Gadsby, J., C.N. Hinshelwood, and K.W. Sykes, Proc. Roy. Soc. (London) **A187**, 129 (1946).
7. Long, F.J., and K.W. Sykes, Proc. Roy. Soc. (London) **A193**, 377 (1948).
8. Blackwood, J.D., and F. McGrory, Aust. J. Chem. **12**, 533 (1959).
9. Johnson, J.L., *Kinetics of Coal Gasification*, John Wiley & Sons, New York, 1979.
10. Curran, G.P., C.E. Fink, and E. Gorin, ACS Div. Fuel Chem. Prepr. **12**, 62 (1968).
11. Ergun, S., U.S. Bur. Mines Bull. (598), 1962.
12. Strickland-Constable, R.F., J. Chim. Phys. **47**, 356 (1950).
13. Bennett, C.O., AIChE J. **13**, 890 (1967).
14. Cutlip, M.B., C.C. Yang, and C.O. Bennett, AIChE J. **18**, 1073 (1972).
15. Luus, R., and T.H.I. Jaakola, AIChE J. **19**, 760 (1973).
16. Ellison, S.E., "Nonlinear Parameter Estimation in Ordinary Differential Equation Systems: Newton-Raphson and Gauss Techniques," Sc.B. Thesis, Division of Applied Mathematics, Brown University, 1984.
17. Kramer, M.A., J.M. Calo, and H. Rabitz, Appl. Math. Model. **5**, 432 (1981).
18. Duval, X., J. Chim. Phys. **47**, 339 (1950).
19. Boulanger, F., X. Duval, and M. Letort, Proc. Third Int. Conf. Carbon, p. 257, Pergamon Press, N.Y. (1959).
20. Blackwood, J.D., D.J. McCarthy, and B.D. Cullis, Aust. J. Chem. **20**, 1561, 2525 (1967).
21. Chang, H.W., and S.K. Rhee, Carbon, **16**, 17 (1978).

**Table I.**

Model parameter values\* obtained with the Luus-Jaaskola search scheme for steam gasification of lignite and coconut char.

**Values for Darco lignite char (PSOC 623):**

$$C_{SO} = 1.6 \times 10^{-6} \exp(+13646/RT), \text{ g mol/g mol C}$$

$$k_1 = 4.86 \times 10^9 \exp(-42286/RT), \text{ min}^{-1} \text{ atm}^{-1}$$

$$k_{-1} = 2.65 \times 10^{10} \exp(-51341/RT), \text{ min}^{-1}$$

$$k_2 = 9.32 \times 10^7 \exp(-33840/RT), \text{ min}^{-1}$$

$$k_3 = 4.21 \times 10^9 \exp(-42075/RT), \text{ min}^{-1}$$

$$k_4 = 5.07 \times 10^{10} \exp(-47262/RT), \text{ min}^{-1}$$

**Values for Fisher activated coconut char:**

$$C_{SO} = 2.21 \times 10^{-8} \exp(+23592/RT), \text{ g mol/g mol C}$$

$$k_1 = 1.41 \times 10^{10} \exp(-45183/RT), \text{ min}^{-1} \text{ atm}^{-1}$$

$$k_{-1} = 1.04 \times 10^7 \exp(-35233/RT), \text{ min}^{-1}$$

$$k_2 = 9.67 \times 10^4 \exp(-19448/RT), \text{ min}^{-1}$$

$$k_3 = 1.20 \times 10^6 \exp(-25995/RT), \text{ min}^{-1}$$

$$k_4 = 2.04 \times 10^6 \exp(-25867/RT), \text{ min}^{-1}$$

\*All activation energies are given in cal/g mol.

**Table II.**

Comparison of kinetic parameters from different studies with coconut char.

Temperature (K)	973.2	1023.2	1063.2
<b>1. Current Work</b>			
$K_1 C_{SO} \times 10^4, [\text{min}^{-1} \text{ atm}^{-1} \text{ g mol/g C}]$	3.6	6.1	8.9
$K_2, [\text{atm}^{-1}]$	1.1	1.8	2.7
<b>2. Gadsby et al. [6]</b>			
$K_1 C_{SO} \times 10^4, [\text{min}^{-1} \text{ atm}^{-1} \text{ g mol/g C}]$	3.6	-	-
$[\text{min}^{-1} \text{ atm}^{-1} \text{ g mol/g C}]$			
$K_2, [\text{atm}^{-1}]$	1.0	-	-
<b>3. Long and Sykes [7]</b>			
$K_1 C_{SO} \times 10^4, [\text{min}^{-1} \text{ atm}^{-1} \text{ g mol/g C}]$	1.6	7.8	25.0
$[\text{min}^{-1} \text{ atm}^{-1} \text{ g mol/g C}]$			
$K_2, [\text{atm}^{-1}]$	0.97	1.61	2.33
<b>4. Blackwood and McGrory [8]</b>			
$K_1 C_{SO} \times 10^4, [\text{min}^{-1} \text{ atm}^{-1} \text{ g mol/g C}]$	-	0.36	1.25
$K_2, [\text{atm}^{-1}]$	-	0.06	0.09

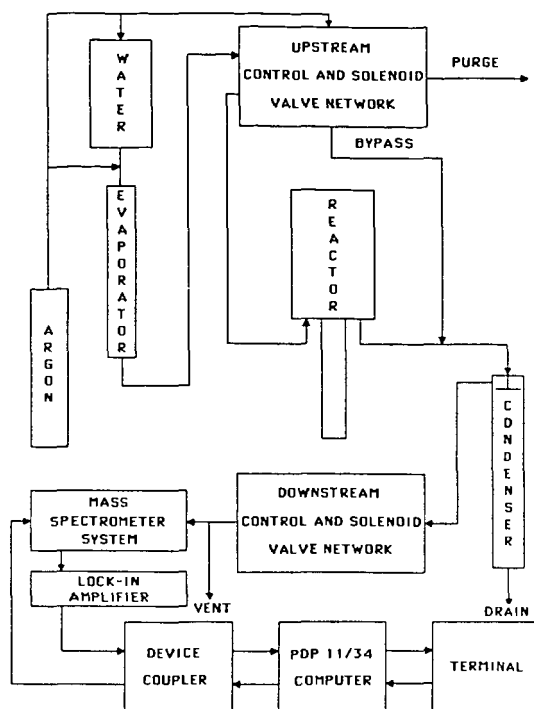


Figure 1. Schematic of experimental system.

# EXPERIMENTAL RESPONSE OF $[CO]$ AND $[H_2]$ VERSUS MODEL PREDICTION

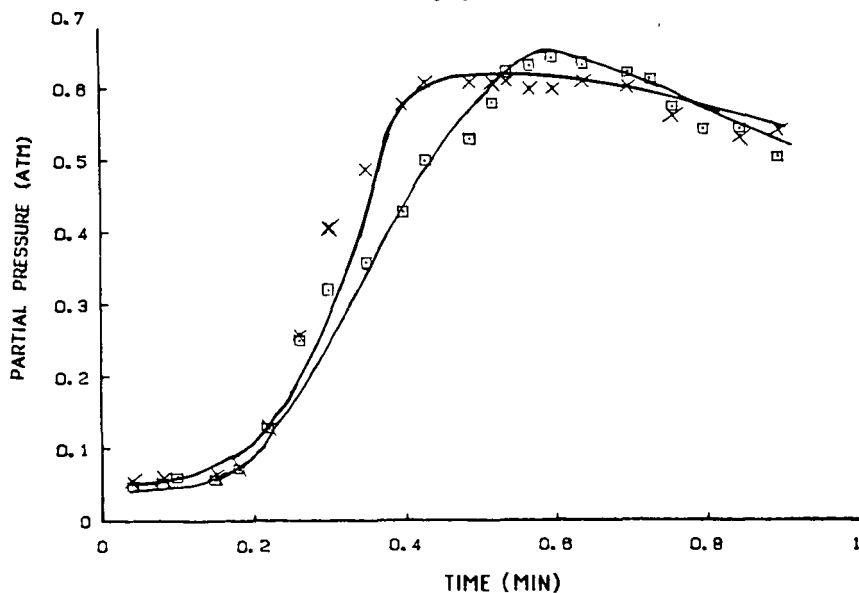


Figure 2. Experimental transient responses of  $CO$  and  $H_2$  versus model predictions for steam gasification of Fisher activated coconut char (2.135 g mol of char;  $T_{bed} = 757^\circ C$ ;  $P_{total} = 13.6$  atm;  $P_{steam} = 7.5$  atm).

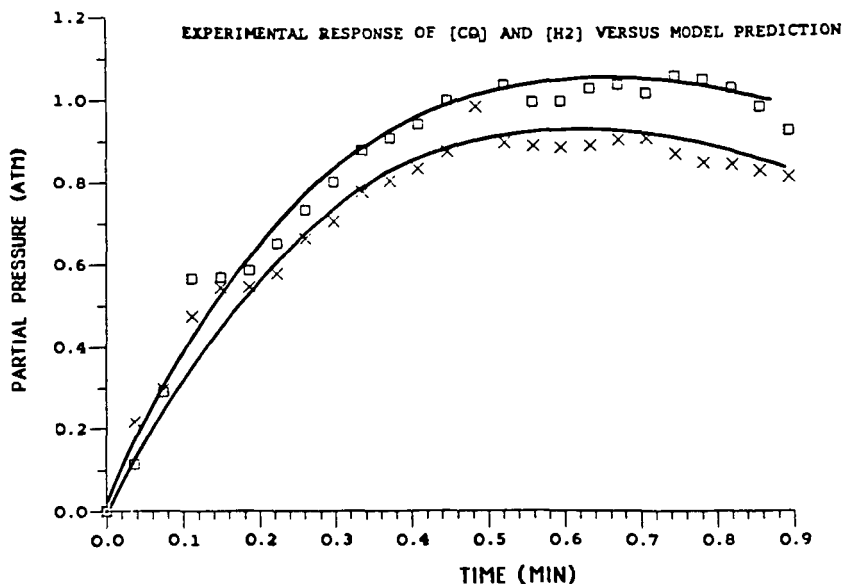


Figure 3. Experimental transient responses of CO and H<sub>2</sub> versus model predictions for steam gasification of Darco lignite (PSOC 623) char (2.903 g mol of char;  $T_{bed}=765^{\circ}\text{C}$ ,  $P_{total}=23.4$  atm;  $P_{steam}=14$  atm).

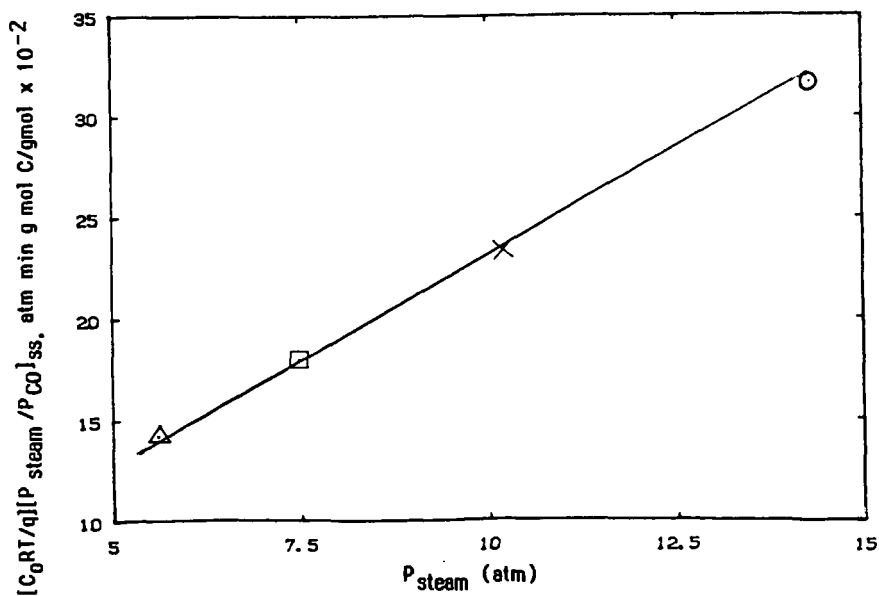


Figure 4. Pseudo-steady-state steam gasification rate data for Fisher activated coconut char ( $T_{gas}=1058$  K, 2.135 g mol of char).



POPULATION AND TURNOVER NUMBER OF ACTIVE POTASSIUM SITES  
ON BITUMINOUS COALS DURING GASIFICATION

C. T. Ratcliffe\*

Corporate Research-Science Laboratory  
Exxon Research and Engineering Company  
Route 22 East, Annandale, N.J. 08801

S. N. Vaughn

Exxon Research and Engineering Company  
P. O. Box 4255  
Baytown, Texas 77520

Introduction

The activity of alkali metal salts as catalysts for steam gasification on carbon surfaces has been well documented.<sup>(1-2)</sup> The kinetics of catalyzed gasification with potassium salts on carbon and the data obtained from characterizing alkali metal treated carbon is consistent with potassium in a highly dispersed and ionic state.<sup>(3-5)</sup>

The rate of potassium catalyzed gasification on bituminous coals, when plotted as a function of carbon conversion, tends to decrease at higher carbon conversions and can be highly variable depending on the source of coal and method of catalyst treatment. The mechanism(s) of catalyst deactivation are not well understood; loss of potassium sites due to reaction with mineral matter, limited mobility after initial reaction, detachment from the coal surface and collapse of pore structure have all been suggested as reasons.<sup>(6-8)</sup> A key factor in developing a fundamental understanding of the change in rate behavior will be the ability to accurately count the population of active alkali sites during gasification as a function of carbon conversion.

We have recently found that carbon dioxide chemisorbs in an irreversible manner on the surface of potassium treated Sphercarb, a high surface area carbon.<sup>(9)</sup> The molar quantity of CO<sub>2</sub> adsorbed on this surface at 300°C, after initial thermal treatment at 850°C, correlated with the level of potassium loading and suggested a facile method of measuring alkali dispersion. The value of 0.5 to 0.6 adsorption sites per K<sub>2</sub>O impregnated on the surface also agreed with the initial number of active sites measured by the derivitization technique.<sup>(10)</sup>

The purpose of this investigation has been to establish CO<sub>2</sub> chemisorption as a tool to selectively measure the population of active alkali sites on gasified coal chars and to determine the specific activity or turnover number of the active sites under gasification conditions.

\* Current address: Union Oil Company of California, Union Science and Technology Division, P. O. Box 76, Brea, California, 92621.

## Experimental

Samples of bituminous coals were obtained in 5 gallon containers from the mines under a nitrogen atmosphere. The coals are identified by mine and state as: Monterey No. 1, Illinois #6, Hawk's Nest, Colorado; Valley Camp, Utah; Walden, Colorado. The samples were sealed in an inert atmosphere for shipment and opened in a controlled atmosphere dry box. Impregnation of the coals with aqueous solutions of potassium carbonate or potassium hydroxide were performed in a controlled atmosphere environment by the method of incipient wetness. Alkali salts were obtained commercially (reagent grade  $K_2CO_3$ , ultra pure KOH,) with aqueous solutions prepared immediately before impregnation. After impregnation, the samples were dried under inert atmosphere and stored in sealed glass vessels. While an apparent dispersion was observed with all KOH treated coals, the  $K_2CO_3$  treated coals required rewetting the samples, followed by stirring and drying to obtain an even dispersion of  $K_2CO_3$ . The loading of potassium was in the range of 7-10%.

Adsorption and gasification studies were performed with a Mettler 2000C TGA/DSC thermal analysis unit equipped with a corrosive gas head <sup>(9)</sup> and a DuPont 951 TGA unit with a pressurized housing for operation up to 500 psig (Figure #1).

## Technique for Adsorption, Gasification

The adsorption properties of bituminous coal and catalyzed coal samples were measured by means of the following procedure. A sample of approximately 80 milligrams was loaded into a ceramic crucible with an equivalent amount of SP-1 graphite prepared in a crucible of identical color and approximately the same mass. The preweighed crucibles were loaded onto the TGA/DSC platform and outgassed at ambient temperature by mild evacuation ( $10^{-3}$ mm) for one half hour. The sample and reference material were subsequently temperature programmed at  $29.9^\circ/\text{min.}$  to  $850^\circ\text{C}$  in flowing helium. After heat treatment, samples were cooled to the desired temperature of  $300^\circ\text{C}$  for adsorption studies. While the sample was maintained at the selected isothermal temperature, a measured flow of  $CO_2$  was introduced into the helium carrier. The reactive gas flow, as measured by the Tylan flow meter, was maintained at 2cc per minute with the carrier flow of 20cc per minute helium; thus a partial pressure ratio of 1:10 of  $CO_2$  to inert carrier was utilized during the adsorption study.

Adsorption of  $CO_2$  was monitored by weight gain recorded on a strip chart. Adsorption was normally rapid with a plateau in total weight reestablished in 15-30 minutes. The mixed gas stream was replaced with a pure helium stream with a second period of 10-15 minutes allowed for any subsequent change in weight. The total adsorbed gas could thus be divided into physical and chemical adsorbed fractions as the former was desorbed when the reactive gas was replaced by helium and the latter was retained as a net weight gain.

A measured flow of  $CO_2$  or  $H_2O$  vapor was mixed with the He carrier gas flows and the temperature of the sample was raised to an isothermal value of  $700-800^\circ\text{C}$  to perform partial gasification of the char. After a steady state period was established, the rate of weight loss per unit time was obtained. The reactive gas flow was subsequently terminated and the above described procedure was repeated for  $CO_2$  measurement of the active site density.

High pressure measurements were performed on a modified DuPont 951 TGA which had been enclosed in a pressurized housing (Figure 1). A similar procedure was used to obtain the rate of gasification; the reactive gas composition was 30%  $H_2O$ , 7%  $CO$ , 13%  $CO_2$ , 15%  $CH_4$  and 35%  $H_2$ . Operating conditions were 500 psig and 705°C. Adsorption measurements with  $CO_2$  were obtained at 300°C, one atmosphere pressure, by the procedure described above with a flow of  $N_2$  as the inert carrier gas.

### Results and Discussion:

Adsorption of  $CO_2$  was examined on each of the neat coals after thermal treatment to 850°C. While physisorption was observed at lower temperatures (100°C) in all cases, only Walden and Valley Camp chars revealed any measureable chemisorption at 300°C. The thermal desorption profile of Walden or Valley Camp chars after  $CO_2$  adsorption identified  $CaCO_3$  formation from  $CO_2$  interaction with  $CaO$  as the source of the chemisorption. The quantity of  $CO_2$  was always an order of magnitude lower than adsorption on alkali treated chars. A display of the quantity of  $CO_2$  adsorbed on  $K_2CO_3$  and  $KOH$  treated coals is shown in Figures 2 and 3. The molar quantity of  $CO_2$  adsorbed (measured by TGA) has been normalized with the molar quantity of impregnated potassium salt to represent relative dispersion values on the ordinate axes. As the chemisorption measurement with  $CO_2$  is performed after each thermal heat cycle to 850°C in inert atmosphere, only active potassium sites which are bonded to the carbon will chemisorb  $CO_2$ . Any free potassium oxide, hydroxide, or basic salt will irreversibly adsorb  $CO_2$  on the first cycle and remain as thermally stable  $K_2CO_3$ . Thus, the efficacy of the technique is its ability to selectively measure only the active potassium complexes bonded to the carbon surface, as they regenerate on each thermal heating cycle to 850°C in  $He$ .

The similarity of the four bituminous coals in their number of available active sites is in contrast to the higher and more constant value of  $K_2CO_3$  impregnated Spherocarb ( $800m^2/g$ , mineral free amorphous carbon) as shown in the dotted line of Figure #2. The low population of active sites on the  $KOH$  and  $K_2CO_3$  treated coal chars may represent a limited surface area, as recently reported by Shadman.<sup>(11)</sup> The lower initial values on  $KOH$  - coals do not correspond to lower surface areas with our BET measurements, but do correlate in a positive manner with lower volatile matter release on initial thermal treatment. Deposition of carbon or non-volatile carbonaceous residue on the active base sites may limit the availability of alkali after initial thermal treatment. Franklin, Peters and Howard have detailed the effect of mineral matter and especially in exchanged alkali on reducing the volatile matter and tar upon pyrolysis of bituminous and sub-bituminous coals.<sup>(12-14)</sup> The greater reduction in volatile matter with  $KOH$  vs.  $K_2CO_3$  treated coals, due to the stronger base, most probably results in a higher localized coating of condensed tar on the active alkali sites. The temporary "poisoning" of the sites to  $CO_2$  adsorption in  $KOH$  or  $K_2CO_3$  treated chars is removed after the initial 5-10% gasification.

The maximum population of sites in the 20-50% char conversion range, representing about 30% dispersion of  $K_2O$ , is only one-half the value obtained with potassium impregnated Spherocarb. Interaction of the basic potassium salts with the mineral matter may well have consumed a portion of the impregnated salt (7) in addition to a possible lower dispersion of the salts on the lower surface area chars. The decline in the site population at 60-90% carbon conversion indicates the continued neutralization of the alkali with mineral matter in addition to the detachment of alkali from the carbon.

When the rate of gasification with  $\text{CO}_2$  is corrected for the population of active sites at each level of char conversion, a specific activity or turnover number can be obtained. The turnover number for Valley Camp and Hawk's Nest coal (both impregnated with KOH) as a function of char conversion are shown in Figure #4 for  $\text{CO}_2$  gasification. The constant value of the turnover number for the entire range of char conversion now establishes the density of active potassium sites as the rate controlling parameter in  $\text{CO}_2$  gasification of these coals. While the results in Figure #4 clearly remove the quantity of carbon in the char as a rate controlling parameter, the change in the concentration or composition of the vapor phase reactant atmosphere is also known to affect catalyzed gasification. Samples of the same impregnated Valley Camp and Hawk's Nest coals have been studied under high pressure conditions with a reactive atmosphere typical of a fluid bed steam/coal gasification environment. The plot of turnover number vs char conversion under this set of reaction conditions is shown in Figure #5. The difference in the average turnover number shown for the two sets of gasification conditions can be attributed to differences in reactivity of the two gas atmospheres. It is again obvious that the constant turnover number for potassium over the range of char conversion confirms the rate controlling nature of the potassium site density for coal gasification.

#### Summary:

Chemisorption of  $\text{CO}_2$  at  $300^\circ\text{C}$  provides a selective and rapid technique to measure the active site density of alkali catalysts on coal at intermittent periods of coal gasification. With a thermal balance/reactor, the specific activity per catalyst site (turnover number) has been measured for catalyzed gasification of  $\text{CO}_2$  or steam/product gases with bituminous coals. The site density of potassium on carbon as the rate controlling parameter in gasification of coal as shown by a constant value for the turnover number over the full range of char conversion.

## REFERENCES

1. International Symposium, Fundamentals of Catalytic Coal and Carbon Gasification, Special Issue, *Fuel*, **62**, 1-261 (1983)
2. For Review, D. W. McKee, *Chem. Phys. of Carbon*, **16**, 1-118 (1981)
3. C. A. Mims, J. J. Chludzinski, J. A. Pabst, R. T. K. Baker, *J. Catalysis*, **88**, 97 (1984)
4. F. J. Long, K. W. Sykes, *J. Chim. Phys.*, **47**, 361 (1950)
5. C. L. Spiro, D. W. McKee, P. G. Kosky, E. J. Lamby, *Fuel* **63**, 686, (1984)
6. F. Kapteijn, J. A. Moulijn, *Fuel* **62**, 205, (1963)
7. L. Kuhn, H. Plogmann, *Fuel*, **62**, 205 (1983)
8. D. Douchanov, G. Angelova, *Fuel* **62**, 231 (1983)
9. C. T. Ratcliffe, Proceedings of the 13th North American Thermal Analysis Society, p.90, September 23-26, 1984, Philadelphia, PA
10. C. A. Mims, K. D. Rose, M. T. Melchior, J. A. Pabst, *J. Am. Chem. Soc.*, **104**, 886 (1982)
11. F. Shadman, D. A. Sams, Div. of Fuel Preprints, **29**(2), 160 (1984)
12. H. D. Franklin, W. A. Peters, J. B. Howard, *Fuel*, **61**, 155, (1982)
13. Ibid, 1214
14. H. D. Franklin, R. G. Cosway, W. A. Peters, *I&EC Process Des. Dev.*, **22**, 42 (1983)

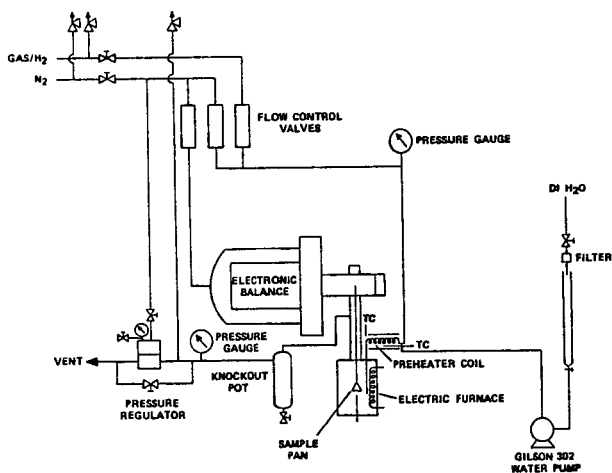


Figure 1. High Pressure TGA Reactor System for Char Gasification

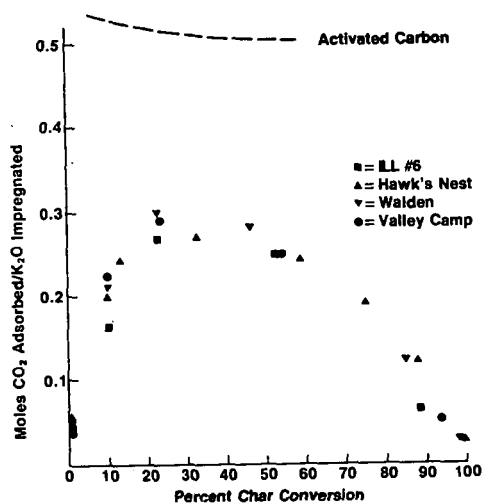


Figure 2, Dispersion of KOH treated coal chars vs carbon conversion as measured by  $\text{CO}_2$  chemisorption at  $300^\circ\text{C}$ .

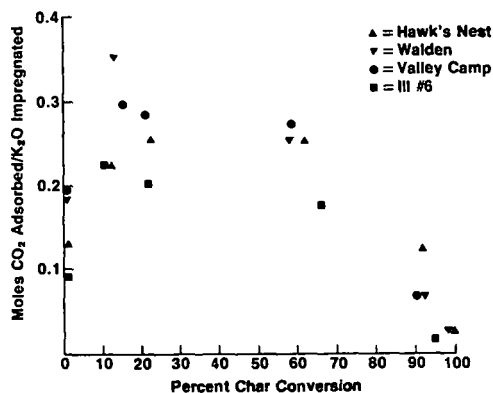


Figure 3. Dispersion of  $\text{K}_2\text{CO}_3$  Treated coal chars vs carbon conversion as measured by  $\text{CO}_2$  chemisorption at  $300^\circ\text{C}$ .

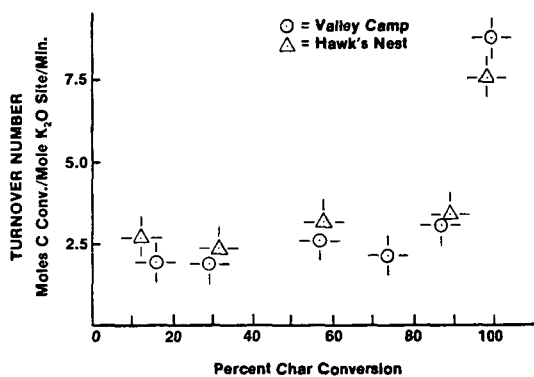


Figure 4. Specific activity per site of KOH treated coals v carbon conversion;  $\text{CO}_2$  gasification,  $\odot$  Valley Camp,  $\triangle$  Hawk's Nest.

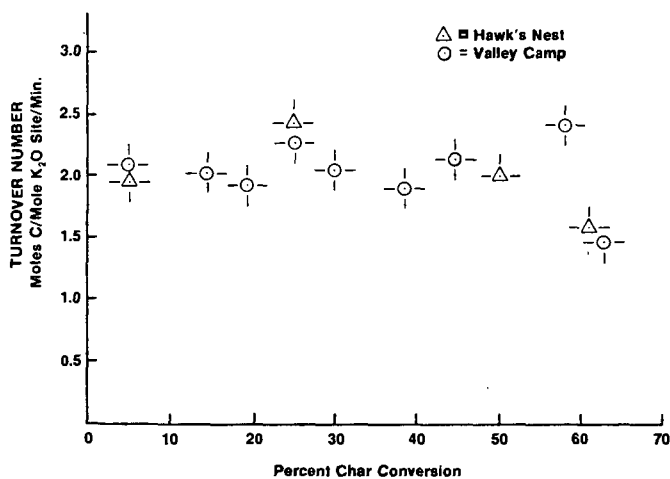


Figure 5. Specific activity per site of KOH treated coals vs carbon conversion;  $\text{H}_2\text{O}/\text{CO}_2$ /recycle atmosphere gasification, 500 psig, vs carbon conversion;  $\odot$  Valley Camp,  $\triangle$  Hawk's Nest.

## THE KINETICS OF CARBON GASIFICATION BY CO<sub>2</sub>

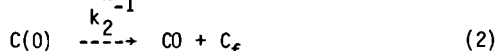
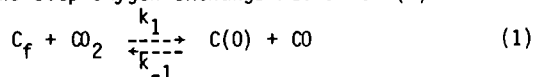
H. Freund

Exxon Research and Engineering Company  
Corporate Research - Science Labs  
Clinton Township, Route 22 East  
Annandale, NJ 08801

### INTRODUCTION

Considerable work has been done in the area of catalytic carbon gasification(1-3) and recently an entire issue of Fuel was devoted to this area.(4) And yet there is still considerable uncertainty about the basic fundamentals. Different kinetic measurements have been reported for similar systems and different theories and mechanisms appear for catalytic gasification.

The mechanism for the gasification of uncatalyzed carbon has been postulated to be a simple two step oxygen exchange mechanism (5):



where  $C_f$  is an available active site, and  $C(O)$  is one which is occupied has been applied to uncatalyzed gasification. In this paper, it will be applied to Ca- and K-catalyzed as well. From a kinetic analysis the rate constant  $k_2'$  can be determined.  $k_2'$  is the product of the active site density and the intrinsic decomposition rate constant,  $k_2$ . It still remains to uncouple the active site density from  $k_2'$  to determine  $k_2$ .

Such an uncoupling can be accomplished by a transient kinetics experiment. Other workers have examined the transient kinetics during the establishment of steady state gasification conditions and have reported  $k_1$  and  $k_2$ . The activation energy for  $k_2$  of 44.8 kcal/mole seems low.(6) In this present paper, the transient kinetics are studied as a steady state gasifying system relaxes when the oxidant is suddenly removed from the system.

Under steady state conditions, in an atmosphere of CO<sub>2</sub>, reaction (1) is driven to the right, populating all available sites and producing one CO molecule for each active site reacted. A second molecule of CO is formed when this complex decomposes. If the oxidant were to be rapidly removed from the system, reaction (1) would be shut down but the surface complex would decay with a characteristic time constant  $k_2$ , if  $k_{-1}[CO]$  were negligible compared to  $k_2$ . One can estimate the magnitude of  $k_2$  and  $k_{-1}$  using the results of Sy and Calo.(6)  $k_{-1}$  can be determined from Sy and Calo's  $k_1$  and Ergun's (5) equilibrium constant. At 1000 K and  $[CO] = 100$  ppm,  $k_{-1}[CO] = 9.1 \times 10^{-4} \text{ min}^{-1}$  and  $k_2 = 1.6 \text{ min}^{-1}$ . Indeed  $k_2 \gg k_{-1}[CO]$ . At sufficiently low temperatures the decay time constant in the transient experiment will be long enough to be measurable. If one were



monitoring CO, one would expect to see ideally an instantaneous decline of the CO to one half of its steady state level followed by an exponential decay of CO.

## EXPERIMENTAL

TGA experiments were done with a Dupont model 951 thermogravimetric analyzer. CO<sub>2</sub>, CO, and Ar were prepurified grade and were used without further purification. The carbon samples used were Analab's Sphero carb (-60+80 mesh), Supelco's Carbosieve S (-120+140 mesh), glassy carbon obtained from Atomergic Chemetals Corp., and a 1000°C char made from Illinois #6 coal. Research grade anhydrous K<sub>2</sub>CO<sub>3</sub> was used as the source of potassium and was co-crushed with the sphero carb to make various mixtures of K<sub>2</sub>CO<sub>3</sub> on sphero carb. The Carbosieve was oxidized overnight in HNO<sub>3</sub> to prepare carboxylic acid sites on the carbon. To prepare Ca-treated carbon this material was then ion-exchanged in an ammoniated Ca (NO<sub>3</sub>)<sub>2</sub> solution.

For a run, approximately 50 mg of sample were loaded into the TGA. All samples were first heated under argon up to a pre-designated temperature (50°/min up to 900°C, for non-potassium samples, 20°/min up to 800°C for potassium samples). Gasification was then generally done at or below these preheat temperatures. This was done to minimize any pyrolysis effects which might occur during gasification. Mixtures of CO and CO<sub>2</sub> (10% CO in CO<sub>2</sub> was the most common) were prepared using Matheson mass flow controllers and passed into the TGA at around 300 cc/min at a pressure of 10 kPag.

The TGA data were obtained measuring sample weight as a function of time. Steady state slopes were usually measured. For the Ca samples, generally the initial rate was taken as there was rather rapid catalyst deactivation. The rate of carbon gasified, R, is defined as  $1/w \, dw/dt$  where w is the weight where the slope (tangent) was drawn and dw/dt is the slope or rate of weight loss. The units of this are g/g/min or grams of C gasified per gram of material per unit time. Figure 1 is an Arrhenius plot for one sample (20% K<sub>2</sub>CO<sub>3</sub> on Sphero carb) showing the effect of the CO/CO<sub>2</sub> ratio.

The flow reactor experiments were done in a 1 cm ID quartz flow reactor within an open ended vertical furnace. The carbon samples sat on a quartz frit, ~20μ pore size. Gas flow was about 1000 cc/min (Ar + CO<sub>2</sub>) and was passed down over the sample. The sample thermocouple passed through a 0.64 cm OD quartz tube through the length of the reactor and was positioned just above the frit.

In order to minimize O<sub>2</sub> contamination, both CO<sub>2</sub> and Ar were passed through an O<sub>2</sub> scrubber. This was a packed bed (45 cm x 1.1 cm ID) of copper chromite catalyst (Harshaw Chem) operated at 150-160°C. The catalyst was activated by H<sub>2</sub> reduction. The bed should reduce O<sub>2</sub> below 1 ppm. CO was monitored using a Thermo Electron Corporation Model 48 CO analyzer. CO<sub>2</sub> was monitored with a Beckman Model 865 infrared analyzer.

The procedure was to charge the reactor with sample and heat to 800-850°C under flowing Ar. This established a common reference condition

for all samples. The temperature was then dropped into the range 570-670°C and 10% CO<sub>2</sub> was added to the gas flow. When steady state was reached, CO<sub>2</sub> was turned off and the decay in CO monitored as a function of time. The observed time constant for CO<sub>2</sub> to be swept out of the system was about 5 sec (10%-90%). The CO analyzer instrumental time constant was 30 sec (0-95%).

## ANALYSIS

In order to properly reduce the TGA data, the effect of the CO/CO<sub>2</sub> ratio had to be taken into account. Using Langmuir-Hinshelwood kinetics and applying the steady state assumption to C(O) in reactions (1) and (2) and assuming that the number of free sites remain constant with burn off, the global surface rate for CO<sub>2</sub> gasification can be shown to be

$$R \equiv \frac{1}{w} \frac{dw}{dt} = \frac{k_1(\text{CO}_2)[C_T]}{1 + k_1/k_2(\text{CO}) + k_1/k_2(\text{CO}_2)} \quad (3)$$

where R is the measured rate of carbon weight loss, (CO<sub>2</sub>) and (CO) are the gas concentrations of CO<sub>2</sub> and CO and [C<sub>T</sub>] is the active site density, g active carbon per g of total carbon. An active site is either free or occupied and hence C<sub>T</sub> = C<sub>f</sub> + C(O). Ergun(5) has shown that Eqn. (3) reduces to

$$R = \frac{k_2[C_T]}{1 + (\text{CO}/\text{CO}_2)K_{eq}} \quad (4)$$

under mild gasification conditions (low T, low pressure). In Equation (4), K<sub>eq</sub> is the equilibrium constant for reaction (1) which is equilibrated at these conditions. Eqn. (4) can be rearranged so that

$$\left(\frac{\text{CO}}{\text{CO}_2}\right) = K_{eq} k_2[C_T] \left(\frac{1}{R}\right) - K_{eq} \quad (5)$$

Hence a plot of CO/CO<sub>2</sub> vs 1/R should yield a straight line with y-axis (CO/CO<sub>2</sub>) intercept of -K<sub>eq</sub> and an x-axis (1/R) intercept of 1/k<sub>2</sub>[C<sub>T</sub>].

The author has applied this mechanism to his data from experiments on catalytic gasification by CO<sub>2</sub> using K and Ca as catalysts as well as experiments with no catalyst present. The CO<sub>2</sub> data for K<sub>eq</sub> is plotted in Figure 2. The curve in Figure 2 is the published Ergun(5) value for K<sub>eq</sub> multiplied by 2. In his paper he mentioned that K<sub>eq</sub> can differ by a factor of 2 depending on which of two algebraic expressions he used to obtain K<sub>eq</sub>. Using K<sub>eq</sub>, a value of k<sub>2</sub>[C<sub>T</sub>] (≅ k<sub>2</sub>) can then be obtained from eqn (4). These have been plotted as Arrhenius plots in Figure 3.

For the flow experiments, two typical CO traces are shown in Figures 4 and 5 for the carbon sample and for the Ca impregnated sample. Note that in Figure 4 there is a substantial dip which occurs when the CO<sub>2</sub> is first turned off. This phenomenon will be discussed later. Two pieces of information were taken from each plot: the steady state value for CO<sub>2</sub> gasification and the rate of CO decay.

The steady state value of CO produced can be converted into the rate constant,  $k_2'$  knowing the total molar gas flow and the carbon loading in the bed. From the overall gasification stoichiometry and the molar gas flow, the observed CO concentration can be related to the moles of carbon being gasified per unit time. Knowing the initial bed weight,  $k_2'$  ( $\equiv 1/w \, dw/dt$ ) can then be determined.

If the rate of CO decay is exponential, the decay constant is the intrinsic rate constant for the decomposition of the surface complex. In most cases, at a given temperature, a small non-zero CO value was obtained in the absence of CO<sub>2</sub>. This value was subtracted out; it was generally less than 10% of the steady state value.

The values of  $k_2'$  derived from the steady state data are shown as an Arrhenius plot in Figure 6. The data scatter about the lines obtained from the TGA work on similar samples. Also included in Figure 6 are the decay constants from the transient experiment, i.e. the intrinsic rate constant,  $k_2$ . Least square analysis yields an average value of:

$$k_2 = 10^{11.6 \pm 2.3} \exp \frac{-53700 \pm 9400}{RT} \text{ min}^{-1}.$$

(uncertainties determined for a 95% confidence limit).

## DISCUSSION

The experimental values for  $K_{eq}$  (Eqn. 1) determined in this work fall quite close to the line determined by Ergun (see Figure 2). This is strongly suggestive that the equilibrium in equation (1) is not affected by the presence of a catalyst. This is further corroborated by the fact that after correcting for the CO/CO<sub>2</sub> ratio in the manner described, the four lines in Figure 1 collapse to one line in Figure 3. Ergun determined the activation energy for uncatalyzed CO<sub>2</sub>-carbon gasification to be 59 kcal/mole. Except for glassy carbon, in the present experiments, least squares analyses on those systems with at least seven points show activation energies within 3.2 kcal of Ergun's value. Because the lines in Figure 3 are parallel to one another, the activation energy for reaction (2), the desorption of CO, is independent of catalyst. This means that the reactive surface intermediate in the catalytic cases must decompose as if the catalyst were not present i.e., it must decompose like reactive adsorbates in uncatalyzed gasification. This author interprets the parallel Arrhenius plots shown in Figure 3 for different carbon-catalyst combinations to mean that the catalyst is effectively acting solely to increase the active site density.

The observation of a decrease in CO in the transient flow experiments of about one half followed by an exponential decay strongly suggests that the two step gasification mechanism is indeed controlling. One can now determine the fraction of total carbons which are "active" ---- dividing  $k_2'$  by  $k_2$  yields the active site density. For the uncatalyzed carbon, one obtains a value,  $4.7 \times 10^{-5}$  active carbon/total C. This exceedingly small value is quite unexpected. In terms of "active surface area", this corresponds to about .019% of the total BET surface area (this was obtained using 1000 m<sup>2</sup>/g as the BET surface area of the carbon and

$8 \times 10^{-16} \text{ cm}^2$  as the area for an active site(7)). This is a factor less than 1/10 that of active surface measured via  $\text{O}_2$  chemisorption of Graphon(4). For high surface area chars, Radovic et al(8) found active surface area/total surface area  $\sim 10\%$ . These chemisorption techniques measure active carbons with respect to  $\text{O}_2$  adsorption. In carbon gasification by  $\text{CO}_2$  it is not the case that all the sites available to  $\text{O}_2$  are assessable by  $\text{CO}_2$ (9). Furthermore not all of the active sites by chemisorption are active in gasification since some represent very active sites which are probably unavailable for reaction because of a stable carbon-oxygen complex while others of low reactivity will form the carbon-oxygen reaction intermediate only very slowly.

The fact that a catalytic system yielded the same  $k_2$  strongly supports the contention that Ca (and presumably other alkaline earth as well as alkalis) catalyze the system by increasing the number of sites. It does not affect  $k_2$ , the rate constant controlling the removal of carbon atoms as CO from the lattice.

The implication of these experiments is that a simple two step oxygen exchange mechanism, although an oversimplification, can still be used to explain  $\text{CO}_2$  gasification. The data herein are self-consistent. The steady state values for  $k_2'$  scatter about extrapolated TGA data obtained earlier for the same samples. Activation energies for  $k_2'$  are  $\sim 58$ -60 kcal/mole. Two different carbon systems which yield  $k_2'$  (c.f. Figure 6) differing by a factor of 100 yield the same  $k_2$  (within the scatter) with an activation energy roughly the same as  $k_2'$ .

The value of  $k_2$  can be compared to the value obtained by Sy and Calo. At 1000 K they obtain  $k_2 = 1.6 \text{ min}^{-1}$ . In this work, at 1000 K,  $k_2 = .71 \text{ min}^{-1}$ , fairly good agreement for a high temperature rate constant. Although the uncertainty in the activation energy is fairly large ( $53.7 \pm 9.4$ ) and encompasses the value determined by Sy and Calo (44.8), this author feels that a  $\Delta E$  closer to that obtained from gasification kinetics<sup>5,10</sup>, i.e.,  $\Delta E \sim 59 \text{ kcal/mole}$  would be most consistent with the available data and the 2-step oxygen exchange mechanism.

There still remain questions regarding the interpretation of the data presented here. One problem can be seen in the Ca plot in Figure 5. After about 60% of the surface complex has decomposed, the rate of CO decrease slows down, i.e. more CO is liberated than expected for an exponential decay. Apparently another mechanism for CO release becomes appreciable; perhaps as just mentioned, complexes of lower reactivity begin to decompose.

In Figure 4, after  $\text{CO}_2$  is turned off, the CO signal dips well below the 50% value before beginning an exponential decay. If one extrapolates back to  $t=0$ , however, it appears to intersect a CO value about half of the initial (because of the dilution effect of the Ar, the value should be 10% larger than 1/2). What appears to be happening is the following: In the case of uncatalyzed carbon, CO initially produced is scavenged by some surface species and can not escape as CO. This scavenging species becomes depleted and CO is able to escape from the bed, thus "resuming" the exponential decay. For Ca-catalyzed carbon either the species does not exist or the effect is swamped by the higher level of CO produced. The

observation of such a large dip suggests more complicated chemistry than a simple two-step oxygen exchange mechanism.

Other carbon systems also suggest more complicated chemistry. A different Ca-catalyzed carbon (Ca-impregnated spherocarb) gave entirely different results: on  $\text{CO}_2$  removal (in the same temperature regime), the  $\text{CO}$  signal dropped to ~90-95% of the steady state value, and no decay constant could be measured. This kind of behavior was observed with  $\text{K}_2\text{CO}_3$ /spherocarb samples. The  $\text{CO}$  concentration dropped to about 90% and declined further slowly with time. In work done subsequent to that reported herein, spherocarb gave a similar rate constant as determined here but the  $\text{CO}$  fell more than half of the steady state value. The results seem to depend on the particular carbon system not on the experimental arrangement. It is not surprising that the structure of the carbon, the micro-pore distribution, the nature of the catalyst or its dispersion may have an effect on the result in these kinds of experiments.

#### Acknowledgements

The technical help of James Pizzulli is gratefully acknowledged.

#### References

1. Walker, P. L., Shelef, M. and Anderson, R. A., Chemistry & Physics of Carbon 4, 287-383 (1968).
2. Wen, W. Y., Catal. Rev. - Sci. Eng., 22, 1-28 (1980).
3. Laurendeau, N., Prog. Energy Combust. Sci. 4 221-270 (1978).
4. Fuel 62 (1983) contains the papers presented at the International Symposium, "Fundamentals of Catalytic Coal and Carbon Gasification," held in Amsterdam the Netherlands, September 27-29, 1982.
5. Ergun, S., J. Phys. Chem. 60, 480-485 (1956).
6. Sy, O. and Calo, J. M., AIChE Annual Meeting, preprint #56b, November 14-18, 1982.
7. Laine, N. R., Vastola, F. J. and Walker, P. L., Jr., J. Phys. Chem. 67, 2030 (1963).
8. Radovic, L. R., Walker, P. L., Jr., Jenkins, R. G., Fuel 62, 849 (1983).
9. Freund, H. and Kelemen, S. R., in preparation.
10. Sundareson, S. and Amundsen, N. R., Ind. Eng. Chem. Fundam. 19, 351 (1980).

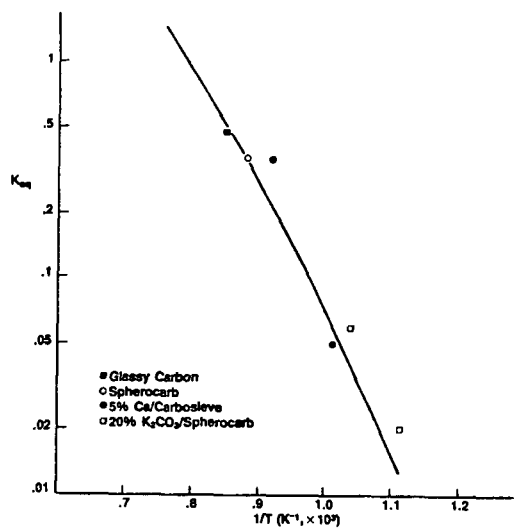


Figure 1: Oxygen Exchange Equilibrium Constant,  $K_{eq}$ , as a Function of Temperature. Line is from Ergun (5), Data are from Present Experiments.

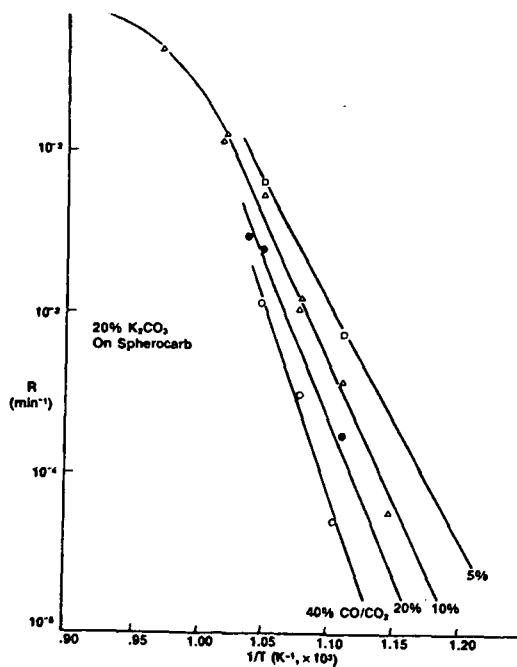


Figure 2: Effect of  $CO/CO_2$  Ratio on Gasification Rate

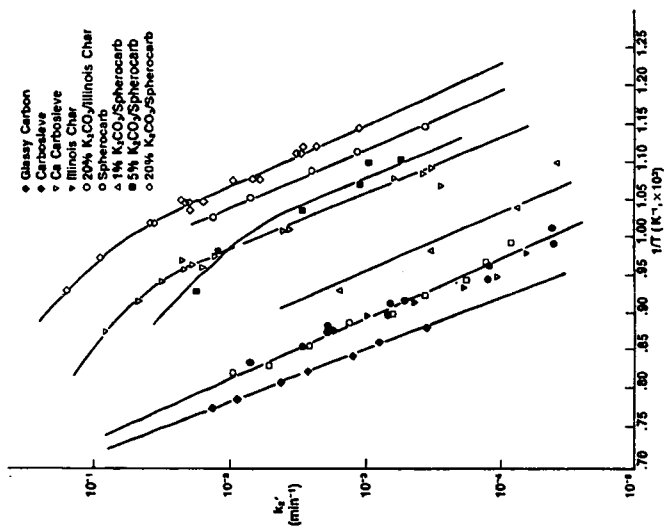


Figure 3 Arrhenius Plots of  $k_2$  for Different Catalytic and Noncatalytic Systems.

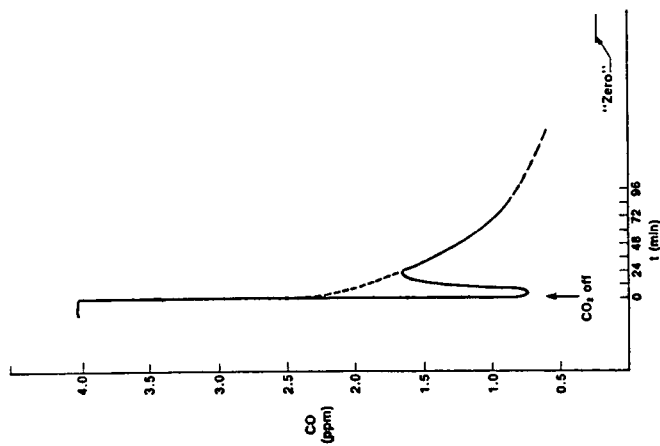


Figure 4 Experimental CO Trace for Uncatalyzed Carbon  $T=607^\circ\text{C}$ .

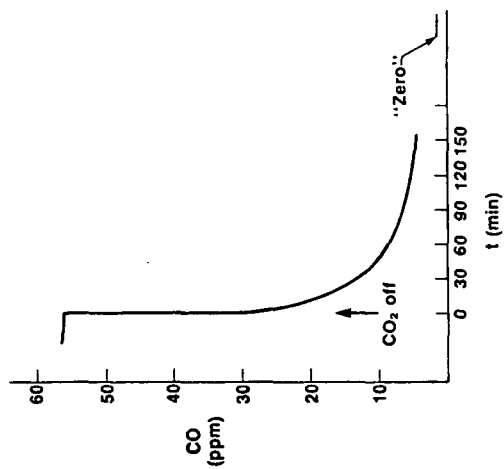


Figure 5: Experiment CO trace for Ca-catalyzed carbon,  $T = 629^{\circ}\text{C}$

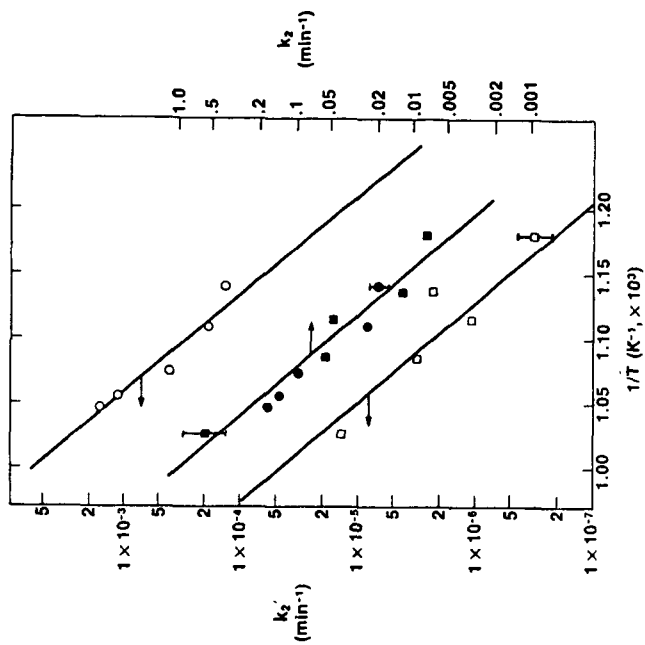


Figure 6: Arrhenius Plot of Rate Constants  $k_2$  and  $k_2'$ ;  $\circ$  and  $\square$  - Ca-catalyzed Carbon; and  $\bullet$  - Uncatalyzed Carbon. The lines of  $k_2$  are from the TGA data.



# CHAR GASIFICATION BY CARBON DIOXIDE: FURTHER EVIDENCE FOR THE TWO-SITE MODEL

P.C. Koenig, R.G. Squires, N.M. Laurendeau

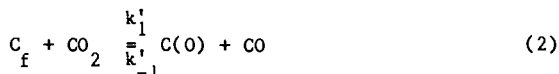
Coal Research Center, Purdue University, West Lafayette, IN 47907

## 1. INTRODUCTION

Several experimental studies of the C-CO<sub>2</sub> gasification reaction have been made. Many investigators have noted that the kinetic data substantiate a rate equation of Langmuir-Hinshelwood form [1,2,3,4]:

$$R = \frac{b_1 [CO_2]}{1 + b_2 [CO] + b_3 [CO_2]} \quad (1)$$

where  $R$  is the intrinsic reactivity (g/m<sup>2</sup> s), and the  $b$ 's represent rate coefficient ratios. Laurendeau [4] summarizes the evidence supporting the following oxygen exchange mechanism which is in agreement with Eqn. (1):



where  $C_f$  represents a free carbon site and  $C(O)$  a chemisorbed oxygen atom. Applying the steady state approximation to  $C(O)$  and a balance on active sites,

$$[C_t] = [C_f] + [C(O)], \quad (4)$$

yields the following values for  $b_1$ ,  $b_2$ , and  $b_3$ :

$$b_1 = m_c k_1' [C_t], \quad b_2 = \frac{k_{-1}'}{k_2}, \quad b_3 = \frac{k_1'}{k_2} \quad (5)$$

where  $m_c$  is the mass of a carbon atom.

Inverting Eqn. (1) gives

$$\frac{1}{R} = \frac{b_3}{b_1} + \frac{b_2}{b_1} \frac{[CO]}{[CO_2]} + \frac{1}{b_1} \frac{1}{[CO_2]}. \quad (6)$$

Thus, the following relationships should exist at constant temperature, if the above model holds:

1.  $1/R$  vs.  $1/[CO_2]$  should be linear for constant  $[CO]$ ;
2.  $1/R$  vs.  $1/[CO_2]$  should be linear for constant  $[CO]/[CO_2]$ ;
3.  $1/R$  vs.  $[CO]$  should be linear for constant  $[CO_2]$ ;
4.  $1/R$  vs.  $1/[CO_2]$  should be linear for near-zero  $[CO]$ .

The purpose of this paper is to examine these relationships for data obtained from our laboratory and the literature. In the course of this analysis, we will show that sufficient experimental evidence exists to question the validity of Eqn. (6) and hence the single-site oxygen exchange mechanism. A two-site model is proposed to explain the available experimental data.

## 2. EXPERIMENTAL PROCEDURE

A differential packed-bed reactor made from 15 mm ID quartz was employed to study the gasification kinetics of Saran char at temperatures between 858 and 956°C, and a total pressure near 1 atm (101.3 kPa). The Saran char was made by heat-treating Dow Chemical Saran polymer in nitrogen at 1300 K for three hours. The reactor was typically loaded with between 0.15 and 3.75 gm of ~250  $\mu$ m char particles yielding a bed height between 0.5 and 10.0 cm. Carbon dioxide, carbon monoxide and argon at 99.99% purity were flowed through the char bed at a total flow rate of between 200 and 1000 cc/min (STP). Carbon dioxide was used as the reactant gas, carbon monoxide was added to study its inhibitive effect on gasification, and argon was employed to vary the inlet  $CO_2$  and CO concentrations. The reaction rates were determined from the amount of CO produced by gasification as measured by an Infrared Industries dual beam nondispersive infrared analyzer (IR-703D). In order to compare the rate data at a common extent of reaction, the rate dependence on  $CO_2$  and CO was determined using a method similar to Tyler and Smith [5]. The percent conversion was maintained below 4.0% to ensure differential conditions. Experimental tests and theoretical criteria indicated the absence of transport limitations. The intrinsic reactivities presented in this study are based on the specific surface area at ~10% burn-off (1285 m<sup>2</sup>/g; Dubinin-Radushkevich isotherm with  $CO_2$  at 298 K).

## 3. RESULTS

Data for  $1/R$  vs.  $1/[CO_2]$  for  $[CO] \sim 15$  kPa and for  $[CO]/[CO_2] \sim 0.25$  were fit using a linear regression analysis and appear in Figs. 1 and 2. The plots are linear with positive intercepts for all temperatures. Strange and Walker [6] noted similar results for SP-1 graphite when  $[CO_2]$  is varied for a fixed  $[CO]$ , and when  $[CO_2]$  is varied for a fixed  $[CO]/[CO_2]$  ratio. Thus, Eqn. (6) adequately fits gasification data in the presence of carbon monoxide.

Plots of  $1/R$  vs.  $[CO]$  for  $[CO_2] \sim 60$  kPa appear in Figure 3. The plots are linear as anticipated with positive intercepts. Gadsby et al. [2] and Wigmans et al. [7] also obtained this result for coconut charcoal and activated peat char, respectively. Consequently, this test also supports Eqn. (6).

Data for  $1/R$  vs.  $1/[CO_2]$  for no CO in the inlet were also fit using a linear regression analysis and appear in Fig. 4. The data exhibit a concave downward curvature about the best-fit lines. From replicate data, the ratio of the mean square "linear-model" error to the mean square experimental error was calculated. A statistical F test indicates that the curvature is not due to random experimental error. Concave downward curves for plots of  $1/R$  vs.  $1/[CO_2]$  with no CO in the inlet can also be discerned [9] in the data of Tyler and Smith [5], Gadsby et al. [2], and in data from our laboratory for coconut char [10]. Turkdogan and Vinters [8] found their gasification rates for no CO in the inlet to be proportional to  $[CO_2]^{0.5}$  over a 100 fold change in  $[CO_2]$ . Although Eqn. (1) allows a fractional order dependence on  $[CO_2]$ , it is not consistent with a constant fractional dependence over a wide  $[CO_2]$  range. These and other results [6,10] suggest that the current single-site model must be modified.

#### 4. DISCUSSION

A suitable modification involves the two-site adsorption of  $CO_2$  shown below [10]:



where  $C^*$  is the two-site surface complex. Temperature programmed desorption and isotopic tracer experiments [3,11,12] indicate that  $[C^*]$  and  $[C(CO)]$  are probably small in comparison to  $[C(O)]$  and  $[C_f]$  during gasification. Thus, using the same site balance as in Eqn. (4) and applying the steady state approximation to each surface species will yield the following equation after rearrangement [10]:

$$[C(O)]^2 \left\{ \frac{k_2 k_{-2} (k_4 - k_{-3} [CO])}{(k_2 + k_{-1}) k_3} + \frac{k_1 k_2 [CO_2]}{(k_2 + k_{-1})} - \frac{k_{-2} (k_4 - k_{-3} [CO])}{k_3} \right\} \\ + [C(O)] [C_f] \left\{ \frac{k_2 k_{-2} k_{-3} [CO]}{(k_2 + k_{-1}) k_3} - \frac{2 k_1 k_2 [CO_2]}{(k_2 + k_{-1})} - \frac{k_{-2} k_{-3} [CO]}{k_3} - k_4 \right\}$$

$$+ [C_t]^2 \frac{k_1 k_2 [CO_2]}{(k_2 + k_{-1})} = 0. \quad (11)$$

The preceding general equation can branch in two directions depending on the amount of  $CO_2$ .

#### 4.1 Case I: Significant $[CO]$

Since Rxn. (10) is irreversible, increasing  $[CO]$  is expected to decrease  $[C(O)]$  via the reverse of Rxns. (8) and (9). If  $[C(O)]$  becomes sufficiently small, then

$$[C_t] \gg [C(O)]. \quad (12)$$

Analysis of the first and second sets of bracketed terms in Eqn. (11) suggests that the sets are similar in magnitude. Eqn. (12) implies that multiplying the first set of bracketed terms by  $[C(O)]^2$  and the second set by  $[C(O)][C_t]$  will make the first term in Eqn. (11) negligible in comparison to the second term. Since

$$R = m_c k_4 [C(O)],$$

Eqn. (11) yields

$$R = \frac{m_c \frac{k_1 k_2}{k_{-1}} [C_t] [CO_2]}{1 + \frac{k_{-2} k_{-3}}{k_3 k_4} [CO] + \frac{2k_1 k_2}{k_{-1} k_4} [CO_2]}, \quad (13)$$

where  $k_{-1}$  has been assumed to be much larger than  $k_2$  (i.e.,  $CO_2$  desorption rate is much faster than  $CO_2$  decomposition rate).

Eqn. (13) is of same form as Eqn. (1) with the following values for  $b_1$ ,  $b_2$ , and  $b_3$ :

$$b_1 = m_c \frac{k_1 k_2}{k_{-1}} [C_t], \quad b_2 = \frac{k_{-2} k_{-3}}{k_3 k_4}, \quad b_3 = \frac{2k_1 k_2}{k_{-1} k_4}. \quad (14)$$

Hence, for significant  $[CO]$ ,  $1/R$  vs.  $1/[CO_2]$  should be linear for constant  $[CO]$  and constant  $[CO]/[CO_2]$ , and  $1/\bar{R}$  vs.  $[CO]$  should be linear for constant  $[CO_2]$  as demonstrated previously. When sufficient  $[CO]$  is available, the previous single-site model and the proposed two-site model are indistinguishable with respect to the final rate expression. Moreover, both explain the available rate data.

The slopes and intercepts from Figs. 1-3 can be used to calculate values for  $m k_4 [C_t]$ ,  $m k_1 k_2 [C_t]/k_{-1}$ , and  $m k_{-2} k_{-3} [C_t]/k_3$  (Table 1). The intercepts of the  $1/R$  vs.  $1/[CO_2]$  plots at constant  $[CO]$  directly yielded  $m k_4 [C_t]$  values. These values also had the least error (95%

confidence limits). Similarly, the slopes of the  $1/R$  vs.  $1/[CO_2]$  plots at constant  $[CO]/[CO_2]$  gave the best  $m k_1 k_2 [C_t]/k_{-1}$  values. Values for  $k_{-2} k_{-3} m [C_t]/k_3$  were calculated from the slopes of the  $1/R$  vs.  $[CO]$  plots at constant  $[CO_2]$  and using the above values for  $k_4 m [C_t]$  and  $k_1 k_2 m [C_t]/k_{-1}$ .

#### 4.2 Case II: Insignificant $[CO]$

If the same assumption regarding the rate coefficients is made as for the first case (i.e.,  $k_{-1} \gg k_2$ ), and any term containing  $[CO]$  is set to zero, Eqn. (11) yields after applying the quadratic equation [10]:

$$R = (m_c k_4) \frac{k_4 + \frac{2k_1 k_2}{k_{-1}} [CO_2] - \sqrt{\frac{4k_1 k_2 k_4}{k_{-1} k_3} (k_{-2} + k_3) [CO_2] + k_4^2}}{\frac{2k_1 k_2}{k_{-1} [C_t]} [CO_2] - \frac{2k_{-2} k_4}{k_3 [C_t]}} \quad (15)$$

If we further assume that  $k_{-2}$  is much larger than  $k_3$  (i.e.,  $C(CO)$  reacts with  $C(O)$  faster than it desorbs from the surface), then it is reasonable to presume that

$$\sqrt{\frac{k_1 k_2 k_4 k_{-2}}{k_{-1} k_3} [CO_2]} \gg \frac{k_1 k_2}{k_{-1}} [CO_2], \quad \text{and} \quad (16)$$

$$\frac{k_{-2} k_4}{k_3} \gg \frac{k_1 k_2}{k_{-1}} [CO_2].$$

Applying Eqn (16) and also assuming that  $k_4^2$  is small compared to the  $CO_2$  term under the square root sign in Eqn. (15), we find that the reaction rate has a square root dependence on  $[CO_2]$ :

$$R = m_c \left[ \frac{k_1 k_2 k_3 k_4}{k_{-1} k_{-2}} \right]^{0.5} [C_t] [CO_2]^{0.5} - m_c \frac{k_3 k_4}{2k_{-2}} [C_t] \quad (17)$$

This predicted square root dependency is consistent with the results of Turkdogan and Vinters [8] with no  $CO$  in the inlet. Moreover, the Saranchar data demonstrates good linear  $R$  vs.  $[CO_2]^{0.5}$  plots with the anticipated negative intercept when no  $CO$  is present in the inlet gases (Fig. 5). However, a slight concave upward curvature can be discerned in all the plots. To test the ability of Eqn. (15) to account for this departure from linearity, we fit the data with the following equation:

$$R = \frac{d_1 + d_2 [CO_2] - \sqrt{d_3 [CO_2] + d_4}}{d_5 [CO_2] - d_6} \quad (18)$$

Parameters  $d_2$  and  $d_5$  were fixed with values from Table 1. Parameters  $d_1$ ,  $d_3$ ,  $d_4$ , and  $d_6$  were determined by a non-linear regression analysis using Marquardt's method. Values for  $k_{4m}[C_t]$  can be calculated from  $d_1$  and  $d_4$  and compared to the values in Table 1. Table 2 demonstrates the agreement. Parameters  $d_1$  and  $d_4$  were not constrained in any way, but still yielded almost identical values for  $k_{4m}[C_t]$ . This agreement supports the proposed two-site model.

## 5. CONCLUSIONS

Proposed models for gasification by  $CO_2$  should account for the following experimental observations obtained in this investigation and the literature:

1.  $1/R$  vs.  $[CO]$  is linear for constant  $[CO_2]$ .
2.  $R$  vs  $[CO_2]^{0.5}$  is near-linear for no  $CO$  in the inlet and differential reaction conditions ( $[CO] \sim 1$  kPa).
3.  $1/R$  vs.  $1/[CO_2]$  is linear for higher concentrations of  $CO$  in the inlet ( $[CO] \sim 10$  kPa).

The model proposed here to account for these observations involves a two-site adsorption and dissociation of  $CO_2$  on the surface.

## ACKNOWLEDGEMENTS

This study was supported by a grant from Conoco, Inc. through the Coal Research Center at Purdue University. We appreciate the helpful comments of Prof. R.P. Andres, Prof. W.N. Delgass, Prof. C.G. Takoudis, and other members of the catalysis group in the Chemical Engineering Department of Purdue University. In addition, we are thankful to P.R. Abel and B.J. Waters for their assistance with this work.

## REFERENCES

1. P.L. Walker, Jr., F. Rusinko, Jr., and L.G. Austin, *Advances in Catalysis*, Vol. 11, p 133. Academic Press, New York (1959).
2. J. Gadsby, F.J. Long, P. Sleightholm, and K.W. Sykes, *Proc. R. Soc., London A103*, 357 (1948).
3. M. Mentser and S. Ergun, "A Study of the Carbon Dioxide-Carbon Reaction by Oxygen Exchange," U.S. Bureau of Mines Bulletin 664 (1973).
4. N.M. Laurendeau, *Prog. Energy Combust. Sci.* 4, 221 (1978).
5. R.J. Tyler and J.W. Smith, *Fuel* 54, 100 (1975).
6. J.F. Strange and P.L. Walker, Jr., *Carbon* 14, 345 (1976).

7. T. Wigmans, A. Hoogland, P. Tromp, and J.A. Moulijn, Carbon 21, 13 (1983).
8. E.T. Turkdogan and J.V. Vinters, Carbon 7, 101 (1969).
9. P.C. Koenig, M.S. Thesis, Purdue University (1983).
10. P.C. Koenig, R.G. Squires, and N.M. Laurendeau, Carbon in press.
11. F. Kapteijn, G. Abbel, and J.A. Moulijn, Fuel 63, 1036 (1984).
12. S.S. Barton and B.H. Harrison, Carbon 13, 283 (1975).

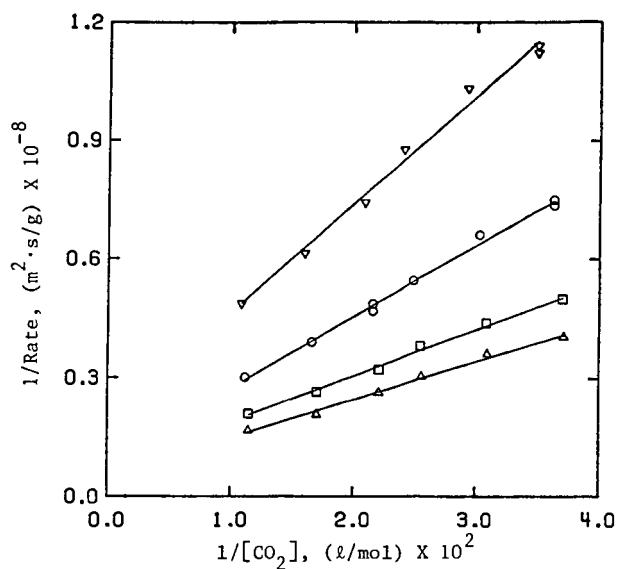


Figure 1. Test of Eqn. (6) for Saran Char with  $[CO] \sim 15$  kPa ( $1.5 \times 10^{-3}$  mol/l).  $\nabla$  - 1189 K,  $\circ$  - 1206 K,  $\square$  - 1217 K,  $\Delta$  - 1229 K.

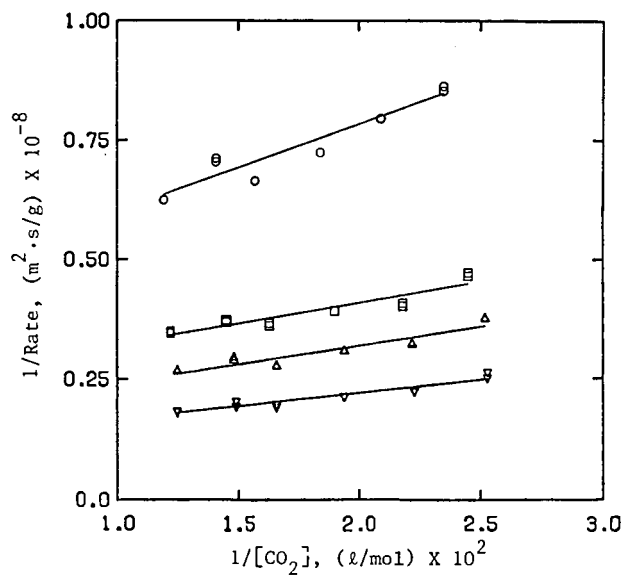


Figure 2. Test of Eqn. (6) for Saran Char with  $[CO]/[CO_2] \sim 0.25$ .  $\circ$  - 1189 K,  $\square$  - 1206 K,  $\Delta$  - 1217 K,  $\nabla$  - 1229 K.



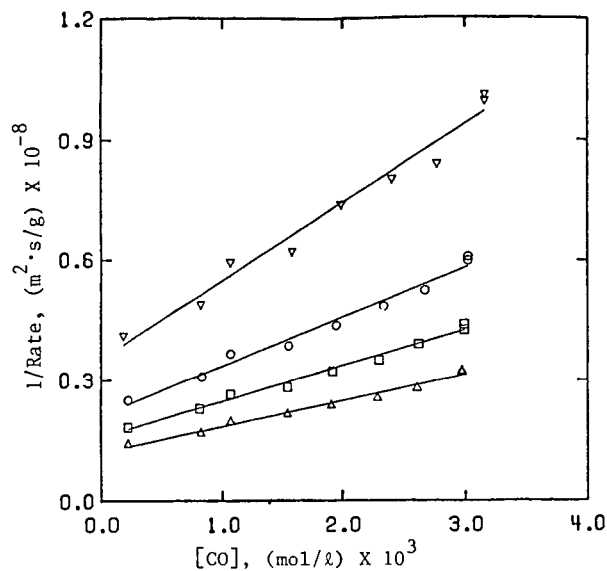


Figure 3. Test of Eqn. (6) for Saran Char with  $[\text{CO}_2] \sim 60 \text{ kPa}$  ( $6 \times 10^{-3} \text{ mol/l}$ ).  $\nabla$  - 1189 K,  $\circ$  - 1206 K,  $\square$  - 1217 K,  $\Delta$  - 1229 K.

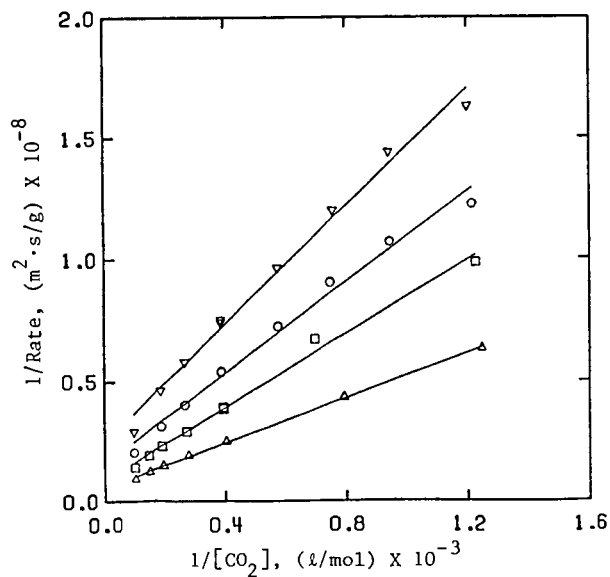


Figure 4. Test of Eqn. (6) for Saran Char with  $[\text{CO}] \sim 1 \text{ kPa}$  ( $1 \times 10^{-4} \text{ mol/l}$ ).  $\nabla$  - 1189 K,  $\circ$  - 1206 K,  $\square$  - 1217 K,  $\Delta$  - 1229 K.

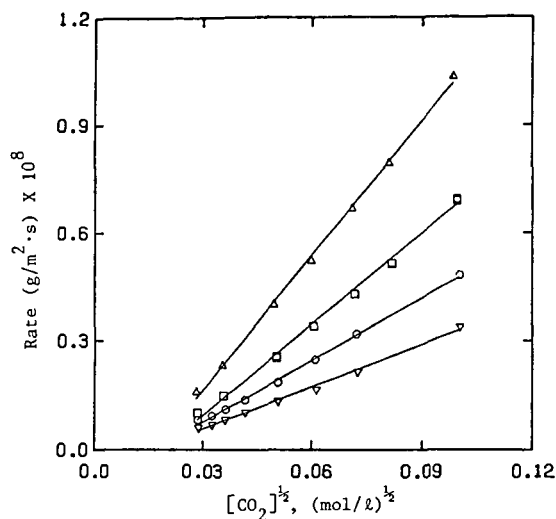


Figure 5. Test of Eqn. (17) for Saran Char with  $[CO] \sim 1 \text{ kPa}$  ( $1 \times 10^{-4} \text{ mol/l}$ ).  $\nabla$  - 1189 K,  $\circ$  - 1206 K,  $\square$  - 1217 K,  $\Delta$  - 1229 K.

Table 1. Experimental Values for Rate Coefficient Ratios.

Temp., K	$m_c k_4 [C_t] \left( \frac{g}{m^2 \cdot s} \times 10^7 \right)$	$m_c \frac{k_1 k_2}{k_{-1}} [C_t] \left( \frac{g}{m^2 \cdot s} \cdot \frac{g}{mol} \times 10^5 \right)$	$m_c \frac{k_{-2} k_{-3}}{k_3} [C_t] \left( \frac{g}{m^2 \cdot s} \cdot \frac{g}{mol} \times 10^4 \right)$
1189	$1.07 \pm 0.46$	$0.55 \pm 0.18$	$0.71 \pm 0.64$
1206	$2.09 \pm 0.72$	$1.15 \pm 0.32$	$1.77 \pm 1.32$
1217	$2.75 \pm 0.86$	$1.27 \pm 0.34$	$1.82 \pm 1.24$
1229	$3.78 \pm 1.52$	$1.85 \pm 0.43$	$2.64 \pm 2.00$

Table 2. Comparison of  $m_c k_4 [C_t] \left( \frac{g}{m^2 \cdot s} \times 10^7 \right)$  Values.

Temp., K	$m_c k_4 [C_t]$ from Table 1	$m_c k_4 [C_t]$ from d1	$m_c k_4 [C_t]$ from d4
1189	$1.07 \pm 0.46$	1.06 (0.77-1.29)	1.08 (0-1.28)
1206	$2.09 \pm 0.72$	2.44 (1.82-2.94)	2.45 (1.70-2.82)
1217	$2.75 \pm 0.86$	2.80 (2.72-2.87)	2.80 (2.72-2.88)
1229	$3.78 \pm 1.52$	3.52 (3.10-3.89)	3.52 (3.00-3.87)

## KINETIC AND MECHANISTIC ASPECTS OF CO<sub>2</sub> GASIFICATION ON ALKALI TREATED CARBON

C. T. Ratcliffe\*

Corporate Research - Science Laboratory  
Exxon Research and Engineering  
Route 22 East, Annandale, N. J. 08801

### Introduction

While catalysis of CO<sub>2</sub> gasification of carbon or coal chars by alkali metals has been the subject of many investigations (1), the state of the catalyst site during gasification and the mechanism involved in the rate limiting step have yet to be resolved. An inherent problem in catalyzed gas-solid reactions at the required high temperatures is the inability to separate the reaction into discrete steps which can be monitored under isothermal reaction conditions. The approach taken in this study has been to decouple the reaction into three steps: catalyst activation, CO<sub>2</sub> chemisorption and reaction/desorption, with only the adsorption step examined under isothermal conditions. The strong chemisorption of CO<sub>2</sub> on thermally activated potassium sites, which showed similarities via our MAS-NMR analysis to the electrostatically held CO<sub>2</sub> on alkali treated Al<sub>2</sub>O<sub>3</sub> or SiO<sub>2</sub>-Al<sub>2</sub>O<sub>3</sub> catalysts as reported by Krupay et al. (2), Sefcik et al. (3,4) and Barrer et al. (5) has allowed the population of active sites to be measured by the quantity of CO<sub>2</sub> that irreversibly chemisorbed at 300°C on the active surface (6). The state of this intermediate is similar to the type suggested much earlier by Long and Sykes (7) and more recently by Mims and Pabst (8), but in disagreement with a mechanism involving K<sub>2</sub>CO<sub>3</sub> formation and subsequent reduction to the metal as proposed by McKee (9) and Vera and Bell (10).

The objective of this study has been to examine the thermochemical reaction(s) of each adsorbed CO<sub>2</sub> complex with an atom of carbon on the surface to eventually yield two molecules of CO. Isotope labelled <sup>13</sup>CO<sub>2</sub> has been adsorbed on the active sites so that the reaction chemistry of CO<sub>2</sub> with the carbon lattice could be monitored by Temperature Programmed Desorption (TPD) with the carbon label differentiated by mass spectral examination of the products. While the TPD analysis technique has been primarily employed for examining desorption of single crystal catalyst surfaces (11), the technique can be applied to porous catalyst materials with proper precautions (12). If discrete desorption states can be identified, details of the kinetics of desorption process can be obtained (13). Feats and Keep have examined graphite (thermal or reactor irradiated) after CO<sub>2</sub> or O<sub>2</sub> adsorption by TPD and found discrete states for desorption of CO and CO<sub>2</sub> (14). Linear TPD analysis and a step-TPD technique were studied by Tremblay et al. to determine the energetics of oxygen removal as CO from non-catalyzed carbons. These authors summarized their results with two major points; more than one functional group is present on carbon and the activation energies for these complexes must be a distributed function (15). Frericks has reported TPD spectra for CO<sub>2</sub> and H<sub>2</sub>O on potassium doped carbon samples but the spectra were not analyzed for kinetic information (16).

\* Present Address: Union Oil Company of California, Science and Technology Division, P. O. Box 76, Brea, California 92621

Discrete desorption states for  $^{13}\text{C}$ -labelled CO and lattice carbon derived CO have been obtained in this study by TPD at one atmosphere in a flowing inert gas stream. Analysis of the TPD spectra by the methods outlined by Redhead, Cvetanovic and Amenomiya and Taylor and Weinberg are presented (11,13,17).

## EXPERIMENTAL

### Samples and Reagents

Spherocarb, a low ash form of activated carbon with a surface area of 800  $\text{m}^2/\text{g}$ , was purchased from Analabs Inc., New Haven, Connecticut. Isotope labelled  $^{13}\text{CO}_2$  (98%  $^{13}\text{C}$ ) was purchased from Isotec, Inc., Centerville, Ohio, with the percentage isotope label verified by M.S. analysis. A high purity source of He (99.9999%) was used as a carrier gas in all experiments. The He stream was passed through a heated trap containing Cu turnings for  $\text{O}_2$  removal followed by molecular sieve traps to insure  $\text{H}_2\text{O}$  removal. The purity of He was found to be critical in adsorption/desorption runs on carbon and was checked periodically by verifying a constant weight of carbon in the TGA/DSC at elevated temperatures (800°C) while flowing a He stream for 2-3 hour period.

Potassium carbonate was purchased from B&A Chemicals (reagent grade). Aqueous solution of  $\text{K}_2\text{CO}_3$  were used to impregnate Spherocarb samples with the volume of the aqueous solution equated to the quantity of moisture required to fully wet the surface but not allow excess solution (method of incipient wetness). After impregnation, samples were dried to 60-70°C in a vacuum oven and sealed in glass containers under inert atmosphere.

Isothermal adsorption and temperature programmed desorption runs were performed in a Mettler 2000C TGA/DSC Analyzer. The balance platform, sample crucibles and chamber were constructed of  $\alpha$ -alumina with no artifacts in adsorption of desorption noted in blank runs. Analysis of the exit gas was performed with a UTI model 100 mass spectrometer that was interfaced with a Spectra Link unit to a M1NC 1123 laboratory computer. Multiple ions could be monitored on a continuous basis during TPD runs. In a typical run, eight amu valves were monitored in a cyclic manner in which data for each mass unit was collected for one second with a total cycle comprising about ten seconds. In this manner, a sufficient number of counts could be obtained for each ion to provide an accurate ratio of partial pressures while the frequency of cycling was fast enough to gain peak temperatures ( $T_p$ ) for CO and  $\text{CO}_2$  fragments at programming rates up to 0.5 K/sec. A small portion (5-10%) of the exit flow from the reaction chamber was differentially pumped through a capillary tube to minimize lag time to the M.S. chamber. The flow pattern, as outlined on Figure #1, was designed to minimize readsorption during TPD experiments (12).

Adsorption of  $\text{CO}_2$  was always performed with 90% He dilution. Samples of  $\text{K}_2\text{CO}_3$ -Spherocarb were preconditioned by heating to 850°C in an inert gas flow prior to the adsorption/TPD study. After an isothermal temperature was established, the adsorption was carried out at 60°C followed by a period of approximately one hour to purge the chamber of residual  $\text{CO}_2$ .

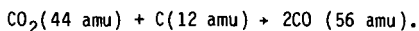
## RESULTS AND DISCUSSION

### Product Formation and Isotope Distribution

The profile of desorbed products, as shown in Figures 2 and 3, identifies three regions of desorption for CO. Desorption of  $\text{CO}_2$  can also be detected in much

lower concentrations with a low temperature peak centered at 170°C and a broad desorption peak at 500°C. The C-13 label on adsorbed CO<sub>2</sub> readily differentiates the source of carbon for both CO and CO<sub>2</sub>. Desorption of CO with mass 29 is clearly present in peaks at 200°, 490°, and 685°, while mass 28 (CO from lattice carbon) is only observed in the 750°C peak. Only labelled CO<sub>2</sub> (mass 45) can be seen in the desorption spectra. The lack of coincidence in desorption states for <sup>13</sup>CO or <sup>12</sup>CO should be noted as it indicates distinct desorption processes. Adsorption of CO<sub>2</sub> at isothermal temperatures from 25-100°C had no effect on the relative ratio of products or the peak maxima. Higher temperature adsorption of CO<sub>2</sub> decreased the contribution of the lower temperature states in the TPD spectrum. Continued evolution of CO above 800°C is also evident in all the spectra. Removal of tightly bound oxygen in chars is known to require very high temperatures (1000°C in vacuum) (18,19) in addition to eventually volatilizing the alkali metal (20). The chemistry in this temperature region was not examined as it is not relevant to the catalytic reaction.

Continued cycling of CO<sub>2</sub> adsorption at 25°C or 100°C followed by TPD programming to 800-850°C demonstrated the reproducible stoichiometry of the Boudouard reaction as monitored during each cycle with the TGA unit:



Thus, separation of the adsorption process and the subsequent thermal desorption into separate steps allowed gasification to be performed on a "one turnover" per cycle basis. That is, for each active site that chemisorbed one molecule of CO<sub>2</sub>, one atom of lattice carbon was reacted during the TPD process to yield two molecules of CO. The quantity of adsorbed CO<sub>2</sub> could readily be controlled by introducing a limited amount of CO<sub>2</sub> into the gas stream and observing the weight gain with the TGA. Thus the effect of desorption at different loading levels could be quantified with the measured weight of adsorbed CO<sub>2</sub> and desorbed CO as known gravimetric values and the isotope contribution determined from the area under the mass spectral profiles. The TPD profiles in Figures 2-4 correspond to desorption of a full saturation of chemisorbed sites (0.6 sites/mole of K<sub>2</sub>CO<sub>3</sub> impregnated). A decline in the total mass of desorbed <sup>13</sup>CO as compared to <sup>12</sup>CO with lower loadings was observed upon integrating the area under the respective M.S. profiles shown in Figures 2 and 4. A similar decrease in the ratio of <sup>13</sup>CO/<sup>12</sup>CO was noted with equal coverages of CO<sub>2</sub> but decreasing ramping rates. Readsorption of <sup>13</sup>CO after its release from lower energy binding states appears probable from these results with a visual illustration of the decline in <sup>13</sup>CO with lower loading shown in Figure 4.

Adsorption of CO<sub>2</sub> at elevated isothermal temperatures was examined up to 500°C. TPD analysis of the surface after adsorption at elevated temperatures showed a dominance of CO desorption in the anticipated 700°C region, with little contribution from the lower states.

#### Determination of Rate Parameters via TPD Analysis

Interpretation of TPD spectra allows the activation energy, frequency factor and order of a process to be determined as the shape of the peaks and the position of the peaks maxima bear a fundamental relationship to the desorption process (11-13).

Data obtained from TPD spectra with variable surface coverage was analyzed from the basic equation,

$$\frac{E_d}{RT_p^2} = \frac{V^n}{\beta} C^{n-1} \exp \frac{-E_d}{RT_p} \quad (1)$$

$n$  = reaction order  
 $C$  = surface conc.  
 $V$  = frequency factor  
 $E_d$  = activation energy  
 $T_p$  = peak desorp. temp.  
 $\beta$  = ramping rate

Rearrangement of this equation reveals the dependence of surface concentration on temperature as a function of reaction order.

$$C^{n-1} = \exp. \frac{E_d}{RT_p} \cdot \frac{E_d \beta}{RT_p^2 V^n} \quad (2)$$

If little change in the energy or frequency factor is assumed as a function of loading level, the relative shift of  $T_p$  as a function of  $C$  will allow a determination of the reaction order. The temperature of the desorption peak for lattice derived carbon ( $^{12}\text{C}$ ) remained constant in the region of surface coverages used in this study (40-100%) and thus represented the profile of a first order desorption process. The three desorption peaks for  $^{13}\text{CO}$  (derived from  $^{13}\text{CO}_2$ ) also showed constant  $T_p$  values at surface coverages in the range mentioned above as shown in Figure #3 which is consistent with first order desorption processes.

TPD experiments were also performed at constant surface coverage values of  $\text{CO}_2$ , as measured with the thermal balance, and at variable heating rates of 0.5 K/sec. to 0.033 K/sec. Surface coverages above 80% were used in all cases. Analysis of the activation energies and preexponential factors could be determined from the log form of equation (1) as mass transfer problems were not anticipated based on the design parameters of Gorte (12) and the effect of readsorption on the preexponential term was small compared to the error in the intercept under the conditions of this study (21). Adsorption of CO on this surface had also been shown by independent studies to be a non-activated process, thus  $\Delta H = E_d$ .

$$2 \ln T_p - \ln \beta = \frac{E_d}{RT_p} - \ln \frac{V^n R}{E_d} \quad (3)$$

The values of  $T_p$  were obtained from both the mass spectral plot and the DTGA peak from the weight loss profile. Desorption of  $^{13}\text{CO}$  in the higher temperature region required dependence on only the M.S. values as the derivative weight loss peak (DTGA) usually appeared as a shoulder on the larger  $^{12}\text{CO}$  peak. The series of M.S. spectra generated from the desorption of  $m/e = 28$  at different  $\beta$  values is shown in Figure 5. The values of  $T_p$ , which required a temperature correction for heat transport effects, were utilized to calculate parameters for activation energies and factors. The desorption energy for the lower temperature release of  $^{13}\text{CO}$ , as shown in Figure 6, gave a value of  $45 \pm 3$  Kcal/mole with a frequency factor of  $4 \times 10^{12}$ . Desorption of  $^{12}\text{CO}$  and  $^{13}\text{CO}$  at the higher temperature region revealed higher energy values of  $73 \pm 3$  Kcal/mole and  $72 \pm 5$  Kcal/mole, respectively with frequency factors of  $10^{15}$ - $10^{16}$  range for both processes (see Figures 7,8). The temperature dependence

plot for  $^{12}\text{CO}$  in Figure 7 displays the experimental values for DTGA and M.S. derived values of  $T_p$  while Figure 6 and 8 were taken from mass spectral profiles.

#### Energetics and Mechanism of CO Formation and Desorption

Exothermic adsorption of  $\text{CO}_2$  on discrete alkali containing sites results in the formation of a  $\text{CO}_2$  containing complex that appears stable up to  $400^\circ\text{C}$ . The chemical shift of  $^{13}\text{C}$  labelled carbon (from adsorbed  $\text{CO}_2$ ) by MAS-NMR clearly showed that  $\text{K}_2\text{CO}_3$  and  $\text{KHCO}_3$  have not formed, but the surface intermediate appears to be "carbonate" in nature. Temperature programmed desorption up to  $400^\circ\text{C}$  in this study revealed no enthalpy changes as noted with the DSC probe, precluding any chemical change involving gain or loss of energy although CO and  $\text{CO}_2$  evolution from weakly held sites occurred at  $200^\circ\text{C}$ . Thus, the breaking of the  $\text{CO}_2$  complex on a potassium salt treated carbon surface to transfer oxygen and the desorption of CO appear to occur as a single endothermic process at  $400^\circ\text{C}$ . This transfer of oxygen and desorption of CO most probably is catalyzed by the potassium site. Bonner and Turkevich (22), Lang and Magnier (23) and Tonge (24) have independently studied the transfer of oxygen from  $\text{CO}_2$  to different forms of non-catalyzed graphite of carbon. Desorption of CO was found to occur at temperatures as low as  $450^\circ\text{C}$  (Tonge) although the rate of exchange of oxygen from  $\text{CO}_2$  to carbon was very low (1700 hrs for completion at  $500^\circ\text{C}$ ) and the surface coverage was minimal ( $7 \times 10^{-6}$  C atom sites/C atom). The inability to desorb all the labelled  $^{13}\text{CO}$  in this study at the  $400^\circ\text{C}$  endothermic transition, either due to readsorption of CO or the presence of more than one type of site, precludes any statement from this study claiming a single event for the first step in the classic mechanism of  $\text{CO}_2$  gasification as outlined by Long and Sykes (25), where (O) refers to an adsorbed oxygen on the carbon surface.



The demonstrated ability of K-Spherocarb to chemisorb CO, with eventual desorption of the majority of the oxygen from a higher dissociated state, places more emphasis on the third step in above mechanism of gasification as shown below:



While readsorption of CO was not found to be significant in the kinetic study with carbon (8,25) it may be important with potassium treated carbon. The desorption energy for the removal of CO at  $490^\circ\text{C}$  from K-Spherocarb via TPD analysis in this study ( $45 \pm 3$  Kcal/mole) with a frequency factor of  $10^{12}$  represent a considerably more facile process than the initial transfer process of Long and Sykes (a) for extracted charcoal ( $E_{\text{act}} = 68$ ,  $V = 3 \times 10^9$ ) or for the original charcoal ( $E_{\text{act}} = 58.8$  Kcal,  $V = 6 \times 10^8$ ) (8). Our studies of CO adsorption on K-Spherocarb showed a non-activated process (thus  $\Delta H_{\text{desorp.}} = E_{\text{act}}$ ); the lower activation energy and higher pre-exponential factor therefore represent the catalytic activity of potassium in this first step (a). The low temperature transition for release of oxygen on alkali treated carbon surfaces is consistent with earlier oxygen exchange studies (19-22) in addition to the aforementioned work by Long and Sykes (8,25).

The energetics and isotope distribution of CO adsorption states allows additional insight on the nature of the surface complexes. The release of CO above  $600^\circ\text{C}$  involves separate and discrete sites for lattice derived carbon and  $\text{CO}_2$

derived carbon as distinguished by the carbon isotope label. The relative increase in the quantity of  $^{13}\text{C}$  desorbed in the 600-700°C region with a decrease in coverage of adsorbed  $^{13}\text{C}_2$  is consistent with preferential bonding to this site (either directly or by readsorption) vs the weaker sites desorbing at 490 and 200°C. As the total quantity of desorbed  $^{13}\text{C}$  is similar to desorbed  $^{12}\text{C}$ , and much greater than the predicted quantity of lattice carbon exposed on the higher surface area Sphero carb, the labelled carbon must be either bonded to or in close proximity to an oxygen atom. The similarity of the desorption enthalpy for  $^{13}\text{C}$  and  $^{12}\text{C}$  above 600°C also implies a similar form of bound intermediate, although the desorption profile always revealed  $^{13}\text{C}$  evolution at a lower temperature than  $^{12}\text{C}$ . The high activation energy for the above processes is equal or greater than values reported for CO release by others from non-catalyzed carbon system. The value of 59 Kcal reported by Ergun (26,27) on three different carbons (Ceylon Graphite, activated graphite and activated carbon) and the value of 67 Kcal for graphite reported by Tyso (28) et al. were obtained under controlled differential flow conditions. A recent steady state kinetic investigation by Freund (29) has shown an activation energy of  $58 \pm 3$  Kcal for  $\text{CO}_2$  gasification of catalyzed and non-catalyzed carbon samples.

The higher energy values obtained in this TPD investigation as compared to steady state kinetic results is probably not due to CO inhibition problems as they have been accounted for in the above quote studies. The inability to measure accurate reaction bed temperatures during the endothermic gasification presents a more plausible explanation. The temperature values obtained in our TPD study, despite the small sample size and low concentration of adsorbed  $\text{CO}_2$ , required a correction at higher temperatures due to the endotherm of CO desorption. The actual temperature of our desorption peaks were corrected with factors determined from DSC measurement of the melting of metals (also an endothermic process) at the desorption temperature. Localized cooling of the bed during any steady state kinetic run would also result in artificially high temperatures from a thermocouple value which would lower the value of the calculated activation energy from a reaction rate vs. reciprocal temperature plot.

## CONCLUSIONS

Isotope labelled TPD under one atmosphere inert gas flow has provided a method of decoupling alkali catalyzed gasification into steps. Distinct desorption states for CO have been identified which help explain the mechanism of  $\text{CO}_2$  interaction with the alkali catalyzed carbon surface. The rate limiting step has been shown to involve removal of lattice carbon as CO. As the activation energy for this step does not appear to be lowered by potassium, alkali serves as a catalyst by increasing the number of active sites in  $\text{CO}_2$  gasification of carbon and exchanging oxygen from  $\text{CO}_2$  to the carbon surface.

## Acknowledgments

The author wishes to thank R. A. Salher for technical assistance in the experimental program.



# REFERENCES

1. W-Y. Wen Catal. Rev. Sci. Eng 22 (1) 1-28, (1980); D. W. McKee, Chemistry and Physics of Carbon, 16, Marcel Dekker, New York, 1981; International Symposium on the Fundamentals of Catalyzed Coal Gasification, Fuel, 62 (1983).
2. B. Krupay, Y. Amenomiya, J. Catalysis 67, 362 (1981).
3. M. D. Sefcik, J. Schaefer, E. O. Stejskal, ACS Symposium Series #40, Molecular Science II, Ed. J. R. Katzer (1977).
4. M. D. Sefcik, H. V. Yuen, Thermochemica Acta 26, 297 (1978).
5. R. M. Barrer, R. M. Gibbons, Trans. Faraday Society, #509 61 (5), 948 (1965).
6. C. T. Ratcliffe, S. N. Vaughn, Div. of Fuel Preprints, Vol. 30, This Symposium.
7. F. J. Long and K. W. Sykes, J. Chem. Phys. 47, 361 (1950).
8. C. A. Mims, J.K. Pabst, Fuel 62(2), 176 (1983).
9. D. W. McKee, Fuel 62(2) 170 (1983).
10. M. J. Vera, A. T. Bell, Fuel, 57, 194 (1978).
11. P. A. Redhead, Vacuum 12, 203 (1962).
12. R. J. Gorte, J. Catalysis, 75 164 (1982).
13. R. J. Cvetanovic and Y. Amenomiya, Adv. in Catalysis, 17, 103 (1967), Catal. Rev. 6 (1), 21-48 (1972).
14. F. S. Feates and C. W. Keep, Trans. Faraday Soc. 66, 3156 (1970).
15. G. Tremblay, F. J. Vastola and P.L. Walker, Jr., Carbon 16, 35 (1978).
16. I. L. C. Freriks, J. M. H. van Wechem, J. C. M. Stuiver, R. Bouwman, Fuel, 60 1463 (1981).
17. J. L. Taylor, W. H. Weinberg, Surf. Sci., 78, 259 (1978).
18. H. Marsh, D. W. Taylor, Fuel, 54, 218 (1975).
19. N. R. Laine, F. J. Vastola, P. L. Walker, Jr., J. Phys. Chem., 67, 2030 (1963).
20. B. J. Wood, R. D. Brittain, K. H. Lau, Division of Fuel Preprints, 28, (1), 55 (1983).
21. J. S. Rieck, A. T. Bell, J. Catalysis 85, 143 (1984).
22. F. Bonner, J. Turkevich, J. Am. Chem. Soc. 73, 561 (1951).
23. F. M. Lang, P. Magnier, Chemistry and Physics of Carbon, Vol. 3, Ed. P. L. Walker, Jr., Marcel Dekker, N. Y., 1968.
24. B. L. Tonge, Proceedings of the Fourth Carbon Conference, Buffalo, pp. 87-93 (1960).
25. F. J. Long, K. W. Sykes, Proc. Roy. Soc. (London) A215, 100, (1952); J. Gadsby, F. J. Long, P. Sleightholm and K. W. Sykes, Proc. Roy. Soc. (London) A193, 357 (1948).
26. S. Ergun, J. Phys. Chem. 60 480 (1956).
27. S. Ergun, M. Mentser, Chemistry and Physics of Carbon, pp.203, Vol. 1, Ed. P. J. Walker, Jr., Marcel Dekker Inc. 1965.
28. W. T. Tyso, J. Carrazza and G. A. Somorjai, Div. of Fuel Preprints, 29 2, 190 (1984).
29. H. Freund, Fuel, (to be published).

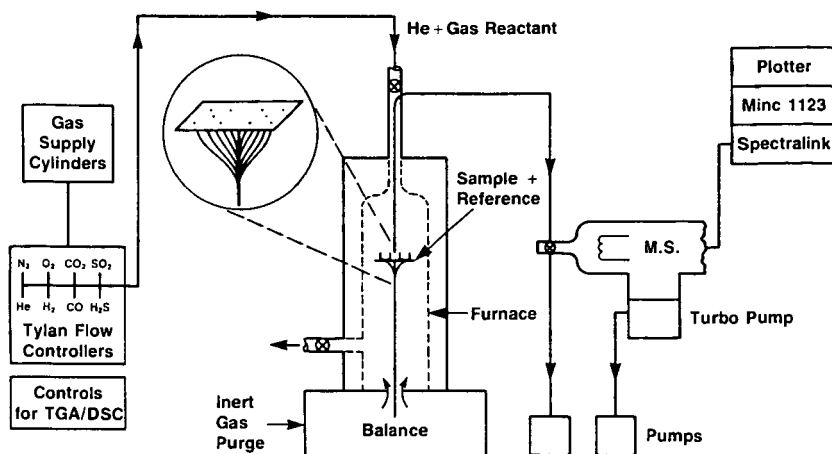


Figure #1. Mettler 2000C Thermal Analysis unit equipped with gas flow control system and on-line M.S. analysis system.

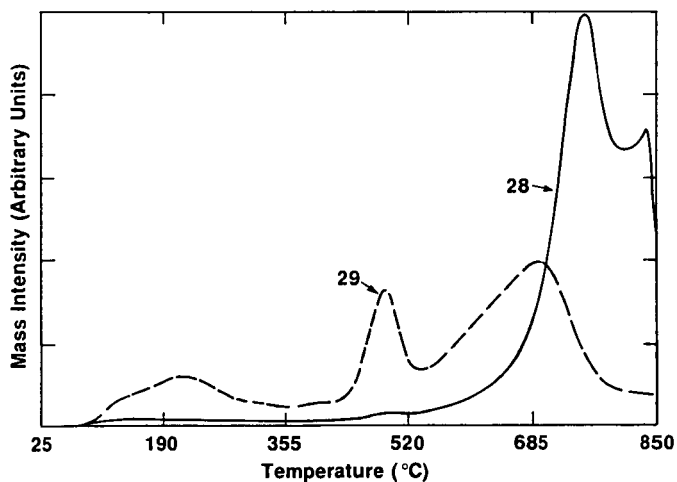


Figure #2. Profile of mass intensity for evolved  $^{13}\text{C}$ O (mp=29) and  $^{12}\text{C}$ O(m/e=28), temperature programming rate of 0.5 K/s, K-treated Spherocharb powder with  $^{13}\text{C}$ O<sub>2</sub> adsorbed ( $\theta \approx 100\%$ ) at 60°C.

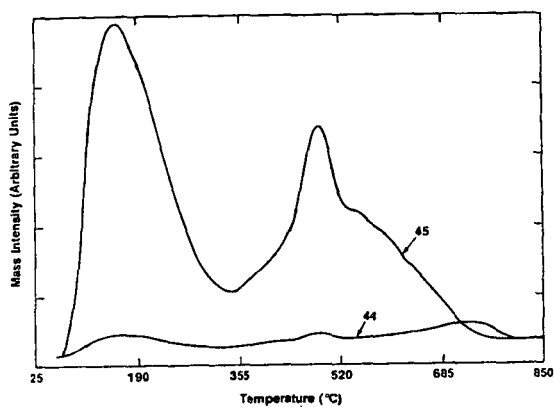


Figure #3. Profile of mass intensities for evolved  $^{13}\text{CO}_2$  ( $m/e = 45$ ) and  $^{12}\text{CO}_2$  ( $m/e = 44$ ), Intensity scale magnified 7.5x, same run as Figure #2.

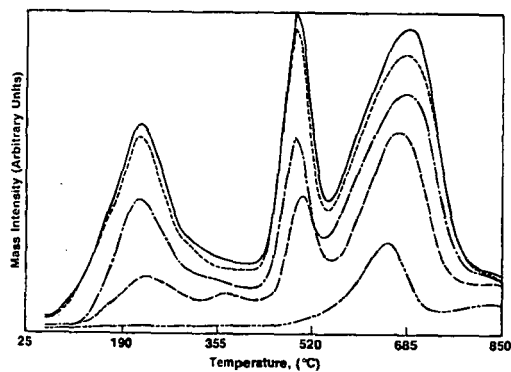


Figure #4. Profile of mass intensity for evolved  $^{13}\text{CO}$  ( $m/e = 29$ ) at different loading levels ( $\theta$  in %) of  $^{13}\text{CO}_2$ . 1, 6%. 2, 16%. 3, 52%. 4, 76%. 5, 100%.

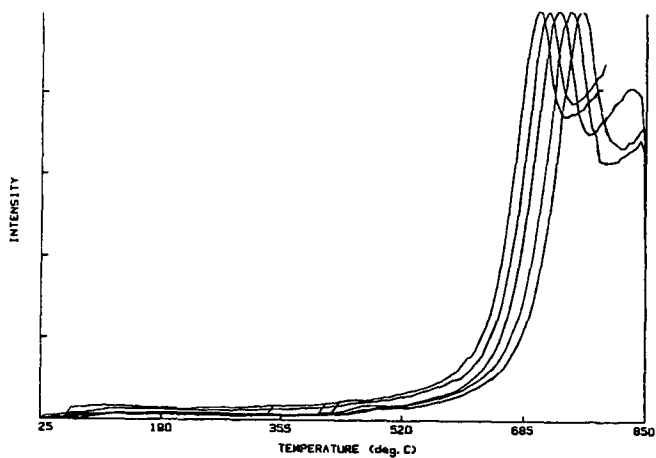


Figure #5. Profile of mass intensities for  $^{12}\text{C}^{18}\text{O}$  desorption ( $m/e = 28$ ) at different ramping rates (8) 1, 0.083K/sec. 2, 0.125K/sec. 3, 0.167K/sec. 4, 0.0333K/sec. 5, 0.5 K/sec.

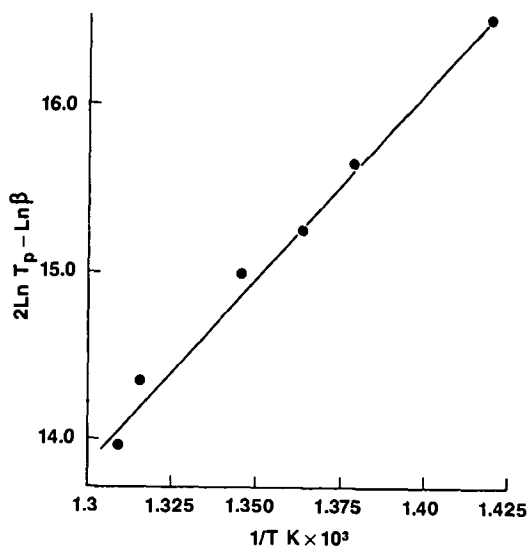


Figure #6. Plot of  $^{13}\text{C}^{18}\text{O}$  desorption values from 420-500°C peak,  $\Delta H$  from slope  $45 \pm 3$  Kcal/mole,  $V_1 = 4 \times 10^{12}$ .

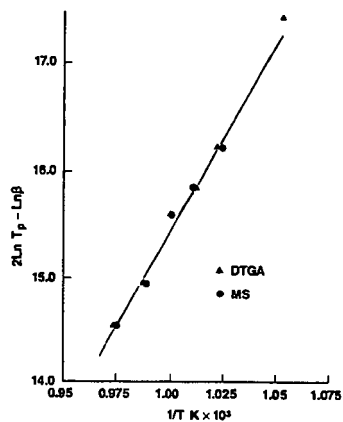


Figure #7. Plot of  $^{12}\text{C}_0$  desorption values from 690°C-750°C peak,  $\Delta H$  from slope  $73 \pm 3$  Kcal/mole,  $V_1 = 2 \times 10^{15}$ .

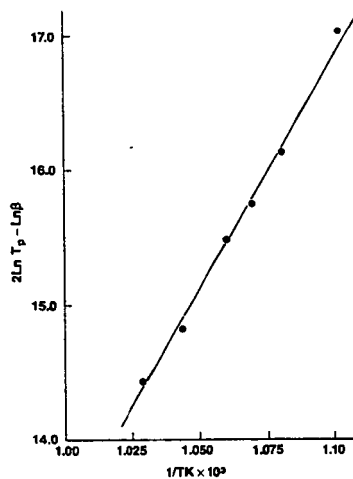


Figure #8. Plot of  $^{13}\text{C}_0$  desorption values from 650°C-690°C peak,  $\Delta H$  from slope =  $72_5$  Kcal/mole,  $V_1 = 2 \times 10^{16}$ .

## TEMPERATURE PROGRAMMED REACTION STUDIES OF POTASSIUM/CARBON INTERACTIONS AND CATALYST LOSS

D.A. Sams, T. Talverdian and F. Shadman

Department of Chemical Engineering  
University of Arizona  
Tucson AZ 85721

### INTRODUCTION

The catalytic effect of alkali metals on the gasification rate of carbonaceous materials has been the subject of a number of studies in recent years (1-16). Despite these efforts, the active form of the catalyst during gasification and the effects of catalyst loss remain unclear. The understanding of the reduction of alkali metal catalysts from its initial oxidized form and the identification of the reduced form are necessary requisites for determining the reaction mechanism. Experimental observations from this laboratory clearly indicate that catalyst loss occurs simultaneously with the reduction (12). In addition, the rate of catalyst loss from the surface is directly influenced by the reduced form it takes. The present study provides insight into this subject by examining the reduction of potassium carbonate on the surface of a pure carbon substrate and the accompanying phenomenon of catalyst loss.

### EXPERIMENTAL

An uncoated graphitized carbon from Supelco, 60/80 Carbopack B (180-250  $\mu\text{m}$ ), with a surface area of approximately 100  $\text{m}^2/\text{g}$  was used as the substrate in this study. The samples were impregnated with potassium by an incipient wetting technique, then dried at room temperature and stored under vacuum.

The data in this study was generated in a thermogravimetric reactor system utilizing an electronic microbalance and a quartz downtube reactor which enclosed the platinum sample tray as shown in Figure 1. The other major components were a movable electric furnace, a temperature controller and an auxiliary type K thermocouple. The system also included a gas preparation section for mixing and metering the feed gas at the desired compositions and flow rates. The reactant gas was a mixture of 15%  $\text{CO}_2$  and 85%  $\text{N}_2$ . Ultra high purity (UHP)  $\text{N}_2$  was used as the purge gas. The product gases were analyzed by an on-line gas chromatograph and nondispersive infrared  $\text{CO}$  and  $\text{CO}_2$  analyzers.

To prepare a run, 20-30 mg of sample were loaded onto the microbalance tray and the reactor was placed in position. The system was purged with UHP  $\text{N}_2$  to remove the oxygen and the furnace was raised to enclose the reactor. Two heat-up procedures were used: a linear  $5^\circ\text{C}/\text{min}$  rate and a rapid one step process where the furnace was preheated to  $800^\circ\text{C}$  and then raised to enclose to reactor.

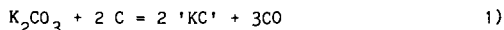
## RESULTS AND DISCUSSION

To examine the interaction of the potassium catalyst with the carbon surface, a series of temperature programmed reaction experiments were conducted where the sample mass and the reaction products were continually monitored. Figure 2 shows typical temporal profiles for the CO and CO<sub>2</sub> peaks when the sample is heated to 800°C in a reducing atmosphere at a moderate rate (5°C/min). For clarity in describing the various processes which occur during the transient heat-up period, the results are divided into five separate stages.

Stage I occurs below 250°C and represents the physical desorption of gases such as CO<sub>2</sub> and H<sub>2</sub>O from the surface. Stage II (250-700°C) corresponds to the evolution of very small amounts of CO<sub>2</sub> due to the partial decomposition of the catalyst and possibly reactions with chemisorbed oxygen. This is followed by Stage III (700-800°C) where the catalyst is reduced through interaction with the carbon surface and large amounts of CO are generated. Stage IV represents an isothermal heat treatment period where the sample is exposed to UHP N<sub>2</sub> at 800°C. Although no measurable amounts of CO or CO<sub>2</sub> are observed during this stage, a steady weight loss occurs. Finally, Stage V represents the gasification of the carbon sample at 800°C.

When a freshly impregnated sample is heated to 250°C (Stage I), both CO<sub>2</sub> and H<sub>2</sub>O are desorbed. The amount of CO<sub>2</sub> generated, normalized with respect to the initial amount of carbon present, is given in Figure 3 as a function of the initial potassium level, (K/C)<sub>0</sub>. A linear response is observed where one mole of CO<sub>2</sub> is desorbed for every two moles of potassium present. This linearity clearly indicates that the potassium strongly influences the amount of CO<sub>2</sub> adsorbed and the stoichiometry suggests that each mole of potassium carbonate interacts with one mole of CO<sub>2</sub>. The amount of CO<sub>2</sub> desorbed was independent of the rate at which the sample was heated to 250°C. The scatter in the data implies that other factors may influence the amount of CO<sub>2</sub> adsorbed.

As the sample temperature approaches 700°C, CO begins to evolve as the catalyst is reduced on the carbon surface (Stage III). The total amount of CO generation is shown in Figure 4 where the CO/C ratio is given as a function of the initial K/C ratio. For each sample, three moles of CO were generated for each mole of potassium carbonate originally present indicating complete reduction of the carbonate:

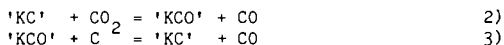


where 'KC' represents the reduced form. The nature of this reduced form is not clearly known but one possibility is a complex involving K, C and possibly O. This unknown complex readily decomposes in the 700-800°C temperature range under reducing conditions and releases alkali metal vapor to the gas phase. The total amount of CO generated during this stage was the same whether the sample was heated at a moderate rate or in one rapid step directly from room temperature to 800°C. For the samples with an initial catalyst concentration high enough to saturate the surface, the rate of CO generation reached a maximum independent of the initial loading and remained constant until the

reduction was nearly complete at which time a normal first order decay profile was observed. In other words, by doubling the initial catalyst concentration, the time for complete catalyst reduction would also be doubled. This phenomenon suggests that the rate is limited by the available surface area.

To analyze the kinetics of catalyst loss by vaporization, the change in the potassium content of several samples undergoing heat treatment was determined both by direct analysis of the samples after quenching and by indirect determination by weight loss measurements. A typical overall temporal profile of catalyst loss when a sample impregnated with potassium carbonate is gradually heated to 800°C in a reducing atmosphere is shown in Figure 5. For comparison, a sample impregnated with potassium hydroxide is also given. The results indicate that a large fraction of the catalyst is lost in a narrow temperature range around 800°C, denoted by Stage III in Figure 2.

Many investigators have suggested that alkali metal catalyzed gasification involves a process where the catalyst continually undergoes an oxidation/reduction cycle (7,13). The catalyst, after first being reduced during the transient start-up period, is oxidized upon the introduction of CO<sub>2</sub> and produces a CO profile characterized by an overshoot. The oxidized form then interacts with the carbon surface to liberate another CO thus returning to the reduced form completing the cycle. Moulijn et al. (1,5) have described this process with a simple two step reaction sequence:



where 'KC' represents the reduced form and 'KCO' the oxidized form. A supporting observation for this type of mechanism is a slight weight gain which accompanies the CO overshoot at the onset of gasification due to the oxidation of the reduced form of the catalyst.

Regardless of the exact chemical form of the catalyst following Stage III, it seems that the formation of the reduced catalyst is a prerequisite for the observed rapid weight loss of catalyst around 800°C. In fact, the rapid weight loss does not seem to be directly related to the melting point of K<sub>2</sub>CO<sub>3</sub> (891°C). Rather, it is due to the fact that at this temperature the catalyst is rapidly converted to its reduced form which is readily vaporized. This speculation is supported by the results obtained from samples impregnated with KOH. As shown in Figure 5, the KOH sample shows the same rapid loss of catalyst around 800°C even though KOH has a melting point of only 380°C.

In conclusion, the process of catalyst reduction appears to be an activated one which requires intimate contact with active sites so that for samples which are initially saturated with catalyst, the rate of reduction is limited by the available surface area. The amount of CO generated during this process indicates that the catalyst is completely reduced. Furthermore, catalyst loss kinetics suggest that the formation of a reduced form of the catalyst is a prerequisite for rapid vaporization and escape to the gas phase.



#### ACKNOWLEDGMENTS

This work was partially supported by the U.S. Department of Energy under grant DE-FG22-82PC50794. David A. Sams appreciates support from a Mining and Mineral Resources Research Institute Fellowship and a Sulzer Scholarship.

#### REFERENCES

1. Cerfontain, M.B. and Moulijn, J.A., 16th Biennial Mtg. of ACS, San Diego, CA. July, 1983.
2. Hamilton, R.T., Sams, D.A. and Shadman, F., Fuel, 63, (7) (1984).
3. Huhn, F., Klein, J. and Juntgen, H., Fuel, 62 (2) (1983).
4. Kapteijn, F., Jurriaans, J. and Moulijn, J.A., Fuel, 62, (2) (1983).
5. Kapteijn, F. and Moulijn, J.A., Fuel, 62 (2) (1983)
6. Kuhn, L. and Plogmann, H., Fuel, 62 (2) (1983).
7. McKee, D.W. and Chatterji, D., Carbon, 16, 53 (1978).
8. McKee, D.W. and Chatterji, D., Carbon, 13, 381 (1975)
9. Mims, C.A. and Pabst, J.K., Am. Chem. Soc., Div. Fuel Chem., Preprints, 25 (3) 258 (1980).
10. Mims, C.A. and Pabst, J.K., Am. Chem. Soc., Div. Fuel Chem., Preprints, 25 (3) 263 (1980).
11. Sams, D.A. and Shadman, F., Fuel, 62 (8) (1983).
12. Talverdian, T., M.S. Thesis, University of Arizona, Dec. 1984.
13. Veraa, M.J. and Bell, A.T., Fuel, 57 (4) (1978).
14. Wigmans, T., Elfring, R. and Moulijn, J.A., Carbon, 21 (1) (1983).
15. Wigmans, T., Groebel, J.C. and Moulijn, J.A., Carbon, 21 (3) (1983).
16. Wigmans, T., Haringa, H. and Moulijn, J.A., Fuel, 63 (6) (1984).

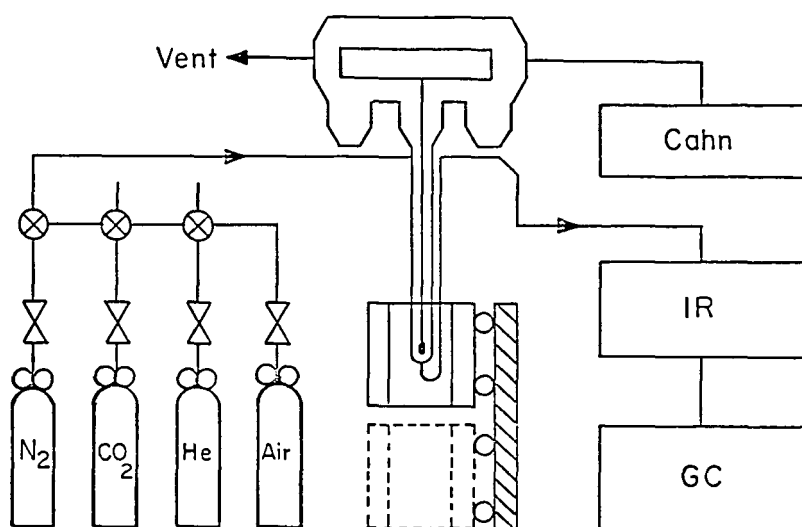


Figure 1. Schematic diagram of the Cahn microbalance system.

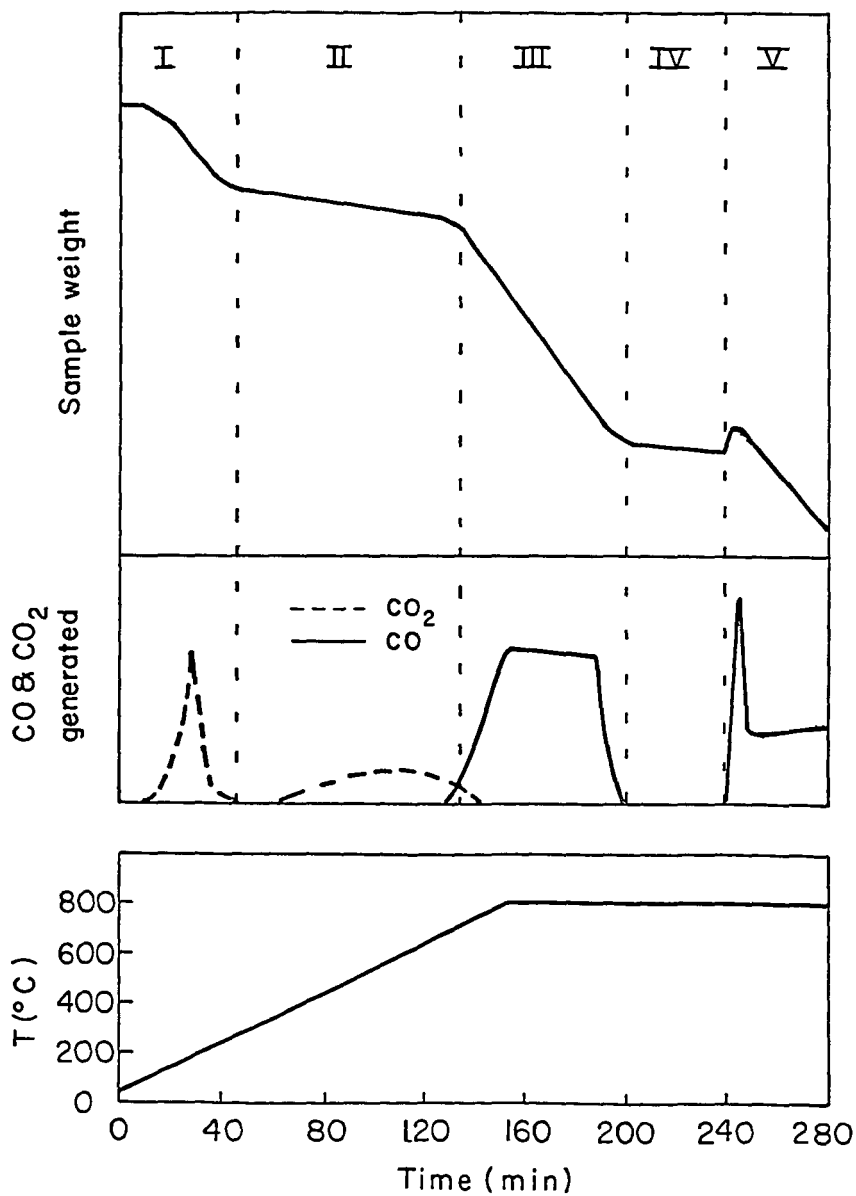


Figure 2. Characteristic stages during a typical TPR experiment.

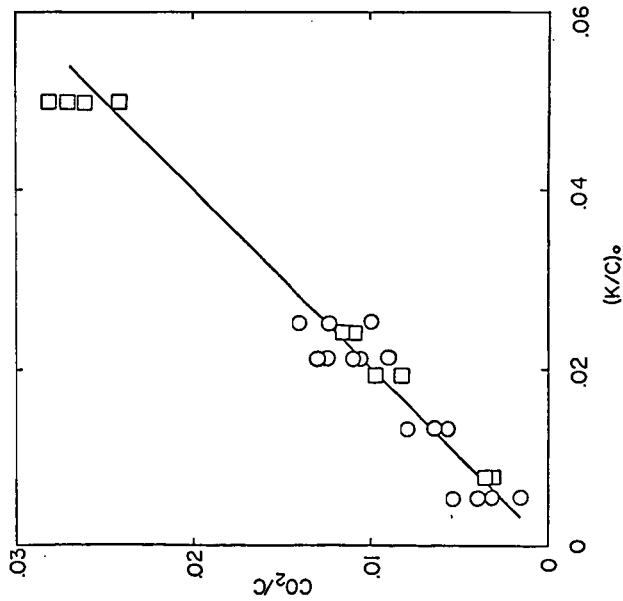


Figure 3. Dependence of low temperature  $\text{CO}_2$  desorption on the initial catalyst loading: (O)  $\text{K}_2\text{CO}_3$ ; (□)  $\text{KOH}$ .

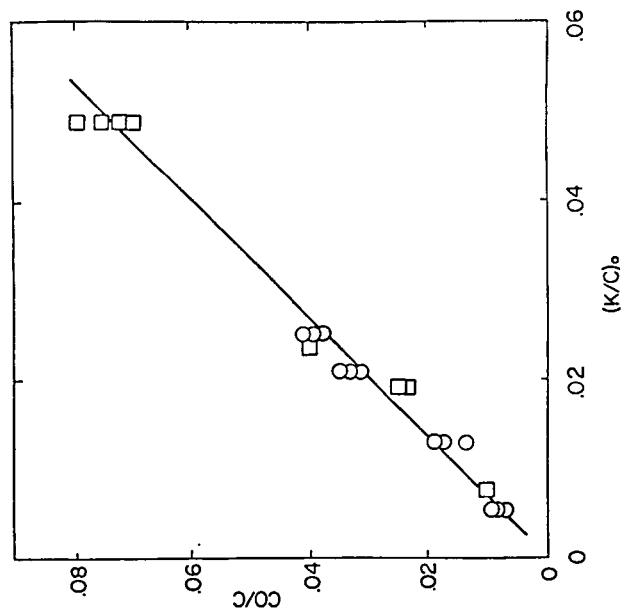


Figure 4. Dependence of high temperature  $\text{CO}$  generation on the initial catalyst loading: (O)  $\text{K}_2\text{CO}_3$ ; (□)  $\text{KOH}$ .

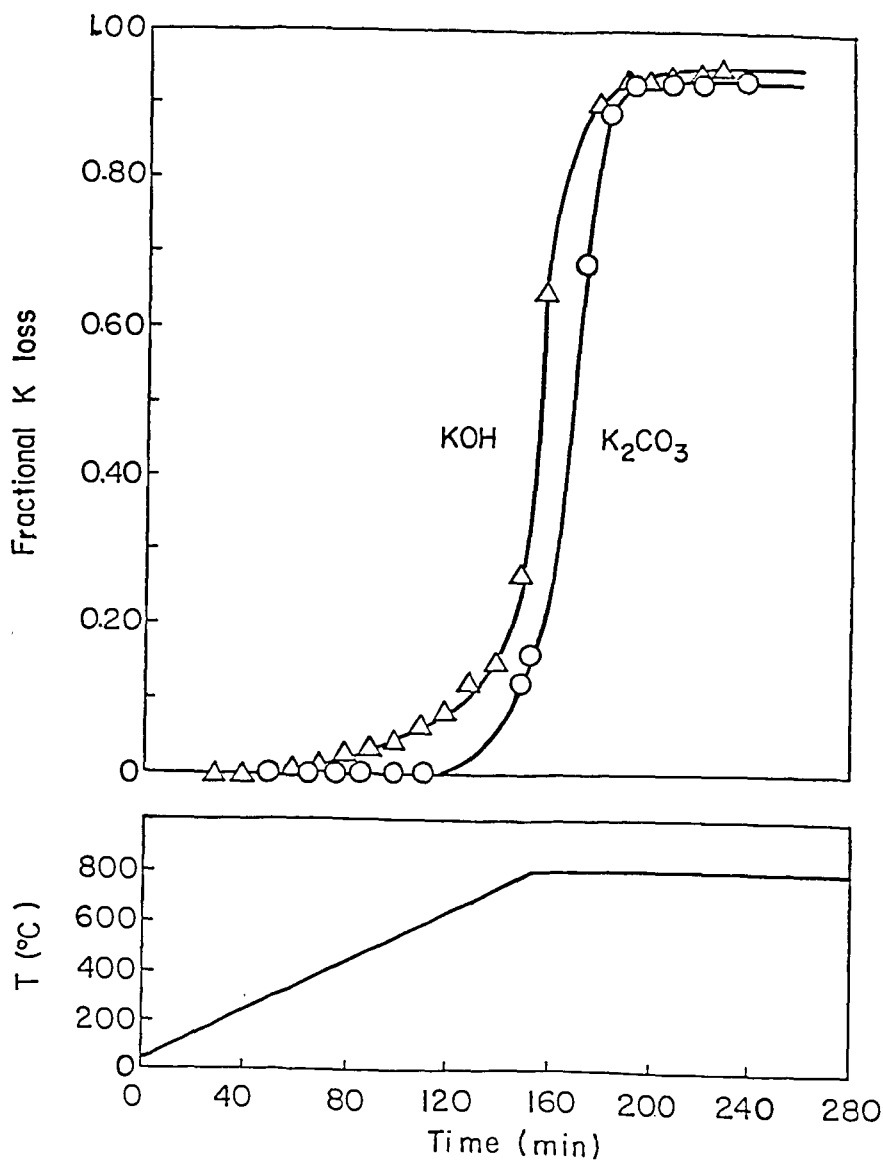


Figure 5. Catalyst loss profiles during a typical TPR experiment.

## CHARACTERIZATION OF POTASSIUM CATALYSTS ADDED AS KOH TO CARBON SURFACES

Simon R. Kelemen  
Howard Freund  
Charles Mims

Exxon Research and Engineering Company  
Corporate Research Science Laboratories  
Clinton Township, Route 22 East  
Annandale, New Jersey 08801

### ABSTRACT

Potassium catalysts active toward gasification of carbon by  $H_2O$  and  $CO_2$  can be generated by addition of KOH to carbon. We have characterized the controlled addition of KOH to the edge surface of graphite and the surface of a glassy carbon using AES, XPS and UPS. Submonolayer concentrations of potassium-oxygen surface species are formed from KOH on pre-oxidized edge graphite and glassy carbon surfaces which are stabilized to 800°C in vacuum. These surfaces have two O(1S) peak envelopes centered near 531 eV and 533 eV. The higher binding energy peak is characteristic of oxygen strongly bound to carbon. Heating to 950° C results in the loss of potassium and the lower binding energy oxygen peak associated with the potassium catalyst. In contrast the interaction of KOH with the atomically clean edge graphite surface does not produce the active potassium form. The initial oxygen content of the carbon surface is important in catalyst preparation from KOH.

### INTRODUCTION

Additions of alkali metal salts to carbon are known to produce catalytic effects toward gasification by  $CO_2$  or  $H_2O$  (1-7). KOH and  $K_2CO_3$  are especially active precursors to catalytically active states on the carbon surface (8). The catalytic form can be prepared by heating a mixture of the sample and the salt in the reactive gaseous environment. In kinetic studies this is usually a temperature greater than the maximum in the range used for the kinetics. The potassium catalyst when in an active form is believed to be mobile on the carbon surface yet stable to vaporization under gasification conditions. The catalyst's stability is demonstrated by the retention of potassium following prolonged heating in an inert environment at the reaction temperature of 700°C subsequent to gasification (9). The active potassium form is found to be associated with surface bound oxygen based on akylation studies (9,10). A better understanding of potassium catalyzed carbon gasification will come from more knowledge of the details of the potassium complex and the carbon surface composition. For this reason the initial interaction of alkali salts such as KOH with well defined carbon substrates are of fundamental interest.

The importance of the oxygen content in relation to the catalytic gasification activity of KOH and  $K_2CO_3$  toward various carbons has been recently emphasized (11,12). The clean oxygen free edge surface of graphite was studied under ultra high vacuum conditions in order to isolate the pure interaction of KOH with active carbon surface sites. The interaction of KOH films contaminated by exposure to  $H_2O$  or  $O_2$  was studied on the "passive" basal

surface of graphite to determine the influence of direct KOH oxidant interaction in the absence of "active" carbon sites. In this way the chemistry of KOH with pre-oxidized carbon surfaces could be differentiated.

### EXPERIMENTAL

Experiments were performed in a standard ultra-high vacuum spectroscopy chamber. A double-pass cylindrical mirror analyzer (Physical Electronics) was used for AES, XPS and UPS measurements. The details of the sample preparation and characterization of the oxygen-free edge surface of graphite and glassy carbon can be found in previous communications (13,14). Two different sample holders were used in the study. One was a standard UHV manipulator which could access a KOH evaporation source. The details of the KOH evaporation source used in the UHV studies appear elsewhere (15). The other holder was a Leybold Heraeus design which allowed rapid introduction of samples from atmospheric pressure to the UHV environment. The carbon samples were oxidized in  $O_2$  at  $300^\circ C$  in an isolated high pressure preparation section. The oxidation kinetics by  $O_2$  of the edge graphite surface and glassy carbon have been examined and conditions chosen which produced substantial amount of surface oxidation.

Nitric acid oxidation of the glassy carbon samples was accomplished by boiling the samples for 4 hours in  $HNO_3$  under reflux conditions. KOH was added to carbon surfaces in laboratory air by physically contacting the carbon surface in air with a moist KOH pellet. This formed a liquid coating across the entire carbon surface. The procedure was accomplished within one minute and the sample was returned to the UHV environment by use of the rapid introduction sample holder.

### RESULTS

#### I. KOH on Basal Graphite With $H_2O$ and $O_2$

When KOH is used as the precursor in gasification catalysis it is usually added from solution or directly added in atmospheric conditions. Furthermore, the carbon surfaces with the salt precursor are exposed to the oxidizing reactant gaseous environment prior to reaction. These are potential sources for chemical modification of parent KOH. In order to examine the effect of direct KOH gas interactions we have performed model experiments on the basal plane of graphite. The basal surface of pyrolytic graphite contains a preponderance of "inactive" carbon sites and provides a suitable surface to examine direct KOH gas interactions. We have found that the surfaces of pure KOH films evaporated in-situ in the UHV chamber will rapidly take up oxygen from exposure to  $H_2O$  and  $O_2$  at room temperature.

The KOH films exposed to  $H_2O$  and  $O_2$  on the basal graphite surface had only slightly greater thermal stabilities toward desorption in UHV than those found for pure KOH films. The vapor pressure of pure KOH is substantial above  $300^\circ C$ . This is also true for surfaces with KOH added in atmosphere. Following KOH addition in air  $H_2O$  was the major gaseous species produced along with KOH upon heating in UHV. Clean basal graphite surfaces were recovered upon heating to  $500^\circ C$  in vacuum.

Addition of KOH to carbon in air will therefore always introduce oxygen containing gases into the system. Basal graphite surfaces which have been contacted by KOH in air have similar thermal stabilities to the  $H_2O$  and  $O_2$  exposed pure KOH films. Although prolonged atmospheric exposure of KOH leads to the uptake of  $CO_2$  and formation of potassium carbonate, our exposures to air were short. Potassium carbonate formation should show itself by increased thermal stability of the potassium species since bulk potassium carbonate decomposes at much higher temperature. We could not find any evidence for appreciable carbonate formation.

## II. KOH On Clean Edge Graphite

We have studied the interaction of KOH on the clean edge graphite surface to determine if stable potassium states are formed on an "active" carbon surface in the absence of oxygen. The potassium, oxygen and carbon AES signals were monitored as a function of coverage following KOH deposition on the oxygen free edge surface of graphite held at room temperature and following heating in vacuum. We will report our AES results in the  $dN(E)/dE$  mode normalized to the carbon substrate signal which circumvents problems associated with absolute intensity calibrations. These results are shown in Figure 1 and are compared to the results obtained on the basal surface in a previous investigation (15).

The studies on the basal graphite surface established that a 1:1 O:K stoichiometry was maintained during room temperature deposition and subsequent heating in vacuum. On the basal surface of graphite an AES K/C ratio  $\sim 0.4$  corresponded to a surface with a coverage of one KOH per eight carbon atoms. On this basis the present AES results for KOH on the edge surface indicate that a 1:1 O:K stoichiometry exists at multilayer as well as submonolayer coverages during the deposition near room temperature and after heating in ultra high vacuum to temperatures where the loss of potassium and oxygen occurs.

The coverage of KOH was monitored by AES following heating to a given temperature for 300 sec in UHV. The initial coverage corresponded to a K/C ratio near 2.0 and represents an amount in excess of a monolayer. The KOH coverage remains almost constant as the surface temperature neared  $200^\circ C$ . The potassium signal decreased between  $200-500^\circ C$ . Above  $300^\circ C$  the vapor pressure of KOH is substantial and this is one likely mode of multilayer loss at these temperatures. Submonolayer coverages of KOH persist in the range of  $400^\circ C$ . The presence of submonolayer concentrations of adsorbate at these higher temperatures is attributed to a stabilizing interaction with the carbon substrate. The same type of behavior was observed for pure KOH on the basal surface of graphite. KOH interacts with the oxygen free edge graphite surface in a manner which does not produce strongly bound potassium-oxygen surface complexes.

## III. KOH on Oxidized Edge Graphite

We have determined the surface elemental composition and the thermal stability of the potassium containing species on the oxidized edge surface of graphite prepared by adding KOH external to the vacuum system in air. The edge surface of graphite was first oxidized in pure  $O_2$  at  $300^\circ C$  near atmospheric pressure and then the KOH was added. This method of preparation of the



KOH overlayer has a dramatic effect on the thermal stability of the potassium complex. The single layer coverage range, AES K/C  $\sim 0.4$ , persists between 700-800°C. The potassium is ultimately lost at temperatures above 800°C. The stability of potassium is very different on the oxidized edge graphite surface. There are also major compositional changes in the KOH overlayer as well as in the carbon surface. Figure 1 shows the oxygen and potassium AES signals relative to the carbon substrate signal for the oxidized sample contacted with KOH. The solid lines in Figure 1 represent integral oxygen to potassium stoichiometric values as defined from the previous results. In the high coverage multilayer regime the KOH overlayer has between 2 and 3 times the oxygen content as the stoichiometric KOH compound. This is evidence that the KOH layers have taken up and retained substantial quantities of oxygen species from atmospheric gases, predominantly  $H_2O$ . Upon heating the sample in UHV the overlayer coverage decreases and the potassium content decreases. Figure 1 shows that as the potassium coverages decrease into a submonolayer regime, AES K/C  $\sim 0.4$ , there is a substantial amount of oxygen present as measured by AES several times the 1:1 stoichiometry. A good portion of this oxygen is associated with the carbon substrate. The carbon surface is heavily oxidized. This has a profound effect on the vacuum stability of the potassium species in the submonolayer coverage range. Oxygen appears to be associated with the species since there is a corresponding loss of a portion of the oxygen.

#### IV. KOH On Oxidized Glassy Carbon

The method of KOH addition to oxidized glassy carbon surface was the same as on the oxidized edge surface. This method of preparation was also used to add KOH to glassy carbon samples which were found to be catalytically active toward  $CO_2$  carbon gasification (16).

We will compare the results for glassy carbon samples which were oxidized differently. One method was oxidation in  $O_2$  at 300°C which was the same method previously used, the other was oxidation by  $HNO_3$  and produced a surface which was oxidized to a greater extent. Figure 2 contains the results of the thermal stability experiments following heating for 300 sec in UHV at each temperature. In both cases a coverage greater than a monolayer was deposited and subsequently heated in UHV. The multilayer coverages were lost in the 500-600°C range on the  $O_2$  oxidized substrate. This is similar to the results on the  $HNO_3$  oxidized sample which are not shown. In both cases the potassium Auger signal persists to much higher temperatures. The potassium levels are approximately three times greater for the  $HNO_3$  oxidized sample for the  $O_2$  case at any given temperature. There are differences in the surface elemental composition of these samples. Figure 3 shows the oxygen and potassium AES signals relative to the carbon substrate signal for the two samples. The solid lines in Figure 3 represent integral oxygen to potassium stoichiometric values as defined from the previous results contained in Figure 1 based on 1:1 oxygen to potassium KOH stoichiometry. In the high coverage multilayer regime the KOH overlayer has between 2 and 3 times the oxygen content as the stoichiometric KOH compound independent of the method of glassy carbon preoxidation. This is again evidence that the KOH layers have taken up substantial quantities of oxygen containing gases from the air. Upon heating the sample in UHV the overlayer coverage decreases and the potassium content decreases. Figure 3 shows that as the potassium coverages decrease into a submonolayer regime, AES K/C  $\sim 0.4$ , there is a substantial amount of oxygen present which is greater than a 1:1 stoichiometry as measured by AES. We see

that as the amount of potassium decreases in the low coverage regime there is a corresponding loss of a fraction of the oxygen present. As in the case with the edge graphite substrate oxygen appears to be associated with the potassium species. In both glassy carbon samples the carbon surface remains heavily oxidized following the loss of potassium. The oxygen Auger signal for the  $\text{HNO}_3$  oxidized sample is slightly more than double that of the sample oxidized in  $\text{O}_2$ . This reflects the different extents of initial oxidation. The vacuum stability of the potassium species is enhanced on the more oxidized surface. The degree of carbon surface oxidation is related to the stability of the potassium species generated from KOH.

We have used XPS in order to characterize the electronic structure of the oxidized glassy carbon surfaces after KOH addition and thermal treatment in vacuum. KOH was added to an  $\text{HNO}_3$  oxidized glassy carbon sample. The  $\text{O}(1\text{S})$  XPS spectra was recorded following 5 min heating to the temperature shown in Figure 4. As previously determined by AES the  $500^\circ\text{C}$  spectrum corresponds to multilayers of the potassium containing overlayer. The  $500^\circ\text{C}$  spectrum has a FWHM of 2.4 eV and a B.E. of 531.7 eV with respect to the Fermi level. This is close to the value reported for KOH (17). We know that the KOH overlayer contains more than the stoichiometric amount of oxygen yet we are unable to resolve different oxygen(1S) peaks. Upon heating to  $800^\circ\text{C}$  the overlayer concentration was decreased into the monolayer regime. The  $800^\circ\text{C}$  XPS spectrum shows a broad  $\text{O}(1\text{S})$  signal, FWHM - 4.5 eV. There appears to be two  $\text{O}(1\text{S})$  peak envelopes, one centered near 531 eV, the other at 533 eV. Heating to  $950^\circ\text{C}$  results in the loss of potassium. A  $\text{O}(1\text{S})$  peak centered near 533 eV remains and this value is associated with oxygen strongly bound to glassy carbon. The 531 eV  $\text{O}(1\text{S})$  peak occurs in the presence submonolayer concentrations of potassium. The work function of the different glassy carbon surfaces were determined from photoelectron spectroscopy. The clean glassy carbon surface had a work function of 4.2 eV. Oxidation by  $\text{O}_2$  increases the work function to 4.4 eV and increases further on a heavily oxidized  $\text{HNO}_3$  sample to a value of 4.5 eV. The oxidized glassy carbon surface with the potassium complex corresponding to the  $800^\circ\text{C}$  XPS spectrum showed a work function decrease to 3.6 eV. If these values are used to estimate binding energies of the oxygen (1S) peaks with respect to the vacuum level we find almost a three eV binding energy difference between the oxygen associated with the potassium species and oxygen bound to carbon. Lower binding energies of a given element are generally identified with more electropositive electronic environments. The carbon surface with the potassium complex therefore shows oxygen in two generally different electronic environments: one associated with potassium and in an electropositive environment; the other in a more electronegative environment which is typically observed on the potassium-free surface.

## DISCUSSION

We have studied the interaction of KOH on clean graphite surfaces in order to isolate the pure interaction of KOH and carbon. AES results show that a constant 1:1 oxygen to potassium stoichiometry is maintained throughout deposition with the edge graphite surface held at  $30^\circ\text{C}$  independent of coverage as well as after heating in vacuum to produce submonolayer coverages. On the basal surface of graphite submonolayer coverages of KOH were thermally stable above the melting point of solid KOH where the KOH vapor pressure is substantial. Likewise the results on the edge surface show an increased stability

for the adsorbate a low concentration. Submonolayer concentrations of potassium species persist up to 500°C. Our results are consistent with the picture that KOH interacts reversibly with the edge surface of graphite. The adsorbate is stabilized with respect to solid KOH by the interaction with the carbon substrate. Pure KOH overlayers on the edge graphite surface do not form stable adsorption states above 500°C.

The interaction of  $H_2O$  and  $O_2$  with a pure KOH overlayer on the basal surface of graphite emphasize direct salt gas interactions. The KOH surface was very active toward  $H_2O$  and  $O_2$  at 30°C. Their presence does not directly lead to a significantly different interaction with the carbon surface. Essentially clean basal graphite surfaces are recovered upon heating in UHV to 500°C. The interaction of KOH with  $H_2O$  or  $O_2$  on a passive basal graphite surface is not sufficient to produce potassium species which are stabilized with respect to vacuum at high temperatures.

The interaction of  $H_2O$  and KOH with the "passive" basal graphite surface or KOH alone on an "active" edge graphite surface does not generate potassium species which are stable above 500°C. Oxygen already bound to carbon is an important element in determining the formation of stable potassium species. Catalytic precursor alkali salts are generally added to carbons under oxidizing conditions of the gaseous environment or the carbon surface. The edge graphite and glassy carbon surfaces were preoxidized to introduced oxygen strongly bound to carbon. The interaction of KOH with these surface produces potassium containing overlayers with enhanced thermal stability. Only submonolayer concentration of a potassium complex remained above 700°C. The concentration of these species was increased with the extent of carbon preoxidation. The potassium form exists on a carbon surface that is heavily oxidized. The carbon surface with the potassium complex shows oxygen in two different electronic environments. One is associated with potassium in an electropositive environment. The other is in a more electronegative environment which is typically observed on the potassium-free surface. We cannot distinguish from these results if potassium is bound to oxygen which is on the carbon surface from potassium which interacts with carbon and promotes the formation of oxygen in a more electropositive configuration bound to carbon. In the latter case this form of oxygen might exist on the carbon surface alone or promoted by materials other than potassium. Species where potassium binds to the surface through oxygen, C-O-K have been postulated to exist on catalyzed carbon surfaces (10,12,18). In the other interpretation potassium would be considered an adsorbate which interacts with an oxidized carbon site. In either case it is the initial oxidation of carbon which leads to their formation from KOH.

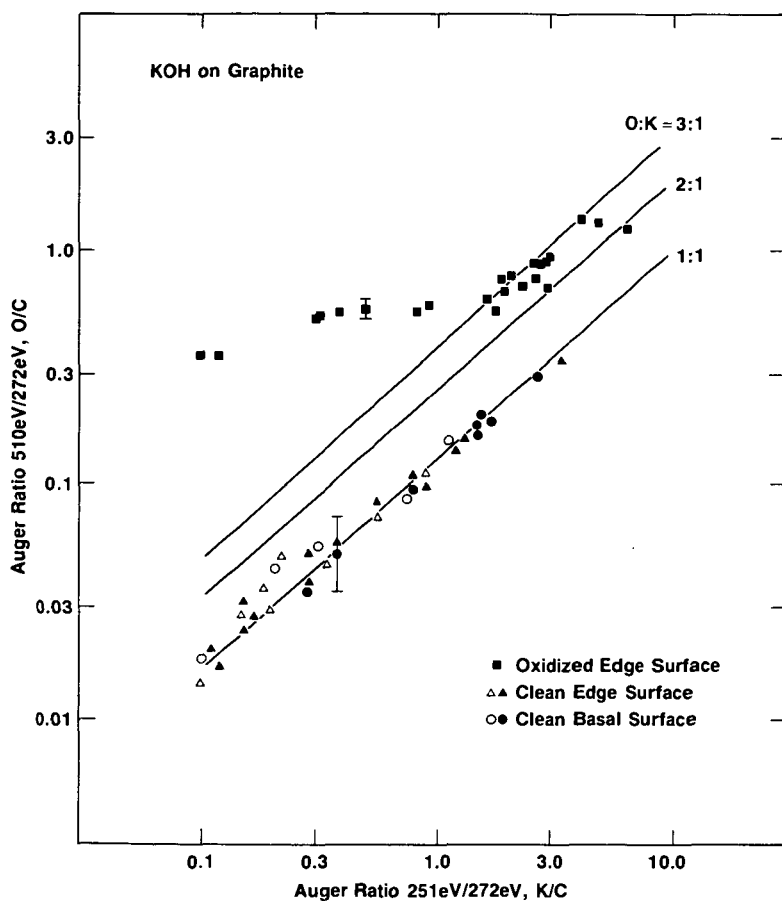
It is generally agreed that no single mechanism can be used to interpret all of the many different manifestations of catalytic carbon gasification. The oxygen transference mechanism has been widely used to explain alkali catalyzed carbon gasification (1,19). The action of the catalyst is to form intermediates in the oxidizing gaseous environment which decompose to oxidize carbon in the proximity. In doing this the catalyst returns to its original state and the action continues (20). Within the class of alkali gasification catalysts for the reaction of carbon with either  $H_2O$  or  $CO_2$  and even for the single element potassium there are a variety of different intermediates postulated for the mechanism (21). Microscopic studies suggest that gasification activity may not be restricted to a single physical form as

catalytic gasification is observed for systems in the presence (22) and absence of discrete particles (23). The mechanisms and intermediates involved in alkali catalyzed carbon gasification by  $H_2O$  and  $CO_2$  are still open issues.

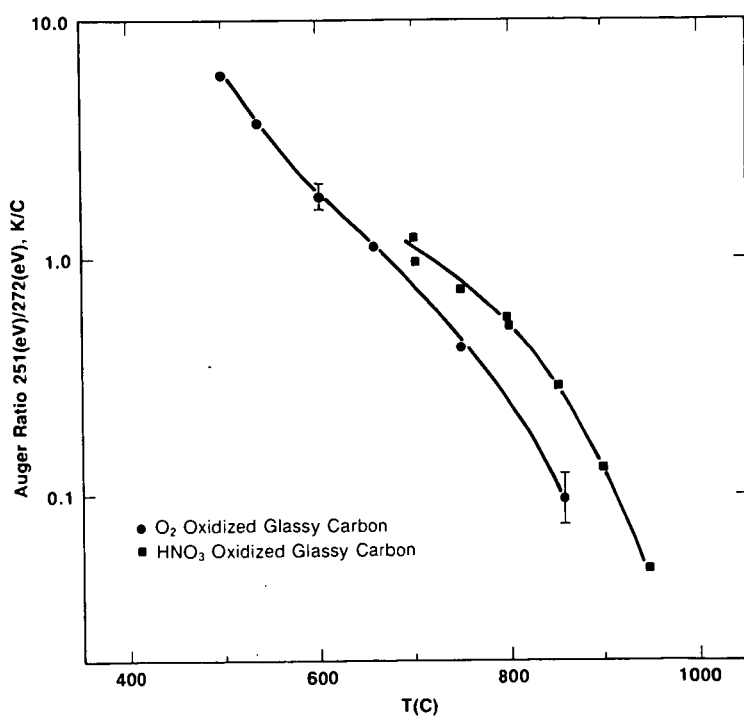
We have found in the study of  $CO_2$  and  $O_2$  interaction with the edge surface of graphite and glassy carbon samples that the surface can possess considerable amounts of oxygen which is strongly bound and much less active for CO formation. The CO formation energy decreases as the total oxygen surface concentration increases (24). The efficiency for producing the needed high oxygen coverages from either  $CO_2$  or  $H_2O$  is extremely low,  $<10^{-14}$  (24). The surface potassium complex is thought to be the active center for gas dissociation whereby CO or  $H_2$  is formed and oxygen transferred to the carbon surface. This increases the carbon surface oxygen concentration in the vicinity of the complex and thus we would expect this to lower the CO formation energy. The action of the catalyst would be to increase the local oxygen coverage in a carbon domain and thereby increase the number of domains having lower CO formation energetics. For glassy carbon these are in the 60-70 kcal/mole range (24). This mechanism would effectively increase the number of sites found in the uncatalyzed reaction.

#### REFERENCES

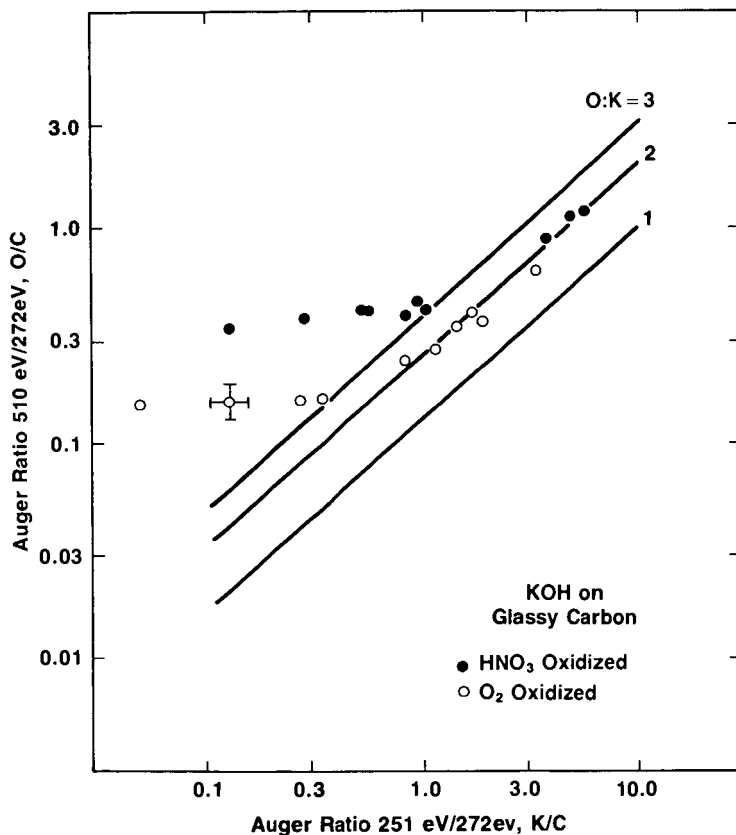
1. D. W. McKee, Chemistry & Physics of Carbon, 16 (1981) 1.
2. C. M. Tessi du Montay and C. R. Marechal Brit. Pat. 2548 (1867).
3. H. S. Taylor and H. A. Neville, J. Am. Chem. Soc., 43 (1921) 2055.
4. C. Kroger, Z. Angew Chem. 52 (1939) 129.
5. Wen-Yang Wen, Catal. Rev. Sci. Eng. 22 (1980).
6. H. Harker, "Proc. 4th Conf. on Carbon" Buffalo, NY 1959, Pergamon Press, NY (1960) pp. 124-139.
7. F. J. Long and K. W. Sykes; J. Chem. Phys. 47 (1950) 361.
8. J. L. Johnson, Catalytic Rev. Sci. Eng. 14 (1976) 131.
9. C. A. Mims and J. K. Pabst, Fuel 62 (1983) 178.
10. C. A. Mims, K. D. Rose, M. T. Melchior and J. K. Pabst, J. Am. Chem. Soc. 104 (1982) 6886.
11. S. Yokoyama, K. Miyahara, K. Tanaka, I. Takakawa and J. Tashior, Fuel 58 (1979) 510.
12. C. A. Mims, and J. K. Pabst, Am. Chem. Soc. Div. Fuel Chem. Preprints 25(3) (1980) 258.
13. S. R. Kelemen and C. A. Mims, Surface Science 136 (1984) L35.
14. S. R. Kelemen, H. Freund and C. A. Mims J. Vac. Sci. and Technol. A(2) (1984) 987.
15. S. R. Kelemen and C. A. Mims, Surface Science 133 (1983) 71.
16. H. Freund, unpublished results.
17. K. Kishi and S. Ikeda, Bull. Chem. Soc. Japan 46 (1973) 342.
18. I. L. C. Frieks, H. M. H. van Wechem, J. C. M. Striver and R. Bouwman Fuel 60 (1981) 463.
19. B. Neumann, C. Kroger and E. Z. Fingas Anorg. Chem. 197 (1931) 321.
20. H. Amariglio and X. Duval Carbon 4 (1966) 423.
21. D. W. McKee Fuel 62 (1983) 170.
22. C. L. Spiro, D. W. McKee, P. G. Kosky, E. J. Lamby, Fuel 63 (1984) 686.
23. C. A. Mims, R. T. K. Baker, J. J. Chludzinski, and J. K. Pabst, Am. Chem. Soc. Div. Fuel Chem., Preprints 28(1) (1983), 71.
24. S. R. Kelemen and H. Freund, Carbon submitted.



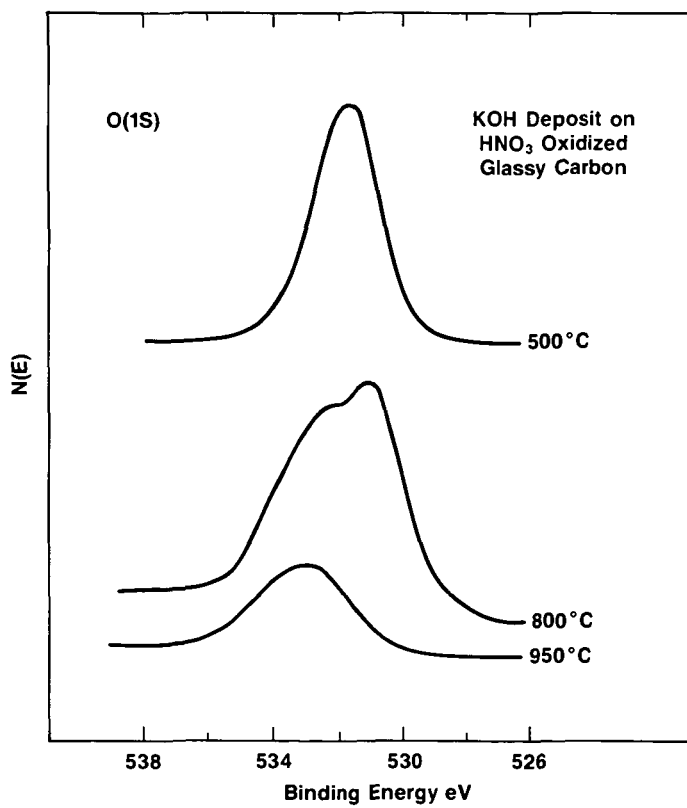
**Figure 1:** Solid triangles are obtained from the prism surface following KOH deposition at room temperature. Open triangles are a result of heating a KOH overlayer on the prism surface. Solid circles are obtained from the basal surface following KOH deposition at room temperature. Open circles are a result of heating the KOH overlayer on the basal surface. Solid squares are a result of heating KOH added to an oxidized edge graphite surface.



**Figure 2:** A comparison of the decrease in the K/C Auger ratio as a function of temperature after KOH addition to glassy carbon surfaces oxidized by O<sub>2</sub> at 300°C and by HNO<sub>3</sub>.



**Figure 3:** Change in the potassium and oxygen AES signals normalized to carbon following KOH addition to oxidized glassy carbon surfaces and subsequent heating in UHV.



**Figure 4:** O(1S) XPS signal after KOH addition to a HNO<sub>3</sub> oxidized glassy carbon sample and heating for 300 sec in UHV at each temperature.



## THERMAL CHEMISTRY PATHWAYS OF 1-NAPHTHOL

R. H. Schlosberg and A. Kurs

Exxon Research and Engineering Company  
Route 22 East, Clinton Township  
Annandale, New Jersey 08801

Previously we have reported our investigations of the thermal chemistry pathways of a number of ether systems under coal conversion like conditions. (1-4). In our studies on naphthalene methyl ether pyrolysis (4), we distinguished three major reaction pathways at 400°C (750°F): O-C alkyl cleavage yielding naphthols and R-H after hydrogen abstraction, an isomerization pathway of the starting ethers and a rearrangement pathway involving initial alkyl C-H hydrogen abstraction. Cleavage of the O-C bond is the most important pathway in this system.

We showed that the decomposition kinetics of the 1-naphthalene methyl ether was faster than that of the 2-isomer and that both naphthalene ethers were thermally more reactive than anisole (Table I). The product slates for the ethers are listed in Table II.

Figure 1 depicts four possible pathways to form naphthalene from 1-naphthalene methyl ether. One way which appeared particularly attractive was hydrodeoxygenation of naphthol. In this study we pursue that question by investigating the high temperature chemistry of 1-naphthol under coal conversion like conditions.

1-Naphthol was heated to 450°C (840°F) in a 30 cc batch autoclave under an initial room temperature pressure of 500 psi (3.5 MPa) of hydrogen. At reaction temperatures, the total pressure of the system rose to ~1000 psi. As shown in Figure 2, under our (largely) gas phase reaction conditions, the major products are naphthalene and tetralin. Other products identified included 1-tetralone and 1-tetralol. The presence of these two C<sub>10</sub> oxygenates is consistent with the results of Poutsma and Dyer (5) who studied the thermal chemistry of 1-naphthol without any external hydrogen. Their work was carried out at 400°C (750°F), a temperature where 1-naphthol exists largely in the liquid phase. In their hydrogen starved system, only a 2% yield of naphthalene was obtained, comparable to our naphthalene yields from the thermolysis of the naphthalene methyl ethers (Table II).

Figure 2 shows that the yield of the hydroaromatic, tetralin, diminishes with time while that of naphthalene grows as a function of time. This is consistent with a continuing hydrogen demand from unreacted naphthol and other hydrogen deficient systems (i.e., radicals, 1-tetralone and 1-tetralol) slowly dehydrogenating tetralin to naphthalene.

Under thermal conditions where Poutsma and Dyer (5) show about 33% conversion, the major products are dinaphthylfuran (53%), 1-tetralone (18%), tetralin (3%) and naphthalene (2%). Under hydrogen at similar levels of conversion (39%), we found tetralin (35%), naphthalene (28%), and 1-tetralone (10%), with only 5% dimeric and higher molecular weight species. Clearly with moderate pressure hydrogen, even without any added catalyst, the dimerization

or "growth" pathway so damaging to high oil yields from coal pyrolyses is superseded by reduction of the hydroxyl-containing ring. We calculate a rate constant for the disappearance of 1-naphthol to be  $2.2 \times 10^{-3} \text{ sec}^{-1}$  at  $450^\circ\text{C}$  under hydrogen and  $1.3 \times 10^{-4} \text{ sec}^{-1}$  at  $400^\circ\text{C}$  without added hydrogen.

Scheme I provides a series of thermal steps which can account for the initial generation of phenolics, then aromatics, and finally hydroaromatics under moderate hydrogen pressure. We begin with aryl alkyl ethers, moieties determined to be important reactive components in lignins (6) and in low rank coals (7). In contrast, when the naphthol is generated without external sources of hydrogen, the dominant pathway is one of condensation to make a dimeric furan (5). Since in a coal system, there will be some available hydrogen (native to the coal) even a pyrolysis will lead to the formation of some aromatic and hydroaromatic compounds as secondary reaction products following the initial ether cleavage pathway to phenols.

#### Experimental

1-Naphthol (Aldrich) was used as received (capillary gc analysis showed a purity >99%). The six batch reactors employed were constructed of 316 stainless steel and have previously been described in detail (8). Each reactor was charged with 2.0g of 1-naphthol and 500 psi (3.5 MPa) of hydrogen, attached to a rack and together plunged into a preheated fluidized sand bath and moderately agitated. Heatup times are on the order of 1.5 minutes. Individual reactors were removed from the hot sand bath at various times and rapidly quenched by plunging them into a water bath. Product analysis was by capillary gc. Use of an external standard (n-hexadecane) permitted identification of >90% by weight of the charged material.

#### Summary

1-Naphthol thermolysis was studied at  $450^\circ\text{C}$  ( $840^\circ\text{F}$ ) under moderate hydrogen pressure of ~1000 psi at reaction temperatures. The surprising result is the marked difference from earlier results reported on thermolysis of 1-naphthol under nitrogen: whereas the condensed products, dinaphthylfuran and 1-tetralone are dominant under nitrogen; in the hydrogen case tetralin and naphthalene are the most important products. This change in reaction product is accounted for by a new, competitive reaction pathway provided to the system by the molecular hydrogen.

#### References

1. R. H. Schlosberg, T. R. Ashe, R. J. Pancirov, and M. Donaldson, *FUEL*, **60**, 155 (1981).
2. R. H. Schlosberg, W. H. Davis, Jr., and T. R. Ashe, *Ibid.*, 201.
3. R. H. Schlosberg, P. F. Szajowski, G. D. Dupre, J. A. Danik, A. Kurs, T. R. Ashe, and W. N. Olmstead, *Ibid.*, **63**, 690 (1983).
4. R. H. Schlosberg, G. D. Dupre, A. Kurs, P. F. Szajowski, T. R. Ashe and R. J. Pancirov, *Liq. Fuels Tech.*, **1**, 115 (1983).
5. M. L. Poutsma and C. W. Dyer, *J. Org. Chem.*, **47**, 3367 (1982).
6. See, e.g., K. Freudenberg, *Ann. Rev. Biochem.*, **8**, 88 (1983).
7. R. Liotta, *J. Amer. Chem. Soc.*, **103**, 1735 (1981).
8. R. C. Neavel, *FUEL*, **55**, 237 (1976).

Table I  
UNIMOLECULAR DECOMPOSITION RATES  
FOR METHYL ARYL ETHERS

Batch Autoclaves, 3.5 MPa N<sub>2</sub>, 0.1 Hr Residence Time

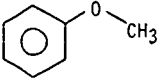
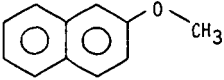
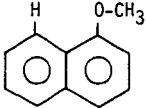
<u>Ether</u>		<u>% Recovered Ether @ T=0.1 Hr 450°C</u>	<u>k(hr<sup>-1</sup>)</u>	
			<u>400°C</u>	<u>450°C</u>
	Anisole	91	-	0.94
	2-Methoxy- Naphthalene	71±2	0.5	4.1
	1-Methoxy- Naphthalene	33±3	1.4	12

Table II

## NAPHTHYL METHYL ETHER PYROLYSIS RESULTS

Batch Autoclave, 0.1 Hr. Residence Time, N<sub>2</sub>

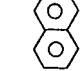
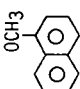
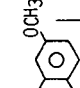
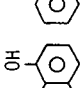
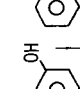
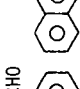
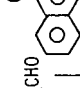
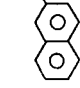
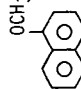
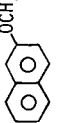
Reactant	Temperature (°C)	% in Liquids by GC Analysis							
									
	400	tr	89 ± 2	-	3 ± 1	-	1 ± 0.3	-	0.6 ± 0.2
	450	4	33	13	5 ± 1	tr	3	-	12
	400	-	-	96 ± 2	-	0.2 ± 0.1	-	-	tr
	450	3	9	71	0.2	1	-	2	tr

Figure 1

POSSIBLE PATHWAYS TO NAPHTHALENE

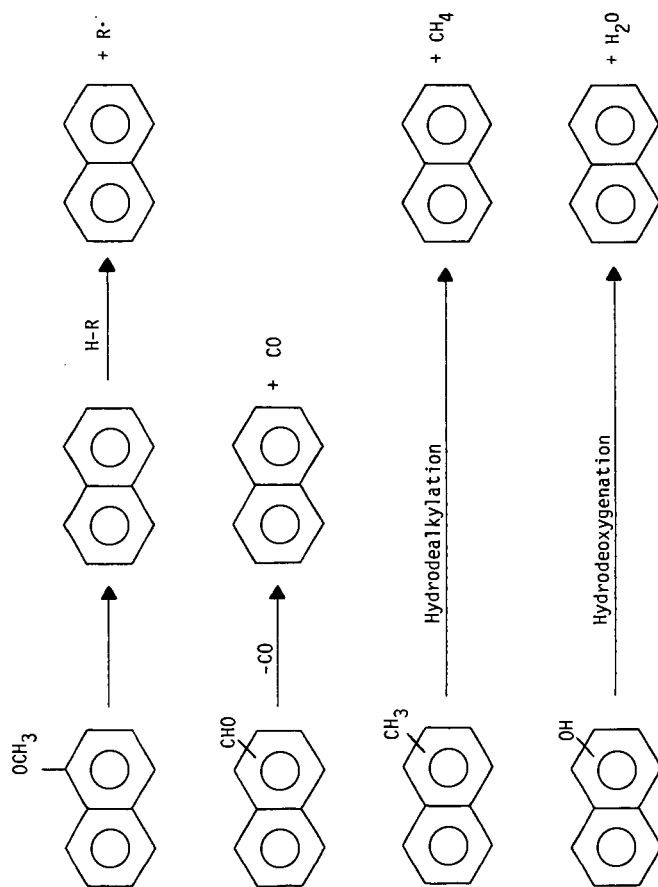
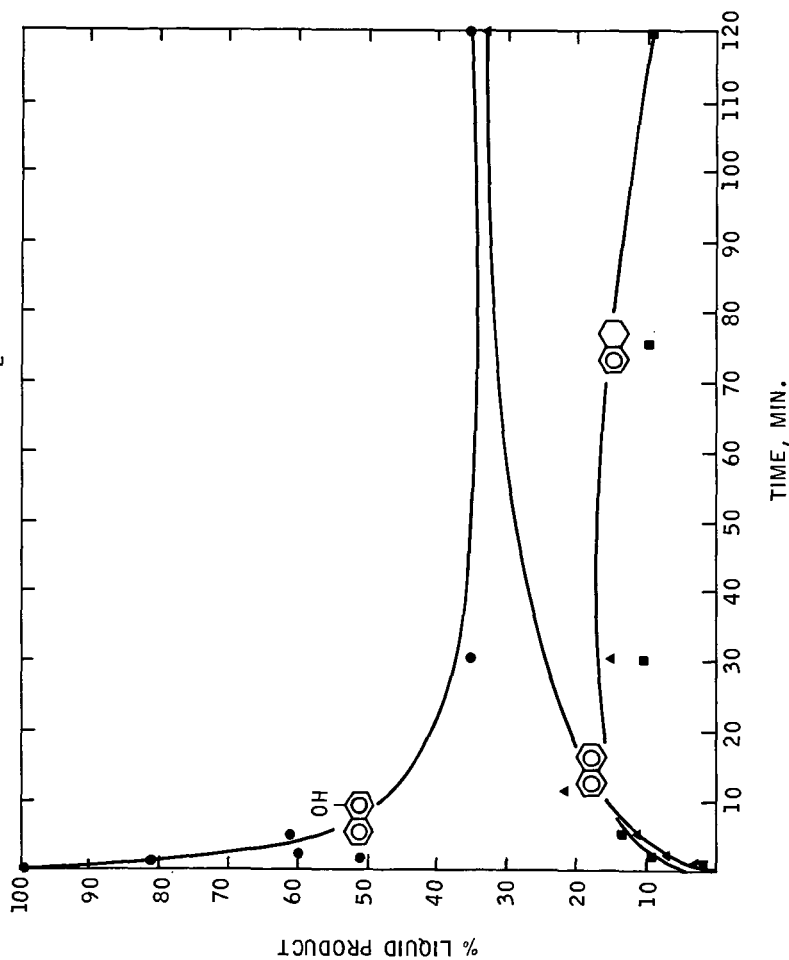


Figure 2

$\alpha$ -NAPHTHOL CONVERSION  
450°C./500 psi H<sub>2</sub>



## THERMOLYSIS OF SUBSTITUTED ANISOLES

Antti I. Vuori and Johan B-son Bredenberg  
Department of Chemistry  
Helsinki University of Technology  
SF-02150 Espoo 15, Finland

### INTRODUCTION

The possibility of using biomass as a chemical feedstock has in recent years attracted increasing interest. Lignin is one of the major components of biomass. It is produced in large amounts during wood pulping but the main part of it is simply burnt. There should, however, be some possibilities to use part of the lignin as raw material for more valuable products (1-3).

The first reaction step in any chemical conversion process of lignin is thermal rupture to smaller units (3, 4). Only the products thus formed are small enough to react with a heterogeneous catalyst to the ultimate products. This behavior corresponds to that found for coal. Thermal reactions of lignin as well as coal are usually very complicated. This makes the interpretation of experimental results from thermal reactions of lignin quite difficult though not impossible (5-7). Study of suitable lignin related model compounds can be of great use in the interpretation of the results. Application of the results of model compound studies on more complicated structures must, however, always be done with care since the reactions of macromolecular structures are not necessarily well represented by simple model compounds as has been noted in connection with coal (8).

Thermolysis of hydroxy, methoxy and methyl substituted anisoles in the presence of tetralin has earlier been studied by Bredenberg and Ceylan (9). Their results are, however, probably influenced by effects caused by the reactor walls. This paper considers the thermolysis of the guaiacyl structure of lignin by comparing the thermal reactions of different hydroxy and methoxyanisoles (and anisole) both neat and in the presence of tetralin at molar ratio 1:1 under conditions where wall effects have been minimized. Some comments about the kinetic parameters of the model compounds studied are also made though the experiments performed are insufficient for a strict kinetic analysis.

#### EXPERIMENTAL

All the model compounds used as well as tetralin were pure or analytical grade and they were used without further purification. Only the meta substituted compounds contained so much impurities (about 2.5 % by GC) that these had to be accounted for in the results.

The experiments were performed in 1 ml boron silicate glass ampoules (Duran 50) under argon atmosphere as described elsewhere (10). The same analytical procedures were also followed. The GC-MS analyses were needed only for the products from the experiments with meta compounds.

In addition to the thermolysis experiments some additional experiments were performed to test the effects of different kinds of materials as well as the possible wall effect on the thermolysis of hydroxyanisoles in the presence of tetralin at 638 K. The materials used for this purpose with all three hydroxyanisoles were sodium glass, AISI 304 and AISI 316 steels, molybdenum powder, and boron silicate glass. Coal ash and silicon carbide were tested only with *o*- and *p*-hydroxyanisole. The reaction time was 3.0 h for *ortho* and *para* compounds and 5.0 h for *meta* compound. The surface



area was approximately doubled in the experiments, except for the experiments with coal ash where the area was more than two hundred times the original. The results showed that sodium glass led to the formation of higher products with all hydroxyanisoles. Molybdenum and coal ash were found to enhance the conversion of the ortho and para compounds while there was no clear trend with the meta compound. No significant difference between the runs with plain boron silicate ampoules and those where boron silicate, silicon carbide or the aforementioned steels had been added were found. It should, however, be noted that molybdenum containing steel alloys have been reported to be activated in hydroliquefaction of coal when treated with pyrocatechol (11, 12).

## RESULTS AND DISCUSSION

Table 1 summarizes the experiments performed. The results are summarized in Figures 1 and 2 which contain the conversions and the selectivities of the formation of the main products from each model compound. Formation of higher products and char is also indicated in Figures 1 and 2.

All hydroxyanisoles gave as the main primary products the correspondingly substituted dihydroxybenzenes and cresols (Figure 1). Neat *m*-hydroxyanisole showed also some formation of methyl-*m*-hydroxyanisoles but because of the low conversions as well as the content of impurities (about 0.7 % methyl-*m*-hydroxyanisoles by GC) these results are uncertain. Figure 2 shows that the *o*- and *p*-methoxyanisoles followed a reaction pattern of same type as the hydroxyanisoles while *m*-methoxyanisole showed a stronger trend than *m*-hydroxyanisole to the formation of ring methylated products with two oxygen atoms. The possible pathways for product formation will be discussed in detail in relation to the C-O bonds reacting.

### The methyl C-O bond

The bond energy of the methyl C-O bond in a guaiacyl structure has been evaluated to be about 247 kJ/mol (3). It is clearly the weakest bond in *o*-hydroxyanisole (guaiacol). The results in Figures 1 and 2 also demonstrate that the majority of the main products from both hydroxy and methoxy-anisoles were formed by breaking of this bond.

Breaking of this bond in all hydroxyanisoles seemed to follow two parallel primary pathways. The formation of pyrocatechol from guaiacol has earlier been explained to take place by a free radical mechanism (13) or by a concerted mechanism (14). A concerted mechanism for the formation of the corresponding dihydroxybenzenes cannot be visualized for *m*- and *p*-hydroxyanisoles.

The question of a concerted versus a free radical mechanism has been widely discussed in the context of both biomass and coal liquefaction. Stein (15) has commented on the mechanistic possibilities of the thermal reactions of guaiacol by noting that there are under conditions of very low pressure pyrolysis where bimolecular reactions cannot occur, methyl radicals but little or no methane as a product. This would indicate a free radical reaction. The mechanism of guaiacol thermolysis is obviously more complicated under high concentration. The presence of water, which is formed during the reaction, has also been found to have a pronounced effect on the thermolysis of guaiacol (16). A combined free radical chain and concerted mechanism has recently been proposed for thermolysis of dibenzyl ether in the presence of tetralin (17).

Our results (Table 2) showed that the rate of decomposition of guaiacol was about one order of magnitude higher than that of any other model compound studied. The apparent first order activation energy found for guaiacol in the presence of tetralin (Table 3) was also unusually low which is in agreement with the values reported elsewhere (14). This

suggests that in addition to the homolytic mechanism an additional reaction mechanism, i.e. the concerted mechanism is also operating. It is in this connection important to note that o-methoxyanisole did not show any similar trend.

The formation of correspondingly substituted cresols from the hydroxyanisoles as well as the formation of correspondingly substituted cresols and methylanisoles from o- and p-methoxyanisoles was the second primary pathway of the methyl C-O bond cleavage. For the para compounds an intramolecular ipso-substitution seems to be the only reasonable explanation. For the ortho and meta compounds an intermolecular methylation is still possible though, especially for the meta compound hardly probable. For the ortho compounds there is, in addition, the possibility of an intramolecular methyl shift to the ortho position from the methoxyl group. Ceylan and Bredenberg (13) have presented an intramolecular rearrangement of guaiacol to o-cresol which takes place via an enolic form of the ortho hydroxyl. No significant interaction between the substituents in m-hydroxyanisole can be expected. Therefore the ipso-substitution requires some other mechanism. Anisole has been explained to react through a phenoxymethyl radical formed by methyl hydrogen abstraction to a benzyloxy radical via a spiranic oxiran intermediate under corresponding reaction conditions (10, 18). The primary products from a benzyloxy radical are, however, benzaldehyde and benzyl alcohol which in turn can then be reduced to toluene. There was no indication of this type of products in any GC or GC-MS analyses made of the thermolysis products of hydroxy and methoxyanisoles during the present work. It should, however, be noted that Kisilitsyn et al. (19) have found both o-hydroxybenzaldehyde and o-hydroxybenzyl alcohol among the products of short contact time pyrolysis of guaiacol at 773 K.

The results of the experiments with m-methoxyanisole (Figure 2) differed from those noted above. The cleavage of the methyl C-O bond to form m-hydroxyanisole corresponds

to the reaction of the other compounds studied. There was, however, no noticeable ipso-substitution of the methyl group despite of the greater proportion of ring methylated dihydroxy compounds. m-Hydroxyanisole also showed a similar trend. This is probably due to the ortho-para-activating effect of both hydroxyl and methoxyl groups. The meta compound has been found to give the greatest proportion of ring methylated products also in catalytic hydrodeoxygenation of hydroxyanisoles (20).

It is also interesting to note that the decomposition rate of neat m-methoxyanisole was roughly twice the decomposition rate of neat anisole (Table 2). This could be interpreted to mean that the methoxyl groups in m-methoxyanisole react fairly independently.

#### The aromatic C-O bond

The bond energy of the aromatic C-O bond of the methoxyl group in a guaiacyl structure has been evaluated to be about 356 kJ/mol, and of the hydroxyl group about 414 kJ/mol (3). For the corresponding homolytic bond scissions a high activation energy is hence required. This correlates well with the fact that guaiacylic model compounds have usually been found to give, under mild thermolysis conditions, only small amounts of products with one oxygen atom (6, 13, 14, 21).

Our results suggest that there was no significant direct scission of the aromatic C-O bonds in guaiacol (Figure 1). The formation of phenol takes place most probably via pyrocatechol. The results of the experiments with m- and p-hydroxyanisole are not as clear.

Anisole and aromatic hydrocarbons were found only in trace amounts in the hydroxyanisole series. The scission of the phenolic C-O bond has been suggested by Stein (15) to take place probably by an ionic mechanism. Tentative experiments

performed with the dihydroxybenzenes in the presence of tetralin gave almost exclusively phenol as a single ring aromatic product from pyrocatechol and hydroquinone whereas no phenol was found in experiments with resorcinol. These experiments also showed that higher products were formed from hydroquinone even in the presence of tetralin, a result which can also be seen in Figure 1.

The results of the methoxyanisole series (Figure 2) showed significant differences in the breaking of the aromatic C-O bonds in comparison with the hydroxyanisole series. In addition to the formation of phenol there was also significant formation of anisole from all three methoxyanisoles. The analyses made also indicated the presence of the products formed in the decomposition of anisole (10).

Anisole has earlier been reported to be formed from *o*-methoxyanisole (22). The formation of anisole from all three methoxyanisoles is not easily explained. It must take place by direct demethoxylation but the presence of a hydroxyl group seems to prevent it for reasons not known.

#### The overall kinetics

The decomposition rates of all the model compounds studied can be fitted into first order kinetics (Table 2) though the gross conversion include parallel reaction pathways. The apparent first order activation energies are shown in Table 3. These values are partly uncertain since in some cases they are based only on a few experiments at two temperatures (Table 1). Hence, only a few comments are made. The unusually low activation energy of guaiacol in the presence of tetralin has already been discussed. The results of neat guaiacol are too few for a proper analysis. Tables 2 and 3 also show that tetralin has, in addition to decreasing the reaction rates, some effect on the apparent activation energies. This is probably due to the quenching effect tetralin has on free radical chain reactions.

## CONCLUSIONS

The main reaction in the thermolysis of all hydroxyanisoles is the breaking of the methyl C-O bond. Two reaction pathways can be distinguished, the first one leading to the formation of the correspondingly substituted dihydroxybenzenes, and the second one leading to the formation of the correspondingly substituted cresols. For guaiacol the former pathway takes partly place, in addition to a homolytic bond breaking, by a concerted mechanism. A concerted mechanism cannot, however, be visualized for *m*- and *p*-hydroxyanisole. The latter pathway is thought to take place via a spiranic oxiran intermediate. For guaiacol there is also the possibility of an intramolecular methyl shift to the ortho position from the methoxyl group. The formation of cresols via methyl-dihydroxybenzenes does not, however, seem to be very probable. Neat *m*-hydroxyanisole shows, in addition, some formation of methyl-*m*-hydroxyanisoles. Breaking of the aromatic C-O bond in the hydroxyanisoles occurs only to a minor extent under mild thermolysis conditions.

The *o*- and *p*-methoxyanisoles follow a reaction pattern of the same type as the hydroxyanisoles while *m*-methoxyanisole gives more ring methylated products with two oxygen atoms. There is, however, no indication of a concerted mechanism for *o*-methoxyanisole. The formation of anisole by direct demethoxylation is significant for all three methoxyanisoles.

The decomposition rate of all the model compounds studied is decreased by the presence of tetralin.

## ACKNOWLEDGEMENTS

This work has been funded in part by grants from the Ministry of Education and Neste OY Foundation. The authors are grateful to Mrs. Eija Kinnunen and Mr. Timo Karinen for their contribution to the experimental part of this work.

# REFERENCES

1. Deglise, X. and Lede, J., *Int Chem.Eng.* 22 (1982), 631-646.
2. Kringstad, K., The challenge of lignin, in *Future sources of organic raw materials - CHEMRAWN I*, ed. by St-Pierre, L.E. and Brown, G.R., Pergamon Press, Oxford etc. 1980, 627-636.
3. Parkhurst, H.J., Jr., Huibers, D.T.A. and Jones, M.W., *Prepr.Pap. ACS Div. Pet.Chem.* 25 (1980), 657-667.
4. Avni, E., Coughlin, R.W., Solomon, P.R. and King, H.H., *Prepr.Pap. ACS Div. Fuel Chem.* 28 (1983), no.5, 307-318.
5. Iatridis, B. and Gavalas, R., *Ind.Eng.Chem.Prod.Res.Dev.* 18 (1979), 127-130.
6. Connors, W.J., Johanson, L.N., Sarkanen, K.V. and Winslow, P., *Holzforsch.* 34 (1980), 29-37.
7. Jegers, H.E. and Klein, M.T., paper submitted to *Ind. Eng.Chem.Process Des.Dev.*
8. McMillen, D.F., Ogier, W.C. and Ross, D.S., *Proc. - Int.Kohlenwiss.Tag, Essen 1981*, 104-109.
9. Bredenberg, J.B. and Ceylan, R., *Fuel* 62 (1983), 342-344.
10. Vuori, A., Karinen, T. and Bredenberg, J.B., *Finn.Chem. Lett.* 1984, in print.
11. Yoshii, T., Yaginuma, R., Yoshikawa, H. and Utoh, S., *Fuel* 61 (1982), 865-866.
12. Yoshii, T., Yaginuma, R., Utoh, S. and Yoshikawa, H., *Fuel* 62 (1983), 47-49.
13. Ceylan, R. and Bredenberg, J.B., *Fuel* 61 (1982), 377-382.
14. Klein, M.T. and Virk, P.S., *Prepr.Pap. ACS Div.Fuel Chem.* 25 (1980), no.4, 180-190.
15. Stein, S.E., *ACS Symp.Ser.* 1981, no.169, 97-129.
16. Lawson, J.R. and Klein, M.T., paper submitted to *Ind. Eng.Chem.Fundam.*
17. Simmons, M.B. and Klein, M.T., paper submitted to *Ind. Eng.Chem.Fundam.*
18. Schlosberg, R.H., Szajowski, P.F., Dupre, G.D., Danik, J.A., Kurs, A., Ashe, T.R. and Olmstead, W.N., *Fuel* 62 (1983), 690-694.
19. Kislitsyn, A.N., Rodionova, Z.M., Savinykh, V.I., Il'ina, E.I. and Abakhumov, G.A., *Sb.Tr.Tsent.Nauch.-Issled. Proekt.Inst.Lesokhim.Prom.* 1971, no.22, 4-16.

20. Bredenberg, J.B., Huuska, M. and Toropainen, P., Proc. 9th Iberoam.Symp.Cat., Lisboa 1984, Vol. I, 650-657.
21. Vuori, A. and Bredenberg, J.B., Holzforsch. 38 (1984), 133-140.
22. Klein, M.T. and Virk, P.S., Report MIT-EL 81-005, 1981, 99 p.

Table 1. Experimental data.

model compound	reaction temperature (K)	reaction time (h)
<u>o</u> -OH-anisole, neat	623	0.6; 1.0; (2.0)
	648	0.5; 1.0; 2.0; 3.0
	673	(1.0; 2.0)
-with tetralin	623	0.75; 1.0; 2.0; 3.0; 4.0
	648	0.5; 0.5; 1.0; 2.0; 2.0; 3.0; 4.0; 4.0
<u>m</u> -OH-anisole, neat	623	2.0; 3.0; 4.0
	648	1.0; 1.0; 2.0; 2.0; 3.0; 4.0
	673	1.0; 1.0; 2.0; 4.0; 4.0
-with tetralin	648	0.5; 1.0; 2.0; 3.0; 4.0; 4.0
	673	0.5; 1.0; 2.0; 2.0; 3.0; 4.0
<u>p</u> -OH-anisole, neat	648	1.0; 2.0; 4.0
	673	0.5; 2.0
-with tetralin	648	0.5; 1.0; 2.0; 2.0; 3.0; 4.0; 4.0
	673	0.5; 1.0; 2.0; 2.0; 3.0; 4.0
<u>o</u> -OCH <sub>3</sub> -anisole, neat	648	1.0; 2.0; 4.0
	673	0.25; 0.5; 2.0
-with tetralin	623	1.33; 2.0; 4.0; 5.0; 7.0
	648	1.0; 1.0; 2.0; 3.0; 4.0
	673	0.5; 1.0; 1.0; 1.5; 2.0
<u>m</u> -OCH <sub>3</sub> -anisole, neat	623	2.0; 3.0; 4.0
	648	1.0; 1.0; 2.0; 4.0
	673	1.0; 2.0; 2.0; 4.0
-with tetralin	648	1.0; 2.0; 2.0; 3.0; 4.0
	673	0.5; 1.0; 1.5; 2.0; 2.0
<u>p</u> -OCH <sub>3</sub> -anisole, neat	648	1.0; 2.0; 4.0
	673	0.25; 0.5; 2.0
-with tetralin	623	1.33; 2.0; 4.0; 5.0; 7.0
	648	1.0; 1.0; 2.0; 3.0; 4.0
	673	0.5; 1.0; 1.0; 1.5; 2.0

-experiments in parentheses are not used for kinetic parameters.



Table 2. The apparent first order rate coefficients of the model compounds.

model compound	623 K		648 K		673 K	
	$10^5 k$ (1/s)	r	$10^5 k$ (1/s)	r	$10^5 k$ (1/s)	r
-neat						
anisole(10)			0.76±0.13	0.959	3.91±0.59	0.957
o-OH	12.5±1.0	0.997	36.2±2.6	0.992		
m-OH	0.43±0.02	0.998	1.34±0.11	0.983	23.7±2.6	0.977
p-OH			5.36±0.83	0.977	54.0±9.4	0.985
o-OCH <sub>3</sub>			7.41±1.05	0.981	70.8±14.2	0.962
m-OCH <sub>3</sub>	0.51±0.13	0.945	1.33±0.16	0.979	8.09±1.67	0.942
p-OCH <sub>3</sub>			6.84±0.75	0.988	57.0±14.4	0.942
-with tetralin						
anisole(10)			0.31±0.04	0.967	2.09±0.16	0.987
o-OH	6.58±0.39	0.993	23.0±1.4	0.987		
m-OH			0.48±0.11	0.897	1.93±0.14	0.986
p-OH			2.50±0.16	0.988	18.5±1.0	0.992
o-OCH <sub>3</sub>	1.52±0.11	0.989	8.01±0.73	0.984	45.7±2.4	0.995
m-OCH <sub>3</sub>			1.00±0.19	0.932	4.58±0.20	0.996
p-OCH <sub>3</sub>	1.02±0.12	0.975	5.82±0.54	0.983	30.3±0.4	1.000

Table 3. The apparent first order Arrhenius parameters of the model compounds.

model compound	$E_A$ (kJ/mol)	$\log_{10} A$ (1/s)
-neat		
anisole(10)	237±46	14.0±3.7
o-OH	143±20	8.1±1.7
m-OH	277±11	17.8±0.9
p-OH	335±49	22.7±3.9
o-OCH <sub>3</sub>	327±51	22.3±4.1
m-OCH <sub>3</sub>	192±31	10.7±2.5
p-OCH <sub>3</sub>	308±57	20.6±4.6
-with tetralin		
anisole(10)	276±30	16.8±2.3
o-OH	168±16	9.9±1.3
m-OH	201±40	10.9±3.1
p-OH	290±17	18.8±1.4
o-OCH <sub>3</sub>	237±9	15.0±0.7
m-OCH <sub>3</sub>	221±32	12.8±2.5
p-OCH <sub>3</sub>	237±9	14.8±0.6

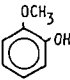
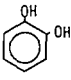
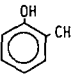
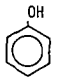
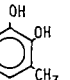
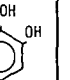
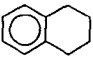
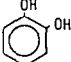
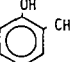
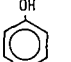
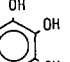
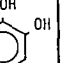
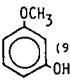
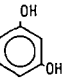
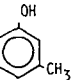
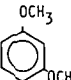
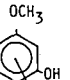
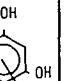
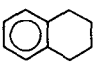
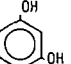
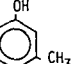
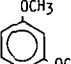
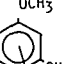
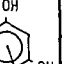
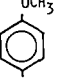
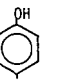
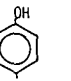
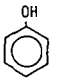
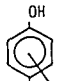
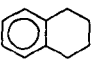
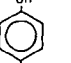
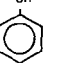
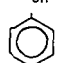
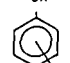
 <p>623 K, 0.6-2.0 h X = 25.8-40.8 % 648 K, 0.5-3.0 h X = 52.3-98.0 % 673 K, 1.0-2.0 h X = 99+ %</p>	<p>HIGHER, 623 K- CHAR, 648 K-</p>      <p>S (%): 14.7-15.8   4.3-6.6   2.7-3.1   1.4-1.6   1.0-1.3 S (%): 7.1-18.2   1.2-5.2   3.0-4.1   0.6-1.5   0.5-1.1 S (%): 4.4-8.5   1.0-1.6   6.5-8.8   0.4-0.6   0.4-0.6</p>
<p>+</p>  <p>623 K, 0.75-4.0 h X = 14.4-60.0 % 648 K, 0.5-4.0 h X = 25.1-96.8 %</p>	     <p>S (%): 71.7-82.0   2.4-7.7   2.7-4.9   6.0-8.1   6.0-7.0 S (%): 64.1-83.6   3.6-10.3   2.0-14.3   4.4-7.2   3.8-5.2</p>
 <p>(97.5%) 623 K, 2.0-4.0 h X = 3.4-6.1 % 648 K, 1.0-4.0 h X = 3.6-17.5 % 673 K, 1.0-4.0 h X = 41.7-97.5 %</p>	<p>HIGHER, 648 K- CHAR, 673 K-</p>      <p>S (%): 34.6-44.9   6.6-12.4   5.9-7.3   27.5-30.2   3.0-5.1 S (%): 42.7-67.1   2.8-5.1   1.3-13.4   17.7-27.9   2.5-5.2 S (%): 0.7-23.1   1.8-5.0   0.3-1.5   0.3-6.0   0.3-2.0</p>
<p>+</p>  <p>648 K, 0.5-4.0 h X = 0-8.4 % 673 K, 0.5-4.0 h X = 3.3-24.7 %</p>	     <p>S (%): 24.7-64.2   -   -   -   4.9-14.7 S (%): 56.7-86.6   8.5-16.3   -   -   10.1-15.4</p>
 <p>648 K, OH 1-4 h X = 26.3-54.7 % 673 K, 0.5-2.0 h X = 81.0-98.3 %</p>	<p>HIGHER, 648 K- CHAR, 673 K-</p>     <p>S (%): 26.6-27.9   8.4-10.6   4.0-5.9   1.7-2.7 S (%): 5.8-24.3   4.4-7.2   7.1-8.3   0.8-2.1</p>
<p>+</p>  <p>648 K, 0.5-4.0 h X = 4.0-31.1 % 673 K, 0.5-4.0 h X = 26.4-93.7 %</p>	<p>HIGHER, 673 K-</p>     <p>S (%): 63.4-82.2   8.4-12.1   1.4-2.4   8.2-9.4 S (%): 30.7-78.5   10.7-12.2   2.1-3.6   5.3-7.2</p>

Figure 1. Main products from the experiments with hydroxy-anisoles.

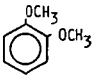
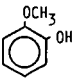
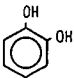
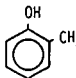
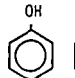
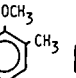
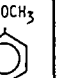
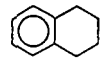
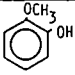
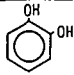
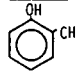
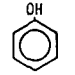
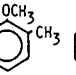
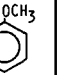
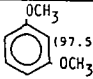
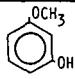
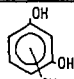
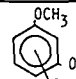
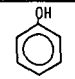
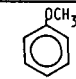
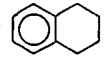
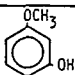
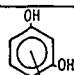
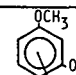
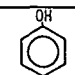
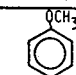
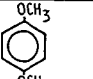
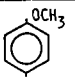
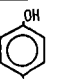
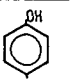
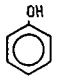
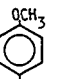
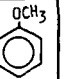
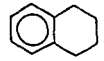
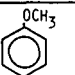
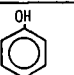
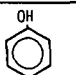
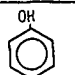
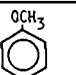
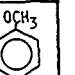
 648 K, 1.0-4.0 h $X = 36.5-67.1\%$ 673 K, 0.25-2.0 h $X = 84.7-99.7\%$	CHAR, 648 K-      
	$S (\%)$ : 14.0-18.8 1.9-5.4 3.1-4.9 0.6-3.4 5.6-7.5 9.8-11.8 $S (\%)$ : 0.2-7.2 4.7-11.2 4.0-4.5 4.1-6.6 0.6-2.6 4.6-9.1
+  623 K, 1.33-7.0 h $X = 5.7-30.5\%$ 648 K, 1.0-4.0 h $X = 17.2-69.8\%$ 673 K, 0.5-2.0 h $X = 55.3-96.3\%$	     
	$S (\%)$ : 34.7-63.8 10.4-22.8 2.3-8.1 7.4-15.4 1.6-4.5 5.4-15.0 $S (\%)$ : 13.7-55.8 6.3-47.0 2.8-7.3 0.7-1.7 9.5-14.4 4.6-7.9 $S (\%)$ : 2.0-19.5 46.3-58.3 2.5-6.9 1.3-4.0 8.3-11.4 4.9-9.3
 (97.5%) 623 K, 2.0-4.0 h $X = 5.8-7.2\%$ 648 K, 1.0-4.0 h $X = 5.6-17.8\%$ 673 K, 1.0-4.0 h $X = 41.4-70.2\%$	HIGHER, 673 K-     
	$S (\%)$ : 26.0-32.2 30.2-34.8 2.4-7.4 - 9.3-11.6 $S (\%)$ : 34.9-39.6 22.7-32.2 4.8-8.2 - 11.5-16.6 $S (\%)$ : 16.6-29.6 1.9-11.4 2.9-5.7 1.3-4.0 17.8-20.5
+  648 K, 1.0-4.0 h $X = 3.5-14.6\%$ 673 K, 0.5-2.0 h $X = 10.9-28.9\%$	    
	$S (\%)$ : 36.7-58.9 12.8-21.0 12.1-14.7 2.7-5.3 8.5-23.2 $S (\%)$ : 44.2-55.1 9.4-15.6 6.4-11.9 1.8-3.8 14.6-21.7
 648 K, 1.0-4.0 h $X = 26.7-62.9\%$ 673 K, 0.25-2.0 h $X = 87.1-99.2\%$	HIGHER, 648 K- CHAR, 673 K-      
	$S (\%)$ : 16.1-23.0 0.5-0.6 0.8-1.5 0.3-0.6 8.8-10.1 10.8-14.6 $S (\%)$ : 3.3-15.4 4.6-4.8 2.3-5.1 2.5-5.8 2.9-6.1 6.6-15.8
+  623 K, 1.33-7.0 h $X = 3.1-21.2\%$ 648 K, 1.0-4.0 h $X = 13.7-58.6\%$ 673 K, 0.5-2.0 h $X = 43.7-88.9\%$	     
	$S (\%)$ : 61.7-73.1 2.2-3.4 (2.0) 6.0-10.9 4.2-6.7 8.8-11.2 $S (\%)$ : 57.7-68.4 2.1-10.6 1.0-3.9 0.8-1.7 9.0-11.5 4.2-9.7 $S (\%)$ : 40.1-66.1 7.2-26.0 1.7-7.1 1.2-1.6 9.3-9.8 8.0-10.8

Figure 2. Main products from the experiments with methoxy-anisoles.

## THERMAL CHEMISTRY PATHWAYS OF ESTERS AND KETONES

by

R. H. Schlosberg, A. Kurs, G. D. Dupre and R. J. Pancirov

Exxon Research and Engineering Company  
Route 22 East, Clinton Township  
Annandale, NJ 08801

### INTRODUCTION

The work described is a continuation of our studies of the thermal chemistry pathways of reactive oxygenates important in fossil fuel hydrocarbons. Esters and ketones are pyrolysis products from carboxylic acids. Ketones have been found to be important components of hydropyrolysis oils from low rank coals, fossil fuels known to contain substantial amounts of carboxylate functionality.

### THERMAL CHEMISTRY PATHWAYS OF ESTERS

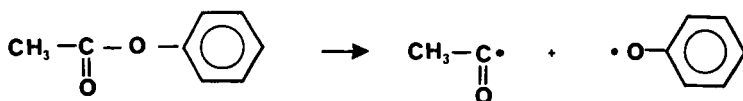
Conventional organic chemistry textbook wisdom describes ester pyrolysis only in terms of olefin elimination, and this only with esters of carboxylic acids. Noller (1) states that "when esters that have hydrogen on the  $\beta$ -carbon of the alkoxy group are heated to 500°C, a molecule of acid is lost with the formation of an olefin". This process is called pyrolytic cis-elimination. The situation with esters lacking  $\beta$ -hydrogens is less well studied and even the textbook cases are somewhat more complex than described.

Hexyl acetate. Hexyl acetate eliminates acetic acid to form 1-hexene according to the textbook mechanism, but this is not the only thermal chemistry event. Our thermal studies were carried out both in a flash pyrolysis unit (Figure 1) and in batch autoclaves. Conditions were set to achieve conversion levels of 10-60%. The thermal chemistry mechanisms are independent of unit. Using the flash pyrolysis unit and establishing a vapor residence time of ~ 1-2 sec, the major components in the gas phase products included hydrogen, methane, ethylene, propylene, water, carbon dioxide, and surprisingly carbon monoxide along with the anticipated 1-hexene (Table I). Experiments at equivalent conditions showed that acetic acid produces acetone, water and carbon dioxide as major products. Since, as we will show below, ketones thermally decarbonylate, the thermal conversion of hexyl acetate proceeds through 1-hexene and acetic acid. Acetic acid itself is thermally reactive and produces water and acetone. The ketone decarbonylates to produce the carbon monoxide observed. Finally, the 1-hexene slowly cracks and according to the results of Rebick (2) produces  $C_1$ - $C_5$  products with a relatively high yield of propylene. Our results are fully consistent with this picture.

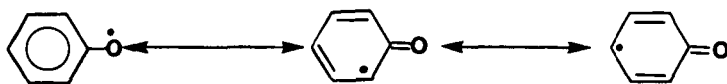
Methyl acetate. This ester does not have the structural properties required for pyrolytic cis-elimination, and at the 18% conversion level produces acetone, methanol and water as the major liquid phase products. This would indicate acyl oxygen, rather than alkyl oxygen, cleavage.

Phenyl acetate. Phenyl acetate unimolecularly decomposes only at the acyl oxygen site due to the influence of the aryl ring. As expected, the only major organic liquid products of any consequence are phenol>>>benzene. The unimolecular rate constant for phenyl acetate decomposition is  $0.35 \text{ min}^{-1}$  s.  $0.44 \text{ min}^{-1}$  for benzoic acid decomposition under similar conditions (3), (4).

A new mechanism is proposed to account for reaction products when olefin elimination is not feasible due to structural constraints. This proposed mechanism is shown in Scheme I for phenyl acetate. Cleavage at the phenolic position has been shown to be a favored pathway in the thermolysis of benzyl phenyl ether (5).  $\text{ArO-H}$  and  $\text{ArCH}_2\text{-H}$  bonds are similar in strength, and



it is reasonable to invoke phenoxy radical formation in the thermal chemistry of phenyl acetate. A contributing driving force for this cleavage reaction at the benzylic position is the enhanced stability of benzyl and/or phenoxy radicals through delocalization of the free electron.

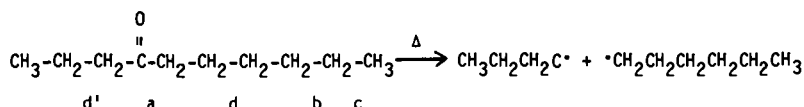


#### THERMAL CHEMISTRY PATHWAYS OF KETONES

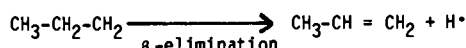
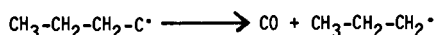
4-Decanone. Treatment of this internal ketone at  $600^\circ\text{C}$  in the flash pyrolysis unit led to conversion levels of 18%. The major fragmentation products (accounting for 85% of the converted ketone) were ethylene, propylene, carbon monoxide and 1-hexene (Table II). The rate constant for the unimolecular decomposition of 4-decanone was calculated to be  $\sim 7.9 \text{ min}^{-1}$ . This experimentally determined activation energy implies a radical chain, since there is no bond this weak ( $\sim 36 \text{ kcal/mol}$ ) in the system. A mechanism which accounts for all of the observed products is shown in Scheme II.

## SCHEME II

### Initiation



### Radical Elimination Reactions



Cleavage at the (b) or (c) bonds can lead to octenones and nonenones and to methane and ethane/ethylene, all identified in the product. Acetone arises from a sequence of reactions ultimately resulting in cleavage at the d and d' positions.

**2-Decanone.** The activation energy was calculated to be ~ 38 Kcal/mol for the unimolecular decomposition of this ketone with a rate constant at 600°C of ~11 min<sup>-1</sup>. Table III presents the product data for the thermolysis of 2-decanone at 550 and 650°C. Here, as found with the 4-isomer, carbon monoxide is a significant product, thus confirming the statement made earlier that acyl radicals decompose releasing carbon monoxide. Ring closure to form aromatic rings becomes an important pathway by 650°C as does formation of solid carbonaceous material.

Aliphatic ketones are formed from the pyrolysis of carboxylic acids. They, in turn, decompose thermally to lighter olefins and acetone, and at sufficiently severe conditions to methane, carbon monoxide and coke.

**1-Tetralone.** A cyclic ketone such as 1-tetralone undergoes a different sequence of thermal transformations. Tetralin, naphthalene and 1-naphthol are the major liquid products when 1-tetralone is treated at 425°C under an inert atmosphere. When hydrogen is present the yields of tetralin and naphthalene increase, consistent with results published earlier (Table IV).

### Acknowledgements

The authors acknowledge the support and counsel of Drs. M. L. Gorbaty and W. N. Olmstead. R. Behul is thanked for his experimental work on the 1-tetralone system.

#### REFERENCES

1. C. R. Noller, "Chemistry of Organic Compounds", W. B. Saunders Co., Philadelphia, 1966, p. 198.
2. C. Rebeck, in "Advances in Chemistry Series. 183", American Chemical Society, 1979, p.1.
3. R. Schlosberg, manuscript submitted for publication.
4. E. Ghibandi and A. J. Colussi, J. Chem. Soc., Chem. Comm. 1984, 433 have shown that at  $T > 680^{\circ}\text{C}$ , phenyl acetate decomposes unimolecularly via a four-centered cyclic transition state giving phenol and ketene.
5. R. T. Morrison and R. N. Boyd, "Organic Chemistry", 2nd Edition, Allyn and Bacon, Inc., Boston, 1967, p. 688.
6. R. H. Schlosberg, W. H. Davis, Jr. and T. R. Ashe, FUEL, 60, 201 (1981).
7. S. Stein in "New Approaches in Coal Chemistry", ACS Symposium Ser. Vol. 69, Blauster, B. D., et. al., Eds., Pittsburg, PA, 1981, pp. 97-130.
8. The thermal chemistry pathways of 1-naphthol has been reported: see M. Poutsma and C. W. Dyer; J. Org. Chem., 47, 3367 (1982).
9. R. H. Schlosberg, P. F. Szajowski, G. D. Dupre, J. A. Danik, A. Kurs, T. R. Ashe and W. N. Olmstead, FUEL, 62, 690 (1983).

TABLE I  
PYROLYSIS OF HEXYL ACETATE  
550°C, ~1-2 SEC. RESIDENCE TIME, HELIUM SWEEP GAS

Gas Analysis, Relative Mole %

<u>H<sub>2</sub></u>	<u>CO</u>	<u>CO<sub>2</sub></u>	<u>CH<sub>4</sub></u>	<u>C<sub>2</sub>H<sub>4</sub></u>	<u>C<sub>2</sub>H<sub>6</sub></u>	<u>C<sub>3</sub>H<sub>6</sub></u>	<u>C<sub>3</sub>H<sub>8</sub></u>	<u>C<sub>4</sub>'S</u>	<u>C<sub>5</sub>'S</u>	<u>C<sub>6</sub>'S</u>	<u>H<sub>2</sub>O</u>
39	12	12	7.7	3.7	-	4.4	1.1	1.8	-	10	5.2

TABLE II  
4-DECANONE THERMOLYSIS  
600°C, ~1-2 SEC. VAPOR RESIDENCE TIME  
3.8g FEED, HELIUM SWEEP GAS

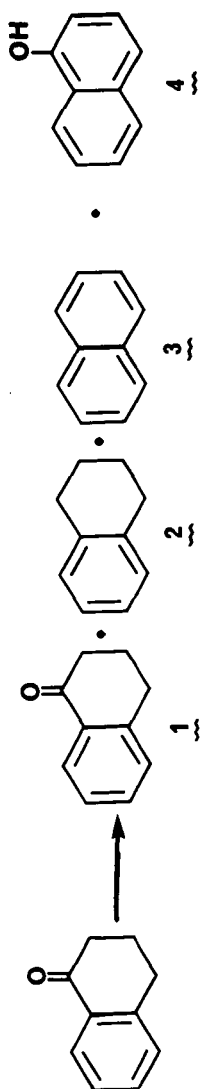
<u>Yields</u>	<u>g</u>	<u>% of Starting Feed</u>
Solid	0.02	0.53
Liquid	3.27	86.3
4-Decanone	3.11	82.1
Acetone	0.024	0.62
1-Hexene	0.049	1.3
n-Hexane	0.002	0.05
Nonenones	0.021	0.56
Others	0.064	1.7
Gases	0.48	12.7
H <sub>2</sub>	0.002	0.05
CH <sub>4</sub>	0.050	1.3
C <sub>2</sub> H <sub>6</sub>	0.035	0.9
C <sub>2</sub> H <sub>4</sub>	0.12	3.1
C <sub>3</sub> H <sub>8</sub>	0.005	0.12
C <sub>3</sub> H <sub>6</sub>	0.10	2.8
C <sub>4</sub> 's	0.038	1.0
C <sub>5</sub> 's	0.014	0.4
CO	0.11	2.8
H <sub>2</sub> O	0.07	0.2
Total Recovered	3.77g	99.4



TABLE III  
2-DECANONE PYROLYSIS  
1-2 SEC. VAPOR RESIDENCE TIME

Yields	g	3.73 g Feed		% of Starting Feed
		550°C	650°C	
		% of Starting Feed	g	
Solid	0.09	2.4	0.45	12.1
Liquid	3.67	98.4	1.81	48.5
2-decanone	3.59	96.2	1.23	33.1
acetone	-	-	0.036	1.0
1-hexene	0.003	0.07	0.039	1.1
n-hexane	-	-	0.011	0.31
2-hexenes/C <sub>6</sub> H <sub>6</sub>	tr	tr	0.101	2.71
1-heptene	0.022	0.61	0.093	2.89
n-hexane	-	-	0.009	0.25
2-heptenes/C <sub>7</sub> H <sub>8</sub>	-	-	0.051	1.37
1-octene	0.029	0.80	0.091	2.45
n-octane	tr	tr	0.010	0.27
2-octenes/EB,XYL	-	-	0.047	1.25
CH <sub>3</sub> CO <sub>6</sub> <sup>=</sup> or CH <sub>3</sub> CO-cyclohexyl	tr	tr	0.015	0.40
others	0.034	0.93	0.87	2.34
Gases	0.093	2.5	0.84	22.5
H <sub>2</sub>	0.005	0.1	0.112	3.0
CH <sub>4</sub>	0.013	0.3	0.115	3.1
C <sub>2</sub> H <sub>6</sub>	-	-	0.053	1.4
C <sub>2</sub> H <sub>4</sub>	0.015	0.4	0.108	2.9
C <sub>3</sub> H <sub>8</sub>	0.001	tr	0.097	2.6
C <sub>4</sub> 's	0.008	0.2	0.033	0.9
C <sub>5</sub> 's	0.024	0.6	0.003	0.1
CO	0.023	0.6	0.303	8.1
H <sub>2</sub> O	0.004	0.1	0.009	0.2
<u>TOTAL RECOVERED</u>	3.85	103.2	3.10	83.1

TABLE IV

THERMAL CHEMISTRY OF  $\alpha$ -TETRALONE

Reaction Atmosphere	Wt. % of Liquids			
	1	2	3	4
3 MPa He	28	19	20	25
3 MPa H <sub>2</sub>	8	52	29	-
5 MPa H <sub>2</sub>	2	56	35	-

## MECHANISTIC MODELING OF THE PYROLYSIS OF ETHYLENE BRIDGED POLYMERS

K.R. Squire, P.R. Solomon, M.B. DiTaranto and R.M. Carangelo

Advanced Fuel Research, Inc., 87 Church Street, East Hartford, CT 06108, USA

Recently, Solomon and King reported a tar formation model applicable to the pyrolysis of softening bituminous coals (1). Their theory combined the random cleavage of weak bonds (similar to a concept used by Gavalas and coworkers (2)) with transport of depolymerization fragments by vaporization and diffusion (like Unger and Suuberg (3)). It predicted char and tar yields and molecular weight distributions and provided several insights into the role of donatable hydrogen and the dependence of product distributions on reaction conditions.

The Solomon and King (SK) theory was developed using model polymers which contain functional groups representative of coal structure. Polymers were studied because coal is generally insoluble, heterogeneous, and chemically complex and is, therefore, difficult to use in validating models. Several types of bridging groups between the aromatic rings in these polymers were considered; it was found that ethylene bridges decompose in the same temperature range where coal evolves tar while oxymethylene bridges cleave at temperatures which are too low and methylene bridges at temperatures which are too high (1,4,5). From these studies it's been found that ethylene bridged polymers are quite valuable in elucidating the mechanisms of tar formation since they have simple, well established chemical structures and melt and produce tars under conditions similar to those where softening bituminous coals form tar. Studies on lignins have also shown that cleavage of oxymethylene and ethylene bridges both play important roles in the formation of tar during pyrolysis of lignins (6).

Although the SK tar formation model has been found to provide reasonable predictions for tar and char yields and for the molecular weight distributions of tars, it contains three significant conceptual problems:

- 1) Reaction yields were controlled in this model by an adjustable parameter which determined how many donatable hydrogens were available for capping the arylmethylene radicals formed when ethylene bridges cleave. This parameter has been found to vary with reaction conditions and not predictable a priori.
- 2) The effect of product olefinic bridges on the bond breaking distributions was not included. The presence of unbreakable double bonds in the oligomer chains should make it less likely that monomers and dimers will form.
- 3) It is difficult to extend the SK model to include realistic chemical mechanisms since the actual concentrations of ethylene and olefinic bridges are not monitored. Attempts to correct this problem have led to excessive computer run-times.

In this paper, a revised version of the SK model is presented which can predict product yields and molecular weight distributions directly from initial polymer structures. In this model all three of these problems have been eliminated. In addition, this new model has been solved using Monte Carlo techniques, is more efficient computationally than the SK model, and can potentially be expanded to detailed simulations of extremely complex polymers such as coal. Furthermore, since this model predicts product spectra directly from polymer structures without use of adjustable parameters, it can be used to investigate the validity of alternative pyrolysis mechanisms. Simulations using this model suggest that ipso substitutions by H radicals occur during thermal decomposition of ethylene bridged polymers and that radical recombination reactions play an important role in determining the molecular weight distributions of pyrolysis tars.

## EXPERIMENTAL

Poly(p-xylylene), 1, was purchased from Frinton Laboratories. As a byproduct of di-p-xylylene (p-cyclophane) synthesis, this polymer was very impure and contaminated with the dimer. It was purified by Soxhlet extraction in toluene for two days.

Poly(1,4-dimethylenenaphthalene), 2, as prepared at Iowa State University using an adaptation of Golden's synthesis for poly(dimethylenedurene) (7). This synthesis was accomplished using phenyllithium to couple the bis(bromomethyl) derivatives which were prepared from dimethylnaphthalenes using N-bromosuccinimide and benzoyl peroxide in  $\text{CCl}_4$ . The degree of polymerization (DP), defined as the number of monomer units in a polymer molecule, is estimated to be 64 (MW = 10,000). Additional use of these polymers as models for coal chemistry was recently described by Squires et al. (8).

Several pyrolysis experiments, including slow heating rate and flash pyrolyses, were carried out on these ethylene bridged polymers using an apparatus which employs an electrically heated grid within an infrared cell to provide on-line, in-situ analysis of evolved products by Fourier Transform Infrared (FT-IR) spectrometry. Details of these experiments have been described previously (1,10). Field Ionization Mass Spectrometry (FIMS) were performed at SRI International and have been described by St. John and coworkers (11).

## THEORY

The original SK tar formation model considered the molecular weight distribution,  $Q_i$  in the reacting polymer and the molecular weight distribution,  $N_i$  of the tar, where  $Q_i$  and  $N_i$  are the molar quantities of the polymeric component with  $\text{DP}=i$  in the reacting polymer and in the tar. The rate of change of  $Q_i$  was written as:

$$dQ_i/dt = (dF_i/dt) - (dB_i/dt) - (dN_i/dt) \quad (1)$$

where  $dF_i/dt$  was the rate of formation for the component with  $\text{DP}=i$  from the decomposition of components with  $\text{DP} > i$  in the reacting polymer;  $dB_i/dt$  was the rate of disappearance by decomposition of the component with  $\text{DP}=i$  in the reacting polymer; and  $dN_i/dt$  was the rate of transport of fragments with  $\text{DP}=i$  from the particle as tar or gas.

The terms of  $dF_i/dt$  and  $dB_i/dt$  were the rate of creation and destruction of oligomers with  $\text{DP}=i$  through the cleavage of weak bonds. The cleavage of these weak bonds was assumed to be a first order process with a rate constant  $k$ , i.e., the rate at which bonds break was  $k$  times the number of breakable bonds. It was further assumed that all bonds in a given oligomer were equivalent and were breakable. Thus, since there were  $(i-1)$  bonds in the polymeric component with  $\text{DP}=i$ , and the breaking of any one of them would remove that component from the distribution parameter  $Q_i$ , the rate of destruction for the component  $i$  was written as

$$dB_i/dt = (i-1)kQ_i \quad (2)$$

Similar arguments were also used to write down the rate at which component  $i$  was created from oligomers with  $\text{DP}=j > i$  (see Eqs. 3 and 4 of Ref. 1).

From Eqs. 1 and 2 it can be seen that this model only kept track of the molar quantities of tar and polymer oligomers; the actual concentrations of ethylene or olefinic bridges were not monitored. Instead, it was assumed that a  $\text{DP}=i$  oligomer always contained  $(i-1)$  breakable ethylene bridges.

Since weak ethylene bridges were not explicitly removed when they donated hydrogens to "cap" free radicals, another parameter was necessary to determine the extent of reaction. In the SK model, the extent of reaction was controlled by an adjustable parameter,  $F_{\text{pqb}}$ , defined as the fraction of weak bonds (ethylene bridges) whose resulting free radicals could be stabilized by donatable hydrogens. The total number of cleaved bonds was continuously monitored during a pyrolysis simulation and, when it

got larger than  $F_{pdb}$ , the reaction was said to have completed. Thus,  $F_{pdb}$  directly controlled char and tar yields in the original SK model. Unfortunately, this parameter varied from polymer to polymer and also depended upon reaction conditions. It could not be predicted from just a knowledge of the polymer's structure and reaction conditions.

This formulation for tar formation led to simple equations which were easy to solve and also produced reasonable predictions for tar molecular weight distributions (1,4). However, it is clearly incorrect to assume that a  $DP=1$  oligomer always contains (1-1) breakable bonds, because as the depolymerization reaction proceeds, many ethylene bridges are converted to olefinic bridges following their use as hydrogen sources. Towards the end of tar formation it is entirely possible that a  $DP=1$  oligomer would contain no breakable ethylene bridges. In a more realistic model the actual numbers of both olefinic and ethylenic bonds need to be monitored.

To take into account the effect of olefinic bridges it is necessary to keep track of the number of oligomers with no double bonds, with 1 double bond, with 2 double bonds, etc. This means that for each  $DP=m$  oligomer, the concentrations of  $m$  double bond combinations need to be monitored. To follow the depolymerization of a polymer with initial chain length  $n$ , the concentrations of approximately  $(n^3)/2$  different oligomers need to be followed. The time evolution of each of these oligomer concentrations is described by a separate differential equation. Thus, even this simple model improvement leads to a dramatic increase in the computational effort necessary to solve it! To avoid solving these complex networks of coupled differential equations, a new approach to the modeling of tar formations has been developed.

The essential problem of modeling polymer pyrolyses is simply that each modified oligomer is technically a new chemical species. As more complex oligomers are treated, the number of differential equations describing the time evolutions of these oligomers rapidly proliferates and becomes computationally unmanageable. An alternative approach is to use Monte Carlo modeling techniques.

In a Monte Carlo simulation, separate differential equations for the concentrations of individual modified oligomers are not explicitly solved. Instead, a small representative sample of polymer molecules is symbolically constructed in the memory of a computer. A bonding array is used to keep track of each monomer's identity, which substituents are attached to a given monomer, and how the monomers are connected to each other. The first four columns of this array are pointers indicating how monomers are attached to other monomers or substituents; the next four columns indicate the bonds involved in each attachment; and the last keeps track of each monomer's identity (e.g. benzene or naphthalene rings). A separate row is stored in this array for each monomer included in the simulation. Pyrolysis is simulated by statistically changing the bonding patterns stored in this array according to the kinetic and vaporization rate laws of the tar formation model.

In the current configuration, 25-40 polymer molecules can be simulated during a single run so that approximately 1200 ethylene bridges are being decomposed. Each monomer can be connected to as many as four other monomers or ring substituents. Up to fifty different monomers and twenty bond types can be used to construct the polymers for each simulation. For example, unreacted polymer 1 would be simulated using only benzene monomers, ethylene bridge connections between monomers, and methyl end groups for the terminal monomers of each polymer chain. As the pyrolysis simulation proceeded, new bond types would be introduced (e.g. olefinic bridges between monomers) to describe the gradual decomposition of the polymer.

Vaporizations are simulated by removing an oligomer from the computer's memory, by adding its mass to the running tar yield, and by putting a count in the appropriate bin of a file describing the molecular weight distribution of the evolving tar. For example, when a molecular weight 312 trimer from polymer 1 vaporizes (composition: 3 benzene monomers, 2 terminal methyl groups, 1 olefinic bridge, 1 ethylene bridge), all its pieces would be removed from the bonding arrays, 312 atomic mass units would be

added to the tar yield, and a single count would be added to bin 312 of the tar's molecular weight distribution file.

A typical simulation proceeds as follows: A series of random numbers are chosen to determine which "global" reactions occur. In the current configuration, oligomer evaporations and a complex network of reactions describing the decomposition of ethylene bridges are the "global" reactions. The random numbers are compared with normalized reaction velocities to see if the pending reaction will occur. If the random number is larger than the velocity, then the program branches to a subroutine which performs the appropriate reaction "chemistry" on the oligomer arrays. If the random number is smaller than the velocity, then the next reaction is tested until the list is exhausted. After every twenty iterations through the reaction list, time is incremented using the observed concentration changes and reaction velocities. The simulation continues until a preset time is reached or no further changes in the bonding arrays are occurring.

The reactions which have been included in the mechanism for ethylene bridge decomposition are presented in Fig. 1. In Step 1, ethylene bridges homolytically cleave to form two arylmethylene radicals. This step is assumed to be rate-limiting and its kinetic rate constants are in good agreement with predictions based upon thermochemical kinetics calculations (5).

The arylmethylene radicals can then react in six ways: they can abstract hydrogens from unreacted ethylene bridges (Step 2) or butylene bridges (Step 3), they can substitute for ethylene bridges (Step 4) or aromatic methyl groups (Step 5), and they can recombine with other arylmethylene radicals (Step 6) or with ethylene bridge radicals (Step 7). Which of these pathways occurs during a given pass through the "chemistry" subroutine is determined by comparing a random number with a set of normalized branching probabilities. In the current program fixed branching probabilities are used to determine how the decomposition proceeds, but in a future model we plan to calculate the individual velocities of the reactions in Fig. 2 using rate constants and steady state radical populations. In these simulations, branching probabilities will be the normalized ratios of these reaction rates.

Steps 2-5 lead to new radicals which continue to react while 6 and 7 produce stable bonds and terminate the reaction. The butylene bridge radicals of Step 3 are assumed to spontaneously decompose via a  $\beta$ -elimination reaction into an ethylene bridge radical and an olefinic bridge, Step 11. The arylethyl and methyl radicals produced in Steps 4 and 5 are assumed to stabilize via abstraction of hydrogens from unreacted ethylene bridges, Steps 15 and 16. Thus, all four of the reactive pathways for arylmethylene radicals eventually form an ethylene bridge radical.

In this model, ethylene bridge radicals are allowed to react in three ways: they can disproportionate (Step 8), they can recombine to form butylene bridges (Step 9), or they can decompose via a  $\beta$ -elimination reaction into a hydrogen radical and an olefinic bridge (Step 10).

The hydrogen radicals formed in Step 10 can then react in three ways: they can abstract hydrogens to stabilize (Step 12), they can substitute for ethylene bridges (Step 13), or they can substitute for aromatic methyl groups (Step 14). The arylethyl and methyl radicals formed in Steps 13 and 14 are assumed to stabilize via hydrogen abstractions from unreacted ethylene bridges, Steps 15 and 16. Thus, all the reactions of hydrogen radicals lead to the formation of new ethylene bridge radicals to replace the ones lost when Step 10 formed H radicals.

This complex network of reactions is an extension of the mechanisms proposed by Stein (12) and Poutsma (13) for the pyrolysis of diphenylethane. In the current Monte Carlo model, these reactions are carried out on the polymer bonding arrays each time the simulation determines that an ethylene bridge has decomposed. Figure 2 is a flow diagram which shows how the "chemistry" is carried out by the simulation.

as predicted by the SK model. With 90% recombination of end radicals (Fig. 5c) the increase in high molecular weight oligomer counts is sizeable, while recombinations of bridge radicals (5d) make high molecular weight oligomers less abundant.

Comparing the experimental FIMS data for polymer 1, Fig. 5a, with these simulated spectra it is apparent that even higher end radical recombination frequencies are necessary to reproduce this polymer's uneven oligomer patterns. Clearly, however, recombinations of bridge radicals can not be contributing to the observed maximum in this polymer's FIMS data.

To understand why recombinations of end radicals lead to increased populations of high molecular weight oligomers while recombinations of bridge radicals decrease their populations, we need to consider the counting statistics for each type of radical: for end radicals the probability of a radical occurring on an oligomer is independent of chain length (they occur only at the ends of chains) while for bridge radicals the probability of a radical occurring on an oligomer increases with chain length (more bridges increase the number of sites where a radical can occur).

When two end radicals recombine, oligomers can be lost in the formation of larger oligomers or they can be formed from smaller ones. For the DP = i oligomer, the terms appearing in the time derivative would be:

$$R_i = \sum_{j=1}^{i-1} f_{i-j} f_j - f_i \sum_{j=1}^a f_j \quad (3)$$

Here the f's are the probabilities of forming each radical oligomer and a is the largest oligomer which can recombine. The first term is due to formations from smaller oligomers and the second is due to losses in the formation of larger oligomers. From the SK tar model we know that roughly equal numbers of each size oligomer are formed by the homolytic bond cleavage reaction (Fig. 5b), so we conclude that  $f_i$  is, to first approximation, a constant and is independent of the degree of polymerization. Putting  $f_i = c$  into equation 3 the result is:

$$R_i = c^2(i-a-1) \quad (4)$$

Thus, recombinations of end radicals decrease the rate of formation of all oligomers but they affect the time derivatives of large radicals less than those of small ones. The net effect is a shift in the tar mass spectrum towards longer chain length oligomers.

When end radicals recombine with bridge radicals, a different result is found. Now the terms appearing in the time derivative are products of the probability of finding end radicals, f's, and the probability of finding radical bridges, g's.

$$R_i = \sum_{j=1}^{i-2} g_{i-j} f_j + \sum_{j=2}^{i-1} f_{i-j} g_j - f_i \sum_{j=2}^a g_j - g_i \sum_{j=1}^a f_j \quad (5)$$

The f's are still independent of the degree of polymerization, i.e.,  $f_i = c$ . However, the g's are proportional to the number of bridges in an oligomer or  $g_i = b(i-1)$ . When these probabilities are inserted in Eq. 5, the sums are slightly more difficult but can still be carried out. We find that

$$R_i = bc(i^2 - (3+a)i + 2 + a - \frac{a(a-1)}{2}) \quad (6)$$

This contribution to the time derivatives is quadratic in the degree of polymerization and reaches a minimum at  $i = (a+3)/2$ . For our simulations, recombinations can occur for at least 40 oligomers (the starting degree of polymerization) so this minimum pa occurs at a DP of at least 21. Inserting  $a = 40$  and some typical values of i into this formula we find:

$$R_1 = -781 bc \quad R_5 = -928 bc \quad R_{10} = -1068 bc \quad R_{15} = -1158 bc \quad (7)$$

Thus, for recombinations between end and bridge radicals, the contributions to the

rates of formation of the oligomers with  $DP < 21$  are all negative and get more negative with increasing chain length. These terms result in the formation of relatively fewer mid-sized oligomers when these recombinations occur than when no recombinations occur.

Similar calculations for recombinations of two bridge radicals can also be carried out and yield a cubic equation for  $R_1$ . This cubic is negative in the range  $DP = 1$  to 15 and gets more negative with increasing oligomer chain lengths. Thus, recombinations of bridge radicals also result in the formation of relatively fewer mid-sized oligomers during pyrolysis of these ethylene bridged polymers.

Both kinds of recombination reactions are probably important in pyrolyses of ethylene bridged polymers, lignins, and coals. The maximum in the FIMS data of polymer 1 seems to be caused by recombination of end radicals while rapid mass drop-offs are observed in the FIMS spectra of lignins (6), lignites (1), and ethylene bridged methoxybenzene polymer (5). Examples of these FIMS spectra will be presented during the talk.

#### ACKNOWLEDGEMENT

The authors would like to thank the Gas Research Institute for their support under contract #5081-260-0582.

#### REFERENCES

1. Solomon, P.R. and King, H.H., *Fuel*, **63**, 1302, (1984).
2. Gavalas, G. R., Cheong, P. H. and Jain, R. "Ind. Eng. Chem. Fundam.," **20**, 113 and 122 (1981).
3. Unger, P. E. and Suuberg, E. M. "Eighteenth Symposium (International) on Combustion", The Combustion Institute, Pittsburgh, PA, (1981), 1203.
4. Solomon, P.R., "Synthesis and Study of Polymer Models Representative of Coal Structure", Gas Research Institute Annual Report for Contract #5081-260-0582. GRI Accession #GRI-83/0171 (April, 1983).
5. Squire, K.R., Solomon, P.R., DiTaranto, M.B., "Synthesis and Study of Polymer Models Representative of Coal Structure", Gas Research Institute Annual Report for Contract #5081-260-0582. GRI Accession #GRI-84/0083 (May, 1984).
6. Squire, K.R. and Solomon, P.R., "Characterization of Biomass as a Source of Chemicals", NSF Final Report under Contract No. CPE-8107453, (1983).
7. Golden, J.H., *J. Chem. Soc.* (1961), 1604-1610.
8. Squires, T.G., Smith, B.F., Winans, R.E., Scott, R. and Hayatsu, R., "International Conference on Coal Science", Pittsburgh, PA, Proceedings, p. 292, (1983).
9. Golden, J.H., *J. Chem. Soc.* (1961), 3741-3738.
10. Solomon, P. R. and Hamblen, D. G., "Chemistry and Physics of Coal Utilization, AIP Conference Proceedings No. 70, Amer. Inst. Phys., New York (1981), pg. 121.
11. St. John, G.A., Buttrill, S.E., Jr., and Anbar, M., "Field Ionization and Field Desorption Mass Spectroscopy Applied to Coal Research, in "Organic Chemistry of Coal", (Ed. J. Larsen), ACS Symposium Series, 71, pg. 223, (1978).
12. Stein, S.E., "New Approaches in Coal Chemistry", (Ed. Blaustein, B.D., Bockrath, D.C., and Friedman, S.), Am. Chem. Soc. Symposium Ser. 169, Washington, DC, pg. 208, (1981).
13. Poutsma, M.L., *Fuel*, **59**, 335, (1980).



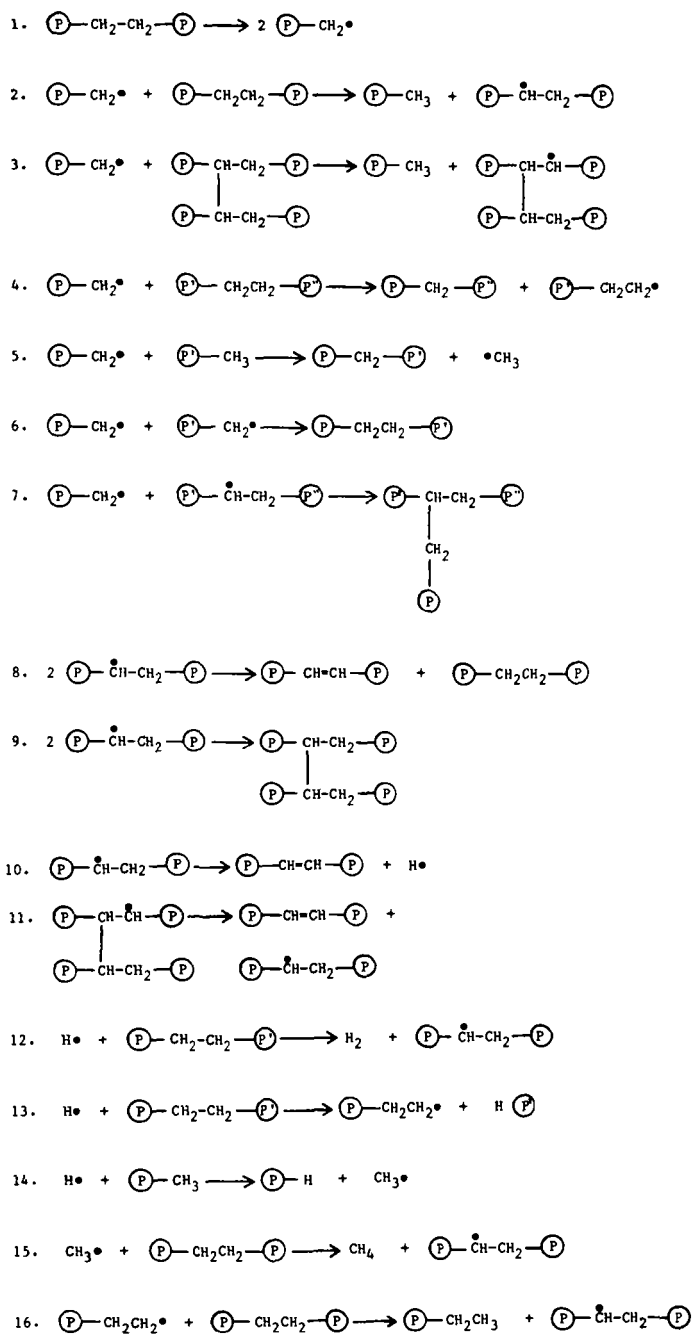


Fig. 1 Proposed Mechanism for the Decomposition of Ethylene Bridges.



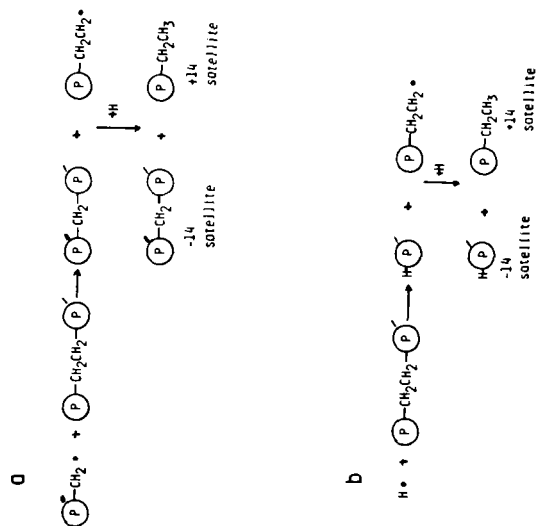


Figure 3. Mechanisms for Ipso Substitution Reactions.  
a) Substitutions by Arylmethylene Radicals. b) Substitutions by H Radicals.

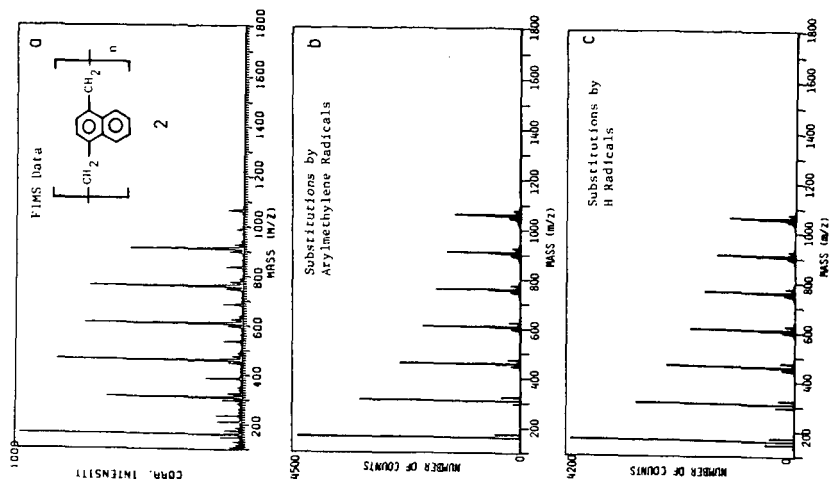


Figure 4. Monte Carlo Simulations for Polymer 2.

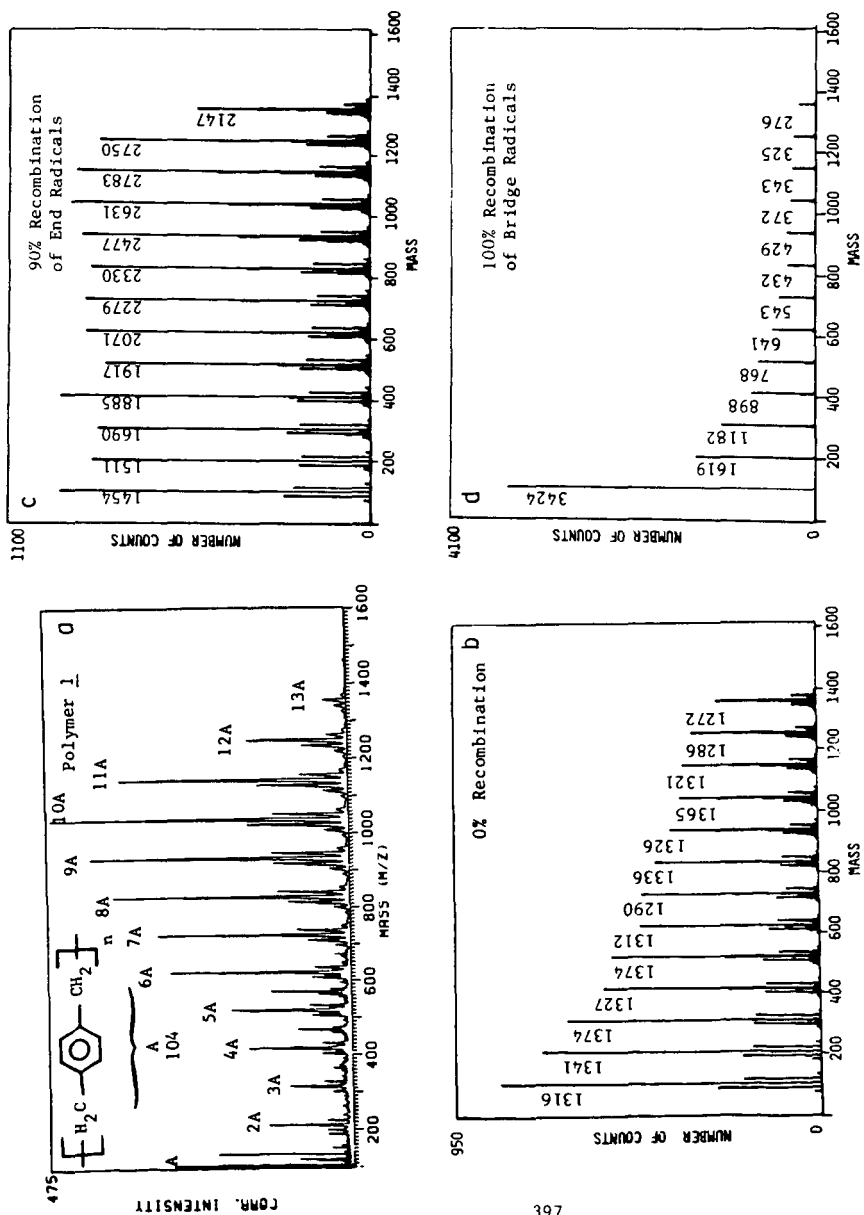


Fig. 5 Monte Carlo Simulations for Polymer 1.

## SOLVENT EFFECTS DURING THE REACTION OF COAL AND BIOMASS MODEL COMPOUNDS IN DENSE WATER

J. R. Lawson, J. R. Obst, M. A. Abraham, S. H. Townsend and M. T. Klein  
University of Delaware  
Department of Chemical Engineering  
Newark, DE 19716

### INTRODUCTION

The chemical reactions that accompany the extraction (1) of volatiles from hydrocarbon resources with supercritical water (SCW) are frequently obscured by the complexities of the reaction system. In contrast, the comparative simplicity of model compound structures and product spectra permit resolution of reaction fundamentals (2) and subsequent inference of the factors that control the reactions of real reacting systems. Herein we use model compounds to probe the kinetics of the pyrolysis and solvolysis reactions that likely occur during the extraction of volatiles from coals and lignins.

A previous study of the reaction of guaiacol (orthomethoxyphenol), a mimic of key structural aspects of lignin, in SCW (3) elucidated parallel pyrolysis and hydrolysis pathways, the selectivity to the latter increasing linearly with water density. Guaiacol decomposition kinetics were interestingly nonlinear in water density, which suggested the possibility of unusual cage or solvent effects attributable to dense fluids. We have observed qualitatively similar behavior for the reaction of each of dibenzyl ether (DBE), benzyl phenyl amine (BPA), and benzyl phenyl sulphide (BPS) in SCW and wish to report a candidate reaction network that unifies the previous and present model compound results.

### RESULTS

Table I summarizes the reaction conditions of temperature, reactants' concentrations and holding time. Measured amounts of tap water and the commercially available (Aldrich) substrates DBE, BPA and BPS were entered into room temperature stainless steel "tubing bombs" that have been described elsewhere (3). Sealed reactors were immersed into a fluidized sand bath held constant at the desired reaction temperature, which was attained by the reactors in about 2 min; this heat-up period was small compared to ultimate reaction times (up to 40 min) and was, in any case, identical for all runs. Products were identified by GC-MS and quantitated by GC as described elsewhere (3,4).

Neat DBE pyrolysis led to toluene and benzaldehyde as major products along with lesser amounts of benzene and benzyl alcohol. DBE reaction in SCW gave benzyl alcohol, toluene, benzaldehyde and high molecular weight oligomers (4) as major products along with 1,2-diphenylethane, diphenylmethane and triphenylmethane as minor products. The influence of water density ( $S$ ) on DBE decomposition kinetics is illustrated in Figure 1, where DBE conversion ( $x$ ) is plotted against water density for parametric values of the reaction time at

374°C. Note that each curve in Figure 1 passes through a minimum value of  $x$ ; these occurred at about  $S = 0.4 \pm 0.05$  in all cases.

Pyrolysis of BPA led to toluene, aniline, benzaniline and oligomers as major products and minor products including 1,2 diphenylethane and 2-benzyl-aniline. BPA reaction in water was to benzyl alcohol and benzaldehyde as well as the neat pyrolysis products. The influence of  $S$  on BPA reaction kinetics at 386°C is illustrated in Figure 2. For each reaction time illustrated in Figure 2, BPA conversion passes through a minimum as water density increases.

Neat pyrolysis of BPS was to the major product toluene as well as thiophenol, phenyldisulfide, and phenylsulfide. Diphenylmethane and 1-2-diphenylethane were minor products. BPS reaction in water led to all of the neat pyrolysis products except diphenylmethane, as well as minor amounts of benzaldehyde. The influence of  $S$  on BPS reaction kinetics at 300°C is illustrated in Figure 3. For each reaction time in Figure 3, BPS conversion passes through a minimum as water density increases.

#### DISCUSSION

Two experimental observations common to the reaction of each of guaiacol, DBE, BPA and BPS merit summary. First, the overall reaction of each substrate in dense water comprised parallel pyrolysis and solvolysis pathways, with the selectivity to the latter increasing continuously with increasing water density. Second, and for a constant reaction temperature and time, each reactant's conversion passed through a minimum as the water density increased. These observations are consistent with the two complementary mechanistic interpretations that form the basis of the model reaction networks of Figures 4a and 4b. We consider these separately.

In the mechanism represented in Figure 4a, the general reactant  $R$  can follow either pyrolysis or solvolysis reaction paths. Neat pyrolytic fragmentation of  $R$  to product spectrum  $P_1$  may, in general, require hydrogen consumption, which will be provided by the reactants themselves. Thus,  $n$  of Figure 4a will typically be 3, 0, 1 and 1 for guaiacol, DBE, BPA and BPS, respectively (3,5). Solvolysis to product spectrum  $P_2$  in Figure 4a is modelled to occur through a solvated reactant intermediate,  $R^S$ , that is caged by  $m$  water molecules. Increases in water density will shift the overall observed reaction product spectrum from  $P_1$  (pyrolysis-like) toward  $P_2$  (solvolysis-like).

Three modelling approximations allowed analytical derivation of a rate expression for the network of Figure 4a. First, reactant solvation was considered to be rapid and in virtual equilibrium at reaction conditions. This is not true during the small heat-up period. Second, solvated reactant molecules were modelled to be caged and thus unable to follow the neat pyrolysis reaction path. Third, the solvated species  $R^S$  was considered to exist only at reaction conditions, and ambient analysis by gas chromatography would thus provide the sum  $R^* = R + R^S$  as the observable for kinetics analysis.

Eq. 1 is a general rate expression for guaiacol, DBE, BPA and BPS disappearance through the network of Figure 4a; the values of the rate expression parameters will be different for each reactant. For the parameter values listed in Table II, the predictions of Eq. 1 and its integration over time

$$r = \frac{-dR^*}{dt} = \left[ \frac{(n+1)k_1}{1 + K_s S^m} + \frac{k_2 S}{(1 + 1/K_s S^m)} \right] R^* \quad 1)$$

are illustrated in Figures 5a and 5b as plots of the reaction rate and conversion, respectively, as a function of S at a fixed temperature and time. Note the predicted minima are quite general and in accord with the experimental observations. The magnitude and occurrence of these minima are clearly dependent upon the values of rate expression parameters.

In the mechanism of Figure 4b the general reactant R fragments directly through either a pyrolysis or solvolysis pathway to product spectrum  $P_1$  or  $P_2$ , respectively. The rate constants  $k_1$  and  $k_2$  of Figure 4b include the activation volume pressure dependence, which was not accounted for in Figure 4a; on the other hand, cage effects and thus solvated reactant  $R^s$  are absent in Figure 4b. Qualitatively, the overall disappearance rate and conversion will pass through a minimum in pressure, and thus water density, if  $k_1$  decreases faster than  $k_2 S$  with increases in solvent concentration S. Cage effects in Figure 4a and pressure-dependent rate constants in Figure 4b thus account for the same experimentally observed behavior.

#### SUMMARY AND CONCLUSIONS

The overall reaction of each of guaiacol, DBE, BPA and BPS in dense water is a superposition of neat pyrolysis and solvolysis reaction pathways. Observed product spectra shift from purely pyrolysis-like to solvolysis-like with increases in water concentration. For a given reaction temperature and time, the reactants' conversions pass through relative minima as the water concentration increases. Two mechanistic interpretations provide consistent predictions. The first comprises parallel pyrolysis and solvolysis reaction pathways, the latter occurring through a solvated reactant intermediate to which pyrolysis is denied. The second is a superposition parallel neat pyrolysis and solvolysis pathway with associated rate constants that are pressure dependent.

#### ACKNOWLEDGMENT

This work was supported by the U.S. DOE under Grant No. DE-FD22-82PC50799 and the USDA Forest Products Laboratory under Grant No. FP-83-0560.

# REFERENCES

- (1) Squires, T.G.; Aida, T.; Chen, Y.; Smith, B.F. ACS Div. Fuel Chem. Preprints, 1983, 28, No. 4, 228.
- (2) Simmons, M.B.; Klein, M.T. "Free Radical and Concerted Pathways in Dibenzyl Ether Thermolysis"; Ind. Eng. Chem. Fundam. (accepted for publication 1985).
- (3) Lawson, J.R.; Klein, M.T. "The Influence of Water on Guaiacol Pyrolysis"; Ind. Eng. Chem. Fundam. (accepted for publication 1984).
- (4) Townsend, S.H.; Klein, M.T. "Dibenzyl Ether as a Probe into the Supercritical Fluid Solvent Extraction of Volatiles from Coal with Water"; Fuel (accepted for publication 1985).
- (5) Abraham, M.A.; Klein, M.T. "Pyrolysis of Benzyl Phenyl Amine Neat and with Tetralin, Methanol and Water Solvents," I&EC Prod. Res. and Dev. (accepted for publication 1984).

Table 1  
Reaction Conditions

<u>Model Compound</u>	<u>Reactant Concentration</u>	<u>Temperature/°C</u>	<u>Holding Time/min</u>
DBE	1.71	374	15
	1.71	374	45
	1.71	374	60
BPA	0.564	386	5
	0.688	386	20
	0.604	386	30
BPS	0.547	300	10
	0.521	300	20

Table 2  
Rate Expression Parameters Used in the Prediction of Figure 5

<u>Parameter</u>	<u>Value</u>
n	1
k <sub>1</sub>	0.06 sec <sup>-1</sup>
k <sub>S</sub>	1.5 mol <sup>-1</sup>
m	1
k <sub>2</sub>	0.3 sec <sup>-1</sup> mol <sup>-1</sup>



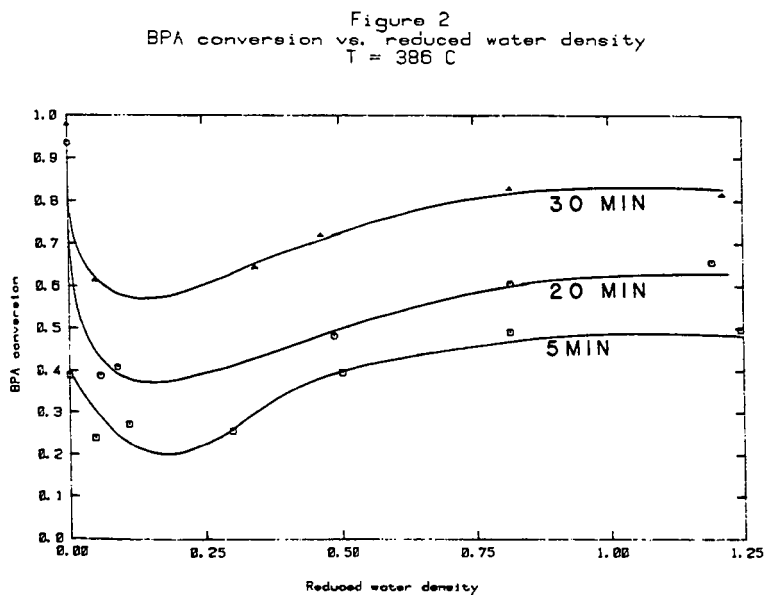
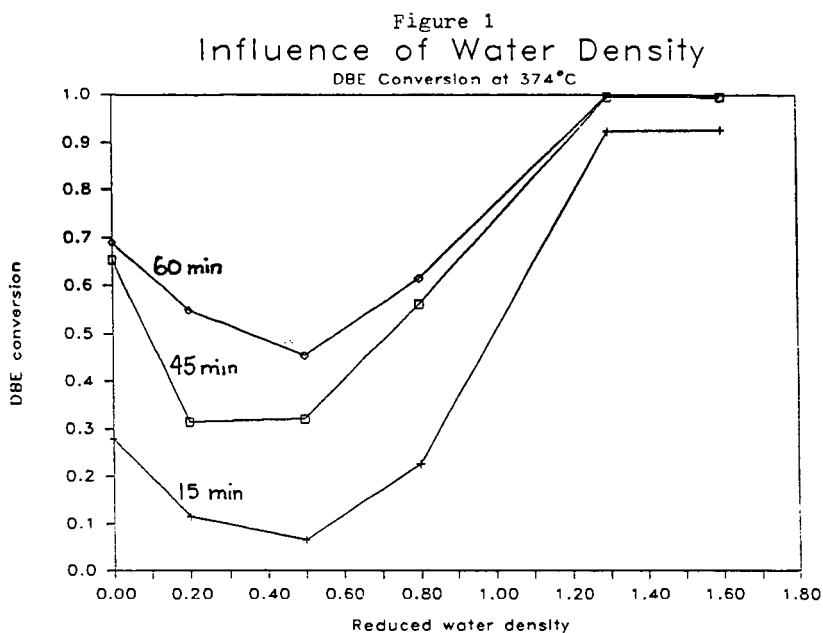


Figure 3  
BPS conversion vs. reduced water density  
 $T = 300\text{ C}$

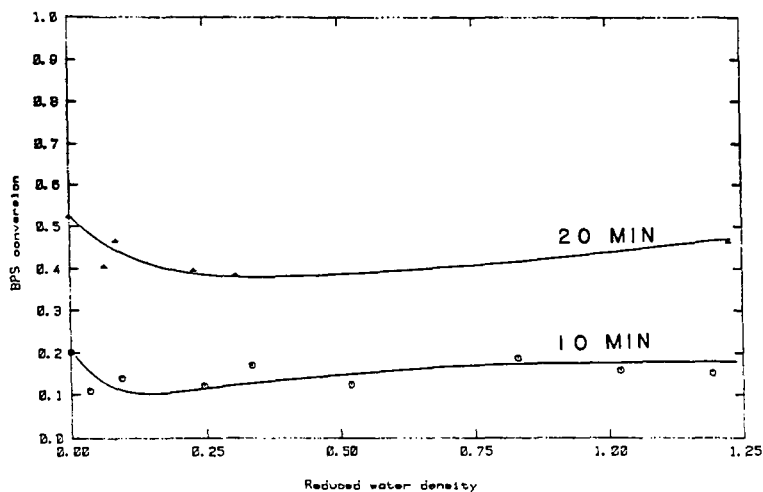


Figure 4: Proposed Reaction Network

Figure 4a: Cage effects

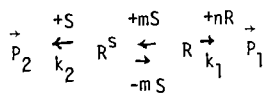


Figure 4b: Pressure-dependent rate constants

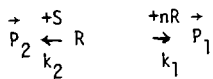


Figure 5A  
Predicted reaction rates vs.  
reduced solvent density

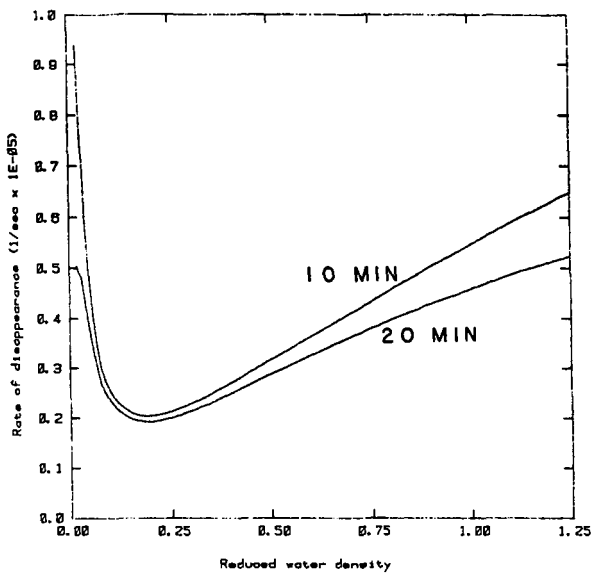
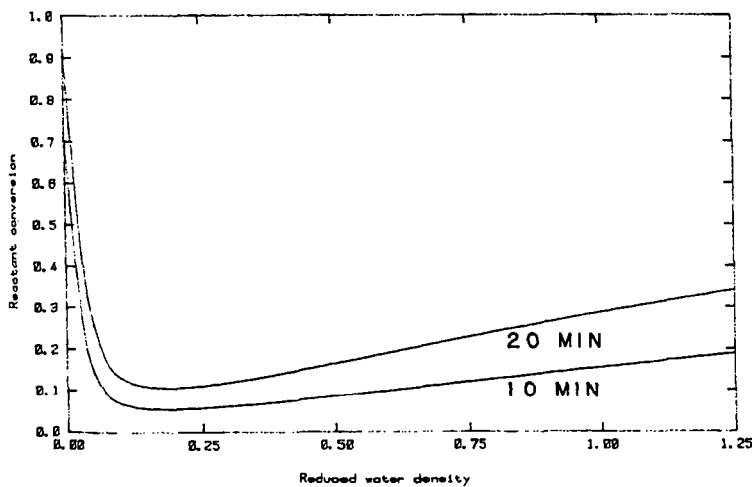


Figure 5B  
Predicted conversion vs.  
reduced solvent density



## Chemical Modelling in the Manipulation of Lignin Pyrolysis Pathways

John B. McDermott, Michael T. Klein and John R. Obst\*

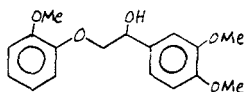
Department of Chemical Engineering, University of Delaware, Newark, DE 19716

\*USDA Forest Products Laboratory, Box 5130, Madison WI 53705

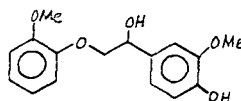
### 1. Introduction

Lignin is an abundant renewable resource of chemical structure apparently amenable to pyrolytic depolymerization to phenolics. However, the utility of recovered products is low, as only 10-15 wt.% of lignin mass is typically recovered as single-ring phenolics and the major products are gases, char and other high-molecular weight materials.

Chemical modelling provides insight into the intrinsic chemical pathways that superimpose to make observable lignin pyrolysis complex. This use of model compound information can also implicate both the favorable and deleterious reaction pathways that may be susceptible to acceleration or circumvention through catalysis or solvolysis. Along these lines, the three classes of experiments reported herein are of : i) lignin pyrolysis; and thusly derived modification strategies of ii) catalytic dehydrogenation of lignin prior to pyrolysis and iii) solvolytic depolymerization of lignin in supercritical water (SCW). We focus on the reactions of the  $\beta$ -ethers that help link lignin into a polymer, of which the glycols veratrylglycol- $\beta$ -guaiacyl ether ( VGE, structure I ) and guaiacylglycol- $\beta$ -guaiacyl ether ( GGE, structure II ) are simple models.



I



II

Thermolyses of pine wood, kraft lignin and a milled wood lignin in SCW also permit scrutiny of the relevance of model results to the reactions of real systems.

### 2. Experimental

Table I summarizes the experiments in terms of the reactants, catalysts and solvents, as well as the associated reaction conditions of temperature, pressure and reactants' concentrations. The reactants VGE and GGE were synthesized as described fully elsewhere (1). The reactor was a 316 stainless steel batch tubing bomb whose construction and use has been described fully elsewhere (2). Product analysis was accomplished by GC and GC-MS, which enabled the calculation of a mass balance index, defined here as the sum of the masses of the product spectra components divided by the initial mass

of substrate charged to the reactor.

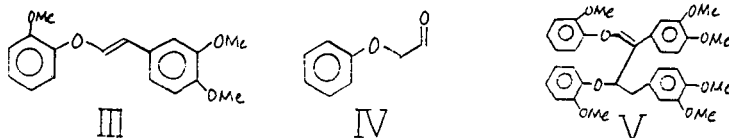
### 3. Results and Discussion

Results are discussed in two major sections. Within the first, three subsections delineate model compound pyrolysis results, a pyrolysis network, and a brief motivation of the modification strategies, respectively. Within the second major section, subsections present the results and implications of model compound, lignin and whole-wood experiments pertaining to the modification strategies.

#### 3.1. Pyrolysis Results and Implications

##### 3.1.1. Products and Kinetics

**VGE.** The four major products of VGE pyrolysis were guaiacol, 3,4-dimethoxyacetophenone (3,4-DMA), and cis and trans forms of the vinyl ether III.

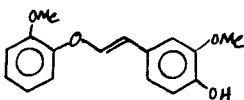


Less abundant products were *o*-cresol, veratrole, 3,4-dihydroxyacetophenone, glycolaldehyde-guaiacol ether (IV),  $\beta$ -hydroxy-3,4-dimethoxyacetophenone and a dimer of the vinyl ether that had a molecular weight of 572 (such as V).

The temporal variations of both the mass balance and the major products' molar yields are shown in Figure 1 for pyrolysis at 315°C. The mass balance nonclosure became more severe as both reaction temperature and time increased and asymptotically approached an approximate value of 0.4. The positive initial slope of the vinyl ether (both *cis* and *trans* forms) is suggestive of primary product formation. Guaiacol appeared with a smaller but nonzero initial slope and was likely a minor primary product; the large ultimate yields of guaiacol indicate that it was also a significant secondary product. Similarly, 3,4-DMA appeared with a small positive slope that suggests primary product formation.

The variation of the product spectrum with pyrolysis temperature is informative. The only observable products at 250°C were the two forms of the vinyl ether, which were asymptotically stable with time, and trace amounts of guaiacol. At the two intermediate temperatures the vinyl ethers appeared with initial slopes far greater than that for guaiacol and attained maxima in yield before undergoing secondary decomposition. Pyrolysis was so facile at 380°C that the initial slopes of both vinyl ethers and guaiacol could not be determined with precision. Guaiacol yields traversed a maximum at this temperature and its secondary decomposition was to *o*-cresol, phenol and catechol products. It is also interesting to note that the yield of guaiacol was always in excess of the sum of the yields of 3,4-DMA and its likely secondary reaction products acetovanillone and 3,4-dihydroxyacetophenone (DHA).

**GGE.** The major products of GGE pyrolysis at 250°C were guaiacol and acetovanillone; lesser amounts of *cis* and *trans* 1-(3-methoxy-4-hydroxyphenyl)-2-(2-methoxyphenoxy) ethylene (vinyl ether VI) and vinyl-guaiacol.



VI

The temporal variations of the molar yields of the major products and the mass balance are shown in Figure 2. The disappearance rate of GGE far exceeded that of VGE. The mass balance approached an approximate value of 0.4, as was observed for VGE pyrolysis. The initial slopes of guaiacol and acetovanillone formation were both positive, suggesting these to be primary products, although that for guaiacol far exceeded that for acetovanillone. The acetovanillone yield passed through a maximum at approximately 30 min whereas guaiacol appeared to be stable with time. Finally, both forms of the vinyl ether VI appeared to be primary products, whereas vinyl-guaiacol appeared to be the product of a secondary reaction.

### 3.1.2. Reaction Pathways

The foregoing suggests that VGE pyrolysis comprised the pathways illustrated in Figure 3. Two primary pathways were operative, the major of which being dehydration to the vinyl ethers and the minor being direct fragmentation to guaiacol and, likely, an enol intermediate capable of rapid tautomerization to 3,4-DMA. Each of the primary products was susceptible to secondary reactions. The detection of the dimer of the vinyl ether as well as the progressive nonclosure of observable products' material balance are both indicative of vinyl ether polymerization to species too heavy to elute during GC analyses. Paring of the vinyl ether or its presumed oligomers was also clearly operative. It is noteworthy that the ultimate material balance of 0.4 is closely equal to the weight fraction of the guaiacol moiety in VGE.

Whereas GGE pyrolysis pathways were analogous to those for VGE, the selectivity to each was markedly different:  $\alpha$ - $\beta$  dehydration of GGE was much less significant than its cleavage to guaiacol and acetovanillone. The large yields of guaiacol, far in excess of the acetovanillone yields, indicate secondary guaiacol formation by the cleavage of the guaiacyl group from the vinyl ether VI or any of its subsequent polymers. Of interest is the presence of vinyl-guaiacol, which could be a product of the homolytic cleavage of vinyl ether VI. Its analogue, vinyl-veratrole, was absent from VGE pyrolysis. Acetovanillone was subject to secondary degradation.

### 3.1.3. Motivation of Catalytic and Solvolytic Modification Strategies

The pyrolysis results detailed above show that a significant  $\beta$ -ether reaction pathway was its undesirable dehydration to a vinyl ether that subsequently underwent yield-reducing polymerization reactions. The ultimate recovery of single-ring products from these substrates could thus be enhanced by reducing the reaction selectivity to the dehydration pathway. Catalytic dehydrogenation of the aliphatic hydroxyls of VGE and GGE to carbonyls would not only prevent the dehydration, and thus circumvent its associated ill effects, but also allow better utilization of the two substrate hydrogen atoms that would otherwise be rejected with the water. For example, shuttling of this hydrogen would allow for the stabilization of free-radicals formed during the subsequent pyrolysis of a dehydrogenated and deoxygenated residue.

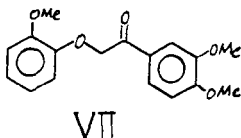
The selectivity of the  $\beta$ -ether reactions may be modified by SCW as well. For example, Lawson and Klein (2) showed that the reaction of guaiacol in SCW was a superposition of parallel pyrolysis and hydrolysis pathways, the selectivity to the latter increasing with increasing water density. The hydrolysis of guaiacol to catechol and methanol was in material balance and the water apparently suppressed a secondary char-forming reaction of catechol. Also, Townsend and Klein (3) showed that the hydrolysis by SCW of DBE to benzyl alcohol competed with the slower pyrolysis of DBE toluene and benzaldehyde. It thus seems reasonable that hydrolysis of the  $\beta$ -ethers by pathways formally similar to those observed for DBE hydrolysis could compete with the formation of the vinyl ethers and circumvent its polymerization. In short, the reactions of guaiacol and DBE in SCW suggest that a suitable modification of the  $\beta$ -ether reaction might be achieved in SCW.

In what follows directly we describe the results of the experiments relevant to both of these strategies

## 3.2. Modification Strategy-Related Results

### 3.2.1. Catalytic Dehydrogenation of VGE and GGE

Catalytic dehydrogenation of VGE over  $\text{Ni/SiO}_2\text{-Al}_2\text{O}_3$  at  $250^\circ\text{C}$  yielded guaiacol, 3,4-DMA, 1-veratryl-2-(2-methoxy-phenoxy)-ethanone-1 (the dehydrogenated form of VGE, structure VII), and trace amounts of vinyl ether. The rate of VGE conversion



was roughly threefold higher in the presence of the catalyst than when VGE was pyrolyzed neat.

Figure 4 illustrates the temporal variations of product molar yields for reaction at  $250^\circ\text{C}$ . The initial

The variation of methanol yield with water density is illustrated in Figure 7. The addition of external water caused a greater than five-fold increase in the mass yield of methanol over that obtained from neat pyrolysis. The insignificant difference between the yields of methanol observed from pyrolysis at the two highest water densities suggests that both of these pyrolyses were at essentially infinite dilution in water.

For both temperatures examined, the sum of the yields of guaiacol, methyl-guaiacol, catechol and methyl-catechol were only slightly sensitive to water density. However, the yields of these phenolics increased monotonically with time during neat thermolysis. In contrast, the yield of guaiacols traversed relative maxima while the yields of catechols increased or were asymptotically stable during reaction in water. Also, the decay of guaiacols was fastest at the highest reduced water density of 1.6 and their maxima in yield occurred at 10 min, compared to 20 min at the intermediate reduced water of 0.8. In general, the total yields of the four major phenolics increased with temperature with the influence of the water being slightly greater but still small at the higher temperature.

Thus the reaction of kraft lignin in SCW included pyrolysis and solvolysis reaction pathways. The hydrolysis of the aromatic methoxyl groups increased methanol yields and shifted the phenolic product spectrum from guaiacols toward catechols. Interestingly, since the mass yield of methanol of 5-6 wt% was higher than the sum of the mass yields of all of the various phenolics, most of the methanol likely resulted from hydrolysis of the methoxyl groups present in the structural skeleton of lignin. These methoxyl groups would be lost to the char fraction under neat pyrolysis conditions.

Milled-wood Lignin. Pyrolysis of milled-wood lignin neat and in the presence of supercritical water at 383°C yielded methanol, guaiacol, methyl-guaiacol, catechol and methyl-catechol as major products.

The temporal variations of the single-ring products are shown in Figure 8. The positive initial slopes of guaiacol and methyl-guaiacol indicate primary formation of these products. The zero initial slope of catechol and methyl-catechol suggest secondary product formation. The guaiacols traversed maxima at approximately 10 min for reaction both neat and in SCW. The sum of the four major phenolic products increased twofold in the presence of SCW. This is markedly different from the kraft lignin results where no net increase of the phenolics was noted.

Figure 9 shows the temporal variations of the methanol yields parametrically with reduced water density. The initial slopes of the methanol yields indicate primary product formation for all cases. The yields of methanol increased approximately fourfold with the addition of external water. The intermediate density produced virtually the same methanol results as the highest density. This is similar to the kraft lignin results.

Loblolly Pine Wood. Neat pyrolysis of loblolly pine wood at 383°C yielded methanol and guaiacol



slopes of both guaiacol and 3,4-DMA are near zero and thus suggestive of secondary product formation. The 1-veratryl-2-(2-methoxy-phenoxy)-ethanone-1 had a small but positive initial slope and was likely a primary product. All products attained maxima at approximately twenty minutes. The maximum yield of single-ring products (guaiacol and 3,4-DMA) was approximately 0.43, which compares with the 0.06 yield obtained from neat thermolysis at 250°C for 30 minutes. Particularly notable in this enhanced product recovery was the large yield of 3,4-DMA which represents the veratryl portion of the VGE molecule. The initial rate of formation of 3,4-DMA approximately equaled that for guaiacol but the ultimate yields of 3,4-DMA were in excess due to the secondary degradation of guaiacol. This portion of VGE recovered as 3,4-DMA was normally lost to the vinyl polymerization during neat pyrolysis.

Thus catalysis by  $\text{Ni/SiO}_2\text{-Al}_2\text{O}_3$  not only effected the desired dehydrogenation but also appeared to crack the resulting keto-ether with hydrogen addition. The net reaction of VGE to guaiacol and 3,4-DMA was thus in hydrogen balance and a selective rearrangement of the hydrogen already present in the substrate.

The catalysis of GGE over  $\text{Ni/SiO}_2\text{-Al}_2\text{O}_3$  yielded the same major products as did its pyrolysis: guaiacol, acetovanillone, vinyl-guaiacol and cis and trans forms of vinyl ether VI. However, the rate of GGE reaction was significantly higher than observed during its pyrolysis, as its conversion was essentially 1.0 after a reaction time of only 10 min. This rate also exceeded the rate of VGE catalysis.

The temporal variations of the product molar yields and mass balance are depicted in Figure 5. The mass balance quickly dropped to 0.2. The only product observed in a significant yield was guaiacol, and its initial rate of formation was higher than for GGE pyrolysis. Guaiacol was also subject to a moderate secondary reaction. The rate of formation of vinyl ether VI was approximately equal to that for neat pyrolysis indicating little or no inhibition of the dehydration pathway by the catalyst. A keto-ether analogous to VII, and hence any evidence of a dehydrogenation pathway, was not observed. The presence of the catalyst thus seemed both to enhance the deleterious dehydration and polymerization pathways as well as to promote charring of guaiacol.

### 3.2.2. Solvolysis in Supercritical Water

**Kraft Lignin.** The major products of kraft lignin pyrolysis both neat and in water were methanol, guaiacol, methyl-guaiacol, catechol and methyl-catechol. Smaller amounts of phenol and cresols were also detected.

Temporal variations of these major products for reaction at 383°C are shown in Figure 6. The positive initial slopes associated with guaiacol and methyl-guaiacol shown in Figure 6 indicate that these were primary products. Slopes for catechol and methyl-catechol of essentially zero indicate that these were secondary products. The small positive initial slope for methanol suggests that it formed by a primary pathway, although it was likely both a primary and a secondary product.

while reaction in the presence of supercritical water at the same temperature yielded methanol, guaiacol, methyl-guaiacol, catechol and methyl-catechol as major products.

The temporal variations of the single-ring products are shown in Figure 10. The initial slope associated with guaiacol yield from neat pyrolysis was too small to be determined conclusively. However, for reaction in SCW, the initial rate of formation of both guaiacol and methyl-guaiacol was positive and these thus appear to have been primary products. Catechol and methyl-catechol were evidently secondary products. The overall yield of single-ring phenolics increased three-fold with the addition of external water.

The temporal variations of the yield of methanol is shown in Figure 11 for two reduced water densities. The initial slopes indicate primary product formation in both cases. The yield of methanol was virtually unaffected by the addition of water, which is consistent with the isolated lignin experiments. During pyrolysis, the carbohydrate fraction of the wood should lead to significant yields of water capable of hydrolyzing the methoxyl groups present in the lignin. Since the milled-wood lignin results demonstrated the attainment of an asymptotic yield as the external water loading increased, the addition of external water to the wood would prove an insignificant increment to the water originating from the carbohydrate pyrolysis.

#### 4. References

1. Landucci, L. L.; Geddes, S. A.; Kirk, T. K. *Holzforschung* 1981, **35**, 1, 67.
2. Lawson J. R.; Klein, M. T. *Ind. Eng. Chem., Fundam.* 1985, accepted.
3. Townsend, S. H., and Klein, M. T. *Fuel* 1985, accepted.

Table I - Summary of Reactants and Reaction Conditions

Reactant	Loading (mg)*	Catalyst	Solvent	Temperature	Pressure (psia)
VGE	15	--	--	250°C	26
VGE	15	--	--	315°C	29
VGE	15	--	--	335°C	30
VGE	15	--	--	380°C	32
GGE	15	--	--	250°C	26
VGE	15	Ni/SiO <sub>2</sub> -Al <sub>2</sub> O <sub>3</sub>	--	250°C	26
GGE	15	Ni/SiO <sub>2</sub> -Al <sub>2</sub> O <sub>3</sub>	--	250°C	26
Kraft Lignin	15	--	--	383°C	32
Kraft Lignin	15	--	H <sub>2</sub> O	383°C	4260
Kraft Lignin	15	--	H <sub>2</sub> O	383°C	3466
Kraft Lignin	15	--	--	408°C	34
Kraft Lignin	15	--	H <sub>2</sub> O	408°C	5750
Milled-Wood Lignin	10	--	--	383°C	32
Milled-Wood Lignin	10	--	H <sub>2</sub> O	383°C	4260
Milled-Wood Lignin	10	--	H <sub>2</sub> O	383°C	2467
Pine Wood	35	--	--	383°C	32
Pine Wood	35	--	H <sub>2</sub> O	383°C	4260

\*Reactor Volume was 0.589 cm<sup>3</sup>

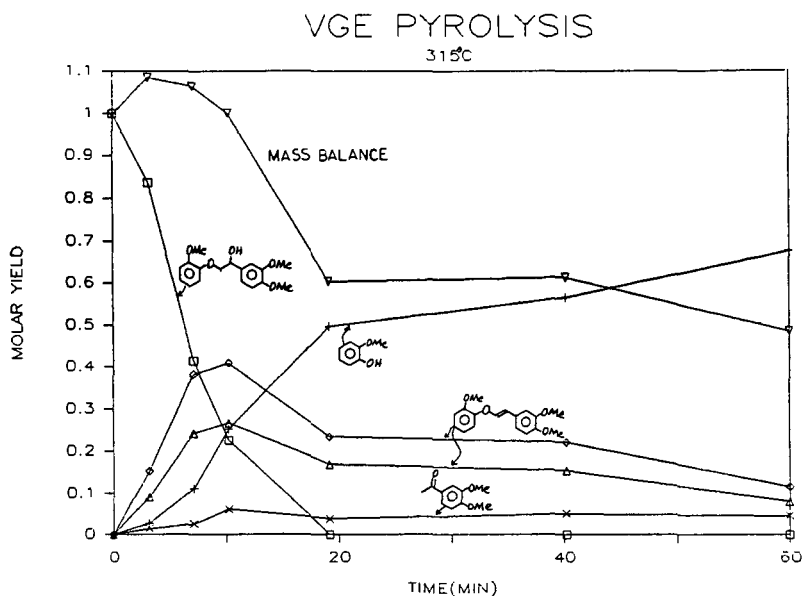


Figure 1. Temporal variations of the yields of the major VGE pyrolysis products at 315°C.

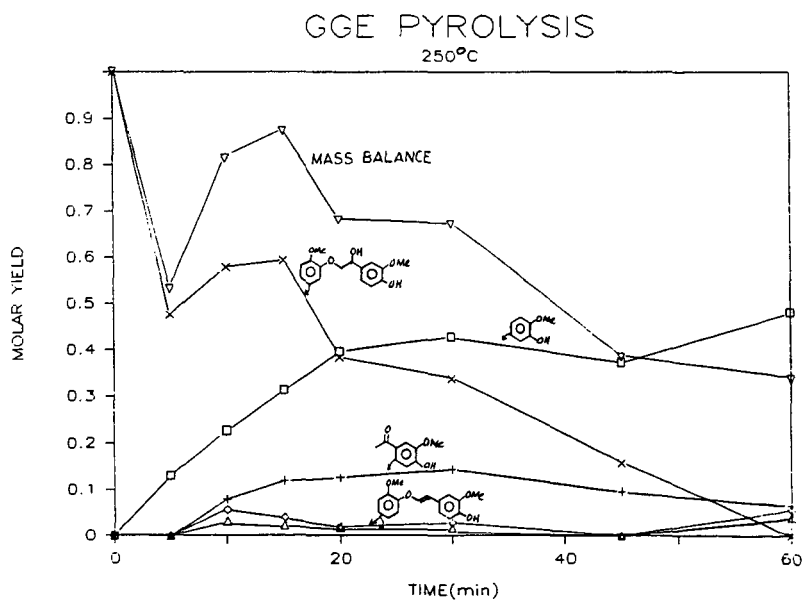


Figure 2. Temporal variations of the yields of the major GGE pyrolysis products at 250°C.

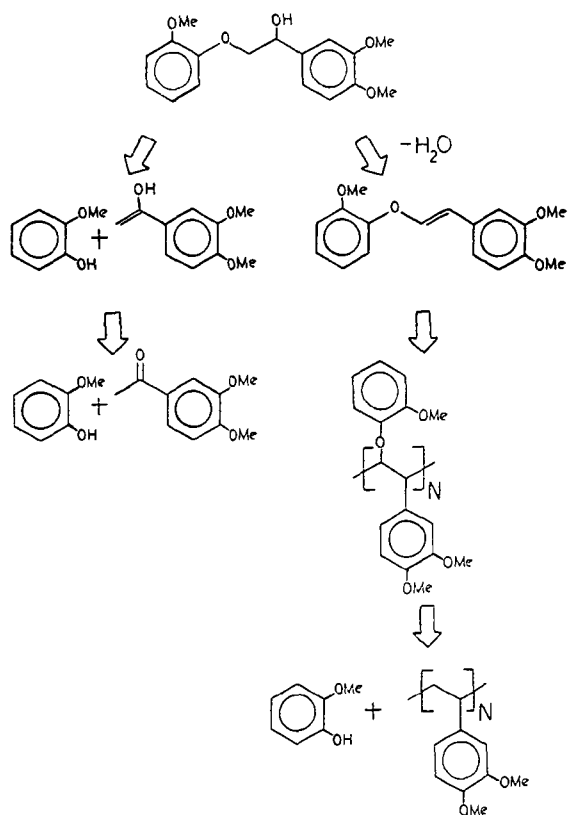


Figure 3. VGE pyrolysis pathways.

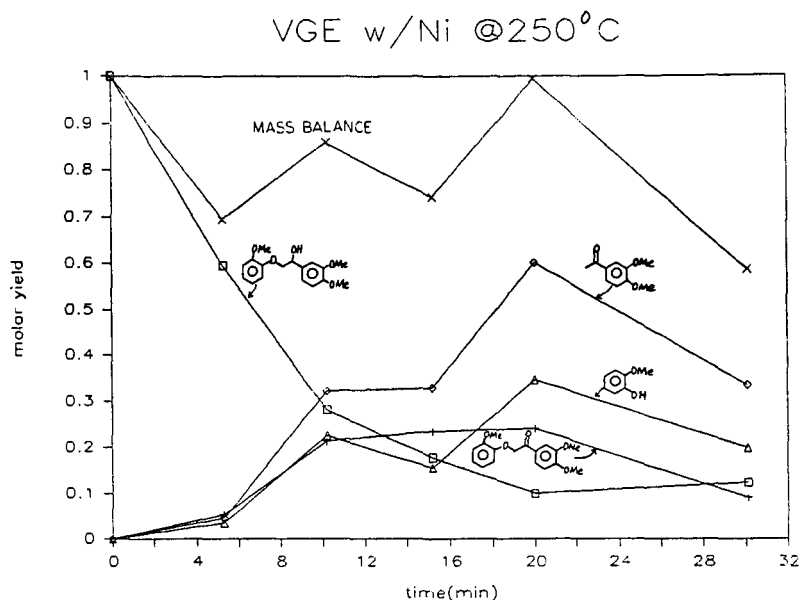


Figure 4. Temporal variations of the yields of the major VGE catalysis products at 250°C.

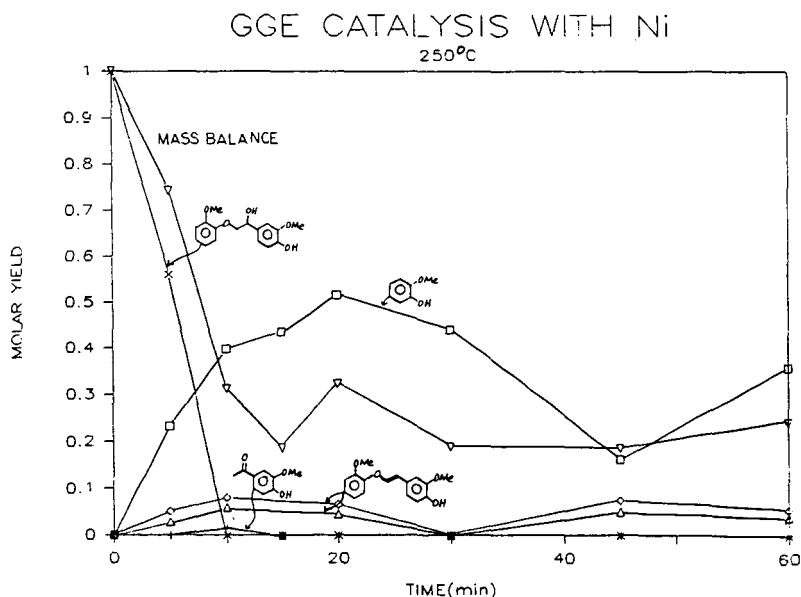


Figure 5. Temporal variations of the yields of the major GGE catalysis products at 250°C.

a) KRAFT LIGNIN PYROLYSIS 383°C  
NEAT

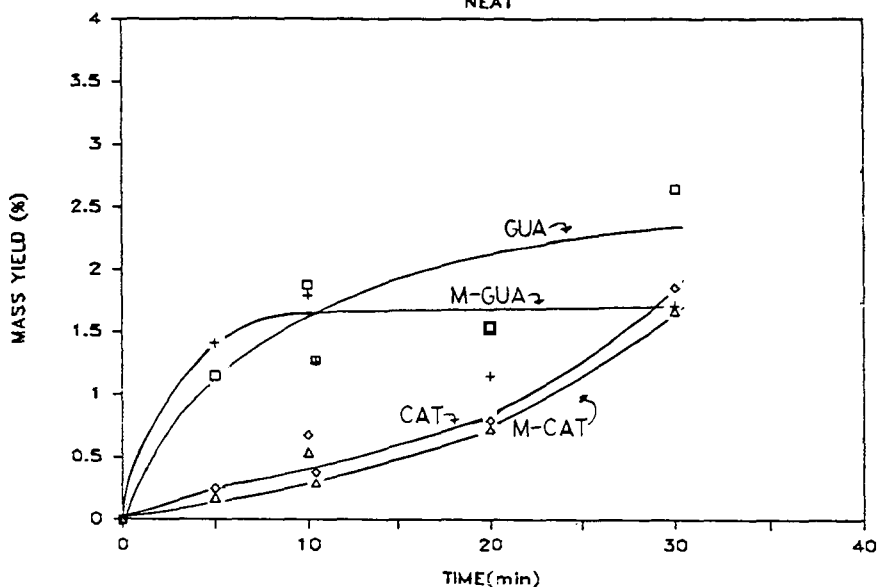
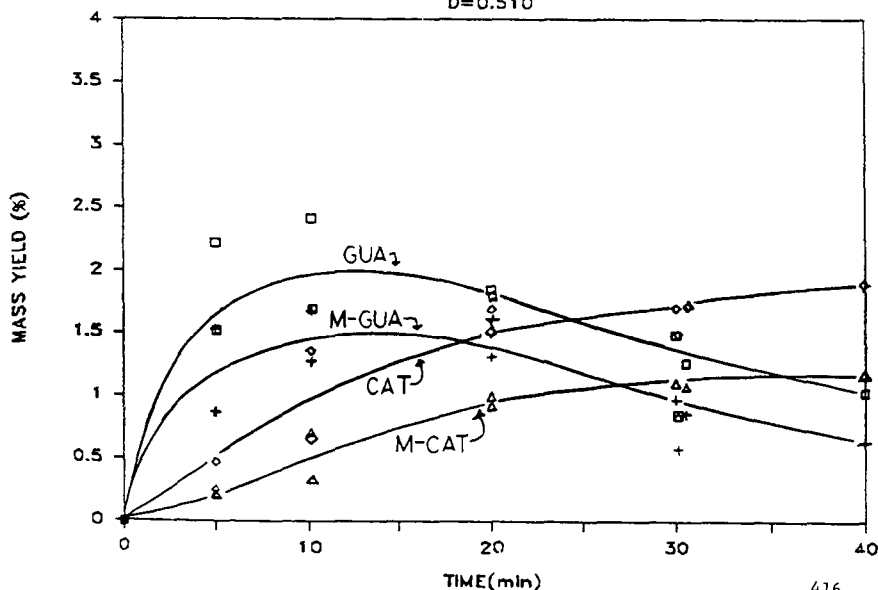


Figure 6. Temporal variations of the yields of the major single-ring products of kraft lignin pyrolysis a) neat b) with water.

b) KRAFT LIGNIN PYROLYSIS 383°C  
D=0.510



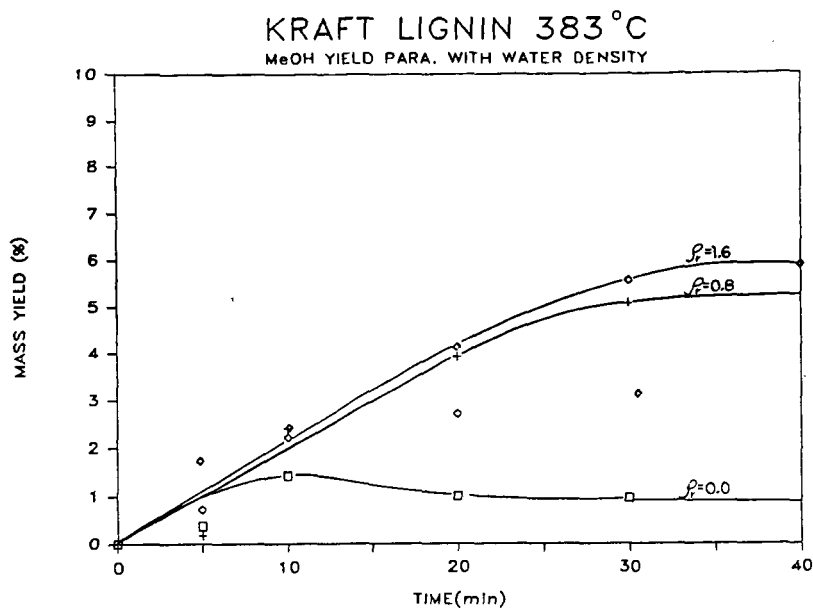


Figure 7. Temporal variation of methanol yield parametric with reduced water density for kraft lignin.

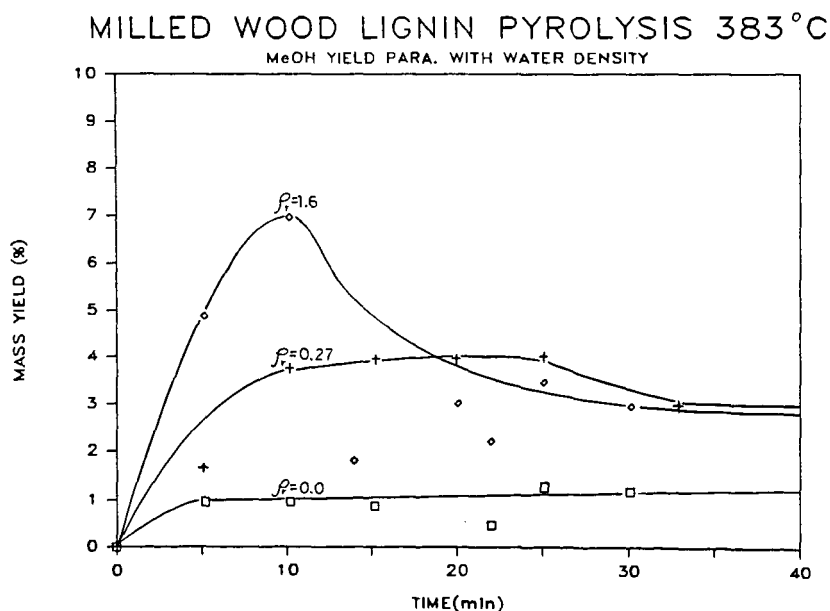


Figure 9. Temporal variation of methanol yield parametric with reduced water density for milled-wood lignin.



a) MILLED WOOD LIGNIN PYROLYSIS 383°C

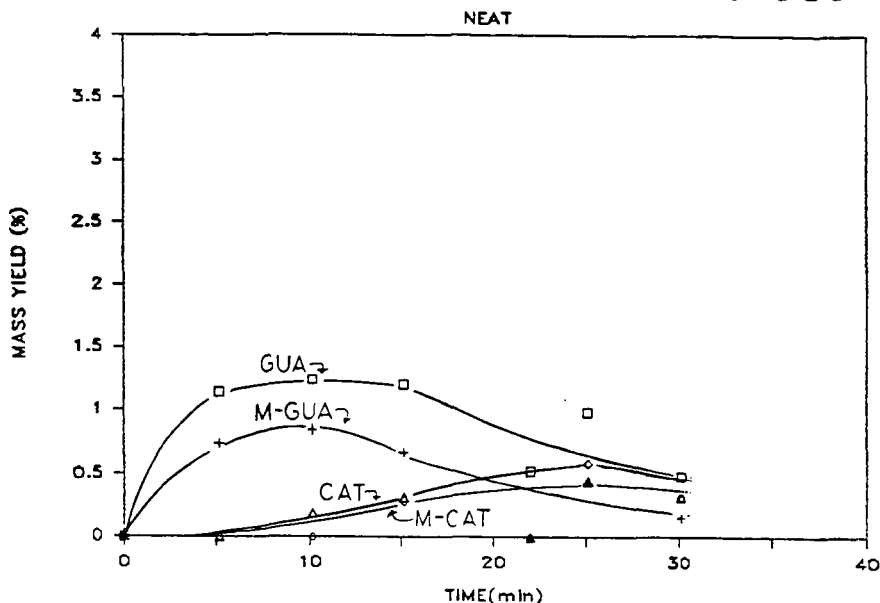
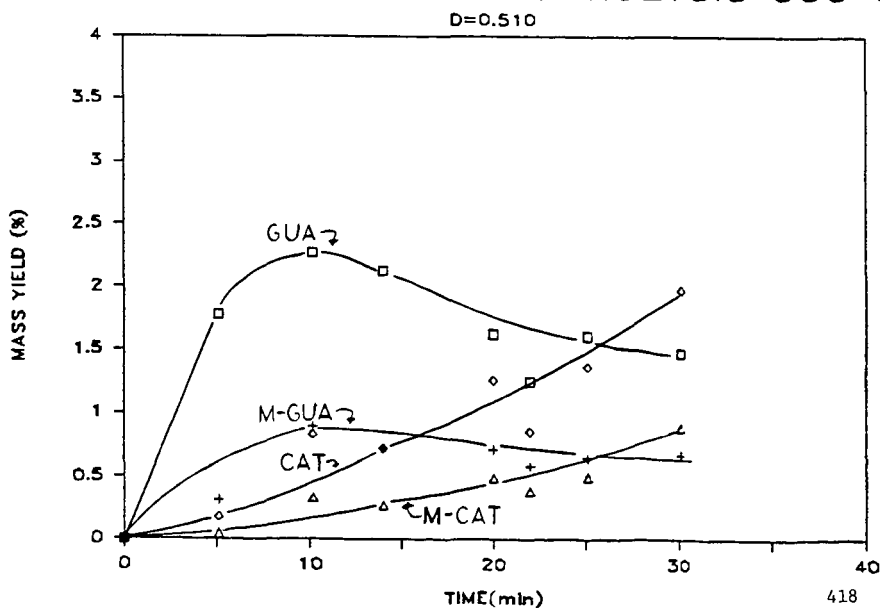


Figure 8. Temporal variations of the yields of major single-ring products of milled-wood lignin pyrolysis a) neat b) with water.

b) MILLED WOOD LIGNIN PYROLYSIS 383°C



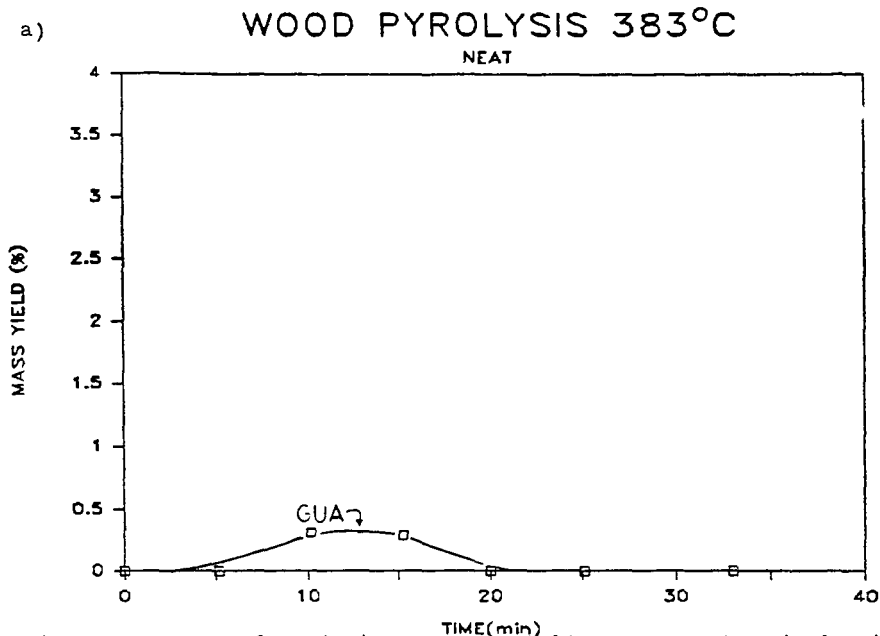
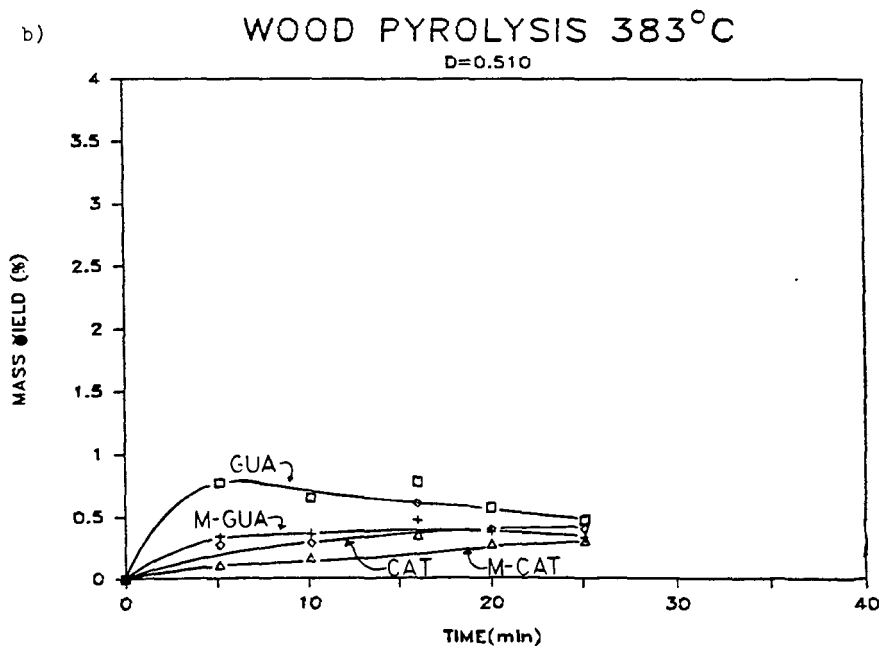


Figure 10. Temporal variations of the yields of the major single-ring products of pine wood pyrolysis a) neat b) with water.



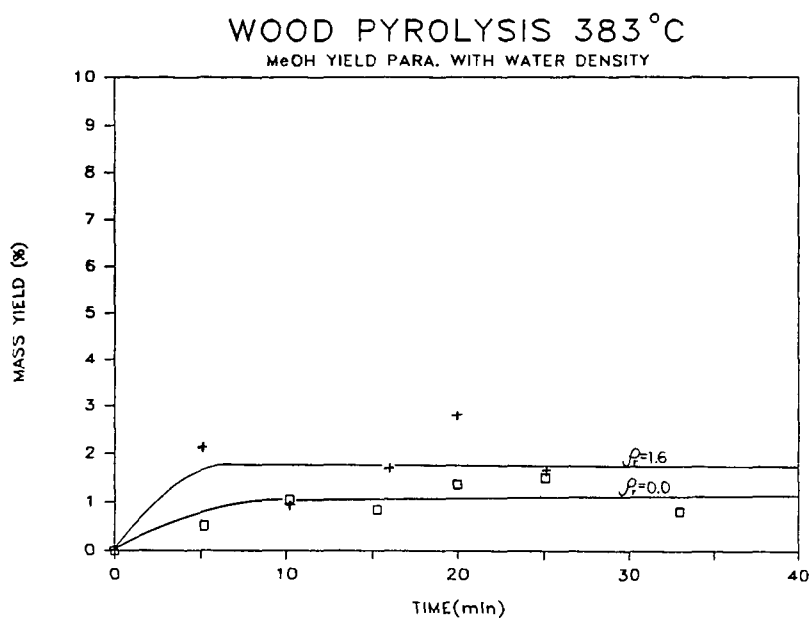


Figure 11. Temporal variation of methanol yield parametric with reduced water density for loblolly pine wood.